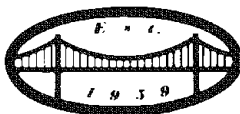


MICROBEAM ANALYSIS

1985

John T. Armstrong, *Editor*

Proceedings of the 20th Annual Conference
of the
Microbeam Analysis Society
Louisville, Kentucky, 5 - 9 August 1985



San Francisco Press, Inc.

Box 6800, San Francisco, CA 94101-6800

Printed in the U.S.A.

PUBLISHER'S NOTICE

Microbeam Analysis Society (MAS) and its publisher, San Francisco Press, Inc., are not responsible for the information and views presented in this volume by the several contributors.

San Francisco Press, Inc., also publishes the Proceedings of the Annual Meeting of the Electron Microscopy Society of America (EMSA), the proceedings of the triennial workshop on Analytical Electron Microscopy (AEM), and the forthcoming Electron Microscopy Safety Handbook. Information on back issues follows. *MAS and EMSA members prepaying by personal check get a 20% discount from the prices listed below.* Overseas orders must be prepaid. California purchasers please add sales tax.

MICROBEAM ANALYSIS

1974, 1975, 1976 (spiral bound)	\$25 each
1977 (full-length papers, Boston meeting)	\$25
1979, 1980, 1981	\$25 each
1982	\$42.50
1983, 1984	\$30
1985	\$40

EMSA PROCEEDINGS

1983, 1984, 1985	\$45 each
------------------	-----------

ANALYTICAL ELECTRON MICROSCOPY

1981	\$25
1984	\$40

Table of Contents*

	Page
Officers of the Microbeam Analysis Society	vii
Sustaining Members' Information	ix
1. LIGHT-ELEMENT ANALYSIS	
Bastin, Heijligers, Quantitative electron-probe microanalysis of very light elements.	1
2. RAMAN AND IR MICROANALYSIS	
Dodd, DeNoyer, Deconvolution of spectra	7
Barbillat, Dhamelincourt, Delhay, Da Silva, Roussel, Nondestructive microprobing by means of a new generation of instruments for Raman and fluorescence spectroscopy.	15
Grayzel, LeClerq, Adar, Hutt, Diem, An automated micro/macro Raman spectrograph system with multichannel and single-channel detectors in a new molecular/crystalline microprobe.	19
Pasteris, Seitz, Wopenka, Compositional interpretation of synthetic C-O-H fluid inclusions by micro-Raman analysis and microthermometry	25
Fisanick, Spatially localized transient spectroscopy as a probe of laser-initiated microchemistry in thin films.	29
Andersen, Delly, Single crystal polarized Raman spectroscopy of microscopically oriented crystalline quartz fragments	33
Adar, Noether, Raman microprobe spectra of spin-oriented and drawn filaments of polyethylene terephthalate: Conformation, orientation, and crystallization.	41
Harvey, Butler, Applications of Raman microprobe spectroscopy in organometallic chemistry	49
Adar, Campbell, Fauchet, Raman microprobe study of changes induced by a pulsed laser.	53
Purcell, Heidersbach, The use of the Raman microprobe for failure analysis of oil field drill pipe.	57
Etz, Newbury, Dunn, Grice, Application of synergistic microanalysis techniques to the study of a possible new mineral-containing light elements	60
Alvarez, Doyle, Deason, Development of a luminescence microprobe.	65
Mehicic, Hazle, Barbour, Grasselli, Some analytical applications of micro IR and micro Raman spectroscopy.	68
Doyle, Alvarez, Microluminescence spectra of Ti-activated $ZrO_2O_2-Y_2O_3$	71
Andersen, Vander Wood, Muggli, Analysis of microzoning in diamond	75
3. QUANTITATIVE X-RAY MICROANALYSIS	
Heinrich, A simple accurate absorption model.	79
Love, Scott, Sewell, Evaluation of recent and improved correction procedures for EPMA	82
Abe, Murata, Cvikevich, Kuptsis, The choice of inner-shell electron ionization cross section in quantitative electron beam analysis.	85
Love, Scott, Analyzing ultra-light elements in the electron microprobe.	93
Packwood, Sastri, Brown, Surface quantification in the electron microprobe.	97
Myklebust, Marinenko, Newbury, Bright, Quantitative calculations for compositional mapping techniques in electron-probe microanalysis.	101
Pouchou, Pichoir, "PAP" $\phi(\rho z)$ procedure for improved quantitative microanalysis	104
Short, Helmold, The effect of imperfect focusing on x-ray intensities in the electron microprobe.	107
4. BIOLOGICAL MICROANALYSIS	
Ingram, Ingram, Evidence for cell volume regulation in rat skeletal muscle.	109
Walsh, Tormey, Electrolyte shifts in the ischemic heart	113
Wheeler-Clark, Tormey, Redistribution of subcellular electrolytes accompanying the increased myocardial contractility produced by low Na	116
Hagler, Buja, Cryosectioning and x-ray microanalysis of cultured myocytes for studies of cell injury.	119
Saubermann, Heyman, Material properties of biological tissue: Implications for cryosectioning.	121

*An Author Index appears on pp. 381-382.

	<i>Page</i>
Brenna, Bernius, Morrison, A cryostage for ultra-low temperature oxygen plasma ashing of frozen tissue samples.	123
Chandra, Morrison, Chiovetti, Correlative ion and electron microscopy of biological soft tissue embedded in low-temperature resins.	125
Myers, Warner, A routine procedure for monitoring sample mass during microanalysis.	129
 5. COMPUTER-ASSISTED MICROANALYSIS	
Russ, Hare, Measurement of edge-intersecting features in SEM images	133
McMillan, Baughman, Schamber, Experience with multiple-least-squares fitting with derivative references	137
Stewart, Russ, Russ, A passive SEM-microcomputer interface for acquisition of electron images and x-ray maps.	141
Ono, Nielsen, Tagata, Seo, High-speed wide-area analysis by electron probe.	145
Vale, Computerized analysis of electron channeling patterns	148
 6. DIGITAL IMAGE PROCESSING AND IMAGE ANALYSIS	
Steel, Myklebust, Bell, Development of an automated digital image acquisition system for AEM	151
Lee, Walker, McCarthy, Micro imaging: A link between microscopy, image analysis, and image processing.	153
Bright, Steel, STEM calibration by analysis of Hough transformed images of optical grating replicas.	155
Marinenko, Myklebust, Bright, Newbury, Wavelength-dispersive techniques for compositional mapping in electron-probe microanalysis.	159
Bright, Steel, Automated method for analyzing images containing electron diffraction spots	163
 7. MATERIALS ANALYSIS AND FAILURE ANALYSIS	
Friel, Analysis of atmospheric corrosion products on metallic coatings.	167
Roeder, Notis, Electron microprobe determination of phase equilibria in the Cu-As-Sn system	170
Follstaedt, Romig, Metastable phase formation in Ni-implanted Al: An analytical electron microscope investigation	173
Cieslak, Romig, Headley, Weld metal hot-cracking of hastelloy alloys C-22 and C-276: A study by analytical electron microscopy.	179
Hellmann, Sorsenson, Carr, Headley, Surface crystallization on metallized 94% alumina ceramics.	189
Davis, Laskowski, Materials analysis of fiberglass-reinforced plastics by scanning electron microscopy	193
Bohning, Microprobe examination of nitrogen and/or oxygen contamination in titanium alloys.	197
 8. GEOLOGICAL AND ENERGY APPLICATIONS	
Calvo, Guilemany, Gómez, SEM morphologies revealed by attack of the structure of Entredicho ore (Ciudad Real, Spain)	199
 9. ADVANCED IMAGING TECHNIQUES	
Newbury, Compositional mapping of thick specimens	204
Levi-Setti, Crow, Wang, High-resolution topographic and isotopic imaging with a 40keV Ga ⁺ scanning ion microprobe	209
Fiori, Leapman, Gorlen, Computer-aided compositional mapping in scanning electron column devices.	219
Hanson, Jones, Gordon, Pounds, Rivers, Schidlovsky, Mapping of trace elements with photon microprobes: X-ray fluorescence with focused synchrotron radiation	227
 10. ENERGY-DISPERSIVE X-RAY ANALYSIS	
Statham, Statistics and wishful thinking in microbeam and image analysis.	230

11. ACCELERATION-BASED MICROSCOPY AND MICROANALYSIS TECHNIQUES

- Benjamin, Rogers, Duffy, Conner, Maggiore, Tesmer, Development and application of the Los Alamos nuclear microprobe: Hardware, software, and calibration. 235
- Fine, Stolper, Mendenhall, Livi, Tombrello, Measurement of the carbon content of silicate glasses by use of the $^{12}\text{C}(\text{d},\text{p}_0)^{13}\text{C}$ reaction 241

12. SURFACE MICROANALYSIS--AUGER ELECTRON SPECTROSCOPY

- Was, Martin, Grain boundary analysis techniques for ductile nickel-base alloys. 246
- Church, McGuire, Recent advances in surface analysis using Auger and x-ray photoelectron spectroscopy 253

13. MICROBEAM ANALYSIS TECHNIQUES IN THE STUDY OF LUNAR, METEORITE, AND COSMIC DUST SAMPLES

- Albee, Microbeam techniques in the study of lunar rocks 255
- Goldstein, Williams, Reuter, Analytical electron microscopy and microbeam analysis of metallic phases in extraterrestrial materials 259
- Grossman, Origins of Ca-, Al-rich inclusions in the Allende meteorite 266
- Brownlee, Electron microbeam analysis of cosmic dust. 269
- Armstrong, Hutcheon, Isotopic analyses of extraterrestrial materials with the ion microprobe. 273
- Nagahara, Matrices of chondrites as the records of pre-solar and early-solar system . . 282
- Jones, Benjamin, Maggiore, Rogers, Duffy, Hollander, Conner, Proton microprobe analysis of maskelynite in the Zagami meteorite. 285
- Clark, Moore, Lewis, Penwell: Unusual meteoritic material 287
- Mackinnon, Rietmeijer, McKay, Zolensky, Microbeam analyses of stratospheric particles . 291

14. MICROANALYSIS MASS SPECTROMETRY--LASER AND ION MICROPROBES

- Mauney, Quantitative laser microprobe mass spectrometry: Potential and constraints. . . 299
- Dennemont, Landry, Mass spectrometric identification of inorganic substances by laser microprobe mass analysis. 305
- Southon, Harris, Kohler, Mullock, Wallach, Quantification and applications of laser-probe microanalysis 310
- Dingle, Griffiths, Examples of quantification in laser ionization mass analyses 315
- Fletcher, Simons, A comparison of two transient recorders for use with the laser microprobe mass analyzer. 319
- Radicati di Brozolo, Odom, Isotopic measurements with a reflection-geometry laser ionization mass spectrometer (LIMS) 322
- Anderson, Heinen, Ramsey, LAMMA/LIMA: A method of controlling the laser power at the specimen for mild fragmentation of organic molecules. 325
- Schmidt, Hagen, Leusmann, Laser microprobe mass analysis of carbonate in apatite of biological concretions. 331
- Musselman, Linton, Simons, The use of laser microprobe mass analysis for nickel speciation in individual particles of micrometer size 337

15. DETECTORS AND INSTRUMENTATION DEVELOPMENTS

- Joy, Si(Li) detectors, dead layers, and incomplete charge 342

16. ANALYTICAL ELECTRON MICROSCOPY--EELS

- Spence, Titchmarsh, Long, Coherent bremsstrahlung--new peaks in EDS: A new unavoidable artifact in thin-crystal x-ray microanalysis. 349
- Statham, Wood, A short study of k-factors for microanalysis of thin films 354
- Klein, Ayer, Williams, Comparison of methods for quantitative thin-film x-ray microanalysis from strongly overlapping peaks. 357

- APPENDIX. Romig, Humphreys, Goldstein, Notis, Solid-state diffusion as measured by microbeam analytical techniques: A comprehensive bibliography 361

- AUTHOR INDEX. 381

Officers of the Microbeam Analysis Society (1985)

MAS Executive Council

President: Dale E. Newbury, National Bureau of Standards, Gaithersburg, Md.
President-Elect: Gordon Cleaver, General Electric Co., Vallecitos Nuclear Center, Pleasanton, Calif.
Past President: David D. Joy, Bell Laboratories, Murray Hill, N.J.
Treasurer: A. D. Romig Jr., Sandia National Laboratories, Albuquerque, N.M.
Secretary: Charles E. Fiori, National Institutes of Health,
Bldg. 13, Rm. 3W13, Bethesda, MD 20205
(301) 496-2599

Directors

John T. Armstrong, California Institute of Technology, Pasadena, Calif.
William F. Chambers, Sandia National Laboratories, Albuquerque, N.M.
Joseph H. Doyle, Rockwell International, Golden, Colo.
Ronald R. Warner, Procter and Gamble Co., Cincinnati, Ohio
Ron Gooley, Los Alamos Scientific Laboratory, Los Alamos, N.M.
David B. Williams, Lehigh University, Bethlehem, Pa.

Honorary Members

L. S. Birks, Naval Research Laboratory, USA
I. B. Borovskii, Academy of Sciences, USSR
Raymond Castaing, University of Paris (Orsay), France
V. E. Cosslett, University of Cambridge, Great Britain
Peter Duncumb, Tube Investments Research Laboratories, Great Britain
K. F. J. Heinrich, National Bureau of Standards, USA
Gunji Shinoda, Osaka University, Japan

Sustaining Members' Information

AMRAY INC.

160 Middlesex Turnpike
Bedord, MA 01730

Contact: Greg Cameron, (617) 275-1400

Product Line: Largest manufacturer of scanning electron microscopes and accessories in the United States.

Sales Offices:

Mark Reynolds, Ohio, (216) 579-0035
George Bruno, New York, (617) 275-8310
Don Pollock, New England, (617) 275-8310
Ken Benoit, New Jersey, (609) 662-3922
William Wehling, Texas, (214) 247-3542
Ken Lindberg Jr., North Carolina, (609) 748-1300
Gerald O'Loughlin, California, (408) 748-1300
Fred Feuerstein, Wisconsin, (312) 695-6117

BAUSCH & LOMB INC.

2930 Baseline Road
Nepean, Ont., Canada K2H 8T5

Contact: Bryce Hanna, (613) 830-9437

Product Line: Scanning electron microscopes and systems for the nondestructive inspection and precision critical-dimension measurement of semiconductors.

Sales Offices:

Western Region, Box 129, Sunland, CA 91040, (213) 352-6011
Central Region, 850 E. Arapaho Rd., Richardson, TX 75081, (214) 238-9264
Eastern Region, 2930 Baseline Rod., Nepean, Ont., Canada K2H 8T5, (613) 820-9437

CAMBRIDGE INSTRUMENTS INC.

40 Robert Pitt Drive
Monsey, NY 10952

Contact: Peter W. Boutell, (914) 356-3331

Product Line: Research scanning electron microscopes and accessories, research production beam microfabrication system, image analysis.

Duane Bellingham, Box 637, Williamstown, MA 01267, (413) 458-5232
Roger Attle, 40 Robert Pitt Drive, Monsey, NY 10952, (914) 356-3331
Mike Webber, 3945 Fairington Drive, Marietta, GA 30066, (404) 926-9636
Richard Russell, 3105 Ira Road, Box 2626, Bath, OH 44210, (216) 666-5331
John Pong, 26011 Falbrook, El Toro, CA 92630, (714) 380-9597
Barbara Stanton, 2840 San Tomas Expressway, #106, Santa Clara, CA 95051, (408) 970-9292
Blaise Fleischmann, 6436 Barnaby Street N.W., Washington, DC 20015 (202) 362-4131
John Wotkyns, 625 Scott Street, #504, San Francisco, CA 94117, (415) 922-8652
Richard Feller, 415 Kewnilworth Avenue, Glen Ellyn, IL 60137, (312) 858-2332

CAMECA INSTRUMENTS INC.

2001 West Main Street
Stamford, CT 06902-4583

Contact: Tom Fisher, (203) 348-5252

Product Line: CAMEBAX-SX series scanning electron probe x-ray microanalyzers. A new series of fully automated high technology electron microprobes. IMS-3F high-resolution secondary ion microanalyzer (SIMS).

Sales Offices:

East: Tom Fisher, Springfield, MA, (413) 734-0617
West: Rob Johnson, San Francisco, CA, (415)

DAPPLE SYSTEMS

355 West Olive, Suite 100
Sunnyvale, CA 94086

Contact: Bill Stewart, (408) 733-3283

Product Line: Microcomputer-based analytical instrumentation including image measurement and processing systems and energy dispersive x-ray analysis.

Sales Offices:

Northeastern Analytical, 17 Sherman Rd., Millis, MA 02054, (617) 376-4132
International Inst., 34 Pine Cone Ct., Vincentown, NJ 08088, (609) 268-8044
Tom Baum Analytical Inst., RR #2, Box 226, Kaufman, TX 75142, (214) 452-3116
The Buhrke Co., 1500 Old Country Rd., Belmont, CA 94002, (415) 592-2904

EDAX INTERNATIONAL INC.

Box 135
Prairie View, IL 60069

Contact: A. O. Sandborg, (312) 634-0600

Product Line: Manufactures energy-dispersive x-ray analysis systems for x-ray microanalysis in SEMs, TEMs, and electron probes; energy-dispersive x-ray fluorescence spectrometers. System configurations from basic qualitative to fully automated quantitative (with computer control and data processing) are available, including an automated WD/ED system with stage and spectrometer controls.

Sales Offices:

V. Balmer, Vermilion, OH, (216) 967-4148
E. Martin, New Rochelle, NY, (914) 576-3117
D. Jimenez, San Ramon, CA, (415) 837-2481
R. Wilson, Prairie View, IL, (312) 634-0600
F. Gibson, Spring, TX, (713) 350-8654

EG&G ORTEC

100 Midland Road
Oak Ridge, TN 37830

Contact: Charles A. Thomas, (615) 482-4411, Ext. 131

Product Line: Energy-dispersive systems for electron optical microscopes of all types. Image analysis systems.

Sales Offices:

Pete Osborn, 16220 Frederick Rd., Suite 404, Gaithersburg, MD 20877, (301) 670-0997
Karen Robbins, 100 Midland Rd., Oak Ridge, TN 37830, (615) 482-4411
Ron Walker, 340 Melvin Dr., Northbrook, IL 60062, (312) 498-5858
Alan Welco, 23342 South Pointe Dr., Laguna Hills, CA 92653, (714) 770-6222

GATAN, INCORPORATED

780 Commonwealth Drive
Warrendale, PA 15086

Contact: Kevin Scudder, (412) 776-5260

Product Line: Specializes in equipment for electron microscopy: electron energy loss spectrometer (EELS); ion beam milling equipment; image intensifier system; analytical stages of beryllium construction; general EM specimen preparation equipment; scanning electron microscopes and freeze fracture equipment.

Sales Office:

Dana Clough, 6678 Owens Dr., Pleasanton, CA 94566, (415) 463-0200

HITACHI SCIENTIFIC INSTRUMENTS
NISSEI SANGYO AMERICA, LTD.

460 E. Middlefield Road
Mountain View, CA 94043

Contact: Hideo Naito, (415) 961-0461

Product Line: Transmission and scanning electron microscopes.

Sales Offices:

Ron Lunn, Tokone, Lakeville, CT 06039, (617) 756-5331
Alan Sandler, 321 Winding Way, Glenside, PA 19038, (215) 925-2683
Morton Harloe, 1701 Golf Rd., Suite 401, Rolling Meadows, IL 60008, (312) 981-8750
Michael Mullen, 2909 Oregon Ct., Unit B-3, Torrance, CA 90503, (213) 328-9700

INTERNATIONAL SCIENTIFIC INSTRUMENTS, INC.

1457 McCarthy Blvd.
Milpitas, CA 95035

Contact: Robert Ruscica, (408) 945-2233

Product Line: A complete line of scanning electron microscopes from inexpensive systems to research-grade high-resolution DS-130 model. Available with a full complement of accessories including x-ray system, image enhancement, electron beam wafer probing, and much more.

Sales Offices:

William Maguire, Avon Park South, 20 Tower Lane, Bldg. 2, Avon, CT 06001, (203) 677-0016

JEOL U.S.A., INC.

11 Dearborn Road
Peabody MA 01960

Contact: Robert Santorelli, (617) 535-5900

Product Line: Manufacturers and dealers of scanning electron microscopes, transmission electron microscopes, scanning transmission electron microscopes, electron probe micro-analyzers, scanning Auger microprobes, energy loss analyzers, and electron beam writing equipment.

Sales Offices:

John Bonnici, American Office Mall, 275 Route #18, East Brunswick, NJ 08816, (201) 254-5600
Thayer Brickman, 1633 Bayshore Highway, Suite 245, Burlingame, CA 94010, (415) 697-9232
Jack Francis, 1402 Rambling Hills Dr., Cincinnati, OH 45230, (513) 232-7350
Ray Gundersdorff, 6236 Gilston Park Rd., Catonsville, MD 21228, (301) 953-2959
Richard Lois, 1 Kingwood Place, Suite 122B, 600 Rockmead Dr., Kingwood, TX 77339 (713) 358-2121
Lewis McDonald, 3223 G Post Woods Dr., Atlanta, GA 30339, (404) 434-9724
Jean-Pierre Slakmon, Soquelec Ltd., 5757 Cavendish Blvd., Suite 101, Montreal, Quebec, Canada H4W 2W8, (514) 482-6427
Robert Steiner, 640 Pearson St., Suite 102, Des Plaines, IL 60016, (312) 825-7164

KEVEX CORPORATION

1101 Chess Drive
Foster City, CA 94404

Contact: Drew Isaacs, (415) 573-5866

Product Line: Materials analysis systems for qualitative and quantitative x-ray and image analysis. Product line includes instrumentation for x-ray energy-dispersive analysis, wavelength-dispersive analysis, Auger and electron energy loss spectrometry, and digital image acquisition and feature analysis. X-ray detectors and digital beam control available for most models of microprobe, SEM, TEM and STEM.

Sales Offices:

9989 Windsor Way, San Ramon, CA 94583, (415) 828-2188
2119 Edsel Avenue, Los Angeles, CA 90066, (213) 306-1033
6417 Glenmoor Avenue, Garland, TX 75043, (214) 226-0182
19635 Cottonwood Trail, Strongsville, OH 44136, (216) 238-8666
8912 N. Skokie Blvd., Suite 2N, Skokie, IL 60077, (312) 676-9313
56 Slater Road, Glastonbury, CT 06033, (203) 633-3102
16 Barberry Hill Road, Gainesville, GA 30506, (404) 887-9965
Box 200, Mercer Island, WA 98040, (206) 232-3444
4536 Stuart Street, Denver, CO 80212

KRISEL CONTROL, INC.

16 Farsta Court
Rockville, MD 20850

Contact: Christos Hadidiacos, (301) 762-1790

Product Line: Automation equipment for electron microprobe/microscope, featuring on-line data acquisition and reduction with Alpha and ZAF correction schemes. Single-crystal automation system for on-line data collection, centering, calculation of orientation matrix, and refinement of cell parameters for an x-ray diffractometer.

LINK ANALYTICAL

3290 W. Bayshore Road
P.O. Box 50910
Palo Alto, CA 94303

Contact: Frank Brown, (415) 856-2726

Product Line: Energy-dispersive microanalysis systems for SEM image processing, Auger and energy loss data handling, and ED/WD automation systems. X-ray fluorescence microanalysis systems.

Sales Offices:

The Buhrke Company, 1500 Old County Rd., Belmont, CA 94002, (415) 592-20-4
Int'l Instrument Corp. 34 Pine Cone Court, Vincentown, NJ 08088, (609) 268-8044
Pulcir, Inc., 9209 Oak Ridge Highway, Oak Ridge, TN 37830, (615) 483-6458
ASI, Inc., 6429 Corporate Drive, Houston, TX 77036, (713) 270-6546
NE Analytical Corp., 17 Sherman Rd., Millis, MA 02054, (617) 376-4123
Contemporary Science, Inc., Box 205, Mt. Prospect, IL 60056, (312) 255-3793

WALTER C. McCRONE ASSOCIATES, INC.

2820 South Michigan Avenue
Chicago, IL 60616

Contact: John Gavrilovic, (312) 842-7100

Product Line: Analytical and consulting services--ultramicroanalysis, small-particle analysis, light microscopy, analytical electron microscopy, scanning electron microscopy, electron microprobe analysis, secondary ion mass spectrometry, micro x-ray diffraction, organic microanalysis for small particles and subnanogram samples. Failure analysis on solid-state devices, bond failures, corrosion problems, thin-film analysis. Microscopy supplies and accessories--microscope sales (Olympus microscope dealer), light microscopy supplies. Asbestos consulting and testing--analysis of suspect materials for asbestos by light microscopy and/or electron microscopy; building surveys, air sampling, monitoring during abatement projects.

Sales Offices:

Ian M. Stewart/Bonnie L. Betty, McCrone Accessories and Components, 2508 S. Michigan Avenue, Chicago, IL 60616, (312) 842-7100
Richard L. Hatfield, McCrone Environmental Services, 5500 Oakbrook Parkway, Suite 200, Norcross, GA 30093, (404) 449-8474 or 8461

MICRON, INC.

3815 Lancaster Pike
Wilmington, DE 19807

Contact: James F. Ficca Jr., (302) 998-1184

Product Line: Scanning electron microscopy, electron spectroscopy, electron probe x-ray analysis, transmission electron microscopy, quantitative image analysis, x-ray diffraction, x-ray fluorescence, optical microscopy and metallography, microhardness, optical emission spectroscopy, differential scanning calorimetry, ultra microtomy, sample preparation.

MICROSPEC CORPORATION

45950 Hotchkiss Street
Fremont, CA 94539

Contact: Joseph Carr, (415) 656-8820

Product Line: WDX-2A wavelength-dispersive x-ray spectrometer systems. X-ray microanalysis systems for use as accessories on scanning electron microscopes and other electron beam instruments. Capable of x-ray analysis of all elements down to beryllium, atomic number 4. Unique design permits attachment to most SEM electron columns.

PERKIN-ELMER

PHYSICAL ELECTRONICS DIVISION

6509 Flying Cloud Drive
Eden Prairie, MN 55344

Contact: Eric Peterson, (612) 828-6300

Product Line: PHI manufactures a full line of analytical instruments for surface and thin film analysis, including Auger, x-ray photoelectron, and secondary ion mass spectroscopies; also molecular beam epitaxy systems for research and production applications. PHI offers contract services for all of these techniques.

Sales Offices:

5600 W. Maple Rd., Suite C-303, W. Bloomfield, MI 48033, (313) 626-8008
5 Progress St., Edison, NJ, (201) 561-6530
1011 S. Sherman St., Richardson, TX, (214) 669-4400
2 Taunton St., Plainville, MA, (617) 695-7181
151 Bernal Rd., San Jose, CA, (408) 629-4343
7310 Ritchie Hwy., Glen Burnie, MD, (301) 761-3053
655 Deep Valley Dr., Rolling Hills, CA (213) 377-7750
1382 Old Freeport Rd., Pittsburgh, PA, (412) 963-6717
6509 Flying Cloud Dr., Eden Prairie, MN, (612) 828-6332
1790 30th St., Boulder, CO 80301, (303) 449-4573
Also: Canada, Hong Kong, Japan, and West Germany

PHILIPS ELECTRONIC INSTRUMENTS, INC.

85 McKee Drive
Mahwah, NJ 07430

Contact: John S. Fahy, (201) 529-3800

Product Line: Transmission analytical electron microscopes, scanning analytical electron microscopes, and analytical accessories for electron microscopes.

Sales Offices:

A. Hugo, 55 Virginia Ave., West Nyack, NY 10994
D. Ahr, 6231 Executive Blvd., Rockville, MD 20852
H. Ittner, 155 N.E. 100th St., Suite 403, Seattle, WA 98125
T. Bates, 7094 Peachtree Industrial Blvd., Suite 220, Norcross, GA 30071
B. Smick, Suite D45, 2525 East Oakton, Arlington Heights, IL 60005
Ms. Jo Long, 7302 Harwin Dr., Suite 106, Houston, TX 77036
S. Spiers, 3000 Scott Blvd., Suite 113, Santa Clara, CA 95050

POLAROID CORPORATION

549 Technology Square
Cambridge, MA 02139

Contact: Carl Schultz, (800) 225-1618

Product Line: Photographic films and cameras of many kinds. Batteries, chemicals, and optics.

Sales Offices:

Atlanta, (404) 346-1717
Cleveland, (216) 433-4884
Dallas, (214) 258-8100
Oakbrook, IL, (312) 654-5200
Paramas, NJ, (201) 265-6900
Santa Ana, CA, (714) 641-1200

PRINCETON GAMMA-TECH, INC.

1200 State Road
Princeton, NJ 08540

Contact: Peter Quigley, (609) 924-7310

Product Line: Manufactures analytical systems for comprehensive microanalysis: energy-dispersive x-ray detectors for all electron microscopes (SEMS, STEMS, TEMS), complete EDS x-ray analysis software, EELS data collection and processing, high resolution digital imaging (ImageCraftTM) from electron or light microscopes which includes image collection and processing, quantitative size/shape measurement software, and unique image comparison capabilities.

Sales Offices:

Scientific Systems Sales Corp., 333 Jericho Turnpike, Jericho, NJ 11753, (516) 822-4880
Don Bishop, 1217 Hampton Lane, Mundelein, IL 60060, (312) 680-8316
Tom Griffin, 701 Morewood Parkway, Rocky River, OH 44116, (216) 331-0120
J. Walter Binns, 1200 State Road, Princeton, NJ 08540, (609) 924-7310
Darlene Zimmerman, 1129 Melrose Drive, Richardson, TX 75080, (214) 644-9419
Richard Stancher, 2206 Broadlawn Ave., Houston, TX 77058, (713) 480-5184
Denny Cannon, Box 36157, Denver, CO 80236, (303) 978-0786
Jake Brown, 568 Weddell Drive, Suite 1, Sunnyvale, CA 94089, (408) 734-8124
Geoffrey Grace, Box 24209, Denver, CO 80222, (303) 329-8554

SPI SUPPLIES

DIVISION OF STRUCTURE PROBE, INC.

535 E. Gay Street
Box 656
West Chester, PA 19380

Contact: Charles A. Garber, (215) 436-5400

Product Line: SPI Supplies: Small instruments and consumable supplies for electron microprobe and electron microscope laboratories including sputter coaters, table-top vacuum evaporators, and microprobe standards. Structure Probe: Independent laboratory providing SEM/EDS, TEM, probe, Auger, XPS, XRD, and other services for industry and government. Member of American Council of Independent Laboratories; accredited by American Association for Laboratory Accreditation.

Laboratories:

230 Forrest St., Metuchen, NJ 08840, (201-549-9350
63 Unquowa Rd., Fairfield, CT 06430, (203) 254-000
1015 Merrick Rd., Copiague, L.I., NY, (516) 789-0100

Sales Office:

SPI Supplies/Canada, Box 44, Station S, Toronto, Ont., Canada MSM 4L6

C. M. TAYLOR CORPORATION

289 Leota Avenue
Sunnyvale, CA 94086

Contact: Dr. Charles M. Taylor, (408) 245-4229

Product Line: Various types of multi-element standards for microbeam analysis by SEM, microprobe, and ion probe using energy, wavelength, and mass spectrometers. The standards available exceed 175 different metals, alloys, glasses, compounds, or minerals. Bence-Albee standards are available. Also manufacture many types of sample holders, polishing jigs, and other types of equipment for sample preparation. Also offers analytical services to customers desiring electron beam microprobe analysis using MAC-5 instrument. Have full ZAF correction capability for microprobe data, using FRAME B or Bence-Albee procedures.

M. E. TAYLOR ENGINEERING INC.

11506 Highview Avenue
Wheaton, MD 20902

Contact: Gene Taylor, (301) 942-3418

Product Line: Scintillators, BSE and SE detectors, unique SEM supplies. SEM contract work, consulting and adhesion testing of coatings through our SEMicro Division.

Sales Offices:

Dave Ballard, SEMicro, 15817 Crabbs Branch Way, Rockville, MD 20855, (301) 330-0077

TRACOR NORTHERN

2551 West Beltline Highway
Middleton, WI 53562

Contact: John Benson, (608) 831-6511

Product Line: Wide range of data-processing instrumentation for qualitative and quantitative x-ray analysis. Products include data acquisition, reduction, and automation for electron microprobe, SEM, TEM, and STEM. Featuring simultaneous EDS/WDS acquisition/reduction, digital beam control allowing for digital mapping, line scans, and other digital image processing. And now particle location, sizing, and elemental characterization. Flexible packaging allows instrument to be used also for ELS, Auger, ESCA, SIMS, etc. Other products are used in nuclear, optical, signal averaging, and medical applications.

Sales Offices:

345 E. Middlefield Rd., Mountain View, CA 94043, (405) 967-0350
3040 Holcomb Bridge Rd., Norcross, GA 30071, (404) 449-4165
134 Franklin Corner Rd., Lawrenceville, NJ 08648, (609) 896-1114

QUANTITATIVE ELECTRON-PROBE MICROANALYSIS OF VERY LIGHT ELEMENTS

G. F. Bastin and H. J. M. Heijligers

Quantitative electron-probe microanalysis of very light elements, such as boron, carbon, nitrogen, or oxygen, brings with it several problems, mostly of a technical nature but also limitations imposed by the physical backgrounds of the technique itself. A major problem is the uncertainty about the performance of the existing matrix correction procedures, which in turn must be attributed to an almost total lack of reliable measurements on which such programs can be tested.

In the past few years considerable efforts have been performed in our laboratory in order to collect a large number of reliable measurements on borides, carbides, and nitrides. In the case of carbon the results have partially been published^{1,2} or submitted for publication; the work on boron has been recently completed; and the measurements on nitrogen were started at the beginning of 1985 and are now in full progress.

It is the objective of the present paper to discuss the various problems that must be expected in light-element analysis. Where possible, solutions to these problems are provided, and the principles and procedures by which accurate intensity measurements should be carried out are discussed. Finally, some results are presented that show that accurate quantitative analysis of light elements is indeed possible, provided that proper care is exercised in the measurements.

Problems in Light-element Analysis

Some of the problems in wavelength-dispersive (WD) analysis of light elements discussed below are not necessarily specific for light elements, as they may also be present in medium- to heavy-element work. They have a tendency to become more pronounced and to become more of a nuisance, due to the rather extreme conditions (e.g., high beam currents, low voltages) one is forced to choose in light-element work.

One of the first problems one has to cope with in light-element analysis is the following.

- Very high demands have to be made on items such as specimen preparation (surface finish, flatness, absence of contaminating agents), correctness of take-off angle, and correctness and stability of probe voltage and current. One has to realize that x-ray generation and emission for these elements is extremely superficial and that in the majority of cases one is almost attempting to perform surface analysis.

As far as the measurements themselves are concerned, the first and quite obvious problem we run into is:

- Low count rates and high backgrounds, in conjunction with a relatively inefficient detection system. Although count rates for boron and carbon can be called quite fair (on elemental standards), the intensities observed for nitrogen are usually desperately low. Nitrogen constitutes, so to speak, almost a "black hole" in WD analysis, since it is right at the top of the absorption edge of carbon and the emerging x-ray beam must pass through a stearate crystal and then through the detector window, both of which contain appreciable amounts of carbon. Efforts to increase the count rate by increasing the beam current may lead to dead-time problems for the metal lines, if these lines have to be measured simultaneously. Resorting to higher orders of reflection can provide a solution.

- Next there is a group of problems that are related to the background determination. As the peak-to-background ratios for light elements are much lower than in the usual work, the correct determination of the background becomes all the more important.

Interference of higher-order metal lines is a well-known nuisance; notorious examples are the metals Cr, Mn, Zr, and Nb in the case of carbon; the elements Ti, Al, and Zr in the case of nitrogen; and Zr, Nb, and Mo in the case of boron. In the last case rather exotic lines like $M\zeta$ -lines show up very close to the $B K\alpha$ peak at very high intensities.

The authors are at the Laboratory for Physical Chemistry, University of Technology, P.O. Box 513, NL-5600 MB Eindhoven, The Netherlands.

The normal solution to interference problems is to apply a rather narrow window in the pulse height analyzer (PHA). However, that may give rise to serious errors in the intensity measurements, due to pulse shifts as a result of the large differences in count rates (easily up to two orders of magnitude) between (elemental) standards and specimens. Figure 1 presents an example of this effect for the B K α pulse. It is evident that an

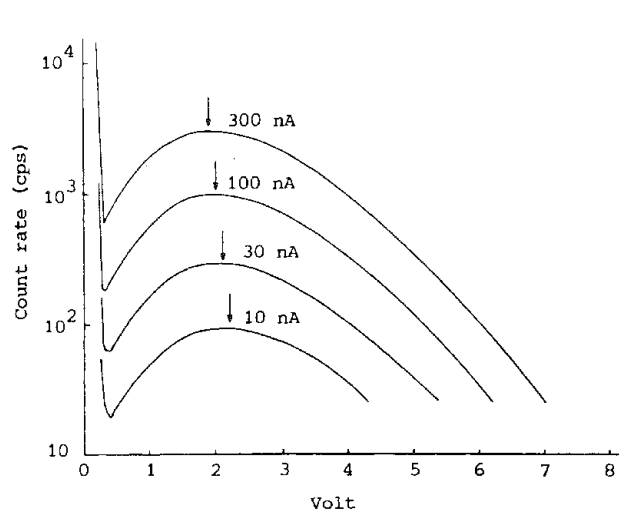


FIG. 1.--Shape of B K α pulse recorded at 10 kV on elemental boron for various probe currents. JEOL Superprobe 733, lead-stearate crystal; gas flow counter (Ar + 10% methane): High tension 1700 V; gain 64×8 , Ortec counting electronics, lower level variable, window 0.2 V.

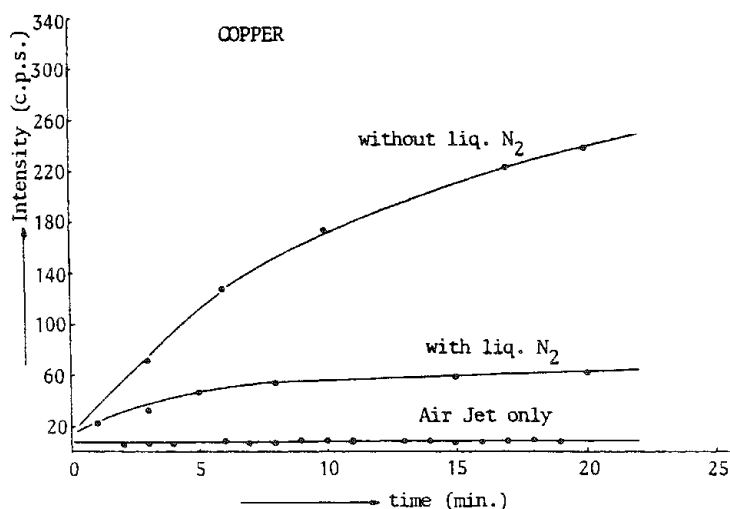


FIG. 2.--Carbon contamination rate on polished copper, without anticontamination device, with cooling finger and with air jet. 10 kV, 100 nA; counter high tension 1700 V; lower level 0.6 V; window 5.0 V; gain 64×5 ; oil-diffusion pumped vacuum system.

increase in count rate by a factor of 3 produces a shift of -0.2 V in the PHA, which can become more than a theoretical problem if a narrow window is applied. Practical solutions to this problem, such as moving the window along with the shift of performing all measurements at the same count rate, are not very attractive. However, one should at least be aware of this effect.

Carbon contamination is a really big problem in the detection of light elements. This effect is of course particularly bad in the analysis of carbon, but it can seriously affect measurements of boron, and certainly nitrogen, as well, and to a certain extent even K-lines of heavier elements. We have conducted a detailed investigation into this effect¹ and found that the best anticontamination device is definitely an air jet. Figure 2 illustrates the perfect functioning of this very cheap device in comparison with the use of a liquid-nitrogen cooling trap. In general it is advisable to use the best possible focus and the highest possible power density in the electron beam in conjunction with the use of the air jet. Even then it is advisable to wait 30-60 s before starting an analysis; the initial carbon count rate is always higher, due to the presence of superficial carbon which has to be burned away first.

The contamination rate can vary appreciably from element to element; it is lowest on B and Si and highest on the transition metals. Probably the thermal conductivity of the specimen plays an important role in this respect. Yet despite all efforts it is not possible to prevent contamination completely. A small but persistent amount of carbon remains and has to be taken into account, especially when low levels of carbon have to be detected.

The effects discussed so far are shown in Fig. 3. A residual carbon peak (at ~ 124 mm) is obviously present on Ti, V, and Fe. We also note the presence of the second-order O K α peak (at 132 mm) on these elements, which shows that oxygen contamination also takes place. The general conclusion from Fig. 3 is that the background for C K α is obviously composed of three parts: a continuous background that may be rather unpredictable,

remnants of higher-order metal lines, and residual contamination. Hence, it is no longer permissible to measure the background on both sides of the peak. A better procedure is probably to measure the backgrounds on the constituent elements at the position of the C K α peak, and to compose them afterward, a procedure similar to the one proposed by Ruste.³

• The choice of a suitable standard can present another problem. In our opinion the use of a complex standard for light-element analysis is strongly advisable, mainly because the anticipated count rates for standard and specimens are closer together, which would rule out problems of pulse shifts. Therefore, in the case of carbon, we have used Fe₃C, which can easily be prepared and has a fixed composition. For the nitrogen measurements, now under way, we chose Cr₂N. Clearly, in this case, an elemental standard is out of the question. Unfortunately, for our boron measurements we were forced to use elemental boron, for reasons that are discussed below.

• After the rather technical problems discussed so far we come to the software problems, which comprise the choice of a suitable matrix correction procedure in conjunction with a consistent set of mass absorption coefficients (MACs). As far as the latter is concerned, it is instructive to realize that for the analysis of carbon, for example, as a rule of thumb, a 1% change in the MAC for C K α can produce a 1% change in the calculated concentration. Hence, the performance of any correction program can at present only be judged in conjunction with the particular set of MACs used. Unfortunately, reported values for C K α radiation may differ up to 50 or 100%.

Concerning the proper functioning of the available programs themselves, one can only say that up to now it could not be tested, simply because of a general lack of reliable data over a sufficiently large range of experimental conditions and a sufficiently large number of specimens.

• So far we have ignored one of the major problems in light-element analysis: How should intensities be measured? Normally in WD analysis we tune at the peak in standard and specimen and determine the peak intensity ratio, under the tacit assumption that the peak intensity is proportional to the integral emitted intensity. Fortunately, that is indeed the case for the vast majority of x-ray lines, but not in light-element analysis. The excitation of a K-line in a light element means that we are exciting the electrons involved in the chemical bond, so that we obtain peak shifts and peak-shape alterations. The former effect is not serious, because we can simply retune the spectrometer; but the latter effect is very serious indeed, as is demonstrated in Fig. 4, where two extreme peak shapes are compared. To facilitate comparison both profiles have been scaled to the same peak intensity. It is immediately obvious that, although the peak intensities are the same (peak intensity ratio equal to 1), the integral intensity from TiC is approximately only half that emitted from glassy carbon (integral or area-intensity ratio equal to 0.5). Hence, it would be completely wrong to compare only peak intensities: TiC would be strongly overrated. The only correct procedure is obviously to measure the intensities in an integral fashion, although this is a rather tedious procedure, especially for nonautomated microprobes.

A considerable reduction in time can be achieved by the introduction of so-called area peak factors^{1,2} (APFs), which are defined as the ratio between the area (integral)

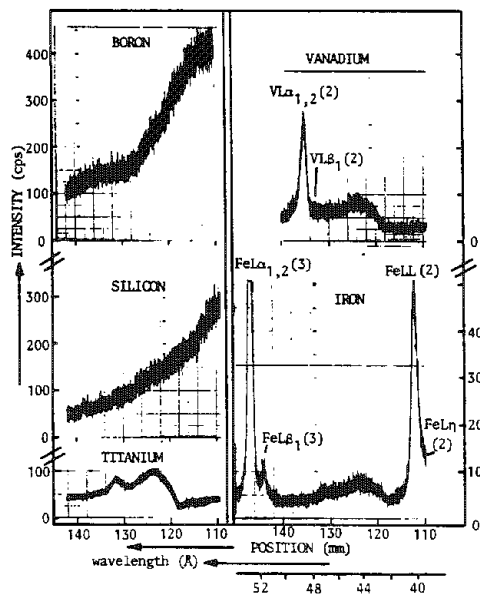


FIG. 3.--Backgrounds recorded in spectral region of C K α peak on various elements; C peak is to be expected at ~ 124 mm. Experimental conditions as in Fig. 2, except beam current 300 nA.

k-ratio and the peak k-ratio for a given binary compound with respect to a given standard and for a given spectrometer. Once such factors are known, future measurements can be simply performed at the peak again and multiplication by the appropriate APF will yield the correct integral intensity ratio. For the example in Fig. 4 it will be clear that the APF has a value of ~ 0.5 .

For many practical purposes the APF can be regarded, apart from a proportionality constant, as the ratio between the width and the height of an emission peak, or even as a kind of weight factor that has to be assigned to a certain peak intensity. An interesting further feature of APFs is that a set measured relative to a certain standard can be easily converted into a new set relative to another standard merely by multiplication of the appropriate factors. A considerable part of the work on light-element analysis has been devoted to the accurate determination of APFs in binary carbides, borides, and (at present) nitrides. The results of this part of the work are discussed next.

Determination of Area/Peak Factors

The experimental procedures used in the measurements were discussed in Refs. 1 and 2 for carbon. The procedures for boron and nitrogen are quite similar and will not be discussed here. The results for carbon were:

1. The APFs in the 13 binary carbides investigated were found to be independent of the accelerating voltage.
2. The individual values (relative to Fe_3C as a standard) were found to vary between ~ 0.7 for strong carbide formers like Ti and Zr, and ~ 1 for B_4C , WC, and W_2C . If glassy carbon had been used as a standard these values would have to be multiplied by 0.7. A plot of APFs vs atomic number of the metal partner showed a conspicuous sawtooth-like appearance, which was synchronous with the beginning and ending of the periods in the periodic system. The immediate consequences of these measurements are that errors of 30-50% (depending on the type of standard) are made if peak shape alterations are ignored. Another consequence would be that one could never hope to get consistent results in certain sequences of carbides, like Ti-, V-, or Cr-carbides, or Zr-, Nb-, or Mo-carbides, if the variations in APFs are not taken into account.

After the work on carbon was completed we hoped that the experience gained so far would permit the work on boron to be accomplished in a fraction of the time, even though we had prepared 28 binary borides. However, a completely new problem arose in addition to those encountered previously.

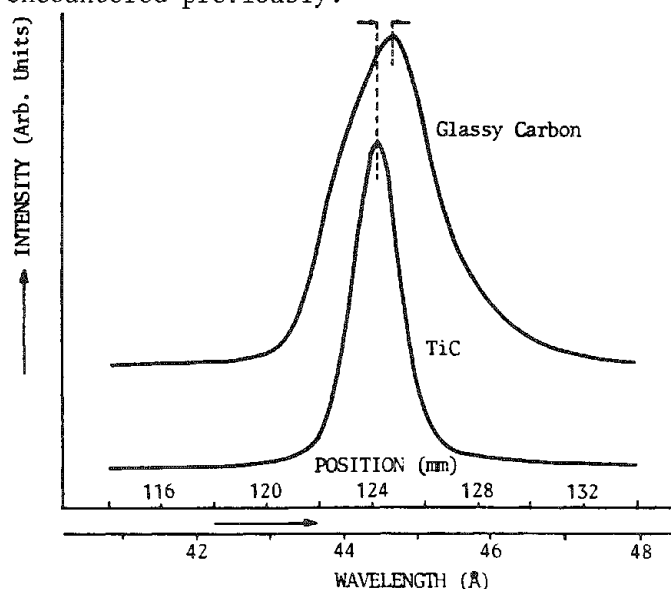


FIG. 4.--Comparison of shapes of C $K\alpha$ peak emitted by TiC and glassy carbon. Both profiles have been scaled to same peak intensity. Experimental conditions as in Fig. 3.

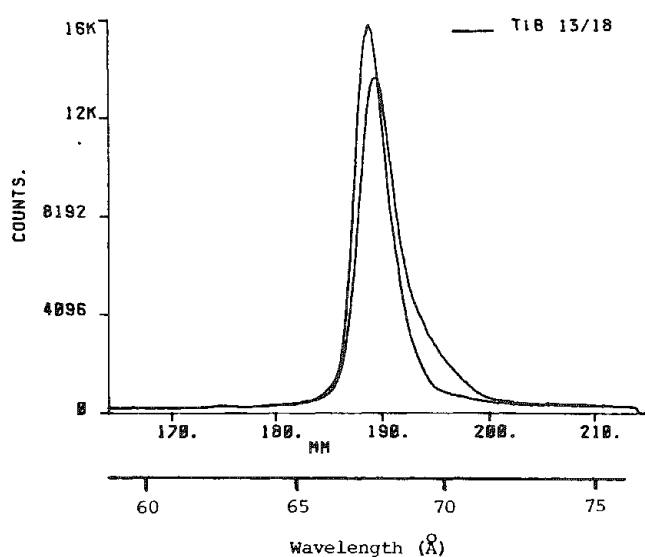


FIG. 5.--Variations that can be observed in shape of B $K\alpha$ peak emitted by various TiB crystals, or upon rotation of same crystal in plane l to electron beam. Exp. conditions same as in Fig. 3, except gain 64×8 and window 3.5 V.

Our first experiments in this connection were made in needle-shaped TiB crystals (orthorhombic crystal structure) grown in a Ti-rich matrix. Since we were used to APF measurements on carbon, which usually showed a reproducibility of better than 2%, we were completely puzzled at first by the very large variation (up to 30%) in these factors for B K α with respect to elemental boron.

The key was that the variation in APF was synchronous with the variation in observed peak position. The lowest APF value (highest peak intensity and narrowest peak) was always found at the lowest peak position (shortest wavelength), and the highest APF was found at the highest peak position. Figure 5 gives two examples of extremes found in the peak shapes of B K α emitted by different TiB crystals. Apparently each individual TiB crystal can yield its own specific B K α peak, both in shape as well in peak position.

Further investigation revealed that each individual crystal could be made to emit peak shapes between the two extremes when the specimen was merely rotated in a plane perpendicular to the electron beam. It is evidently not so much the position of the specimen with respect to the electron beam that matters, but the position of the specimen with respect to the analyzing crystal. In extreme cases a rotation of 90° was enough to shift the maximum in the B K α peak almost over 1 mm, from the maximum to the minimum position; further rotation of 90° brought it back to the original position, and so on. The situation is as when a noncubic specimen is used under an optical microscope with crossed Nicol's prisms; a literature research revealed that the effects observed were indeed due to polarization effects in the emitted x radiation. The phenomenon itself has been known since 1969⁴ and is explained by the presence of polarized components in the emitted x radiation. It can be expected⁵ in all compounds with a symmetry lower than cubic and higher than triclinic. Polarization takes place in two mutually perpendicular planes, which are aligned along the principal crystallographic directions of the crystal lattice. Unfortunately, for quantitative analysis, the analyzing crystal can assume the function of a polarization filter and its action as such is optimal when the angle of incidence of the x rays on the crystal is 45°. As it happens this angle for B K α radiation in our spectrometer (JEOL 733, lead-stearate crystal) is 42.5° which explains a great deal of the exciting and interesting phenomena observed.

The most pronounced effects found so far have been in ZrB₂ (hexagonal), with almost 40% variation in APF and shifts of ~1 mm. As might be expected, the few cubic borides (such as LaB₆) did not show this effect and could thus be used as complex standards. Unfortunately, due to the low MAC of B K α in these compounds, the emitted intensity is 30-50% of that from pure boron. Boron itself does not show these polarization effects although its structure (rhombohedral) would allow it, so we were ultimately forced to use this as a standard.

An immediate implication of the polarization phenomena is that anyone who is unaware of these effects could make large errors even on measurements performed with the same compound as a standard and with the spectrometer retuned for each individual measurement. One could easily come to the conclusion that the boron content of TiB₂, for example, showed variations of 25%, whereas it actually has a very limited homogeneity range.

For quantitative analysis these effects are of course a great nuisance because one is forced either to measure all intensities in an integral fashion or to determine first the variation of APF with peak position for each noncubic binary. We have done the latter for all 28 borides and the general results are that the area (integral) intensities showed a small variation of ± 2 -3% relative to the average values. Obviously, there is also a small effect of crystallographic orientation. However, reasonably accurate intensity measurements are indeed possible for a light element such as boron, although the fundamental uncertainty in k-ratio is ± 2 -3% to start with. The rest of the error in the final concentration is doubtless due to the matrix correction program.

As we have done before for the carbon analyses, large series of peak-intensity measurements were performed, for most of the compounds between 4 and 15 kV, and for some low-absorbing systems up to 30 kV. Afterward all peak intensity ratios were multiplied by the APFs appropriate to the peak positions observed, in order to obtain the correct integral intensity ratios. A total of 180 boron measurements were thus collected, in addition to the already available set of 117 carbon measurements.

The measurements on nitrogen have been only recently started. A big problem has been the preparation of homogeneous and massive nitride specimens suitable for electron-probe microanalysis. In fact, it took us the best part of a year to prepare 18 nitrides spread over 12 systems and to have them chemically analyzed for nitrogen as well as oxygen. The measurements on these specimens are now in progress and the preliminary results indicate

that peak shape alterations are much less pronounced than for boron and carbon; presumably the APFs are within 10% from unity. However, new practical problems show up here: very low N K α intensities are observed and the background can present some problems because of a slight curvature and the presence of persistent interferences.

Ultimately we hope to collect 162 intensity ratios relative to Cr₂N over the range 4-30 kV. Afterward we hope to proceed to oxygen as well.

Final Results Obtained so Far

Once a reliable set of measurements is available one can take the last step in the procedure: the conversion of measured integral k-ratios into concentration units.

On previous occasions we have shown^{1,2} that unexpectedly good results can be obtained for the analysis of carbon. The application of our own correction program,^{6,7} in conjunction with our own consistent set of mass absorption coefficients, led to a relative root-mean-square value (calculated over nominal concentration) of 3.7%. This result is all the more remarkable if one considers that the data file was obtained for the very wide range of 4-30 kV. Even better results might be expected if this range were restricted to 8-15 kV (somewhat more realistic values in which to measure carbon).

As was to be expected the preliminary results for boron (using Henke's⁸ MACs) were considerably less satisfactory, partly perhaps because we were forced to use B as a standard. Hence, the amount of correction necessary is correspondingly larger than for a complex standard. We must also realize that the wavelength of B K α (67.6 Å) is ~ 1.5 times that of C K α (44.7 Å), and that the overvoltage ratio U_0 (accelerating voltage/critical excitation voltage) for B K α at 30 kV amounts to ~ 160 , compared to ~ 100 for C K α . Moreover, we obtained the equations being used at present in our $\phi(\rho z)$ program through optimization⁷ using an old data file. The measurements in this file were limited to elements heavier than Al and accelerating voltages of 10-40 kV; hence, U_0 varied between 1 and 22 at the most. Since U_0 (raised to some power) is present in most equations in the $\phi(\rho z)$ approach, one can understand that the present set of equations is probably no longer adequate to cope with such extreme conditions as in the analysis of boron. The newly collected set of 180 boron measurements will be doubtless extremely valuable in the necessary critical reexamination of the present equations, perhaps precisely because the conditions are so extreme.

As long as the intensity measurements can be carried out with an accuracy of, say, $\pm 5\%$, there is no fundamental reason to expect nor to accept a much poorer figure in the calculated concentrations. This last is obviously a problem of further improving the existing matrix correction procedure(s) and as such it is a matter of time, dedication, and effort.

References

1. G. F. Bastin and H. J. M. Heijligers, *Quantitative Electron Probe Microanalysis of Carbon in Binary Carbides*, Internal Report, University of Technology, Eindhoven, The Netherlands, March 1984 (in English), ISBN 90-6819-002-4.
2. G. F. Bastin and H. J. M. Heijligers, "Quantitative electron probe microanalysis of carbon in binary carbides," *Microbeam Analysis--1984*, 291.
3. J. Ruste, "Principes généraux de la micronalyse quantitative appliquées aux éléments très légers," *J. Microsc. Electron.* 4: 123, 1979.
4. O. Brümmner, G. Dräger, and K. Machlitt (quoted in Ref. 5), in V. V. Nemoshkalenko, Ed., *Proc. Intern. Symp. X-ray Spectra and Electronic Structure of Matter*, Kiev: Inst. Met. Phys., Acad. Sci. Ukr. SSR, 1969, 300.
5. G. Dräger and O. Brümmner, "Polarized x-ray emission spectra of single crystals," *Phys. Stat. Sol.* B124: 11, 1984.
6. G. F. Bastin, F. J. J. van Loo, and H. J. M. Heijligers, "Evaluation of the use of Gaussian $\phi(\rho z)$ curves in quantitative electron probe microanalysis: A new optimization," *X-ray Spec.* 13: 91, 1984.
7. G. F. Bastin, H. J. M. Heijligers, and F. J. J. van Loo, "The performance of the modified $\phi(\rho z)$ approach as compared to the Love and Scott, Ruste, and standard ZAF correction procedures in quantitative electron probe microanalysis," *Scanning* 6: 58, 1984.
8. B. L. Henke et al., "Low energy x-ray interaction coefficients: Photoabsorption, scattering, and reflection," *Atomic Data and Nuclear Data Tables* 27: 1-144, 1982.

DECONVOLUTION OF SPECTRA

Raman and IR microanalysis

J. G. Dodd and L. K. DeNoyer

Experimentally determined spectra are often limited in resolution by the resolving power of the spectrometer. It may be infeasible, or even impossible (as in the case of x-ray spectra obtained by energy-dispersive detectors), to "close down the slits" to improve resolution. Using both Van Cittert-Jansson and maximum entropy methods in the spectral domain, we show that in many such cases the transfer function of the instrument may be removed, with resolution enhancements of two to four.

The maximum entropy algorithm provides the most probable arrangement of photons in object space, and is cognizant of the noise present in the data. The Van Cittert algorithm gives more spectacular resolution, but has difficulty with high spatial frequency noise. We show applications of both algorithms to real (noisy) data. Implementations of these algorithms for small desk-top computers run in reasonable times (5-15 min) for spectra of a few hundred data points.

Spectroscopy

Spectroscopy is the study of structure in the response function of a system. A system may respond to either external or internal (spontaneous) perturbations. The response function may be measured in energy, frequency, wavelength, or any domain in which a response function can be defined and measured. In no case is the response function of a real system a delta function. The uncertainty principle forbids this outcome and always requires some irreducible "line width," and hence some kind of "line shape." This characteristic width obeys the inequality

$$W \gtrsim h/T \quad (1)$$

where T is the characteristic response time of the system. In most cases, of course, the line width is dominated not by the uncertainty principle but by other effects, which arise because one usually does not observe an isolated system (atom, molecule) but an ensemble of systems that are either not all quite identical--such as a Doppler-broadened gas in which molecules have slightly different energies in the observer's frame, or/and interact with (perturb) one another, as in the case of a solid or liquid.

In any case, sources never speak *ex cathedra*, but through some instrument that has its own response function. What is delivered to the observer is the convolution of the instrument's response function with that of the process from which the signal originates. This convolution, or "folding" operation carried out on a process response $R(E)$, by an instrument with a response $S(E)$, produces the observed "signal"

$$I(E) = \int R(E')S(E - E') dE' = R(E)*S(E) \quad (2)$$

where the range of the variable E' is that of E and $*$ is the convolution operator.

Unless $S(E - E')$ is a delta function, the observed spectrum $I(E)$ is never the same as the process response function $R(E)$.

But the goal of spectroscopy is to find $R(E)$; that is, to characterize the process, not the instrument. It would be very helpful if one could undo the convolution of Eq. (2), deducing what $R(E)$ must be if $I(E)$ is observed. The extraction of $R(E)$ from $I(E)$ is called *deconvolution*.

But why bother? Why not just close down the slits?

The Cost of Resolution

If we critically sample a spectrum at a given resolution, taking N data points in time T , then what is the cost in time of working at one-fourth the original slit width?

First, the flux falling on the detector is reduced by a factor of 16. If the system

The authors are at Colgate University, Hamilton, N.Y. They wish to acknowledge the support and encouragement of McCrone Associates during this undertaking; they are especially grateful to Mark Andersen who provided the Raman spectra for deconvolution.

is detector noise limited, then to achieve the same signal/noise ratio requires 256 times to scan time. But in addition, four times as many points must be sampled to meet the condition of critical sampling, and so the time penalty is a factor of 1024!

In other cases, such as x-ray spectra taken with energy-dispersive detectors, the detector response function is "built into" the instrument. There is no handy knob that will improve it even if one is willing to pay the time cost. Then there is really no alternative; one either deconvolves or puts up with poorly resolved spectra.

Deconvolution

Formally, deconvolution is quite simple. The Fourier transform of $I(E)$ is

$$I'(t) = R'(t)S'(t) \quad (3)$$

where t is the independent variable conjugate to E and primes indicate that the function is in Fourier space. If $S'(t)$ is known, then

$$R'(t) = I'(t)/S'(t) \quad (4)$$

and the inverse Fourier transform of Eq. (4) yields $R(E)$, the desired source function.

This simple process hardly ever works. By its nature, $S'(t)$ must be small over some of the range of t , else $S(E)$ would be nearly a delta function, and $I(E) \approx R(E)$. But where $S'(t)$ is small, the presence of noise causes large fluctuations in the calculated values of $R'(t)$; that is, the result is very noisy. Direct inversion is therefore seldom useful, since noise is always present and the wings of $S'(t)$ are always small.¹

Noise is always present in $I(E)$ also, often high-frequency noise that has been added by the electronics. A common solution to this problem is "smoothing," or application of a filter that attenuates everything in the signal and line shape spectra lying above some arbitrary cutoff frequency. This process at least gets rid of frequencies that cannot possibly have passed through the instrument, and so are certainly noise; but of course such a crude process also removes any signal information in that part of frequency space. However, it may be at least possible then to do a direct inversion. If the loss of higher signal frequencies due to the filter is too severe, however, the restoration algorithm converges to a source function not very different from the observed spectrum. Then other means should be employed.

It is the entire thrust of deconvolution algorithm research to find some way to discriminate signals from noise through the use of suitably chosen equations of constraint.

The Use of A Priori Knowledge

We may know more about a spectrum than is explicit in the data. For example, if the spectrum is a set of intensities, we know it cannot be negative anywhere. If it is an absorption spectrum, it normally has an upper bound of 1. We also may know that the spectrum is band limited; that is, everything that comes from the source must pass through a measuring instrument with a transfer function $S(E)$, and so there should be no features in the observed spectrum $I(E)$ "sharper" than $S(E)$. If there are, then these features are post-instrument noise.

Other constraints may apply in special cases. In mass spectroscopy where the purpose is quantitative analysis, we often know what elements may be present. Their positions are determined by *a priori* knowledge, and the only question is their relative amplitudes. Each such constraint is a potential discriminant against noise.

The deconvolution process may be thus thought of as the solution of Eq. (2) for an $R(E)$ that satisfies both Eq. (2) and a set of *a priori* constraints. It is the presence of these constraints which makes the problem soluble, or else noise would dominate and Eq. (2) would have no solution.

The Van Cittert-Jansson Algorithm

In 1931 Van Cittert showed that the iterative algorithm

$$R^{n+1} = R^n + e(I - R^n * S) \quad (5)$$

where e is a dimensionless constant less than 1, converges, in the absence of noise and for e not too large, to $R(E')$ if S is sufficiently well behaved.² For sufficiently small e , Eq. (5) may be written

$$dR = (I - R*S)de \quad (6)$$

where * denotes the convolution operator.

Fourier transformation of Eq. (6) yields

$$dR' = (I' - R'S')de \quad (7)$$

which may be integrated to obtain

$$I' - R'S' = I'(1 - S')\exp(-eS') \quad (8)$$

showing that with suitable restrictions on S' the right side goes exponentially to zero with e , and so on the left R' does converge to I'/S' , just as Van Cittert said. But the restrictions on S' are severe: where it is small convergence is slow, and where it goes negative, the algorithm diverges. This result shows that Van Cittert's algorithm may be no better than direct inversion. It is at best equivalent to it, failing just where direct inversion fails. That is true if no further constraints due to *a priori* knowledge are invoked. But the Van Cittert algorithm accepts many such constraints rather gracefully, which is not true of direct inversion.

If the spectrum is known to be non-negative, then during the iteration of Eq. (5), the current approximation to R may be tested at every point for a negative value, and if one is found then R may be set to zero at that point. And since one of the diseases of any kind of inversion is that noise tends to be amplified into "peaks" during division by small values of S' , we may replace the constant k by a function $k(R)$ such as kR , which encourages large peaks to grow larger but tends to suppress small fluctuations in the "grass" of the baseline.

The weighting function

$$k(R) = R(1 - R) \quad (9)$$

is often used for absorption spectra, since it limits growth of a peak to about unity height, and tends to drive small fluctuations toward zero. Such nonlinear weighting functions are the Jansson contribution to the Van Cittert algorithm.³⁻⁵

However, it is clear from this kind of language that we have left even Van Cittert's modest rigor far behind. With such weighting functions, it is no longer possible to predict what will happen in the presence or absence of noise; to prove that the algorithm will or won't converge; or if it does converge, what it will converge to. We have left the realm of science and have entered the domain of mysticism, or at least of art.

But it works. Blass and Halsey have experimented extensively with this algorithm on IR spectra with excellent results.⁶ Improvements in resolution of factors of two to three are routinely obtained on experimental data, with conservation of area under the peak within 15%, and excellent peak position stability. The limit of resolution enhancement seems to be determined only by the amount of noise present in the data.

We have made modest resolution improvements in the Van Cittert method by using a carefully chosen starting spectrum for iteration (the usual choice is simply the observed spectrum). An example is shown in Fig. 1. Here, a Raman spectrum of multiplet structure in a CCl_4 symmetric stretch band, recorded at a resolution of 4 wavenumbers (solid line), is deconvolved (coarse dotted line), and compared to the same spectrum recorded at a resolution of 1 wavenumber.

Is It Real?

When one sees detail in a spectrum "grow out of" an unpromising undulating low-resolution recording as in Fig. 1, the professional instinct is to be suspicious. No one can describe in mathematical detail just how these various nonlinear implementations of Van Cittert's algorithm work, so how do we know they do?

In fact, convergence is probably not unique, but in the best case only to a member of a large set located within a small radius in solution space. In other words, starting from a different initial set of conditions it seems possible to converge to different "source spectra" which however usually seem quite similar except in degree of resolution.

On the other hand things can go wrong, too, especially if the prefiltering step is not carried out properly, as the restoration of a similar Raman spectrum shows in Fig. 2. The presence of splitting where there should be none, and even completely fictitious peaks, warns us that a stable restoration to a unique end point should not be assumed. A more careful treatment of the same spectrum is shown in Fig. 3. Clearly, interaction of the

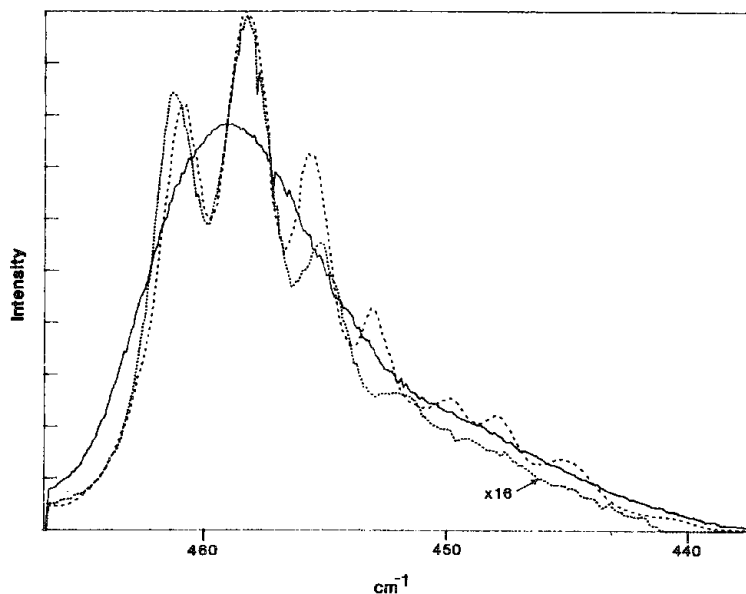


FIG. 1.--Raman spectrum of multiplet structure in CCL_4 symmetric stretch band. Solid line is original spectrum recorded at resolution of 4 cm^{-1} , coarse dotted line is deconvolved spectrum. Fine dotted line is same spectrum recorded at 1.0 cm^{-1} .

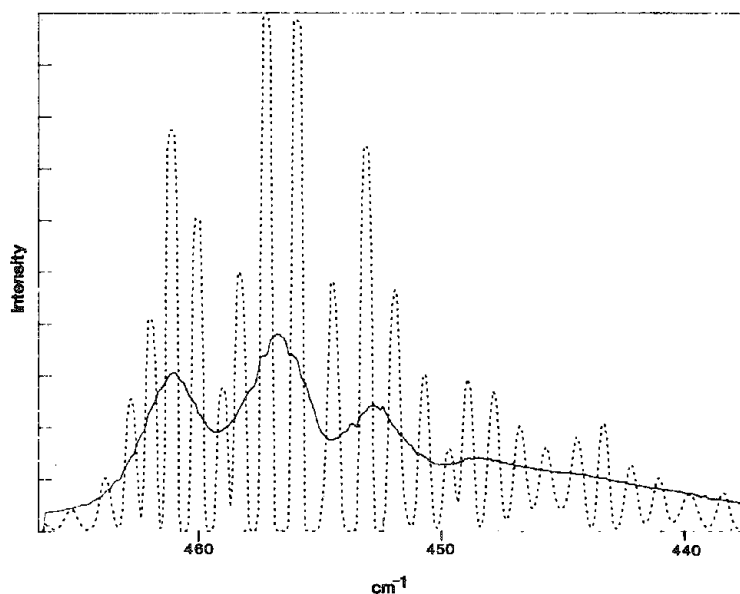


FIG. 2.--Raman spectrum of CCL_4 . Solid line recorded at 1 cm^{-1} , dotted line is improperly deconvolved spectrum.

experimenter can guide the algorithm to a successful result.

This process is not as alarming as it sounds.

Suppose we review the much-beloved least-square fit. Given four assortments of points as in Fig. 4, we may decide that we should draw a straight line through each. Never mind why; one might justify some other function as easily on the basis of some *a priori* information. That is, we think we know the *line shape*, and we now want to deconvolve the data. The result of the familiar calculation will be four straight lines *with the same slopes, intercepts, t statistics, sums of squares, regression sums of squares, residual sums of squares, and correlation coefficients!*⁷

Still, we all use the least-square fit with the knowledge that it does something definite and understandable and *objective* to the data. It may have its problems, but we are used to them and can bring care and even skepticism to its use. We must be willing to bring a similar care and skepticism to the use of the less familiar deconvolution algorithms.

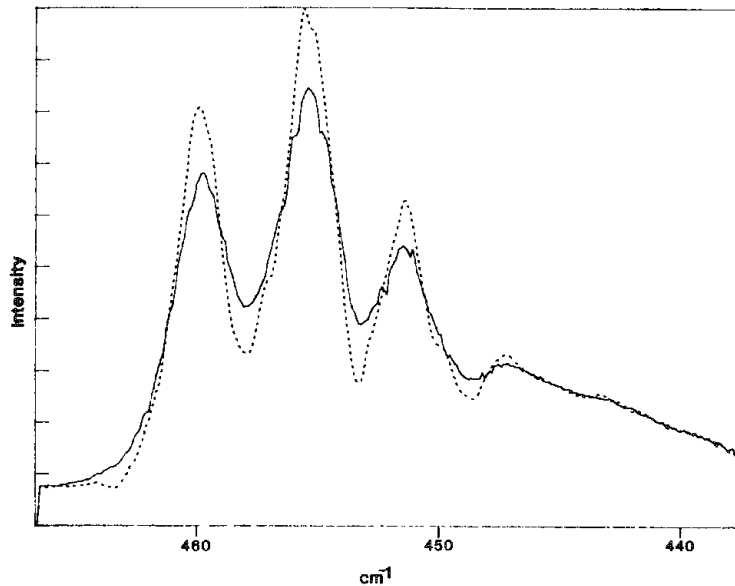


FIG. 3.--Raman spectrum of CCL_4 . Solid line recorded at 1 cm^{-1} , dotted line is properly deconvoluted spectrum.

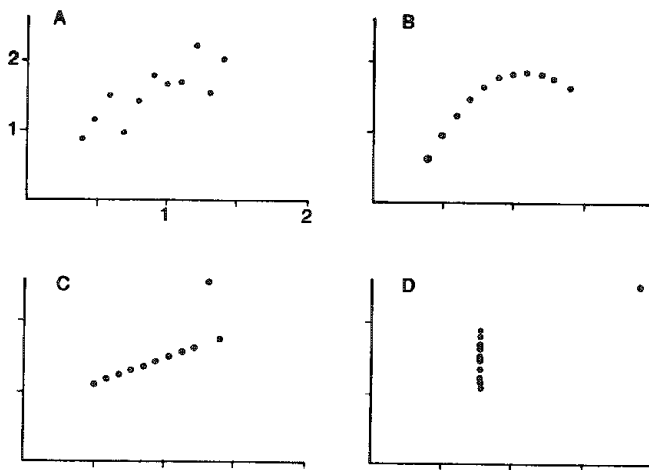


FIG. 4.--Four different data sets having identical linear least-squares fit. (From F. J. Anscombe, "Graphs in statistical analysis," *American Statistician* 27: 17-21, 1973.)

Maximum Entropy Deconvolution

It would be better to be able to work from secure general principles than to cobble up algorithms and then wonder why they do or do not work. Such a secure general principle forms the basis of maximum-entropy methods of data processing.

Think of each photon as a Maxwell-Boltzmann (distinguishable) particle. A particular spectrum in object space, represented as a string of boxes j each containing a certain number of photons o_j , can be generated in many different ways simply by exchange of photons between pairs of boxes. The number of ways W that can be done is

$$W(o_1, \dots, o_j) = O! / (o_1! o_2! \dots o_j!), \quad (10)$$

where the o are the photon numbers in each box and O is the total number of object elements. Using Stirling's approximation for the factorials we obtain

$$W \ln(W) = o_j \ln(o_j) \quad (11)$$

(O is large, and repeated indices are summed.)

We might have made this argument, and do, for atoms in energy states in a gas in equilibrium. The expression is the same in either case, and in either case $W \ln(W)$ is called the *entropy* of the system.

Of course, we do not observe object space, but image space. The image is the object convolved with an instrument transfer function, and so may be written

$$I_m = O_j S_{mj} + n_m \quad (12)$$

We always sum over repeated indices.

Note the inclusion of noise (the term n_m) in the image. We may as well have it; it is always there! We may assign an entropy to it as well; the expression looks just like Eq. (10) except that n and N replace o and O .

We now wish to find the most probable source distribution and the most probable noise distribution, subject to some set of constraints. These constraints (we will assume) are:

1. The distribution must yield the above image points, within the uncertainty of the noise.
2. The intensity must everywhere be positive (no negative occupancies of any state).
3. The total number of photons is conserved (in statistical mechanics this means that the chemical potential is different from zero).

Since noise and signal are assumed to be independent in this model, the entropy of the system is the sum of the entropies of noise and signal. We therefore construct this total entropy, and add the constraint functions using Lagrangian multipliers, and then--exactly as we would in the statistical mechanics of gases--maximize this entropy to find the characteristic equations of the state that can be achieved in the maximum number of different ways. We assume that the object function of this state is the best estimate of the process spectrum.

The characteristic equations then turn out to be:

$$O_j = \exp[-1 - u - k_m S_{mj}] \quad (13)$$

$$N_m = \exp[-1 - k_m/r] \quad (14)$$

$$I_m = O_j S + N_m - B \quad (15)$$

$$P_O = \text{SUM}_j (O_j) = \text{SUM}_m (I_m) \quad (16)$$

where

- I_m are the measured data points (the observed image)
- O_j are the estimated source object points
- N_m are the estimated noise fluctuations
- P_O is the total signal power
- S_{mj} is the point spread function (line shape)
- r is the target signal/noise ratio
- B is the estimated peak negative noise fluctuation
- u, k are the Lagrange multipliers

and summation over repeated indices is assumed.⁸

The solution of this system of equations for the object function is not easy or fast. On the other hand, the deconvolutions obtained by maximum entropy methods are far more robust (immune to noise) than those obtained by the Van Cittert family of algorithms, being useful for image spectra contaminated by as much as 40% noise. Further, MEM solutions are unique. And finally, we really do know what the computation does. There is a general principle.

It is instructive to examine the estimated object function a little more closely. Eliminate u from the object function expression, using the constraint equation of total power. This operation yields

$$O_j = P_O [\exp(k_i S_{ij})] P_f \quad (17)$$

where P_f signifies the usual partition function expression for a Maxwell-Boltzmann distribution,

$$P_f = \exp(k_j S_{ij}) \quad (18)$$

The estimated object point O_j is proportional to the normalized probability of finding the system in the state described by Eq. (17).

The image, in turn, is simply the convolution of the transfer function with the estimated object function, with some added noise.

Does it work?

Figure 5 shows an MEM deconvolution, and Fig. 6 a modified Van Cittert restoration of the same Raman spectrum. The MEM result shows less enhancement. Why?

The two algorithms approach the data differently.

A Van Cittert algorithm treats the data not as a sample of a process, but as the process itself. Since it does not search object space for more than one solution, it does not necessarily find the most probable solution. Furthermore, the smoothing of the data, which is essential to avoid nonphysical spectra in the Van Cittert case, actually modifies the data and hence changes the process treated by the algorithm in a way that is outside the algorithm, and in fact is arbitrary--up to the experimenter. In this way the experimenter adds a priori knowledge to the data treatment, and so guides the algorithm to a particular solution in object space.

On the other hand, MEM methods do not require pre-smoothing of the data because the noise, as well as the signal, can be estimated by the algorithm. The MEM algorithms treat the data as a *sample* of the process, and return the data set most nearly representative of the process, given the presence of the noise. It is really a more conservative, and certainly a more defensible approach.

The computational cost of MEM can be considerable. The nonlinearity of the equations requires iterative methods. Convergence is slow and not always successful. We have employed a fixed-point method of iteration, which turns out to be quite efficient. When it converges (which depends upon how well one guesses the parameter B), it does so in a dozen iterations; when it does not (if B is chosen too small), one knows almost at once. The smallest value of B that permits satisfactory convergence is then a measure of the peak noise fluctuations of the estimated image.

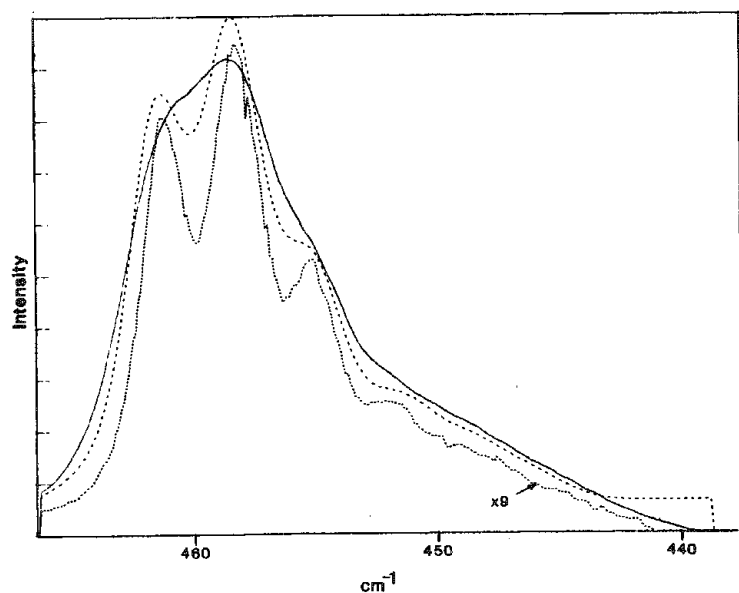


FIG. 5.--Raman spectrum of CCL_4 . Solid line recorded at 3 cm^{-1} , coarse dotted line is MEM deconvolution. Fine dotted line is same spectrum recorded at 1 cm^{-1} .

Use Which?

The practicing spectroscopist who usually knows approximately what he should see is often happier with the Van Cittert approach because he can tinker with it until he likes the picture. That sounds cynical, but it is merely the application of implicit a priori knowledge. It is perfectly proper if the knowledge is correct.

Nevertheless, MEM can be defended in the same way as the least-squares fit: it is an objective estimate of the process, given a typical sample, and a set of explicitly imposed constraints.

The difference between the two algorithms is not merely in degree of enhancement. MEM tends to restore large peaks more fully than small peaks, in that large peaks appear sharper than small peaks after deconvolution. The Van Cittert algorithm tends to produce the same peak shape for any peak height. This

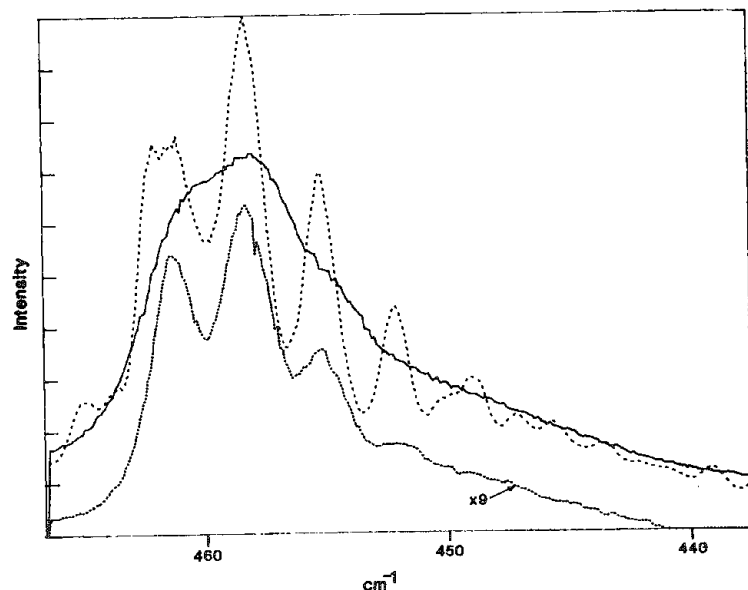


FIG. 6.--Raman spectrum of CCL_4 . Solid line recorded at 3 cm^{-1} , coarse dotted line is Van Cittert deconvolution. Fine dotted line is same spectrum recorded at 1 cm^{-1} .

difference is not incidental, but reflects again a fundamental difference between the way the two algorithms view the data. The Van Cittert algorithm does, if given the chance, turn every upward fluctuation into a peak of some kind. MEM, on the other hand, does not allow a peak to sharpen beyond the ability of the data to define it in the presence of the noise.

Hardware Requirements

We have programmed both algorithms in FORTRAN 77 and have tested them using the IBM PC with 8087 support, a 68000 coprocessor (HSC, 6 MHz) which uses a CPM 8-bit machine as host, and a VAX780.

These algorithms are subroutines in a comprehensive spectral data manipulation program. Running times on the VAX for data arrays of 256 points are under 1 min, on the 68000 about five or six VAX times, and on the IBM PC about eight to ten VAX times. The program may be run on 8-bit machines or on the PC without the 8087, but of course it is quite slow, typically 40 VAX times for either.

Conclusions

The Van Cittert and maximum-entropy deconvolution algorithms have been discussed and examples given of their use on Raman spectral data. Resolution enhancement of factors of 2-4 have been obtained with good agreement with spectra taken at the higher resolution. Hardware requirements and typical running times were reported.

References

1. W. Halsey and W. E. Blass, *Appl. Opt.* 16: 286, 1977.
2. P. H. Van Cittert, *Z. Phys.* 69: 298, 1931.
3. P. A. Jansson, *J. Opt. Soc. Am.* 58: 1665, 1968.
4. P. A. Jansson, *J. Opt. Soc. Am.* 60: 184, 1970.
5. P. A. Jansson, R. H. Hunt, and E. K. Plyler, *J. Opt. Soc. Am.* 60: 596, 1970.
6. W. E. Blass and G. W. Halsey, *Deconvolution of Absorption Spectra*, New York: Academic Press, 1981.
7. E. R. Tufte, *The Visual Display of Quantitative Information*, Cheshire, Conn.: Graphics Press, 1983.
8. B. Roy Frieden, *J. Opt. Soc. Am.* 62: 511, 1972.

NONDESTRUCTIVE MICROPROBING BY MEANS OF A NEW GENERATION OF INSTRUMENTS FOR RAMAN AND FLUORESCENCE SPECTROSCOPY

Jacques Barbillat, Paul Dhamelincourt, Michel Delhayé, Edouard da Silva, and Bernard Roussel

In the past the major limitation on the use of a Raman microprobe with a scanning monochromator and a single photomultiplier has been that the measurement times are generally too long for fragile materials. The high radiation over a long exposure time in the small sample volume may cause significant microprobe degradation. Extensive research has been performed into procedures that would allow increased sensitivity and higher signal-to-noise ratios while decreasing the power of the laser at the sample so as to preserve the non-destructive nature of Raman microanalysis. Since 1980 CNRS in collaboration with French industry (DILOR) has made a special effort to develop a multichannel Raman micro-analyzer.¹⁻³ That research resulted in a new commercial instrument, the DILOR Microdil 28, which takes full advantage of recent microchannel plate (MCP) intensifier tube and photodiode array technology.

The multichannel technique based on a MCP intensifier tube and a diode array allows the simultaneous recording of a large number of elements with a sensitivity per channel comparable to that of a photomultiplier tube. The advantage to this increase in sensitivity is two-fold. First, very weak signals can be observed over long integration times followed by computer analysis of the data. Second, sample degradation can be avoided when a laser beam with lower power and shorter exposure times is used.

This paper begins with a description of the Microdil 28. Some examples are then shown that illustrate its capabilities for the analysis of microsamples which are subject to degradation through prolonged exposure to the laser beam.

In principle, the extension of multichannel micro-Raman techniques to the domain of microfluorescence spectroscopy is feasible by means of minor modifications of the microprobe system: both broader spectral field and a lower resolution are required for microfluorescence spectroscopy. After a preliminary study of fluorescence instrumentation the development of a new laser microfluorimeter was undertaken in a new cooperative group (G.I.P. instrumentation and spectroscopy) which has been formed by CNRS, university laboratories, and the DILOR company.⁴

Some of the features of this instrument with reference to biological applications are outlined below.

Micro-Raman Analyzer: Microdil 28

Each component has been carefully designed to integrate with the multichannel detector and the result is a high-quality, reliable, and easy-to-use instrument specially designed for Raman microanalysis. The Microdil 28 uses an Olympus optical microscope as the sample carrier and the same microscope objective is used for laser illumination and scattered light collection (Fig. 1). A special optical device (optical scanner) is placed between the microscope and the spectrometer so that one may analyze any point in the field of the microscope with a spatial resolution better than 1 μm without moving the sample. Since the exploration is performed in the back image space of the microscope, one benefits from the magnification of the objective. Thus a variety of cumbersome samples (cooling or heating stage, pieces of art, or industrial materials) can be analyzed with high accuracy over a wide field.

The spectrometer consists of a double foremonochromator (with subtractive or additive dispersion) followed by a stigmatic spectrograph of a conventional design with a plane grating and large aperture objectives. Two gratings (600 g/mm and 1800 g/mm) mounted back to back in a turret provide various dispersions in the focal plane of the spectrograph.

A specially built multichannel detector head (MCP intensifier tube coupled to a 512 photodiode array) cooled at -20 °C by a Peltier element is used to detect Raman spectra.

Authors Barbillat, Dhamelincourt, and Delhayé are at the CNRS Laboratoire de Spectrochimie Infrarouge et Raman, Université de Lille, F-59655 Villeneuve d'Ascq, France; authors Da Silva and Roussel are with DILOR, 244 rue des Bois Blancs, F-59000 Lille, France.

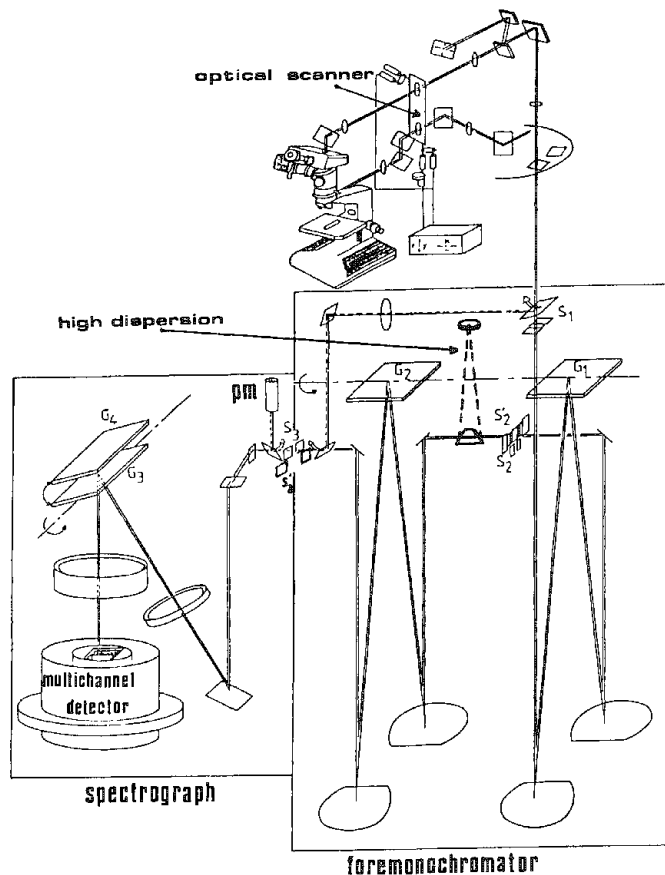


FIG. 1.--Optical schematic of Microdil 28.

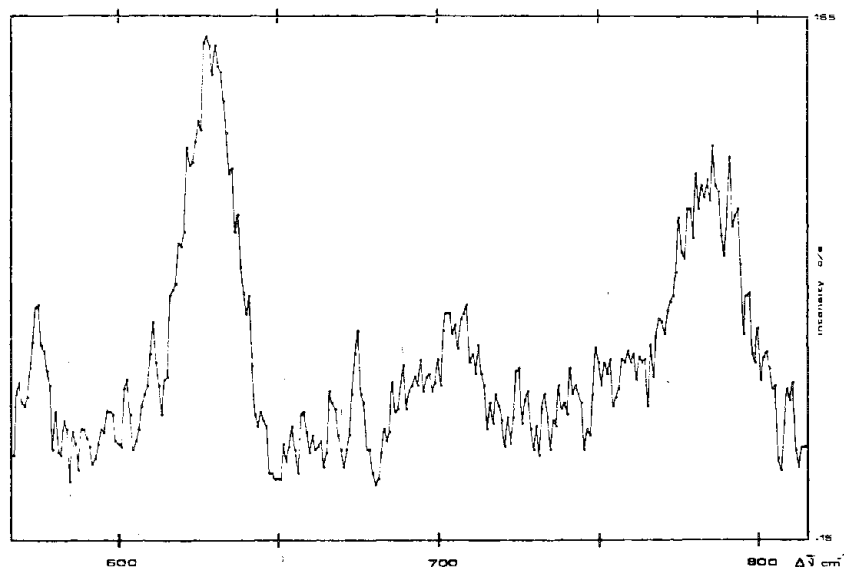


FIG. 2.--Raman spectrum of spherocrystal inside insect fat body. Measurement parameters: exciting wavelength, 514.5 nm; laser power (at sample), 250 μ W; spectral resolution, 7 cm^{-1} ; integration time, 20 s; number of scans, 20.

The signal from the diode array is sampled, multiplexed, and then sent to a fast 12-bit A/D converter (data available during 5 μ s every 9 μ s). Typically a single cycle of data acquisition consists of a signal integration period (from 120 ms to 60 s) with a signal readout, followed by a period to integrate and read a dark-current offset on the detector. There are two different methods for the actual processing of the data from the A/D converter.

1. Data may be stored directly into the memory of a fast computer with direct memory access.
2. For each acquisition cycle, data may be stored in two different memories (one for signal sweep, the other for dark sweep). Then an arithmetic unit performs the subtraction of the dark sweep from the signal sweep to eliminate the dark current and the fixed pattern signal. Subtracted data are then compatible with currently available micro-computers.

The actual data system includes: (1) an Apple II computer system with 64K, with interfaces for multichannel and photon counting detection systems, a dual disk drive, a video monitor, and a plotter; and (2) the software package, which consists of acquisition mode selection (visualization, single/multichannel, signal averaging) and data treatment (smoothing, integration, base line correction, normalization). In this instrumental configuration the spectrometer may be used in different ways, depending mainly on the nature of the sample.

- For samples with Raman lines at a sufficient distance from the exciting line, the scattered light can be directly focused onto the entrance slit of the spectrograph through a colored filter that cuts off the exciting line. As a result one benefits from the high luminosity of the spectrograph and the low dispersion of the 600g/mm grating to observe wide spectral field with a low resolution. Typical spectral coverages of 2300 cm^{-1} are achievable at 500 nm with the 600g/mm grating and 540 cm^{-1} with the 1800g/mm grating.

- By using the zero-dispersion foremonochromator to reject the exciting line, one can record spectra close to the Rayleigh line with a medium dispersion. At 500 nm Raman spectral coverages of 540 cm^{-1} are available on the multichannel detector with a dispersion of about 0.7 cm^{-1} /diode, giving a practical resolution of about 5 cm^{-1} (slit width 100 μ m).

- Better resolution may be obtained by an increase in the global dispersion of the instrument. The subtractive foremonochromator is automatically changed into an additive double monochromator by means of an optical device that reverses the dispersion of one stage. As a result the spectrometer then consists of three additive monochromators and field coverages of 180 cm^{-1} are achievable with a dispersion of about 1.5 cm^{-1} at 500 nm (slit width 100 μ m).

- In addition to the multichannel detection the foremonochromator can be operated as a scanning double spectrometer (with additive or subtractive dispersion) with photon counting detection.

Biological Applications

The micro-Raman technique offers a unique method for the in situ identification of small inclusions or local concentrations of compounds in biological tissues or histological sections. Applications of micro-Raman to biological samples are essentially limited by the threshold of degradation. With nonresonant excitation for which the absorption of laser light can be neglected, a few picograms of matter can be unambiguously identified by their vibrational spectra by use of laser power as low as 0.2 to 1 μ W. As an example, we present the spectrum of spherocrystals recorded in a histological section of insect fat body (*Blattella germanica*) with only 250 μ W at the sample (Fig. 2). Another example shows the identification of a rabbit kidney stone induced by mercury and cadmium intoxication. This kidney stone has been identified as calcium phosphate by a recording of its Raman spectrum with 7 μ W at the sample and an acquisition time of 2 min (Fig. 3).

These applications clearly illustrate the advantage of multichannel detection for the analysis of microsamples that are subject to modifications through prolonged exposure to the laser beam. Several spectra were recorded after various illumination periods from 5 to 30 min. One can observe some modifications in the spectra with long exposure times (15 and 30 min) that reveal a change in the nature of the sample being analyzed.

Laser Microfluorimeter

The multichannel technique developed for the Raman microprobe has been extended to microfluorescence spectroscopy and results in a very sensitive microfluorimeter for biological applications (Fig. 4). It consists of the following components.

(1) An optical microscope that focuses the laser beam onto the sample to a spot of about 1 μm in diameter and collects the fluorescence radiations.

(2) The necessary optics to couple the microscope to a spectrograph. The same optical scanner used with the Microdil 28 forms a part of the coupling optics and permits scanning of the sample by the focused laser radiation.

(3) A spectrograph equipped with plane gratings (F/2 aperture) with an automatic wavelength-setting system (coupled to a computer) that permits, depending on the grating in use, the observation of a spectral domain of 300 or 30 nm with a spectral resolution of respectively 3 and 0.3 nm, respectively.

(4) A multichannel detection system (optical solid-state sensor coupled by optical fibers to a MCP intensifier tube) whose high sensitivity allows recording of spectra with low power at the sample (typically a few tens of microwatts) and short irradiation times.

(5) A computer for total system control (optical scanner, wavelength setting) and acquisition and treatments of the signals.

(6) An optional interference filter, which may be placed between the microscope and the spectrograph in order to record Raman spectra between 350 and 3500 cm^{-1} .

(7) The system can obtain fluorescence spectra of the various species distributed throughout the sample, which allows the collection of intensity profiles and mapping of the sample at preset wavelengths of fluorescence emission. Information on the precise characteristics of this new instrument and some applications in the study of intracellular fluorescence of chemotherapeutic agents in single cells is available.

References

1. M. Delhaye et al., "A new generation of laser Raman microspectrometer: Micromars," *Microbeam Analysis--1982*, 275-278.
2. J. Barbillat, doctoral thesis, University of Lille, 1983.
3. A. Deffontaine et al., "The third generation of multichannel Raman spectrometers," *Rev. Phys. Appl.* 19: 415-421, 1984.
4. P. Dhamelincourt et al., "Development of a laser microfluorimeter equipped with a multichannel detector," *Horizon de l'Optique*, 1985.

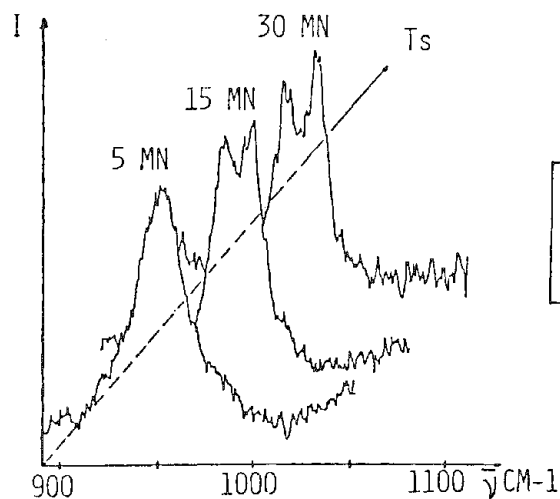


FIG. 3.--Raman spectra of rabbit kidney stone after various exposure times to the laser beam. Measurement parameters: exciting wavelength, 5.4.5 nm; laser power (at sample), 7 μW ; spectral resolution, 7 cm^{-1} ; acquisition time, 2 min for each spectrum.

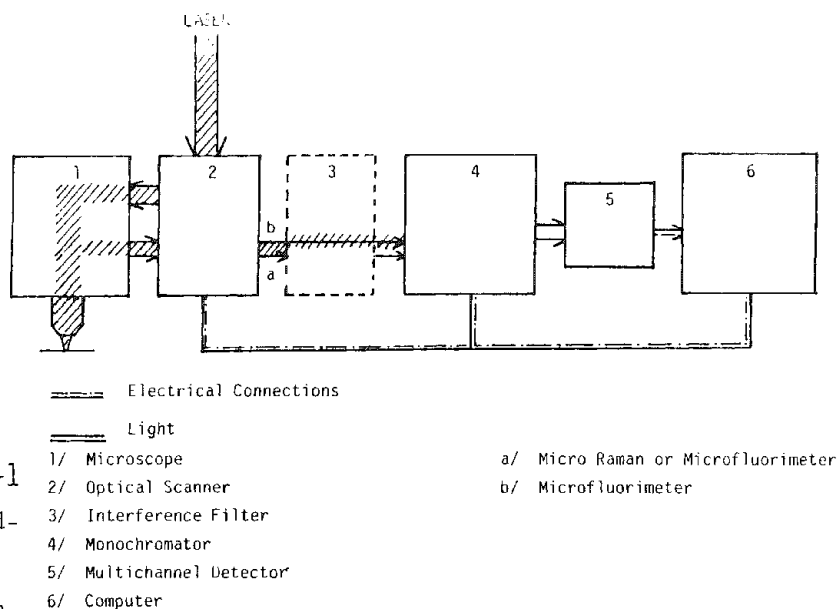


FIG. 4.--Schematic of microfluorimeter.

AN AUTOMATED MICRO/MACRO RAMAN SPECTROGRAPH SYSTEM WITH MULTICHANNEL AND SINGLE-CHANNEL DETECTORS IN A NEW MOLECULAR/CRYSTALLINE MICROPROBE

R. Grayzel, M. LeClercq, F. Adar, M. Hutt, and M. Diem

A new fully computerized triple spectrograph/spectrometer system with integrated software solves the complex instrumental control and safety problems associated with the present generation of Raman spectrographs in which detectors and spectrometers must be independently controlled. The primary design objective in creating this instrument was to offer the industrial analytical chemist a fully integrated, safe, and easy-to-operate Raman system that requires minimal instrumental adjustments and provides the high sample throughput that follows from the decreased acquisition time when one is operating in the spectrograph mode. Computerized reformatting of spectra acquired with the diode array into constant Raman wavenumber shifted spacings makes comparison of data with all published Raman spectra possible.

The development of the Raman microprobe (RMP) MOLE® in the mid- to late 1970s has provided the impetus for the practical implementation of Raman spectroscopy in the industrial analytical laboratory.¹⁻³ There are many examples where spectra acquired with an RMP provide information complementary to results from infrared (IR) absorption, x-ray diffraction (XRD), electron microprobe (x-ray fluorescence and Auger emission), electron diffraction, electron spectroscopy for chemical analysis (ESCA), and ion microprobe.

In the case of IR, the spatial resolution of an RMP is about 10 times better and the Raman spectra tend to be sensitive to different molecular vibrations; that is, Raman scattering can probe double and triple bonds between two carbon atoms or between carbon and nitrogen whereas these bands are often inactive in the infrared. In the case of XRD and ESCA data acquisition of samples smaller than 1 mm³ is difficult. In addition, there are cases in which intermediate range order has been monitored by Raman spectroscopy more effectively than XRD (see Ref. 1 for some examples). All techniques other than IR and XRD require a vacuum for sample examination. The ion microprobe provides inferential information on molecular composition but destroys the sample. Elemental information acquired by an electron microprobe is often not adequate to identify a contaminating source or model the deposition of material without molecular and/or crystalline information. Electron diffraction provides detailed information on a sample but requires sample thinning to the point that preparation-induced modification can be a concern.

Many applications of the RMP have shown that there are several analytical problems that can be addressed by the RMP and provide information complementary to the techniques mentioned above.³ However, a deterrent to the use of a RMP in many locations has been the long acquisition time required in a monochannel instrument (typically 10 min to 10 h). Because of the inherent weakness of Raman signals, and the requirements for rejection of the unshifted laser light, the Raman instruments tend to be large and no foreseeable improvements in the optics or single channel detectors of such instruments are expected to decrease acquisition times by an order of magnitude. The availability of multichannel optical detectors, however, provides the potential for sample throughput because of the well-known multiplex advantage. It was early recognized that such detectors would prove quite useful when incorporated in a RMP.⁴ The work described here was performed on an instrument fully controlled on a single computer. The instrument was designed to provide a safe and easy-to-operate Raman microprobe system for rapid sample turnaround times.

Instrument Design

Figure 1 is a schematic of the instrument. The core of the instrument is a Raman triple spectrograph composed of a double subtractive monochromator (DHR320) and a 0.64m spectrograph (HR640). The function of the pre-monochromator is to define a bandpass (i.e., spectral region) that the spectrograph outfitted with a diode array will detect. By limiting the spectral region passed into the spectrograph, high stray-light rejection

Authors Grayzel, LeClercq, Adar, and Hutt are at Instruments SA, Inc., 173 Essex Ave., Metuchen, NJ 08840; author Diem is at the Department of Chemistry, Hunter College, City University of New York, NY 10021.

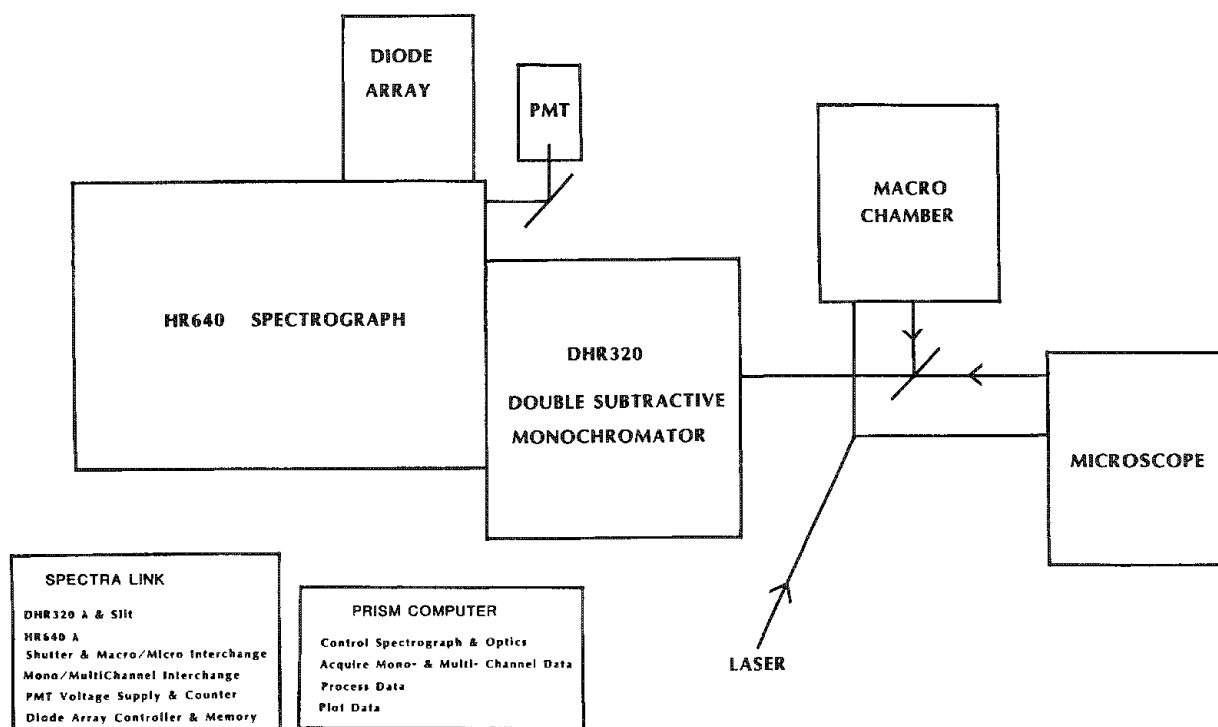


FIG. 1.--Schematic of MOLE[®] triple spectrograph.

can be offered, a requirement for work on powdered bulk samples and for most work on the microprobe. The software enables control of the spectrograph parameters in both wavelength and wavenumber shifted units. For Raman work, where wavenumber shift from the laser is the relevant parameter (reflecting a molecular or crystalline vibrational frequency), the user chooses low and high Raman frequency shifts that define the covered spectral region and the computer calculates the central wavelength and scans both the HR640 and DHR320 drive systems. It also calculates and controls the second slit in the DHR320 which determines the bandpass. Interchange between the macro and micro sampling optics is under computer control; a single motor exchanges the laser input to the samples and the imaging of the Raman light onto the DHR320 entrance slit. The photomultiplier tube (PMT) and diode array can be interchanged as well and standard scanning software has been implemented on this system. Safety features in both the hardware and software protect against conditions that may allow the excitation source to damage the detectors.

The intensified diode array that has been incorporated in the system is provided by Princeton Instruments. The intensifier is of the microchannel plate design which permits negligible image distortion onto the diode array and enables spectra to be calibrated accurately over the full range of the array.

Computer Control

All functions of the instrument, including rotation of the gratings, setting of the intermediate aperture bandpass, control of both photodiode array and photomultiplier detectors, and the choice of sampling optics are handled by a single multitasking computer. The system eliminates the need for calculating grating wavelength positions and intermediate aperture settings for wavenumber shifted data. The software automatically sets the minimum aperture for the desired coverage to optimize stray-light rejection.

Further innovations to the system include an automatic background subtraction subroutine that will collect a background spectrum immediately after each multichannel acquisition or pull a valid background spectrum from disk memory. An autocalibration routine with a built-in hollow-cathode lamp standard provides automatic calibration of spectral peak position.

Results

Testing of the system was designed first to evaluate optical performance and then the performance of the diode array.

Throughput, resolution, and stray-light rejection were measured with a standard photon counting system using an RCA GaAs photomultiplier (C31034). Spectra recorded by scanning of the triple monochromator were compared to data recorded on the U1000 double 1m monochromator on the same sample in the same sample chamber.

Figure 2 shows Raman spectra of a pellet of dibenzothiophene recorded by scanning of the U1000 and the new triple spectrometer. Differences in throughput were within the predictions based on differences in total reflectivity of the two systems. Small differences in resolution can be observed by examination of closely spaced lines (for instance, the doublet at ca. 1300 cm^{-1}).

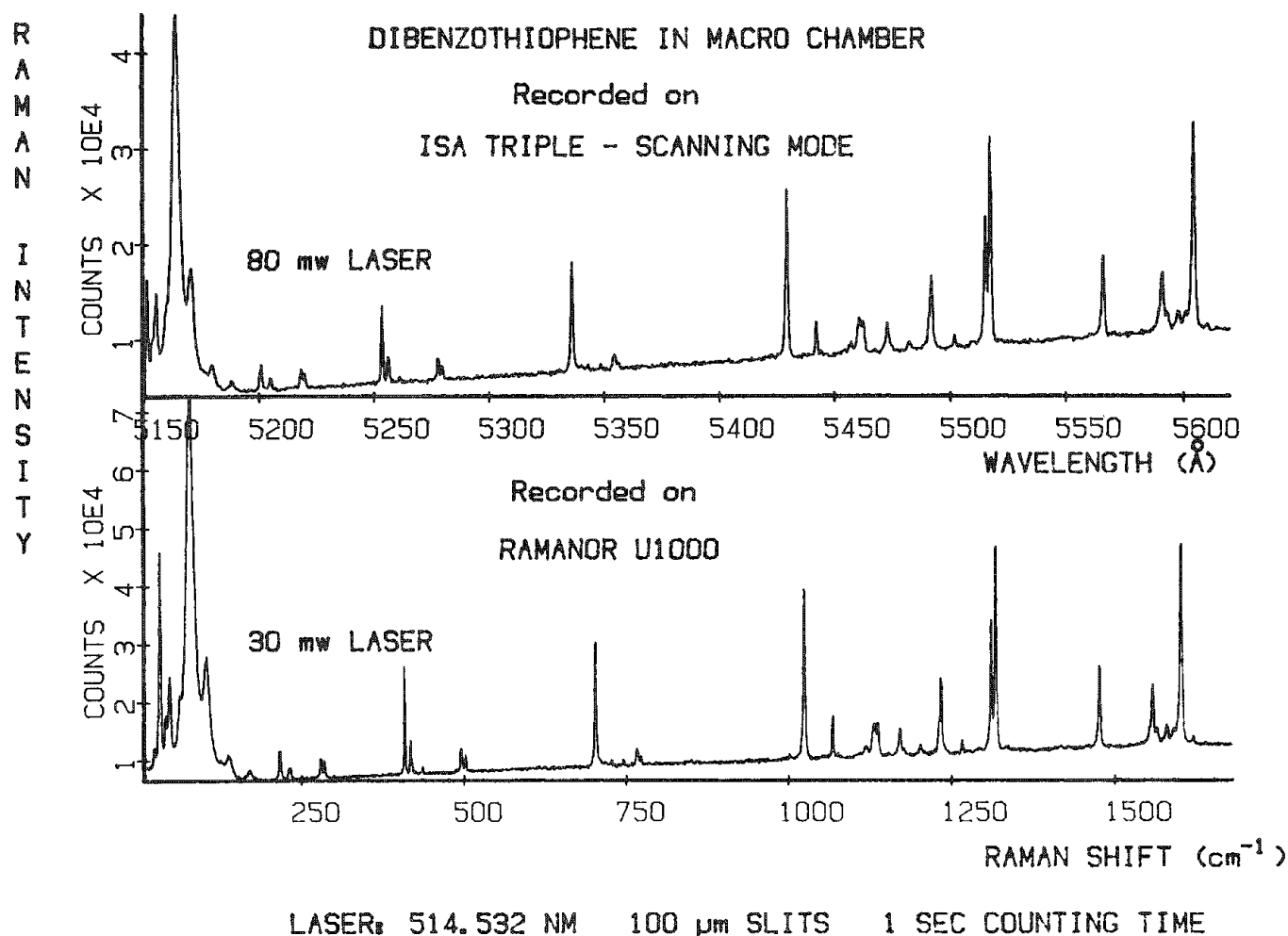


FIG. 2.--Raman spectrum of a pellet of dibenzothiophene recorded on triple spectrometer in scanning mode compared to spectrum recorded on the U1000.

Preliminary data recorded on the triple in the scanning and spectrograph modes show a gain in speed of recording spectra of about an order of magnitude.

Figure 3 shows three mercury lines through the triple spectrograph as detected by the diode array. The insert in the upper right of the figure shows the unprocessed data; the minimum detectable linewidth is 3-4 diodes, which is the specification for an intensified diode array.

Figure 4 shows data taken in the spectrograph mode of dibenzothiophene and sulfur in the macro and micro modes. Pellets were examined in the sample chamber and single particles (5-10 μm) were examined on the microscope stage.

Data Reformatting and Linearization

The computer on the system provides for reformatting of spectra taken with the multichannel detection system from the original presentation in linear diode spacing to either linear wavelength or wavenumber spacing. The algorithm describing the conversion is based on the focal length of the HR640 monochromator, the included angle at the grating, and the groove density of the grating.⁵ This conversion allows direct comparison between data in the multichannel mode with all standard published Raman data and with data acquired on the standard double monochromator whose scanning increments are constant-frequency intervals.

Figure 5 shows a diode array spectrum of dibenzothiophene compared to a spectrum recorded on the U1000 before and after linearization of the diode array spectrum. The bands in the reformatted file accurately overlay the bands in the Raman U1000 file.

In conclusion, it is to be anticipated that this new instrument design will enhance the usefulness of the Raman microprobe MOLE in industrial analytical laboratories where the ability to acquire molecular and/or crystalline information from unaltered microscopic samples rapidly will aid in product development and quality control.

References

1. F. Adar, *Microbeam Analysis--1981*, 67-72.
2. M. E. Andersen, *Microbeam Analysis--1984*, 115-120.
3. F. Adar, *Proc. 31st Sagamore Materials Research Conference*, August 1984 (to be published by Plenum).
4. T. Hirschfeld, *J. Opt. Soc. Am.* 63: 476-477, 1973.
5. M. Diem, F. Adar, and R. Grayzel (in preparation).

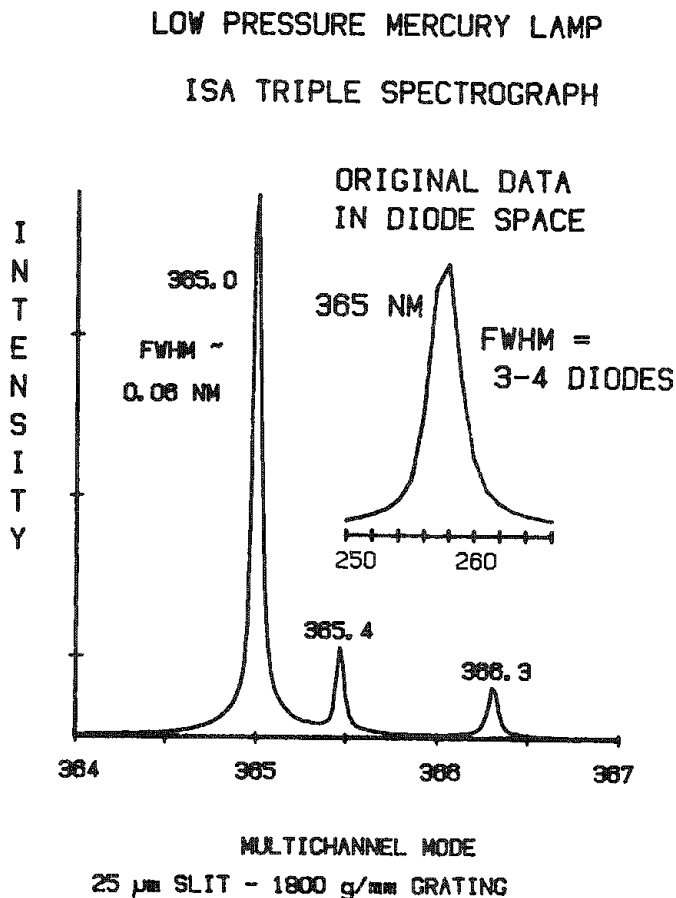


FIG. 3.--Mercury spectrum detected by diode array on triple spectrograph.

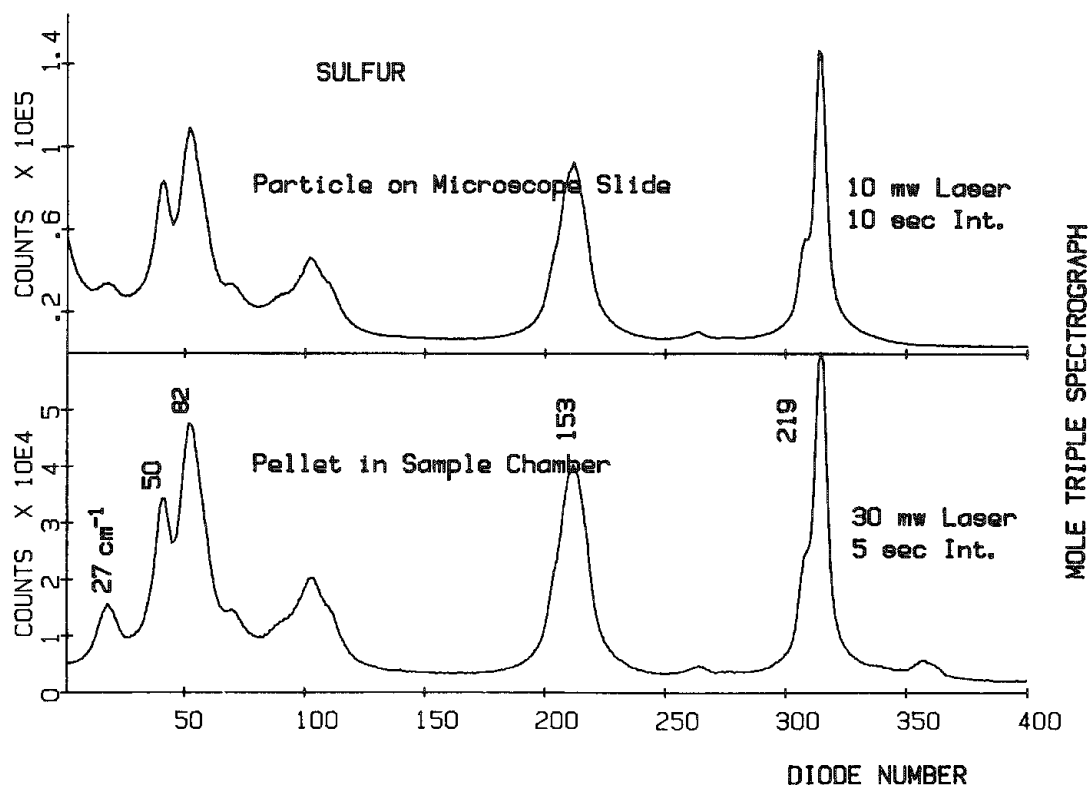
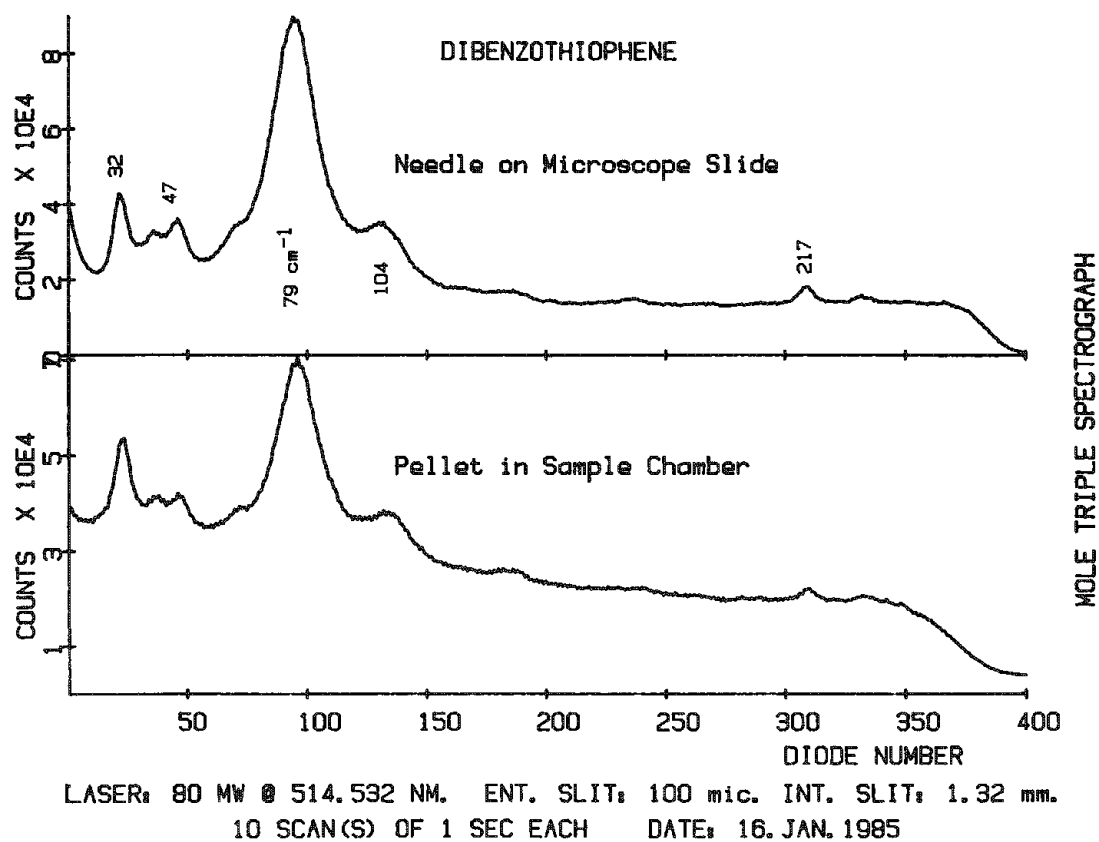


FIG. 4.--Micro vs macro spectra of (a) dibenzothiophene, (b) sulfur.

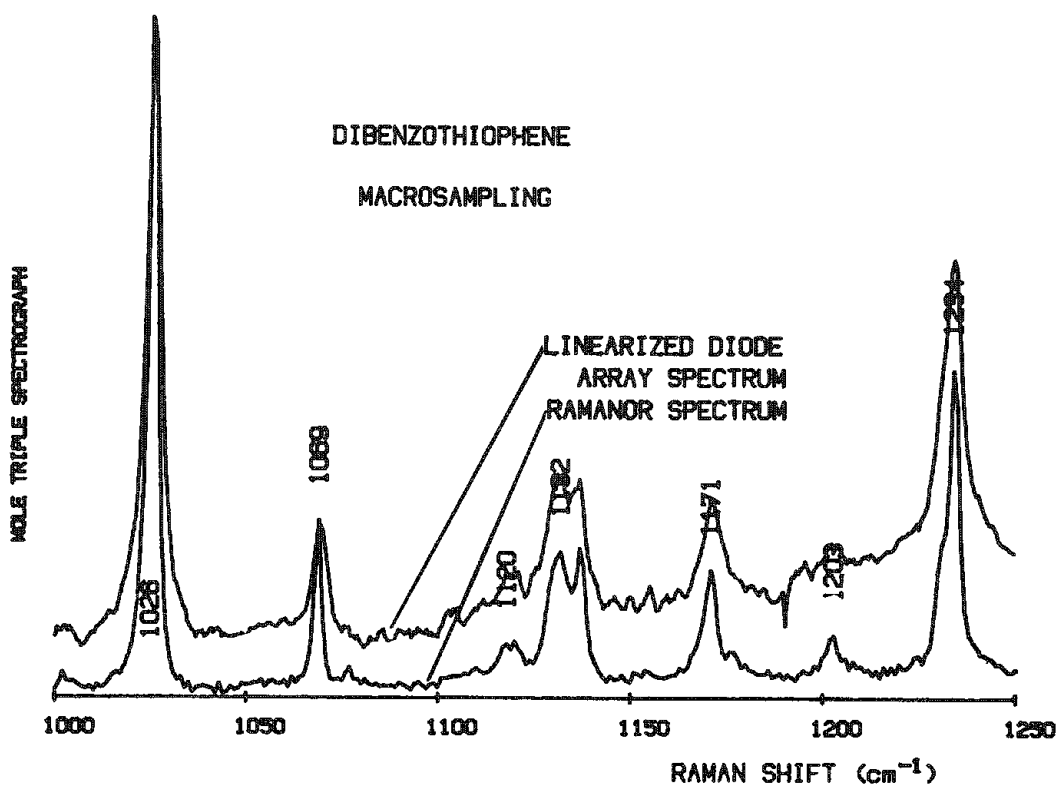
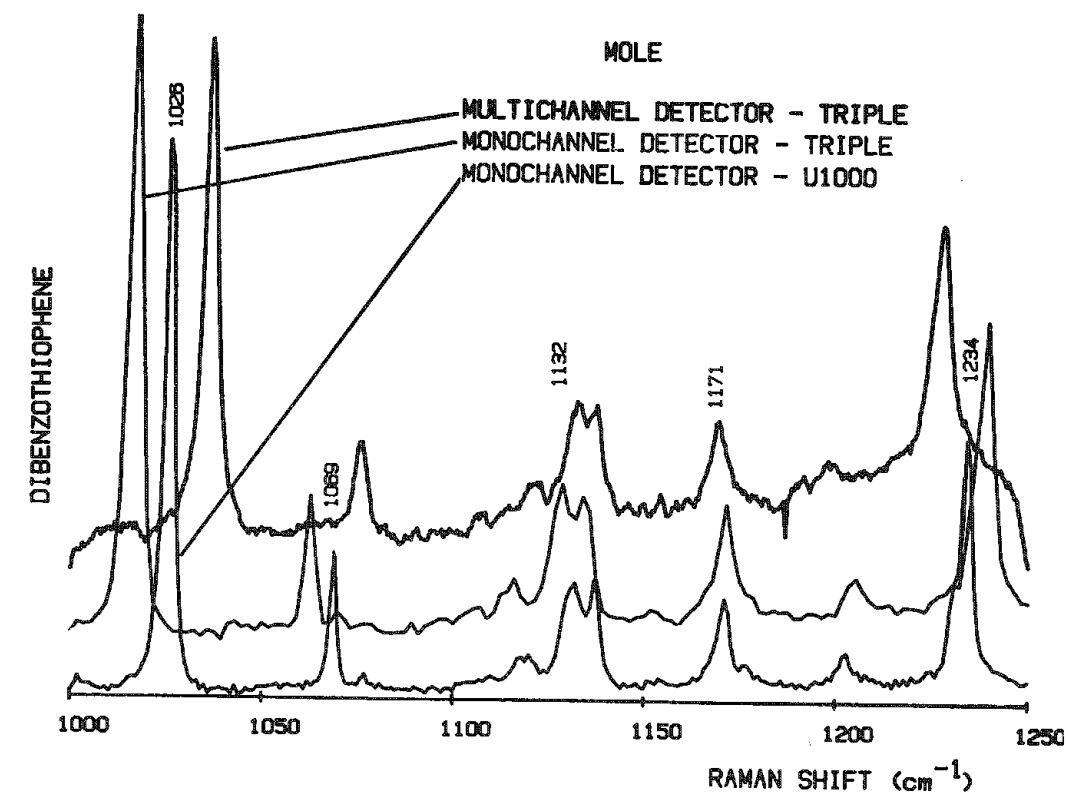


FIG. 5.--(a) Raman spectrum of dibenzothiophene recorded on Ramanor U1000 (bottom) compared to spectrum recorded on Triple MOLE in scanning mode (middle) and in multichannel spectrograph mode (top); (b) linearized diode array spectrum vs Ramanor U1000 spectrum.

COMPOSITIONAL INTERPRETATION OF SYNTHETIC C-O-H FLUID INCLUSIONS BY MICRO-RAMAN ANALYSIS AND MICROTHERMOMETRY

J. D. Pasteris, J. C. Seitz, and Brigitte Wopenka

Geologists attempt to determine the compositions of fluid inclusions (usually $< 100 \mu\text{m}$) in minerals in order to infer the chemical and physical conditions under which their host rocks crystallized or subsequently were altered.^{1,2} The conventional method of analysis is microthermometry. However, in recent years laser Raman microprobe (LRM) spectroscopy has proved to be a very useful technique³⁻⁸ for the detection and quantification of non-ionic species in fluid inclusions (e.g., CO_2 , CH_4 , H_2S , N_2). This paper compares the LRM and microthermometric results of synthetic fluid inclusions⁹ and illustrates how both techniques are needed to infer the bulk composition of a C-O-H fluid. This comparative study also helps to reveal some inherent weaknesses in assumptions underlying the application of both of these techniques.

Methods

In microthermometry, inclusion-bearing chips of the rock are cooled until the fluids solidify. The chip is slowly heated, and the equilibrium melting temperature T_m of the fluid is observed under a microscope. T_m is used to help identify the composition of the fluid. Although microthermometry is very useful for simple chemical systems, there are several limitations to this method: (1) The inclusions may be very small ($< 3 \mu\text{m}$) and/or optically unclear. (2) For complex mixtures of two or more compounds, fluid inclusions of exactly the same composition can have different T_m 's if their densities differ.¹⁰ (3) Small amounts of gas species frequently are not detected by microthermometry.

In LRM analysis, a monochromatic laser beam is focused through a microscope into a solid, liquid, or gas inclusion in a mineral. The Raman-scattered radiation within a narrow cone whose axis is 180° to the exciting beam is collected by a microscope objective, then passes through a double monochromator and is detected by a monochannel photon-counting system. Solid inclusions $\geq 1 \mu\text{m}$ and fluid inclusions $\geq 3 \mu\text{m}$ in diameter readily can be analyzed. Our instrument is a RAMANOR U-1000, manufactured by Instruments SA.

Synthetic C-O-H Fluid Inclusions

The C-O-H system includes, among others, the geologically important species CO_2 , H_2O , and CH_4 . In order to understand the behavior of these species in natural inclusions, Sterner and Bodnar⁹ prepared synthetic C-O-H inclusions of known bulk composition by healing fractures in Brazilian quartz. The fluid was generated from acetic acid plus water at 600 C and 3 kb in a closed hydrothermal system. The resulting synthetic fluid inclusions generally range from 2 to $50^+ \mu\text{m}$ in length and have excellent optical clarity. At room temperature, most of them contain an aqueous liquid (mostly H_2O with minor dissolved CO_2 and CH_4), a carbonic liquid ($\text{CH}_4 + \text{CO}_2$), and graphite (Fig. 1).

Sterner and Bodnar provided us with three different samples, each having different bulk compositions, which we initially intended to use as external standards to check our ability to do quantitative LRM analyses. Sterner and Bodnar subsequently determined that not all the inclusions from a single experimental run had the same microthermometric properties, such as melting and homogenization temperatures.¹¹ Furthermore, almost all the inclusions in each of the three samples contain visible graphite, but the bulk composition of the fluid had been calculated assuming the stoichiometric breakdown of acetic acid to produce only CO_2 and CH_4 . Thus, the bulk *fluid* composition was unknown and not what had been predicted. The inclusions could not be used as standards for quantitative LRM analysis, i.e., to check the accuracy of the analysis. However, they still could be used to check the precision of the method, after it subsequently was established by LRM

The authors are in the Department of Earth and Planetary Sciences at Washington University, St. Louis, MO 63130. They are grateful to Michael Sterner and Robert Bodnar for providing them with the C-O-H synthetic inclusions. This research was funded in part by NSF grant EAR-8408004 and by the McDonnell Center for the Space Sciences at Washington University.

analysis that all the inclusions in one chip (AA3) have the same bulk fluid composition. Only the results from chip AA3 are reported in this study.

Quantitative Micro-Raman Analysis

The LRM was used to obtain spectra of each of the three phases in 25 fluid inclusions. Particular interest was focused on the CO_2 - CH_4 molar ratio in the carbonic liquid (Fig. 1), a geologically important parameter.

Placzek showed that the relative molar proportions of two species in a homogeneous mixture vary *directly* with the ratio of the areas of their Raman peaks and *inversely* with the ratio of their Raman scattering efficiencies.¹² The Raman scattering efficiency of a certain vibrational mode is expressed as the relative normalized differential Raman scattering (RNDRS) cross section. These RNDRS cross sections have been determined experimentally relative to nitrogen for most gases of geological interest, and are tabulated.¹³⁻¹⁴

The scanning intervals in this study were 1370 - 1400 cm^{-1} for CO_2 (symmetric C-O stretching vibration at 1388 cm^{-1} for low-pressure gas phase) and 2900 - 2930 cm^{-1} for CH_4 (symmetric C-H stretching vibration at 2917 cm^{-1} for low-pressure gas phase). Peak areas (Fig. 2) were determined with an uncertainty of ± 3 relative % due to counting statistics. The instrumental reproducibility was excellent, since the uncertainty of the CH_4 - CO_2 peak area ratio was determined mainly by counting statistics.¹⁵ Application of Placzek's¹² formula and values for RNDRS cross sections for CO_2 and CH_4 from Schrötter and Klöckner¹³ produced consistent values of ~ 15 mole% CH_4 (15 ± 2 mole%) in the CO_2 - CH_4 liquid in fluid inclusions in three different regions of the synthetic chip. The uncertainty of this result is a function of the errors of the four variables, namely the two peak areas and the two RNDRS cross sections, as determined by error propagation.

These analysis results provide a strong confirmation that all the inclusions have the same CO_2 - CH_4 composition. The standard deviations of results among different inclusions do not differ significantly from those for repeated analysis of the same inclusions.¹⁵ However, the *exact* proportions of CH_4 and CO_2 are still unknown, and thus the accuracy of the result is questionable. The major uncertainties in a Placzek-type calculation are the values for the RNDRS cross sections of the species. First, there is at least a 10 relative % uncertainty in these values at 1 bar pressure, the condition at which these values were experimentally determined for gas phases. Second, our fluid inclusions are at 10's of bars pressure and are liquid. Third, the RNDRS cross sections are reported for a 90° scattering geometry, which applies to neither the RAMANOR U-1000 nor its predecessor, the MOLE. (Both instruments have a 180° scattering geometry.) Thus, the accuracy of the present results is not known.

Microthermometry Combined with Micro-Raman Analysis

As an independent check on the compositional information, microthermometry was done on the same inclusions that had been analyzed by the LRM. Two of the measured parameters are plotted in Fig. 3: melting temperatures T_m of the carbonic phase and temperature of homogenization T_{hb} of the gas bubble that forms in the carbonic phase upon cooling. It is clear from Fig. 3 that the T_m 's and T_{hb} 's are not the same for all the inclusions. However, as mentioned above, in a multicomponent system these temperatures reflect both composition and density.

Without the LRM analyses, the inclusions probably would have been considered different in composition. However, the consistent Raman data and the linear relationship of T_m vs

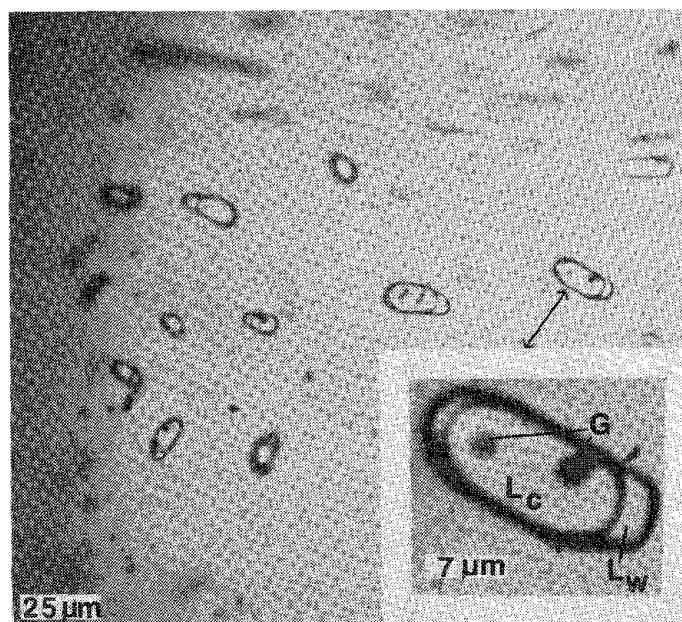


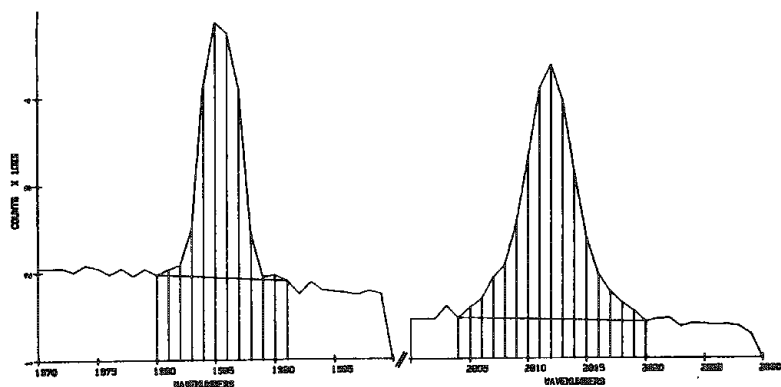
FIG. 1.--Photomicrograph of some of synthetic C-O-H fluid inclusions in quartz that were analyzed by both LRM and microthermometry. Central carbonic (CO_2 - CH_4) liquid (L_c). Envelope of aqueous liquid (mostly H_2O , with minor dissolved CO_2 and CH_4 ; L_w). Small black graphite particles (G).

CO₂

TOTAL AREA : 28771 +/- 170 COUNTS
 BACKGROUND AREA : 17955 +/- 284 COUNTS
 PEAK AREA : 10816 +/- 331 COUNTS

CH₄

TOTAL AREA : 37783 +/- 184 COUNTS
 BACKGROUND AREA : 22515 +/- 411 COUNTS
 PEAK AREA : 15248 +/- 435 COUNTS



LASER: 10 MW AT SAMPLE SURFACE @ 514 NM. SLITS: 500 MIC. 30 SECS/POINT. POINTS SPACED BY 1 WAVENUMBER

FIG. 2.--Peak area determinations for CO₂ (Fermi resonance of C-O symmetric stretching vibration) and CH₄ (C-H symmetric stretching vibration) in carbonic liquid phase of single synthetic fluid inclusion.

T_{hb} (Fig. 3) suggest that the inclusions have the same composition but somewhat different densities.

It is difficult to make a compositional interpretation of the above microthermometry data, because no reliable pressure-volume-temperature data are available for the system CO₂-CH₄-H₂O. The assumption was made that since there is little mutual solubility of the aqueous and carbonic components below room temperature, one could use experimental data for the subsystem CO₂-CH₄.¹⁰⁻¹⁶

Application of Swanenberg's method¹⁶ to the carbonic portion of these fluid inclusions (which involves estimating volumes of phases present in an inclusion at a standard temperature) produces a wide range of CH₄-CO₂ ratios (casting doubt on its applicability in the more complex system containing H₂O), many of which are in the range of 20-30⁺ mole% CH₄. The method of Burruss¹⁰ (which involves plots of T_m vs T_{hb}) was attempted, but our microthermometry data are not compatible with his diagrams for CO₂-CH₄ inclusions. However, Burruss¹⁰ had inferred that within the CO₂-CH₄-H₂O system, if, upon heating, the bubble in the carbonic liquid homogenizes (T_{hb}) before the solid clathrate (CO₂-H₂O phase) melts, then there probably is more than 20 mole% CH₄ in the carbonic liquid. This indeed describes the melting behavior in all inclusions analyzed in this study, where the clathrate melts at up to 25 C above T_{hb} . Thus, inferences from both the Swanenberg¹⁶ and Burruss¹⁰ studies suggest considerably *greater* than 20 mole% CH₄, rather than only 15 mole% as calculated from the LRM spectra by the Placzek method.

Conclusions

It has been known for several years that the LRM can provide semiquantitative analysis of nonionic species in fluid inclusions. The present study confirms how the combined use of LRM and microthermometric data can be helpful in constraining both compositional and density differences among inclusions. In the present study, in which it was known that only C-O-H species could occur, each technique also pointed out a weak assumption in the other.

It cannot be assumed that the ratio of the RNDRS sections for CH₄ and CO₂ remains the same at all pressures. It therefore certainly cannot be assumed that this ratio is the same for a liquid phase as it is for the low-pressure gas phase for which the ratio was experimentally determined. These two factors probably are the major reasons that the Placzek-type calculations on the LRM data consistently yielded low CH₄ ratios.

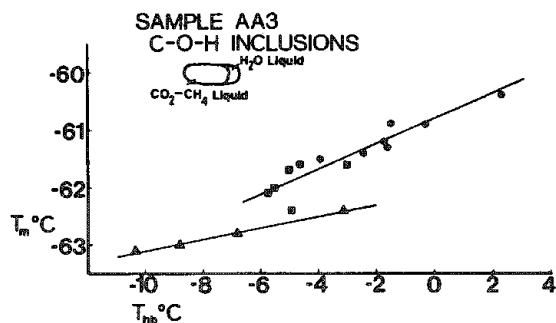


FIG. 3.--Plot of melting temperature T_m vs homogenization temperature of gas bubble T_{hb} in carbonic liquid of C-O-H synthetic fluid inclusions. Two lines are least-squares fits to inclusions in three different regions of same quartz chip, as indicated by three different symbols. All inclusions along same line are assumed to have same bulk fluid composition, but different densities. Why there are two distinguishable populations (lines) is under investigation.

Knowledge from the LRM data showed all the inclusions to have approximately the same CH_4 - CO_2 ratio, although the microthermometric parameters differed among inclusions (Fig. 1). This finding permitted confirmation of Burruss's¹⁰ statement that inclusions of the same composition can have different microthermometric parameters if they have different densities. It also permitted us to demonstrate that it is not a simple matter properly to interpret CO_2 - CH_4 - H_2O inclusions by use of data for the CO_2 - CH_4 subsystem.

This work again has confirmed that micro-Raman analysis and microthermometry are complementary analytical techniques and that both methods are needed for the compositional interpretation of C-O-H fluid inclusions. However, at the present levels of knowledge, the true composition (i.e., quantitative analysis) of the synthetic fluid inclusions cannot be determined with high accuracy by either method. RNDRS cross-section values applicable to geological problems (i.e., high-pressure gas and liquid phases) as well as reliable thermometric data for the CO_2 - CH_4 - H_2O system would be required to accomplish this.

References

1. L. S. Hollister and M. L. Crawford, Eds., *Short Course in Fluid Inclusions: Applications to Petrology*, Calgary: Mineralogical Association of Canada, 1981.
2. E. Roedder, *Fluid Inclusions*, Washington, D.C.: Mineralogical Society of America, 1984.
3. G. J. Rosasco et al., "Laser-excited Raman spectroscopy for nondestructive partial analysis of individual phases in fluid inclusions in minerals," *Science* 190: 557-560, 1975.
4. P. Dhamelincourt et al., "Analyse d'inclusions fluides à la microsonde MOLE à effet Raman," *Bull. Mineral.* 102: 600-610, 1979.
5. J. Dubessy et al., "The use of the Raman microprobe MOLE in the determination of the electrolytes dissolved in the aqueous phase of fluid inclusions," *Chem. Geology* 37: 137-150, 1982.
6. J. Dubessy et al., "Reconnaissance par microspectrométrie Raman, dans les inclusions fluides, de H_2S et CO_2 solides à domaine de fusion comparable," *Bull. Mineral.* 107: 189-192, 1984.
7. A. Cheilletz et al., "Les fluides moléculaires d'un filon de quartz hydrothermal: Comparaison de techniques analytiques ponctuelles et globales, contamination des fluides occlus par des composés carbonés," *Bull. Mineral.* 107: 169-180, 1984.
8. J. D. Pasteris et al., "Applications of the laser Raman microprobe RAMANOR U-1000 to hydrothermal ore deposits: Carlin as an example," *Econ. Geol.*, submitted 1984.
9. S. M. Sterner and R. J. Bodnar, "Synthetic fluid inclusions in natural quartz: I. Compositional types synthesized and applications to experimental geochemistry," *Geochim. Cosmochim. Acta* 48: 2659-2668, 1984.
10. R. C. Burruss, "Analysis of phase equilibria in C-O-H-S fluid inclusions," in L. S. Hollister and M. L. Crawford, Eds., *Short Course in Fluid Inclusions: Applications to Petrology*, Calgary: Mineralogical Association of Canada, 1981, 39-74.
11. S. M. Sterner and R. J. Bodnar, personal communication, 1983.
12. G. Placzek, "Die Rayleigh und Raman Streuung," in E. Marx, Ed., *Handbuch der Radiologie*, Leipzig: Akademische Verlagsgesellschaft, 1934, 209-374.
13. H. W. Schrötter and H. W. Klöckner, "Raman scattering cross-sections in gases and liquids," in A. Weber, Ed., *Raman Spectroscopy of Gases and Liquids*, New York: Springer-Verlag, 1979, 123-166.
14. W. R. Fenner et al., "Raman cross section of some simple gases," *J. Opt. Soc. Am.* 63: 73-77, 1973.
15. B. Wopenka and J. D. Pasteris, "Limitations to quantitative analysis of fluid inclusions in geological samples by laser Raman microprobe spectroscopy," *Appl. Spectros.*, submitted 1985.
16. H. E. C. Swanenberg, "Phase equilibria in carbonic systems and their application to freezing studies of fluid inclusions," *Contrib. Mineral. Petrol.* 68: 303-306, 1979.

SPATIALLY LOCALIZED TRANSIENT SPECTROSCOPY AS A PROBE OF LASER-INITIATED MICROCHEMISTRY IN THIN FILMS

G. J. Fisanick

Chemical reactions localized to the micron or submicron level have become of major interest in the microelectronics industry for repair and customization of lithographic masks and devices. Laser-initiated chemistry using beams focused to near diffraction-limited diameters has provided one technique for obtaining such features; in particular, we have focused on the local thermal decomposition of metallopolymer films for metal deposition. Using a modified Raman microprobe for generation of the laser-initiated reaction, we have simultaneously probed the reaction dynamics using spatially localized transient absorption and reflection spectroscopy. The reaction kinetics in these systems are complicated by the very rapid thermal ramping rates (up to 10^9 K/s) obtained when using highly focused laser beams for heating, a regime far from that normally accessible.

In addition, for cases where the local metal pattern is to be used for conduction, the purity of the remaining deposit (or equivalently the extent of reaction) is a major issue. Reaction profiles obtained by scanning Auger microscopy complement the dynamic measurements described above, and lend additional insight into the local reaction kinetics.

Experimental

An Instruments S.A. Raman Microprobe was the core apparatus for these experiments. We modified the system by replacing the viewing screen with a video monitoring system, adding 0.1 μ m Klinger computer-controlled stepping motor stages for rastering sample position, and introducing a polarizer at the microscope exit to direct the reflected light to an aper-tured fast photodiode. A second apertured photodiode was aligned with the transmitted laser beam. A gated OMA has been added to the system for future Raman or luminescence spectroscopy as well. The input optical train was also modified by inclusion of a Coherent Noise Reduction System, followed by an acoustico-optic modulator to provide variable width, sharp rise time (< 100 ns) pulses when triggered by a computer controlled BNC pulse generator, a NRC variable attenuator, and a spatial filter.

Besides the high-power 5145 Å Ar⁺ laser beam used to generate the chemical reaction (0-3 mW in a 0.8 μ m FWHM spot on target), a second weak HeNe (0.5 mW in a 1.2 m FWHM spot on target) probe beam was introduced through the input optical train, at a variable spatial offset (0-10 μ m) from the generating beam. We measured beam diameters in the focal plane by translating a sample with an abrupt (< 0.1 μ m width) reflectivity step through the beams. Color filters were used to select either pump or probe beam for presentation to the photodiodes. The transient signal from the photodiodes during reaction was digitized by a Le Croy/CAMAC transient digitizer, and averaged and plotted using a DEC 11/23 computer.

The material used for deposition of Au features was Engelhard NW Bright Gold Screen ink, consisting of a Au mercaptide and additional polymer binders. The material produces a homogeneous, uniformly thick brown glassy film when spun on substrates using a commercial spinner such as those used for deposition of photoresist. The film was prebaked at 90 C for 20 min to remove excess solvent and later written; then unreacted material was removed with a CH₂Cl₂ to leave behind adherent metallic-looking features, which were analyzed by scanning Auger microanalysis in a JEOL system.

Results

Typical laser-written features on a thin nonthermally conducting substrate are shown in Fig. 1, where the laser beam was CW, and the sample was rastered at variable speeds. A remarkable variety of structure is generated as a laser power and scan speeds are varied. This structure has been postulated¹⁻³ to result from the competition between the energy input from the laser, and the heat released from the highly exothermic oxidative pyrolysis of the metallopolymer. The heat released from the reaction causes the reaction front to propagate rapidly far beyond the laser-illuminated region, until it is quenched by thermal conduction losses. The scanning laser then catches up and reinitiates the reaction which

The author is at AT&T Bell Laboratories, Murray Hill, NJ 07974.

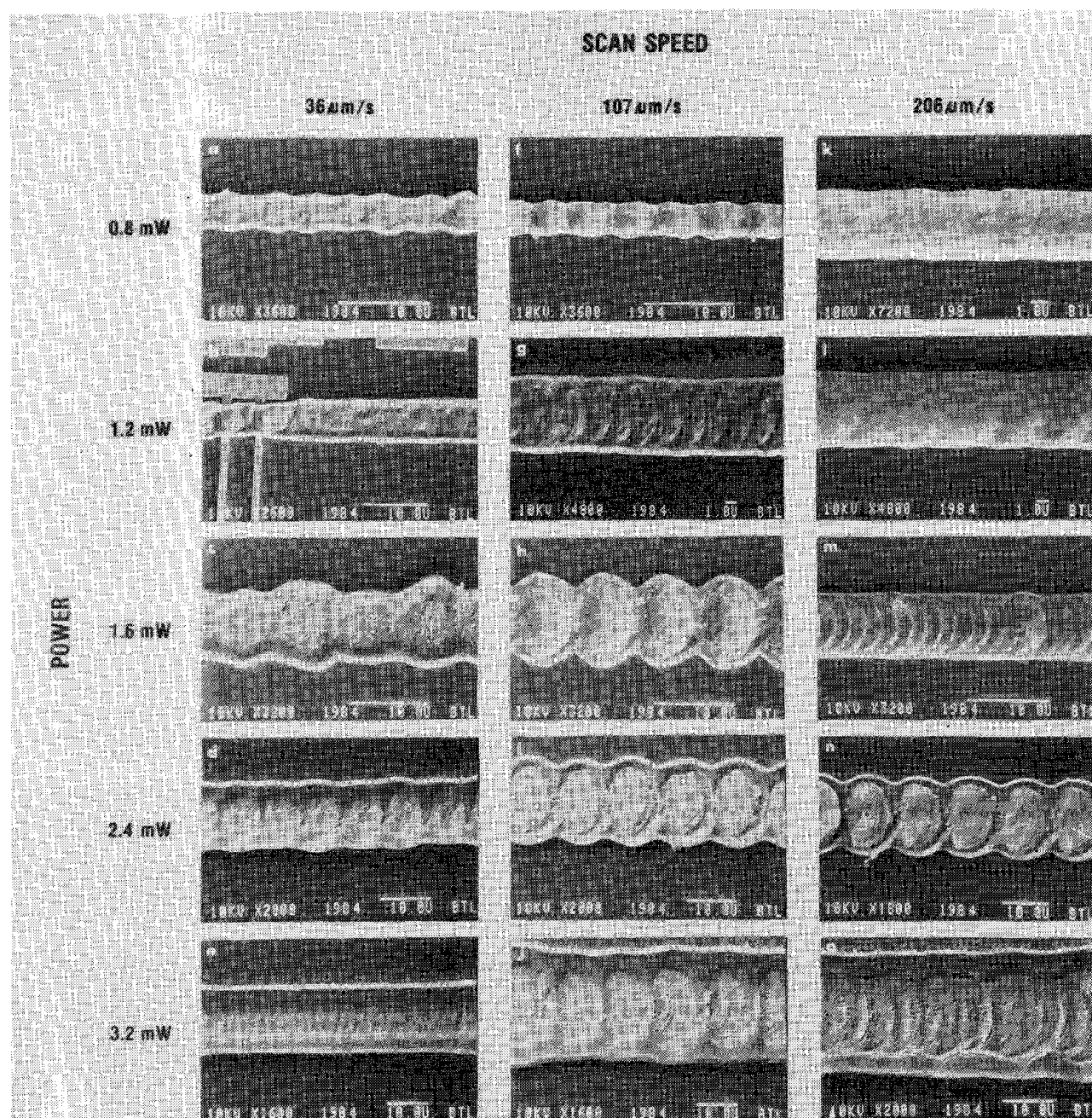


FIG. 1.--SEMs of periodic structure as a function of laser conditions; scan direction from left to right.

runs ahead; the process repeats indefinitely and leads to the strongly periodic structure observed.

In Fig. 2, the relation of this structure to reaction profiles is demonstrated by a comparison of an SEM of a periodic feature with an 8-tone Auger map of local carbon contamination. It is clear the Auger map can be superimposed on the periodic structure, and that reaction has nearly gone to completion at the center of the feature. Modification of the development conditions can remove the carbon contaminated feature wings.

The dynamical behavior of the system is illustrated in Fig. 3, where self-transmission data of the Ar^+ laser as a function of laser power are shown; and Fig. 4, where HeNe laser transmission as a function of distance is shown, both for a static pulsed exposure. In Fig. 3, the transmission initially falls as a function of time as an opaque deposit is formed. The decay rate is not simple exponential due to the thick film limit of the absorption, and to the heating during reaction. However, the reaction time scale is in the

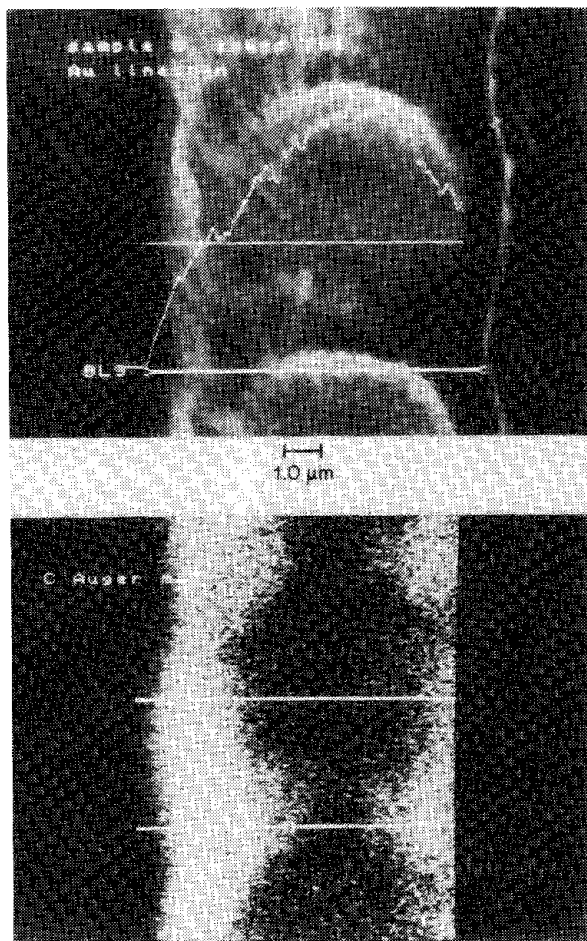


FIG. 2.--SEM and scanning Auger map of C concentration. Auger spot size is 0.3 μm .

3. G. J. Fisanick, J. B. Hopkins, M. E. Gross, M. D. Fennell, and K. J. Schnoes, "Laser-initiated microchemistry: Dynamic probes of metallopolymer thin film decomposition," *Appl. Phys. Lett.* (accepted for publication).

microsecond regime. At higher powers, for later times, the transmission increases, corresponding to material ablation at the center of the spot. At the highest power, Fig. 4 shows the spatially resolved dynamics. Ablation at the spot is still evident, but at larger distances from the center there is no increase in transmission at later times, the reaction rate slows, and there is a finite induction time prior to the onset of reaction. This time may be related to a reaction front velocity, which propagates outward at a rate of 0.3-0.5 m/s.

Conclusion

Clearly, dynamic measurements of spatially localized reactions, coupled with standard microanalysis techniques, can provide detailed information on reaction mechanisms. Spatially localized reactions on micron or submicron scales are becoming of even greater interest on the microelectronics community, and analysis techniques that can address these processes will be increasingly in demand.

References

1. G. J. Fisanick, M. E. Gross, J. B. Hopkins, M. D. Fennell, K. J. Schnoes, and A. Katzir, "Laser-initiated microchemistry in thin films: Development of new types of periodic structure," *J. Appl. Phys.* 57: 1139, 1985.
2. M. E. Gross, G. J. Fisanick, P. K. Gallagher, K. J. Schnoes, and M. D. Fennell, "Laser-induced deposition reactions: Microchemistry in thin organometallic polymer films," *Appl. Phys. Lett.* (accepted for publication).

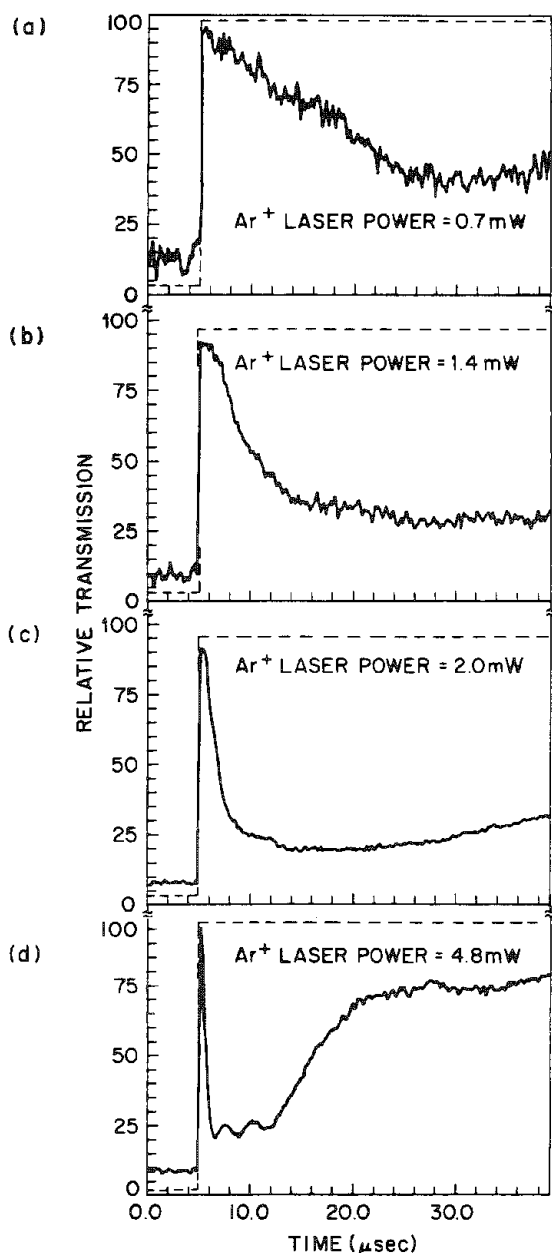


FIG. 3.--Transient self-transmission spectroscopy of Ar^+ generating laser as a function of laser power for stationary pulsed exposure. Increase in transmission in panel d at later times is due to ablation at center of spot.

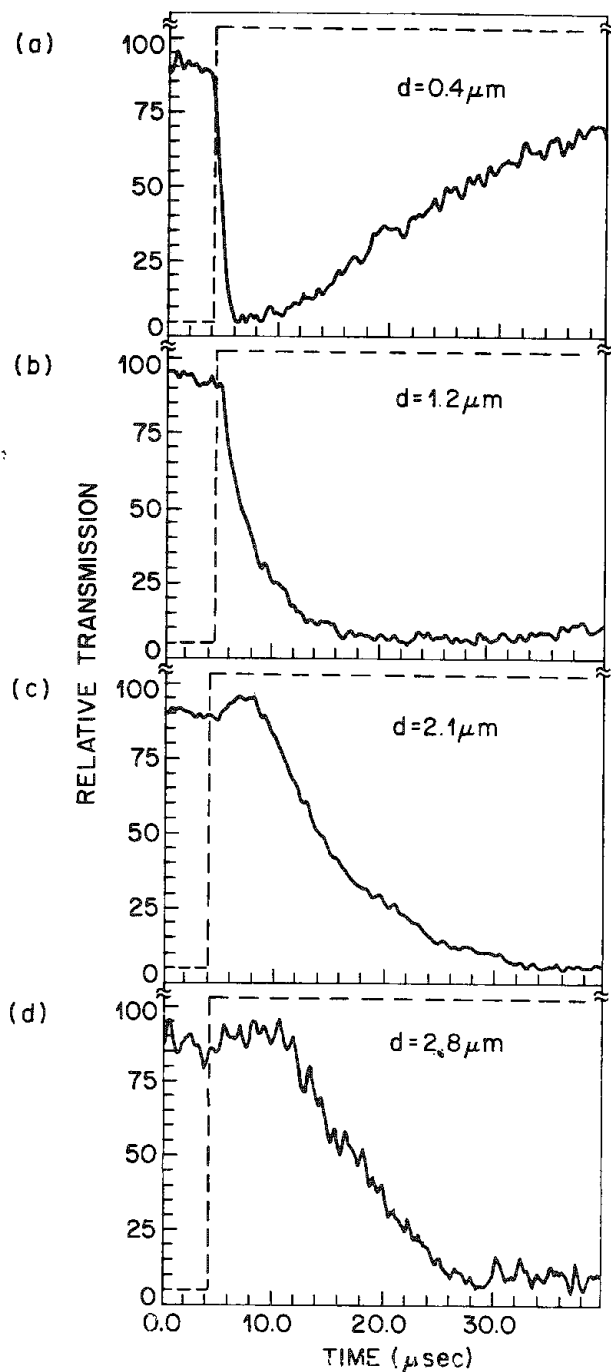


FIG. 4.--Spatially resolved probe transmission as a function of distance between generating and probe spots.

SINGLE-CRYSTAL POLARIZED RAMAN SPECTROSCOPY OF MICROSCOPICALLY ORIENTED CRYSTALLINE QUARTZ FRAGMENTS

M. E. Andersen and J. G. Delly

Polarized Raman spectra are often used to assign particular vibrational modes to peaks in the observed spectra. Such assignments can help determine, for instance, the orientation of a molecule within a crystal structure or polymer fiber. Quantitative measurements of band intensities as a function of single crystal orientation is of interest in the theoretical understanding of materials.¹ Studies of this kind have been made with standard Raman instruments, but only recently have Raman microprobe instruments been applied to polymer fibers²⁻⁴ and silicon.^{5,6} Raman microprobes allow measurement of polarized spectra with high spatial resolution. Some materials that are difficult to grow into crystals large enough for polarized macro-Raman measurements can now be analyzed by the Raman microprobe. In this paper we describe the procedure one can use to orient optically single crystals as small as about 10 μm ; polarized Raman data can subsequently be obtained.

Polarized-light Microscopy (PLM)

The single-crystal orientations used in the present Raman spectroscopic studies were made with the use of a polarized-light microscope, a spindle stage, and the principles of optical crystallography. To characterize optically homogeneous, transparent materials we need to take advantage of the fact that the refractive optical properties of such materials can be represented by three principal refractive indices, which are mutually at right angles to one another. In the case of substances crystallizing in the cubic system, the three refractive indices are numerically the same, and determining the value of that index n is sufficient to optically characterize the substance. For uniaxial substances crystallizing in the hexagonal or tetragonal systems, two principal refractive index values (ϵ and ω) need to be determined to characterize the substance. For biaxial materials crystallizing in the orthorhombic, monoclinic, or triclinic system, three principal refractive indices α , β , γ need to be determined. The relationship between the refractive indices and the crystallographic axes can be determined. The specific methods for accomplishing these tasks are described in several standard reference works on microscopy and optical crystallography.⁷⁻¹⁰ For the present study we are concerned primarily in locating the vibration directions within a single, morphologically imperfect (i.e., lacking well-formed faces and angles; comminuted) uniaxial quartz particle, and maintaining those vibration directions in known orientations for the purpose of conducting Raman spectroscopic studies along known crystallographic planes. This procedure is applicable to any hexagonal or tetragonal transparent material.

Crystal orientation is achieved through the use of a spindle stage on the rotating stage of a polarized-light microscope. Figure 1 illustrates the various freedoms of motion available. The principles and practice of the spindle stage have been described by Bloss.¹¹ The spindle stage is about 3.8 \times 5.0 cm at the base, with a 180° protractor mounted upright at one end. A needle holder made from stainless-steel hypodermic needle tubing is bent to a right angle and forms a handle that travels around the protractor. The protractor scale is graduated in 5° intervals with detents. In rotating the handle, it clicks into the detents, indicating the number of degrees the needle holder is being rotated. The actual spindle consists of a fine embroidery needle, which fits into the needle holder. The crystal is mounted on the tip of the needle with a minimum of flexible collodion in amyl acetate; a stereomicroscope is used to observe the process. Thus, rotating the handle around the protractor allows for rotating the crystal 180° about the spindle axis. The spindle stage (which is available commercially from Technical Enterprises, 2008 Carrol St., Blacksburg, VA 24060) allows room for a microscope slide so that if desired the crystal may be immersed in liquids (e.g., water for cooling, refractive-index liquids, etc.) and covered with a coverglass while still being capable of being rotated. From

The authors are at Walter C. McCrone Associates, Inc., Chicago, IL 60616.

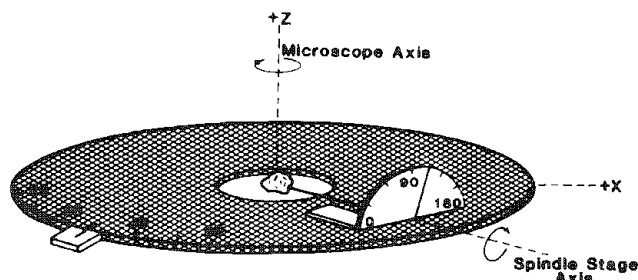


FIG. 1

Fig. 1 it will be seen that, because the spindle stage is fastened to a rotating, graduated microscope stage, the entire apparatus bearing the crystal may be rotated 360° about the vertical microscope axis. Between these two rotations, crystals may be properly oriented.

To illustrate the crystal orientation procedure step by step, we have constructed a model spindle stage and crystal. Alpha-quartz is a uniaxial, positive material with two principal refractive indices, $n_D = 1.5533$ (ϵ)

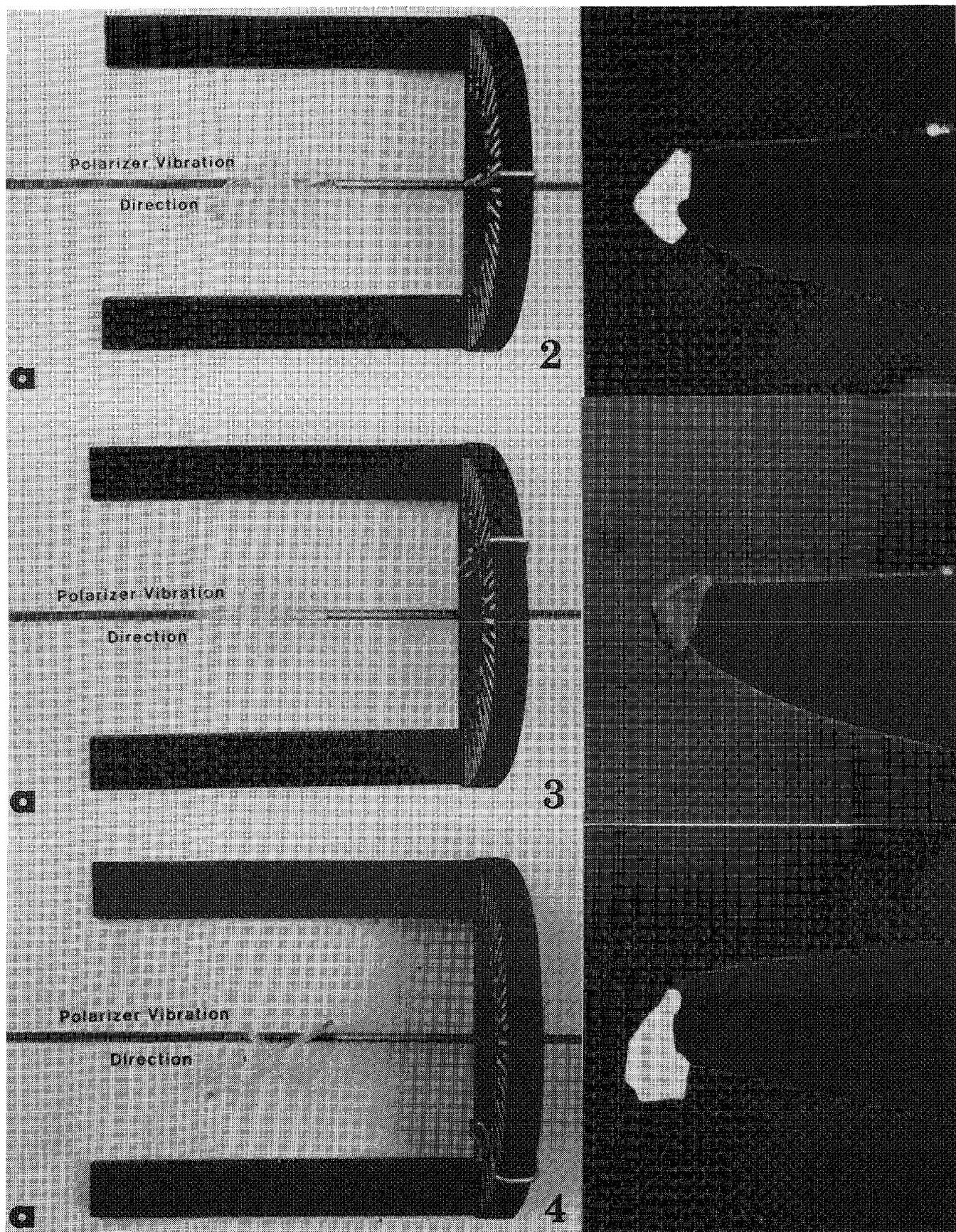
and $n_D = 1.5442$ (ω). We have used Fletcher's concept of the uniaxial indicatrix as an ellipsoid of revolution in constructing the plastic model of the crystal.

Figure 2(a) represents the quartz crystal attached to the needle tip with adhesive. The "crystal" has been mounted in the worst possible case (that is, the needle axis direction does *not* correspond to any crystallographic axis), and the spindle handle has been initially set straight up, at 90° . Figure 2(b) is an actual photomicrograph showing the microscopical appearance of just such a randomly mounted and oriented, comminuted quartz grain, as it is seen between almost fully crossed polarizers. (In actual practice, the polarizers are fully crossed, but are here very slightly uncrossed so as to demonstrate the needle position relative to the crystal.) Under these conditions, the anisotropic nature of the birefringent crystal is evident as a lighted object against a black background; the actual colors are a function of the birefringence (i.e., the numerical difference between the refractive indices, 0.009 for quartz) and the thickness of the crystal. Neither vibration direction corresponds (i.e., is parallel) to the East/West vibration direction of the microscope's substage polarizer.

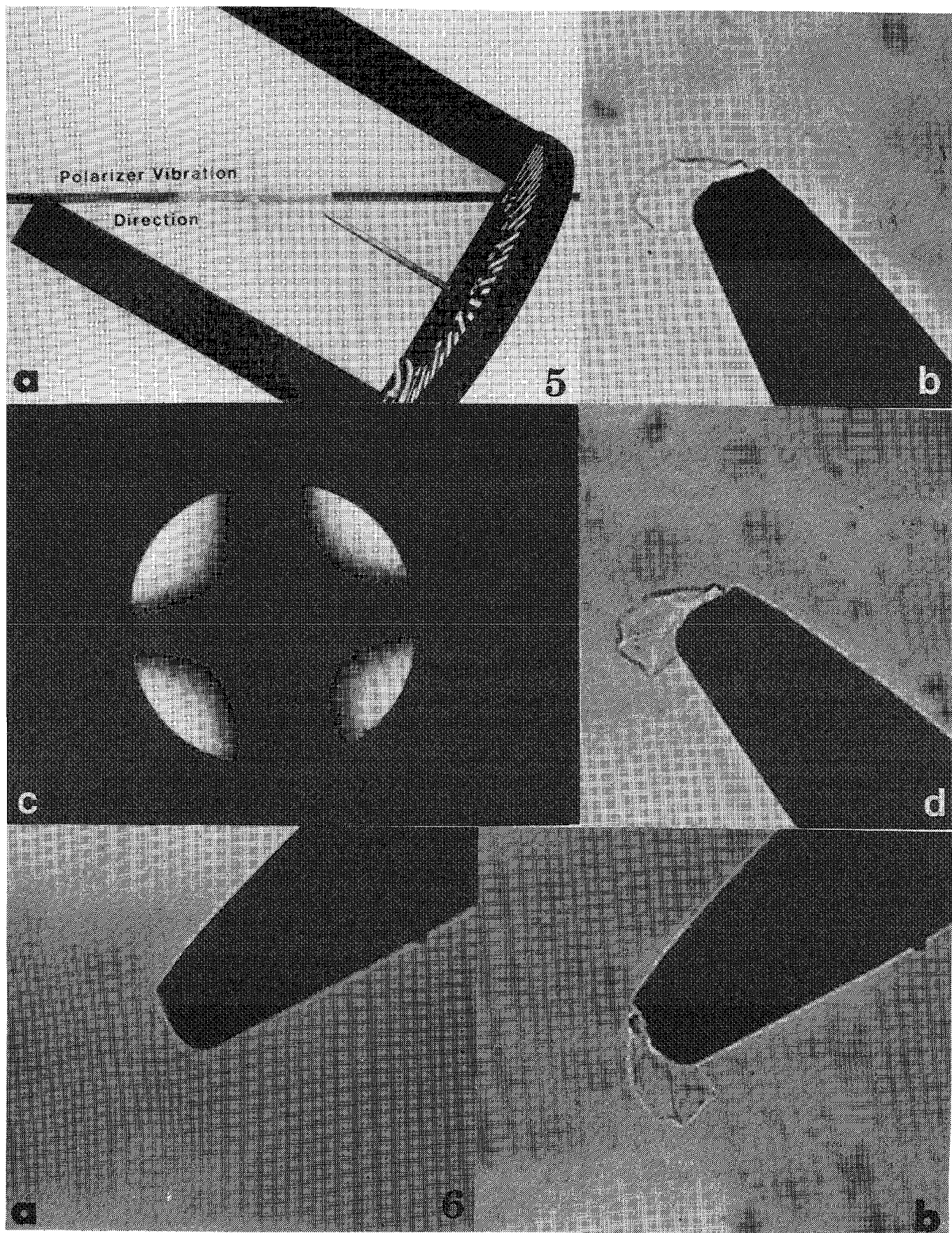
Next, the handle is rotated around the protractor in either direction while the crystal is kept under observation between fully crossed polarizers. The handle is rotated until the crystal comes to extinction and the entire field of view is black, as happens when one of the crystal's vibration direction corresponds to that of the polarizer or analyzer. Figure 3(a) shows this condition; the major axis of the model is parallel to the polarizer vibration direction. Figure 3(b) is the microscopical appearance (again, the analyzer has been slightly uncrossed so as to outline the crystal and needle). This step aligns one of the vibration directions; the other is 90° from this point. The spindle stage protractor reading is now made (note handle position in Fig. 3a) and then the handle is rotated exactly 90° from that reading. Figure 4 shows (a) the new crystal model position and (b) the microscopical appearance.

The final step, after the handle has been rotated 90° from the first extinction position, is to rotate the microscope stage that bears the spindle stage, while observing the crystal between fully crossed polarizers until it again becomes extinct (i.e., field of view completely black). Figure 5(a) shows that this occurs when now both crystal principal vibration directions exactly correspond to the polarizer and analyzer vibration directions; compare Figs. 5(a) and 2(a). Figure 5(b) is the microscopical appearance. In this orientation, ϵ and ω lie in the plane of the field of view, and the conoscopic appearance (i.e., with Bertrand lens or phase telescope inserted) is that of an optic normal flash figure, ideally illustrated in Fig. 5(c).

We have seen how to orient a uniaxial crystal (quartz) so that both ϵ and ω lie in the plane of the field of view, but we still do not know which is which; i.e., does ϵ lie North/South or East/West? To answer this question we select a refractive index liquid whose value lies between ϵ and ω (say, $n_D = 1.549$) in which to mount the crystal originally. Then, with the analyzer OUT and with a Sodium D (589nm) filter in the light path, the aperture diaphragm is closed and we focus UP (i.e., increase distance between objective and specimen). A halo of light surrounding the crystal when in best focus, on focusing up, moves either *into* the crystal or *outward* into the surrounding mounting medium. The halo always moves in the direction of higher refractive index (the Becke test). Figure 5(d) illustrates this procedure with the crystal left as in Fig. 5(a) and 5(b). The halo has moved into the crystal indicating that the *higher* refractive index (ϵ) is parallel to the East/West oriented polarizer, i.e., the 1.5533 direction in the crystal is East/West; the other vibration direction is perpendicular, and although one need not do



FIGS. 2-4



FIGS. 5 and 6

so, we illustrate that by taking a reading from the microscope graduated stage with the crystal as in Fig. 5(d), then rotate the microscope stage bearing the spindle stage 90° , so that the microscopic appearance is that of Fig. 6(a). Again applying the Becke test, we see (Fig. 6b) that the halo moves outward, indicating that with the crystal oriented thus, the refractive index of the liquid is higher than that of the crystal, which is to say the smaller (ω) refractive index direction, 1.5442, now lies East/West. In practice, it is enough simply to rotate the stage back and forth to see the Becke line cross over the crystal boundary first into and then away from the crystal.

With the vibration directions known, the Raman spectroscopic studies may now be conducted with confidence as to crystal orientation. We have selected a $40\mu\text{m}$ crystal to illustrate this step-by-step orientation procedure. In practice, we have gone down to $10\mu\text{m}$ crystals and have found no difficulty in making the observations necessary to orient the crystal. This orientation procedure may be applied to any uniaxial crystal; a different procedure for biaxial materials is necessitated by the two optic axes and the need to consider three principal refractive indices.⁷

Raman Spectroscopy

Figure 7 is a schematic definition of the laboratory frame of reference with regard to the light path for the MOLE® Raman Microprobe. The electric vector of the laser was oriented for maximum reflectance from the beam splitter; that is, the electric vector was parallel to y in the laboratory frame of reference. The presence of the beam splitter can seriously affect the polarization measurements and for quantitative work its effects must be compensated. The analyzer is placed in a plane of the collected beam where the light rays diverge only slightly. A polarization scrambler (quartz wedge) is placed immediately after the analyzer to minimize the polarizing effect of the gratings. Finally, an aperture diaphragm is placed in the enlarged conjugate image plane of the microscope objective back focal plane. This aperture diaphragm can be closed to limit the effective numerical aperture (NA) of the objective. An adjustable aperture diaphragm gives the spectroscopist two additional analytical advantages: first, the presence of this aperture eliminates stray light which may be introduced when a microscope objective is used that is not optically matched to the system.^{2,12} For instance, when a $50\times/0.85$ NA objective is used, the Raman signal increases as the numerical aperture increases (Fig. 8) until the gratings are filled. Any further increase in the numerical aperture (beyond NA:0.77 in this example) results in additional stray light with no increase in the Raman signal. In polarized Raman spectroscopy, the high numerical aperture of the microscope objective introduces an error in the measurement. This error has most recently been discussed with regard to Raman microprobes by Turrell.¹³ Using the relationships derived in that paper one can maintain high numerical aperture optics and the resultant small spot size, and correct the measured signal. Alternatively, if the signal is sufficiently intense one can reduce the effect of the high numerical aperture of collection by closing down the aperture diaphragm.

Quartz was the material selected for this Raman study because it is uniaxial and has been well characterized in previous studies on a macro scale.¹ The mounted crystal is oriented so that the y axis of Fig. 7 (that is, the electric vector of the laser) is parallel to the c axis of the crystal. A $50\times/0.85$ NA objective was used and the crystal was first examined in air. Two spectra were recorded with the analyzer rotated 90° between spectra (Fig. 9). It is evident that the discrimination between polarized features in this figure is quite poor. A number of hypothetical reasons for this lack of discrimination can be considered. Certainly a minor effect arises from the polarization scrambling of the objective.¹³ Other effects might be attributed to the birefringence of the crystal affecting the polarization of both the incoming laser beam and the Raman scattered radiation. In addition, the material is optically active, which would also affect the polarization of the incoming and outgoing beams. Considering the very small volume that is excited in quartz with a highly focused laser beam (of the order of a few micrometers with this objective) such effects are unlikely to cause the significant polarization scrambling observed in these spectra. Rather, the most likely explanation is due to the scattering of the light by the very rough surface of the crystal itself. In order to eliminate this scatter one should immerse the crystal in a liquid whose refractive index very nearly matches that of quartz; that is, around $n_D = 1.55$. However, such immersion liquids have Raman spectra that can be relatively intense, or they may be

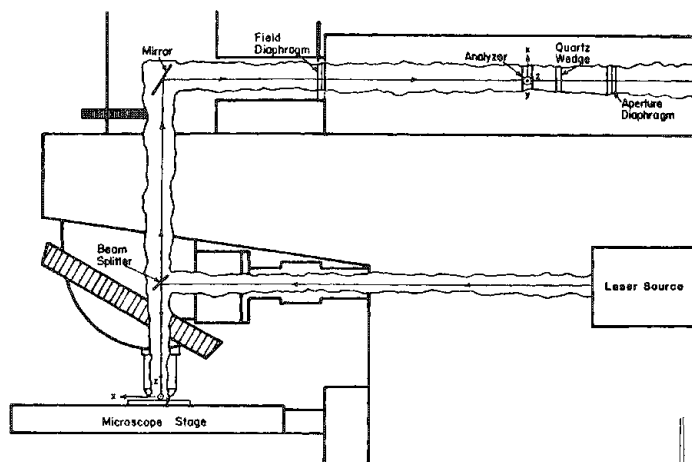


FIG. 7

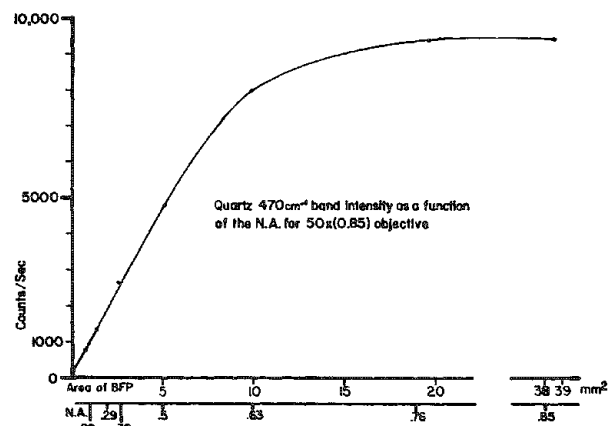


FIG. 8

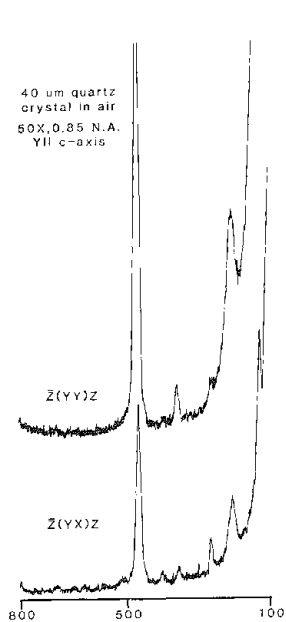


FIG. 9

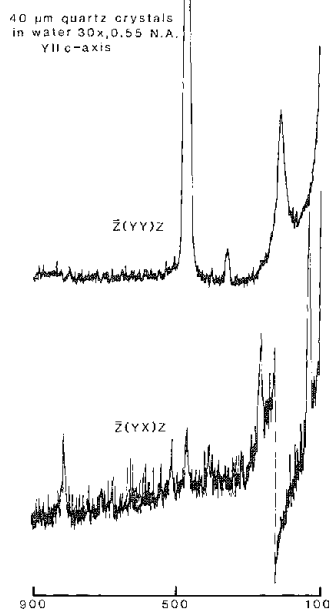


FIG. 10

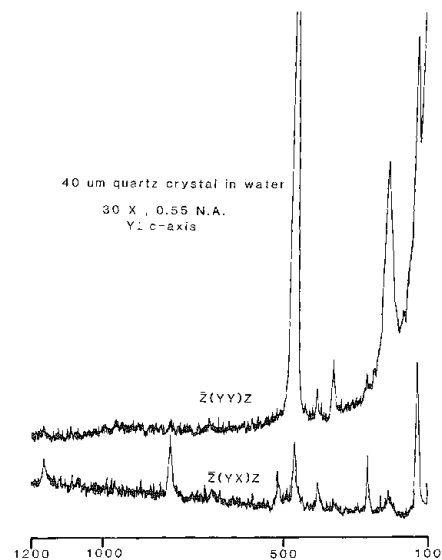


FIG. 11

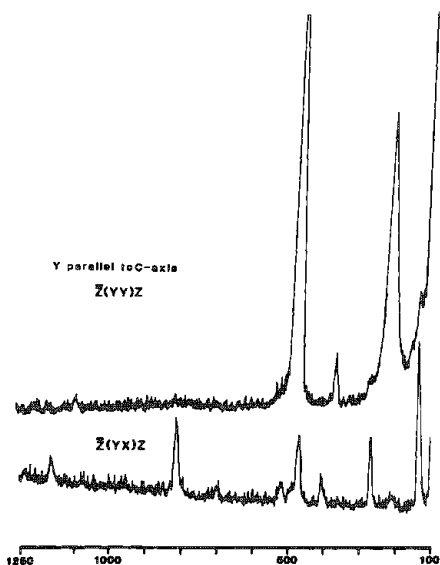


FIG. 12

fluorescent and interfere with the measurement. An ideal immersion liquid for Raman measurements is water with a refractive index of $n_D = 1.33$. Although this value does not match the immersed crystal, it significantly cuts down light scatter when compared to air (refractive index $n_D = 1.00$). Thus the crystal was immersed in water and examined through a cover glass. In order to record a Raman spectrum from the crystal, a long working distance objective (a Nikon 30 \times /0.55 NA with correction collar) had to be used since the working distance of the 50 \times objective was inadequate for examination through a cover glass. The resulting spectrum is shown in Fig. 10. In the top figure the A_1 modes are shown; in the bottom, the E modes. Any misorientation of the crystal or polarization scrambling is indicated by leakage of the most intense A_1 mode into the bottom spectrum. This band at 464 wavenumbers is present in the lower spectrum but its intensity is quite low. In Fig. 11, the microscope stage has been rotated 90° and two additional Raman spectra have been recorded. In this orientation both A_1 and E modes are present in the upper spectrum, whereas in the lower spectrum only the E modes are detected, although there is still a small amount of leakage due to some misalignment or polarization scrambling.

A second crystal, also examined in detail, was a naturally rounded grain of quartz sand, the surface of which was much less light scattering than the previous crystal. The polarized Raman spectra of this sample were recorded immersed in air with the 50 \times /0.85 NA objective. Some polarization scrambling has obviously occurred (Fig. 12) as evidenced by a leakage of the 464 wavenumber quartz band into the lower spectrum, but the smoother surface of this sand grain has minimized the deleterious effects of the light scatter

Conclusion

With the use of standard polarized-light microscopical techniques and a spindle stage, randomly shaped and oriented, uniaxial birefringent crystals as small as 10 μ m in maximum dimension have been oriented for polarized Raman microprobe measurements. Although spindle stage sample orientation procedures have been previously applied on a routine basis to x-ray diffraction, this is the first time these procedures have been applied to Raman spectroscopy. Any small biaxial transparent single crystal can similarly be crystallographically oriented for polarized Raman microprobe analyses. With the recent application of multichannel detection systems to Raman spectroscopy, crystal orientations can be monitored and optimized in "real time."

References

1. J. F. Scott and S. P. S. Porto, "Longitudinal and transverse optical lattice vibrations in quartz," *Phys. Rev.* 161: 903, 1967.
2. M. E. Andersen and R. Z. Muggli, "Microscopical techniques with the molecular optics laser examiner Raman microprobe," *Anal. Chem.* 53: 1772, 1981.
3. B. W. Cook and G. D. Ogilvie, "Microanalysis of industrial polymers by Raman spectroscopy," *Microbeam Analysis--1982*, 294.
4. M. E. Andersen, "Molecular optical laser examiner (MOLE) application to problems encountered by electron microscopists in the analysis of polymers," in C. D. Craver, Ed., *ACS Advances in Chemistry Series, No. 203 Polymer Characterization: Spectroscopic, Chromatographic, and Physical Instrumental Methods*, Am. Chem. Soc., 1983, 383.
5. J. B. Hopkins, L. A. Farrow, and G. J. Fisanick, "Raman microprobe determination of local crystal orientation in laser annealed silicon," *Appl. Phys. Lett.* 44: 535, 1984.
6. S. Nakashima, Y. Inoue, and A. Mitsuishi, "The evaluation of the crystallinity of laser annealed polycrystalline silicon-on-silicon structures by Raman microprobe polarization measurements," *J. Appl. Phys.* 56: 2989, 1984.
7. F. D. Bloss, *An Introduction to the Methods of Optical Crystallography*, New York: Holt, Rinehart and Winston, 1961.
8. N. H. Hartshorne and A. Stuart, *Crystals and the Polarizing Microscope*, London: Edward Arnold, 1970, 4th ed.
9. W. C. McCrone, L. B. McCrone, and J. G. Delly, *Polarized Light Microscopy*, Ann Arbor, Mich.: Ann Arbor Science Publishers, 1978.
10. E. E. Wahlstrom, *Optical Crystallography*, New York: Wiley, 1960, 3d ed.
11. F. D. Bloss, *The Spindle Stage: Principles and Practice*, New York: Cambridge University Press, 1981.

12. P. Dhamelincourt, "Instrumentation and recent applications in micro-Raman spectroscopy," *Microbeam Analysis--1982*, 261.
13. G. Turrell, "Analysis of polarization measurements in Raman spectroscopy," *J. Raman Spectros.* 15: 103, 1984.

RAMAN MICROPROBE SPECTRA OF SPIN-ORIENTED AND DRAWN FILAMENTS OF POLYETHYLENE TEREPHTHALATE: CONFORMATION, ORIENTATION, AND CRYSTALLIZATION

Fran Adar and H. Noether

Polarized Raman spectra of single filaments of spin-oriented and drawn fibers of polyethylene terephthalate were recorded. Because the degrees of crystallinity and orientation were known from x-ray diffraction (XRD), density, and optical birefringence, it became possible to identify features of the Raman spectra which correlated with (1) orientation of the chains and (2) crystallinity, and (3) to monitor independently the conformation of the glycol linkage.

The degree of orientation, as a function of take-up speed or draw ratio, was correlated with the intensity ratios of the various polarization components.

The width of the carbonyl band, which is the classical indicator of the amorphous or crystalline character of PET, correlated well with the known degree of crystallinity of the samples examined.

The appearance and increases in intensity of bands due to transglycol conformations and the disappearance of the gauche bands with increasing orientation could be followed readily. It appears that some of the Raman bands earlier assigned to crystallinity in PET actually represent the transconformation of the glycol group as is observed in IR spectra. This conclusion is based on the observation that in spin-oriented amorphous materials, the transconformation bands increase in intensity in parallel with increasing birefringence. A cold-drawn amorphous highly oriented fiber shows these same transconformation bands with high intensity. But the width of the carbonyl band in this same fiber confirmed the amorphous nature of this sample.

X-ray diffraction (XRD) studies¹ of polyethylene terephthalate (PET) show that in the crystalline form, molecular chains are aligned so that the glycol units between aromatic rings are in the all-transconformation, the carbonyl units are coplanar with the rings, and all aromatic rings are parallel but with each successive unit slightly displaced in a direction normal to the ring (Fig. 1). In principle, all C-C and C-O bonds between the aromatic groups allow some rotational freedom which may occur in noncrystalline material. Our present understanding of the crystallization process assumes that the ethylene glycol units align in the all-transconformation and that the carbonyl groups rotate into the aromatic planes. X-ray diffraction can quantify the degree of orientation of crystalline material; optical birefringence can measure total orientation,² and that of both amorphous and crystalline material. Although it is possible to prepare samples with close to 100% uniaxial orientation (the polymer axis almost parallel to the macroscopic axis and no orientation order perpendicular to this axis), the most highly crystallized samples are only approximately 50% crystalline. Because oriented noncrystalline material cannot be studied by XRD, other methods such as birefringence and vibrational spectroscopy have also been used to characterize orientational amorphous and crystalline features of PET.

The aim of this project was the study of a series of PET yarn samples of both drawn and spin-oriented materials in order to aid in correlation of their structural and morphological characteristics with physical properties.

In this work we have recorded polarized Raman spectra of individual spin-oriented and drawn filaments of PET. Systematic comparison of spectra shows the development of orientation and crystallization of the polymer. Reliance on band assignments of previous authors makes it possible to separate features due to molecular alignment, conformation, and crystallization.³ It will become clear that the orientation of the polymeric chains can be monitored independent of the crystallization, which occurs subsequent to orientation in the spin-line.

The data presented in this work were acquired from single filaments approximately 20 μm diameter) positioned on a microscope stage where the beam waist was 1 μm and the

Author Adar is at Instruments SA, Inc., Metuchen, NJ 08840; author Noether is at the Textile Research Institute, Princeton, NJ 08542. They wish to thank Drs. Heuvel and Huisman (Enka, The Netherlands) for providing the samples and some of their physical characterization. They also thank Sigrid Ruetsch (TRI) for her birefringence measurements and Otto Burkhardt (Celanese) for the density data.

depth of focus approximately 10 μm . The ability to acquire polarized RMP spectra of single filaments has been previously documented.^{4,5} Spectra of various polarization combinations from a single spot on a given fiber were acquired and intensity ratios compared to those of fibers spun under other conditions. Because these measurements were not totally analogous to those of earlier workers, the underlying rationale must be described explicitly.

Rationale of Polarized Raman Measurements of Spin-oriented Fibers

In an oriented system, the laser and Raman polarizations can be aligned along molecular/crystalline axes. In such cases it is common for certain asymmetric vibrations to have higher intensities for off-diagonal components. In addition, in uniaxial systems the diagonal intensities along different directions can be quite different.

The Z axis of these samples is defined as the macroscopic fiber axis. We define an R axis as one of the radial directions (perpendicular to Z). There are three independent measurements that can be made on fibers examined radially; the fiber lies on the stage and the laser and Raman beams propagate along radial directions. From a single spot on a fiber from each sample spectra labeled ZZ, ZR, and RR were acquired. The first letter indicates the laser polarization, the second the Raman polarization.

Two criteria for detecting orientation in spin-oriented and drawn fibers of PET can be described.

Increasing the take-up speed of spin-oriented PET fibers or increasing their draw ratio improves the degree to which the polymer axis is aligned along the fiber axis Z. The R and Z directions are quite different in well-oriented fibers, but indistinguishable in unoriented samples. Thus the first criterion for orientation is inequivalence of RR and ZA spectra of PET.

The second criterion follows the work of Boerio and Bailey.⁵ These authors use polarization measurements of an oriented rod of PET to determine that the only asymmetric type vibration observed in their Raman spectrum of PET occurred at 800 cm^{-1} . Our second criterion for orientation is thus a higher intensity of the asymmetric mode such as that at 800 cm^{-1} in the ZR spectrum rather than in the ZZ or RR spectra.

Sample Mount

Individual fibers of PET were examined on a rotating stage of the Raman microprobe. The fiber bundles were picked apart slightly before they were mounted on a standard microscope slide with adhesive tape, with a minimum of tension applied to keep the fibers stationary. Viewed on the monitor the fiber could be accurately positioned vertically or horizontally. When the sample is mounted on a rotation stage the input laser beam which is polarized in the horizontal direction, can be oriented along the fiber axis or perpendicular to it. The polarization of the Raman light can be chosen to be horizontal or vertical, independent of the fiber orientation.

Samples

PET fibers were provided by Drs. H. M. Heuvel and R. Huisman of the Enka BV, Research Institute, NL-6800 AB Arnhem, The Netherlands. One series of fibers was spun to a yarn count of 165 dtex (for 30 filaments) with wind-up velocities of 1500, 2500, 3500, 4500, and 5500 m/min.

A fiber from another set had been spun at a wind-up velocity of 500 m/min and subsequently drawn at a different ratio of 5.0:1 in two steps with pins adjusted to 90 C and 150 C.

In addition, we drew at room temperature one of the fibers spun at 1500 m/min to a ratio of 2.5:1.

Heuvel and Huisman provided density measurements and x-ray diffraction evaluation (axis dimensions, crystal density of the unit cells, and crystalline orientation factors) as described in their publications.⁶

In addition Otto Burkhardt (Celanese Research) measured the densities (in a calcium nitrate/water column) and Sigrid Ruetsch (Textile Research Institute) obtained the birefringences data with an interference microscope of these samples. These physical parameters are tabulated in a publication describing this work.³

The density, unit cell dimensions, crystallinity, birefringence, and crystalline

FIG. 1.--Molecular structure of polyethylene terephthalate (PET) chain when glycol unit is in all-trans conformation and packing of those all-trans chains in crystalline phase. (From C. W. Bunn, in Rowland Hill, Ed., *Fibers from Synthetic polymers*, New York: Elsevier, 1953; p. 295, Figs. 11.5 and 11.6.)

GLYCOL

AROMATIC RING

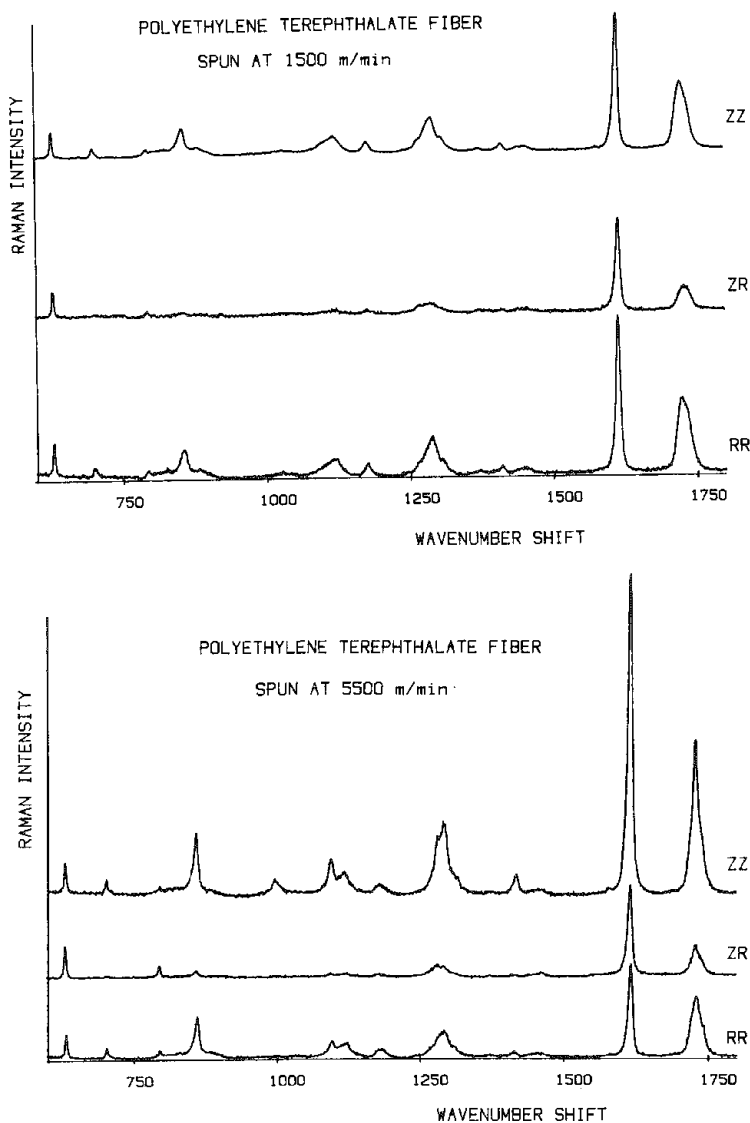
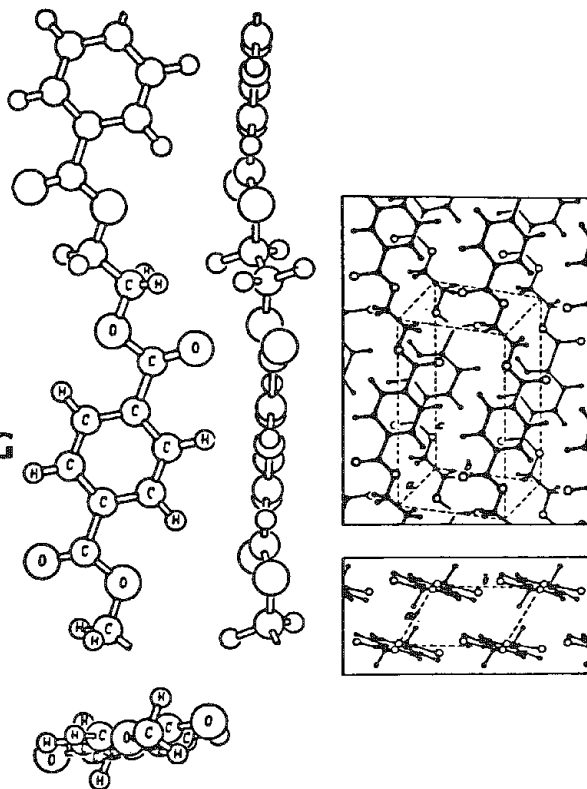


FIG. 2.--Polarized Raman spectra between 600 and 1800 cm^{-1} of single 20m fiber of polyethylene terephthalate spin-oriented at 1500 m.min. Laser intensity at sample, 2.5 mW. Spectra are displayed so that relative intensities represent scattering intensity differences due to polarization differences. ZZ (RR) indicates that laser and Raman polarization are parallel (perpendicular) to fiber axis; ZR indicates that laser polarization is parallel to fiber axis and Raman polarization is perpendicular to it. Differences in signal-to-noise ratio arise from differences in integration times which have been normalized in plotted intensities.

FIG. 3.--Polarized Raman spectra of single 20m fiber of PET spin-oriented at 5500 m/min. Laser intensity at sample, 4 mW. All other comments in Fig. 2 apply.

orientation factor of the high-temperature drawn sample indicate that the crystallinity of this sample is about 30%. For the spin-oriented materials, only the samples with wind-up velocities of 4500 and 5500 m/min are crystalline on the basis of x-ray diffraction data; the crystalline orientation functions are as high as for the drawn materials, but their percentage crystallinity is lower. The overall orientation for the drawn sample is high as shown by the high value of the birefringences. The spin-oriented samples show a gradual increase in birefringence with take-up velocity to a considerably lower maximum value than for drawn fibers. This feature is generally observed in spin-oriented polyethylene terephthalate fibers⁷ and indicates considerably lower orientation in the non-crystalline regions of this type of PET fiber. Birefringence and XRD of the fiber drawn at room temperature showed it to be highly oriented but noncrystalline.

Results

Figure 2 presents polarized Raman spectra from a single point in a fiber spun at 1500 m/min. Spectra from the ZZ, ZR, and RR polarization combinations are presented. The vertical intensity scales have been normalized to make comparison of intensities among the three scans possible. Absolute intensities were reproducible to 15%. Within this 15% variability, the ZZ and RR spectra are indistinguishable. All bands in the ZR spectrum except for the 632 and 800 cm^{-1} bands are diminished in intensity; the intensities of these bands are comparable to those of the diagonal spectra.

Figure 3 reproduces similar spectra from a point on a fiber spun at 5500 m/min. In this case the RR intensity is significantly reduced relative to that of the ZZ spectrum. In the off-diagonal (ZR) spectrum all bands except those at 632 and 800 cm^{-1} show intensities lower than those in the ZZ or RR spectra.

The comparable or stronger intensities of the 632 and 800 cm^{-1} bands in the ZR spectra relative to their intensities in ZZ or RR scans confirm these bands to have B_g , rather than A_g , character.

The intensity ratios of the major bands have been calculated and tabulated in Table 1. Since the intensities are considered to be reproducible to $\pm 15\%$, there will be ca. $\pm 30\%$ uncertainty in the ratios as calculated from these spectra ($0.85/1.15 = 0.75$, $1.15/0.85 = 1.35$). These numbers are presented as *typical* for a series of scans recorded, not necessarily definitive.

The development of orientation can be monitored by examination of the trends in the intensity ratios as a function of take-up speed. For instance, $I_{RR}:I_{ZZ}$ of the 1615 cm^{-1} band decreases from approximately 1.1 to 0.1 in the series of fibers examined. Other bands exhibit similar decreases in $I_{RR}:I_{ZZ}$. As described earlier, the inequivalence of the macroscopic Z and R axes is consistent with alignment of the molecular axes during spinning and/or drawing.

Changes in molecular alignment and interchain packing of polymer units can be monitored by the appearance and disappearance of several bands. Conformational and/or packing changes of the glycol units can be observed in bands in the 900-122 cm^{-1} range. Spectra recorded in this region are shown in Fig. 4. All fibers have well-defined bands at 1120 and 1175 cm^{-1} . Fibers spun at low take-up speeds consistently show weak, poorly defined features at about 1030 and 11 cm^{-1} . As the take-up speed is increased, the diffuse band at 1030 cm^{-1} is replaced by a well-defined, relatively sharp band at 1000 cm^{-1} . (The 1000 cm^{-1} band is highly polarized, appearing only in the ZZ spectrum of "crystalline" fibers.) In addition, the shoulder in the 1100 cm^{-1} range becomes the most intense, sharpest band (1096 cm^{-1}) in this region of the spectrum. Both bands have been correlated with "crystallinity" in PET.

Crystallization has also been correlated with the width of the carbonyl band at 1730 cm^{-1} . Melveger⁸ showed a correlation between the density of a PET sample and the half width of the carbonyl band at 1725-1730 cm^{-1} .

Figure 5 gives some of the preliminary data of the 1725-1730 cm^{-1} band for two samples spun at 1500 and 5500 m/min and the room high temperature drawn sample for ZZ = RZ, and RR polarizations. The spectra are displayed with Y axis expansions, which give equivalent maximum intensities to each spectrum. The differences in the shape of the carbonyl bands represent a multiplicity of conformations, which will have to be analyzed by curve-resolving techniques. This is shown most clearly for the amorphous Sample 5, which shows three maxima at 1721, 1726, and 1731 cm^{-1} . The crystalline samples have one main peak at 1725 cm^{-1} , but it is clear that the other two components are also present (1730 cm^{-1} in the

ZR and 1721 cm^{-1} in the RR spectra). The half-width data reported here fit Melveger's correlation with density.

Full spectra from the fiber drawn at room temperature, below T_g , are presented in Fig. 6. These filaments show glycol bands at 1000 and 1096 cm^{-1} . Although previous authors have associated these bands with crystalline PET, XRD indicates the sample to be amorphous. Also the width at half maximum intensity of the carbonyl band is not appreciably different from that of the undrawn sample spun at 1500 m/min . However, XRD and birefringence are consistent with the high orientation derived from the Raman intensity ratios and indicate very good orientation of the polymer chains.

A comment regarding the band at 1080 cm^{-1} should be made. Careful inspection of the spectra of all the fibers reveal a more or less intense shoulder in this region. The shoulder is very strong in the room-temperature drawn fiber and is also clearly present in the high-temperature drawn fibers and the fiber spin-oriented at 3500 m/min . It is least visible in the fiber spin-oriented at 5500 m/min . It is our feeling that this band correlates with a transglycol unit in the amorphous phase.

Discussion

Orientation vs Crystallization. Previous investigations of the Raman spectra of PET and perhaps other polyesters either dealt with amorphous or crystalline (semicrystalline) unoriented materials or they dealt with oriented materials which because of their method of preparation (drawing above T_g) of necessity were crystalline. The Raman spectrum of an oriented, noncrystalline material does not seem to have been investigated in detail.

Implicit in most previous Raman studies of oriented PET is the coupling of orientation and crystallization. This coupling is due to the fact that preparation of the materials used by these authors, be it fiber or film, involved orientation by drawing of the unoriented material at or above the glass transition temperature T_g , and therefore simultaneously produced crystallization. In these drawing processes, the degree of orientation can be obviously changed by adjustment of the draw ratio, and the crystallinity can be modified by changing the drawing temperature, the number of drawing steps, and the annealing conditions of the drawn product. Normally this drawing process leads to samples in which orientation and crystallization occur simultaneously.

In contrast, the spin-orientation process can lead to materials with a range of orientations: some of the fibers are amorphous, others partially crystalline (as determined by wide-angle x-ray diffraction methods), depending on spinning conditions (yarn take-up, spin stress, extrusion temperature, polymer molecular weight, etc.). Thus, for example, some PET yarns spun by this method in a range of take-up speeds between 1500 to 3500 m/min (so-called POY materials: Partially Oriented Yarns) show increasing orientation but are all amorphous. Yarns spun at or above 400 m/min take-up speed (4000 - $10\,000\text{ m/min}$) are usually crystalline and have highly oriented crystalline areas. Again, the amount of crystalline material depends on spinning and annealing conditions.

Conformation of the Glycol Unit. In the noncrystalline state, the coplanarity and transconformation of the carbonyl groups is not required and the gauche conformation in the glycol unit is prevalent. However, some transconformation of this unit seems to be present even in unoriented amorphous PET (approximately 10%). Thus it is essential to be able to differentiate transconformations in various environments--i.e., in the amorphous or in the crystalline regions.

The Raman peaks measured between 900 and 1220 cm^{-1} correlate with conformational changes and interchain effects rather than amorphous-crystalline differences. Both the 1000 and 1096 cm^{-1} bands appear in the spectrum of the amorphous sample spin-oriented at 3500 m/min . In the other spectra their intensities increase with take-up speeds. Their intensities are also quite clear in the spectrum of the 1500 m/min fiber drawn at room temperature. The behavior of the 1030 cm^{-1} band fits assignment to a gauche structure of the glycol group; its replacement by a band at 1000 cm^{-1} in the trans form is also consistent with the polarization orientation behavior. Extended polyester chains *require* the transconformation in the glycol units. Our data show the 100 cm^{-1} band only in ZZ spectra of oriented fibers. The 1030 cm^{-1} band, however, appears in ZZ as well as RR traces. In addition the amorphous trans Raman band at 1080 cm^{-1} appears only in amorphous oriented PET. Taken together these observations imply simultaneous occurrence of the transconformation and chain orientation.

FIG. 4.--ZZ component of Raman spectra between 950 and 1220 cm^{-1} of five samples spin-oriented with take-up speeds (TUS) of 1500, 2500, 3500, 4500, and 5500 m/min, and two drawn samples. Spectrum at top of figure was recorded from fiber spin-oriented at 500 m/min and drawn 5 \times over pins held at 90 and 150 C; spectrum at bottom of figure, from fiber spin-oriented at 1500 m/min and drawn 2.5 \times at room temperature.

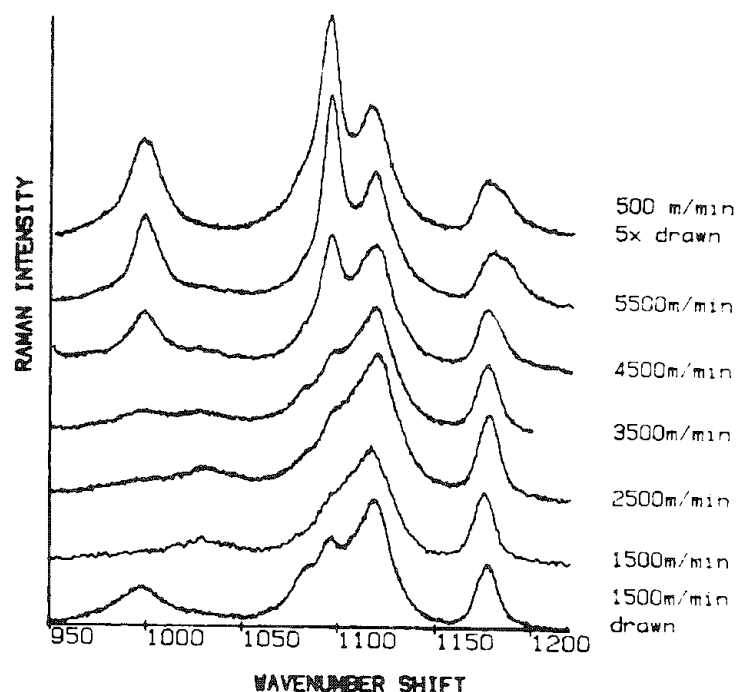


TABLE 1.--(a) Peak height ratios: I_{RR}/I_{ZZ} .

cm^{-1}	SAMPLE #							
	5	6	7	8	9		1	5' DRAWN
632	1.3	1.0	.6	1.0	.8		.7	.8
704	1.1	.9	.7	.7	.8		.8	.9
797	1.1	1.93	.8	.9	1.1		.8	.8
850, br, amorph.	.9	.7	.5	.8	1.0		1.4	1.1
858	.9	.8	.6	.8	.6		.6	.5
999	-	-	-	.0	.1		0	0
1030	1.7	1.2	?	-	-		-	2
1096	-	-	.6	.5	.5		.5	.5
1117	.9	.8	.6	.7	.7		.6	.5
1177	1.3	.9	.6	.8	.9		1.0	.8
1293	1.1	.7	.4	.5	.4		.3	.3
1371	1.7	.7	.7	1.3	-		-	-
1419	1.0	.6	.4	.4	.3		.2	.2
1453	1.2	.9	.6	.9	.9		.5	.5
1615	1.1	.7	.4	.4	.3		.1	.2
1729	1.1	.7	.5	.5	.4		.3	.4

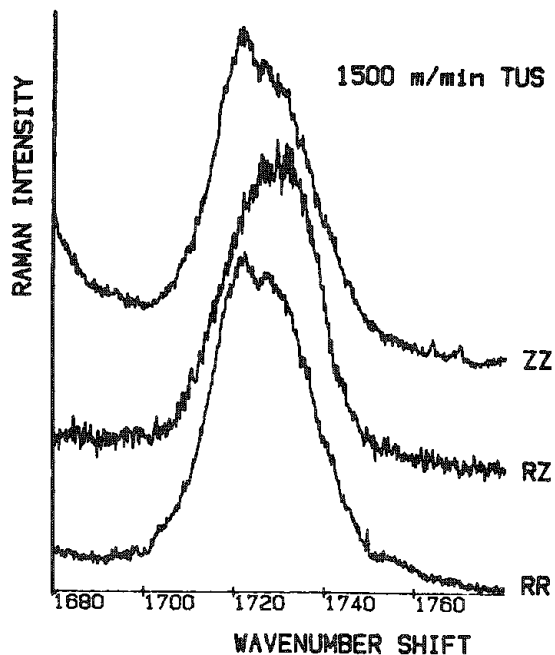
References

1. R. Daubeney, C. W. Bunn, and C. J. Brown, *Proc. Roy. Soc.* 2(6): 531, 1954.
2. See, for example, F. W. Billmeyer Jr., *Textbook of Polymer Science*, New York: Wiley, 1971, 2d ed.
3. The Raman literature has been reviewed in a more complete description of this work submitted for publication in *Polymer*.
4. M. E. Andersen, in C. D. Craver, Ed., *Polymer Characterization: Spectroscopic, Chromatographic, and Physical Instrumental Methods*, New York: ACS, 1983, 383-400.
5. F. ADar, and H. Noether, *Microbeam Analysis--1983*, 269-273.
6. F. J. Boerio, and R. A. Bailey, *J. Polym. Sci.: Polym Lett.* 12: 433-437, 1974.
7. R. Huisman, and H. M. Heuvel, *J. Appl. Polym. Sci.* 22: 943-965, 2229-2243, 1978.
8. H. R. E. Frankfort and B. H. Knox, U.S. Patents 4 134 882 (1979) and 4 195 051 (1980); S. K. Garg, *J. Appl. Polym. Sci.* 27: 2857-2867, 1982.
9. A. J. Melveger, *J. Polym. Sci.* A-2(10): 317-322, 1972.

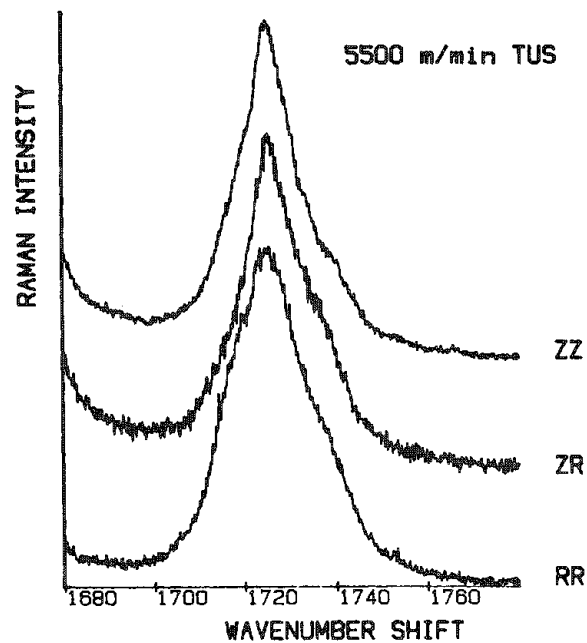
TABLE 1 (cont'd).--(b) Peak height ratios: I_{ZR}/I_{ZZ} .

cm ⁻¹	5	SAMPLE #			8	9		1	5' DRAWN
		6	7						
632	1.1	1.0	1.1		1.6	1.1		1.1	1.3
704	0	0	.2		.1	.1		.1	0
797	1.5	1.2	1.8		2.1	2.5		2.2	1.8
850, br, amorph.	.2	.2	.2		.1	.2		0	.3
858	.1	.1	.1		.2	.1		.1	.1
999	-	-	-		.1	0		.3	.1
1030	.7	1.0	-		-	-		-	-
1096	-	-	.2		.1	.1		.1	.1
1117	.2	.2	.2		.2	.2		.2	.1
1177	.3	.3	.3		.3	.4		.3	.4
1293	.3	.3	.2		.2	.2		.1	.2
1371	1.3	.4	.9		1.3	-		.2	-
1419	.4	.3	.3		.3	.1		.1	.2
1453	.7	.9	1.0		1.0	.9		.4	.6
1615	.7	.6	.5		.5	.3		.2	.2
1729	.3	.3	.3		.3	.2		.2	.2

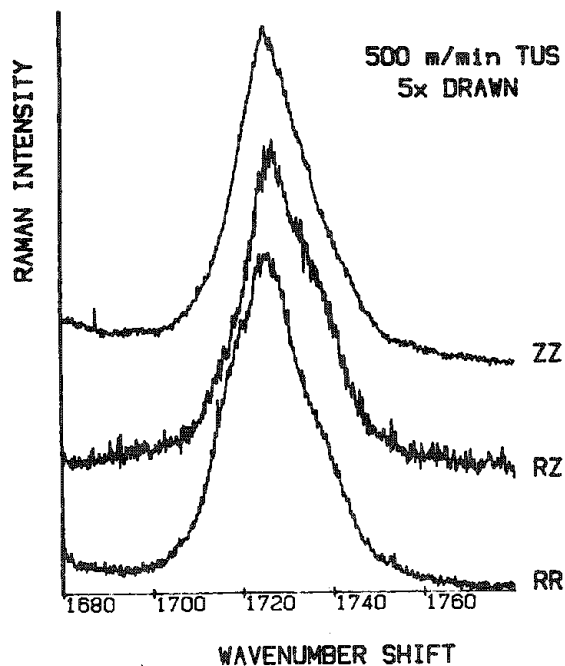
These data were collected with 1 point/cm⁻¹ and 300μm slits (optical resolution ca. 3 cm⁻¹).



(a)



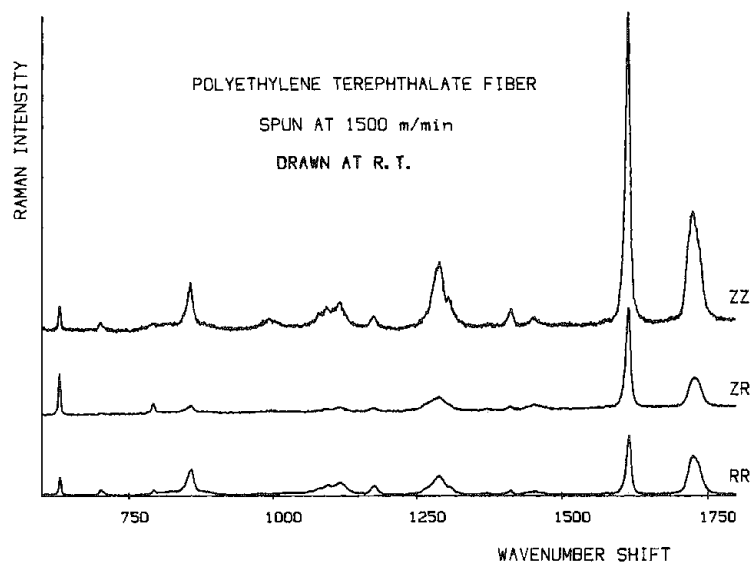
(b)



(c)

FIG. 5.--Polarized Raman spectra in carbonyl region. All spectra were displayed with bands fully expanded in Y direction. Fibers oriented at (a) 1500, (b) 5500, (c) 500 m/min, and drawn 5× at 90 and 150 C.

FIG. 6.--Polarized Raman spectra between 600 and 1800 cm^{-1} of single fiber spin-oriented at 1500 m/min and drawn 5× at room temperature. Laser intensity at sample, 4 mW. All other comments in Fig. 2 apply.



APPLICATIONS OF RAMAN MICROPROBE SPECTROSCOPY IN ORGANOMETALLIC CHEMISTRY

P. D. Harvey and I. S. Butler

Two of the most important features of the rapidly developing technique of Raman microprobe (or microRaman) spectroscopy are the small sample areas ($<50 \mu\text{m}^2$) that can be routinely examined and the very low laser powers needed for sample excitation owing to the high collection efficiency of the microscopic optics employed. Laser-induced thermal damage to samples can almost always be avoided and Raman spectra can now be obtained for compounds earlier considered totally unsuitable to the technique.

Transition metal organometallic compounds are well known to chemists as being air- and light-sensitive materials, many of which have important industrial applications, e.g., as catalysts, fuel additives, electrode coatings, biological markers, reagents in organic synthesis, etc.¹ In the work described here, the Raman microprobe spectra of some typical organometallic systems, which were available only in milligram quantities, were examined in an attempt to gauge the potential of the technique as another structural method available to scientists working in the field.

Several different systems were selected for analysis: $\text{Re}_2(\text{CO})_{10-n}(\text{CNR})_n$ (R = alkyl, aryl; n = 0-4), $(\eta^5\text{-C}_5\text{H}_4\text{R})(\eta^5\text{-C}_5\text{H}_4\text{R}')\text{Fe}$, $(\eta^6\text{-Arene})\text{Cr}(\text{CO})_3$, Cp_2ME_x (Cp = $\eta^5\text{-C}_5\text{H}_5$; M = Ti, Zr, Hf, etc.; E = S, Se; x = 2-5), and $[(\eta^7\text{-C}_7\text{H}_7)\text{Mo}(\text{CO})_3]^+ \text{BF}_4^-$. Some of the structures of these compounds are shown in Fig. 1. The rhenium compounds are prototypes of an important class of metal-metal bonded molecules known as "metal clusters" that are currently considered as good models for metal surfaces during catalysis. We were particularly interested in ascertaining the effects on the vibrational spectra of sequential CO group replacement by the more strongly bonding isonitrile ligands (CNR) and whether these perturbations had any structural-prediction utility. The derivatives of the famous "sandwich" molecule, ferrocene (Cp_2Fe), may find use as coatings for electrodes and as polymer-supported catalysts. The metal polysulfane and polyselenane complexes are interesting molecules for probing the properties of chalcogen rings of differing sizes and their relationship to the parent molecules, S_8 and Se_8 . Finally, the metal tricarbonyl complexes are members of the "piano-stool" family of molecules, many of which are proving extremely useful as catalysts (e.g., for hydrogenation) in organic syntheses.

Experimental

The Raman spectra were recorded for samples sealed in Pyrex glass capillaries on an Instruments SA Raman microprobe spectrometer equipped with a U-1000, 1.0-m double monochromator, a Columbia Data Products minicomputer, and a $32\times$ long-range microscope objective. With this system, multiscanning was straightforward and high-quality data were obtained in almost every case. A Spectra Physics Model 164 argon-ion laser (5 W) was used as the excitation source, usually the 514.5nm green line, with typically about 20 mW laser power at the samples. In the case of

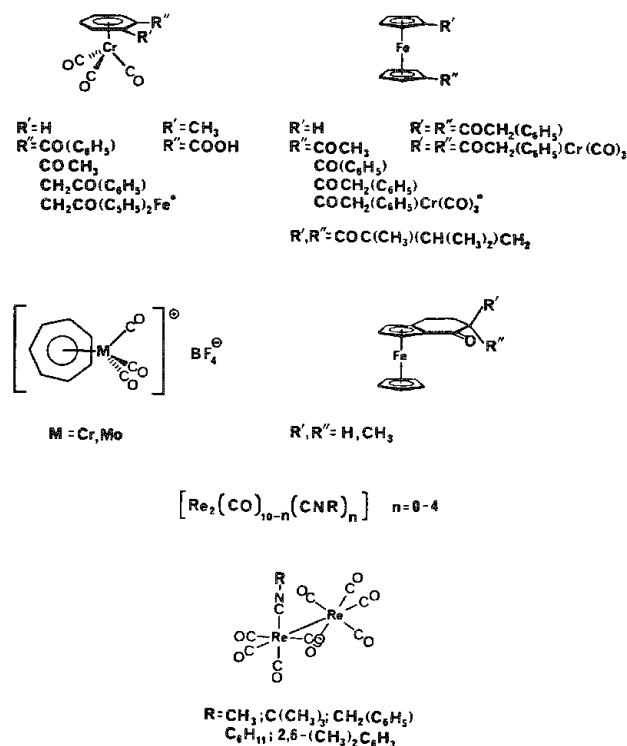


FIG. 1.--Structure of transition metal organometallic complexes investigated in this work.

The authors are at McGill University (Department of Chemistry), Montreal, Quebec, Canada H3A 2K6. NSERC (Canada) and FCAC (Quebec) financial support is gratefully acknowledged.

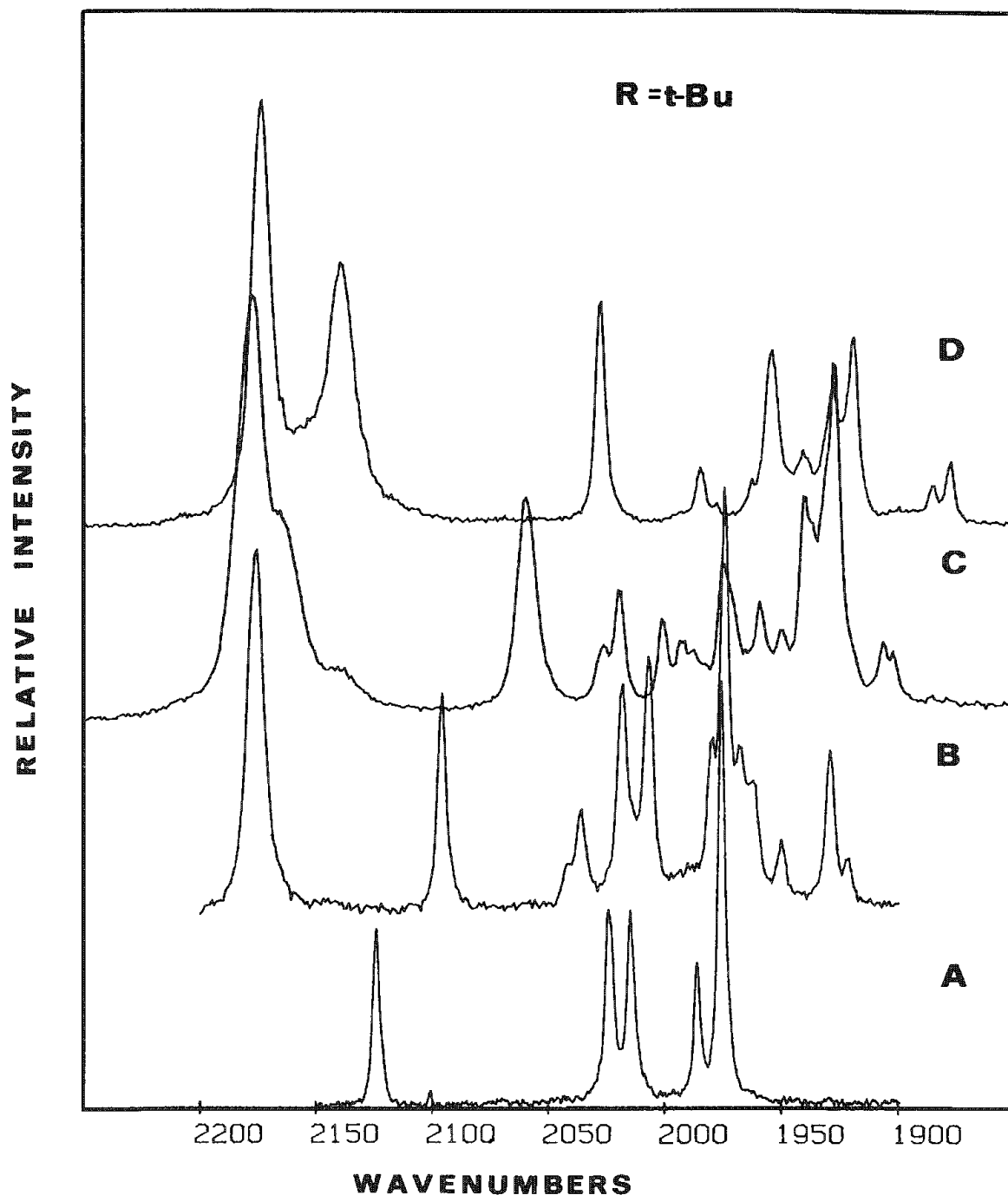


FIG. 2.--Raman microprobe spectra of solid rhenium carbonyl-*t*-butylisonitrile complexes in 2250-1850 cm^{-1} region: (a) $\text{Re}_2(\text{CO})_{10}$, (b) $\text{Re}_2(\text{CO})_9[\text{CN}(\text{t-Bu})]$, (c) $\text{Re}_2(\text{CO})_8[\text{CN}(\text{t-Bu})]_2$, (d) $\text{Re}_2(\text{CO})_7[\text{CN}(\text{t-Bu})]_3$. Spectral conditions: 514.5nm excitation (20 mW at sample), 300 μm slits, 2 scans (4 s point $^{-1}$, 1 cm^{-1} steps), 32 \times magnification.

the ferrocene derivatives, however, laser powers of 0.5 mW had to be used to avoid sample burning but satisfactory spectra could still be obtained. Such low laser powers would have been completely impractical in conventional Raman measurements.

Conclusions

As an illustration of the sort of information obtained from our Raman microprobe investigations of organometallic complexes, some of the results for two of the series of complexes are presented below.

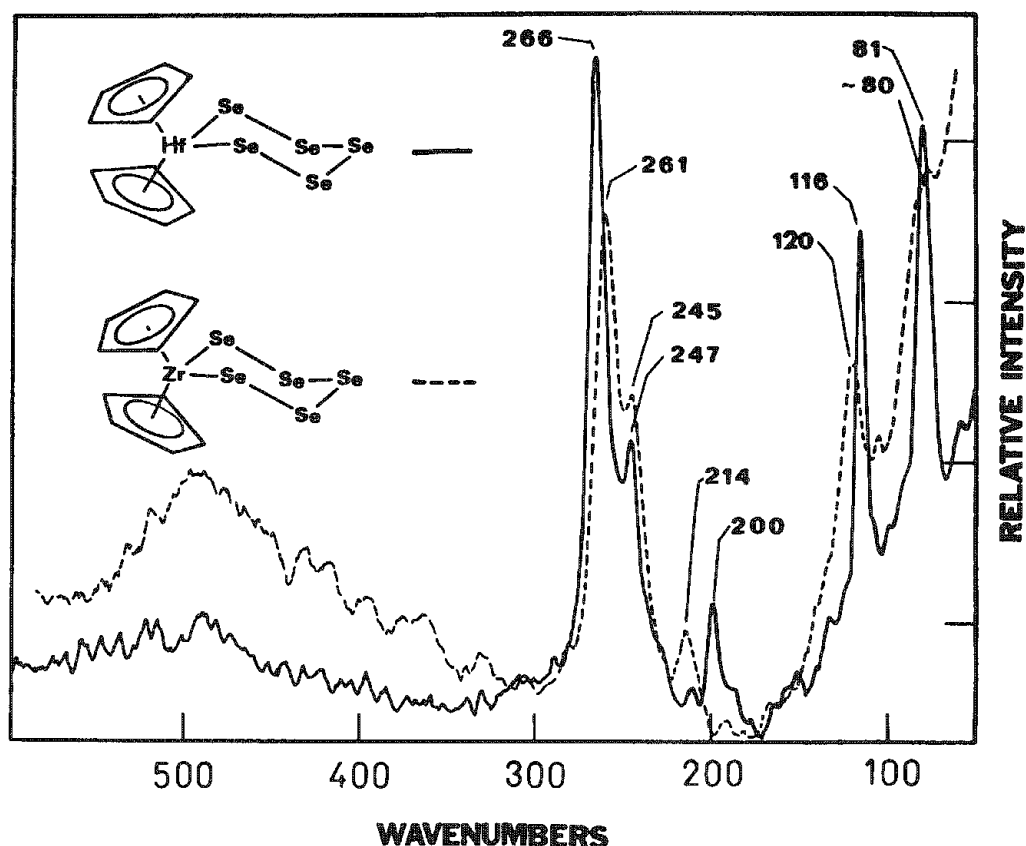


FIG. 3.--Raman microprobe spectra of solid zirconium and hafnium pentaselenido complexes in 600-500 cm^{-1} region. Spectral conditions: 514.5nm excitation (30 mW at samples), 400 μm slits, 2 scans (1 s point $^{-1}$ 1 cm^{-1} steps), 32 \times magnification.

1. The effect of sequential CO replacement in $\text{Re}_2(\text{CO})_{10}$ by $\text{CN}(\text{t-Bu})$ groups is shown dramatically by the changes in the $\nu(\text{CO})$ region of the spectra shown in Fig. 2. The solitary peak at about 2130 cm^{-1} in $\text{Re}_2(\text{CO})_{10}$ ² steadily decreases upon isonitrile substitution to around 2040 cm^{-1} and it is clear that the position of this peak can be used as an indicator of the extent of CO replacement by $\text{CN}(\text{t-Bu})$ ligands. Similar results are obtained for the other isonitrile ligands investigated.

2. Little information is available in the literature on the effect of ring size in polysulfanes on the S-S stretching modes and on the location of the Se-Se and M-Se stretching modes in metal-selenido chelate complexes. From our work, the symmetric S-S stretching mode in the Cp_2MS_x complexes decreases monotonically in energy from 530-470 cm^{-1} upon increase of the ring size from MS_2 to MS_5 , and the Se-Se and M-Se stretching fundamentals in the analogous polyselenanes appear around 250 cm^{-1} (Fig. 3).

In conclusion, our study has shown, for the first time, that Raman microprobe spectroscopy shows considerable promise for obtaining structural data on organometallic compounds previously thought to be totally unsuitable for Raman measurements. Such studies will doubtless become more common in the future.

References

1. C. M. Lukehart, *Fundamental Transition Metal Organometallic Chemistry*, Monterey, Calif.: Brooks/Cole Publishing Co., 1985.
2. P. D. Harvey and I. S. Butler, "Low-temperature Raman and Fourier transform infrared spectra of dodecacarbonyldirhenium(0), $\text{Re}_2(\text{CO})_{10}$," *Can. J. Chem.*, in press (1985).

RAMAN MICROPROBE STUDY OF CHANGES INDUCED BY A PULSED LASER

F. Adar, I. H. Campbell, and P. M. Fauchet

The behavior of solids under pulsed laser illumination is of interest to researchers in various fields, including laser processing of semiconducting materials¹ and laser-induced damage to optical materials.² One topic of special interest is the understanding and characterization of the subtle subthreshold effects that occur during repeated illumination by laser pulses below the single-shot damage threshold which eventually lead to irreversible transformations of solid surfaces.³ Due to the lack of nondestructive, quantitative probes that can be used in situ, our understanding of these mechanisms has been very limited. We show here that the Raman microprobe is a sensitive detector probe of the structural changes produced by single or repeated illumination of thin films with laser pulses below and above single-shot damage threshold. Our results to date have been obtained primarily with silicon thin films since the effects of stress and microcrystallinity in these films have been well characterized; however, similar results should be obtainable with other materials as well.

Experimental

In the experiments reported here, the damaging beam is produced by a modelocked Nd:YAG laser. The laser is fired at a 10Hz repetition rate; each shot is in fact composed of approximately 20 individual modelocked pulses, each pulse lasting approximately 100 ps, under a 100ns envelope. The experiments discussed below were all performed at 1.064 μm . The laser beam is focused to a spot approximately 150 μm on the sample, where the beam profile is Gaussian. The intensity of the beam is controlled with a half-wave plate followed by a polarizer. The pulse energy, monitored by a photodiode on a shot-to-shot basis, is constant to better than $\pm 10\%$. A predetermined number of identical pulses is incident on one area of the sample; the sample is then translated and another area is illuminated with a different number of identical pulses. The number of pulses varies from 1 to more than 1000. The sequence is then repeated with a different pulse intensity. The Raman Stokes line at various locations in and around the illuminated area is then recorded with a Ramanor U-1000 double-grating spectrometer optically and mechanically coupled to a research grade optical microscope. Spatial resolution of 1 μm is achieved with objectives whose numerical apertures are 0.75 or greater. As shown in Fig. 1, the Raman spectra were collected reproducibly to $\pm 0.1 \text{ cm}^{-1}$. The spectral resolution is routinely set at approximately 3 cm^{-1} and the spectra discussed below consist of points spaced by 0.1 or 0.2 cm^{-1} taken with 1-4 s exposure times. The laser power is kept at or below 3 mW at the sample to avoid broadening and shifting of the Stokes line of silicon. The samples discussed here are 1 μm thick films of silicon on insulator (SOI), grown at 625 C by low-pressure chemical vapor deposition. These films are expected to be polycrystalline and under tensile stress because of the difference in thermal expansion coefficients between silicon and fused quartz.

Results and Discussion

In a first set of experiments, we exposed the selected areas of an SOI sample to a single shot of variable intensity in order to determine the single-shot damage threshold. At threshold, damage occurs as a few randomly distributed worm-like features, 1 to 2 μm in size. High-resolution Nomarski optical microscopy is used to observe the surface. These highly localized damaged areas are thought to be associated with local imperfections in the material. Well above threshold, single-shot damage is accompanied with melting and/or vaporization of the illuminated area.⁴ At threshold, melting and vaporization occurs only at selected sites. In Fig. 2, we show the resolution of the Stokes line as the focused Raman probe beam moves away from the center of one of these worm-like damage sites. Though

Author Adar is at Instruments SA, Inc., 173 Essex Avenue, Metuchen, NJ 08840; authors Campbell and Fauchet are at Princeton University, Princeton, NJ 08540. The aid of Dr. N. Johnson (who provided the SOI samples) and Dr. C. Paddock's technical assistance are gratefully acknowledged.

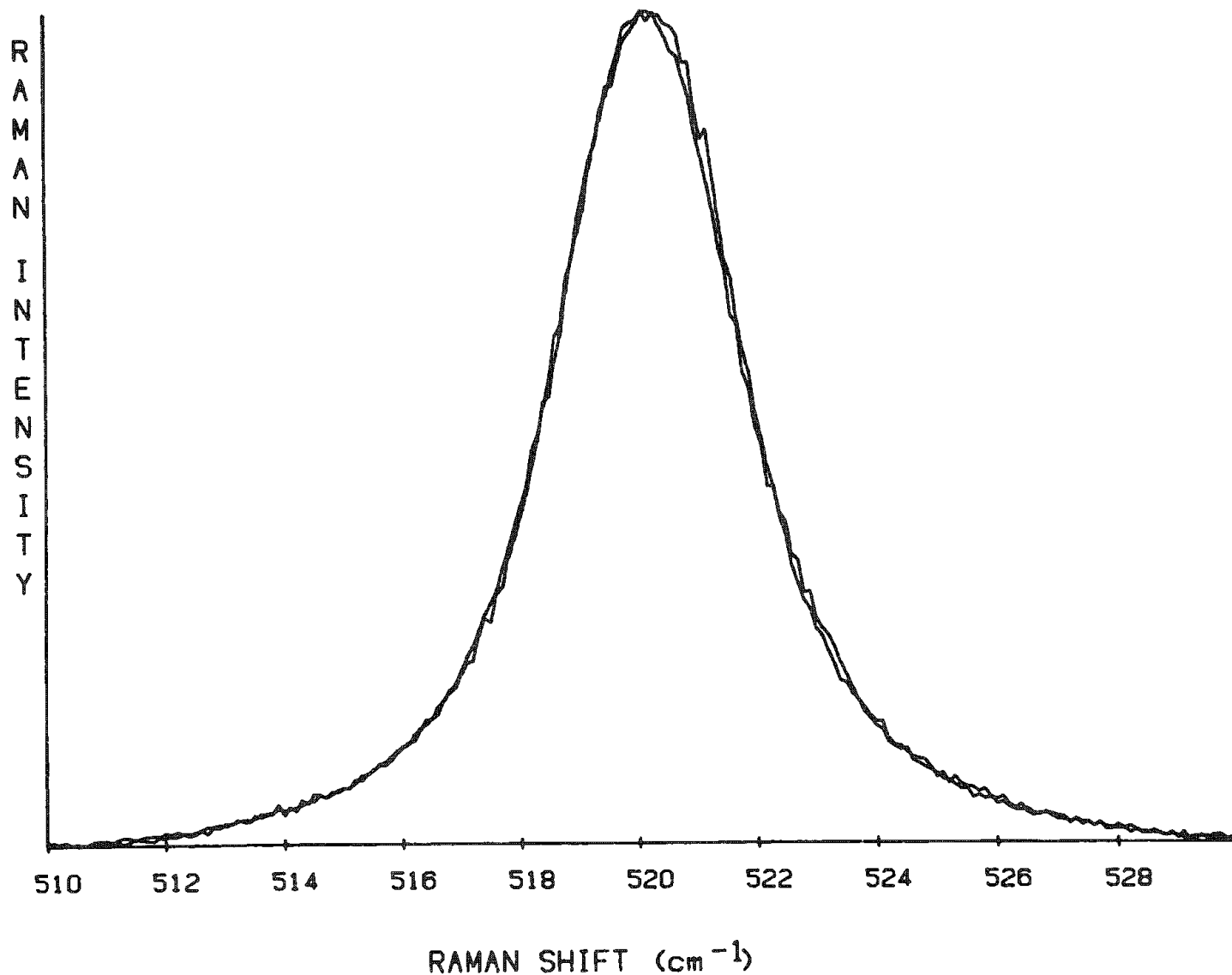


FIG. 1.--Three identical scans of Raman phonon of single crystal silicon recorded with 0.1cm^{-1} intervals.

the Stokes line of the virgin SOI is broad, asymmetric and down-shifted by less than 2 cm^{-1} from the Stokes line of unstressed, single-crystal silicon, it gradually sharpens, becomes more symmetric, and moves towards a smaller Stokes shift as the probe beam moves away from the damage site. High-resolution Nomarski microscopy identifies the damage site but does not allow us to observe the gradual modification of the structural properties of the SOI away from the worm-like feature. These spectra also exhibit a shoulder at about 490 cm^{-1} , which disappears close to the damage site. We associate this shoulder with some amorphous material⁵ which is present in the virgin film. After melting and recrystallization, the material becomes entirely crystalline. The size of the grains increases dramatically as indicated by the symmetry of the line.⁶ However, a large tensile stress remains (approximately $10^{10}\text{ dynes/cm}^2$) and the line is broader than that of crystalline silicon. The stress dependence of the Raman band has been characterized by Anastassakis et al.⁷ and used to map local strain in SOI.⁸⁻¹¹ A hypothesis to explain our observations is as follows: the initial material, which is composed of many tiny microcrystallites separated by amorphous-like highly distorted boundary regions, is not expected to be as dense as single crystal silicon. However, the damaged material, which regrows as one or a few large grains, is under large tensile stress with respect to the neighboring material.

Structural changes produced by multiple pulse illumination below damage threshold were

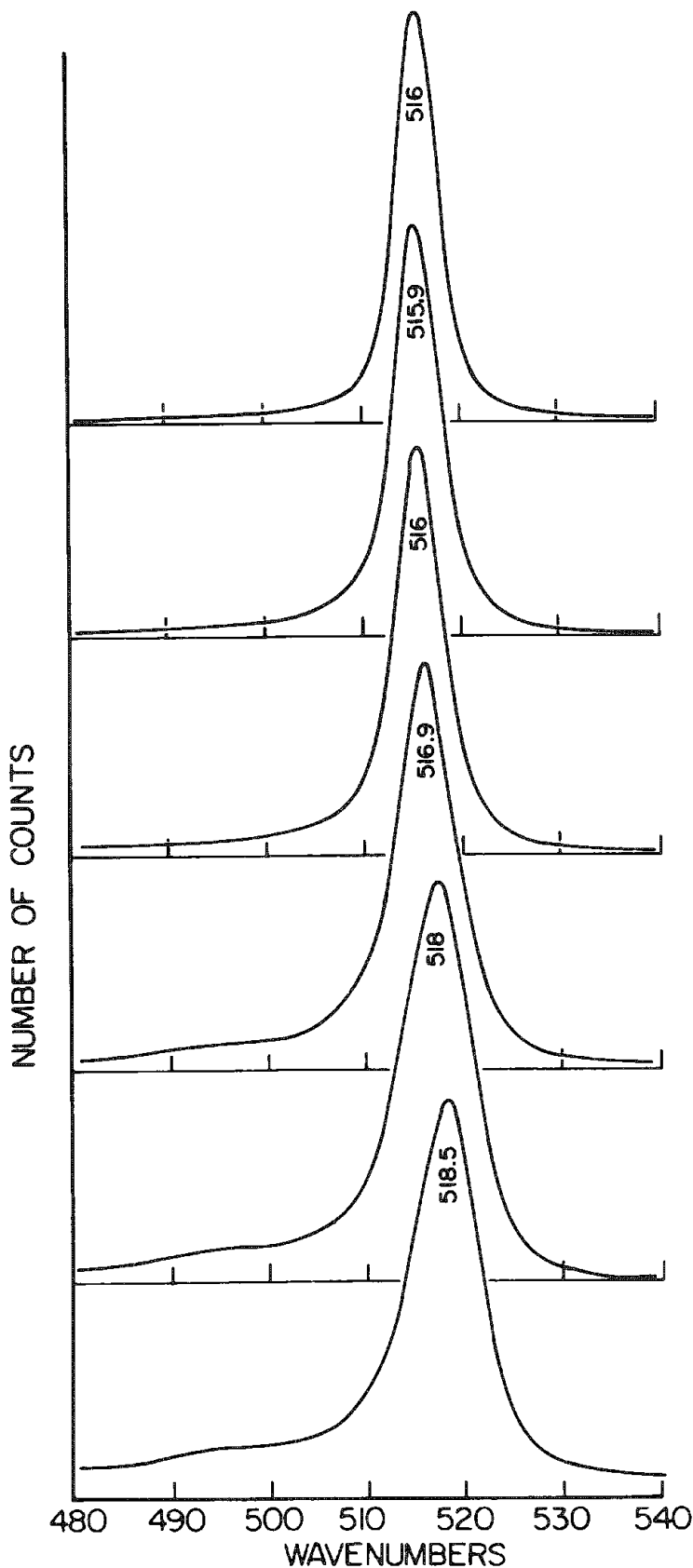


FIG. 2.--Stokes Raman line of silicon (a) at center of micron-size damage feature, (b) on the edge, (c)-(e) ~ 3 , ~ 6 , and ~ 3 μm array, and (f) Stokes line of virgin SOI. From (a) to (f), line shifts, widens, and becomes asymmetric. Note amorphous shoulder at 450 cm^{-1} .

subsequently investigated. After 600 shots at $2/3$ of threshold, the sample is damaged. Figure 3 shows the peak frequency of the Stokes line as a function of radial distance from the center of a damaged area. Inside the damaged area, ω_0 is down-shifted by approximately 2 cm^{-1} compared to that of the virgin SOI. At the boundary between damaged and undamaged regions, determined by optical microscopy, ω_0 is discontinuous. However, only when regions approximately $20\text{ }\mu\text{m}$ from the boundary of the damaged region were probed was a spectrum comparable to SOI recorded. A similar plot (Fig. 4) of the full-width half maximum vs the asymmetry Γ_a/Γ_b , implies that the stress extends approximately $20\text{ }\mu\text{m}$ beyond the damaged area in the microcrystalline region. In the damaged region, the stress is observed to be heterogeneous. Close to the center, where the intensity is largest, the surface is very distorted; the strain of protruding regions should be smaller because of the existence of a large free surface, in agreement with the increase of ω_0 .

In Fig. 4, we plot a small fraction of our data, together with the result of a calculation where the increased asymmetry and full width at half maximum of the Stokes line of silicon is produced by microcrystallites of decreasing sizes. In that calculation, the finite microcrystallite size ΔX causes an uncertainty in the phonon wavevector Δq approximately equal to $1/\Delta X$.⁶ For very small size crystallites ($\sim 100\text{ }\text{\AA}$), Δq becomes so large that contributions from optic phonons away from the center of the Brillouin zone must be included. Since the phonon frequency in silicon decreases for increasing wave vector, the resulting peak shifts to lower frequency and the line broadens. The asymmetry is brought about by the weighting factor of phonons with different wave vectors. Although the trend is similar for theory and experiments, there is a large quantitative discrepancy, which is explained by the presence of a large heterogeneous stress. A quantitative determination of stress and microcrystallite size is under way but is complicated by the possible stress variation from microcrystallite to microcrystallite.

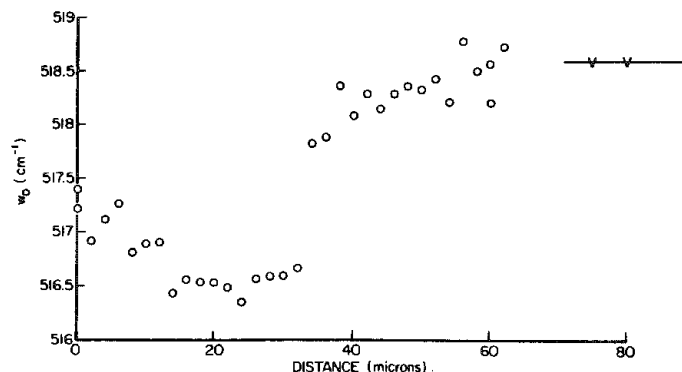


FIG. 3.--Peak frequency of Stokes line in and outside damaged area after repeated illumination below threshold. The uncertainty on ω_0 is less than $\pm 0.2 \text{ cm}^{-1}$.

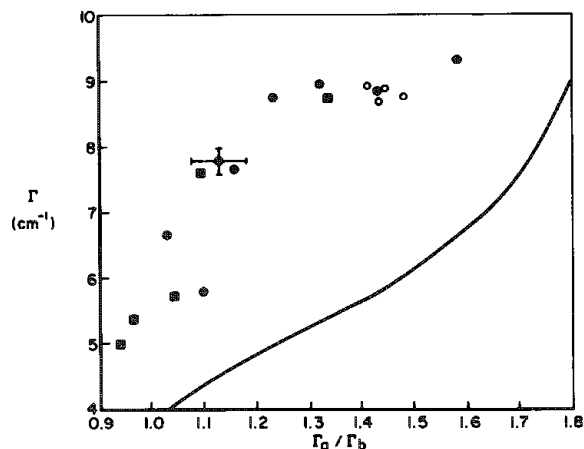


FIG. 4.--Measured full-width half maximum Γ and symmetry Γ_a/Γ_b (where Γ_a is half width on low-frequency side and Γ_b is half width on high-frequency side) for virgin SOI (o), at various locations in an area illuminated with 600 pulses at half the threshold (\bullet), and for the first five spectra shown in Fig. 2 (\blacksquare). Curve results from a calculation in which increase in Γ and Γ_a/Γ_b is produced by decrease in micro-crystalline size.

Conclusion

We have shown that micro-Raman scattering is an excellent probe of the structural change produced by one or many laser pulses. Variations not detected by high-resolution Nomarski microscopy are clearly observed with the Raman microprobe. We are at present developing a model that will quantitatively explain our results and are continuing experiments on samples exposed to multiple shots at power densities well below single shot power levels for damage threshold.

References

1. See the various Proceedings of the Annual Materials Research Society meetings.
2. See the Proceedings of the Annual Symposium on Optical Materials for High Power Lasers.
3. P. M. Fauchet, *Phys. Lett.* 93A: 155, 1982.
4. P. M. Fauchet and A. E. Siegman, *Appl. Phys. Lett.* 43: 1043, 1983.
5. D. Bermejo and M. Cardona, *J. Non-Crystall. Solids* 32: 405, 1973.
6. H. Richter, Z. P. Wang, and L. Ley, *Solid State Commun.* 39: 625, 1981.
7. E. Anastassakis, A. Pinczuk, E. Burstein, F. H. Pollak, and M. Cardona, *Solid State Commun.* 8: 133, 1970.
8. P. Zorabedian and F. Adar, *Appl. Phys. Lett.* 43: 177, 1983.
9. J. B. Hopkins, L. A. Farrow, and G. J. Fisanick, *Appl. Phys. Lett.* 44: 535-537, 1984.
10. S. Nakashima, Y. Inoue, M. Miyauchi, A. Mitsuishi, T. Niskimura, T. Fukumoto, and Y. Akasaka, *J. Appl. Phys.* 54: 2611-2617, 1983.
11. S. R. J. Brueck, in D. Bauerle, Ed., *Laser Processing and Diagnostics*, Springer-Verlag, 1984, 446-457.

THE USE OF THE RAMAN MICROPROBE FOR FAILURE ANALYSIS OF OIL FIELD DRILL PIPE

F. Purcell and R. Heidersbach

The Raman microprobe is earning itself a unique position in the arsenal of techniques for metallurgical failure analysis.^{1,2} A natural complement to standard elemental methods, micro-Raman spectroscopy can provide detailed molecular and structural information from microscopic particles.

Corrosion of metal surfaces involves complex reactions between the surface material and the surrounding environment. If unchecked, these reactions ultimately lead to metallurgical failure. Efforts to control corrosion (including the development of new alloys, protective coatings, and chemical inhibitors) require an understanding of the particular interactions between a material and its environment. Critical information about the corrosion process can be inferred from examination of the reaction products on the corroded surface.

Accurate determination of corrosion reaction products usually requires a combination of analytical techniques. Elements on the corroded surface can be identified with a scanning electron microscope and energy-dispersive x-ray spectrometer (SEM-EDXS) or with other surface techniques such as secondary ion mass spectroscopy (SIMS), Auger electron spectroscopy (AES), or electron spectroscopy for chemical analysis (ESCA). However, these elemental techniques provide limited information about the structure of the compounds formed by the identified elements.³ Molecular information is essential for complete characterization of corrosion samples. X-ray diffraction provides structural information about crystalline materials, but amorphous compounds, which are frequently found on corroded metal surfaces, cannot be detected by this method.

Micro-Raman spectroscopy is proving to be an excellent technique for identifying corrosion compounds on metal surfaces. Raman spectra can distinguish between similar compounds (between two iron oxides, for example) and between different geometrical forms of the same compound. The Raman microprobe yields structural information for crystalline and amorphous samples; in fact, Raman spectra can provide information about the degree of crystallinity of a material. Moreover, micro-Raman spectroscopy is an inherently nondestructive technique that can be applied to microscopic particles. Because Raman spectra can be obtained *in situ*, corrosion product alteration can be minimized.

The results of a preliminary investigation of corrosion products from oil-field drill pipes illustrate the capability of the Raman microprobe for corrosion analysis. Oil-field drill pipe is subjected to a harsh combination of corrosion and fatigue loading environments, and the consequences of metal failure in the pipe are costly. Various proprietary corrosion inhibitors can be added to the drilling mud to prevent corrosion fatigue of the drill pipe. To evaluate the relative effectiveness of various chemical inhibitors, corrosion-monitoring rings are placed in the joints of the drill pipe with their inside surfaces exposed to the drilling mud.

This paper presents the results of a surface analysis performed with a Raman microprobe on corrosion-monitoring rings from various oil drilling sites. The identity of the minerals on the surface may help to determine why some corrosion inhibitors are more effective than others.

The Raman Microprobe

The Raman microprobe, a relatively new variation of the commercial laser-Raman system, consists of a laser source, a microscope/illuminator for focusing the laser onto the sample, a spectrometer for analyzing the light scattered by the sample, and the necessary optics to couple the microscope to the spectrometer. With the sample positioned on the microscope stage, the excitation beam is focused onto the sample with a spot size of approximately 1 μm . The scattered radiation is collected back through the microscope objective and focused onto the entrance slit of the spectrometer.

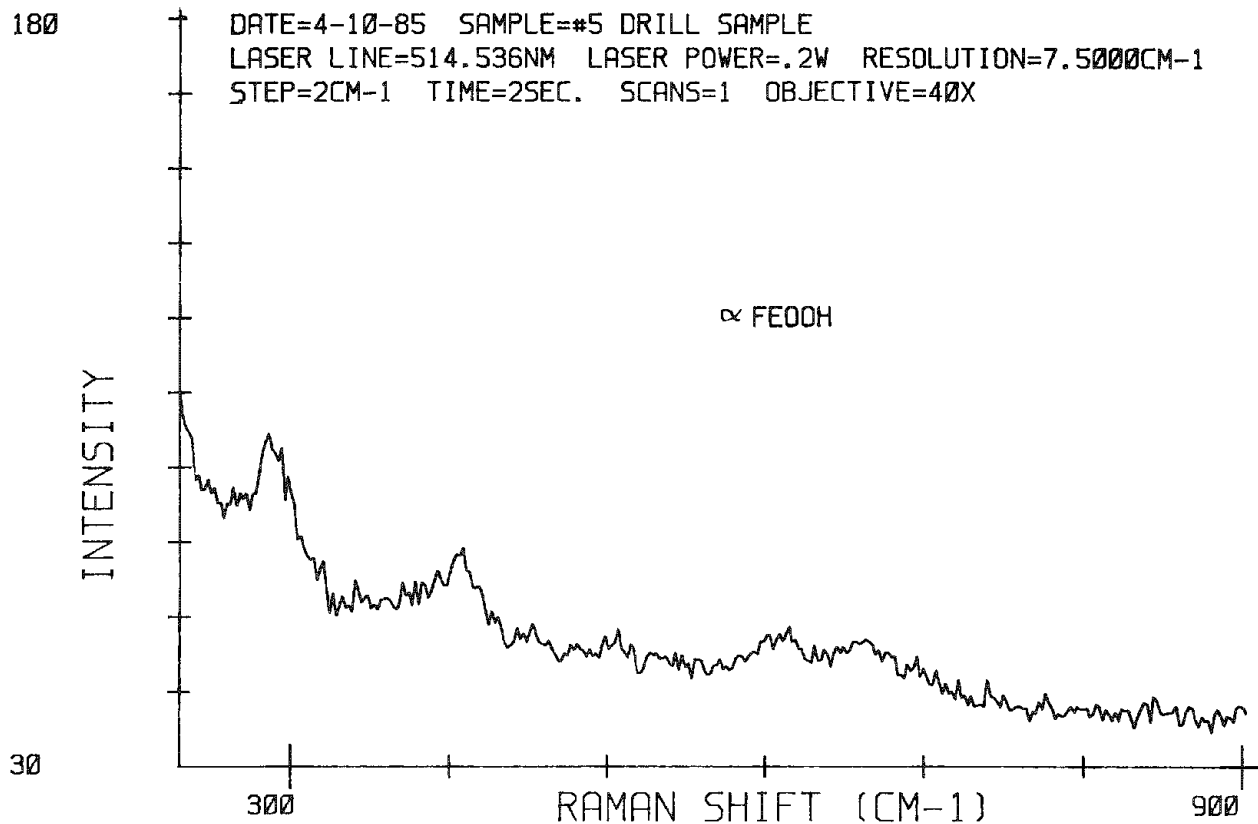


FIG. 1.--Micro-Raman spectrum of corroded region on one drill pipe ring, attributed to α -FeOOH.

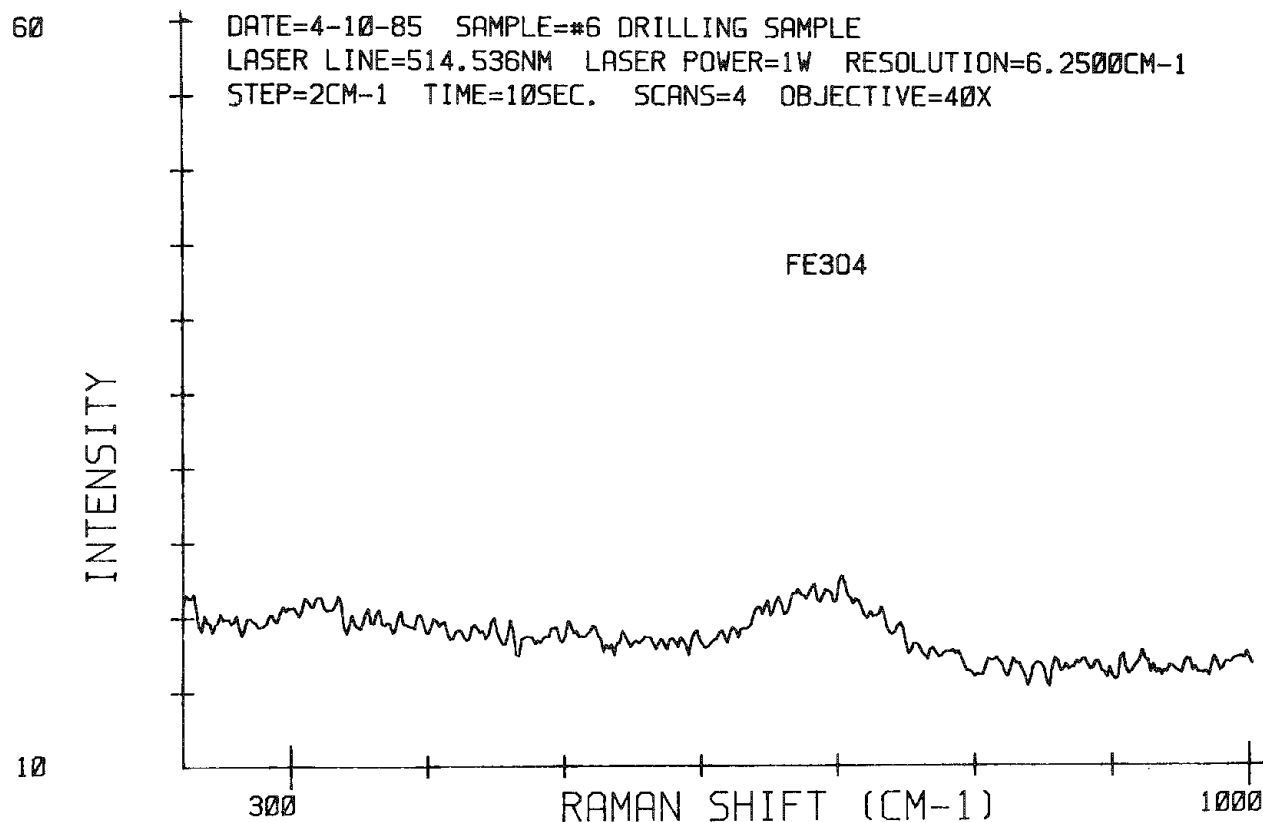


FIG. 2.--Micro-Raman spectrum of Fe₃O₄ from black deposit on another drill-pipe corrosion ring.

Experimental

Small sections of six corrosion-monitoring rings from oil-field drill pipes were obtained for analysis with the Raman microprobe. The inside surfaces of the rings exhibited varying degrees of corrosion.

Analysis was performed on a SPEX RAMALOG micro-Raman instrument system. (An optical diagram of the system appears elsewhere.⁴) Each ring sample was positioned on the microscope stage to permit spot analysis of the inside surface. A TV camera and viewing screen were used to locate corrosion features. A 4W Coherent argon ion laser (Innova-70) with laser line at 514.5 nm was then focused on the spot of interest using a 40× objective.

Results and Discussion

Preliminary results from a micro-Raman analysis of the corrosion rings indicate the presence of various iron oxides. The bands in general are broad compared to pure oxide spectra, suggesting a mixture of components.

The Raman spectra for the drill-pipe samples exhibit some similarities to those obtained in the weathering steel study, in spite of differences in surface composition and environmental conditions. (The weathering steel, a structural steel much lower in carbon than the steel used in the drill pipes, was exposed to simulated atmospheric weathering.) Amorphous Fe_3O_4 was found on the surface of both the drill pipe and weathering steel samples. However, the difference in structural forms of FeOOH on the two sample types suggests a possible difference in the corrosion mechanisms. The Fe_3O_4 and $\gamma\text{-FeOOH}$ found together on one of the weathering steel samples could be different stages of a single process, since the gamma form of FeOOH reduces to Fe_3O_4 ; but because $\alpha\text{-FeOOH}$ is not reducible to Fe_3O_4 , the determination of both of these compounds on the drill-pipe rings suggests that probably at least two different mechanisms were involved in the drill pipe corrosion.

The simplicity of Raman spectra of iron oxides permits determination of mixtures of oxides like those found on the drill pipe rings. Even amorphous compounds such as Fe_3O_4 are readily identified. The relative narrowness of Raman bands compared to the broad overlapping bands of infrared spectra aids in the rapid identification of individual compounds of a mixture. Superior spatial resolution of the Raman microprobe, on the order of 1 μm with a 40× objective, makes it possible to distinguish positional variations in the composition of a corrosion film.

Conclusions

Results from this study suggest that the Raman microprobe can provide significant information about corrosion reaction products on metal surfaces. Such information is valuable in studies of corrosion mechanisms and ultimately in the development of effective corrosion inhibitors.

Among the capabilities that make the Raman microprobe ideal for corrosion analysis are the following:

- permits nondestructive, *in situ* analysis, with no vacuum
- provides molecular and structural information
- can be used to identify amorphous or crystalline material
- allow spatial resolution of individual features to 1 μm

References

1. F. Purcell and R. Heidersbach, "Use of the Raman probe for metallurgical failure analysis," *American Laboratory*, 118-121.
2. R. Heidersbach and F. Purcell, "Analysis of corrosion products with the use of the Raman microprobe," *Microbeam Analysis--1984*, 61-64.
3. R. Thibau et al., *J. Electrochem. Soc.* 127: 37, 1980.
4. F. Purcell and W. White, "A Raman microprobe study of phase-separated minerals," *Microbeam Analysis--1983*, 289-292.

APPLICATION OF SYNERGISTIC MICROANALYSIS TECHNIQUES TO THE STUDY OF A POSSIBLE NEW MINERAL CONTAINING LIGHT ELEMENTS

E. S. Etz, D. E. Newbury, P. J. Dunn, and J. D. Grice

The analysis of samples containing light elements (atomic number < 11) presents considerable difficulties to conventional electron probe microanalysis. Although x-ray spectra can be measured for elements with atomic number as low as 5 (boron), the sensitivity of detection for the light elements is significantly poorer than that for heavier elements. The energy of the characteristic x rays of the light elements is low, so that the specimen self-absorption is extremely high. A further consequence of the high absorption is that a large uncertainty arises in the accuracy of quantitative analysis for the light elements. In particular, it becomes very difficult to assess the stoichiometric relationships among the constituents of the sample.

The development of analytical techniques complementary to conventional electron probe microanalysis has presented the analyst with new methods of attacking the problem of light-element analysis, and in particular the question of the stoichiometric relationships. In a study of a possible candidate for a new mineral, an opportunity arose to apply two of these techniques, secondary ion mass spectrometry (SIMS) and laser Raman microanalysis (LRM), to the analysis of the light-element fraction.

Experimental Procedures

Electron probe microanalysis (EPMA) of a potentially new mineral species from Evans-Lou Mine near Wakefield, Quebec, revealed only the presence of yttrium as a major constituent in the sample, with minor amounts of calcium and rare earth elements (Table 1). The low total obtained with EPMA inevitably suggested the possible presence of light elements, presumably including oxygen. Carbon might also be present, based upon the environment in which the specimen was found, which included tengerite, a hydrated calcium yttrium carbonate. Studies of the optical properties of the mineral also suggested the possibility of a carbonate-bearing phase. It was therefore decided to examine the specimen for light elements by SIMS, which has complete coverage of the periodic table and adequate sensitivity of the light elements; and further, to attempt to deduce the stoichiometry of the sample by LRM, which can directly detect molecular species.

TABLE 1.--Electron-probe analysis of possible new mineral species. (Total of analysis: 48.7 wt.%.)

Oxide	Weight Percent	Oxide	Weight Percent
Y ₂ O ₃	35.3	Ho ₂ O ₃	2.7
Ce ₂ O ₃	0.8	Sm ₂ O ₃	1.2
Nd ₂ O ₃	1.3	Gd ₂ O ₃	3.3
Dy ₂ O ₃	3.7	CaO	0.4

SIMS Analysis

The specimen was analyzed in an ion microscope, a spatially resolved SIMS instrument, both in the form of a polished section and in the form of particles. A primary beam of negative oxygen ions at an effective energy at the sample of 5.5 keV was employed for sputtering. Secondary-ion signals were collected from apertured areas 60 and 20 μ m in diameter. The technique of energy filtering was used to reduce the amount of molecular ions in the spectrum. An example of the resulting SIMS spectrum is shown in Fig. 1. In addition to the major yttrium and minor calcium and rare earth elements detected with the electron microprobe, the SIMS spectrum also reveals the presence of boron and carbon in

Authors Etz and Newbury are with the Center for Analytical Chemistry, National Bureau of Standards, Gaithersburg, MD 20899; author Dunn is with the Department of Mineral Sciences, Smithsonian Institution, Washington, DC 20560; author Grice is with the Division of Mineral Sciences, National Museum of Natural Sciences, Ottawa, Ont., Canada K1A 0M8.

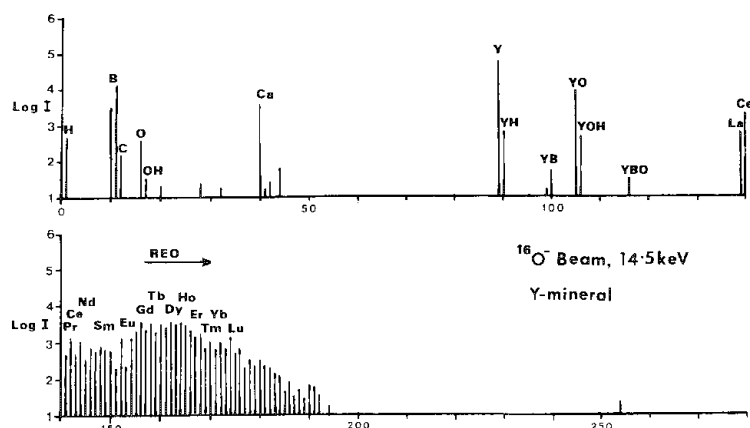


FIG. 1.--SIMS spectrum of candidate new yttrium-bearing mineral.

ate species in addition to the carbonate ion. Based on these findings, it seemed appropriate to examine the spectra of yttrium borates and carbonates and of several natural minerals containing both borate and carbonate species. Thus, spectra were acquired of yttrium oxide, Y_2O_3 ; yttrium carbonate, $Y_2(CO_3)_3 \cdot 3H_2O$; and a stoichiometric solid phase of yttrium borate, YBO_3 . The mineral samples studied include the following natural borates, carboborates, and borates containing other species as a second anion:

Colemanite, $Ca_2B_6O_{11} \cdot 5H_2O$
 Canavesite, $Mg_2(CO_3)(HBO_3) \cdot 5H_2O$
 Gaufreyite, $Ca_4Mn_3X^{3+}(BO_3)_3(CO_3)(O,OH)_3$
 Cahnite, $Ca_2[B(OH)_4][AsO_4]$
 Seamanite, $Mn_3^{2+}(OH)_2[B(OH)_4][PO_4]$

The structural diversity and complexity of borate minerals is apparent from the suite of samples examined in this work. Even with the best data on elemental composition, it is often difficult to elucidate the relationships pertaining to mineral chemistry and structure.

Vibrational spectroscopy, especially infrared, has been extensively used for the structural and molecular characterization of minerals.¹⁻³ Yet, Raman data on borate minerals are quite sparse. For minerals with several molecular groupings, a general assumption is that the spectra are made up of a set of internal modes of each of the molecular units (e.g., CO_3^{2-} , BO_3^{3-} , SO_4^{2-} , H_2O) in the crystal, plus a set of lattice modes characteristic of individual crystal structures. The spectra of borate minerals show great variety and complexity, arising from the many possible anions that these materials may contain.¹ They contain either 3- or 4-coordinated boron resulting in trigonal or tetrahedral coordination, or both. Furthermore, in these minerals polynuclear ions can be formed from these coordination polyhedra, as well as poly-ions of hydrated borates. Among the many possible groups of atoms or species that indicate this structural diversity are BO_3^{3-} , $(B_3O_6)^{3-}$, BO_4^{5-} , and $B(OH)_4^-$, and each vibrating unit has its distinct vibrational spectrum. The measurements described here seek to clarify these implicit structural relationships: first, to distinguish between 3- or 4-coordinated boron; second, to establish whether the oxygen atoms around boron exist as part of hydroxyl groups or as bare oxygen; and third, to obtain information about the presence of discrete water molecules.

The Raman spectra were acquired with the laser-Raman microprobe developed at the National Bureau of Standards.⁴⁻⁵ The instrument employs a scanning double monochromator with cooled photomultiplier tube detection and signal processing by photon counting. The microprobe has been fully automated and uses a computer.⁵ In previous work, the instrument has been applied in a similar fashion to the characterization of biological minerals in calcified tissues.⁶

All spectra were excited with the 514.5nm line of an argon-krypton laser. No serious spectral interferences due to the potential fluorescence of such samples were encountered for any of the mineral specimens. Irradiance levels, directed at the sample in a beam spot $\sim 10 \mu m$ in diameter, ranged from 20 to 50 kW/cm². All spectra were recorded with

the sample. The observed oxygen signal arises at least in part from the oxygen implanted by the primary ion beam.

LRM Analysis

Laser-Raman microanalysis (LRM) was performed on the candidate new mineral and on a series of reference samples that had some relation to the presumed molecular composition of the unknown mineral. The choice of appropriate standards for spectral characterization was governed by results from x-ray crystal structure determinations of the yttrium/boron/carbon (Y/B/C) mineral, which indicated the possible presence of tetrahedral borate

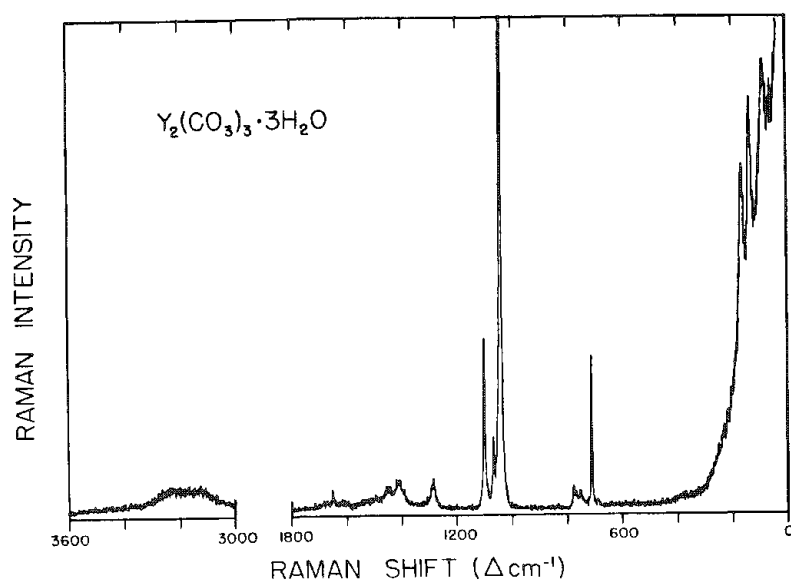


FIG. 2.--Micro-Raman spectrum of yttrium carbonate.

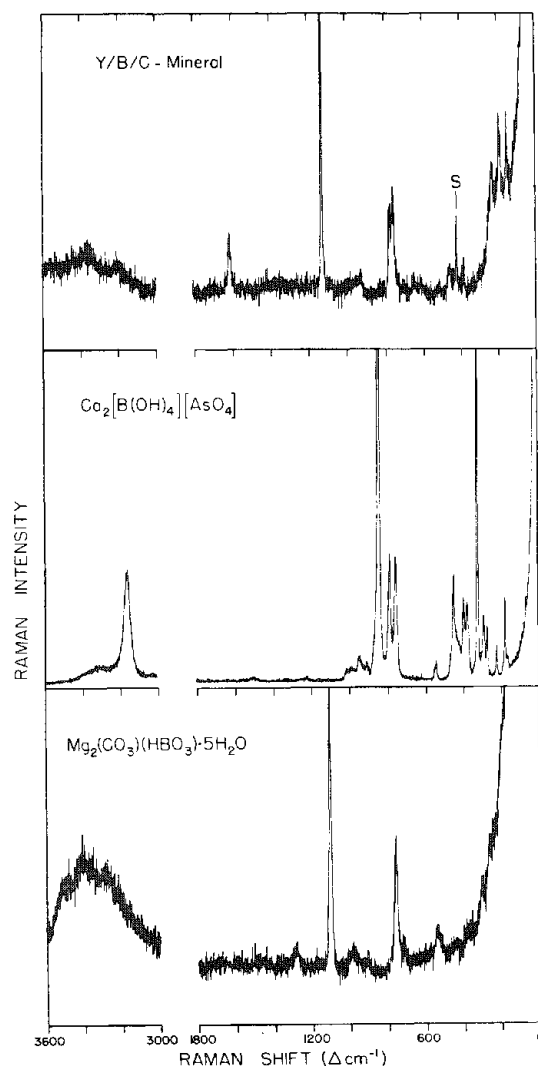


FIG. 3.--Raman spectra of microscopic fragments of three natural minerals: (a) candidate new yttrium-bearing mineral analyzed on a sapphire (S) substrate, (b) borate/arsenate mineral caninite, (c) carborborate mineral canavesite.

5cm^{-1} resolution. They were obtained either from polished sections of the mineral embedded in epoxy, or from microscopic ($\sim 10\text{-}30\ \mu\text{m}$) fragments or crystallites sampled from the bulk and analyzed on either lithium fluoride or sapphire substrates. The spectra are presented in a uniform format. The region from 1800 to $3000\ \text{cm}^{-1}$ has been deleted since no prominent spectral features were observed in this frequency domain.

The initial assumption, that the unknown mineral might consist largely of an impure phase of yttrium carbonate, can be ruled out by comparison of the spectrum of yttrium carbonate hydrate (Fig. 2) with the spectrum of the unknown mineral (Fig. 3a). Raman data have not been reported for any of the rare earth carbonates, though these compounds (some anhydrous and others as hydrates) have been studied by infrared and their spectra correlated with structure.^{3,7,8} Aside from several well-defined lattice modes in the low-frequency region, the prominent feature in the spectrum of the carbonate is the complex band centered around $1080\ \text{cm}^{-1}$ appearing as a triplet ($1046, 1072, 1106\ \text{cm}^{-1}$). This feature is attributed to the symmetric stretching mode (ν_1) of the carbonate ion. In other particle spectra of this compound, the relative intensities of these three components vary. The same is true for the carbonate bands (ν_4 modes, in-plane bending motions) in the $700\text{-}800\ \text{cm}^{-1}$ region, which consist of a more or less well-resolved triplet ($717, 757, 783\ \text{cm}^{-1}$). The group of weak and broad bands in the region from 1250 to $1700\ \text{cm}^{-1}$ includes the carbonate asymmetric stretching vibrations (ν_3 modes) expected around $1400\ \text{cm}^{-1}$ for yttrium carbonate.⁷ The weak, broad band between 3000 and $3400\ \text{cm}^{-1}$ is indicative of OH stretching modes associated with waters of hydration. The spectrum of the unknown Y/B/C mineral has as its prominent features several lattice modes; a medium-intensity doublet centered around $765\ \text{cm}^{-1}$; and a strong, sharp band with peak at $1124\ \text{cm}^{-1}$ (ν_1 carbonate). Other Raman

modes due to carbonate, though much weaker, can be identified as well. The assignment of certain bands to fundamental modes of the CO_3^{2-} ion leaves several other features unaccounted for; they must be considered as arising from scattering by a second vibrational grouping and possibly also hydroxyl species. Since SIMS analysis reveals the presence of boron as a major element, it is reasonable to examine the spectrum for scattering contributions by borate species. To that effect, the spectra of two other complex borates are examined here. One is the spectrum of cahnite (Fig. 3b) and the other is that of canavesite (Fig. 3c). Cahnite is a natural mineral containing the tetrahydroxoborate group, $\text{B}(\text{OH})_4^-$, and the arsenate ion, AsO_4^{3-} . It is one of only a few complex mineral borates for which Raman and infrared data have been reported.⁹ In the micro-Raman study of this mineral, the expected vibrations of the tetrahedral $\text{B}(\text{OH})_4^-$ grouping are observed at 378/397 cm^{-1} (ν_2 modes), at 542/551 cm^{-1} (ν_4 modes), and at 757 cm^{-1} attributed to the ν_1 stretching mode. The adjacent 788 cm^{-1} band is not a fundamental $\text{B}(\text{OH})_4^-$ mode. The grouping of weak bands in the region 900-1000 cm^{-1} is assigned to the ν_3 modes of the tetrahedral ion.⁹ Other bands in the spectrum of cahnite arise from fundamentals of the arsenate ion and vibrations of the OH groups. The frequencies of the AsO_4^{3-} ion are observed in the spectrum as the strong ν_1 mode at 845 cm^{-1} , at 272/290 and 448 cm^{-1} (ν_2 modes), at 323 and 788/843 cm^{-1} (ν_3 modes), and at 419/448 cm^{-1} (ν_4 modes). Cahnite is nonhydrated, so that the band centered at 3162 cm^{-1} is attributed to OH-stretching of the $\text{B}(\text{OH})_4^-$ ion.

Further examination of the spectrum (Fig. 3a) of the unknown mineral in light of the band assignments for $\text{B}(\text{OH})_4^-$ in cahnite reveals sufficient spectral similarities to suggest the existence of tetrahydroxoborate species in this specimen. Thus, the weak features at ~ 385 cm^{-1} , the band at 758 cm^{-1} , and the weak features around 925 cm^{-1} are in the correct frequency regions for $\text{B}(\text{OH})_4^-$, by analogy with the spectra of borate minerals of this type.⁹

Canavesite is a recently discovered mineral and has not yet been characterized by vibrational spectroscopy. Its chemical composition is that of a carboborate of 1:1 carbon-to-boron ratio. The mineral is fibrous; the spectrum of a typical microscopic fiber is shown in Fig. 3(c). Bands due to carbonate vibrations appear at the expected frequency shifts. Most prominent is the carbonate band at 1106 cm^{-1} (ν_1). Other carbonate bands are much weaker, as is the case for the unknown mineral. Overall, the spectrum bears close resemblance to that of the unknown mineral and is in appearance much less complex than that of cahnite. It is now of interest to identify the Raman features that can be attributed to scattering by the HBO_3^{2-} species, the protonated ortho-borate ion. The borate fundamentals in various minerals containing discrete BO_3^{3-} units fall into the range 870-1020 cm^{-1} (ν_1), 680-810 cm^{-1} (ν_2), 1100-1300 cm^{-1} (ν_3), and 550-670 cm^{-1} (ν_4).³ This feature should in principle allow a distinction between vibrations of the $\text{B}(\text{OH})_4^-$ versus the BO_3^{3-} ions. By assigning the band centered at 766 cm^{-1} to the ν_2 bending mode of BO_3^{3-} , one can argue equally well that this band may be attributed to the ν_1 stretching frequency (at 757 cm^{-1} for cahnite) of the BOH vibrating unit of the HBO_2^{2-} ion. Thus, this aspect of the spectrum remains unclear though other features can be uniquely assigned to normal modes of the BO_3^{3-} grouping.

This interpretation of the borate spectra gathered here supports other experimental findings that the structure of the candidate new mineral includes borate functional groups most likely bonded to hydrogen. Our present understanding of the subtleties of these spectra and their relation to structural variances does not allow us to draw definite conclusions regarding the presence of either trigonal or tetrahedral borate in the structure of the unknown mineral. Further work through the application of all synergistic micro-analysis techniques available to us is expected to resolve some of the remaining uncertainties.

References

1. V. C. Farmer, Ed., *The Infrared Spectra of Minerals*, London: The Mineralogical Society, 1974.
2. W. P. Griffith, "Raman spectroscopy of terrestrial minerals," in C. Karr Jr., Ed., *Infrared and Raman Spectroscopy of Lunar and Terrestrial Minerals*, New York: Academic Press, 1975, chap. 12, 299-323.
3. S. D. Ross, *Inorganic Infrared and Raman Spectra*, Maidenhead, Berks., England: McGraw-Hill, 1972.
4. E. S. Etz, "Raman microprobe analysis: Principles and applications," *SEM/1979 I*, 67-82.

5. J. J. Blaha, R. L. Myklebust, and E. S. Etz, "Automation of NBS laser-Raman microprobe," *Microbeam Analysis--1981*, 61-64.
6. M. D. Gryn timer, E. S. Etz, and W. J. Landis, "Studies of calcified tissues by Raman microprobe analysis," *Microbeam Analysis--1982*, 333-337.
7. J. A. Goldsmith and S. D. Ross, "Factors affecting the infrared spectra of some planar anions with D_{3h} symmetry: III. The spectra of rare-earth carbonates and their thermal decomposition products." *Spectrochim. Acta* 23A: 1909-1915, 1967.
8. P. E. Caro, J. O. Sawyer, and LeRoy Eyring, "The infrared spectra of rare-earth carbonates," *Spectrochim. Acta* 28A: 1167-1173, 1972.
9. S. D. Ross, "The vibrational spectra of some minerals containing tetrahedrally coordinated boron," *Spectrochim. Acta* 28A: 1555-1561, 1972.

DEVELOPMENT OF A LUMINESCENCE MICROPROBE

J. L. Alvarez, T. E. Doyle, and V. A. Deason

A luminescence microprobe was developed to supplement measurements from a Raman microprobe. Many crystals that are non-Raman active luminesce, which yields both chemical and crystalline information. This instrument (Fig. 1) was built specifically for crystals with the NaCl structure and for Raman active crystals that exhibit impurity luminescence. Luminescence is defined as the emission of nonthermal, electromagnetic radiation, usually in the visible region. Luminescence includes fluorescence, characterized by an exponential decay rate that is independent of temperature; and phosphorescence, which decays more slowly and with more complex kinetics.¹

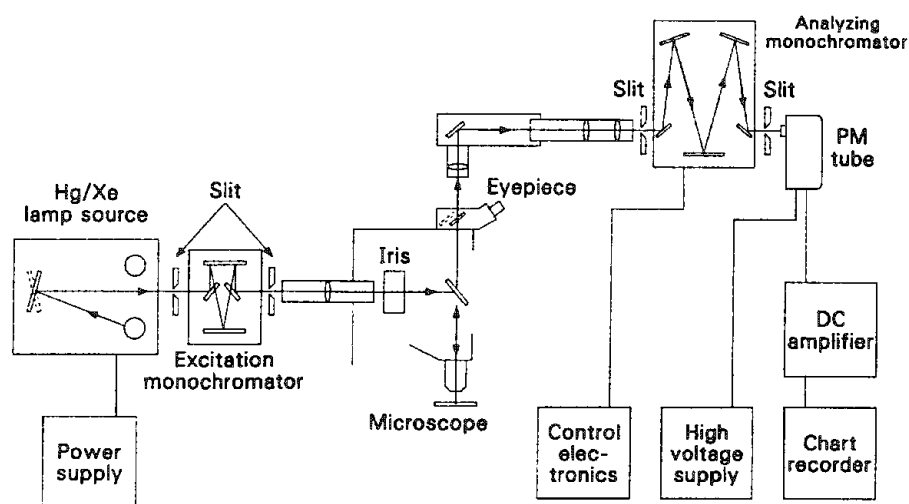


FIG. 1.--Schematic of luminescence microprobe.

The excitation source is either a high-pressure mercury or xenon lamp. The xenon provides a broadband source; the mercury lamp can give selected higher-intensity lines. The source is focused to a narrow beam that is spatially defined by a slit and iris. The source can be monochromatized by means of a 0.125m monochromator with a 1200 lines/mm holographic grating. The grating can be stepped manually to give a 10nm resolution, which allows the observation of the excitation spectrum of the luminescence, i.e., the frequencies of the source that cause the maximum excitation. The source beam is directed through the microscope objective by a half-silvered mirror. The sample can be viewed through the mirror via a UV blocking eyepiece. A white light source is also available for viewing non-luminescing samples. The UV objective is 16 \times .

The luminescence from the source is collected by the objective and passed via a half-silvered mirror to the analyzing monochromator. The optical characteristics of the microscope and monochromator differ, and must be matched by a three-lens system to optimize the signal. The analyzing monochromator is a 0.32m instrument with a holographic grating having 2400 lines/mm and driven by a stepping motor at 0.01nm increments, yielding a resolution of 0.05 nm. At present, resolution of this order is not attainable since the slits on the analyzing monochromator are opened to a width to achieve sufficient throughput. The detector is a UV sensitive, side-window photomultiplier tube mounted in an ambient-temperature housing. The signal from the PM tube is routed to a DC amplifier and a chart recorder.

The combination of the luminescence and excitation spectra is sufficient for compound and crystal identification in most cases. The resolution is not adequate for investigating phonon mediated fluorescence and luminescence line widths.

The authors are at EG&G Idaho, Inc., Idaho Falls, ID 83415. Work performed for the Nuclear Regulatory Commission.

Instrument Description

The microprobe can obtain a luminescence and an excitation spectrum from an area as small as 30 μ m. The system is designed around a modular UV microscope. The source can be broadband or monochromatic. The excitation beam is directed normally upon the sample through the microscope optics. The luminescence is collected by the same optics for transmission to the analyzing monochromator.

Results

The microprobe was developed specifically to identify fission-product CsI. It has been postulated that most of the iodine produced in nuclear reactors resides in the fuel rods as CsI. The form of the iodine and its chemistry upon release from the fuel are important in hazard analysis and protection schemes. Samples from a deliberately failed test reactor were to be examined by the microprobe to determine the existence of CsI.

Cesium iodide crystals exhibit broadband luminescence centered at 420 nm. The line width at half maximum is 63 nm.² This luminescence is the result of defects in the crystal.³⁻⁵ Broadband luminescence is far from sufficient for identification since many crystals exhibit the same or nearly the same luminescence. The frequency that excites the luminescence can be diagnostic. The excitation frequency for the CsI luminescence is centered at 240 nm with a line width at half maximum of 10 nm.²

Work on standards to determine the ability of the microprobe to observe the luminescence and excitation spectra on small particles has revealed several difficulties in obtaining the spectra that are the direct result of CsI chemistry. The observations eliminate several proposed reactions at low temperature on solids but investigations have not been made at high temperature on vapors.

Cesium iodide crystals stored open to the atmosphere at room temperature or as received from a vendor do not exhibit luminescence. The cause appears to be quenching by waters of hydration on the surface. A luminescence spectrum is obtained if the crystal is crushed and a particle from the center is examined. The strength of the luminescence decreases with exposure to the atmosphere but regains strength if heated. No Raman spectra are observed from either the fresh or the stored crystals. This seems to indicate that the reaction occurring is $\text{CsI} + x\text{H}_2\text{O} \rightarrow \text{CsI} \cdot x\text{H}_2\text{O}$ and not $\text{CsI} + x\text{H}_2\text{O} \rightarrow \text{CsOH} + \text{HI}$ or $\text{CsIO}_3 + \text{HIO}$.

The iodates have characteristic Raman spectra and CsOH reacts with CO_2 in the air to give CsHCO_3 , which is also Raman active.

These results and further planned experiments may elucidate the expected chemistry and chemical forms of the CsI when nuclear reactor samples are examined.

Possible Improvements

The present instrument was constructed to demonstrate the feasibility of a micro-luminescence instrument and to solve a specific problem, the identification of CsI. It was built at an equipment cost of approximately \$40K. Several improvements are possible to increase the sensitivity and resolution and decrease the spot size.

The sensitivity can be increased by three methods. The first is to increase the power of the source. Brighter lamps are available as are UV lasers. The latter are very inefficient and require high-power lasers with frequency doubling systems. These high-power, high-cost systems may be advantageous for some applications. Such a laser would cost \$100K. The second method is to lower the noise in the detection system. High-sensitivity, low-noise, cooled photomultiplier systems are available at moderate costs, roughly 10% of the present system parts. The third method of sensitivity improvement would also reduce the spot size. This goal can be accomplished by incorporating a 74× objective, which increases the resolving power by 4.6× and should reduce the spot size (area) by 1/20. The spot size can be further reduced but with a loss of intensity by use of a smaller source diaphragm opening.

Resolution can be increased, at the expense of throughput, by use of higher-resolution monochromators. A double monochromator would be particularly advantageous for the analyzer and would eliminate second-order diffraction interferences. The higher resolution would allow investigation of impurity luminescence and phonon-mediated luminescence that is currently being done with visible excitation frequencies. UV excitation dependence would be very helpful in explaining the interactions and may enhance weak lines or produce new lines.

A UV laser or higher-resolution monochromator may improve the excitation frequency information. A UV laser would also contribute to a smaller spot size, since a narrow, parallel beam is produced.

Conclusions

A luminescence microprobe has been developed that demonstrates the possibility and usefulness of such a system. It is adequate to its original purpose of detecting micro quantities of CsI. The instrument in conjunction with a Raman microprobe has demonstrated CsI chemistry under some conditions and indicates methods of examining for CsI on nuclear reactor samples.

Several modifications can be made in the system for specialized or general purpose use.

References

1. F. Williams, "Theoretical basis for solid-state luminescence," in P. Goldberg, Ed., *Luminescence of Inorganic Solids*, New York: Academic Press, 1966, 1-52.
2. Z. L. Morgenshtern, "Luminescence of unactivated CsI monocrystals," *Optics and Spectroscopy* 7: 146-148, 1959.
3. Z. L. Morgenshtern, "Luminescence of unactivated CsI crystals: II," *Optics and Spectroscopy* 8: 355-357, 1960.
4. K. Teegarden, "Halide lattices," in P. Goldberg, Ed., *Luminescence of Inorganic Solids*, New York: Academic Press, 1966, 53-118.
5. T. Iida, Y. Nakaoka, J. P. Van der Weid, and M. A. Aegerter, "Self-trapped exciton in cesium iodide: I. Theory," *J. Physics* C13: 983-992, 1980.

SOME ANALYTICAL APPLICATIONS OF MICRO IR AND MICRO RAMAN SPECTROSCOPY

M. Mehicic, M. A. Hazle, R. L. Barbour, and J. G. Grasselli

Many microprobe techniques are available in the laboratory today and are used with various types of analytical spectroscopy. Electron and ion beam microprobes are generally very good for atom concentration determination, although SIMS can provide very useful molecular information under proper conditions. Molecular information is much better approached by the relatively recent development of vibrational spectroscopy microprobes, i.e., infrared and Raman microspectroscopy.¹⁻⁶ In an industrial analytical spectroscopy laboratory, where material identification is one of the typical problems, these techniques are developing into very important tools. This paper presents some typical applications.

Catalysts

In both fixed and fluid bed heterogeneous catalysts, catalyst particle homogeneity is a very important question. Many industrial catalysts are multiphase systems, usually consisting of a support material (Al_2O_3 or SiO_2) and the active phase, which is either one or more metals or metal oxides. Many of the active phases have inhomogeneities either through deliberate preparation or because of use. The ability to detect these phases is important, as they seriously affect the catalyst's performance. An example of the use of the Raman Microprobe to detect different phases is shown in Fig. 1. These catalyst particles show different color regions. Spectra were obtained from a dark colored particle and a light colored particle. In both cases particles were less than $5 \times 10 \mu\text{m}$. The differences in the relative amount of $\text{Fe}_2(\text{MoO}_4)_3$ (789 cm^{-1}), and the other molybdates ($900\text{-}1000 \text{ cm}^{-1}$ region), are easily recognized. Obtaining comparable information with Micro IR is very difficult because of low transmission and reflectance. Raman spectroscopy, in general, is a better technique for studying active phases in supported heterogeneous catalysts because most common supports (SiO_2 , Al_2O_3) are strong IR absorbers and poor Raman scatterers.

Ferrography

Ferrography is the study of shape, concentration, composition, size, and distribution of wear particles in lubricating and hydraulic fluids.⁷ Infrared spectroscopy provides additional information on the extent and type of oil degradation and microspectroscopy techniques can be used to provide even better chemical characterization of particles (AES for atomic and micro IR/R for molecular).

Minerals

Traditionally minerals analysis is the domain of electron microscopy and elemental analysis techniques associated with it (energy-dispersive x-ray analysis), but vibrational spectroscopy is making an impact, particularly in situations where atomic composition is not sufficient to determine the chemistry of the particle. Problems are associated with mineral inclusions, flotation problems, separations, etc.

Corrosion

The economic impact of corrosion in the oil industry is enormous, providing an impetus for extensive scientific research. Many analytical methods are applied in corrosion problems; electron beam excited AES/SAM and microscopy are probably the most common methods for study of many problems such as embrittlement, crack formation, segregation/boundaries, etc. Microvibrational spectroscopy has much to offer in this area. There are applications to the study of filliform corrosion⁸ which occurs on painted metals (pipe-lines, storage areas).

The authors are at The Standard Oil Company, Research and Development, Cleveland, OH 44128.

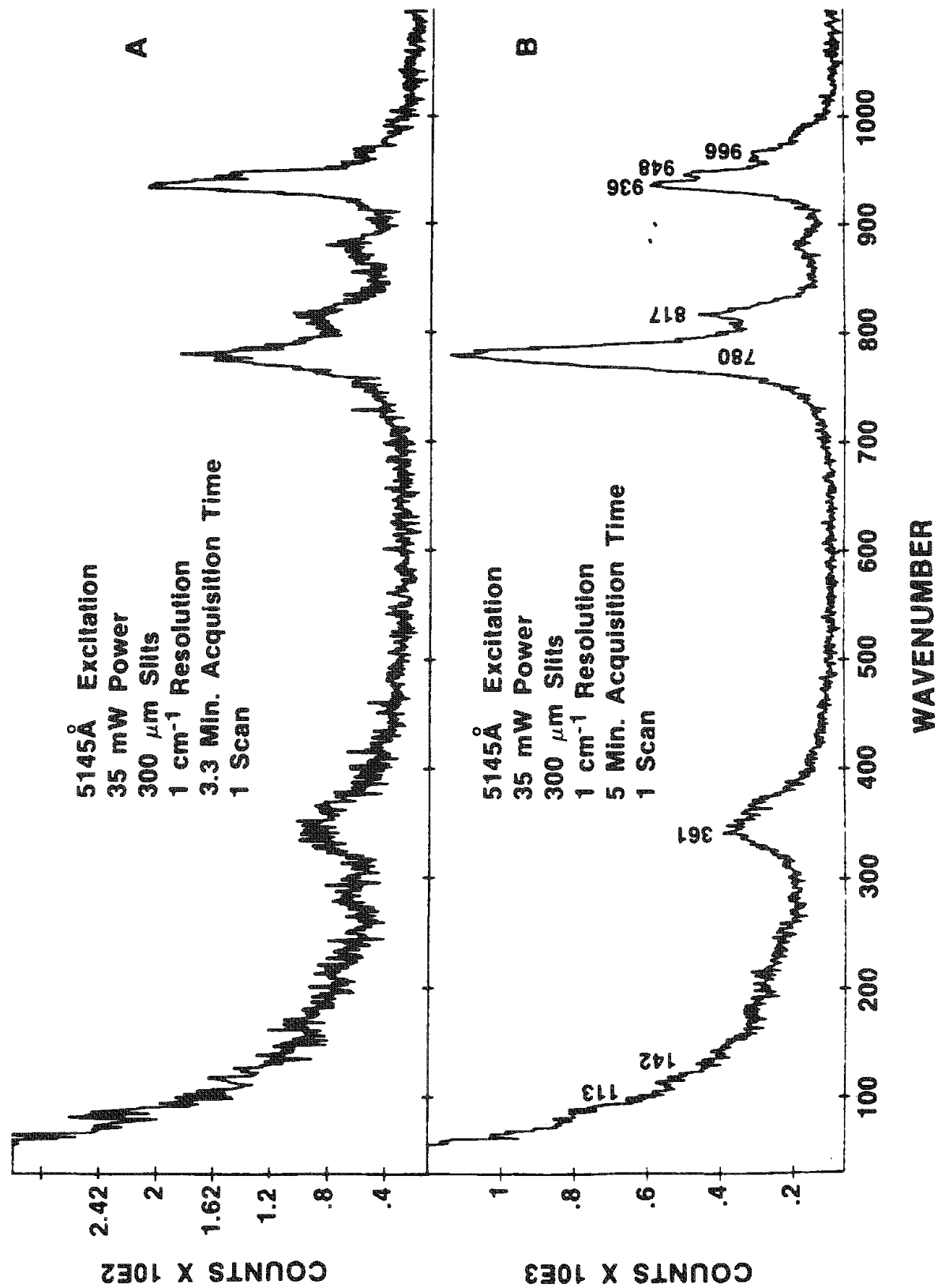


FIG. 1.--Raman microprobe spectra of ammoxidation catalyst particles.

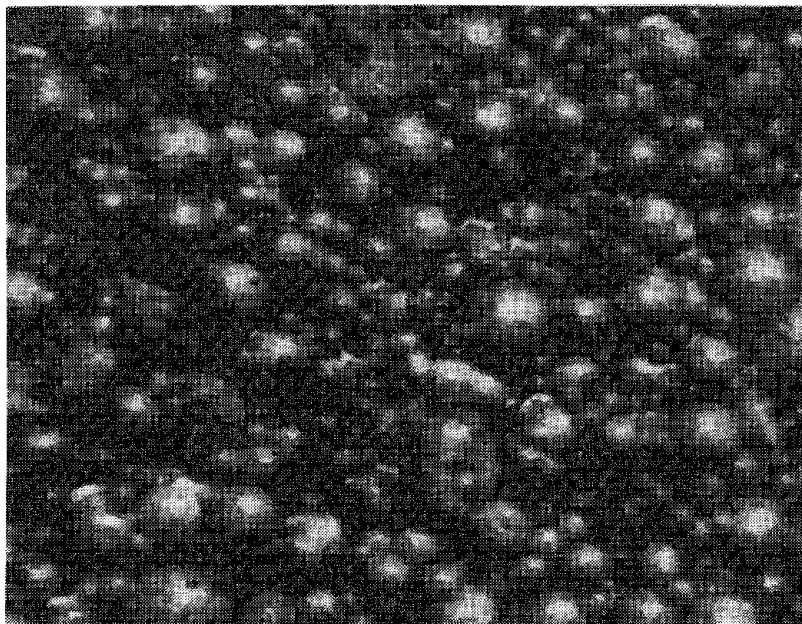


FIG. 2.--Ammoxidation catalyst particles, 128 \times .

Polymers

Microspectroscopy can be very useful in the study of polymers. There are a variety of problems such as inclusions, separation of phases, bubbles, etc.

Other applications include environmental problems (solid particles trapped in smoke stacks or liquid-phase filters), fossil fuels (inhomogeneties and chemistry of coals, tar sands, and shale rock), and ceramic materials.

References

1. G. J. Rosasco, "Raman microprobe spectroscopy," in R. J. H. Clark and R. H. Hester, Eds., *Advances in Infrared and Raman Spectroscopy*, London: Heyden, 1980, vol. 7.
2. F. Adar, "Developments in Raman microanalysis," *Microbeam Analysis--1981*, 67-72.
3. J. W. Brasch, R. J. Yakobsen, and C. J. Riggle, "Development and use of a combined beam condenser microscope for FT-IR spectroscopy," *Microbeam Analysis--1982*, 000.
4. H. H. Hausdorff and V. J. Coates, "Microspectrophotometers for small-sample analysis," *ibid.*, pp. 233-237.
5. C. J. Curry, M. J. Whitehouse, and J. M. Chalmers, "Ultramicrosampling in infrared spectroscopy using small apertures," *Appl. Spectrosc.* 39: 174, 1985.
6. P. J. Miller, G. J. Piermarini, and S. Block, "An FT-IR microspectroscopic method for kinetic measurements at high temperatures and high pressures," *ibid.*, 38: 680, 1984.
7. Y. Laskowski, "Ferrography: Powerful maintenance technique," *Oil and Gas J.*, 5 November 1984.
8. R. T. Ruggeri and T. R. Beck, "An analysis of mass transfer in filliform corrosion," *Corrosion-NACE* 32: 452, 1983.

MICROLUMINESCENCE SPECTRA OF Ti-ACTIVATED $\text{ZrO}_2\text{-Y}_2\text{O}_3$

T. E. Doyle and J. L. Alvarez

Sharp-line luminescence of titanium impurities in the system $\text{ZrO}_2\text{-Y}_2\text{O}_3$ has been investigated. Cubic ZrO_2 and $\text{Zr}_3\text{Y}_4\text{O}_{12}$ exhibit broadening of the luminescence lines that can be attributed to structural disorder. The sharp-line luminescence also provides a method for determining the phonon modes in cubic ZrO_2 .

Investigators have observed luminescence in zirconia as a blue-white broadband emission¹ and sharp-line emissions in the green region of the spectrum.² Both the broadband and sharp-line luminescence can be ascribed to trace impurities of titanium in solid solution with the ZrO_2 .^{1,2} Asher et al.² proposed that the sharp-line luminescence arises from phonon-mediated de-excitation of excited states rather than direct electronic transitions. The excited states, consisting of three closely spaced energy levels, decay by producing both a photon and a single long-wavelength optical phonon. Therefore, the frequencies of the luminescence peaks correspond directly to discrete phonon energies.

Although sharp-line luminescence in Ti-activated ZrO_2 has been previously reported,² we have not found a discussion of sharp-line luminescence in ZrO_2 binary systems in the literature. The present study examined the sharp-line luminescence spectra of solid solutions and an intermediate compound in the system $\text{ZrO}_2\text{-Y}_2\text{O}_3$. Our experiments indicate that structural disorder in cubic ZrO_2 and in $\text{Zr}_3\text{Y}_4\text{O}_{12}$ broadens the luminescence lines. However, individual luminescence lines and thus their associated phonon frequencies are still discernible and allow phonon mode determination for cubic ZrO_2 . The results demonstrate the use of luminescence for probing crystal structures in zirconia binary systems.

Experimental

We made $\text{ZrO}_2\text{-Y}_2\text{O}_3$ solid solutions and an intermediate compound by a coprecipitation method adapted from Garvie.³ Proportioned amounts of zirconyl nitrate and yttrium nitrate were separately dissolved in distilled water and mixed. The hydroxides were precipitated by the addition of ammonium hydroxide until the solution became basic. The precipitate was centrifuged, decanted, and dried under a heat lamp for 2 h to evaporate excess water and ammonia. It was then heated in a muffle furnace at 1000 C for 16 h to drive off water from the hydrous oxide. ICP analysis confirmed that the zirconyl nitrate contained sufficient amounts of titanium impurities to cause luminescence in the resultant solid solutions and compound. We also made CaO-stabilized cubic ZrO_2 using the coprecipitation method and heating the precipitate to 1000 C.

Sample particles were mounted on glass slides and placed under the microscope of an Instruments SA MOLE 77 Raman microprobe for analysis. Spectra were taken of the particles by monochannel scanning and photon counting. The excitation source was an Ar^+ laser at wavelengths of 488.0 nm (blue) and 514.5 nm (green). The luminescence peaks were differentiated from the Raman peaks by changing the excitation wavelength.

Results and Discussion

Figure 1 is the phase diagram of the system $\text{ZrO}_2\text{-Y}_2\text{O}_3$.⁴ The circles in the phase diagram represent the compositions of three samples we made and the temperatures reached. Raman spectra of sample particles acquired simultaneously with the luminescence spectra verified that the tetragonal and cubic phases were achieved. The Raman spectrum of the sample containing 40 mol % Y_2O_3 was different from the spectra of the three ZrO_2 polymorphs, and is probably the spectrum of $\text{Zr}_3\text{Y}_4\text{O}_{12}$. The x-ray diffraction pattern of the sample indicated $\text{Y}_{0.15}\text{Zr}_{0.85}\text{O}_{1.93}$ with some d-spacing shift, and a mixed phase was most probably present in the sample.⁵ Cubic ZrO_2 stabilized with 20 mol % CaO was also made, with the cubic phase verified by Raman spectroscopy.

Figure 2 displays the Raman and luminescence spectra of the three $\text{ZrO}_2\text{-Y}_2\text{O}_3$ samples. The 514.5nm line was the excitation wavelength. Tetragonal ZrO_2 (top) produced 8 sharp, distinct luminescence lines and 4 broader luminescence lines between 900 and 1700 cm^{-1} .

The authors are at EG&G Idaho, Inc., Idaho Falls, ID 83415. Work performed for the Nuclear Regulatory Commission.

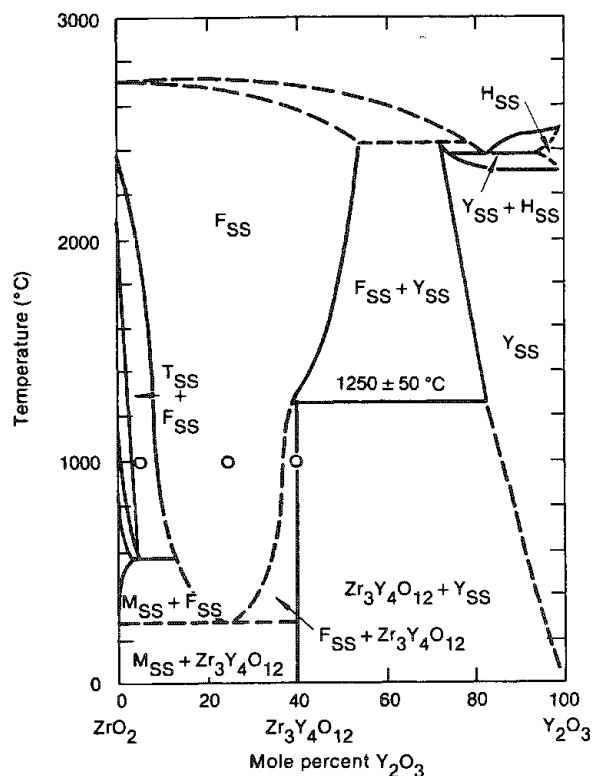


FIG. 1.--Phase diagram of system $\text{ZrO}_2\text{-Y}_2\text{O}_3$ (Ref. 4). Circles represent sample composition and treatment temperature.

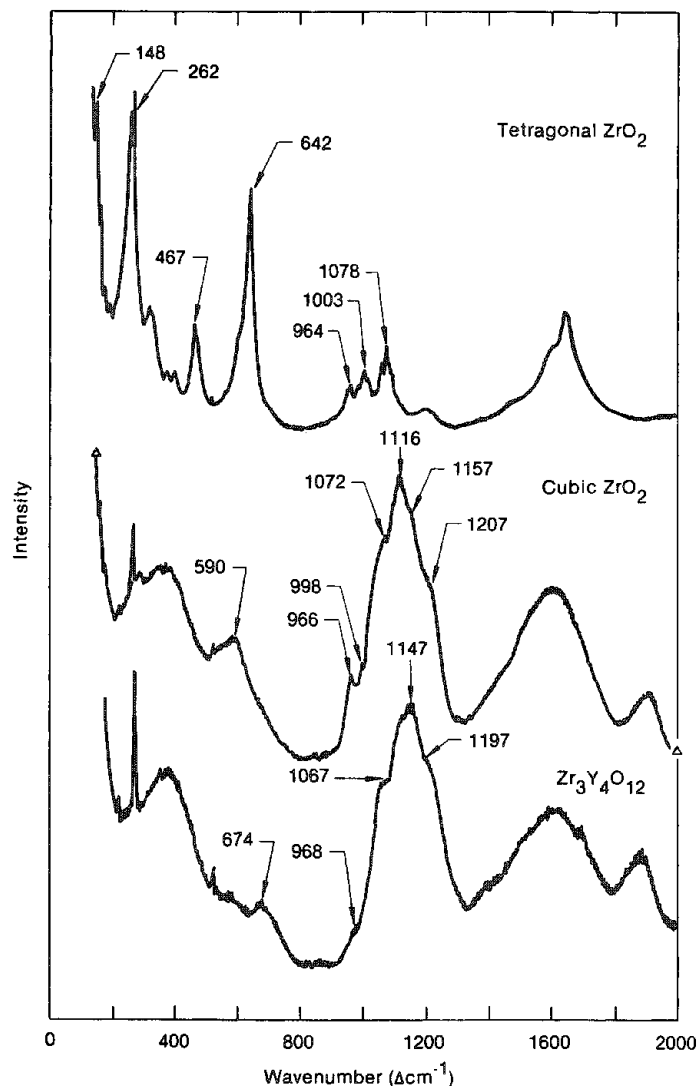


FIG. 2.--Raman and luminescence spectra of three $\text{ZrO}_2\text{-Y}_2\text{O}_3$ samples.

Cubic ZrO_2 (middle) produced 6 broad lines and 1 sharp line between 900 and 1700 cm^{-1} , and an additional broad peak appears at 1900 cm^{-1} . $\text{Zr}_3\text{Y}_4\text{O}_{12}$ (bottom) displayed a broad Raman band at 674 cm^{-1} . Seven broad luminescence lines were discernible with $\text{Zr}_3\text{Y}_4\text{O}_{12}$ from 900 to 1700 cm^{-1} , with an additional peak appearing at 1870 cm^{-1} .

Both cubic ZrO_2 and $\text{Zr}_3\text{Y}_4\text{O}_{12}$ exhibit a defect structure primarily associated with oxygen vacancies.⁶ In cubic ZrO_2 , the oxygen ions are also shifted from their ideal fluorite lattice sites.⁷ $\text{Zr}_3\text{Y}_4\text{O}_{12}$ has a rhombohedral crystal structure, with oxygen vacancies lying along the $[111]$ crystal axis.⁶ In general, structural disorder in a crystalline compound results in a broadening of the luminescence lines.⁸

It is evident from the spectra that a definite broadening of the luminescence lines occurs with cubic ZrO_2 and $\text{Zr}_3\text{Y}_4\text{O}_{12}$, and is most likely associated with the defect structure. Also noticeable is the change in frequency of the luminescence lines with the different samples, probably resulting from the change in crystal structure that alters the phonon frequencies in the lattice. We also observed lesser effects due to crystal orientation.

We obtained similar results from the luminescence spectra of CaO -stabilized cubic ZrO_2 and CaZrO_3 . Spectra of the CaO -stabilized cubic ZrO_2 revealed broadening of the luminescence lines. Broadening was not apparent in the spectra of CaZrO_3 , which has an orthorhombic perovskite crystal structure.

Because the frequencies of the luminescence peaks correspond directly to discrete phonon energies, luminescence can be used to determine the phonon modes of cubic ZrO_2 and various zirconate compounds. This technique would be especially useful since the Raman

spectra are weak and yield limited information on the phonon modes. For example, the Raman spectrum of cubic ZrO_2 is a weak continuum representing a density-of-states function caused by structural disorder in the form of oxygen vacancies creating a breakdown of the $k = 0$ selection rule.^{9,10}

Using the values for the energy levels of $\text{ZrO}_2:\text{Ti}^{4+}$ derived by Asher et al.,² we can calculate the phonon modes of Y_2O_3 -stabilized cubic ZrO_2 from the luminescence lines. Table 1 displays the values for the energy levels (absolute wavenumbers), luminescence line frequencies (Raman frequency, centered at 514.5 nm), and the corresponding phonon frequencies.

Because they both have a cubic fluorite structure, the phonon modes of cubic ZrO_2 should be similar to those of UO_2 . On examination (Table 2), we find fair agreement. Vibrations of the oxygen ions in the crystal lattice produce these phonon modes. We are at present working to deconvolute the cubic ZrO_2 luminescence spectrum to interpret the data more accurately.

TABLE 1.--Luminescence line frequencies and corresponding phonon modes for cubic ZrO_2 .

Luminescence lines (cm^{-1})	Energy level (cm^{-1})	Phonon frequency (cm^{-1})
966	18705	236
998		268
1072	18687	324
1116		368
1157 (shoulder)		409
1207 (shoulder)		449

TABLE 2.--Comparison of cubic ZrO_2 and UO_2 phonon modes.

Cubic ZrO_2 phonon modes (cm^{-1})	UO_2 phonon modes (Ref. 11) (cm^{-1})
236	233 $[\text{M}_5]$
268	284 $[\text{T}_{1\text{u}}(\text{T0})]$
324	328 $[\Sigma_3(01)]$
368	352 $[\text{L}_3]$
409	407 $[\text{L}_3']$
449	447 $[\Gamma_{25}']$

Summary

We have used the sharp-line luminescence of titanium impurities to probe crystal structures in the system $\text{ZrO}_2\text{-Y}_2\text{O}_3$. The presence of Y_2O_3 in the crystal lattice alters the frequencies of the luminescence lines, probably as a result of the change in crystal structure and phonon modes. Luminescence line broadening was observed in both cubic ZrO_2 and $\text{Zr}_3\text{Y}_4\text{O}_{12}$, and can be attributed to structural disorder. The phonon modes in cubic ZrO_2 were determined from the luminescence lines, and the phonon frequencies appear to correspond to those of UO_2 .

References

1. J. F. Sarver, "Preparation and luminescent properties of Ti-activated zirconia," *J. Electrochem. Soc.* 113: 124-148, 1966.
2. I. M. Asher, B. Papanicolaou, and E. Anastassakis, "Laser excited luminescence spectra of zirconia," *J. Phys. Chem. Solids* 37: 221-225, 1976.
3. R. C. Garvie, "The occurrence of metastable tetragonal zirconia as a crystallite size effect," *J. Phys. Chem.* 69: 1238-1243, 1965.

4. V. S. Stubican, R. C. Hink, and S. P. Ray, "Phase equilibria and ordering in the system $\text{ZrO}_2\text{-Y}_2\text{O}_3$," *J. Am. Ceram. Soc.* 61: 17-21, 1978.
5. S. P. Ray, V. S. Stubican, and D. E. Cox, "Neutron diffraction investigation of $\text{Zr}_3\text{Y}_4\text{O}_{12}$," *Mat. Res. Bull.* 15: 1419-1423, 1980.
6. V. S. Stubican and J. R. Hellman, "Phase equilibria in some zirconia systems," in A. H. Heuer and L. W. Hobbs, Eds., *Science and Technology of Zirconia*, Columbus, Ohio: The American Ceramic Society, 1981, 25-36.
7. E. C. Subbarao, "Zirconia: An overview," *ibid.*, 1-24.
8. G. E. Rindone, "Luminescence in the glassy state," in P. Goldberg, Ed., *Luminescence of Inorganic Solids*, New York: Academic Press, 1966, 422.
9. V. G. Keramidas and W. B. White, "Raman scattering from $\text{Ca}_x\text{Zr}_{1-x}\text{O}_{2-x}\square_x$: A system with massive point defects," *J. Phys. Chem. Solids* 34: 1873-1878, 1973.
10. A. Feinberg and C. H. Perry, "Structural disorder and phase transitions in $\text{ZrO}_2\text{-Y}_2\text{O}_3$ system," *J. Phys. Chem. Solids* 42: 513-518, 1981.
11. G. Dolling, R. A. Cowley, and A. D. B. Woods, "The crystal dynamics of uranium dioxide," *Can. J. Phys.* 43: 1397-1413, 1965.

ANALYSIS OF MICROZONING IN DIAMOND

M. E. Andersen, T. B. Vander Wood, and R. Z. Muggli

Diamond has long held an interest for people as a result of its unique physical properties. The best known of these properties include hardness and high refractive index, both of which are important gem qualities. Other applications for diamond can be found, however. For instance, its hardness would be an advantage as a protective layer on a product such as a computer disk. In addition, diamond has a thermal conductivity which is higher than copper metal;¹ thus, there is great interest in it for utilization in semiconductors. Geologists have always viewed diamonds with interest because they are a phase that is thermodynamically stable only at high pressure; so its persistence at atmospheric pressure, where it can be studied, has given geologists the opportunity to gain information about the earth's interior by studying the phase relations of diamond and associated minerals and the inclusions and trace elements within the diamond (e.g., Ref. 2).

Diamond has been previously widely studied on a macro scale. One of the most prominent of the elements present in diamond, other than carbon, is nitrogen. Nitrogen is most readily detected by its effect on the infrared spectrum of diamond. Boron has also been found in diamonds and renders them semiconducting.³ On a micro scale the phases included within diamonds have been studied both in situ and after removal from the diamond matrix.

We recently began study of a unique diamond that had been cleaved to produce surfaces parallel to the (100) plane. This diamond displayed a peculiar zoning pattern shown by variations in birefringence (Fig. 1) and, when exposed to long-wavelength (365nm) UV (Fig. 2), the diamond showed oscillatory zoning in its fluorescence pattern. The oscillations are displayed on an extremely fine scale, so that a determination of the cause of this oscillatory zoning requires microprobe techniques. In this paper we discuss the application of two microprobes to the study of this unique diamond.

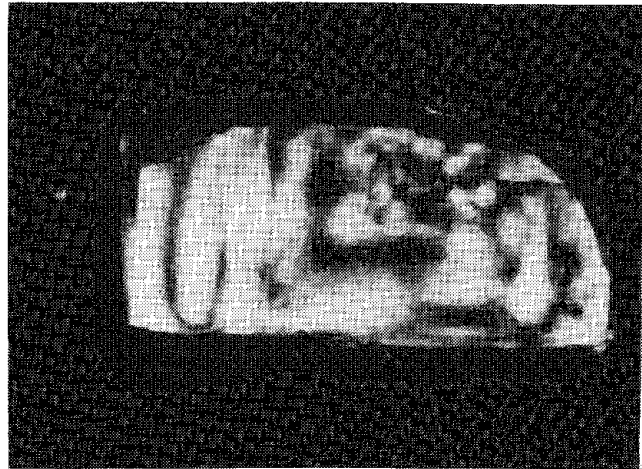


FIG. 1.--Zoning in diamond sample shown by variations in birefringence.

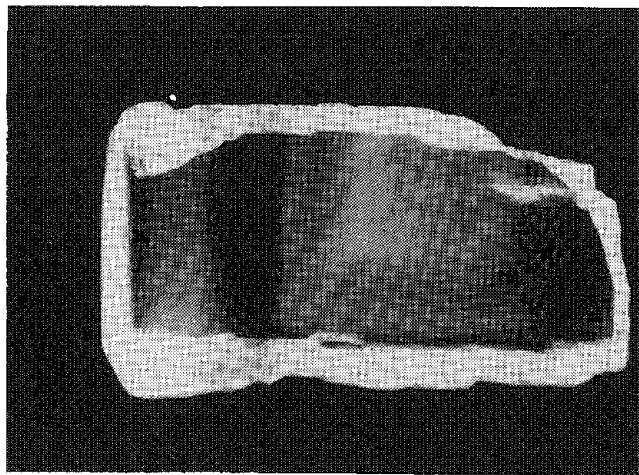


FIG. 2.00Same diamond as in Fig. 1, displaying oscillatory zoning in ultraviolet fluorescence.

Micro IR Spectroscopy

We have taken a Perkin-Elmer Model 85 infrared microscope and merged it with our Digilab FTIR (Fig. 3). This system allows us to image a sample at approximately 150× magnifications using a condensing system and a matched objective with a numerical aperture of approximately 0.75. Apertures are placed in an intermediate magnified image plane, which allows one to control the width and length of the region being studied. Because these

The authors are with Walter C. McCrone Associates, 2820 S. Michigan Avenue, Chicago, IL 60616.

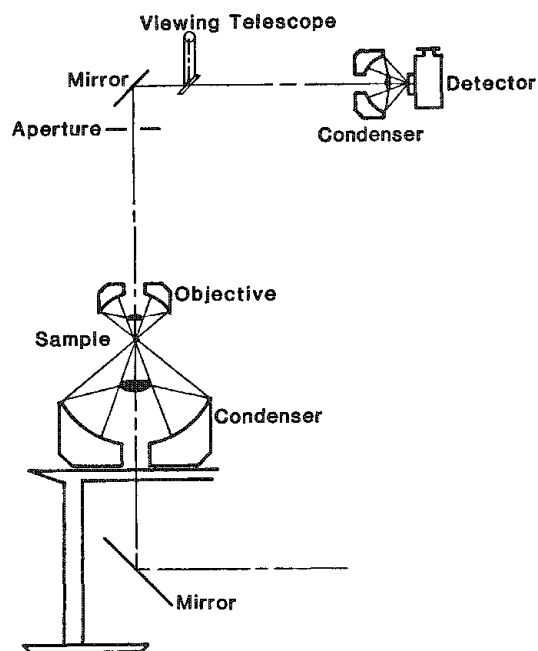


FIG. 3.--Schematic of micro-infrared absorption spectrometer used in these analyses.

attributed to a "B" type aggregate, believed to contain more nitrogen atoms than the Ia type. Both of these features are quite common in Type Ia diamonds.

Synthetic diamonds are characterized by atomically dispersed, not aggregated, nitrogen atoms. These diamonds yield a strong band at approximately 1120 wavenumbers, and are termed Type Ib diamonds. Numerous diamonds also contain "platelets" of nitrogen. The infrared band associated with these platelets occurs at 1370 wavenumbers, known as the "B'" feature. Some micro data supporting the correlation of these platelets with nitrogen have been found but the abundance of platelets does not correspond to the total amount of nitrogen in a diamond.⁴ In Fig. 5 we plot the intensities of the absorbance vs distance across a prominent zone of the diamond after normalizing to the diamond bands. It is apparent that the nitrogen content drops off precipitously in the low-fluorescence zone as indicated by the drop off in the intensity of Type A and B features. It is significant that the B' features, associated with the nitrogen platelets, also drop off in a like manner. This effect is certainly consistent with the interpretation that the platelets are related to nitrogen.

Ion Microprobe Results

The diamond was also mounted for analysis by ion microprobe. The instrument used was the Instruments SA Riber Model MIQ 156. This instrument is an ultrahigh-vacuum (10^{-11} Torr) quadrupole system. Utilizing an ultrahigh vacuum minimizes hydride formation from residual water vapor and makes the interpretation of the resulting mass spectrum simpler. The analyzing beam was a $^{40}\text{Ar}^+$ beam accelerated through 20 kV; an electron gun was used for charge neutralization.

Two areas of the diamond were analyzed in this initial study. One was a highly UV fluorescent area; the other was a low-fluorescence area which corresponds to the regions analyzed by micro infrared. Ion intensities were normalized to ^{12}C for each region and the ratio of high fluorescence to low fluorescence areas was taken. The low-fluorescence region exhibited a lower concentration of most elements (Fig. 6). It can be seen that the highly fluorescent region is significantly enriched in nitrogen, consistent with the infrared data. However, this region is also highly enriched (by an order of magnitude) in sodium, potassium, aluminum, etc. These elements correspond to the elements of an eclogite association of minerals in the mantle source regions of diamonds. The platelet band intensity at 1370 cm^{-1} is also correlated with element variations other than nitrogen.

apertures are in the magnified image plane, diffraction effects are much less important than if one attempted to aperture at the sample. An image of the sample is focused onto the detector, which is a liquid-nitrogen-cooled MCT type. Because this microscope incorporates all reflecting objectives, there is no dispersion and one can conveniently image in white light to orient and bring the sample into proper focus. For this particular experiment, the diamond was oriented so that one set of apertures was parallel to the direction of the banding. We set the width of the apertures to approximately $20\text{ }\mu\text{m}$ and the length to approximately $100\text{ }\mu\text{m}$.

A number of extreme regions, in terms of ultra-violet fluorescence, were known to be present and we stepped the diamond across the interface between a low- and high-fluorescence region. The spectra from two such regions are shown in Fig. 4. The bands in the region from 1600 to 2800 wavenumbers are intrinsic to diamond and these features were used to normalize the nitrogen features. This diamond is a Type Ia diamond, which implies the presence of nitrogen. The broad band at 1280 wavenumbers arises from "A" features, which correspond to a pair of nearest-neighbor nitrogen atoms substituted for carbon in the diamond lattice. The band at 1170 wavenumbers is

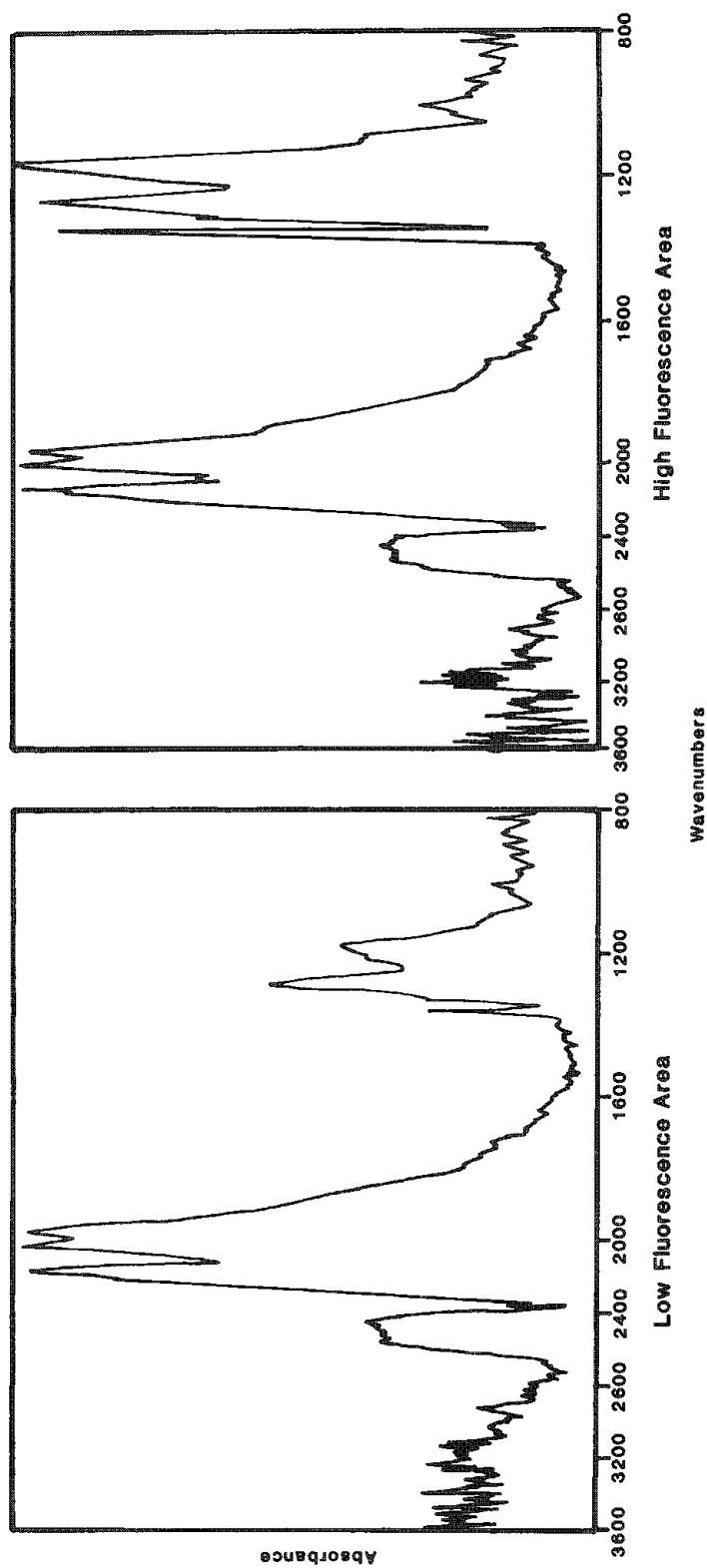


FIG. 5.--Infrared absorption spectra obtained from two regions showing extremes in ultraviolet fluorescence.

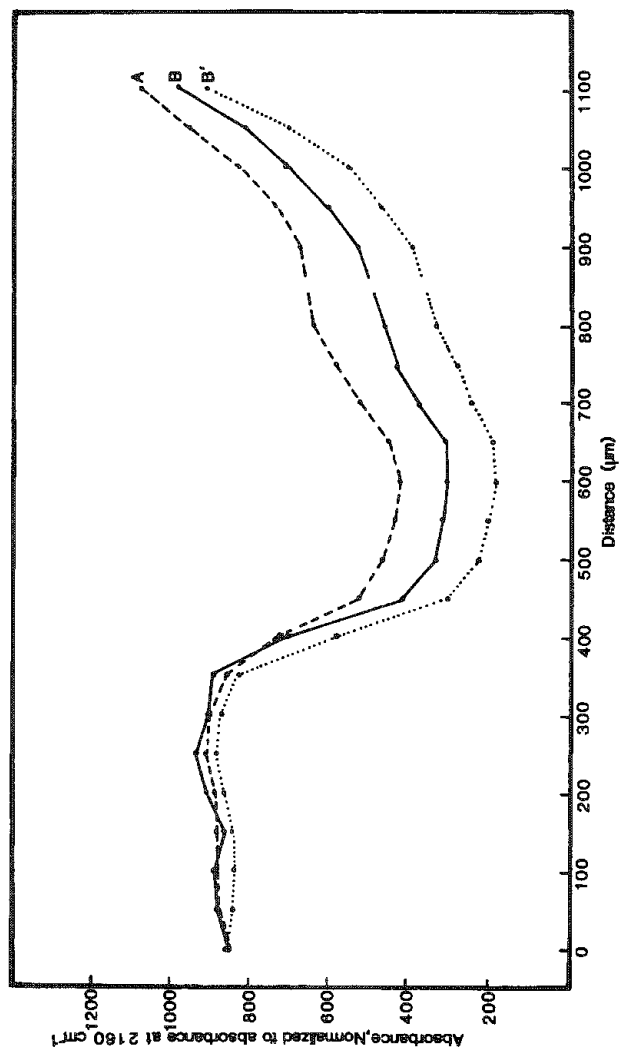


FIG. 4.--Nitrogen-related feature absorption intensity variations along transect across boundary between high and low fluorescence zones.

Conclusions

The oscillatory zoning pattern detected in the diamond by fluorescence and birefringence is shown to be associated with distinct chemical oscillations. These oscillations are certainly related to the growth of the diamond, possibly indicating variations in growth rate, so that rapid growth allows incorporation of the extraneous elements associated with the source region. Alternatively, the diamond has found its way into a variety of source regions, perhaps through convection; or the composition of the source region varied during diamond growth. Additional finer-scale ion microprobe work should help resolve this question, particularly in conjunction with the sensitive micro IR technique.

References

1. E. A. Burgemeister, "Thermal conductivity of natural diamond between 320 and 450 K," *Physica* 93B: 165-179, 1978.
2. E. M. Bibby, H. W. Fesq, and J. P. F. Sellschop, "Trace elements in diamonds of different types," *Nature* 276: 379-381, 1978.
3. R. M. Chrenko, "Boron, the dominant acceptor in semiconducting diamond," *Phys. Rev. B* 7: 4560-4567, 1973.
4. S. D. Berger and S. J. Pennycook, "Detection of nitrogen at [100] platelets in diamond," *Nature* 298: 635-637, 1982.

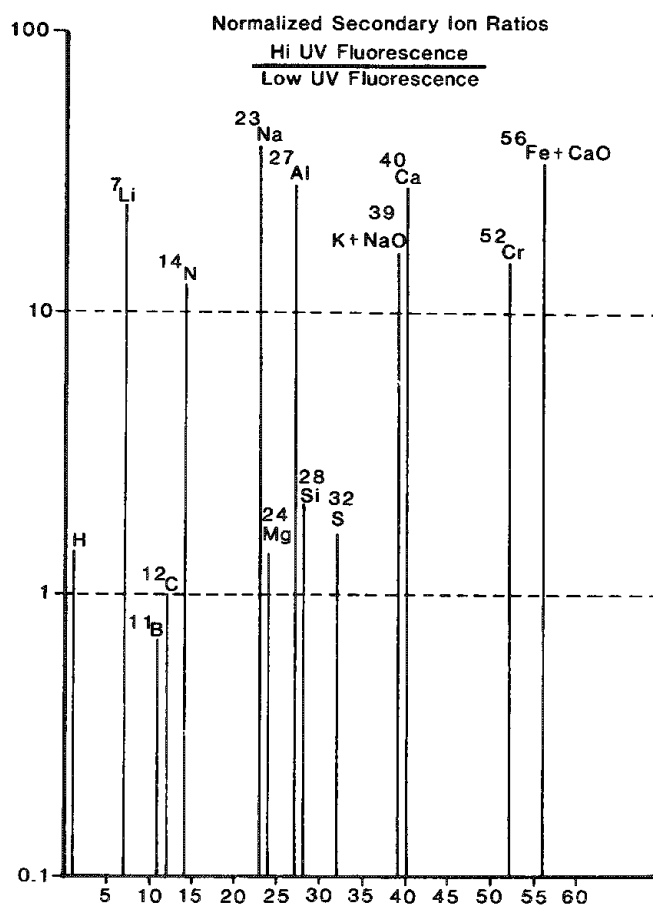


FIG. 6.--Ratio of ion intensities (normalized to ¹²C) detected from high- and low-fluorescence zones by secondary ion mass spectroscopy.

3 Quantitative X-ray Microanalysis

A SIMPLE ACCURATE ABSORPTION MODEL

K. F. J. Heinrich

The model for distribution in depth of direct x-ray generation proposed by Philibert, with modifications by Duncumb² and Heinrich,³ has been widely used in microanalytical practice. This model was intended to be used for moderate absorption losses and performs very well under these conditions. As pointed out by Yakowitz and Heinrich,⁴ in the case of severe absorption losses the accuracy is inherently limited by the inaccuracies in all applicable parameters, as can be easily seen from error propagation. Analytical programs such as FRAME⁵ and its variant for solid-state detectors⁶ were provided with warnings against use for lines of elements of atomic numbers below 11. However, such warnings are frequently disregarded by users, who work out of the intended range of operating conditions but are surprised to obtain poor analytical results. In FRAME, for instance, the absorption edges in the region beyond 11 Å are not programmed in the calculation of mass absorption coefficients. Hence, the program is not merely inaccurate in this region, it does not work at all.

The interest in determining elements of low atomic number ($Z < 11$) is nevertheless very great, and since the warnings against the use of general analytical programs are usually disregarded, it is preferable to provide general analytical schemes with absorption models that work well for high x-ray absorption in the target. The present work attempts to lay the foundations for this goal.

The general form of the equation for depth distribution of x-ray generation corresponding to the (simple) Philibert type correction is:

$$\phi(z) = \sum c_i \exp(-d_i z) \quad (1)$$

In this equation z is the distance from the surface (in g/cm²) and c and d are constants. The number of terms (k) is two in the Philibert equation.¹ At depth zero this function attains the value of zero, in striking contradiction to theoretical prediction and experimental evidence.⁷ When the absorption is high, the observed radiation comes mainly from shallow depth, and thus the Philibert model becomes unsuitable. The importance of the proper fit of $\phi(z)$ close to the surface was shown by the success of the rectangular model for $\phi(z)$ proposed by Bishop, which despite a poor fit over most of the region of electron penetration gives better results in cases of high x-ray absorption than the conventional models.⁸ However, the general use of a model so deviant from physical reality does not appear desirable. One would like to use a model that fits the experimental evidence well, particularly close to the specimen surface.

The absorption correction is applied in the usual correction procedures as a Laplacian transform of the $\phi(z)$ function:

$$f(\chi) = \int \phi(z) e^{-\chi z} dz / \int \phi(z) dz \quad (2)$$

In this equation, $\chi = \mu \csc \psi$, μ is the mass absorption coefficient of the x radiation in the target, and ψ the average emergence angle of the x rays. If we use a normalized depth distribution such that $\int \phi(z) dz$ over the entire depth range is equal to unity,⁷ we obtain

$$f(\chi) = \int_0^\infty \phi(z) e^{-\chi z} dz \quad (3)$$

The function $f(\chi)$ gives the probability that an x-ray photon being emitted into the solid angle covered by the spectrometer system (or the energy-dispersive detector) survives absorption within the target. In the ZAF procedures, in which the correction terms are multiplicative factors, the absorption correction is:

$$f(\chi)_{\text{specimen}} / f(\chi)_{\text{standard}}$$

The author is with the Office of International Relations, National Bureau of Standards, Gaithersburg, MD 20899.

Because much of the experimental evidence concerning x-ray absorption in the target is related to the tracer experiments which yield $\phi(z)$, whereas the performance of the absorption correction requires $f(\chi)$, a practical model for $\phi(z)$ should lend itself easily to transformation into $f(\chi)$ via the Laplace transform, so that the model can be readily tested and applied.

The Proposed New Model

Castaing⁸ observed in his thesis that at great depth within the target the function $\phi(z)$ approaches an exponential function. This function is that of Eq. (1) with $i = 1$:

$$\phi(z) = (1/a\gamma)\exp(-z/a\gamma) \quad (4)$$

Here, γ is a term that depends on the operating potential V_0 and the critical excitation potential for the relevant x-ray emission V_q ,

$$\gamma = V_0^{1.65} - V_q^{1.65}$$

and a is a constant. The corresponding expression for $f(\chi)$ is:

$$f(\chi) = (1 + a\gamma\chi)^{-1} \quad (5)$$

This expression was used by several authors,⁹⁻¹¹ and experimental evidence on $f(\chi)$ indicates a reasonably good fit where no significant fluorescent radiation is emitted. The model does not fit the shape of $\phi(z)$, because the electrons diffuse rapidly within the target, and the ionization cross section is a function of electron energy. Unlike the simplified Philibert formula, the exponential curve does not go to zero at zero depth: [$\phi(0) = 1/a\gamma$], but has at this point its highest value (for positive values of z), diminishing rapidly with increasing depth.

As shown previously,¹² a model of the form

$$f(\chi) = (1 + a\gamma\chi)^{-2} \quad (a = 1.2 \times 10^{-6}) \quad (6)$$

(quadratic model) can be fitted very well to the experimental data at moderate absorption levels. The corresponding form for $\phi(z)$,

$$\phi(z) = z/(a^2\gamma^2)\exp(-z/a\gamma) \quad (7)$$

provides a reasonably good fit to experimental $\phi(z)$ curves from tracer experiments, except at very small values of z at which $\phi(z)$ again vanishes. By combining additively the exponential and the quadratic models, one can obtain a good fit over the whole range.

$$\phi(z) = \alpha[(a\gamma)^{-1} \exp(-z/a\gamma)] + (1 - \alpha)[(z/(a\gamma)^2) \exp(-z/a\gamma)] \quad (8)$$

The corresponding $f(\chi)$ function is readily obtained:

$$f(\chi) = [1 + \alpha(a\gamma\chi)]/(1 + a\gamma\chi)^2 \quad (9)$$

The parameters α and a depend on the specimen composition, χ on the absorption conditions, and γ on the operating and minimum excitation voltages.

Examples of the fit of Eqs. (8) and (9) to experimental data are shown in Figs. 1 and 2.

The variation of α with target composition is more important than that of a ; a satisfactory fit to the experimental values of $\phi(z)$ and $f(\chi)$ for normal beam incidence can be obtained with

$$\alpha = 0.180 + 2/\gamma + 0.008V_q + 0.005Z^{1/2}$$

$$a = 1.65e^{-6}$$

where V_q is the critical excitation potential and Z the atomic number.

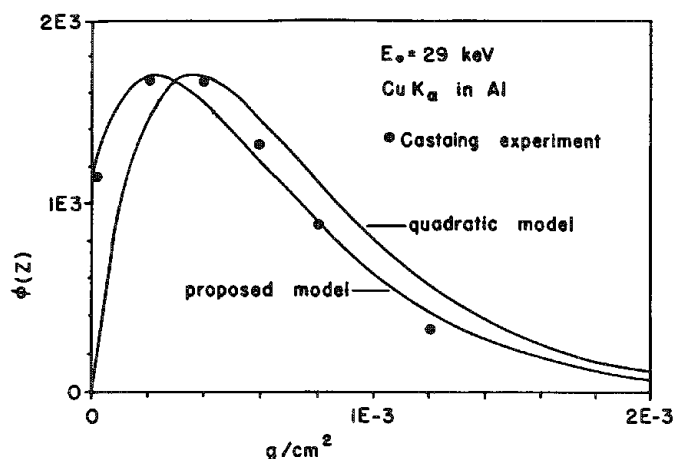


FIG. 1.--Ionization function $\phi(z)$ for Al tracer in Cu; $E_0 = 29$ keV. Data of Castaing & fit of quadratic & proposed model.⁸

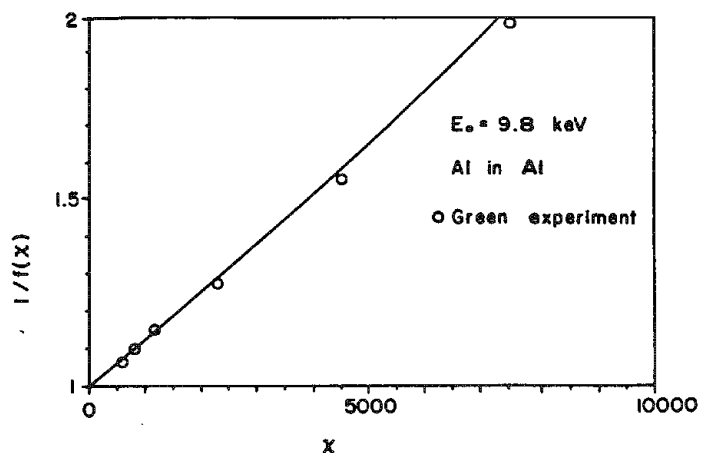


FIG. 2.--Absorption parameter $1/f(\chi)$ vs χ as predicted by proposed model, compared with experimental data of Green, for Al.¹²

The limits for further refinement of this model are set by internal inconsistencies among experimental results. It should be easy to adapt the equation to oblique beam incidence. A test of this model on analyses of material of known composition is planned for the near future.

References

1. J. Philibert, in H. H. Pattee, V. E. Cosslett, and A. Engstrom, Eds., *Proc. 3rd Conf. on X-ray Optics and Microanalysis*, New York: Academic Press, 1963, 379.
2. P. Duncumb and P. K. Shields, in T. D. McKinley, K. F. J. Heinrich, and D. B. Wittry, Eds., *The Electron Microprobe*, New York: Wiley, 1966, 284.
3. K. F. J. Heinrich, NBS Tech. Note 521, Washington, D.C.: National Bureau of Standards, U.S. Department of Commerce, 1970.
4. H. Yakowitz and K. F. J. Heinrich, *Mikrochim. Acta* 1968, p. 182.
5. H. Yakowitz, R. L. Myklebust, and K. F. J. Heinrich, *FRAME: An Outline Correction Procedure for Quantitative Electron Probe Microanalysis*, NBS Tech. Note 796, October 1973.
6. R. L. Myklebust, C. E. Fiori, and K. F. J. Heinrich, *FRAME C*, Note 1106, Washington, D.C.: U.S. Department of Commerce, 1979.
7. K. F. J. Heinrich, *Electron Beam X-ray Microanalysis*, New York: Van Nostrand Reinhold, 1981.
8. R. Castaing, Thesis, University of Paris, 1951.
9. T. O. Ziebold and R. E. Ogilvie, *Anal. Chem.* 36: 322, 1964.
10. J. A. Belk, in R. Castaing, P. Deschamps and J. Philibert, Eds., *Proc. Int. Congr. on X-ray Optics and Microanalysis*, Paris: Hermann, 1966, 214.
11. I. B. Borovsky and V. I. Rydnik, in K. F. J. Heinrich, Ed., *Quantitative Electron Probe Microanalysis*, NBS Special Publ. 298, Washington, D.C.: National Bureau of Standards, 1968, 35.
12. M. Green, Thesis, University of Cambridge, 1962.

EVALUATION OF RECENT AND IMPROVED CORRECTION PROCEDURES FOR EPMA

Glyn Love, V. D. Scott, and D. A. Sewell

In electron probe microanalysis, three principal factors have to be taken into account when correcting x-ray intensity ratios recorded from specimen and standard: atomic number Z , absorption A , and fluorescence F corrections; their magnitudes are computed separately in a ZAF routine. Although the formulas developed in the 1960s for calculating these factors are still widely used today, improved correction procedures are required to deal with ultra-light element ($Z < 10$) analysis and to translate the better-quality x-ray data achievable with modern instruments into more accurate estimates of specimen composition.

The atomic number and absorption (particularly absorption) corrections tend to be the largest and both may be calculated from knowledge of the distribution of generated x rays with mass depth (ρz) in the specimen [commonly referred to as the $\phi(\rho z)$ curve]. The four recent correction procedures examined in this paper are, unlike earlier methods, largely empirical in that their formulas are based upon experimental x-ray depth distributions which have been obtained by tracer measurements or by Monte Carlo simulation. This is a logical approach because (a) the physical processes involved in the excitation of x rays by electrons are insufficiently well understood to develop a wholly theoretical treatment, (b) more extensive experimental $\phi(\rho z)$ data have become available for curve fitting purposes, and (c) the complex formulas that tend to be generated using this method can now be readily dealt with by modern mini- and micro-computers and provide on-line correction of microanalysis data. The basis of each correction method is outlined below.

Correction Models Evaluated

Tanuma.--The approach of Tanuma and Nagashima¹ is founded upon an idea of Wittry² that the $\phi(\rho z)$ curve could be represented as a Gaussian function whose peak is displaced from the origin along the positive ρz axis by an amount proportional to its half width. Unfortunately this means that it is not possible to obtain simultaneously the correct peak height in the $\phi(\rho z)$ distribution and the appropriate x-ray generation at the specimen surface. Probably for this reason Tanuma has chosen to use the procedure for calculating absorption effects only and to deal with atomic-number effects separately. The atomic-number correction selected is a curious hybrid which involves calculating the electron stopping power by the classical method of Duncumb and Reed³ (but using a different form of the mean ionization potential) and calculating the backscatter factor by the method of Love et al.⁴

Bastin.--In this model the $\phi(\rho z)$ curve is used to produce a combined atomic number and absorption correction: the curve is described by a modified Gaussian shape with its origin centered at the specimen surface. The introduction of a transient function allows the x-ray generation from the surface of the specimen to be properly represented. This concept was first suggested by Packwood and Brown⁵ but subsequently the formulas have been adjusted and those assessed here, due to Bastin et al.,⁶ have the advantage that they do not require time-consuming numerical integration.

Love-Scott I.--Here the $\phi(\rho z)$ curve is represented by a rather crude rectangular shape⁷ such that the x-ray generation with depth in the specimen is constant until twice the mean depth of x-ray generation ($\bar{\rho z}$) is reached, when it falls abruptly to zero. It is based on work of Bishop,⁸ who showed that $\bar{\rho z}$ controls the size of the absorption correction provided that absorption effects are not very large (say, less than 50%). However, the model is totally inadequate for calculating an atomic-number correction and the method of Love et al.⁴

The authors are at the School of Materials Science, University of Bath, Claverton Down, Bath, England BA2 7AY. SERC support of this program is acknowledged.

is adopted in which a modified form of the Bethe energy loss law is used to describe the electron stopping power and the backscatter factor is derived from Monte Carlo calculations.⁹

Love-Scott II.--This is essentially an extension of the preceding model but now the x-ray depth distribution is represented by a quadrilateral shape;¹⁰ the key parameters are $\bar{\rho z}$, the value of the surface ionization, the height of the peak in the $\phi(\rho z)$ curve, and its position along the ρz axis. This more accurate representation is intended to deal with cases where absorption is very large such as in ultra-light-element analysis. At the same time by retaining $\bar{\rho z}$ as an explicit parameter performance should not be compromised when absorption effects are less severe. The atomic number correction is the same as that used in Love-Scott I.

Test of the Correction Models

The four correction models have been assessed first by use of a wide range of microanalysis results on binary alloys¹⁰ (554 results). Second, a database¹⁰ consisting of 94 oxygen and fluorine measurements has been compiled to evaluate performance for ultra-light-element analysis.

For x radiations with energy greater than 2 keV the formulas of Springer and Nolan¹¹ were used to calculate mass absorption coefficients and for lower energy radiation the values of Henke et al.¹² were employed.

All correction models were combined with the characteristic fluorescence correction of Reed,¹³ but no continuum fluorescence correction was applied as it was negligible for almost all systems examined.

The performance of each model was assessed by a comparison of the measured intensity ratios k with the intensity ratios k' predicted by the correction procedure from a prior knowledge of specimen composition. An accurate correction procedure should give k'/k values close to unity and assessment is facilitated by plotting of the data in the form of histograms.

The results of applying all four correction models to the binary alloy data are shown by the histograms in Fig. 1 and the percentage root mean square (RMS) errors listed in Table 1. Examination of Fig. 1 reveals that both the Love-Scott models have similar sized peaks. This is not an unexpected result in view of the fact that both use the same formula for $\bar{\rho z}$ and this parameter controls the size of the absorption correction in many of the binary alloys. However, the Love-Scott II histogram has a narrower base, which is reflected in the smaller percentage RMS error--2.9%, compared with 3.5% given by Love-Scott I. Histograms constructed by the correction models of Tanuma and Bastin both have peaks which are significantly lower than either of the Love-Scott methods but the corrected data are still relatively good as illustrated by the RMS errors.

Application of the models to the ultra-light elements (oxygen and fluorine) is a more stringent test of the absorption correction. No histograms were produced because of the limited amount of data but RMS errors are given in Table 1. These errors show that the method of Tanuma cannot be recommended for ultra-light element work and illustrate the deficiencies of the Love-Scott I procedure now that absorption effects are large. The performance of the Bastin model is reasonable but it is bettered by that of Love-Scott II.

From an examination of alloy systems where atomic number effects were larger than those of absorption it was deduced that all the atomic number corrections worked fairly well, the percentage RMS errors ranging from 2.9% (both Love-Scott methods) to 3.4% (Tanuma).

The assessment shows that the correction models of Bastin and Love-Scott II work particularly well and, based on our experience, would outperform the ZAF procedures currently in use. At present specimen tilt factors are being introduced into our model so that it will provide a "universal" correction procedure which can be confidently applied to all systems and analysis conditions.

References

1. S. Tanuma and K. Nagashima, "Evaluation of an improved absorption correction based on the Gaussian ionization distribution model for quantitative electron probe microanalysis," *Microchimica Acta* 1: 299-313, 1983.
2. D. B. Wittry, "Resolution of electron probe microanalysis," *J. Appl. Phys.* 29: 1543-

TABLE 1.--Percentage RMS errors given by correction procedures when applied to microanalysis data.

Element range	Tanuma	Bastin	Love-Scott I	Love-Scott II
Z > 10	3.8	3.7	3.5	2.9
Z < 10	11.8	7.0	9.7	4.8

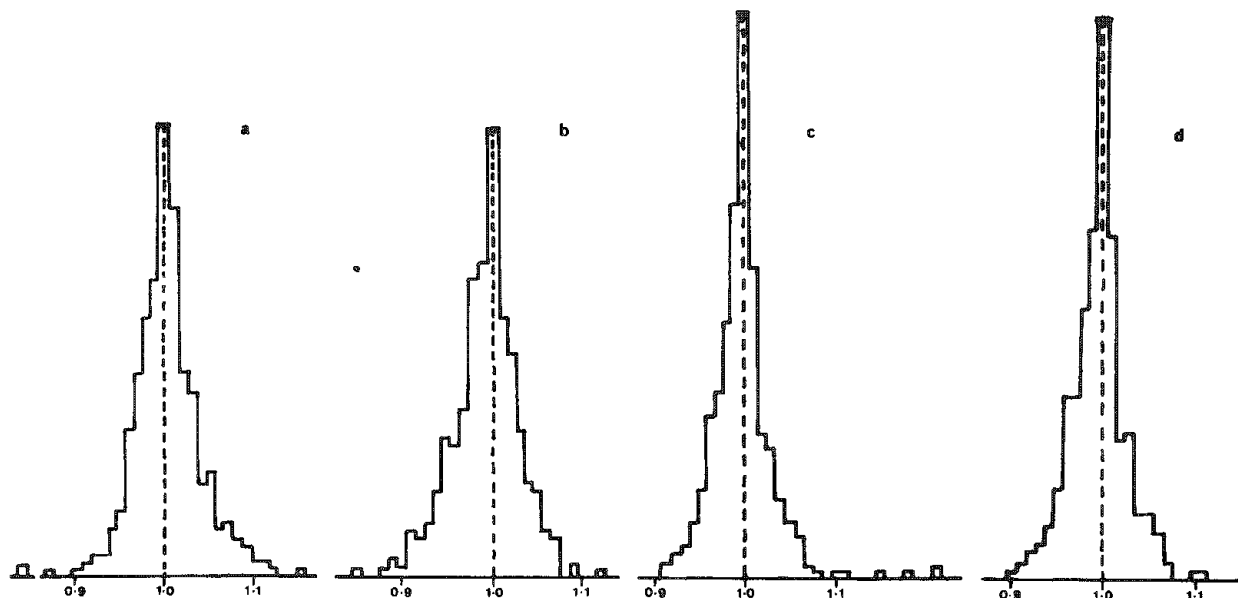


FIG. 1.--Histograms of corrected microanalysis data (Z > 10, 554 results) plotted as k'/k , where k' is x-ray intensity ratio predicted by model and k is measured value: (a) Tanuma, (b) Bastin, (c) Love-Scott I, (d) Love-Scott II.

1548, 1958.

3. P. Duncumb and S. J. B. Reed, *The Calculation of Stopping Power and Backscatter Effects in Electron Probe Microanalysis*, NBS Spec. Publ. 298: 133-154, 1968.

4. G. Love, M. G. C. Cox, and V. D. Scott, "A versatile atomic number correction for electron probe microanalysis," *J. Phys. D* 11: 7-21, 1978.

5. R. H. Packwood and J. D. Brown, "A Gaussian expression to describe $\phi(\rho z)$ curves for quantitative electron probe microanalysis," *X-ray Spectrom.* 10: 138-145, 1981.

6. G. F. Bastin, F. J. J. van Loo, and H. J. M. Heijligers, "Evaluation of the use of Gaussian $\phi(\rho z)$ curves in quantitative electron probe microanalysis: A new optimization," *X-ray Spectrom.* 13: 91-97, 1984.

7. G. Love and V. D. Scott, "Evaluation of a new correction procedure for quantitative electron probe microanalysis," *J. Phys. D* 11: 1369-1376, 1978.

8. H. E. Bishop, "The prospects for an improved absorption correction in electron probe microanalysis," *J. Phys. D* 7: 2009-2020, 1974.

9. G. Love, M. G. C. Cox, and V. D. Scott, "A simple Monte Carlo method for simulating electron interactions and its application to electron probe microanalysis," *J. Phys. D* 10: 7-23, 1977.

10. D. A. Sewell, G. Love, and V. D. Scott, "A universal correction procedure for electron probe microanalysis: Part 2. The absorption correction," *J. Phys. D* (in press).

11. G. Springer and B. Nolan, "Mathematical expression for the evaluation of x ray emission and critical energies, and of mass absorption coefficients," *Canad. J. Spectrosc.* 21: 134-138, 1976.

12. B. L. Henke, P. Lee, T. J. Tanaka, R. L. Shimabukuro, and B. K. Fujikawa, "Low energy x-ray interaction coefficients: photoabsorption, scattering and reflection," *Atomic Data and Nuclear Data Tables* 27: 1-144, 1982.

13. S. J. B. Reed, "Characteristic fluorescence corrections in electron probe microanalysis," *Brit. J. Appl. Phys.* 16: 913-926, 1965.

THE CHOICE OF INNER-SHELL ELECTRON IONIZATION CROSS SECTION IN QUANTITATIVE ELECTRON-BEAM ANALYSIS

Hiroshi Abe, Kenji Murata, Serge Cvikevich, and J. D. Kuptsis

The exact knowledge of the ionization cross section $Q(U)$ for the case of the ionization of inner-shell electrons, which takes place in electron beam solid interactions, can be disregarded in conventional electron-beam microanalysis of bulk samples. The use of unknown-to-standard characteristic x-ray intensity ratios (k-ratios) significantly compensates for the uncertainty in the expression chosen to describe the ionization cross section. However, significant errors are to be expected in the case of standardless bulk analysis and quantitative analysis of thin films or small particles.

The Monte Carlo simulation approach has been used by Murata et al.^{1,2} for quantitative electron microprobe analysis of thin films on substrates with reasonable success. In their more recent work, Murata et al.² have observed that, for Cu-Pd-Au alloy films, the best agreement with Rutherford backscattering spectroscopy (RBS) data is achieved by use of the Hutchins cross section³ (with exponent $m = 0.7$) for the Pd $L\alpha$ and Au $M\alpha$ x-ray lines, and that the best agreement with RBS results is obtained by the use of the Worthington-Tomlin cross section⁴ for the Cu $K\alpha$ radiation. This observation pointed to the need for a more general ionization cross-section expression and motivated us to look at all the currently available ionization cross-section data.

Survey of Currently Available Ionization Cross-section Data

Powell has extensively reviewed the expressions that have been developed for inner-shell electron ionization⁵ as well as the ionization cross-section data available up to 1975.⁶ An up-to-date summary of ionization cross-section measurements is given in Table 1. Ionization cross sections for the relatively lower atomic number elements were determined mostly by Auger electron spectroscopy on gaseous samples. Measurements of ionization cross sections of higher atomic number elements were done on thin elemental films by electron microprobe analysis (EMPA). Figures 1 to 5 summarize these experimental data, which are presented in a normalized form for ease of comparison. The data are grouped according to the specific ground level electron shell involved in the ionization process. Figure 4 shows the ionization cross section for the lower atomic number L-shell transitions separately, and Fig. 5 compares the L-shell cross-section data for higher atomic number elements with the cross-section expressions proposed by Hutchins (with $m = 0.7$) and Worthington and Tomlin. In general, the data show a mild atomic number dependence with the data for higher atomic number elements descending more steeply from the maximum value with increasing overvoltage U .

A Study of the Ionization Cross Section by a Monte Carlo Simulation Method

We have compared our experimental measurements on Mo to the x-ray intensities generated by simulations that used the expressions for ionization cross section proposed by Hutchins ($m = 0.7$ and $m = 1.0$), by Worthington and Tomlin, and by Gryzinski.⁷ The Monte Carlo simulation procedure described elsewhere² involved the use of Mott cross sections for elastic scattering, the values of Duncumb and Reed for the mean ionization potential,⁸ and Heinrich's mass absorption coefficients.⁹ To obtain the cross-section value at any arbitrary value of overvoltage U , a linear interpolation between adjacent data points was used during the Monte Carlo simulation runs.

In Fig. 6 the experimental intensity measurements made on a bulk Mo target are compared to Monte Carlo simulation results obtained from both the Hutchins ($m = 0.7$) and the Worthington and Tomlin ionization cross-section expressions. The calculated and experimental results were matched at 10 keV. Although agreement is good at the lower values of

Author Abe's permanent address is IBM Japan, Yasu, Siga, Japan; author Murata's permanent address is University of Osaka Prefecture, Sakai, Osaka, Japan; author Cvikevich is at IBM East Fishkill, Hopewell Junction, NY 12533; author Kuptsis is at IBM San Jose Research Laboratory, San Jose, CA 95193.

TABLE 1.--Compilation of ionization cross-section data references.

Authors	Shell	Sample	Phase	Z	EC(keV)	References
Pockman et.al (1947)	K	Ni	solid	28	8.322	(10)
Hink, Ziegler (1969)	K	Al	solid	13	1.560	(11)
Hink, Paschke (1971)	K	C	solid	6	0.284	(12,13)
Glupe, Mehlhorn (1967) (1971)	K	C	gas	6	0.284	(14) (15)
	K	N	gas	7	0.400	
	K	O	gas	8	0.532	
Glupe (1972)	K	Ne	gas	10	0.867	(16)
Bekk (1974)	K	Ne	gas	10	0.867	(17)
Vrakking, Meyer (1974)	L	P	gas	15	0.189	(18)
	L	S	gas	16	0.229	
	L	Cl	gas	17	0.270	
Ogurtsov (1973)	L	Ar	gas	18	0.320	(19)
Christofzik (1970)	L	Ar	gas	18	0.320	(20)
Kyser, Geiss (1977)	K	Si	solid	14	1.837	(21)
	L	Zr	solid	40	2.220	
Butz, Wagner (1972)	K	Al	solid	13	1.560	(22)
	M	W	solid	74	1.814	
	L	Nb	solid	41	2.371	
	L	Mo	solid	42	2.523	
Kuptsis (1978)	M	Pt	solid	78	2.133	(23)
	K	Al	solid	13	1.560	
	L	Mo	solid	42	2.523	
	L	Nb	solid	31	2.371	

TABLE 2.--Comparison of Mo L α k-ratios obtained by experiment and simulation with various ionization cross sections at 15 keV.

Method	Experimental	Hutchins m = 0.7	Hutchins m = 1.0	Worth.- Tomlin	Gryzinski	Experimental Q(U)
K-ratio	0.1938	0.1899	0.1783	0.1733	0.1876	0.1883
% Deviation						
from	-	-2.0	-8.0	-10.6	-3.2	-2.8
Experiment						

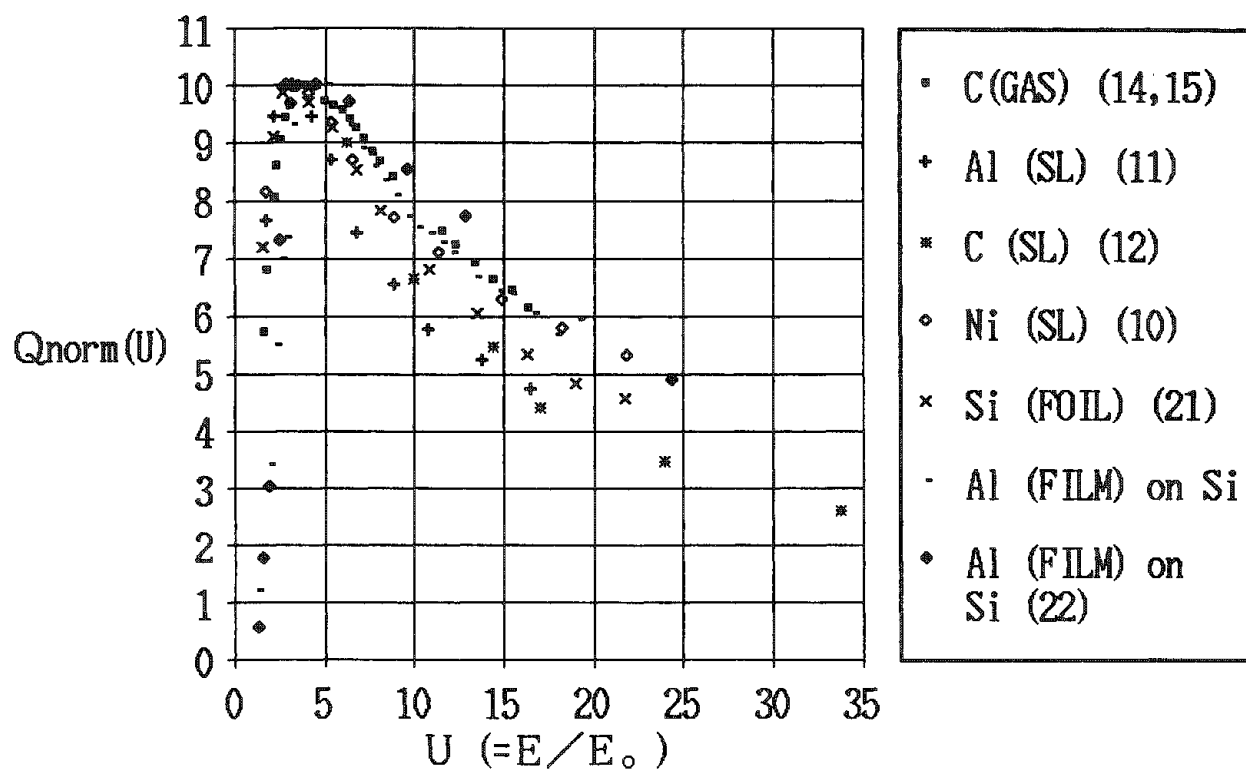


FIG. 1.--Normalized ionization cross section as function of overvoltage U (K-shells).

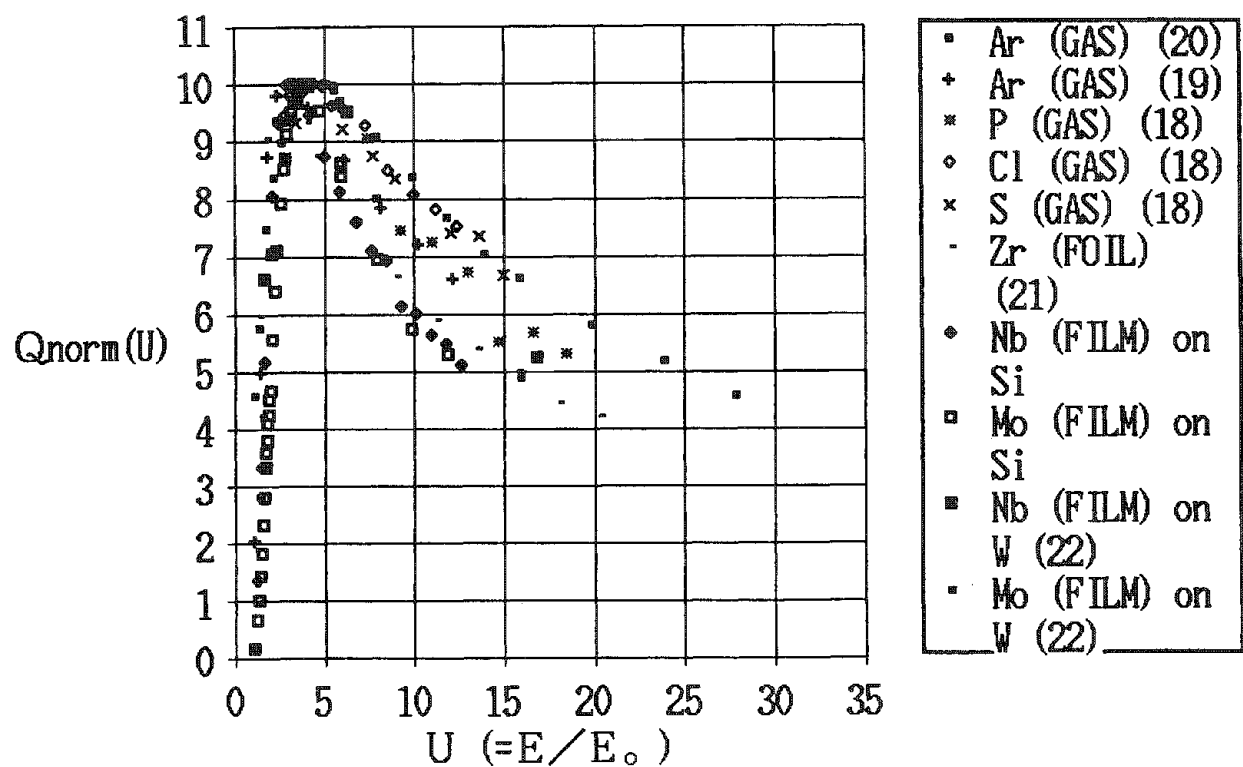


FIG. 2.--Normalized ionization cross section as function of overvoltage U (L-shells).

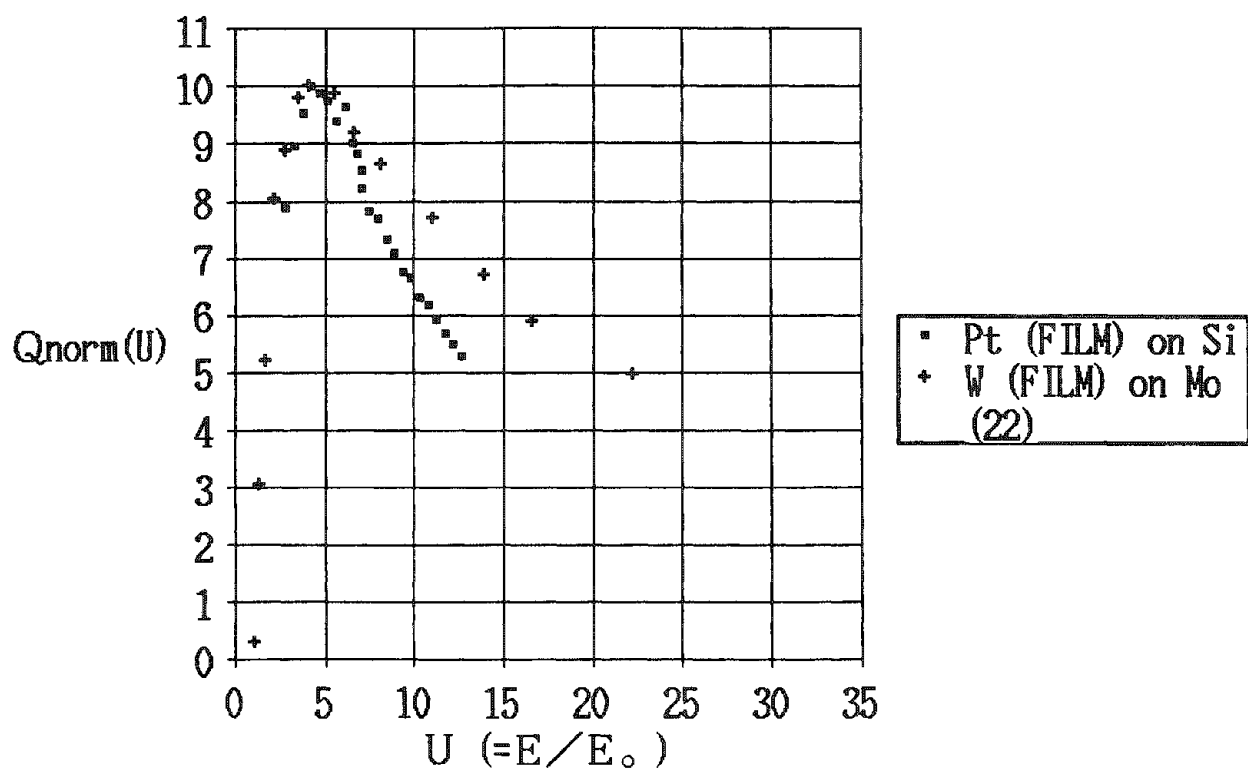


FIG. 3.--Normalized ionization cross section as function of overvoltage U (M-shells).

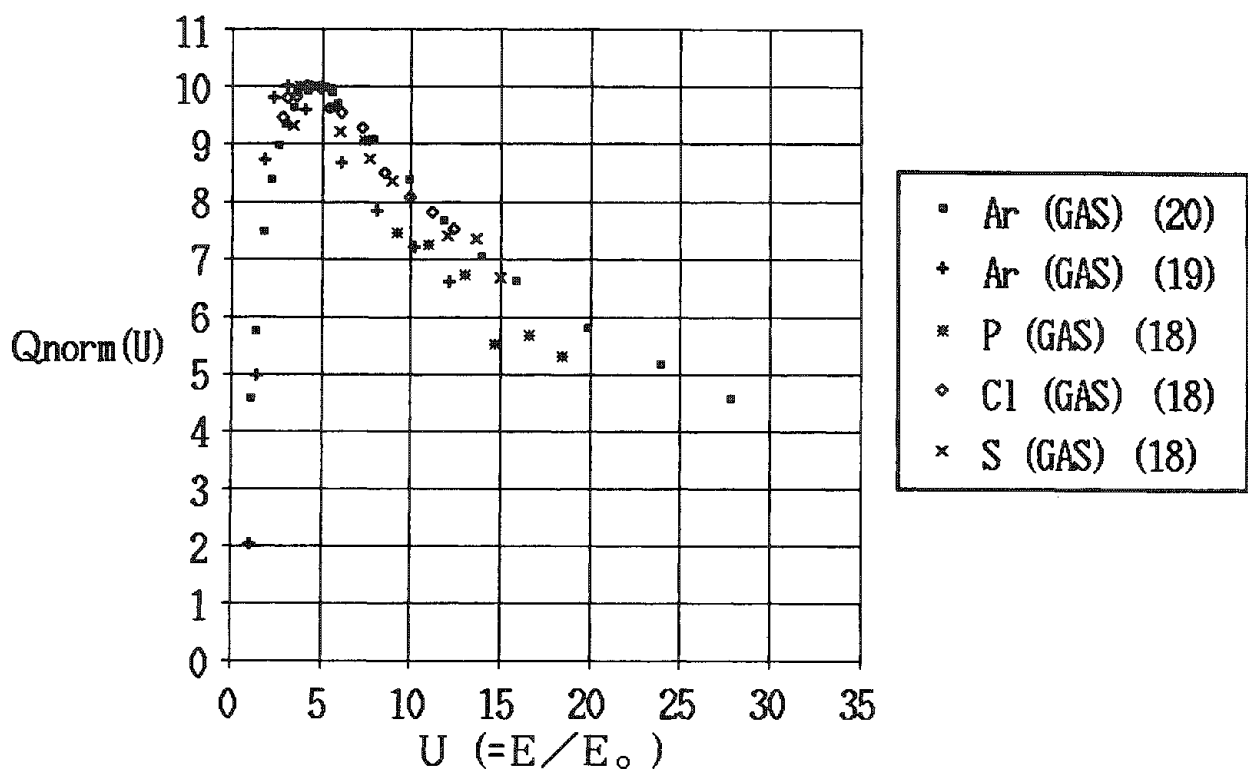


FIG. 4.--Normalized ionization cross section as function of overvoltage U (L-shells of lower atomic number elements).

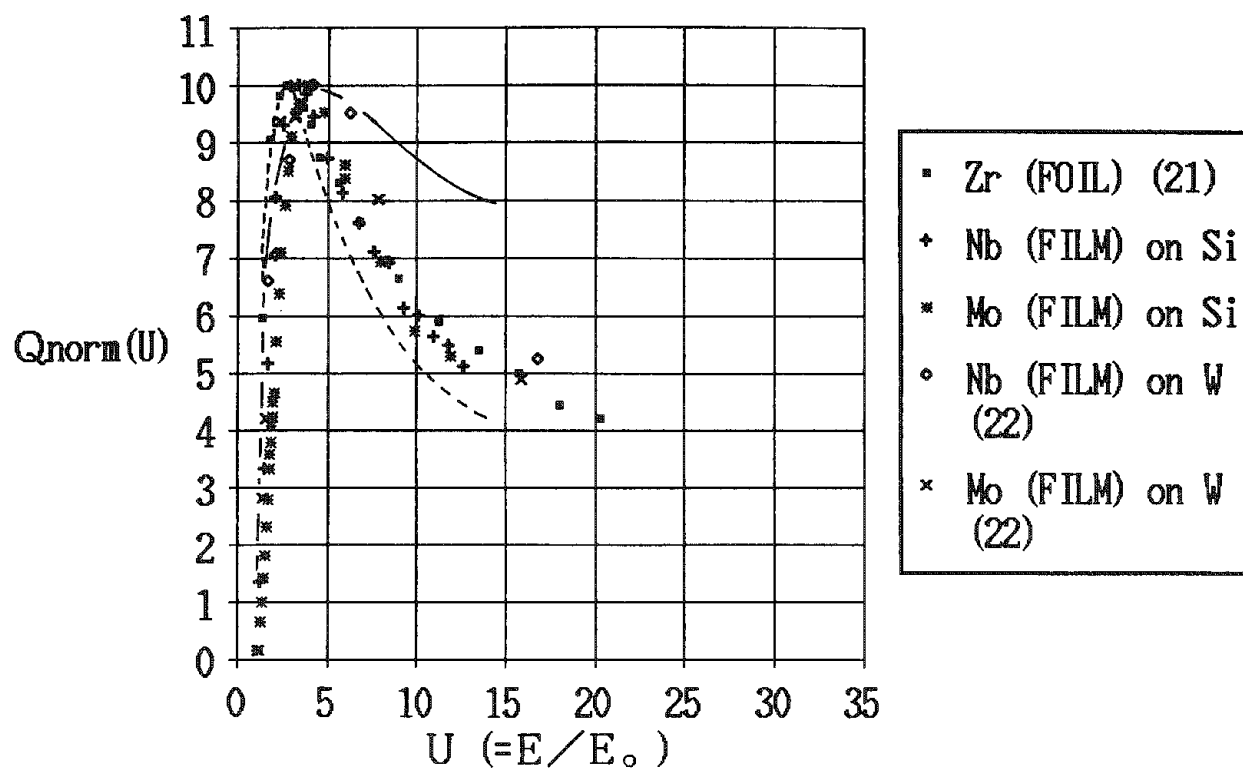


FIG. 5.--Normalized ionization cross section as function of overvoltage U (L-shells of higher atomic number elements). Hutchins (—), Worthington-Tomlin (---) ionization cross section.

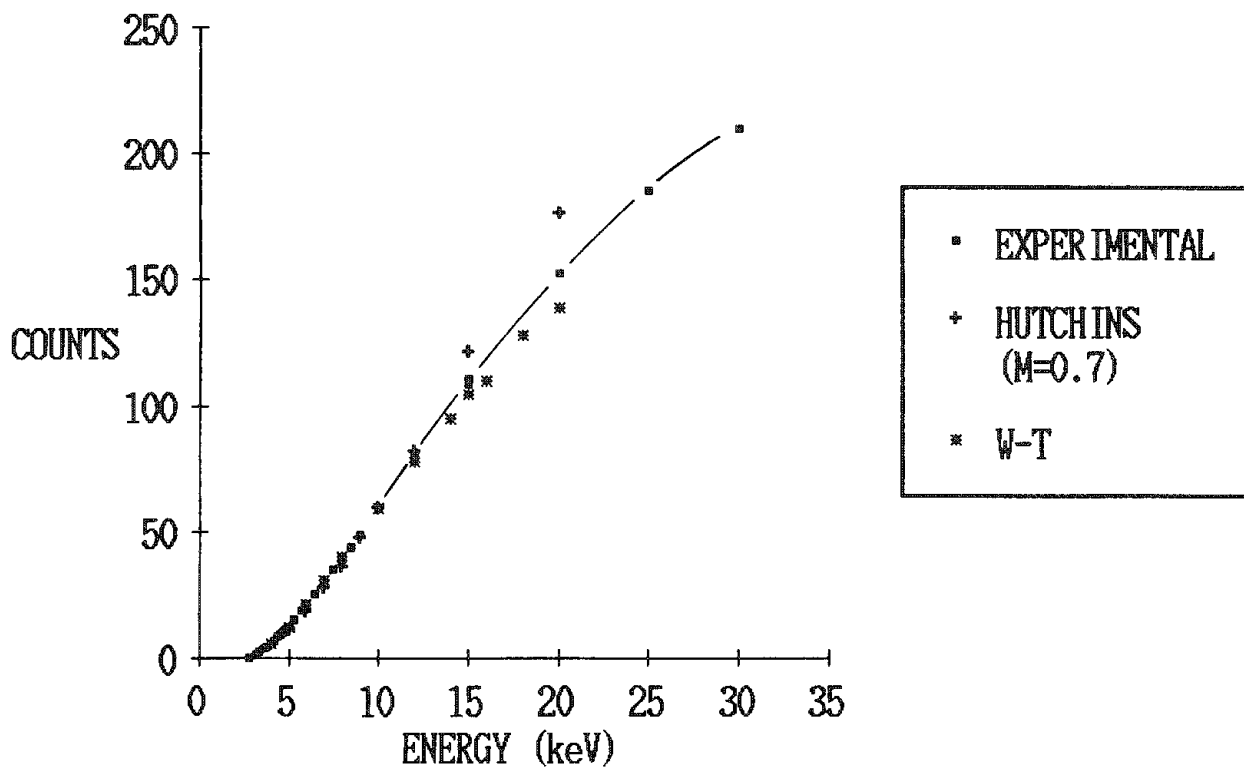


FIG. 6.--X-ray intensities from Mo standard vs electron energy. Experimental (■), simulated by Hutchins (+) ($m = 0.7$), and Worthington-Tomlin (*) cross section.

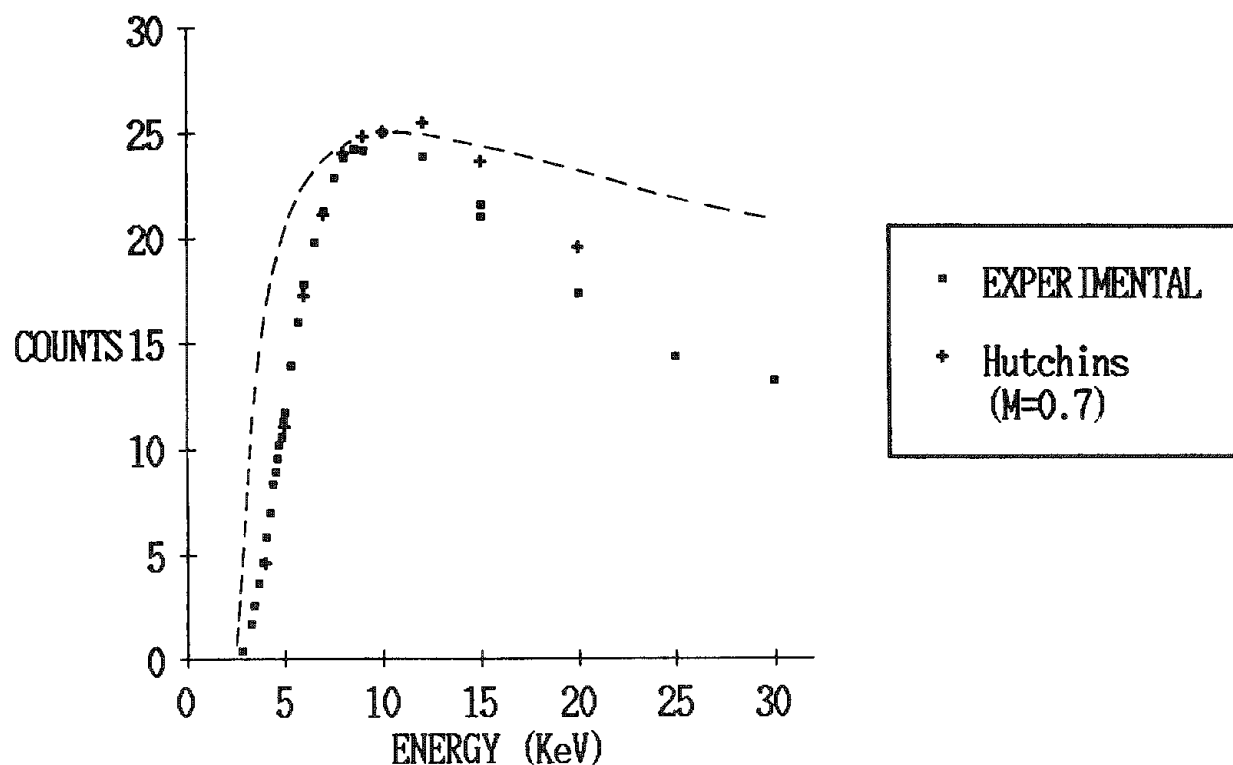


FIG. 7.--X-ray intensities from the thin Mo film vs electron energy. Experimental (■), simulated by Hutchins (+) ($m = 0.7$) cross section and normalized plot of the Hutchins ($m = 0.7$) cross-section formula (---).

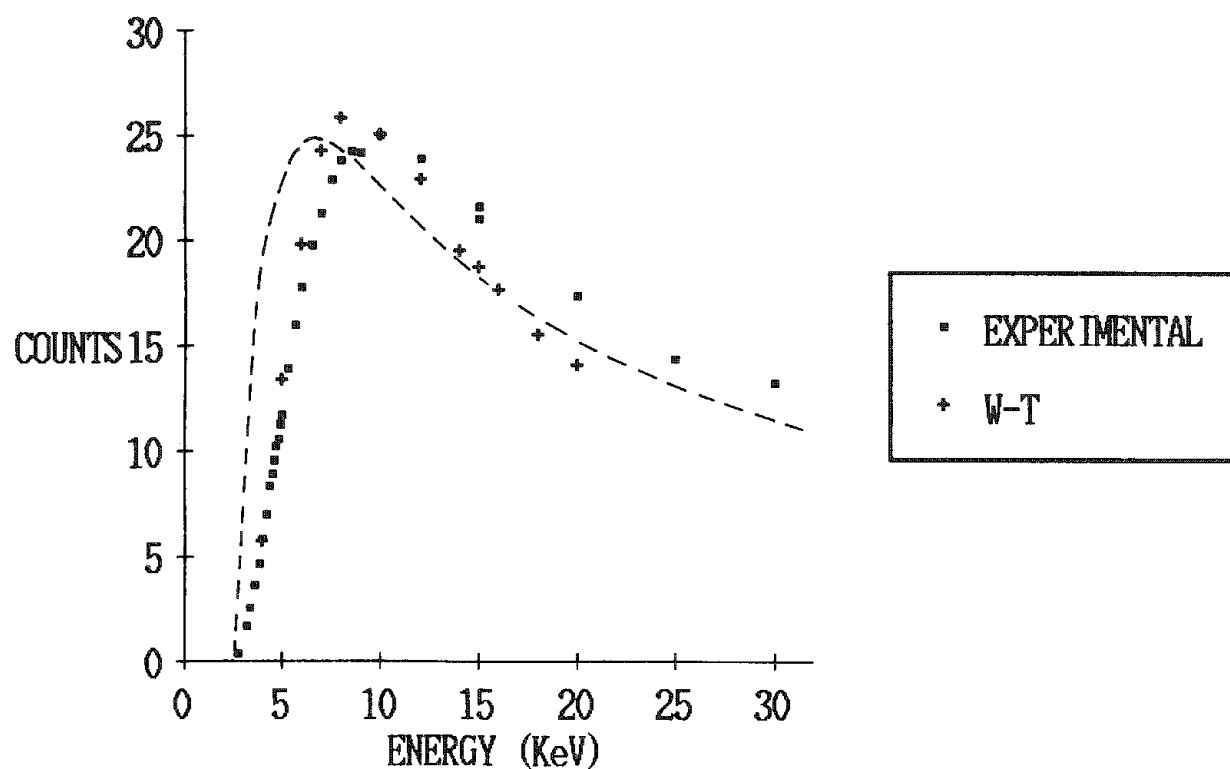


FIG. 8.--X-ray intensities from a thin Mo film vs electron energy. Experimental (■), simulated by Worthington-Tomlin cross section (+), and normalized plot of Worthington-Tomlin cross section formula (---).

electron energies, the Monte Carlo results diverge from experiment at higher energies. The Hutchins cross-section results diverge positively, and the simulation results using the Worthington-Tomlin cross section exhibit a negative divergence. In Fig. 7 the characteristic x-ray intensities obtained from measurements on a thin (700Å) Mo film (deposited on a Si substrate) are compared to those generated by Monte Carlo simulation using the Hutchins cross section with $m = 0.7$. In addition to these results, the Hutchins cross section $Q(U)$ is superimposed on this graph. The calculated intensity values obtained by using the Hutchins ionization cross-section expression ($m = 0.7$) are in good agreement with the measured intensity values. A comparison of our experimental data and the Hutchins cross-section expression leads us to conclude that experimental intensity measurements on such films do not directly yield the values of the ionization cross section. For the case of a 700Å Mo film on Si, our Monte Carlo simulation runs show that there is a strong variation in the generation of characteristic x rays with depth even for an initial electron impact energy of 10 keV. Therefore the effective x-ray generation volume within the film will vary with film thickness and atomic number.

The corresponding experimental and simulated results for Mo when the Worthington-Tomlin cross section is used are shown in Fig. 8. The agreement between simulated and experimental data is clearly less satisfactory. In order to minimize the in-depth variation of x-ray generation and the substrate effect, we chose to make the comparison between the Monte Carlo simulation results that used a variety of cross sections, and the experimental measurements made at an electron beam energy of 15 keV.

Table 2 summarizes the experimental k-ratio and the k-ratios obtained by Monte Carlo simulation technique with five different ionization cross-section expressions for an electron beam energy of 15 keV and a Mo film with a mass-thickness of $71.4 \mu\text{g}/\text{cm}^2$ ($\sim 700\text{\AA}$) on Si. The Mo $L\alpha$ ($E_c = 2.52 \text{ keV}$) characteristic x radiation is used. From this we find that the Hutchins cross section (with $m = 0.7$) and the cross section determined from the data in Fig. 7 yield the best agreement with experiment.

Summary

Currently available inner-shell ionization cross-section data were reviewed. These data show a mild atomic number dependence, but, due to an extensive scatter of data points, they do not lend themselves to description by relatively simple empirical expressions.

The effect of the choice of ionization cross-section expression on k-ratios was evaluated by Monte Carlo simulation. The cross sections of Hutchins ($m = 0.7$ and $m = 1.0$), Worthington and Tomlin, and Gryzinski were considered, and experimental measurements on a thin film of Mo on a Si substrate were used. The Hutchins cross section (with $m = 0.7$) and the cross section determined from intensity measurement on a 700Å Mo film yielded the best agreement with experiment in that order.

References

1. D. F. Kyser and K. Murata, *IBM J. Res. Develop.* 18: 352, 1974.
2. K. Murata, S. Cvikevich, and J. D. Kuptsis, *Microbeam Analysis--1983; ICOM 10 Proceedings*, Toulouse, 1983.
3. G. A. Hutchins, in P. K. Kane and G. B. Larrabee, Eds., *Characterization of Solid Surfaces*, New York: Plenum Press, 1974, 441.
4. C. R. Worthington and S. G. Tomlin, *Proc. Phys. Soc. A* 69: 401, 1956.
5. C. J. Powell, NBS Special Publication 460, 1975, 97.
6. C. J. Powell, *Rev. Modern Physics* 48: 33, 1976.
7. M. Gryzinski, *Phys. Rev.* 138: A336, 1965.
8. P. Duncumb and S. J. B. Reed, in K. F. J. Heinrich, Ed., *Quantitative Electron Probe Microanalysis*, NBS Special Publication 298, 1968, 133.
9. K. F. J. Heinrich, in T. D. McKinley, K. F. J. Heinrich, and D. B. Wittry, Eds., *The Electron Microprobe*, New York: Wiley, 1966, 296.
10. L. T. Pockman, D. L. Webster, P. Kirkpatrick, and H. Harwroth, *Phys. Rev.* 71: 330, 1974.
11. W. Hink and A. Ziegler, *Z. Phys.* 226: 222, 1969.
12. W. Hink and H. Paschke, *Z. Phys.* 224: 140, 1971.
13. W. Hink and H. Paschke, *Phys. Rev. A* 4: 507, 1971.
14. G. Glupe and W. Mehlhorn, *Phys. Lett.* 25A: 274, 1967.
15. G. Glupe and W. Mehlhorn, *J. Phys. (Paris)* C4: 40, 1971.

16. G. Glupe, Ph.D. Thesis, University of Münster, 1972.
17. K. J. Bekk, Diplom Thesis, University of Freiburg, 1974.
18. J. J. Vrakking and F. Meyer, *Phys. Rev. A* 9: 1932, 1974.
19. G. N. Ogurtsov, *Sov. Phys. - JETP* 37: 584, 1973.
20. H. J. Christofzik, Diplom Thesis, University of Münster.
21. D. F. Kyser and R. H. Geiss, *8th International Conference of X-ray Optics and Microanalysis*, 1977.
22. R. Butz and H. Wagner, *Surface Science* 34: 693, 1973.
23. W. Reuter, J. D. Kuptsis, A. Lurio, and D. F. Kyser, *J. Phys.* D11: 2633, 1978.

ANALYZING ULTRA-LIGHT ELEMENTS IN THE ELECTRON MICROPROBE

Glyn Love and V. D. Scott

Electron-probe microanalysis of the ultra-light ($Z < 11$) elements presents far more problems than analysis of heavier elements mainly because (a) the low (< 1 keV) energies involved are readily absorbed on their way to the detector and (b) this region of the x-ray spectrum contains many lines (L and M spectra from heavier elements) that may overlap the K spectra from ultra-light elements and interfere with analysis. Fortunately, recent improvements in the performance of both wavelength-dispersive (WD) and energy-dispersive (ED) techniques of x-ray analysis have enhanced the prospects of success in this area. Furthermore, in parallel with progress in instrumentation, correction procedures have now been developed that may be applied universally to all systems including the ultra-light elements. This paper reports on progress and prospects for the future.

Wavelength-dispersive Analysis

A large number of diffracting crystals, with d spacings ranging from 12 up to 70 Å have been developed for dispersing low-energy x-ray emissions but relatively few are available commercially; the majority of ultra-light element analyses are carried out with a stearate crystal ($d \approx 50$ Å). The quality of diffracting crystals depends upon several interrelated criteria: (a) spectral dispersion and (b) spectral resolution, both of which are important for separating the proliferation of x-ray lines that may appear in this region of the spectrum; and (c) diffraction efficiency, in order to obtain useful element detection sensitivities.

Table 1 lists the spectral resolution for three commercially available crystals as measured from the oxygen K emission ($23.6 \text{ Å} \approx 525 \text{ eV}$) obtained from Al_2O_3 . They indicate clearly the superiority of the TAP crystal ($d \approx 13 \text{ Å}$) over the laurate ($d \approx 35 \text{ Å}$) and stearate ($d \approx 50 \text{ Å}$); the resolution for TAP approaches the natural bandwidth for oxygen ($\sim 2 \text{ eV}$). The difference in performance is underlined by the separation of the chromium $L\alpha$ and $L\beta$ emissions using TAP (Fig. 1a) but not with laurate (Fig. 1b). Good spectral

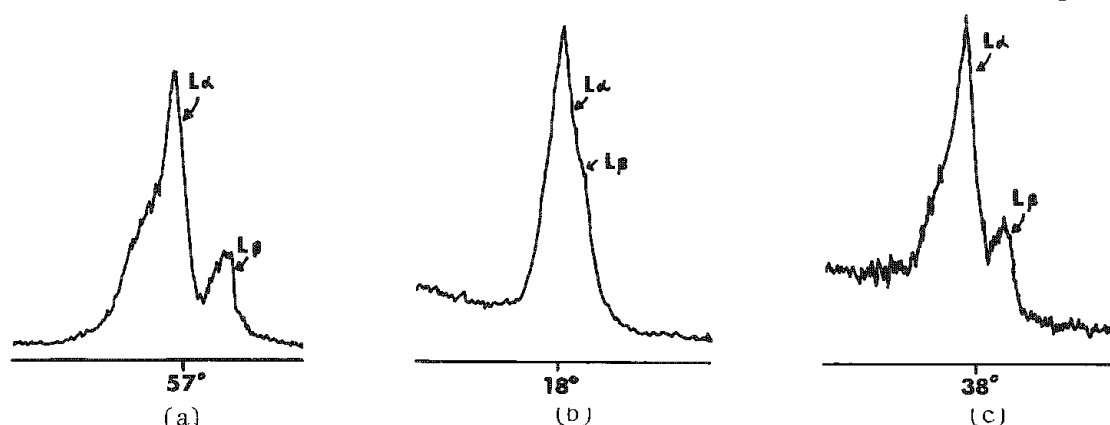


FIG. 1.--Cr $L\alpha$ and $L\beta$ peaks: (a) TAP, (b) laurate 1st order, (c) laurate 2nd order.

resolution of the diffracting crystal is needed also when the detailed structure of the characteristic x-ray emission (peak shape modifications) is being explored since it can be related to the nature of the chemical bond between constituent atoms. Such effects are well documented and accurate measurement of x-ray emission profiles can provide useful complementary information on the structure of the specimen. As an example (Fig. 2a) oxygen peaks obtained with TAP show that CuO (upper curve) may be clearly distinguished from Cu_2O (lower curve). Such chemical shift effects occur whenever valence electrons are involved in the transitions that lead to x-ray production, and Fig. 2(b) shows iron L

The authors are at the School of Materials Science, University of Bath, England BA2 7AY. The aid of SERC for supporting this research is gratefully acknowledged.

spectra from metal and from oxides. Note that the $L\alpha/L\beta$ intensity ratio increases with increase in oxidation state.

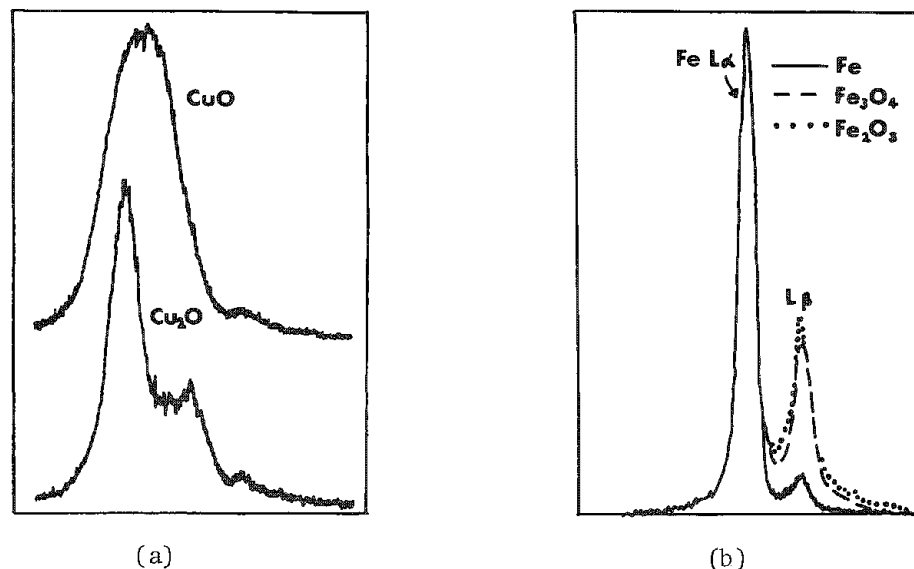


FIG. 2.--TAP analyzing crystal: (a) oxygen peaks from copper oxide, (b) iron L peaks from iron and iron oxides.

The ability of a diffracting crystal to separate closely spaced x-ray lines is also affected by the Bragg angle at which the lines are diffracted, i.e., the dispersion of the crystal. The Cr $L\alpha$ and Cr $L\beta$ lines are not normally resolved with either stearate or laurate (see Fig. 1b from laurate, where $\theta = 18^\circ$), but can be separated by use of a second-order reflection (Fig. 1c, $\theta = 38.2^\circ$). This result indicates that, whenever feasible, advantages may be gained by operating at a high Bragg angle. However, for quantitative analysis the total characteristic x-ray intensity is needed, which means that the full width of the peak must be integrated in such measurements. The minimum detection limit (MDL) is determined by spectral resolution and by diffraction efficiency of the crystal and may be calculated from $MDL = 3c\sqrt{B/P}$, where c is the weight concentration, B the background, and P the peak intensity. Values of MDL for carbon, nitrogen, and oxygen obtained with different analyzing crystals are given in Table 1. These values depend on

TABLE 1.--A = Spectral resolution in eV. B = Minimum detection levels in wt%; 200 s counting time; 7kV for C and N, 12kV for O; beam currents WD 200nA, ED 10nA.

		WD			ED
		TAP	Laurate	Stearate	
Oxygen (Al_2O_3)	A	2.8	8.8	12.4	100
	B	0.019	0.015	0.017	0.12
Nitrogen (Si_3N_4)	A	—	7.6	9.6	95
	B	—	0.070	0.076	0.41
Carbon (SiC)	A	—	4.8	5.4	120
	B	—	0.038	0.024	0.33

the applied probe voltage (the optimum values being given here) and also on matrix composition. For example, estimates of nitrogen sensitivity would appear inferior when based upon titanium nitride, due to higher absorption and higher background, but better when measurements are referred to boron nitride. Although not apparent from Table 1, dispersion also affects the MDL, as illustrated in Fig. 4 obtained from 18Cr-8Ni-Fe alloy containing 0.5 wt% nitrogen. The nitrogen peak is clearly revealed using the laurate

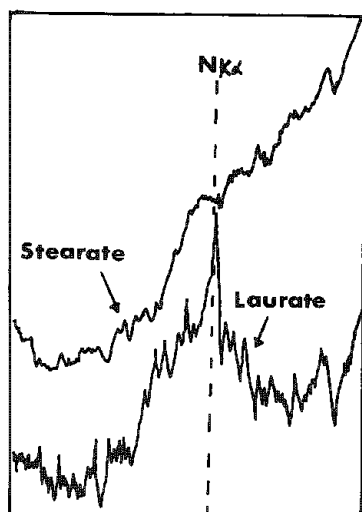


FIG. 3.-- Trace through nitrogen peak position on steel containing 0.5% nitrogen; upper curve stearate crystal, lower curve laurate crystal.

analyzing crystal, Fig. 3 (lower curve), and indeed much lower levels are detectable (Table 1). With the stearate crystal, however, the nitrogen peak is not visible owing to the high and steeply sloping background (upper curve), because interfering second-order NiL radiation has not been effectively dispersed at the lower Bragg angle (18.8° for stearate compared with 26.8° for laurate).

Before concluding this section, we should mention the problem of specimen contamination. Surface layers of carbon contamination present difficulties when low carbon concentrations are measured in, for example, steels and the reader is referred to Hren¹ and Love et al.² for further details. These problems can be overcome, however; Fig. 4, obtained from a nitrocarburized austenitic alloy,³ is an interesting example of what can be achieved by use of WD spectrometers.

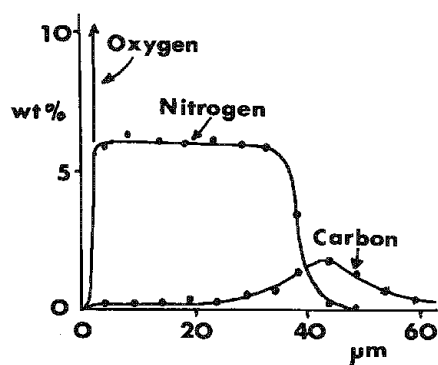


FIG. 4.--Diffusion profiles for carbon, oxygen, and nitrogen in tufftrided steel.

Energy-dispersive Analysis

Energy-dispersive analysis of ultra-light elements has become available only recently, since the introduction of "windowless" or thin-window systems. However, not only does the method suffer from inherently poor spectral resolution (Table 1), but a number of spectrum-processing problems have to be solved. First, a spectrum artifact arising from electronic noise must be dealt with by recording the noise with the electron beam switched off and then subtracting it from the spectrum of interest. Second, a small upturn in the noise-free spectrum occurs, possibly owing to incomplete charge collection, which needs to be separated from the genuine background by, for example, mathematical modeling.⁴ Only then can a method of background subtraction be applied for obtaining true peak intensities, but here another problem emerges since methods suitable for heavy-element analysis are found to be quite inappropriate in the low-energy region of the spectrum. However, a method has been recently developed⁵ that has been shown to work well: MDLs for ultra-light elements obtained by this spectrum-processing technique are given in Table 1. The figures show that element detection sensitivities are some *ten* times worse than those obtained with WDS, a situation not dissimilar to that for heavier element analysis. In point of fact, even these EDS values are probably overoptimistic because of the overlap problems arising in much practical work. Certainly, the 0.5 wt.% nitrogen level in steel clearly revealed when WD is used (Fig. 3, laurate crystal) was undetectable with ED. Nevertheless, Fig. 5(a) illustrates that higher levels (~ 6 wt.% nitrogen in a nitride layer on steel) can be measured satisfactorily, provided that an accurate background (dotted line) is established, from which an informative nitrogen diffusion profile may then be constructed (Fig. 5b).

Correction Procedure for Quantitative Analysis

The majority of quantitative programs include an absorption correction based on the method of Philibert;⁶ since it cannot deal adequately with ultra-light elements⁷ and because the absorption correction is the largest of the factors incorporated into a quantitative

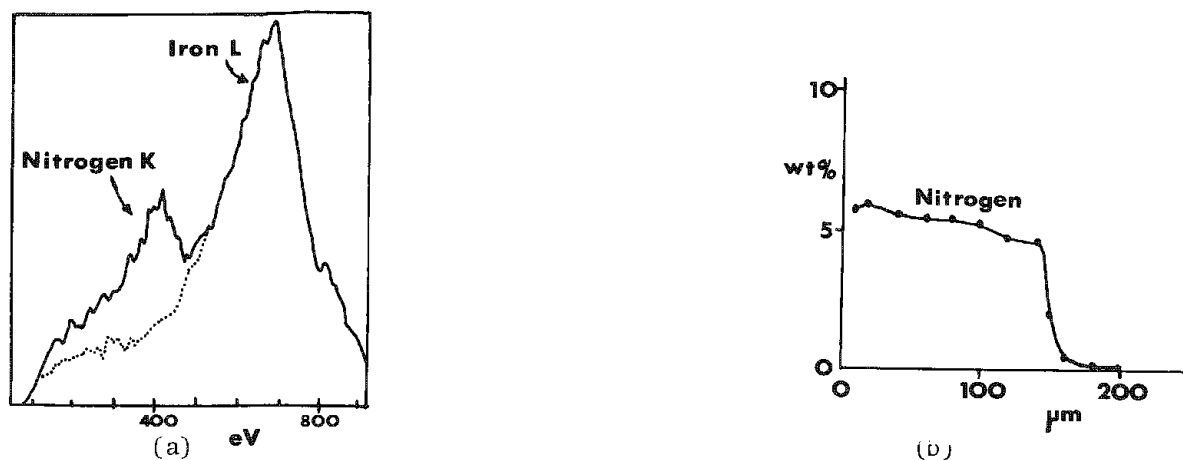


FIG. 5.--ED analysis of nitrided steel: (a) nitrogen peak from nitrided case, (b) nitrogen diffusion profile.

routine, it is not surprising that corrected light-element data obtained by this method are inaccurate, in many cases by as much as 20%. Improvements in correction programs have therefore concentrated on the absorption correction and new procedures have now been developed in which the RMS errors for ultra-light elements have been reduced to less than 5%, and for the heavier elements to ~3%. For a more detailed discussion of these new methods, the reader is referred to our other paper in this volume.⁸

Concluding Remarks

WD spectrometry may be successfully applied to the analysis of ultra-light elements down to concentrations of 0.02 wt.%, depending on the system studied and provided that the experimental conditions are optimized. However, ED methods are much less sensitive and in some systems even a few percent may remain undetected. Nevertheless, ED has still a useful role to play in ultra-light element analysis, especially when one is dealing with beam-sensitive materials,² because much lower beam currents are needed. Also, WDS may be usefully applied to studies of chemical shifts, whereas EDS is quite inappropriate there. Finally, suitable spectrum-processing methods are now available for ED work in the low-energy region and correction procedures have been developed that may be confidently applied to quantitative analysis of ultra-light elements as well as heavier elements.

References

1. J. J. Hren, "Barriers to AEM: Contamination and etching," in J. J. Hren, J. I. Goldstein, and D. C. Joy, Eds., *Introduction to Analytical Electron Microscopy*, New York: Plenum Press, 1979, 481-505.
2. G. Love, V. D. Scott, N. M. T. Dennis, and L. Laurenson, "Sources of contamination in electron optical equipment," *Scanning* 4: 32-39, 1981.
3. R. D. T. Whittle, G. Love, and V. D. Scott, "EPMA of surface reactions between light elements and austenitic alloys," *Inst. Phys. Conf. Ser.* 68, Bristol: Inst. Phys., 1984, 301-306.
4. D. J. Bloomfield, G. Love, and V. D. Scott, "Quantitative light-element analysis using an energy dispersive detector: Part 1. Dead time and the low-energy spectrum," *X-ray Spectrom.* 13: 69-77, 1984.
5. D. J. Bloomfield and G. Love, "Quantitative light-element analysis using an energy dispersive detector: Part 2. Continuum removal and peak deconvolution," *X-ray Spectrom.* 14: 8-15, 1985.
6. J. Philibert, "A method for calculating the absorption correction in electron-probe microanalysis, H. H. Pattee et al., Eds., *Microanalysis*, New York: Academic Press, 1963, 379-392.
7. G. Love, M. G. C. Cox, and V. D. Scott, "Assessment of Philibert's absorption correction models in electron probe microanalysis," *J. Phys.* D8: 1686-1701, 1975.
8. G. Love, V. D. Scott, and D. A. Sewell, "Evaluation of recent and improved correction procedures for EPMA," *Microbeam Analysis--1985*, 82.

SURFACE QUANTIFICATION IN THE ELECTRON MICROPROBE

Rod Packwood, V. S. Sastri, and J. D. Brown

It has been noted elsewhere¹ that the microprobe can detect a single monolayer of atoms. In fact the x-ray signal generated by 10kV electrons is large enough and the background generally small enough so that one can expect to see surface concentrations down to 0.1 monolayer equivalent without going to extremes in terms of electron beam current or counting times.

Surface Quantitation

Although the microprobe is not a surface analysis instrument that only senses the outer layers of a sample, there are circumstances when surface quantification is not only possible with the microprobe but when the microprobe may even be the method of choice. Those circumstances are as follows.

1. When the specimen of interest is, in the surface analysis sense, contaminated; when, in other words, it would require cleaning prior to analysis and hence might be changed in the process. An electron beam will pass unaffected through modest amounts of surface contamination to generate x rays in the layer; in turn, x rays can escape through the contamination without appreciable loss in intensity.

2. If quantitative information is required, then the microprobe really excels; the physical parameters required for quantification, ϕ_0 ; the ionization potential $\phi(\rho z)$ in terms of γ_0 , α , and β^2 ; the absorption coefficients, etc., are all known with sufficient accuracy that one can expect to make absolute measurements with errors of less than 10%.

3. If an unused or untreated surface is available for reference, measurements are that much easier because the necessity to determine background intensities by offsetting the spectrometers is eliminated. It also helps to know what elements may be present or what a client may have tried to do with a specimen. In principle, one could search for each of the more than fifty elements that may exist on a surface. However, analysts with the necessary patience are normally only to be found at monasteries in mountainous regions.

In the above it is taken for granted that the layer of interest is chemically different from its surroundings and will not be vaporized by the electron beam.

Some aspects of condition (2) are worthy of further explanation. The observed intensity ratio for element A, $K_S(A)$, is given by

$$K_S(A) = \phi_0 C_S(A) / \int_0^{\infty} \phi(\rho z)_A \exp(-\chi \rho z) d\rho z \quad (1)$$

where $C_S(A)$ is the surface concentration of A; the integral refers to pure A and can be evaluated very easily. $\phi(\rho z)$ is given by the modified Gaussian formulation^{3,4}

$$\phi(\rho z) = \gamma_0 \exp(-\alpha^2 \rho z^2) - (\gamma_0 - \phi_0) \exp(-\alpha^2 \rho z^2 - \beta \rho z) \quad (2)$$

and α is given by⁵

Authors Packwood and Sastri are at the Canadian Center for Mineral and Energy Technology, 568 Booth Street, Ottawa, Ontario, K1A 0G1; author Brown is at Engineering Science, University of Western Ontario, London, N6A 5B9. The authors thank Dr. J. R. Brown for the ion-milling and V. E. Moore and V. C. Chartrand for their technical assistance.

$$\alpha \approx \frac{6.7 \times 10^5}{E_0^{1.45}} \frac{Z}{A} \left(\frac{\ln(1.166E_0/J)}{R(E_0 - E_C)} \right)^{0.5} \quad (3)$$

where R is the backscatter correction factor of Duncumb and Reed⁶ and the other symbols have their usual meanings. γ_0 and β are listed in reference 2. For x rays in the soft x-ray region, i.e., below 1 keV, generated in a medium atomic number and density material by a beam of 5 kV electrons, the $3/2\alpha$ range will be of the order of 1000 Å. When large values for the x-ray absorption coefficients which are the norm for this region are taken into account, the mean penetration depth observed in the microprobe is typically 200 Å or less. Choosing a low x-ray take-off angle by tilting the specimen and/or inclining the electron beam with respect to the surface will further decrease the effective penetration and enhance the relative importance of the surface layers.

Langmuir-Blodgett Layers

Although there are some reports in the literature of submonolayer detection limits with the microprobe and related instruments,^{7,8} for the most part the limits are based upon extrapolation from thicker layers. There appeared to be a lack of known monolayer specimen material for use as standards. On the other hand the Langmuir-Blodgett layers of the lead stearate pseudo crystals used on the microprobe to diffract soft x rays would seem to have just the right sort of properties.⁹ The layers are relatively easy to manufacture,^{10,11} and although some care must be taken to insure that the desired metal-stearate reaction is complete, they can be formed for a number of bivalent metals and carry one metal atom per 40 Å squared. The layers are formed in pairs when a substrate is dipped in and out of the solution in the Langmuir trough. Thus, a single dip cycle should leave on the substrate one metal atom per 20 Å squared of surface embedded within close packed pairs of stearate molecules on the surface, representing a thickness of approximately 50 Å of hydrocarbon film. This idea was tested for a number of metals. Shown in Fig. 1 are preliminary results obtained with magnesium, calcium, and barium stearates deposited on polished aluminum sheet. The linear relationship between intensity and numbers of dipping cycles is very gratifying. For magnesium stearate, the surface concentration per double layer is predicted to be 1.93×10^{-8} g cm⁻². The amount observed was 1.8×10^{-8} g cm⁻². Obviously, the magnesium stearate was not fully formed at the pH used for these deposits. Compared with magnesium metal, the Langmuir-Blodgett double layer contains $\sim 2/3$ of a mono-layer equivalent of metal.

Depth Distribution

Although the x-ray signal comes from an overall depth of material it is possible to deduce something concerning the whereabouts of surface or near surface deposits. One can do so either by changing the accelerating potential and observing the changes in apparent concentration ratio,¹ or by taking a leaf out of the ESCA-Auger operating manual and using the ion-mill in conjunction with the microprobe as a means of depth profiling. Most microprobes have no ion guns, so that any ion-milling will have to be done elsewhere. The curve shown in Fig. 2 was obtained in just this fashion. A thin copper film was evaporated onto a stainless-steel specimen and subsequently ion-milled at a constant rate for different times. Although exploratory, the results clearly indicate the potential gains to be made by mounting an ion gun to the microprobe. The alternate method that varies the accelerating potential is beautifully expounded in the work by Butz and Wagner,⁸ who show that the intensity from a surface film of tungsten (36 Å) on molybdenum is first observed at about 3 kV and from there increases rapidly rather like the excitation cross section, whereas 0.24 wt% tungsten in molybdenum only becomes detectable at around 10 kV and then increases in roughly the same manner as the electron range, i.e., as $(E_0 - E_C)^2$.

Surface Analysis with Energy-dispersive X-ray Spectrometer (EDXS)

The implicit assumption to this point that a microprobe equipped with a good crystal spectrometer is used for analysis begs the question whether anything can be done on an SEM with an EDXS. Figure 3 shows a sequence of spectra from a stainless-steel specimen that had

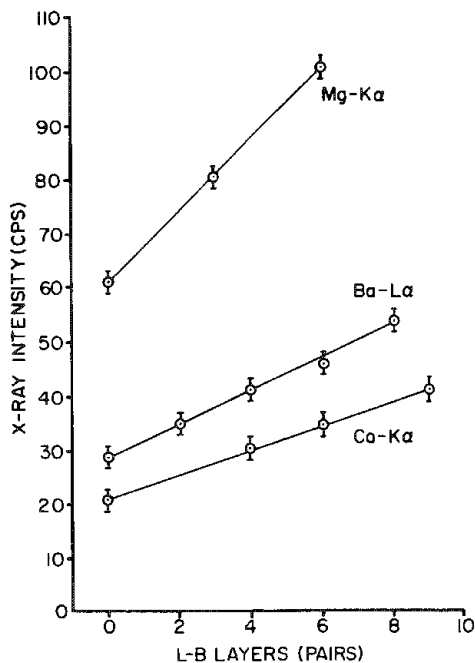


FIG. 1.--X-ray intensities vs dipping cycles for magnesium, calcium, and barium stearate Langmuir-Blodgett layers.

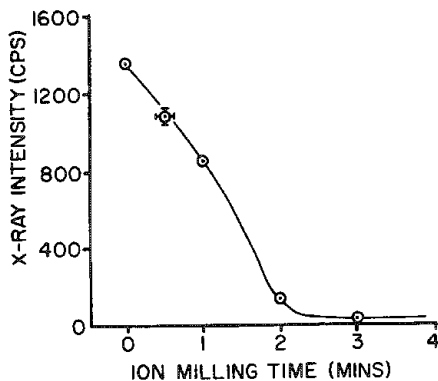


FIG. 2.--Cu L α x-ray intensity vs ion milling time on 375Å copper on stainless steel; 10kV accelerating potential.

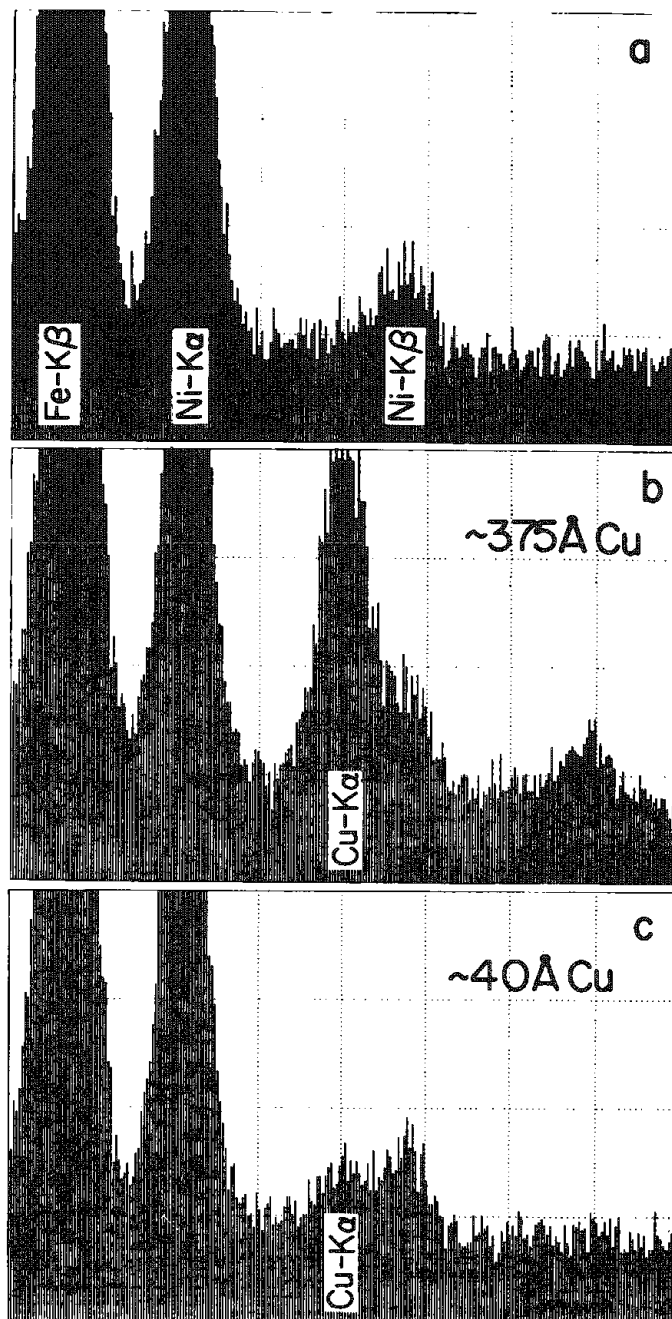


FIG. 3.--EDXS spectra from copper films on stainless steel: (a) none, (b) 375 Å copper, (c) ~40 Å copper; 20kV accelerating potential and 200 s counting time.

35-40 Å of copper and 375 Å of copper deposited on its surface. In making the analyses, care was taken to insure that all samples were at the same angle of tilt and height with respect to the electron beam and the EDXS. The x-ray counts in the Fe K α peak was used to control the counting time, thus effectively integrating the electron beam current.

Conclusions

Given certain conditions, the microprobe can perform adequately as a surface analysis instrument; i.e., it is possible to determine most of the species present on a substrate and their depth concentration profiles. The SEM-EDXS combination is not as powerful a combination, but is capable of detecting, for example, 40 Å of copper on stainless steel.

References

1. R. H. Packwood et al., " $\phi(\rho z)$," *Microbeam Analysis--1983*, 89-96.
2. R. H. Packwood and J. D. Brown, "A new theory for microprobe analysis," *Can. Metall. Quarterly* 20: 211-217, 1983.
3. R. H. Packwood and J. D. Brown, "Concerning x-ray production and quantitative analysis," *Microbeam Analysis--1980*, 45-48.
4. R. H. Packwood and J. D. Brown, "A Gaussian expression to describe $\phi(\rho z)$ curves for quantitative electron probe microanalysis," *X-ray Spectrom.* 10: 138-146, 1981.
5. R. H. Packwood and J. D. Brown, "Surface analysis in the electron microprobe," *Int. Chem. Cong. Pacific Basic Soc.*, 1984 (unpublished proceedings).
6. P. Duncumb and S. J. B. Reed, "The calculation of stopping power and backscatter effects in electron probe microanalysis," in K. F. J. Heinrich, Ed., *Quantitative Electron Probe Microanalysis*, Washington: NBS (SP 298), 1968, 133-154.
7. K. H. Ecker, "Sub-monolayer detection by electron microprobe analysis," *J. Phys.* D6: 2150-2156, 1973.
8. R. Butz and H. Wagner, "The determination of thin layer thicknesses with an electron microprobe," *Surface Science* 34: 693-704, 1973.
9. M. W. Charles, "Optimization of multilayer soap crystals for ultrasoft x-ray diffraction," *J. Appl. Phys.* 42: 3329-3360, 1971.
10. K. B. Blodgett, "Films built by depositing successive monomolecular layers on a solid surface," *J. Amer. Chem. Soc.* 57: 1007-1022, 1935.
11. B. L. Henke, "X-ray fluorescence analysis for sodium, fluorine, oxygen, nitrogen, carbon and boron," *Adv. X-ray Analysis* 7: 460-488, 1964.

QUANTITATIVE CALCULATIONS FOR COMPOSITIONAL MAPPING TECHNIQUES IN ELECTRON PROBE MICROANALYSIS

R. L. Myklebust, R. B. Marinenko, D. E. Newbury, and D. S. Bright

X-ray maps of various elements in a specimen have been a popular method for presenting electron microprobe data for many years.¹ These maps have been an effective way of localizing the elements within the specimen; however, no quantitative information could be obtained from the maps. With the advent of computer-controlled electron microprobes, it has become possible digitally to step the electron beam in a raster pattern across the specimen surface, pausing at each point to accumulate x rays for each element. The data collected at each of these points can then accumulate for background and compared to a standard to obtain an intensity ratio (k-value). These k-values are then processed by a quantitative data-reduction program such as the NBS FRAME program to obtain quantitative elemental information at each point.² Display of these arrays as images gives a true compositional map of each element in the specimen, because the brightness of each point (pixel) is directly proportional to the amount of the element present at that point.

Instrumentation and Data Acquisition

The techniques for collecting the data with wavelength-dispersive spectrometers is described in a separate paper in the present volume by Marinenko et al.³ Maps of x-ray intensities on standard specimens and on unknown specimens have been collected by these techniques and have been transferred to a Digital Equipment Corporation VAX 11/780* for processing and display on a DeAnza IP8500* image analysis system.

Calculations

The images collected at low magnification (200-800 \times) suffer from severe spectrometer defocusing on both the standards and unknowns. The background is almost entirely continuum which should show the defocusing effect if a single wavelength only were measured. However, the spectrometer is always focused on some wavelength of the continuum that varies with beam position. Since the continuum intensities can be considered equal over the small range of wavelengths involved, the background counts do not demonstrate any defocusing, and a single value for the background counts for each element could be used. As a first step in the data reduction, all counts are converted to counts per second and corrected for dead time. The dead-time correction is particularly important in this case since high count rates are used to minimize the data collection time.

The k-ratios for each element are then computed at each point in the array by division of the counts from the unknown by the counts from the standard at the corresponding point in the standard array. We assume that this technique of computing k-values corrects for the spectrometer defocusing, since the defocusing should be the same for both the standard and the unknown if nothing else is changed. A matrix correction procedure (FRAME) is then used to compute the concentrations for each element at each pixel. The resulting concentration maps are then displayed through the image analysis system.

To test the validity of this approach, SRMs known to be homogeneous on a micrometer scale were mapped and the resulting data were statistically analyzed. The maps for homogeneous gold-silver alloys are shown in Fig. 1, together with the intensity maps for the pure element standards. The contours on the intensity maps show the spectrometer defocusing for each of the spectrometers. The lack of contours on the concentration maps shows that all of the concentration data were within one gray-level ramp ($\pm 10\%$ concentration) for these images. Table 1 lists the compositions obtained from nine different regions of one of the alloys and the corresponding intensities for the same regions.

The authors are at the Center for Analytical Chemistry, National Bureau of Standards, Gaithersburg, MD 20899. *Certain commercial equipment, instruments, or materials are identified in this paper to specify adequately the experimental procedure. Such identification does not imply recommendation or endorsement by the National Bureau of Standards, nor does it imply that the materials or equipment identified are necessarily the best available for the purpose.

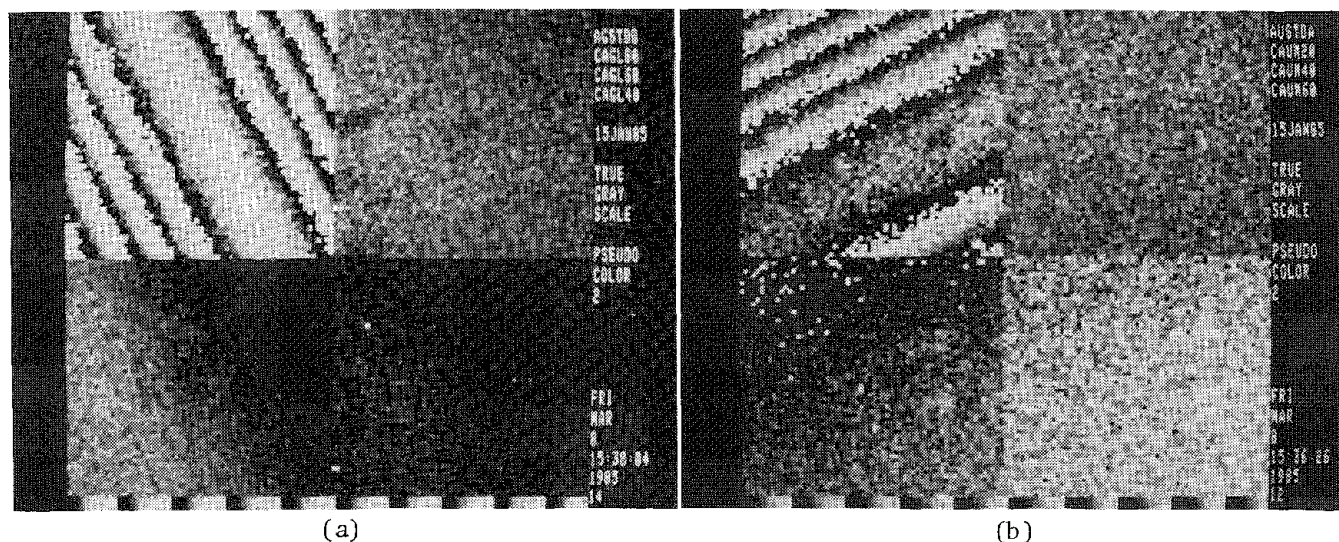


FIG. 1.--Concentration maps of gold-silver alloys: (a) silver maps, (b) gold maps. In each group of four, pure-element intensity map is at upper left. Upper right is the concentration map of the 80Ag-20Au alloy, lower left is the 60Ag-40Au alloy, and lower right is the 40Ag-60Au alloy. The strip along the bottom shows gray-level ramps in images.

TABLE 1.--Comparison of x-ray intensities and concentrations from different areas on an alloy specimen of 80Ag:20Au. Intensities are in counts and concentrations are in mass fractions. The population standard deviation for the concentrations is 0.006 for both silver and gold. The nine areas are arranged in three rows of three columns as shown in the following pattern.

1 2 3
4 5 6
7 8 9

Area no.	Intensity AgL	Conc. Ag	Intensity AuM	Conc. Au
1	22451	0.781	1107	0.215
2	22868	.772	1312	.215
3	17265	.765	1481	.213
4	19647	.779	1467	.214
5	23506	.773	1577	.211
6	20633	.770	1632	.211
7	16714	.780	1629	.212
8	22194	.780	1598	.211
9	23108	.773	1507	.210

Discussion

The compositional maps appear to be quite uniform even though the intensity maps from which they were generated showed serious defocusing problems. The lithium-drifted-silicon [Li(Si)] energy-dispersive detector can produce these images much easier since it can look at a rather large area on the specimen without any loss in intensity due to defocusing. Another advantage of the Li(Si) detector is the ability to collect data on any number of elements simultaneously. However, there are some serious disadvantages to using a Li(Si) detector for compositional maps. The Li(Si) detector must look at the entire spectrum instead of only the x-ray energy of interest; therefore, the counting rate on each element is considerably lower than for the wavelength spectrometer and each data point requires a longer counting time. A lower beam current must also be used for a Li(Si) detector to keep the dead time from becoming too large.

The wavelength-dispersive spectrometer can collect data at a high counting rate, which reduces the time required to collect an image. The high peak-to-background ratio for the

wavelength-dispersive spectrometer allows elements with low concentrations to be measured in a reasonable length of time. It is particularly useful at high magnifications, where the defocusing problem is minimized.

We are studying some other methods of correcting for the defocusing problem, such as attempting to model the intensities across an image. This would eliminate the necessity of measuring an entire array on each pure element standard.

References

1. H. Yakowitz and K. F. J. Heinrich, *J. Res. Nat. Bur. Standards*, 73A: 113, 1969.
2. H. Yakowitz, R. L. Myklebust, and K. F. J. Heinrich, "FRAME: An on-line procedure for quantitative electron probe microanalysis," NBS Tech. Note 796, October, 1973.
3. R. B. Marinenko et al., *Microbeam Analysis--1985*, 159.

"PAP" $\phi(\rho z)$ PROCEDURE FOR IMPROVED QUANTITATIVE MICROANALYSIS

J. L. Pouchou and F. Pichoir

A new general model for quantitative microanalysis of homogeneous or layered samples has been developed¹⁻⁵ and incorporated to the CAMECA software under the name "PAP." As opposed to the usual models (generally conceived for computing moderate correction factors), the "PAP" model has been designed for computing accurately the characteristic emerging x-ray intensities, even when absorption and atomic number effects are large.

Basic Concepts

The principal feature of the "PAP" program resides in a novel description of the ionization functions $\phi(\rho z)$ allowing a combined computation of the absorption and Z effects. Considering that the modified Gaussian form we had tried some years ago was too restrictive, we have now adopted for $\phi(\rho z)$ a polynomial expression, the coefficients of which are deduced from four parameters which characterize the distribution $\phi(\rho z)$: the surface ionization $\phi(0)$, the ultimate depth of ionization R_X , the depth R_m of maximum ionization, and the integral F of the distribution, which represents the number n_j of primary ionizations produced on a given level j:

$$n_j = C_A Q_j^A(E_0) \cdot N/A \int_0^{R_X} \phi(\rho z) d(\rho z)$$

This approach differs basically from other recent $\phi(\rho z)$ approaches,^{7,8} since the integral F of $\phi(\rho z)$ does not depend on any empirical shape parameters, but is calculated theoretically before being used as one of the parameters characteristic of the distribution. This particular procedure insures the area of the distribution is realistic in all cases and varies correctly with the electron energy.

The primary intensity is computed from a modified form of the Coulon-Zeller⁹ model for the backscattering factor R, an ionization cross section proportional to $\ln(U)/U^m$ (with m close to 0.9 for K levels and close to 0.8 for L and M levels), and a semi-empirical electron retardation law¹⁰ that reduces the computation time and is claimed to be more adequate than the usual Bethe's expression at low accelerating voltages.

The ultimate ionization depth R_X is expressed as a fraction $Q(U, Z)$ of the total ionization range R_0 , which is calculated using the above-mentioned retardation law.

The depth R_m corresponding to the maximum of $\phi(\rho z)$ is expressed as a function of R_X , Z, and U.

The surface ionization $\phi(0)$ is a function of the backscattering coefficient η , the over-voltage U, and the atomic number Z.

Application to Conventional Microanalysis

The realistic $\phi(\rho z)$ functions involved in the "PAP" procedure allow to perform highly reliable quantitative analysis with soft x rays, even at high accelerating voltages. Therefore, this model is particularly suited for light and ultralight elements analysis, medium Z elements analysis by L lines, and heavy elements analysis by M lines. Several examples will show the improvements of the results obtained in these fields (Fig. 1).

Apart from the computation of corrective factors in conventional microanalysis, the "PAP" model may be applied to an other type of application: the determination of unknown or uncertain mass absorption coefficients of soft x rays. For this purpose, a program called "PAPMAC" has been included recently in the CAMECA software that deduces the mass absorption coefficient from an automatic fit of the emerging intensity data measured at variable accelerating voltage on a known sample. Examples relative to ultralight emitters (B, C) and to L lines of medium Z elements (Ni, Cu, Ga, As) illustrate the reliability of the method.

The authors are at the Office National d'Etudes et de Recherches Aéropatiales, 29 Avenue de la Division Leclerc, F-92320 Chatillon, France.

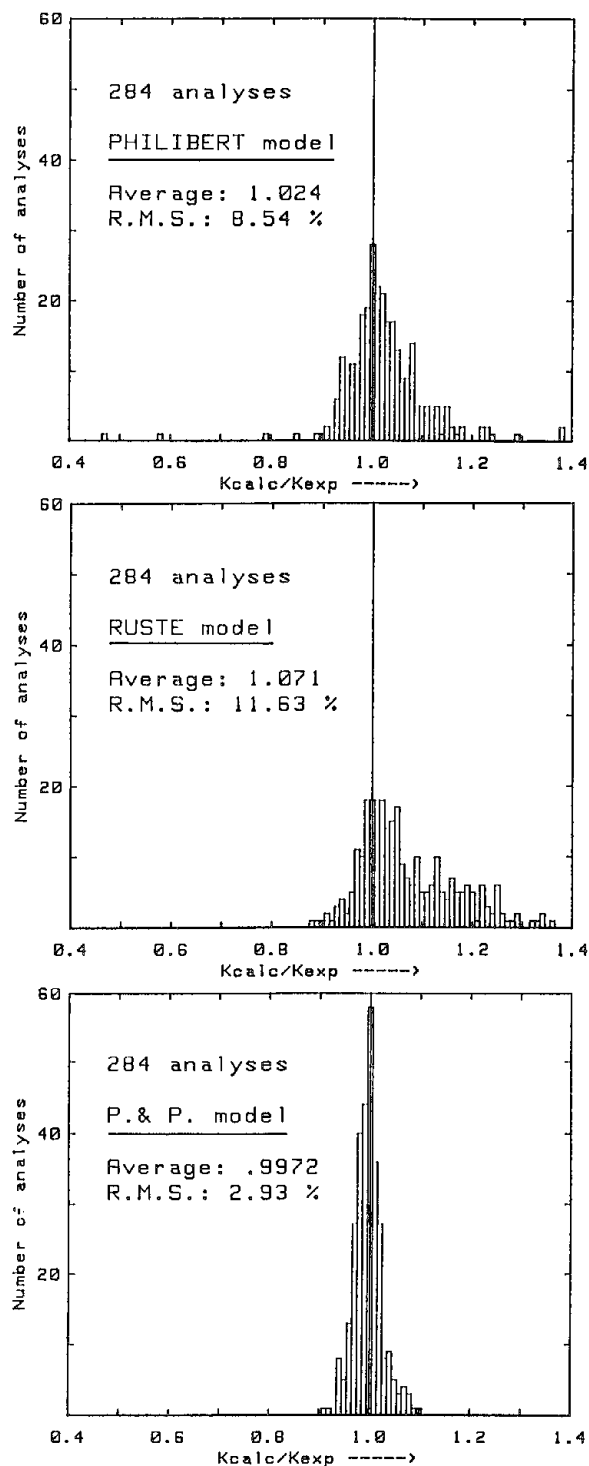


FIG. 1.--Error histograms obtained using Philibert, Ruste, and "PAP" models for 234 analyses involving strong absorption corrections.

Application to Superficial Analysis

The realistic character of its $\phi(\rho z)$ functions allows the "PAP" model to be extended to the quantitative analysis of specimens having a depth-dependent composition (particularly layered specimens). Even when a noticeable variation of atomic number is associated with the layered structure, the principle of a continuous ionization function may be maintained; each of its four characteristic parameters is equivalent to those of fictitious homogeneous samples defined from the distributions in depth of the elements present in the real specimen.

A graphic restitution by a conversational program of the K-ratios measured at variable accelerating voltage gives simultaneously access to the composition and mass thickness of superficial layers, in the typical range 10-1000 nm.

In the particular case of a single layer on a substrate of known composition, it may be sufficient for a complete characterization of the layer to operate only at one accelerating voltage, providing that ultimate ionization depth corresponding to this operating condition is significantly greater than the film thickness. Several examples illustrate the quantitative capabilities of "PAP" model for thin superficial films analysis.

References

1. J. L. Pouchou and F. Pichoir, "Extension des possibilités quantitatives de la microanalyse X par une formulation nouvelle des effets de matrice," ICXOM 10, *J. Physique Colloq.* 45(c2): 17-20, 1984.
2. J. L. Pouchou and F. Pichoir, "Analyse d'échantillons stratifiés à la microsonde électronique," ICXOM 10, *J. Physique Colloq.* 45(C2): 47-50, 1984.
3. J. L. Pouchou and F. Pichoir, "A new model for quantitative analysis: Part I. Application to the analysis of homogeneous samples," *La Recherche Aéronautique* 3: 13-38, 1984.
4. J. L. Pouchou and F. Pichoir, "A new model for quantitative analysis: Part II. Application to in-depth analysis of heterogeneous samples," *La Recherche Aéronautique* 5: 47-65, 1984.
5. J. L. Pouchou and F. Pichoir, "Possibilités d'analyse en profondeur à la microsonde électronique," *J. Micr. Spectrosc. Electron.* 9: 99-100, 1984.
6. J. L. Pouchou, F. Pichoir, and F. Girard, "Application de la méthode de Monte-Carlo à l'analyse de couches minces déposées sur substrat," *J. Micro. Spectr. Elect.* 5: 425-441, 1980.
7. R. H. Packwood and J. D. Brown, "A Gaussian expression to describe $\phi(\rho z)$ curves for quantitative electron probe microanalysis," *X-ray Spectrometry* 10: 138-146, 1981.
8. G. F. Bastin, H. J. M. Heijligers, and F. J. J. Van Loo, "Evaluation of the use of Gaussian $\phi(\rho z)$ curves in quantitative electron probe microanalysis: A new optimization,"

X-ray Spectrom. 13(2): 91-97, 1984.

9. C. Zeller and J. Coulon, "Détermination théorique du facteur de rétrodiffusion en microanalyse par émission X," *C. R. Acad. Sci.* 276(B): 215-218, 1973.

10. J. L. Pouchou, "In-depth analysis of layered samples using the electron microprobe," *TP ONERA* 109: 1-10, 1984.

THE EFFECT OF IMPERFECT FOCUSING ON X-RAY INTENSITIES IN THE ELECTRON MICROPROBE

M. A. Short and K. P. Helmold

The focusing of x rays by linear crystal spectrometers has been discussed in some detail by Heinrich.¹ He comments, in particular, on the difference in sensitivity between vertical and inclined spectrometers due to variations in specimen elevation. This difference has been graphically illustrated by Bishop² (as quoted by Ruste³) who measured intensity changes over a distance of more than 3000 μm . For practical electron microprobe analysis, however, we are concerned with changes in intensity associated with difficulties in the exact focusing of the sample on the Rowland circle. Experience shows that it is most unlikely that the error in elevation will exceed $\pm 10 \mu\text{m}$.

In this paper we present the results of measurements of x-ray intensity losses over a range of $\pm 10 \mu\text{m}$ from the nominal focusing circle for both vertical and inclined crystal spectrometers. The results include measurements for different crystals and for different Bragg angles.

Experimental

All measurements were made on a Cameca MBX electron microprobe equipped with both vertical and inclined spectrometers with LiF, PET, and TAP crystals for Bragg angles ranging from 14° to 43° . Two separate determinations of x-ray intensity were made at each different sample elevation for each combination of crystal, spectrometer, and Bragg angle used. The two determinations were: (a) with the crystal spectrometer aligned (peaked) with the sample on the Rowland circle, as determined by the optical microscope, and left at that setting for measuring the intensity at the different sample elevations; and (b) with the crystal spectrometer realigned at each sample elevation prior to measuring the x-ray intensity. The usual precautions were taken to insure that any changes in intensity that might occur were not obfuscated by the buildup of carbon contamination or by the accumulation of total counts which were not statistically meaningful.⁴ When ambiguous results caused by only very small changes in intensity were encountered, experiments were repeated until plausible and consistent results were obtained.

Results

The results for a selection of crystals, spectrometers, and Bragg angles are shown in Table 1. The table shows percentage change in intensity per $10 \mu\text{m}$ change in elevation and the change in the sine of the Bragg angle per $10 \mu\text{m}$ interval found in those measurements in which the Bragg angle was redetermined as the sample was elevated.

From the results shown in Table 1, it is evident that the following generalizations can be made:

1. As expected, the change both in x-ray intensity and in Bragg angle with respect to sample elevation over a range of $\pm 10 \mu\text{m}$ from the Rowland circle for the inclined spectrometer is essentially zero for all combinations of spectrometer, crystal, and angle.
2. Changes in x-ray intensity with respect to sample elevation over the same range were observed for the vertical spectrometers, reaching 0.2% per $1 \mu\text{m}$ for Si K determined with a TAP crystal. In all cases this change can be reduced to insignificant proportions by refocusing (peaking) the crystal spectrometer prior to measuring the x-ray intensity.

An assessment of the overall accuracy of the measurements shown in Table 1 can be obtained from a comparison of the expected and measured standard deviations (which are shown to one significant figure only).

The authors are at Cities Service Oil and Gas Corporation, Box 3908, Tulsa, OK 74102.

The measured intensity changes for inclined spectrometer/TAP/Si K and Al K require some comment. A large number of repetitive measurements for all three scenarios showed no statistically significant intensity changes at all for a distance of 20 μm on each side of the Rowland circle. As the sample passed through the point of best optical focus, however, there was found every time an abrupt change of 0.2% in x-ray intensity. We do not know the reason.

Conclusions

The results suggest a preferred experimental procedure for cases where the optically determined sample elevation may be in error by more than 1 μm . This procedure is to determine all major elements on vertical spectrometers, in principle refocusing a spectrometer each time before measuring the x-ray intensity; in practice this is of greatest significance only for low values of $\sin \theta$. Minor elements (where the x-ray intensity is too low to determine the spectrometer peak position accurately) may be measured on an inclined spectrometer where the sample elevation does not affect the x-ray intensity.

It is also clear that when Si K x-ray intensities are measured on a vertical spectrometer with a TAP crystal the spectrometer peak position should always be redetermined prior to measurement of the x-ray intensities unless there is absolute confidence in the elevation of the sample. We have found experimentally that the best results for both Si K and Al K are obtained if the spectrometer is refocused for every measurement.

References

1. K. F. H. Heinrich, *Electron Beam X-Ray Microanalysis*, New York: Van Nostrand Reinhold, 1981, 111.
2. H. E. Bishop, AERE R-8413, 1976.
3. J. Ruste, in F. Maurice, L. Meny, and R. Tixier, Eds., *Microanalysis and Scanning Electron Microscopy*, Orsay: Editions de Physique, 1979, 255.
4. M. A. Short, "Statistical considerations in x-ray fluorescence analysis," *Advances in X-ray Analysis* 19: 53, 1976.

TABLE 1.--Intensity and Bragg angle changes for a selection of spectrometers, crystals, and radiations.

Spectrometer Geometry	Crystal	Radiation	Approximate $\sin \theta$	Peak Position Redetermined	Measured Intensity Change per 10 μm	Standard Deviation from N^2	Standard Deviation Measured	Measured Change in $\sin \theta$ per 10 μm
Inclined	LiF	TiK	0.68	Yes	0	0.2%	0.2%	± 0.00002 over 40 μm
Vertical	LiF	TiK	0.68	Yes	0	0.2%	0.2%	0.00003
Inclined	LiF	TiK	0.68	No	0	0.2%	0.2%	--
Vertical	LiF	TiK	0.68	No	0.3%	--	--	--
Vertical	PET	MnK	0.24	No	0.8%	--	--	--
Vertical	PET	MnK	0.24	Yes	0	0.1%	0.1%	0.00009
Vertical	PET	PdL	0.50	No	0.3%	--	--	--
Vertical	PET	PdL	0.50	Yes	0	0.5%	0.5%	0.00005
Inclined	LiF	FeK	0.48	Yes	0	0.5%	0.5%	± 0.00002 over 80 μm
Inclined	LiF	FeK	0.48	No	0	0.08%	0.08%	--
Vertical	LiF	FeK	0.48	Yes	0	0.5%	0.6%	0.00004
Vertical	LiF	FeK	0.48	No	0.3%	--	--	--
Vertical	TAP	ZnL	0.48	Yes	0	0.1%	--	0.00004
Vertical	TAP	ZnL	0.48	No	0.2%	--	--	--
Vertical	TAP	SiK	0.28	No	2.0%	--	--	--
Vertical	TAP	SiK	0.28	Yes	0.1%	--	--	0.00009
Inclined	TAP	SiK	0.28	Yes	$\pm 0.1\%$ over 40 μm	0.06%	--	± 0.00001 over 60 μm
Inclined	TAP	SiK	0.28	No	$\pm 0.1\%$ over 40 μm	0.06%	--	--
Inclined	TAP	AlK	0.32	No	$\pm 0.1\%$ over 40 μm	0.06%	--	--

EVIDENCE FOR CELL VOLUME REGULATION IN RAT SKELETAL MUSCLE

Mary Jo Ingram and F. D. Ingram

When exposed to a hypertonic bathing medium, many types of cells respond with a regulatory volume increase that returns cell volume toward normal after an initial shrinkage.¹⁻³ In vivo studies of cell volume regulation are complicated by central systems that control plasma osmolality and may mask intrinsic properties of the cell. Pollock and Arieff⁴ presented data from in vivo studies suggesting that skeletal muscle may not have volume regulation properties. The present study examined the response of isolated intact muscle to hypertonic challenge to determine whether cell volume regulation is an intrinsic property of rat skeletal muscle.

Although electron probe microanalysis is labor intensive and hence not the method of choice for most cell volume regulation studies, nevertheless, it provides a number of advantages for studying cell volume regulation. With the proper choice of preparation methods and operating parameters, cell volume, intracellular water, and important intracellular electrolyte concentrations can be measured simultaneously in individual cells. With conventional methods, most of those parameters can be computed only indirectly.

Measurement of cell water is straightforward when tissue is either frozen hydrated or embedded with an appropriate embedding medium.⁵ For studies of cell volume regulation, in which only change in volume is needed rather than absolute cell volume, change in cell volume is assessed from the characteristic x-ray data of an element endogenous to tissue solids. Sulfur has been found useful for this purpose with freeze-dried, embedded tissue. If the concentration of tissue solids [TS] is proportional to sulfur concentration [S],

$$[TS] = a[S] \quad (1)$$

where a is the constant of proportionality. Further, assume that no detectable change in cell solids content occurs in response to an osmotic stress; i.e.,

$$(TS \text{ Mass})_e = (TS \text{ Mass})_c \quad (2)$$

By definition

$$[TS] = \frac{(TS \text{ Mass})}{V} \quad (3)$$

or

$$(TS \text{ Mass}) = V[TS] \quad (4)$$

where V is cell volume.

Then from Eq. (2),

$$V_e[TS]_e = V_c[TS]_c \quad (5)$$

and from Eq. (1)

$$V_e a[S]_c = V_c a[S]_c \quad (6)$$

or

$$\frac{V_e}{V_c} = \frac{[S]_c}{[S]_e} \quad (7)$$

The determination of cell volume change by use of the S K α signal is not possible unless tissue is embedded or fully hydrated. In addition, the ZAF correction factor for the S K α signal must be identical for both the experimental and control tissue. In the work presented here, both control and experimental tissue are embedded in the same plastic. Because the embedding material makes up approximately 80% of the sample, the criterion that the ZAF correction factors be identical in both sets of tissue is met. Yet the estimation of cell volume change from the ratio of characteristic S K α x-ray signals will not be accurate if appreciable sulfur enters or leaves the cells.

Alternatively, cell volume change can be determined from information on tissue solids derived from the intracellular water data. Similar to the sulfur ratio method, cell

The authors are at the USDA/ARS Children's Nutrition Research Center, Department of Pediatrics and the Department of Physiology, Baylor College of Medicine, Houston, TX 77030. USDA/ARS support is acknowledged.

volume change can be determined from the ratio of experimental to control cell solids concentration, which comes directly from Eqs. (2) and (4). The determination of cell volume change from data on tissue solids will be accurate only if there is no net movement of tissue solids across the cell membrane. The cell volume size will be underestimated with the tissue solids method if sufficient material enters the cell to change the mass of solids in experimental cells. Agreement between the two methods of estimating cell volume change provides strong evidence that mass of cell solids has not changed as a result of the experimental procedure. When there is disagreement between the two estimations of cell volume change, it can be determined by the sense of the disagreement whether solids have entered or have left the cell.

A third method to estimate cell volume change proposed by Tosteson and Hoffman⁶ for use with conventional methods could also be used with electron probe microanalysis. The method involves comparing the sum of intracellular electrolyte concentrations, $[] + [Na] + [Cl]$, in control tissue with the sum of electrolyte concentrations in experimental tissue. The method is too simplistic for general application, however, because it assumes that the only response of cells to an osmotic challenge is the movement of electrolytes and water across the cell membrane; i.e., it does not accommodate the involvement of other entities such as H^+ ions or amino acids in the cellular response to osmotic challenge. It also assumes that the activity of each electrolyte is the same as the concentration.

Lumbricals from the hind feet of young rats were selected for the study of the response of skeletal muscle to osmotic challenge because of their size, nature, and number. Six muscles of a uniform fiber type, approximately 8 mm long and 0.5 mm thick, can be obtained from each animal. The lumbricals are sufficiently numerous to simplify the treatment of controls, and their small size insures good perfusion of incubation solutions and permits excellent cryofixation by quench-freezing or freeze-clamping.

Methods

Intact lumbricals were removed from anesthetized 250g rats. Each muscle was stretched to approximately 125% of resting length and mounted on simple, individual plastic forms with one of a series of color-coded threads. After dissection, the muscles were placed in normal, buffered, oxygenated bathing solution at 37 C for approximately 1 h. The muscles then were distributed among a series of bathing solutions described in Table 1. A minimum of one muscle from each animal was incubated in the control solution. Composition of the various solutions was identical except for solution osmolality which was adjusted with lactose. After a 40 min incubation at 37 C and gentle bubbling with 95% O_2 and 5% CO_2 , the muscles were removed from the vials and plunged by hand into chilled liquid propane. Frozen muscles were stored under liquid nitrogen until a portion of the frozen muscle was mounted in a freeze-dry apparatus. Tissue was dried at approximately -80 C, fixed with osmium tetroxide vapor, and embedded in EPON 826 containing approximately 80 mmol kg^{-1} Br. Embedded tissue blocks were sectioned with a dry glass knife to expose muscle fibers in cross section, and a thin section was stained and mounted for light microscopy. The faced block was mounted for thick sample analysis along with a set of pure crystal secondary standards and coated with approximately 20 nm carbon.⁶ The prepared tissue blocks were analyzed with a 10keV, 50nA electron beam in a fully automated, Applied Research Laboratories, Model SEMQ, electron microprobe. Data were collected simultaneously from four wavelength-dispersive spectrometers and a KEVEX Si(Li) energy detector.⁷ Diffraction crystals used for this work were: PET (pentaerythritol) for S $K\alpha$ and Cl $K\alpha$; TAP (thallium acid phthalate) for Br $L\alpha$; and RAP (Rubidium acid phthalate) for Na $K\alpha$. Continuum from 4.2 to 7.2 keV and K $K\alpha$ were collected with the Si(Li) detector.

Electron microprobe signals for the electrolytes were converted to numbers representing wet weight concentrations by referencing characteristic x-ray counting rates through pure crystal secondary standards to counting rates on fabricated albumin standards.⁶ Tissue water was assessed by observing the reduction in embedding plastic Br $L\alpha$ signal as a result of dilution of the plastic by tissue solids.⁴ Change in cell volume was inferred independently from the ratio of control-tissue S $K\alpha$ signal to experimental-tissue S $K\alpha$ signal.

TABLE 1.--Incubation solutions for osmotic experiment using isolated rat skeletal muscle (mEq/L).

mOsM/L	K ⁺	Cl ⁻	Na ⁺	Ca ⁺⁺	Mg ⁺⁺	HCO ₃ ⁻	HPO ₄ ⁻	ACET	GLU	ALA	LEUC	LACT
309	4.6	114	147	1.8	1	25	2.3	8	8	5	5	5
353	4.5	114	144	1.8	1	25	2.3	8	8	5	5	45
381	4.5	114	145	1.8	1	25	2.3	8	8	5	5	76
406	4.5	114	145	1.8	1	25	2.3	8	8	5	5	100

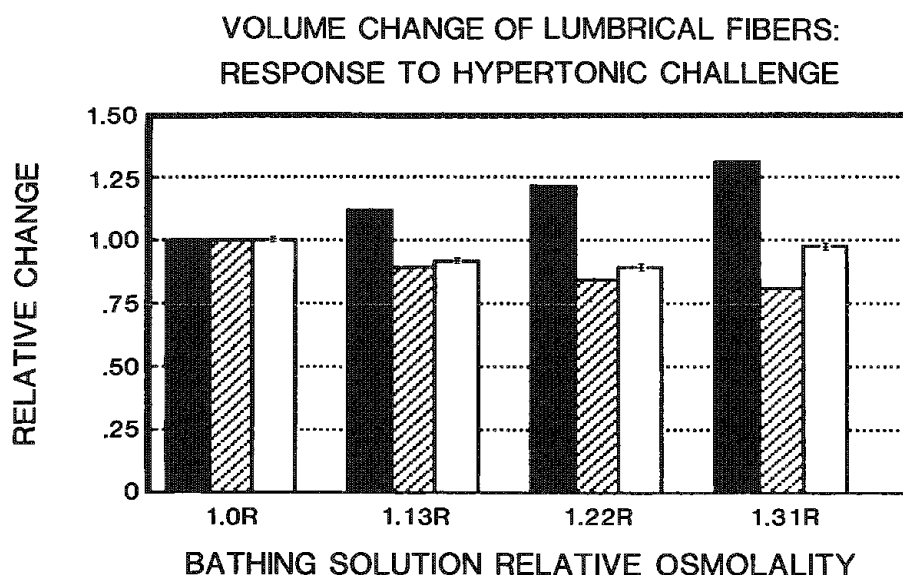


FIG. 1.--Cell volume change with hyperosmotic solutions. Solid bars represent relative osmolality, hatched bars represent expected volume change, and open bars represent measured volume change.

Results

Fibers from each of the muscles incubated in hypertonic solutions shrank, but not to the extent expected of a perfect osmometer (Fig. 1). The volume of fibers incubated in the hypertonic solutions, in fact, had returned almost to the volume of control fibers. The expected volume change (depicted by the hatched bar in Fig. 1) was computed from the Van't Hoff relationship between osmolality and cell water volume. The open bar is the ratio of S K α signal from control lumbrical fibers to S K α signal from experimental animal lumbrical fibers. This ratio of sulfur signals was interpreted as the volume change in experimental animals in response to the osmotic challenge.

Discussion

More effective cell volume regulation was demonstrated in the lumbrical fibers that were incubated in the more hypertonic solutions. In a study of the response to hypertonicity as a function of time, we have observed that volume regulation was complete in less than 4 min for lumbricals incubated in a 385mosm l⁻¹ solutions. Because regulation may occur at a slower rate for fibers stressed with less hypertonic solutions, future

studies will be of longer duration to determine whether muscles incubated in less hypertonic solutions are capable of regulating cell volume as effectively as those in more hypertonic solutions. Special attention will be given to the mechanisms that effect regulatory volume increase when cells are challenged with hypertonic solutions.

References

1. A. D. C. Macknight and A. Leaf, "Regulation of cellular volume," in T. E. Andreoli, J. F. Hoffman, and D. D. Fanestil, Eds., *Physiology of Membrane Disorders*, New York: Plenum, 1978, pp. 315-334.
2. R. Gilles, "Intracellular free amino acids and cell volume regulation during osmotic stresses," in C. B. Jorgensen and E. Skadhange, Eds., *Osmotic and Volume Regulation*, New York: Academic Press, 1978, pp. 470-499.
3. P. Cala, "Volume regulation by amphiuma red blood cells," *J. Gen. Physiol.* 76: 683-708, 1980.
4. A. S. Pollock and A. I. Arieff, "Abnormalities of cell volume regulation and their functional consequences," *Am. J. Physiol.* 239: F195-F205, 1980.
5. M. J. Ingram and F. D. Ingram, "Electron microprobe calibration measurement of intracellular water," *SEM/1983 III*, 1249-1254.
6. D. C. Tosteson and J. F. Hoffman, "Regulation of cell volume by active cation transport in high and low potassium sheep red cells," *J. Gen. Physiol.* 44: 169-194, 1960.
7. F. D. Ingram and M. J. Ingram, "Quantitative analysis with the freeze-dried, plastic-embedded specimen," *J. Micros. Biol. Cell.* 22: 193-204, 1975.
8. F. D. Ingram and M. J. Ingram, "Combined energy detector-wavelength dispersive spectrometer electron probe microanalysis of biological soft tissue," *SEM/1983 II*, 853-860.

ELECTROLYTE SHIFTS IN THE ISCHEMIC HEART

L. G. Walsh and J. McD. Tormey

Myocardial ischemia (impaired blood flow to the heart) commonly leads to myocardial infarction, the leading cause of death in the United States. The mechanisms by which ischemia leads to cell death are poorly understood, but are known to involve major shifts of electrolytes both within cells and across cell membranes. The most dramatic changes tend to occur not during ischemia itself but shortly after reestablishment of normal blood flow.

Such electrolyte shifts are difficult to study by conventional techniques. The susceptibility of individual cells and regions to cell death is highly variable. Attempts to study electrolytes in ischemia have mostly involved measurements of gross changes at the tissue level. Electron probe microanalysis (EPMA) is well suited for studying these phenomena, because damaged cells and subcellular constituents can be individually analyzed apart from dead cells and extracellular fluid.

Materials and Methods

Male rabbits were anesthetized, their hearts were excised, and the right ventricular walls were removed and perfused via the right coronary artery. The perfusing solution included 1mM Ca and 5% dextran, and the ventricular walls were maintained at 37 C and pH 7.35-7.40. The preparations were stimulated at 72 beats/min and their force development was monitored. Three conditions were selected for study. (1) *Control* preparations were frozen after 30 min at 37 C. (2) *Ischemic* preparations were frozen after an additional 60 min of anoxia and no perfusion. (3) *Reperfused* preparations first received the same treatment as ischemic, but were frozen 5 min after perfusion was reestablished in a normoxic atmosphere. Tissue was frozen between polished copper blocks that were cooled in LN₂. Pieces were glued¹ to mounts, and thin cryosections were cut at -120 C. With the use of a Gatan cryotransfer stage in a JEOL 100CX microscope, sections were freeze-dried at temperatures up to -90 C, and were analyzed² at -120 C.

Results and Discussion

Figure 1 summarizes the EPMA data. Separate bar graphs depict results from whole cells (exclusive of nuclei), myofibrils, and mitochondria. Four conditions are depicted. The reperfused measurements are divided into "dead" and "live" groups, based on the criterion that dead cells have a cell [K] less than 100 mM/kg dry weight.

Although myofibrils and mitochondria constitute approximately 60% and 35%, respectively, of the normal sarcoplasmic volume, they do not include an additional ~5% that contributes to our cell measurements. [Much of this extra component is associated with T-tubules and sarcoplasmic reticulum (SR).] In the case of control hearts, the [Ca] of myofibrils and mitochondria (weighted by 0.60 and 0.35, respectively) explains 90% of the [Ca] measured over the cells.

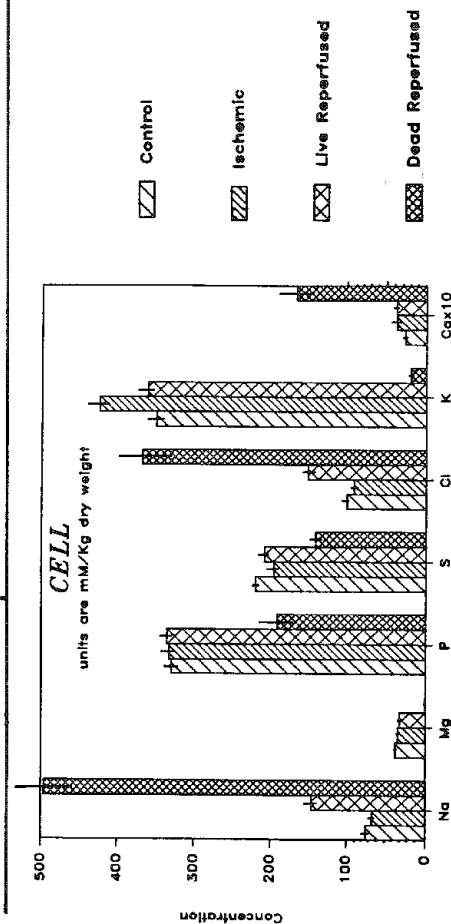
The control concentrations differ from those we previously reported for rabbit papillary (heart) muscles.³ Cell [Na] and [Ca] are greater and [K] is lower than in the papillary preparation. These differences are related to the 5× higher contraction frequency and 10° higher temperature in the present study.

The authors are at the UCLA Department of Physiology, Center for Health Sciences, Los Angeles, CA 90024. LGW has been supported by M. L. Schulte and NIH fellowships. The work has been supported in part by Grant R01 HL 31249 from the National Heart, Lung, and Blood Institute and by grants from the American Heart Association Greater Los Angeles Affiliate and the Muscular Dystrophy Association.

TABLE 1.--Comparison of [Ca] before, during, and after ischemia. Ca concentrations are in mmoles/kg dry weight. Probability levels are from two-tailed Student's t-test.

	Ca Concentration			
	Control	Ischemic	Live Reperfused	
Cell	Mean SEM	2.65 0.4	3.67 0.9	3.76 0.6
Myofibrils	Mean SEM	3.07 0.5	1.84 0.5	4.21 0.5
Mitochondria	Mean SEM	1.13 0.2	0.95 0.3	2.21 0.4

	Comparison			
	Control: Ischemia	Control: Reperfused	Ischemia: Reperfused	
Cell	n.s.	P<.2	n.s.	
Myofibrils	P<.1	P<.2	P<.01	
Mitochondria	n.s.	P<.01	P<.01	



from six muscles with 79, 68, and 70 measurements of cells, myofibrils, and mitochondria, respectively; ischemia data are from eight muscles with 92, 91, and 145 measurements of cells, myofibrils, and mitochondria, respectively; reperfusion data are from six muscles with 27, 26, and 29 measurements of cells, myofibrils, and mitochondria from live cells, and 27, 26, and 29 measurements of cells, myofibrils, and mitochondria from dead cells.

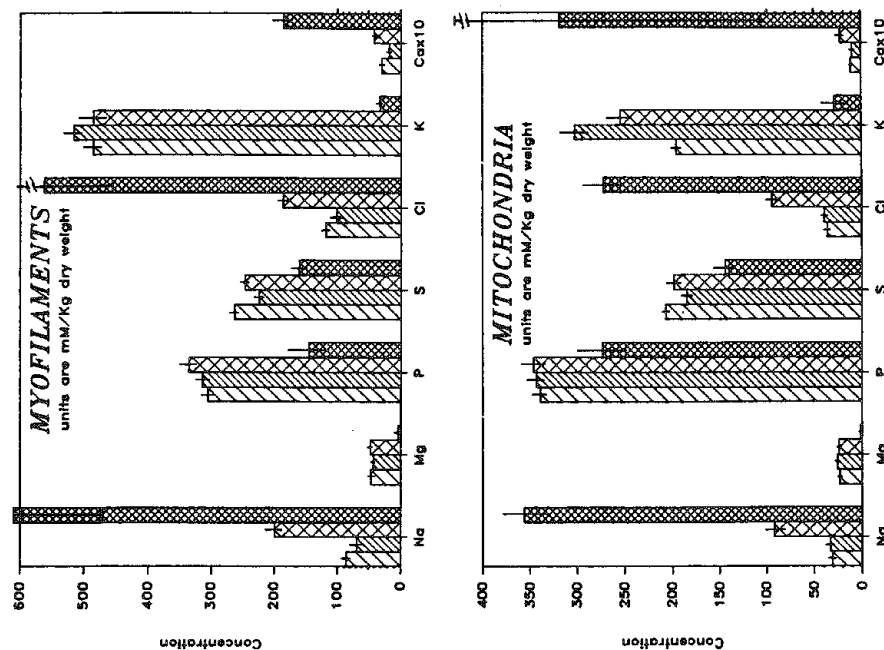


FIG. 1.--Mean elemental concentrations before, during, and after ischemia. Error bars indicate standard errors of mean. Control data are from four muscles with 56 measurements each of cells, myofibrils, and mitochondria, respectively; ischemia data are from six muscles with 92, 91, and 145 measurements of cells, myofibrils, and mitochondria, respectively; reperfusion data are from six muscles with 27, 26, and 29 measurements of cells, myofibrils, and mitochondria from live cells, and 27, 26, and 29 measurements of cells, myofibrils, and mitochondria from dead cells.

Ischemia markedly increases cellular [K]. Most of the increase is due to a 50% increase in [K] in the mitochondrial compartment. This increase is associated with a marked increase in mitochondrial hydration, presumably due to the inhibitory effects of hypoxia on ion transport by this structure.

Ischemia produces a different pattern of Ca shifts: myofibrillar [Ca] is decreased, but mitochondrial and cellular [Ca] are unchanged. The data in Table 1 suggest that a substantial fraction of cellular [Ca] is not attributable to myofibrils and mitochondria. Thus the "third" compartment, as defined above, has become significantly Ca loaded. The Ca-accumulating component of this compartment is probably sarcoplasmic reticulum (SR). The low myofibrillar [Ca] also shows that the increased resting muscle tension accompanying ischemia is not directly due to increased Ca levels.

The standard deviations for the ischemic muscles are nearly identical to the controls. Thus, with the possible exception of cellular Ca, ischemia causes no increase in cell-to-cell variation for the analyzed elements; i.e., the cells that are destined to live and those that are destined to die upon reperfusion have virtually identical electrolyte distributions.

After 5 min of reperfusion a marked dichotomy, both morphological and microchemical, becomes obvious.

The cells exhibit wide variations in damage, but two cell types can easily be distinguished. The more damaged cells have contraction bands (regions of condensed myofilaments), no sarcomeres, condensed nuclei, and mitochondria that are swollen and rarified. At no time are any dense, Ca-rich granules observed within the mitochondria. The less damaged group shows sarcomeric structure of varying density, no contraction bands, and mitochondria that are nearly normal in density and size. These changes are similar to those described by others using conventional preparations for TEM.⁴

These morphological differences correlate closely with the dead and live groups defined by EPMA. The contents of the "more damaged" cells indicate that they are in fact dead, i.e., that their sarcolemmas are so severely damaged that their electrolyte contents approach those of the ECF. In the live-reperfused group, most of the electrolyte shifts that develop after an hour of ischemia have at least partially reversed. In fact the [Na] and [Cl] in all compartments are twice control values, whereas the decreases in [K] are moderate. The overall cell [Ca] is not different from that in ischemia, but it is distributed differently (Table 1): the myofibrillar [Ca] has risen significantly, which suggests that the high rest tension at this time might be due to Ca overload. The increase in mitochondrial [Ca] indicates that mitochondria are playing a significant Ca buffering role, now that a Ca overload has developed. However, as was true with the controls, 90% of the cell Ca can be accounted for by the mitochondria and myofibrils. This suggests that, in spite of the Ca overload, the SR has released the Ca accumulated during ischemia.

Though much remains to be done, it is clear that EPMA offers unique information to elucidate an extremely complex pathophysiological problem.

References

1. R. D. Karp, J. C. Silcox, and A. V. Somlyo, "Cryoultramicrotomy: Evidence against melting and the use of a low temperature cement for specimen orientation," *J. of Microsc.* 125: 157-165, 1982.
2. J. McD. Tormey, "Improved methods for x-ray microanalysis of cardiac muscle," *Microbeam Analysis--1983*, 221-228.
3. J. McD. Tormey, "Accuracy and precision of biological x-ray microanalysis," *Microbeam Analysis--1984*, 272-276.
4. R. B. Jennings and C.E. Ganote, "Structural changes in myocardium during acute ischemia," *Circ. Res. Suppl.* III, 156-172, 1974.

REDISTRIBUTION OF SUBCELLULAR ELECTROLYTES ACCOMPANYING THE INCREASED MYOCARDIAL CONTRACTILITY PRODUCED BY LOW Na

E. S. Wheeler-Clark and J. McD. Tormey

Reducing the Na concentration in aqueous solutions bathing heart muscle is well known to produce positive inotropy (increased cardiac contractility).^{1,3} Although this inotropy is presumably mediated by Ca, the mechanisms by which low Na makes more Ca available to the myofibrils are unclear. Recent isotopic measurements suggest an increased association of Ca with sarcolemmal sites in response to reduced external [Na], which would thus presumably make more Ca available from extracellular sources.² Ca also appears to accumulate within the muscle cells, as evidenced by a substantial increase in ⁴⁵Ca contained in a slow washout component from heart muscle.³ However, isotope uptake and efflux measurements alone (whether of whole or fractionated cells) are inadequate to determine the exact subcellular sites involved in the uptake and transfer of Ca. Therefore we have turned to electron probe microanalysis to measure directly the elemental redistribution that accompanies the positive inotropic effects of low external [Na].

Methods

Papillary muscles were removed from the right ventricles of anesthetized rabbit hearts; they were then perfused at 28 C and electrically stimulated at 0.3 Hz while their force development was monitored. The oxygenated perfusing solution included 1 mM Ca, 5 mM K, 5% dextran, and HEPES buffer at pH 7.4. After an initial period, half the muscles were bathed either in a *control* solution that included 139 mM NaCl or in a *low-Na* solution that contained only 36 mM NaCl plus enough sucrose to maintain isosmolality. After 30 min in one of these solutions, the muscles were frozen against a liquid helium cooled block as described previously.⁴ Thin cryosections were cut at -120 C and then transferred in the frozen hydrated state into a JEOL 100CX microscope with the use of a Gatan cryotransfer stage. They were freeze-dried in the microscope at -120 to -90 C, and then analyzed at -120 by x-ray microanalytical methods described before.⁴

Results and Discussion

All subcellular compartments of heart muscles bathed in low Na solution show statistically significant decreases in [Na] and [Cl]. Compartments analyzed include cells (excluding nuclei), myofibrils, mitochondria, sarcolemmae (cell boundary region), transverse (T) tubules, and junctional sarcoplasmic reticulum (JSR). Table 1, by way of example, summarizes the composition of myofibrils under control and low-Na conditions.

TABLE 1.--Elemental analysis of myofibrils in control vs low Na⁺ muscles. Values are mean ±S.E., expressed in mmol/kg dry wt. Asterisk denotes values significantly different (p < 0.001) from control muscles for this element by t-test.

	Na	Mg	P	S	Cl	K	Ca
Control (N=16)	82.2 ±8.6	55.2 ±4.6	288.8 ±17.8	300.8 ±18.8	164.7 ±9.3	534.1 ±43.4	1.0 ±1.0
Low Na (N=23)	30.9* ±4.0	54.4 ±3.4	285.3 ±12.4	341.6 ±14.2	70.7* ±4.5	476.6 ±20.1	2.7 ±0.7

The authors are at the Department of Physiology, Center for Health Sciences, UCLA, Los Angeles, CA 90024. ESW is recipient of an Advanced Fellowship from the American Heart Association Greater Los Angeles Affiliate. The work has been supported in part by Grant R01 HL 31249 from the National Heart Lung and Blood Institute and by grants from the American Heart Association and the Muscular Dystrophy Association.

Alterations in Ca compartmentalization are presented in Fig. 1. Low Na clearly causes [Ca] to double in both the sarcolemmal region and the JSR. In spite of the relatively small number of measurements, these differences are highly significant ($p < 0.01$). Increased [Ca] is also associated with T-tubule sarcolemmae and with myofibrils, although the amount of data collected to date is insufficient to determine statistical significance. Mitochondria, by contrast, show no change. Other compartments (not shown), including cell, tissue, and extracellular fluid, also show no significant changes in Ca.

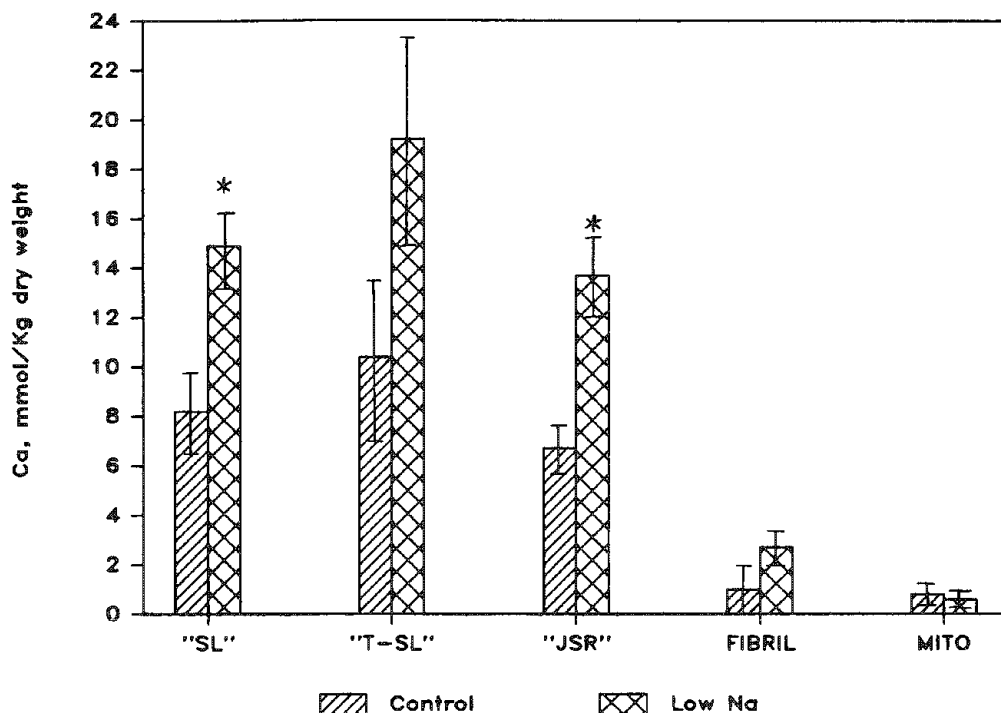


FIG. 1--Ca concentrations (\pm S.E.) in control vs low Na⁺ muscles for sarcolemmal boundary regions ("SL"), T-tubule boundaries ("T-SL"), junctional sarco-plasmic reticulum (JSR), myofibrils (FIBRIL), and mitochondria (MITO). N ranged from 8-23. Asterisk denotes values significantly different from controls ($p < 0.01$) by t-test.

The doubling of Ca associated with the sarcolemma is consistent with the interpretation of isotopic uptake studies on isolated cardiac cells.² Our data also help define the previously unknown location(s) of the slowly exchanging Ca pool defined by ⁴⁵Ca washout studies.³ At least part of this pool involves increased accumulation of Ca in the JSR. The mitochondria are definitely not involved. On the other hand, a second, major component may be associated with the myofibrils themselves; more data are required to determine whether the observed increase is statistically significant.

Caution should be observed in interpreting Fig. 1. Relatively large values of [Ca] in a particular compartment do not necessarily indicate large aqueous concentrations, because microanalysis yields concentrations in mmol/kg *dry* weight, and because hydration of various compartments varies markedly. For example, [Ca] in extracellular fluid averages 19.1 mmol/kg, which corresponds to only 1 mM/kg wet weight, because only about 5% of the wet weight of this compartment consists of dry solids. Thus the concentrations measured in highly hydrated regions cannot be simply compared with those from much less highly hydrated regions such as JSR or myofibrils. However, unless a particular experimental condition produces marked hydration changes, the differences in [Ca] measured in a particular compartment have a straightforward interpretation.

Also, measurements of the sarcolemmal boundary region unavoidably include x-ray contributions from adjacent regions. To measure this region, long, narrow rasters (ca 22 nm wide) are centered over the sarcolemmal boundaries (visualized by abrupt density changes) along the cell edge. The resulting spectra are compared with spectra obtained within 75 nm on either side of the boundary. Given such factors as the distribution of electrons within the probe and section thickness, it is inevitable that x rays will originate from adjacent regions. Therefore, accurate quantitation of such regions is difficult at best. In spite of this difficulty, our data demonstrate that [Ca] in the

sarcolemmal region has approximately doubled. Furthermore, this increase cannot be correlated with changes in [Ca] in the bulk phases of the immediately adjacent regions.

Our measurements of very small subcellular structures such as JSR and sarcolemmal regions are near the limit of what is currently achievable with x-ray microanalysis of biological specimens. It is therefore encouraging to be able to define significant changes of [Ca] in these small but physiologically dynamic regions of heart cells.

References

1. J. H. Tillisch et al., "Transient and steady-state effects of sodium and calcium on myocardial contractile response," *J. Mol. Cell. Cardiol.* 11: 137-148, 1979.
2. G. A. Langer and L. M. Nudd, "Calcium compartmentation in cardiac tissue culture: The effects of extracellular sodium depletion," *J. Mol. Cell. Cardiol.* 16: 1047-1057, 1984.
3. M. Fintel et al., "Effects of low sodium perfusion on cardiac caffeine sensitivity and calcium uptake," *J. Mol. Cell. Cardiol.* 16: 1037-1045, 1984.
4. J. McD. Tormey, "Improved methods for x-ray microanalysis of cardiac muscle," *Microbeam Analysis--1983*, 221-228.

CRYOSECTIONING AND X-RAY MICROANALYSIS OF CULTURED MYOCYTES FOR STUDIES OF CELL INJURY

H. K. Hagler and L. M. Buja

The neonatal rat cardiac myocyte in culture is being used as a model to study a variety of cell injury mechanisms. For this study the metabolic inhibitor, iodoacetic acid, is introduced into the culture medium and cells are harvested at various time periods after introduction of the inhibitor. Any cell injury results in a heterogeneous population of cells, which makes it advantageous to be able to make measurements on individual cells. The rapid freezing of the cells using liquid nitrogen-cooled copper pliers provides a means of preserving the cells in their in vitro state. The cells are then transferred to a Dupont Sorvall MT 50000 and FS 1000 cryoultramicrotome for thin sectioning at a nominal thickness of 120 nm. The hydrated thin sections are then transferred to the electron microscope in a Gatan Model 626 cryotransfer stage and freeze dried in the microscope at -80 C prior to x-ray microanalysis.^{1,2}

One of the difficulties with the heterogeneous state of the cells is how to analyze the x-ray data to show not only changes occurring in the individual cells, but changes in the total population of myocytes. Toward this end we are collecting x-ray spectra from three different locations (nucleus, cytoplasm, and mitochondria) and making three measurements at each site in each cell. Data were collected from each time point of injury until measurements from 10 cells were accumulated. An ANOVA was performed on all spectra to show shifts of the elements measured as a function of time exposure. An additional series of measures was performed based on classifying cells as normal or abnormal. For each cell, the three measurements were averaged to obtain average values for nucleus, cytoplasm, and mitochondria of each cell. For this work an abnormal elemental concentration was defined as an elemental concentration greater than two standard deviations from the control measurements in the direction of the expected change with cell injury. Table 1 shows data from a typical ANOVA on all spectra collected from populations of cells; Table 2 presents data for cells with normal and abnormal elemental concentrations based on the criteria defined above.

The use of cryofixation and cryosectioning insure the preservation of diffusable elements in the natural location and provide sufficient high resolution morphology to be able to identify individual cells and subcellular locations for x-ray microanalysis. The use of the statistical measurements provides a better approach to identifying changes in the population of injured cells and a better way to correlate elemental changes and structural changes with other parameters such as biochemical measurements that cannot be made on a cell-by-cell basis. Thus, these techniques provide insight into the heterogeneity of injury occurring in populations of cultured myocytes.

References

1. H. K. Hagler and L. M. Buja, "New techniques for the preparation of thin freeze dried cryosections for x-ray microanalysis," in J. P. Revel et al., Ed., *The Science of Biological Specimen Preparation for Microscopy and Microanalysis*, AMF O'Hare, Ill.: SEM Inc., 1984, 161-166.
2. H. K. Hagler, "Cryotransfer of ultrathin cryosections for x-ray microanalysis," *Microbeam Analysis--1984*, 290.

The authors are at the Department of Pathology, University of Texas Health Science Center at Dallas, 5323 Harry Hines, Dallas, TX 75235. (Supported in part by the National Institutes of Health Ischemic Heart Disease Specialized Center of Research, Grant HL17669.)

TABLE 1.--Elemental concentrations in cytoplasm of control and iodoacetate treated cardiac myocytes.

GROUP	Na	Mg	Cl	K	Ca
CONTROL (n=27)	16.4 ^A ± 21.8	9.7 ^A ± 6.3	62.5 ^A ± 18.4	451.2 ^A ± 196.8	-.2 ^A ± 4.5
1 HR. IAA (n=36)	89.8 ^B ± 132.0	-.4 ^B ± 12.4	100.8 ^B ± 66.1	418.5 ^A ± 254.1	5.9 ^A ± 16.3
1.5 HR. IAA (n=30)	234.2 ^C ± 102.6	-18.7 ^C ± 10.5	79.3 ^{AB} ± 44.7	71.3 ^B ± 54.5	12.0 ^A ± 11.9
2 HR. IAA (n=38)	263.0 ^C ± 166.1	-22.3 ^C ± 20.2	149.0 ^C ± 112.0	127.8 ^B ± 134.3	25.9 ^B ± 48.2

Data are expressed as mean values (mMoles/kg dry weight) ± standard deviation.
n=number of spectra collected.

In Tables 1 and 2, superscripts indicate results of analysis of variance tests comparing values of control and IAA groups for each element. For each vertical column, values with the same letter superscript are not significantly different and those with different superscripts are significantly different from each other.

TABLE 2.--Elemental concentrations in normal and abnormal cells and numbers of abnormal cells from control and iodoacetate cytoplasm of treated myocyte cultures.

	SODIUM			MAGNESIUM			CHLORINE			POTASSIUM			CALCIUM		
	Norm Cells	Abnor Cells	No.Cells Abno/tot	Norm Cells	Abnor Cells	No.Cells Abno/tot	Norm Cells	Abnor Cells	No.Cells Abno/tot	Norm Cells	Abnor Cells	No.Cells Abno/tot	Norm Cells	Abnor Cells	No.Cells Abno/tot
CONTROL	16.4 ±14.6	---	0/9 ^A	9.7 ±4.4	---	0/9 ^A	62.5 ±13.4	---	0/9 ^A	451.2 ±194.9	---	0/9 ^A	-.2 ±2.8	---	0/9 ^A
1 HR. IAA	17.9 ±11.3	161.7 ±139.0	6/12 ^B	5.6 ±3.3	-6.3 ±10.9	6/12 ^B	57.5 ±23.5	144.1 ± 32.8	6/12 ^B	451.5 ±187.5	55.7	1/12 ^B	1.2 ±2.8	20.1 ±20.5	3/12 ^B
1.5 HR. IAA	---	234.2 ± 88.3	10/10 ^{BC}	---	-18.7 ± 7.7	10/10 ^{BC}	62.8 ±12.5	117.9 ± 28.7	3/10 ^{AB}	95.8 ±33.7	34.5 ±13.5	4/10 ^B	4.6 ± .8	13.9 ± 9.5	8/10 ^{BC}
2 HR. IAA	---	253.5 ±149.5	12/12 ^C	---	-21.3 ± 18.4	12/12 ^{BC}	61.5 ±10.3	173.1 ±100.4	8/12 ^B	210.0 ±133.2	26.2 ± 3.4	5/12 ^B	1.5 ±2.9	39.4 ±33.7	8/12 ^{BC}

Data are expressed as mean values (mMoles/kg dry weight) ± standard deviation.

MATERIAL PROPERTIES OF BIOLOGICAL TISSUE: IMPLICATIONS FOR CRYOSECTIONING

A. J. Saubermann and R. V. Heyman

Cryosectioning is an important preparative step for x-ray microanalysis of biological specimens. Yet, the process of cryosectioning is poorly understood. Little is known about the mechanical properties of frozen biological material, although such information is fundamental to cryosectioning since the physical properties of a material determine how it reacts to stress. Therefore, the purpose of these studies is to determine the effects of temperature on the stress/strain relationship of a nonbotanical biological tissue (rat liver).

Experimental

A device to determine compression as a function of load at low temperature was constructed (Fig. 1). This device consisted of two parallel load plates with connecting rods, a loading bolt, a load transducer, and a micrometer. The load plates were located in an insulated chamber cooled by cold N_2 gas. Cubes of rat liver ($\sim 3 \text{ mm}^3$) were prepared by cutting of the tissue with a special double, and parallel, bladed knife. The specimens were quickly frozen in melting freon and stored in liquid nitrogen. Cubes ($\sim 3 \text{ mm}^3$) of polycrystalline ice were also prepared by freezing of tap water in a small mold at -30°C . Loading curves used to correct for instrument compression were obtained at room temperature (22°C) and at -30°C , -60°C , and -90°C and were found to be identical. Loading occurred over sufficient time to allow sample relaxation to cease for each 2kg load increment from 1 to 42 kg. The results demonstrate that ductility decreased with decreasing temperature. Liver at -30°C and -60°C was compressible, but at -90°C liver fractured under compression at loads less than 10 kg, at a calculated stress of 11 MN/m^2 . The polycrystalline ice exhibited large creep as expected, which was a function of temperature. The ice samples fractured under compression at loads of 6 kg at -60°C and at 10 kg at -90°C . The ice samples did not fracture at -30°C .

Conclusion

These results demonstrate the importance of temperature in determining material properties of a tissue. It appears that the material properties of tissue are not determined by the properties of ice alone. For this discussion we are defining cryosectioning as the process of continuous chip formation from a frozen block of tissue. Our previous measurement of the force of cryosectioning allows calculation of the stress in cryosectioning (force/area)¹; if we assume that the load is distributed over a $1 \times 500 \mu\text{m}$ area on the knife edge, the stress ranged from 10 to 60 MN/m^2 . These values are in the range at which liver, at -90°C , fails by fracture during compression (11 MN/m^2). Material failure is known to occur in shear where shear stress is a function of Young's modulus; such shear stress is likely to be less than compressive stress. Therefore, we are led to the conclusion that if the temperature of the material (liver) is actually -90°C in the shear plane (assuming no heat input from the cutting work), failure would occur and the material could not be cryosectioned. Thus, these data suggest that cryosectioning rat liver at specimen temperatures below -90°C is not possible because of the material properties of that tissue. Those who report that they cryosection at colder temperatures are likely to do so by warming the shear zone through heat generated from the work of cutting and friction until a temperature is reached at which the material becomes ductile. At that point the work of sectioning would be decreased and the material would undergo plastic deformation under shear stress rather than fracturing. Plastic deformation in the shear plane favors continuous chip formation (de-

The authors are at the Department of Anesthesiology of the University of Texas Health Science Center and the Microprobe Center, Houston, TX 77225.

sired condition). These data show again that cryosectioning can be explained by application of conventional metal machining theory.

References

1. A. J. Saubermann et al., "Cutting work in thick section cryomicrotomy," *J. Microscop.* 111: 39-49, 1977.

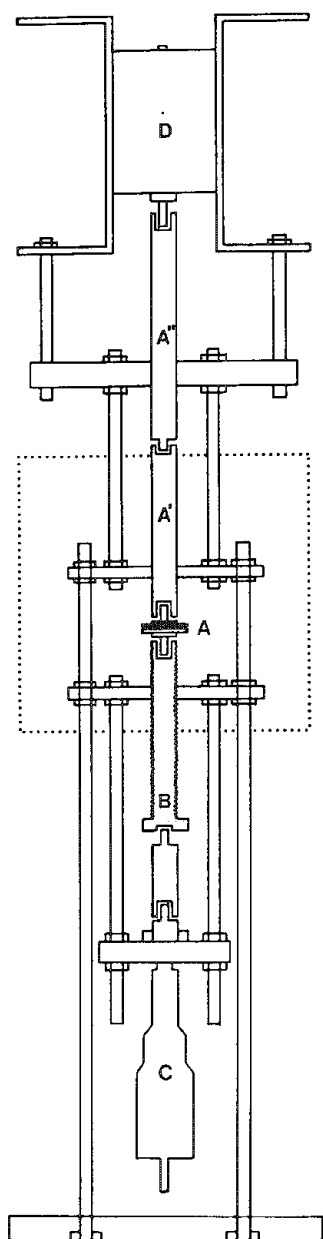


FIG. 1.--Compression device schematic. Dotted area represents cooled area. Note parallel load plates A with connecting rods A', A'', loading bolt B, micrometer C, and load transducer D.

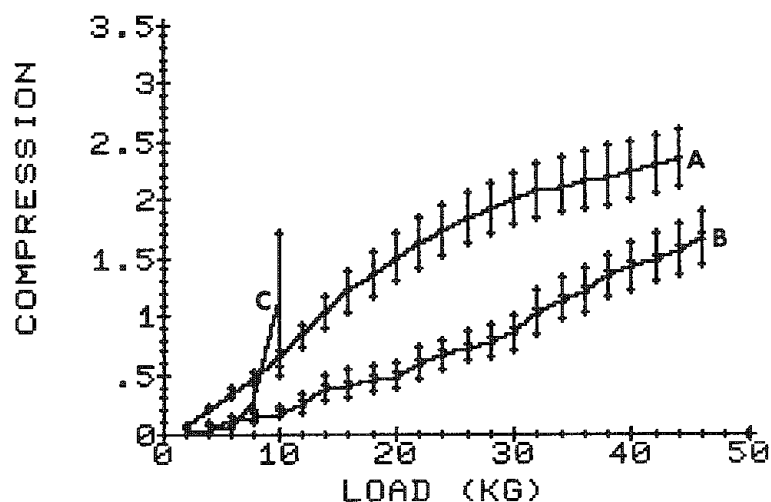


FIG. 2.--Compression (in mm) of 3mm^2 cubes of frozen rat liver as function of load at -30°C (A), -60°C (B), and 90°C (C). Values shown as means \pm SEM.

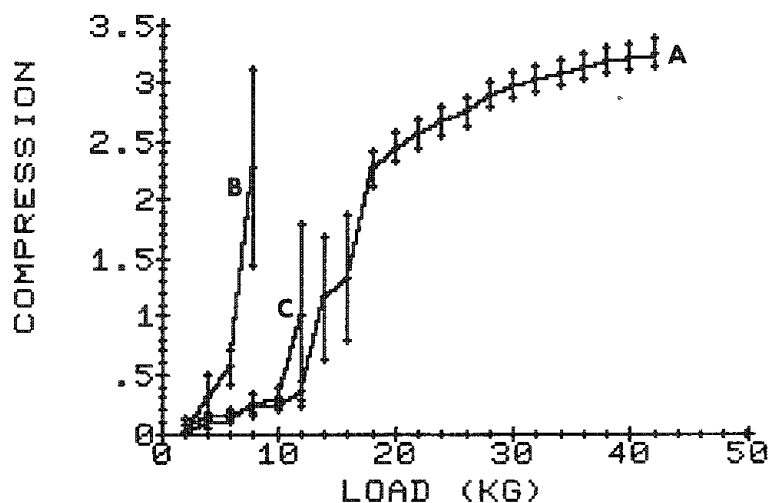


FIG. 3.--Compression (in mm) of 3mm^2 cubes of polycrystalline ice as function of load at -30°C (A), -60°C (B), and -90°C (C). Values shown as means \pm SEM.

A CRYOSTAGE FOR ULTRA-LOW TEMPERATURE OXYGEN PLASMA ASHING OF FROZEN TISSUE SAMPLES

J. T. Brenna, M. T. Bernius, and G. H. Morrison

Low-temperature oxygen plasma ashing (LTA) recently has been shown to be a useful technique for enhancing elemental sensitivities in the ion microscopical analysis of plastic embedded biological section.^{1,2} In this method, an oxygen plasma afterglow is slowly passed over the surface of the section and allowed to react with the organic molecules making up the matrix. These organic matrix elements (C, N, H) are gently converted into the gaseous products of combustion and are swept away with the stream. This process, under mild conditions, completely and efficiently removes the organic matrix at relatively low temperatures (100 C) while preserving elemental morphology.

Conversion of biological specimens into a form compatible with high-vacuum systems used in elemental analysis is a topic which has received a great deal of attention. The literature is replete with reports indicating that conventional methods involving aqueous fixatives cause elemental loss and relocation.³ Freeze-substitution methods improve the situation, but results vary depending on the specific sample and element. The only generally accepted method for sample preparation valid from tissue to tissue and element to element is fast freezing followed by cryosectioning (in the case of bulk tissue) and either direct analysis or freeze-drying followed by analysis. In order to extend the analytical advantages of LTA to frozen-hydrated samples, we have constructed a cryostage fitted to a commercial LTA apparatus for either sequential or simultaneous freeze-drying and ashing, i.e., complete matrix removal from cryo-samples at low temperatures (L²TA). This device will allow determination of the applicability of complete matrix removal for these types of samples.

Details of specific design consideration and construction of the stage have been reported elsewhere.⁴ Within one hour of initial start-up, the stage is at its operating temperature of -70 C. It maintains this temperature in the presence of the radiofrequency field (used to power the oxygen plasma) indefinitely.

Human squamous epithelial cells obtained from fresh cheek scrapes were used as a convenient model system for optimization of the instrumental parameters. The cells are mounted on smooth silicon wafers, fast frozen by plunging into nitrogen slush, and carefully transferred to the ashing chamber for treatment.

Appearance of the ash residue in reflected light and ion microscopy was used to assess morphological preservation. Our results indicate that satisfactory preservation of micro-anatomy and elemental integrity is achieved with careful choice of treatment parameters. These data indicate that simultaneous freeze-drying/ashing is potentially a powerful method for preparing frozen-hydrated samples for elemental analysis.

References

1. J. T. Brenna and G. H. Morrison, "Low temperature oxygen plasma ashing for elemental localization in biological soft tissue by ion microscopy," *Anal. Chem.* 56: 2791-2797, 1984.
2. J. T. Brenna and G. H. Morrison, "Low temperature ashing preconcentration for elemental localization in ion microscopy," in *Microbeam Analysis--1984*, 265-266.
3. M. A. Hayat, Ed., *Principles of Techniques of Electron Microscopy*, Baltimore: University Park, 1980, vol. 1, 2d ed.
4. M. T. Bernius, J. T. Brenna, and G. H. Morrison, "A temperature stage for ultra-low temperature oxygen plasma ashing (L²TA)," submitted to *Rev. Sci. Instr.*

The authors are at the Department of Chemistry, Cornell University, Ithaca, NY 14853-1301.

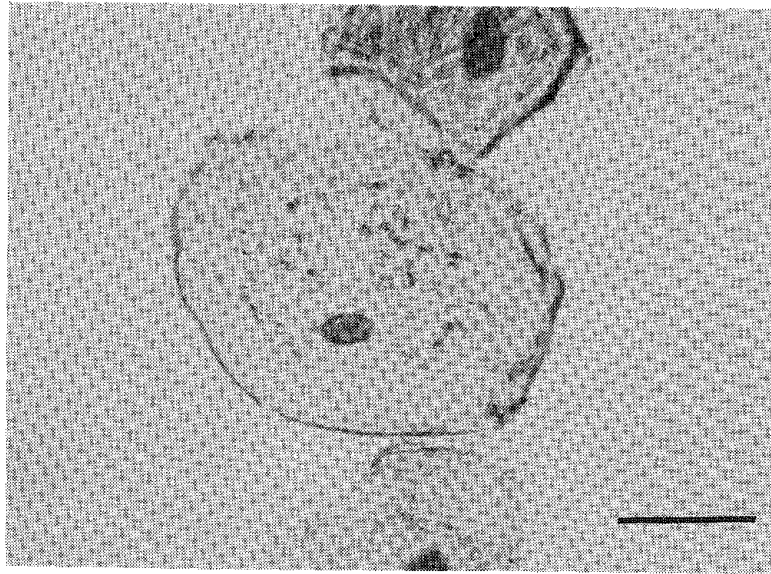


FIG. 1.--Transmitted-light micrograph of fresh human squamous epithelial cell obtained from cheek scrape. Cells is stained with toluidine blue. Prominent features include nucleus and granular cytoplasm.

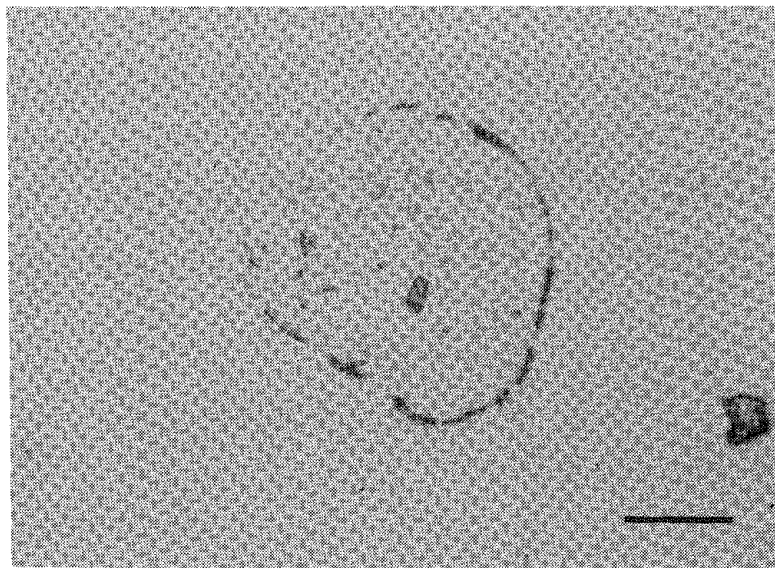


FIG. 2.--Reflected-light micrograph of L²TA-treated cell. Nucleus, cytoplasmic granules, and peripheral cell membrane remain intact after treatment. Bars are nominally 20 μ m long.

CORRELATIVE ION AND ELECTRON MICROSCOPY OF BIOLOGICAL SOFT TISSUE EMBEDDED IN LOW-TEMPERATURE RESINS

Subhash Chandra, G. H. Morrison, and Robert Chiovetti Jr.

The ion microscope, based on secondary ion mass spectrometry (SIMS), is a powerful tool for studying the elemental (isotopic) distribution in biological systems.^{1,2} The technique is capable of 3-D analysis and detecting all elements and isotopes from hydrogen through uranium with sensitivities generally in the parts-per-million range. The unique ion optics of the ion microscope allows direct microscopic imaging of ions in relation to tissue morphology with a spatial resolution of $\sim 0.5 \mu\text{m}$. Ion microscopy coupled with electron microscopy provides a potentially powerful combination for elemental microanalysis in biological systems. Histochemical information obtained by correlating tissue morphology with elemental distribution allows a better understanding of various processes in physiology and pathology. The highly diffusible nature of physiologically important elements and the hydrated matrix of soft biological tissue require cryotechniques for a reliable sample preparation before such studies can be undertaken.

The present study explores the potential of correlative ion and electron microscopy and investigates the feasibility of low-temperature embedment of soft biological tissue for ion microanalysis. Segments of smooth muscle from rabbit renal artery were used as the model tissue and Lowicryl K4M as the low temperature resin. The slam-frozen, lyophilized tissue was compared with conventionally fixed tissue for Na, K, and Mg distributions. The transmission and scanning electron microscopy complemented SIMS ion microanalysis.

Experimental

Approximately 1mm^2 pieces of smooth muscle from rabbit renal artery were slam-frozen on a polished copper bar cooled in liquid nitrogen and lyophilized as described previously.³ The lyophilization took approximately 4 days during which the temperature was raised from -190°C to -90°C . The tissue was then infiltrated in pure Lowicryl K4M starting at -20°C under vacuum according to a newly developed methodology.⁴ The Lowicryl was polymerized with 366nm UV at -20°C for 24 h. The final polymerization took place at room temperature for 72 h. The conventional fixation included tissue fixation at 4°C for 1 h in 1.5% formaldehyde/1.0% glutaraldehyde in 0.1M sodium cacodylate buffer at pH 7.2. The tissue was then washed several times in 10mM lysine HCl in the same buffer. The specimens were dehydrated in graded ethanol solutions and infiltrated in Lowicryl K4M. The Lowicryl was polymerized by the same procedure as described for the freeze-dried tissue. The thin ($\sim 100\text{nm}$) and thick ($\sim 0.5\mu\text{m}$) sections were cut dry and on distilled water using a Sorval-MT2B ultramicrotome. The thin sections were transferred to the copper grids for TEM analysis; the thick ones were mounted on polished silicon wafers for ion microanalysis.

An Hitachi 11-C electron microscope operated at 80 kV was used to evaluate the morphological preservation of these treatments.

A CAMECA IMS-3f ion microscope operated with a 8.0kV O_2^+ primary ion beam and monitoring positive secondary ions was used for the study. A primary beam of 300 nA ($100 \mu\text{m}$ diameter) was rastered over an area of $250 \times 250 \mu\text{m}$. The ion images were recorded on Kodak Tri-X ASA 400 film with a 35mm camera.

A JEOL JSM-35CF scanning electron microscope was used to complement SIMS analysis. The secondary electron images were recorded on Type 52 Polaroids.

Authors Chandra and Morrison are at the Department of Chemistry, Cornell University, Ithaca, NY 14853-1301; author Chiovetti is at the Department of Biology, University of New Mexico, Albuquerque, NM 87131. This work was supported by National Institutes of Health.

Results and Discussion

The transmission electron microscopy revealed good morphological preservation in conventional glutaraldehyde fixed and Lowicryl-embedded smooth muscle (Fig. 1). The nuclei, mitochondria, contractile filament, and extracellular spaces are well preserved and can be easily recognized. The frozen, lyophilized, and low temperature embedded tissue also shows a reasonably good morphological preservation (Fig. 2).

The distribution of Na, K, and Mg, and a comparison between treatments from sections cut on distilled water is shown in Fig. 3. The left column represents the ion images from conventional and the right column from frozen, lyophilized, and Lowicryl-embedded tissue. Ion microscopy, however, does not possess the resolving power of electron microscopy but a geometric-fit elemental distribution with cell morphology is revealed by these ion micrographs. Brightness indicates higher ion emission. It is clearly evident that the nuclei contain slightly higher intensities of Na and K than the surrounding cytoplasm. Such differences are intensified for Mg distribution in both treatments. It seems that the conventional sample preparation intensifies differences between the nuclei and the cytoplasm at least for Na and K distribution in this tissue. Dry sectioning of frozen, lyophilized, and Lowicryl-embedded tissue showed qualitative distributional differences from wet sectioning for Mg distribution alone (Fig. 3a). After dry sectioning, high intensities of Mg were not observed in nuclei. Although Na and K distributions remained the same, quantitative leaching of these elements cannot be ruled out on wet sectioning.

The scanning electron microscopy provides a geometric-fit recognition of the morphological details after ion microanalysis due to the preferential etching of plastic embedded tissue. The secondary electron micrograph can be matched perfectly with K, Na, and Mg distributions shown for the conventional treatment in Fig. 3 and facilitates the morphological recognition (Fig. 4 match arrows in Fig. 3 and Fig. 4).

It should be realized that these small differences observed in elemental distribution between treatments do not insure the authenticity of elemental distribution in freeze-fixed, lyophilized, and cold-temperature Lowicryl-embedded tissue. The comparisons have to be made with frozen-hydrated or frozen-freeze-dried cryosections for this purpose. Although higher intensities of potassium in nuclei are in agreement with previous observations on cryosections,⁵ a detailed study is needed to further these observations. The greatest advantage of cold-temperature-embedded tissue for elemental microscopy lies in the ease of sectioning. The planar section would be an advantage for the quantitative research in ion microscopy.

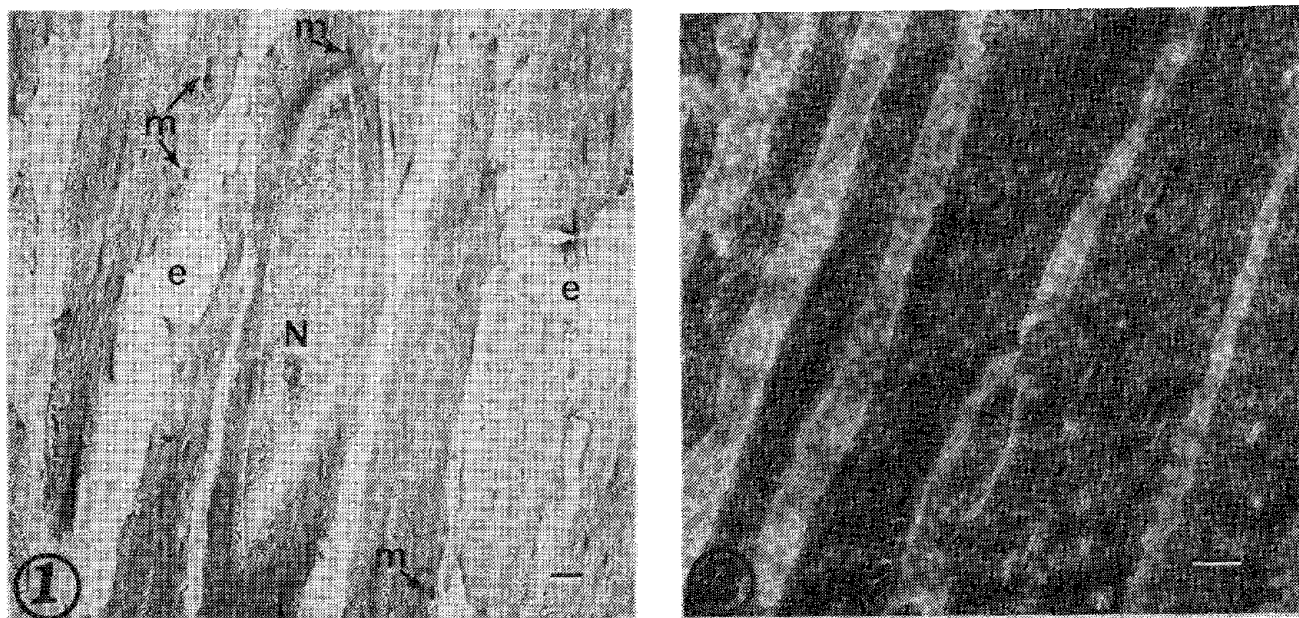


FIG. 1.--Smooth muscle cells of rabbit renal artery after glutaraldehyde fixation and Lowicryl K4M embedment. Cells are separated from one another by extracellular spaces (e). Within cell, mitochondria (m), nuclei (N), and contractile filament can be easily recognized. Bar = $1\ \mu\text{m} \times 42,00$. FIG. 2.--Smooth muscle cells of rabbit renal artery in frozen, lyophilized, and low-temperature embedded tissue. Cells show no evidence of gross morphological damage. Bar = $1\ \mu\text{m} \times 72,00$.

CONVENTIONAL

FROZEN, LYOPHILIZED

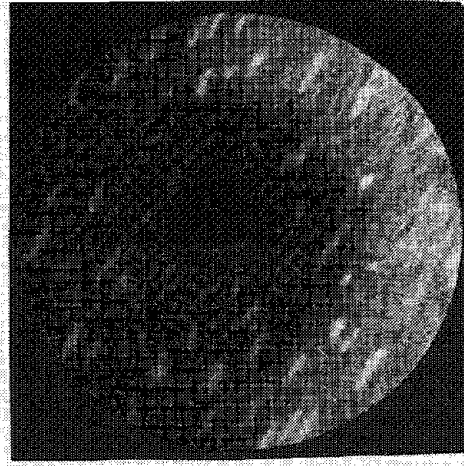
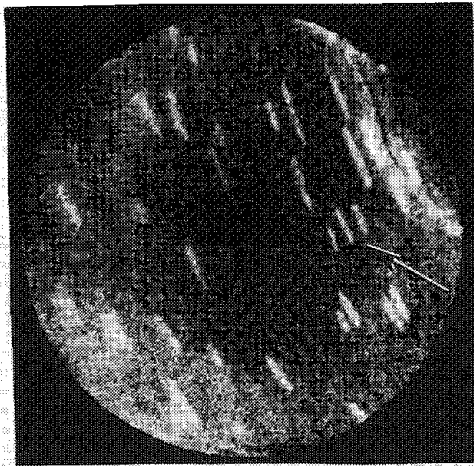
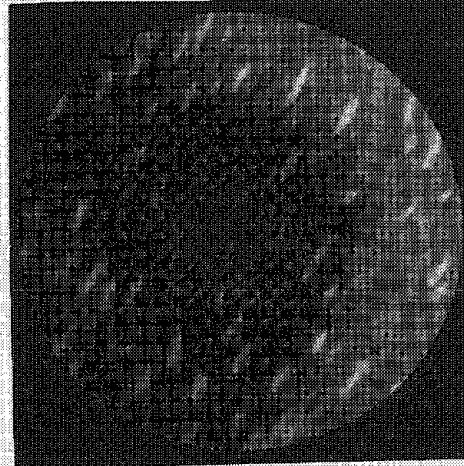
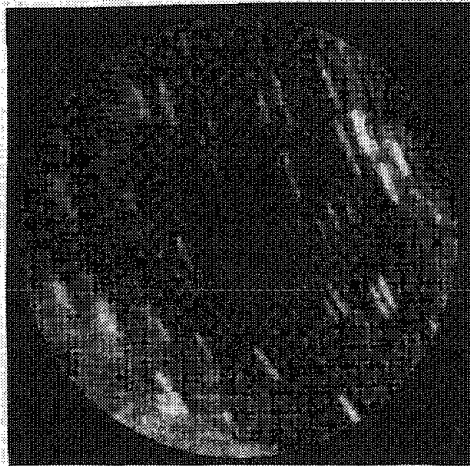
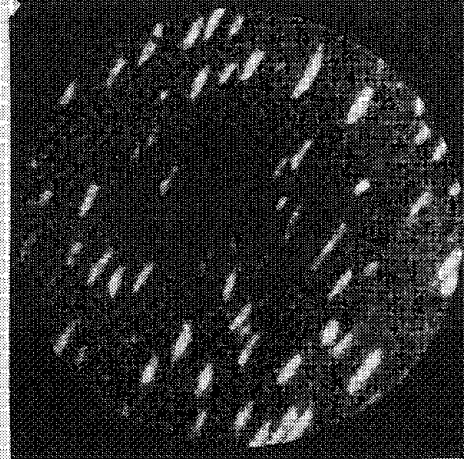
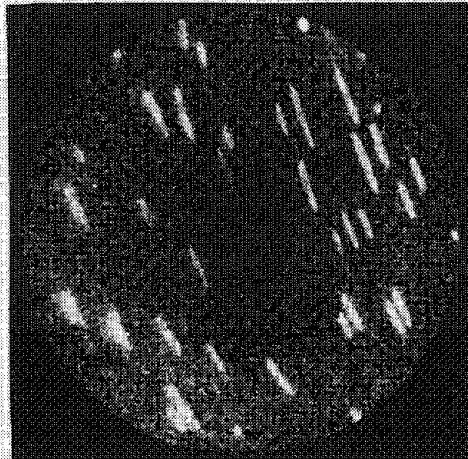
K**Na****Mg**

FIG. 3.--Distribution of K, Na, and Mg from conventionally prepared (left column) and frozen, lyophilized, and low-temperature embedded tissue (right column) as revealed by ion microscopy. Nuclei and muscle fiber can be easily recognized. Arrow in potassium image helps in matching morphological details with secondary electron micrograph of Fig. 4. Fields of view, 150 μ m.

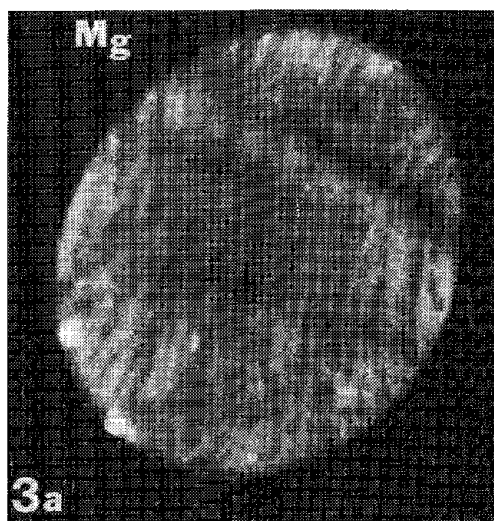


FIG. 3(a).--Distribution of Mg from dry-sectioned frozen, lyophilized, and Lowicryl embedded smooth muscle cells. Darker areas represent folds, a typical feature of dry-sectioned tissue. Field of view, 150 μ m.

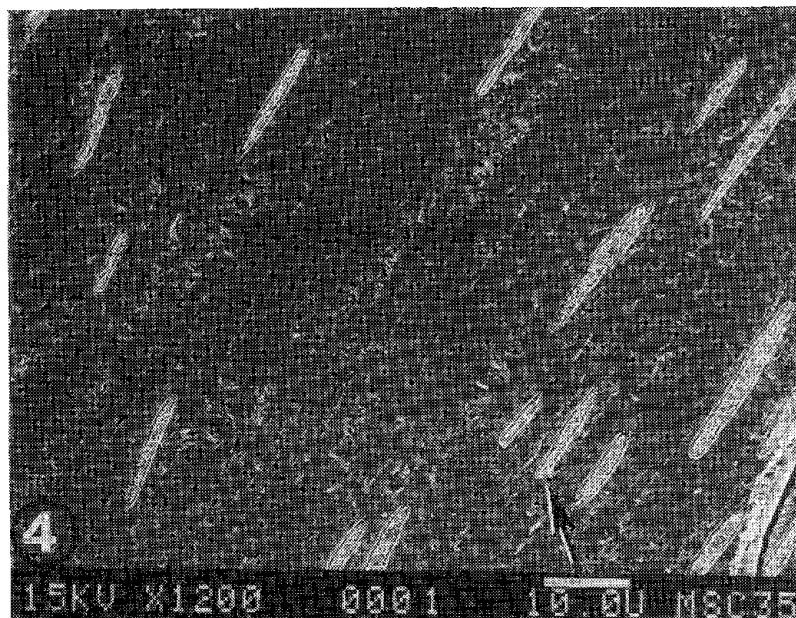


FIG. 4.--Secondary electron image taken after SIMS analysis from same region as shown in K, Na, and Mg conventional tissue ion images of Fig. 3. Perfect correlation of ion and electron microscopy is shown by arrows.

In summary, the present study demonstrates the potential of correlative ion and electron microscopy for elemental microanalysis in biological systems. The low-temperature embedment of frozen and lyophilized soft biological tissue shows good morphological preservation and differs slightly in elemental distribution from conventionally prepared tissue.

References

1. G. H. Morrison and G. Slodzian, "Ion microscopy," *Anal. Chem.* 47: 932A-943A, 1975.
2. A. R. Spurr, "Application of SIMS in biology and medicine," *Scanning* 3: 97-109, 1980.
3. L. J. McGuffee, L. Hurwitz, S. A. Little, and B. E. Skipper, "A ^{45}Ca autoradiographic and stereological study of freeze-dried smooth muscle of the guinea pig vas deferens," *J. Cell Biol.* 90: 201-210, 1981.
4. R. Chiovetti Jr. and L. J. McGuffee, "A new approach to low temperature embedding: Quick freezing, lyophilization, and direct infiltration in Lowicryl resins," *J. Cell Biol.* 99: 268A, 1984.
5. A. P. Somlyo, A. V. Somlyo, and H. Shuman, "Electron probe analysis of vascular smooth muscle: Composition of mitochondria, nuclei, and cytoplasm," *J. Cell Biol.* 81: 316-335, 1979.

A ROUTINE PROCEDURE FOR MONITORING SAMPLE MASS DURING MICROANALYSIS

M. C. Myers and R. R. Warner

Quantitative biological electron probe microanalysis of thin specimens by the continuum-normalization method proposed by Hall¹ requires an accurate determination of the sample mass, which is obtained by measurement of the continuum x rays generated from the sample. During analysis, sample mass loss or gain can result in an error in the continuum measurement.² A practical method of monitoring the sample mass of a thin specimen during energy-dispersive (EDS) x-ray analysis has been examined. With this technique, changes in sample mass as small as 10% may be detected. When analysis conditions cannot be defined to avoid sample mass changes, a corrected mass value may be calculated from the experimental data.

One of the more challenging aspects of the Hall method of biological quantitation is to obtain a continuum measurement from the sample only. Factors affecting the continuum measurement include contributions from the sample support film, peak-associated extraneous continuum, nonhomogeneous peakless continuum,³ and sample mass gain (contamination)⁴ or loss (etching)⁵ during analysis. Correction procedures and instrument modifications have been devised to minimize extraneous contributions from the support film and the microscope;^{1,6-11} sample contamination has been minimized with improved microscope vacuum systems. It is a controversial point, however, whether sample mass changes, particularly mass loss, can be entirely eliminated at electron doses that provide sufficient x-ray counting statistics.¹² In spite of our efforts to minimize sample mass change during analysis, we find problems can still occur. As a result, we routinely monitor the sample mass during each analysis.

Methods and Results

Samples were examined in a Hitachi H-500 TEM-STEM equipped with a Kevex EDS detector and a Tracor Northern 5500 EDS spectrometer. Our procedure for monitoring sample mass changes, described below, has progressed from a completely manual procedure through a variety of computer software aides. At present our procedure has been incorporated into the quantitative biological microanalysis software package 'BIOQ' available from Tracor Northern. Beam current and transmitted sample current were monitored with a Keithly digital electrometer. A Gatan Model 626 cryotransfer specimen holder with variable temperature control was employed to cool the specimen.

To investigate a wide range of irradiation doses, it was useful to analyze samples that were relatively homogeneous over large dimensions. Studies were done on 2 μ m-thick polycarbonate films (Makrofol, Siemens) coated with 100 nm of evaporated Al; on sections of Spurr's epoxy resin cut at nominal thicknesses of 100, 500, and 900 nm; and on uncoated, unsupported chlorinated rubber films. Inorganic salts, sulfur-containing protein crystals, and cryosections of biological tissue mounted on formvar and carbon-coated nickel slot grids were also examined. Samples were analyzed at 100 kV for 200 s at room temperatures ranging from ambient to -170 C. Beam currents of 0.05 or 1.0 nA were used to deliver a total accumulated electron dose ranging from 10^{-3} to 10^{+5} coulombs/cm². To study accurately changes in sample mass during analysis, it was essential to maintain a constant beam current.

We employ a graphical procedure to evaluate changes in specimen mass. Rather than monitoring the x-ray counting rate, as others have done,^{2,6,13} we examine the cumulative x-ray counts versus time.¹⁴ The advantage of this method is that statistical accuracy constantly improves as the accumulating counts are summed. The plotted data thus contain sufficient statistical precision to detect small changes in sample mass, even at relatively low excitation currents or relatively short acquisition times. At low excitation currents, a plot of the change in count rate versus time is statistically noisy and

The authors are at Miami Valley Laboratories, Procter & Gamble Co., Box 39175, Cincinnati, OH 45247. Dr. Ted Hall's gift of Makrofol polycarbonate films is gratefully acknowledged.

typically will not reflect small changes in the sample mass unless extremely long acquisition times are used or a number of separate analyses are combined. From the plot of integrated counts, extrapolation of the later (statistically more accurate) points toward the origin will result in a positive Y-intercept if mass loss has occurred, or a negative Y-intercept if the specimen has gained mass.

An example of this technique is shown in Fig. 1. Continuum counts were monitored from a 2 μ m-thick polycarbonate film irradiated at room temperature with a total dose of 2.5×10^4 coulombs/cm². The concave curvature of the line indicates that a nonlinear gain in sample mass occurred during analysis. By extrapolation of the initial slope, it was calculated that the sample mass increased by 11% during analysis. A corrected continuum value obtained from this extrapolation was equivalent to that determined with the same beam current but a 10^5 -fold lower electron dose during which no mass change was detected. Figure 2 is from the 2 μ m polycarbonate film analyzed at -170 C with a total accumulated dose of 40 coulombs/cm². The convex curvature of the continuum data and the positive Y-intercept of the extrapolated line indicate mass loss occurred during analysis; in this example, a mass loss of 9% was calculated. Again, excellent agreement was found between the corrected continuum value and the value obtained using a much lower electron dose (but identical current) during which no mass loss was detected.

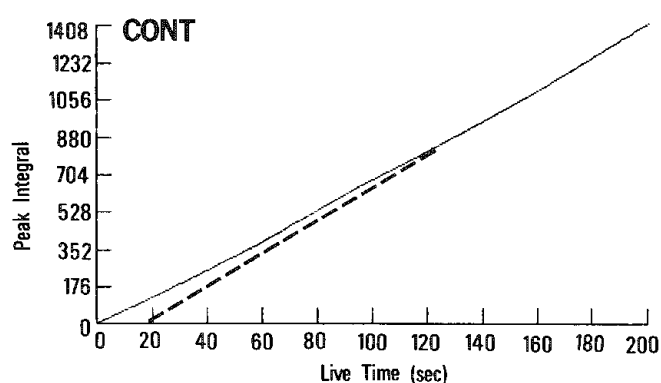


FIG. 1.--Continuum counts (4.00-6.25 keV) from 2 μ m-thick polycarbonate film plotted as accumulated counts vs time. Concave curvature of line and negative Y-intercept indicate mass gain occurred during analysis.

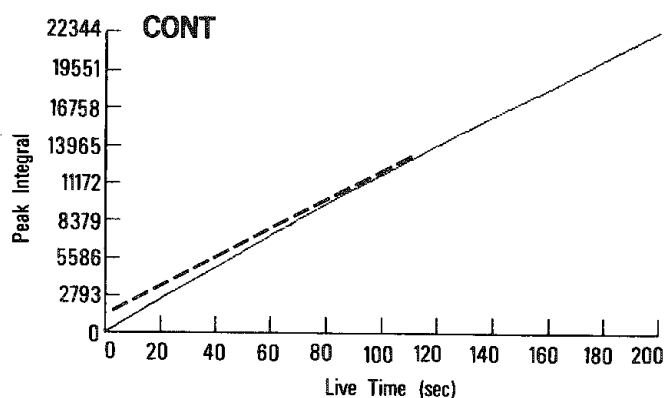


FIG. 2.--Plot of continuum counts (4.00-6.25 keV) from analysis of a 2 μ m polycarbonate film. Convex curvature of line and positive Y-intercept indicate mass loss occurred during analysis.

Limitations of the Technique

This method of data analysis is not foolproof. We have found two circumstances that could lead to misinterpretation of the results. If the sample mass changes linearly with time, it will not be detected in the plotted continuum data; a linear increase in sample mass would still result in a linear plot intercepting the origin. Also, when extremely beam-sensitive materials are analyzed or high probe current densities ($>10^3$ coulombs/cm²) are used, a large fraction of the sample mass can be lost in the first seconds of electron irradiation;¹⁵ this change in mass can go undetected in the plotted x-ray data. To avoid misinterpreting the plotted x-ray data, we also monitor the current transmitted through the specimen during analysis.¹⁵ The transmitted current provides an instantaneous relative measure of the specimen mass and is extremely sensitive to mass changes. By combining these two approaches, limitations in monitoring specimen mass by the graphical procedure can be avoided.

Conclusion

We use the mass-monitoring techniques: (1) initially, to select analytical conditions that minimize mass change during analysis; (2) to insure that contamination or etching does not occur in subsequent analyses; and (3) if mass changes are unavoidable (but small),

to approximate the sample mass by extrapolating the initial slope of the plotted continuum. The graphical technique must be used with some caution, whereas monitoring both the accumulated x-ray counts and the transmitted current provides a very reliable method for assessing sample mass change during analysis. The graphical technique can also be used to monitor sample element content.

References

1. T. A. Hall, "The microprobe assay of chemical elements," in G. Oster, Ed., *Physical Techniques in Biochemical Research*, New York: Academic Press, 1971, 157.
2. T. A. Hall and B. L. Gupta, "Measurement of mass loss in biological specimens under an electron microbeam," in T. Hall, P. Echlin, and R. Kaufmann, Eds., *Microprobe Analysis as Applied to Cells and Tissues*, New York: Academic Press, 1974, 147-158.
3. R. R. Warner, M. C. Myers, and D. A. Taylor, "Inaccuracies with the Hall technique due to continuum variation in the analytical microscope," *J. Microscopy*, in press.
4. J. J. Hren, "Contamination and etching," in J. J. Hren, J. I. Goldstein, and D. C. Joy, Eds., *Introduction to Analytical Electron Microscopy*, New York: Plenum Press, 1979, 481-505.
5. R. M. Glaeser, "Radiation damage with biological specimens and organic materials," *ibid.*, 423-426.
6. Henry Schuman, A. V. Somlyo, and A. P. Somlyo, "Quantitative electron probe analysis of biological thin sections: Methods and validity," *Ultramicroscopy* 1: 317, 1976.
7. T. A. Hall, "Problems of the continuum-normalization method for the quantitative analysis of sections of soft tissue," in C. P. Lechene and R. R. Warner, Eds., *Microbeam Analysis in Biology*, New York: Academic Press, 1979, 185-208.
8. W. A. P. Nicholson et al., "Optimizing thin film x-ray spectra for quantitative analysis," *J. Microscopy* 125: 25, 1982.
9. L. F. Allard and D. F. Blake, "The practice of modifying an analytical electron microscope to produce clean x-ray spectra," *Microprobe--1982*, 8-20.
10. J. Bentley et al., "Optimization of an analytical electron microscope for x-ray microanalysis: Instrumental problems," *SEM/1979 II*, 581-594.
11. N. J. Zaluzec, "Quantitative x-ray microanalysis: Instrumental considerations and applications to materials science," in J. J. Hren, J. I. Goldstein, and D. C. Joy, Eds., *Introduction to Analytical Electron Microscopy*, New York: Plenum Press, 1979, 121-167.
12. T. A. Hall, "EDS quantitation and application to biology," *ibid.*, 169-197.
13. J. G. Hecker and T. E. Hutchinson, "Measurement of mass loss during microanalysis: Methods and preliminary results," in T. E. Hutchinson and A. P. Somlyo, Eds., *Microprobe Analysis of Biological Systems*, New York: Academic Press, 1981, 83-100.
14. M. C. Myers, Janet Van, and R. R. Warner, "Ultrastructural distribution of sulfur in human hair," *Microbeam Analysis--1981*, 210-212.
15. B. P. Halloran and R. G. Kirk, "Quantitative electron probe microanalysis of ultrathin biological sections," in C. P. Lechene and R. R. Warner, Eds., *Microbeam Analysis in Biology*, New York: Academic Press, 1979, 571-589.

5 Computer-assisted Microanalysis

MEASUREMENT OF EDGE-INTERSECTING FEATURES IN SEM IMAGES

John C. Russ and T. M. Hare

The application of stereometric methods to images from the electron microscope is a growing field, but one in which some new practical limitations must be faced. One of them occurs when one is trying to determine the size distribution of features, either particles on a substrate or a phase within a matrix. Automatic computer-based systems can discriminate the features of interest based on the brightness, typically in the backscattered electron image, and sometimes hole-filling operations are needed to correct for contrast changes on rounded particles, or smoothing algorithms may be needed to reduce noise in the image,¹ but after these initial operations the image appears to be ready for measurement and counting just as an image from a conventional light microscope.²

One problem that remains, however, is dealing properly with distributions of features, some of which intersect the edge of the image frame (typically a square or rectangle). Simple counting operations (to determine, for instance, the number of particles or grains per square millimeter) usually count 1 for each discrete feature and 1/2 for each feature that touches any edge. However, when the size of features is required (for instance to obtain a histogram of number vs size), it is not possible to determine the size of any feature that touches an edge.

One approach that has been used for some time with light microscope images is to introduce a "guard frame" around the central, or active, measurement region. Ideally, this can be described as having an active measurement frame that covers the upper left quarter of the image, with the remaining three quarters constituting the guard frame. Any feature that intersects the upper or left edge of the image is ignored entirely, and features that extend from the measurement region into the guard area, but do not intersect the far image edge, can be measured entirely. This procedure allows features as large as could fit into the active region to be measured, and delivers statistically correct values for both the number and size of features. Of course, the size data (area, perimeter, length, breadth, etc.) can then be used further to derive feature-specific parameters of further interest, such as volume, surface area, and so on.

For SEM images this method is not often practical, because the image resolution is limited by the backscattered electron image to about 1 μm , and at a magnification low enough so that large features do not exceed the size of the measurement area, small features may be undefined pinpoints. Furthermore, it is desirable to use all of the image area for measurement as this means that four times as much information is available. It is often essential to collect information at several different magnifications, and then combine the data in proportion to the amount of image area covered at each magnification to produce an overall size distribution.

But if the measured size data are obtained from the entire image, it is still necessary to reject features that intersect an edge, and cannot be measured. For features that are all of the same size, one must simply correct the reference area (the amount of sample covered by the measurements), by multiplying the area of the image by the ratio of the sum of all measured feature areas to the total area of all detected features (including ones that touch edges). If the features are all of the same shape (e.g., circles), but of varying sizes, it is possible to calculate a series of correction factors that adjust the total for each bin in the size distribution histogram by the probability that randomly located features of that size will intersect the edge of the image. For the most important case of real features, which are irregular in shape and may be preferentially oriented, this calculation is not possible.

The authors are at the School of Engineering, North Carolina State University, Raleigh, NC 27695.

We present here an alternate method³ which adds very little computational overhead to the measurement process, and yields correct size distributions for all features which can be measured within the size of the image. The method measures and counts each feature which lies within the image (without intersecting any edge). But instead of counting each feature as 1 in the histogram bin that corresponds to its size (area, length, equivalent circular diameter, or any other measure of size), an adjusted count is computed and used instead. The width of the image in the X- and Y-directions (W_X and W_Y) and the Feret's diameters of each feature (F_X and F_Y) are used. The Feret's diameters (also called the shadow length or projected length) are very easy to determine: they are simply the difference between the extreme values of X and Y coordinates around the periphery of the feature.

The adjusted count is then $W_X W_Y / [(W_X - F_X)(W_Y - F_Y)]$, which is a value greater than 1. It compensates for the fact that very large features are more likely to intersect an edge of the image and be rejected from measurement, than are small ones. The adjusted count can also be used to weight parameters such as area that may be summed in a distribution.

Figure 1 shows SEM images of particles (glass fragments), with varying shapes and sizes. Histograms of number of features vs size (using the equivalent spherical diameter, arbitrarily divided into 20 logarithmic size classes from 0.015 to 0.58 μm) were accumulated from a series of images covering over 100 μm^2 on this sample, with and without the correction. The results depend on the magnification used, as shown in Fig. 2. The measured data (bars) and adjusted values (lines) are essentially identical for the smaller size particles which predominate (and are not likely to intersect an edge). But for larger sizes, the bars understate the number of particles, and at 5000 \times (where each image covers one-quarter as much area), more large features touch edges and are rejected. At higher magnifications, smaller features would be measurable but the drop in count for large ones would occur sooner.

This difference is more dramatic when the volume (estimated as the volume of a prolate ellipsoid of revolution with length and breadth given by the maximum and minimum projected diameters sampled in 32 directions) is plotted against size (Fig. 3). Here the small particles, though numerous, contribute very little and the large ones predominate so that the differences between the measurements at the two magnifications are evident. The corrected curves agree closely considering the limited statistics (there are only 22 measured features at 2500 \times in the largest five size classes, and only 1 in the single largest class).

Figure 4 shows the cumulative volume plot, which illustrates perhaps most clearly the loss of information due to edge-touching large features at different magnifications, and the effect of the correction. At 5000 \times , more than half of the total volume of fragments would be missed without the correction.

For grain size measurements, the same phenomenon is obtained. Figure 5 shows a diagram of grain boundaries, from a synthesized (Johnson-Mehl) microstructure. Figures 6 and 7 illustrate the change in the measured distribution of grain sizes when the adjusted count is applied. The size classes are linear, using the square root of grain area. Without the correction, increasing the image magnification cuts off the larger features and alters the shape of the distribution. With the correction, the curves agree quite closely (the statistical scatter present reflects the fact that each set of data come from different random sections through the microstructure). Note that the curves for the highest magnification ($\times 6$ and $\times 8$) cut off at the largest sizes because these grains are actually larger than the image size at those magnifications, yet the balance of the distribution is essentially correct.

When the adjusted counts are used to weight the individual grain areas, the effects are also dramatic. Figures 8 and 9 show plots of cumulative area vs size class for the as-measured and adjusted data. The as-measured curves are different for each magnification; the adjusted curves agree closely. The curves for the highest magnification deviate at large sizes where no features can be measured, but lie along the actual curve up to that point. Since the total adjusted area of features and the total image area are known, the difference represents the unmeasurable large features, and these can be determined from supplemental measurements at lower magnifications.

In conclusion, the use of an adjusted count for each measured feature allows accurate size distributions to be obtained for images in which some features intersect the image edge, without requiring the use of a guard frame to reduce the actual measurement area. The method is applicable to any shape, distribution, or orientation of features, and to nonsquare images. It provides an estimate of the fraction of the size distribution which has been missed in the case where there are features too large for measurement at the current magnifi-

cation, and allows data obtained at different magnifications to be combined in proportion to the image area examined. Although particularly suited to the needs of SEM images, and easily implemented by the small computer-based image measurement systems used with them, it is also recommended for light microscope systems because of its accuracy and simplicity.

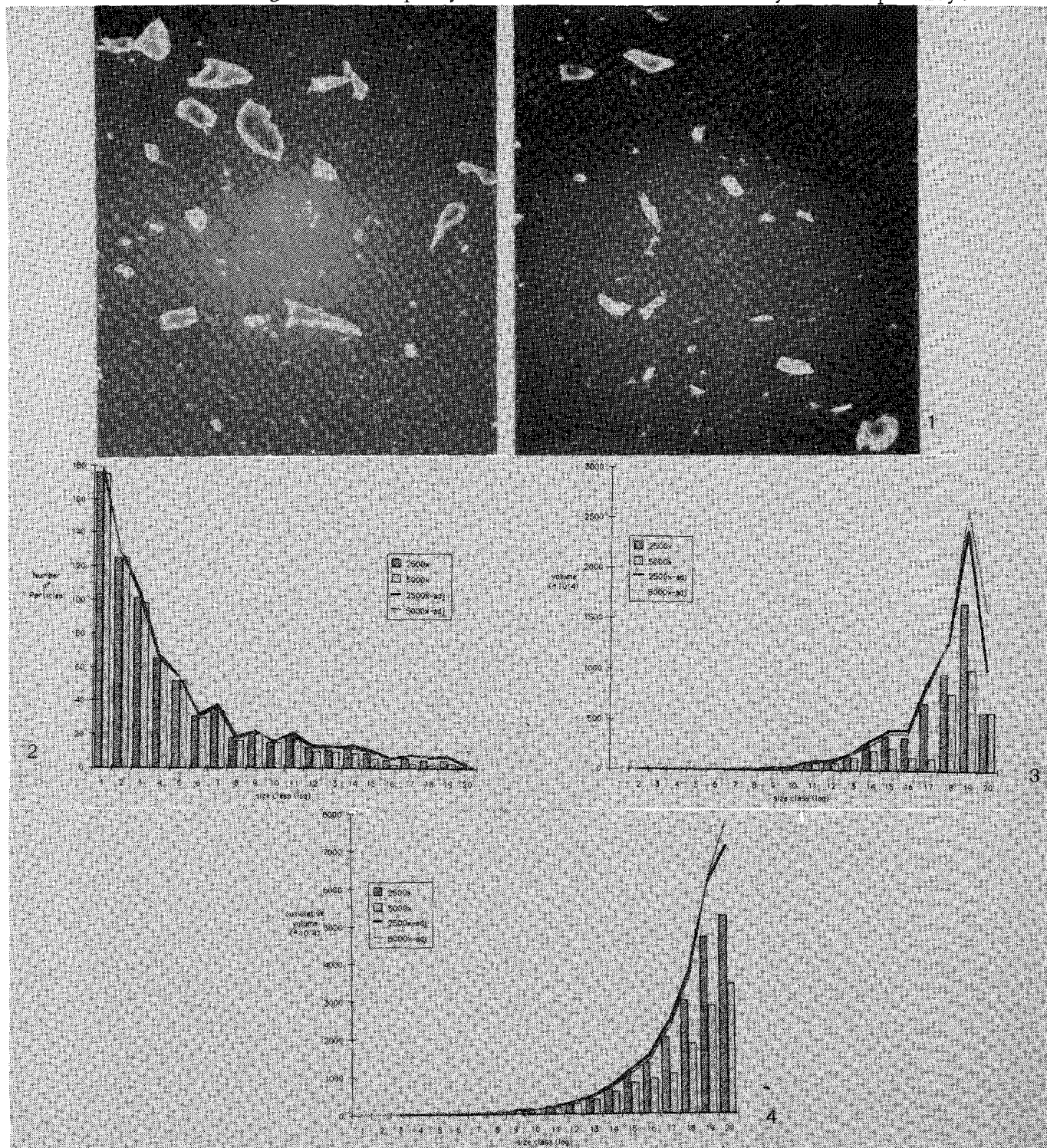


FIG. 1.--SEM images of glass fragments (original magnification 200 \times). FIG. 2.--Size-distribution plot for number of particles. Size classes are logarithmic, in 20% steps, from 0.015 to 0.58 μ m equivalent spherical diameter. FIG. 3.--Size-distribution plot for summed particle volumes in each size classes (classes as in Fig. 2.). FIG. 4.--Cumulative volume plot from Fig. 3.

References

1. J. C. Russ and J. C. Russ, "Image processing in a general purpose microcomputer," *J. of Microscopy* 135: 89-102, 1984.
2. J. C. Russ and W. D. Stewart, "Quantitative image measurement using a microcomputer system," *American Laboratory* 15(No. 12): 70-75, Dec. 1983.
3. T. M. Hare and J. C. Russ, "Accurate feature size distributions without a guard frame," *J. Microscopy* (in press).

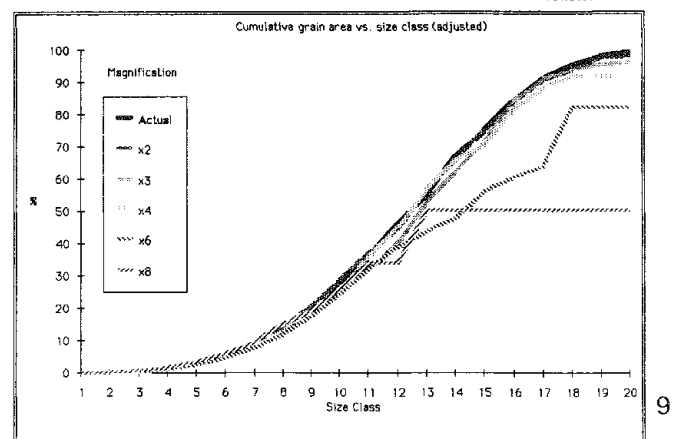
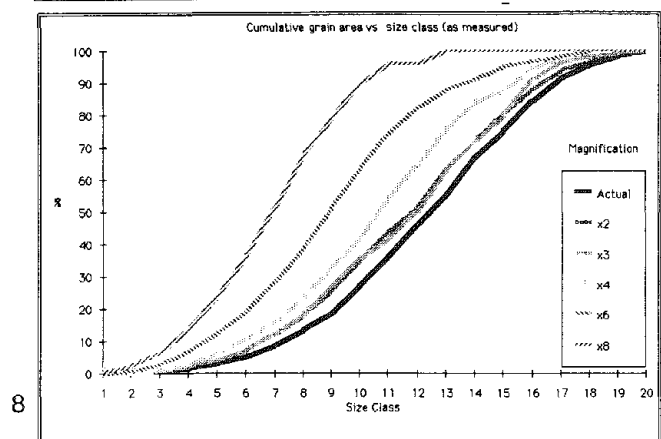
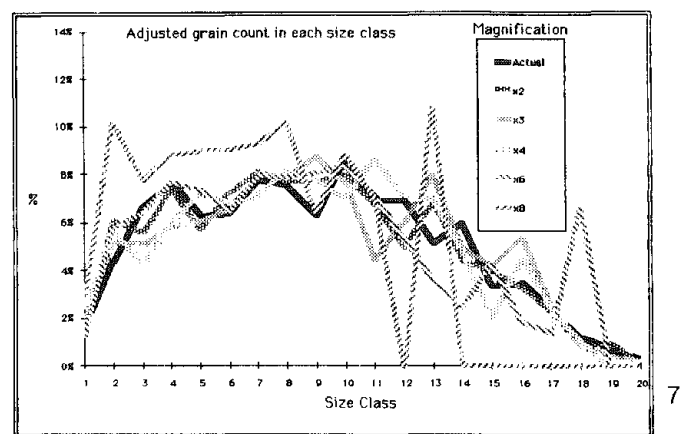
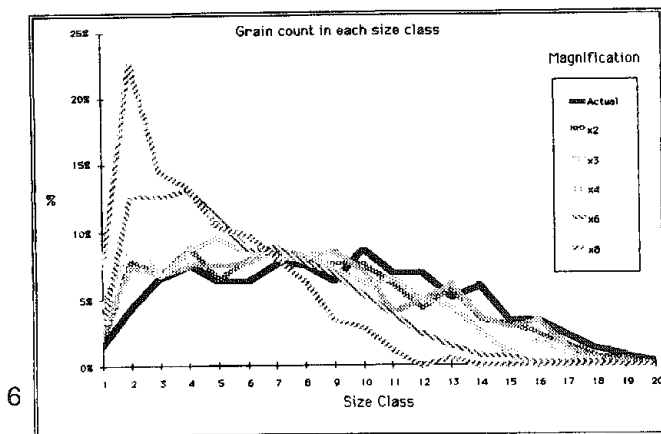
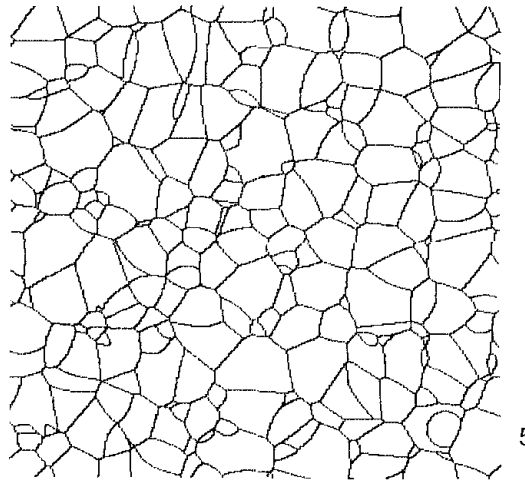


FIG. 5.--Grain structure from computer-simulated microstructure. FIG. 6.--Size-distribution plot for grains at various magnifications. FIG. 7.--Plot from Fig. 6 with the use of adjusted count described in text. FIG. 8.--Plot of cumulative grain area vs size. FIG. 9.--Fig. 8 plot weighted by adjusted count.

EXPERIENCE WITH MULTIPLE-LEAST-SQUARES FITTING WITH DERIVATIVE REFERENCES

D. J. McMillan, G. D. Baughman, and F. H. Schamber

For over a decade the technique of multiple-least-squares (MLS) fitting has been used successfully to quantify x-ray peak intensities from x-ray spectra obtained from lithium-drifted silicon [Si(Li)] detectors. The technique¹⁻⁴ involves collecting reference spectra for each element that has characteristic peaks in the spectrum to be analyzed. These reference spectra are then "fitted" to the analyzed spectrum by the method of least squares. The method returns a series of constants or K-ratios, one for each reference component used in the fit, that represent the amounts of each of the reference components in the analyzed spectrum.

One implicit assumption in this procedure is that an element's reference spectrum accurately represents that element's spectral component in the unknown spectrum. There can be no variations of peak position or of peak width between reference spectra and analyzed spectra. In most cases these requirements are easily met by routine calibration procedures. However, from time to time situations arise in which differences between reference spectra and unknown spectra cannot be eliminated. In the past, these differences resulted in unavoidable systematic errors in the intensity information that was extracted with the MLS technique. Recently, however, Kitazawa et al.⁵ presented a procedure that allows the MLS technique to be used even in cases where differences in references and the unknown spectra exist. We were interested in determining the usefulness of this procedure and its range of applicability. The results of our investigations will be summarized in this paper.

Theory

Assume that a MLS reference spectrum $S(E)$ is represented by a Gaussian peak with an energy E_0 and a width parameter σ :

$$S(E) = \frac{1}{\sqrt{4\pi}\sigma} \exp \left[-\frac{(E - E_0)^2}{2\sigma^2} \right] \quad (1)$$

Also assume that the spectrum to be fitted by MLS is a Gaussian peak with a different peak energy $E_0 + \epsilon$ and a different peak width represented by $\sigma + \rho$:

$$S'(E, \epsilon, \rho) = \frac{1}{\sqrt{4\pi}(\sigma + \rho)} \exp \left[-\frac{(E - E_0 - \epsilon)^2}{2(\sigma + \rho)^2} \right] \quad (2)$$

If the quantities ϵ and ρ are small, we can approximate the perturbed Gaussian peak by the Taylor expansion

$$S'(E, \epsilon, \rho) = S'(E, 0, 0) + \epsilon \left. \frac{\partial S'}{\partial \epsilon} \right|_{E, 0, 0} + \rho \left. \frac{\partial S'}{\partial \rho} \right|_{E, 0, 0} + \frac{1}{2} \epsilon^2 \left. \frac{\partial^2 S'}{\partial \epsilon^2} \right|_{E, 0, 0} + \dots \quad (3)$$

By evaluating Eq. (2) and its partial derivatives for $\epsilon = 0$ and $\rho = 0$, and by taking the first and second derivatives with respect to E of Eq. (1), we can show that

$$\frac{dS}{dE} = -\frac{\partial S'}{\partial \epsilon} \quad (4)$$

$$\frac{d^2S}{dE^2} = \frac{1}{\sigma} \frac{\partial S'}{\partial \rho} = \frac{\partial^2 S'}{\partial \epsilon^2} \quad (5)$$

Substituting these results into Eq. (3), we have the relationship

The authors are at Tracor Northern, Inc., Middleton, WI 53562.

$$S'(E, \epsilon, \rho) \approx S(E) - \epsilon \frac{dS}{dE} + (\rho\sigma + \frac{1}{2} \epsilon^2) \frac{d^2S}{dE^2} \quad (6)$$

Thus, we see that the modified Gaussian spectrum can be approximated by the original Gaussian spectrum plus a linear combination of the first and second derivatives of the original Gaussian spectrum. This result is similar to that obtained in earlier work⁵ which was based upon more general assumptions of the analytical expression of the reference spectrum $S(E)$. Equation (6), however, explicitly shows the functional dependence of the Gaussian width parameter σ in the relationship and is therefore useful when the approximation is applied to the MLS fitting process.

Although Eq. (6) is based upon a single Gaussian peak, it can also be shown to be valid for a linear combination of Gaussian peak components which have all been broadened and shifted by the same amount. Thus, the above relationship holds for any reference spectrum that is made up of a series of Gaussian peak shapes.

The first and second derivatives of a reference spectrum can be easily computed by applying Savitsky-Golay⁶ derivative coefficients to the original reference spectrum. These calculated derivative spectra are themselves included as references during the MLS fitting procedure. If correct normalization is maintained when the derivative spectra are calculated, the constants returned by the MLS procedure for the derivative references can be related to the coefficients of the derivative terms in Eq. (6).

Tests with Simulated Data

In order to determine the effectiveness of MLS fitting with references plus derivatives, several tests utilizing simulated data were conducted. In the first test a Gaussian peak located at 6.0 keV with a full-width-at-half-maximum (FWHM) of 160 eV was set up as a reference spectrum and used to fit a series of spectra made up of identical Gaussian peaks shifted by varying amounts from the 6.0 keV location of the reference peak. Figure 1(a) shows the error in the fitted peak intensity as a function of shifted position. Note that a shift of 30 eV results in a reduction in the fitted intensity of over 20% and that a shift of 10 eV corresponds to a reduction in intensity of over 2%.

The same test was repeated after the first and second derivatives of the Gaussian reference were calculated numerically by using five-point Savitsky-Golay⁶ coefficients and included as fitting references. The addition of these derivative references has a dramatic effect in reducing the intensity error as indicated in Fig. 1(a). Errors of less than 1% are observed even for shifts as large as 30 eV. In fact, errors less than 0.1% are observed for all spectrum shifts 20 eV or less.

A similar test was conducted to determine the effect of derivative references in compensating for changes in peak width. Again, a Gaussian reference at 6.0 keV with a FWHM = 160 eV was used as a reference to fit a series of spectra of similar Gaussian peaks located at 6.0 keV but with varying FWHM values. Figure 1(b) shows the results of these measurements. In this case, a change in the FWHM value of the fitted peak of 10 eV resulted in an error of 5% or more. By including derivative references in the fitting procedure, the errors are reduced to less than 0.5% for a 10eV change in peak resolution.

Another test was conducted to confirm the results of the Kitazawa et al.⁵ in their application of the method. In this test Gaussian peaks were used to simulate the $K\alpha$ and $K\beta$ lines of potassium (K) and the $K\alpha$ line of calcium (Ca). The K $K\beta$ line is separated from the Ca $K\alpha$ line by approximately 100 eV. These simulated spectra were used as references to fit a series of spectra containing only the simulated K $K\alpha$ and $K\beta$ lines shifted by varying amounts from the calibrated position. The intensity assigned to the nonexistent Ca $K\alpha$ component was used as an indicator of the error in the fitting process. Measurements were taken with only the K and Ca references and with these references plus the K first and second derivative references. The results of these tests are shown in Fig. 1(c). Again the effect of the derivative reference fit is to reduce the erroneous intensity assigned to the Ca component dramatically. Note that the data for the derivative fit have been multiplied by a factor of 10 in Fig. 1(c) in order to show the deviation from zero. The assigned Ca intensity is reduced by a factor of about 50 for a K spectrum shift of 5 eV when derivative references are used. This is in agreement with the results presented earlier.⁵

Figure 1(d) shows the effect of differing peak resolution of potassium on the

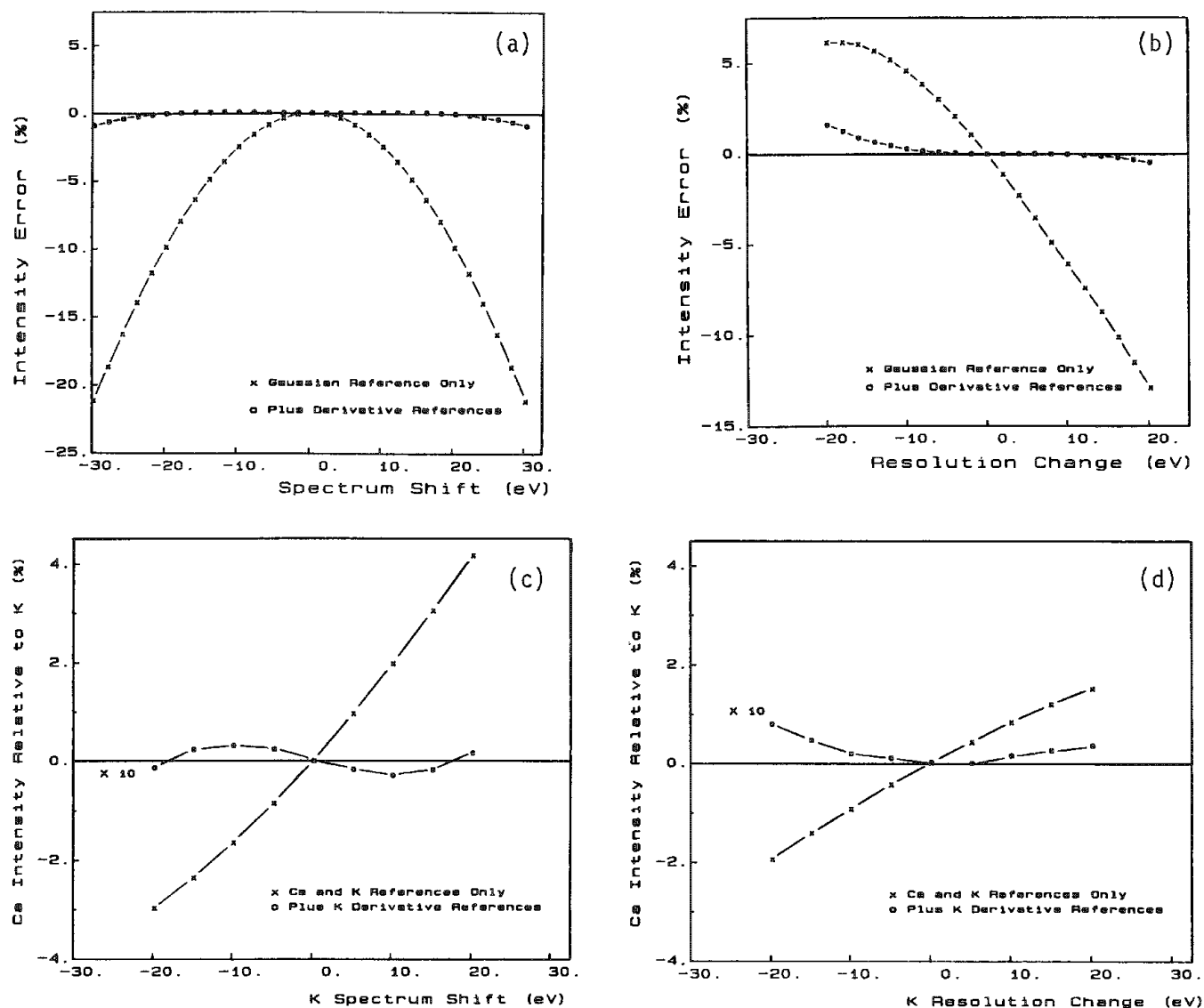


FIG. 1.--Intensity error for Gaussian peak spectra versus (a) peak shift, (b) resolution change from the reference spectrum; and intensity extracted for absent Ca $K\alpha$ peak as (c) K peaks are shifted from calibrated reference spectrum position, (d) K peak resolution is changed from reference spectrum resolution.

quantification of a nonexistent calcium component. The addition of K derivative reference spectra substantially decreases the error in measuring the Ca intensity. The data for the derivative reference results have been multiplied by a factor of 10 in Fig. 1(d). An improvement of a factor of approximately 50 is obtained when derivative references are used to compensate for a K spectrum resolution change of 5 eV.

Measurement of Peak Shift

As shown by Eq. (6), the coefficient of the first derivative term gives a measurement of the spectrum shift ϵ between an x-ray reference spectrum and its component in a spectrum being analyzed. Since the MLS procedure returns a constant for each of the reference spectra used in the fitting process, the constant returned for a correctly normalized first derivative reference can be used as a measure of the spectrum shift. To test the accuracy of this relationship, a series of manganese (Mn) K x-ray spectra generated by an Fe-55 radioactive source was acquired with the Mn $K\alpha$ line calibrated at various energies over a range of ± 15 eV from its normal 5.890 keV position. These spectra

were analyzed with the MLS procedure and by Gaussian fitting. In the latter case, Gaussian peaks of equal width were placed at the locations of the $K\alpha$ and $K\beta$ lines. A nonlinear least-squares procedure was used to determine the peak position, intensity, and width that would best fit the Mn K x-ray data. A small tailing component on the low energy side of the peak was added to the Gaussian lineshape to adjust the model to the x-ray data. The results of these measurements are presented in Table 1. The agreement between the spectral shift calculated by the MLS method and that calculated by Gaussian fitting is within 1 eV for all but one case. This result indicates that accurate measurements of peak shift can be obtained by the MLS method if derivative references are used.

TABLE 1.--Measurement of Mn $K\alpha$ peak shift.

Calibrated Shift (eV)	Measured Shift (eV)	
	MLS with Derivative Reference	Gaussian Fit
-15	-15.0	-13.4
-10	- 9.3	- 9.0
- 5	- 5.2	- 4.9
5	6.1	5.5
10	11.6	11.5
15	17.1	16.2

Conclusions

This study shows that first and second derivative reference spectra can be used to compensate for peak shift problems and/or spectral resolution changes when x-ray spectra are analyzed by the MLS method. In addition, the magnitude of the compensation required to obtain accurate results can be estimated from parameters returned by the MLS procedure. These characteristics make the addition of derivative references a valuable tool when used with the MLS method to extract elemental x-ray intensities.

References

1. F. H. Schamber, "A new technique for deconvolution of complex x-ray energy spectra," *Microbeam Analysis--1973*, 85.
2. F. H. Schamber, "A modification of the linear least-squares fitting method which provides continuum suppression," in T. G. Dzubay, Ed., *X-Ray Fluorescence Analysis of Environmental Samples*, Ann Arbor, Mich.: Ann Arbor Science Pub., 1977, 241-257.
3. J. J. McCarthy and F. H. Schamber, "Least-squares fit with digital filter: A status report," in K. F. J. Heinrich, Ed., *Workshop on Energy Dispersive X-Ray Spectrometry*, Washington, D.C.: NBS Special Publication, 1980, 273-296.
4. J. J. McCarthy, "Analysis of x-ray spectra by filtered least-squares fitting," *SEM/1980 II*, 259-270.
5. T. Kitazawa et al., "Quantitative electron probe analysis: Problems and solutions," *Ultramicroscopy* 11: 251-261, 1983.
6. A. Savitzky and M. J. E. Golay, "Smoothing and differentiation of data by simplified least squares procedures," *Anal. Chem.* 36: 1627-1639, 1964.

A PASSIVE SEM-MICROCOMPUTER INTERFACE FOR ACQUISITION OF ELECTRON IMAGES AND X-RAY MAPS

W. D. Stewart, J. Christian Russ, and John C. Russ

Scanning electron microscopes have been connected to mini- and microcomputers for many years, although the trend is now accelerating rapidly as the advantages of having the image information in a form available for processing become more widely known. The kinds of operations that are useful include false or pseudo-color displays, image combination and enhancement, and measurement of features within the image. All these applications have been well reported in the literature and are now available in various degrees in commercial systems.

The usual method employed for the interface is to have the microcomputer take control of the beam scan, using digital-to-analog converters (DACs) to generate voltages which drive the deflection coils in the SEM. However, as there are a great many different SEM designs that use unique voltage levels and in some cases rely on a close match between the characteristics of the electron optics and the built-in analog scan generators, this interfacing method is not always straightforward. Indeed, for some older instruments it is quite impractical.

A much less expensive and easier interface can be achieved without bypassing (or attempting to drive with external signals) the built-in SEM scan generators. This method simply requires locating the appropriate signals within the SEM and bringing them out so that they can be measured and tracked by the computer. Then the internal scan generators control the beam scan at all times, and the computer acquires the image by reading the voltages that tell it where the beam is located on the sample, and what the image signal is at that location.

Figure 1 illustrates the setup schematically. The only connections from the SEM are passive. The voltages from the X- and Y-scan generators, which produce sawtooth voltages to drive the beam deflection coils, are brought out to an analog-to-digital converter (ADC) which has multiple inputs. (The one we use, which is typical of many modern designs, can actually accept 16 different inputs through a multiplexer and select any of them for reading.) The successive-approximation ADCs used in these single-chip devices typically have conversion times of 30-80 μ s. Because the voltages may range from several volts to millivolts, depending on where in the SEM circuitry it is convenient to tap the signals, and also to provide a high impedance which will not load down the scan generators, operational amplifiers are used. Op-amps are inexpensive devices that can be readily configured to produce positive or negative voltages with various ranges. A common input voltage range for ADCs is ± 5 V.

A similar op-amp is used to bring out the image signal, as shown. Since most SEMs have at least a secondary electron detector and some way to detect backscattered electrons, and may also have cathodoluminescence, electron-beam induced conductivity, or other types of signals, it is usually most convenient to tap the signal after the video amplifier (which will have the appropriate input selector and adjustable contrast and level controls). Alternately, it is possible when appropriate to connect each signal source to its own input on the ADC card, so that all images are available to the computer.

The operational amplifiers can be purchased and a chassis built to house them, or commercially available attachments such as the G&W model 100, which provide these outputs, may be used. The three (or more) signals are brought to the computer by shielded cable to minimize interference from the plethora of radiating signals in the environment of both the SEM and the computer. The ADC card itself resides within the computer, connected to its system

Author Stewart is at Dapple Systems, Sunnyvale, CA; author J. Christian Russ, at the University of Michigan in Ann Arbor; and author John C. Russ, at the School of Engineering, North Carolina State University, Raleigh, NC 27695.

bus.

For normal acquisition of images, we use ADCs with 8-bit resolution (1 part in 256), which produce images 256 points wide. Higher resolutions (12 or even 16 bit ADCs) are readily available; the practical limitations to image size arise from storage space and processing time. Figure 2 shows an example SEM image as photographed normally, and as digitized and redisplayed with 256-point lateral resolution. Further modification to sharpen edges or adjust the gray scale range for optimum viewing can also be applied, as shown.¹ The resolution is entirely adequate for measurement of features in the images.²

The simplest way to acquire an SEM image using this passive scheme is to have the computer program constantly monitor all three ADCs (X-position, Y-position, and image brightness) in a repetitive loop. The brightness can be stored in a memory location corresponding to the X- and Y-position of the beam (a 256×256 pixel image takes 65K bytes of storage) until the user determines that the entire image has been scanned and stops the program.

There are several ways to improve this simple approach. First, by noting the Y-voltage when the image acquisition is begun (which need not be at the top of the image scan raster), the program can decide for itself when the image is complete. The Y-voltage increases to its maximum, drops sharply to its minimum, and then passes the original voltage. When it exceeds it by some small amount (e.g., 10%), the image should be complete.

Another problem that may arise is missing pixels in the image. Many analog scan generators are not perfectly linear. That does not matter much for purposes of normal SEM viewing, because the same generator drives both the SEM beam and the display CRT, so that mapping of points from one to the other is still accurate. However, at moderate scan rates, the nonlinearities may cause the voltage to increase so rapidly past an intermediate voltage level that some points are missed along a scan line, or even an entire scan line might be missed if a Y-value was skipped over.

This problem can be handled in software. For both the X- and Y-voltages, the program can allow the digitized value to increment only by one. Further, the Y-value can be allowed to increment only after an entire X-line has been read in. The use of a "sticky" increment prevents blank spots in the image, even with quite nonlinear or noisy scan circuitry, as we have found in some (especially older or "low-cost") SEMs.

The typical minimum acquisition time for a complete image is 5-10 s by this approach. Of course slower scans can also be used, in which case loss of pixels is much less likely to occur. Another modification that can be introduced for slow scans is signal averaging, where each pixel is actually read several times and the mean brightness value is recorded. This technique produces smoother images with less statistical noise, particularly with low beam currents. An alternate approach is to acquire several single scans and average them together afterward. Our software has the capability to store multiple images and combine them in varying proportions, and this feature can also be used with images of the same area using different detectors (e.g., secondary and backscattered electrons).

Optionally, the system may also allow x-ray maps to be collected. If this is the case, then there are two ways to transfer the information to the computer. One is to use a conventional separate x-ray system, and to route the pulse output normally used to drive the SEM display to an interrupt input on the computer. The other is to use a pulse-measuring ADC card directly inside the computer. In the latter case, the computer may also be used as the multichannel analyzer, with complete facilities to collect, display, and process spectra and perform quantitative analysis.^{3,4} For x-ray mapping, the user defines upper and lower energy limits (actually, limits on the pulse height coming from the pulse amplifier). When an event occurs that lies within those limits, an interrupt is generated within the system and the computer reads the DC voltages from the multiple input ADC which specify the current location of the beam.

The program then increments by one the value stored at the memory location that corresponds to that X-Y position. This process builds up, over time, an x-ray image that differs significantly from the traditional "dot map" image. The brightness at each image point is proportional to x-ray intensity, and the gray-scale image can be processed (for instance by smoothing) before display. It is also possible to set discriminators to cut off a background dot level to suppress the continuum background in the map, to use nonlinear brightness functions (or false color tables) in the display to enhance selected details, or to combine the x-ray images with electron images, as we have previously described.⁵

Acquiring an x-ray map with enough information (enough x-ray counts) to produce a good

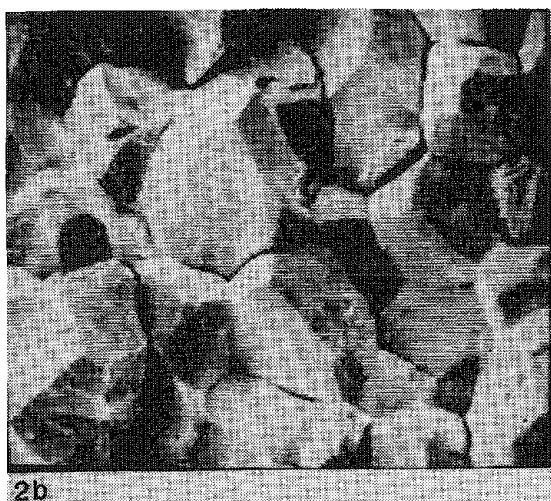
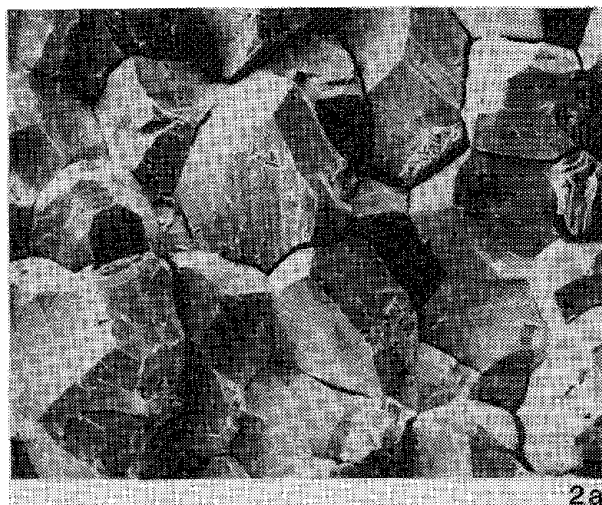
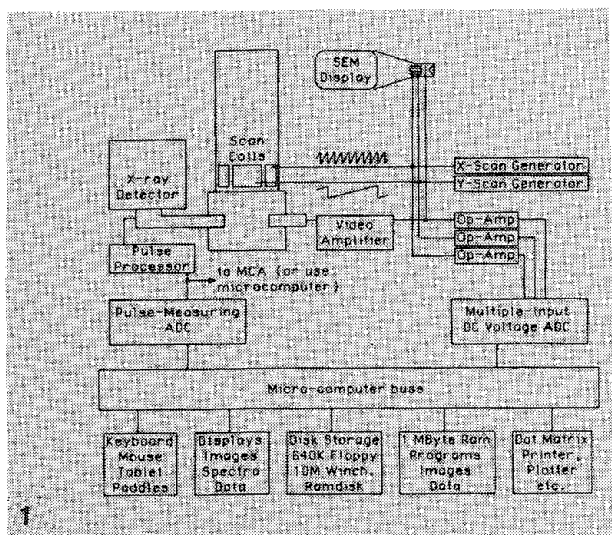


FIG. 1.--Schematic diagram of connections from SEM to microcomputer (Apple IIe).

FIG. 2.--SEM image of fracture surface in ceramic: (a) as photographed from SEM, (b) as digitized in microcomputer and redisplayed, (c) redisplayed after processing to sharpen edges and modify contrast function.

gray-scale image frequently takes much longer than getting a conventional "dot" map, but the gray-scale mode of display gives much cleaner outlines to features and boundaries, and permits interpretation of variations in intensity directly. It is notoriously difficult to judge variations in dot density in a conventional map. Figure 3 shows an example of a gray-scale x-ray map of a copper grid on a nickel stub, compared to a minimal x-ray dot map of the same specimen. Note in these images that the "background" intensity is actually counts of Ni K β x rays from the substrate. The conventional map was acquired in a single 250s sweep; the gray-scale x-ray image required about $\frac{1}{2}$ h of continuous scanning. The latter image is well suited to processing or measurement. Figure 4 shows contour and Y-modulation displays of the image after smoothing.

In conclusion, the principal advantage of the passive interface method is simplicity and low cost, as compared to direct beam control using computer-controlled DACs. In some cases it also minimizes nonlinearities that arise when the scan coils and circuits designed by the SEM manufacturer are not used together. It is much easier to locate the required signals within the SEM and bring them out for reading by the computer, than to implement ways to switch back to normal SEM operation. Once acquired, the images may be used in all the normal ways, for processing, measurement, and enhanced display.

References

1. J. C. Russ and J. Ch. Russ, "Image processing in a general purpose microcomputer," *J. Microscopy* 135: 89-102, 1984.
2. J. C. Russ and W. D. Stewart, "Quantitative image measurement using a microcomputer system," *American Laboratory*, Dec. 1983, 70-75.
3. D. Hale, J. C. Russ, and D. E. Leyden, "Operation of a microcomputer-based multi-channel analyzer with energy-dispersive detectors," *Microbeam Analysis--1982*, 473-478.
4. J. C. Russ, "Processing x-ray spectra, data, and line scans in a 'personal' computer," *Microbeam Analysis--1982*, 479-486.
5. J. Ch. Russ and J. C. Russ, "Enhancement and combination of x-ray maps and electron images," *Microbeam Analysis--1984*, 161-164.

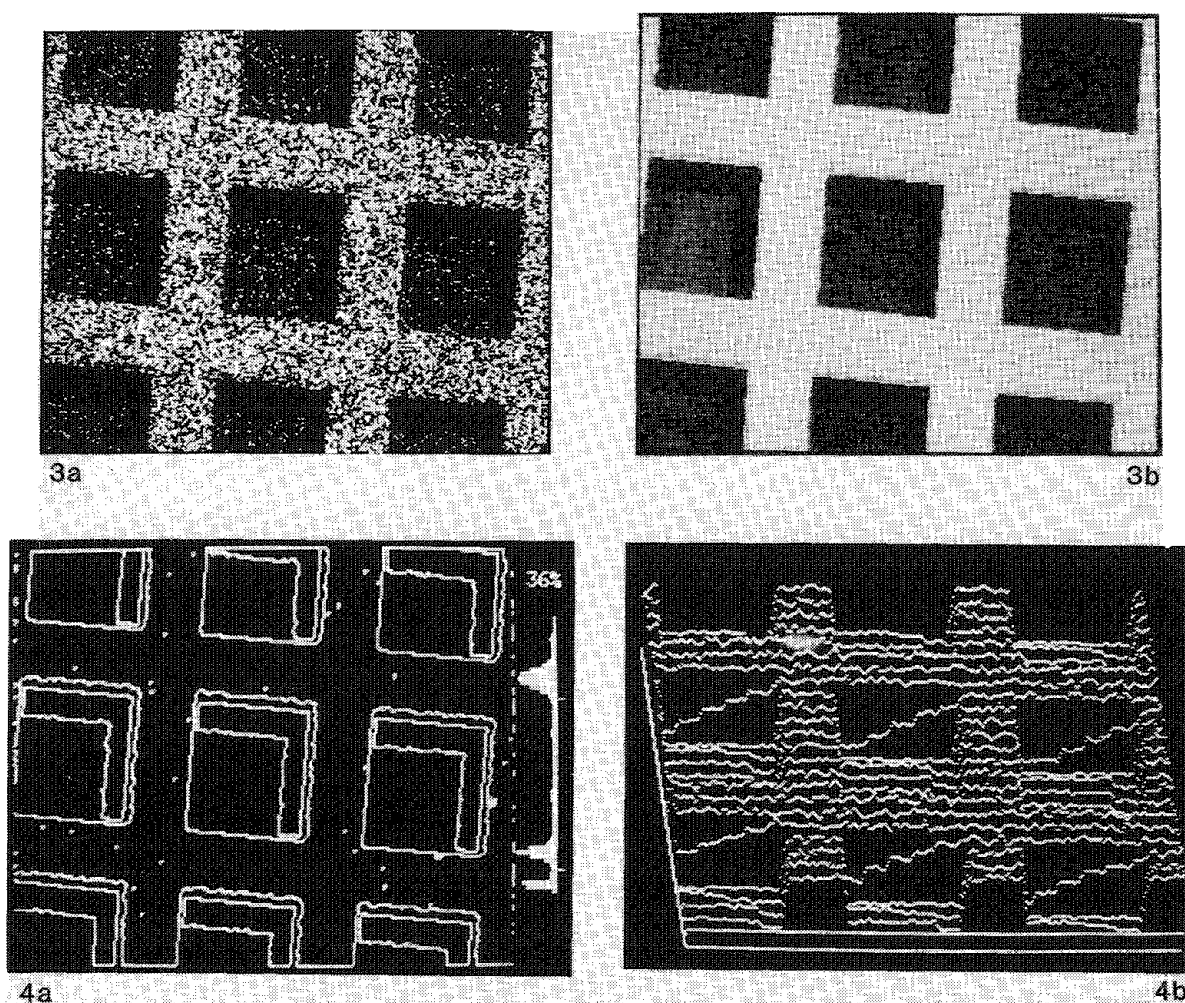


FIG. 3.--X-ray maps for Cu from copper grid on nickel substrate: (a) conventional, acquired in single 250s scan, (b) gray-scale image stored during continuous scanning for approximately 30 min.

FIG. 4.--Gray-scale x-ray map image from Fig. 3, smoothed and shown in (a) contour, (b) isometric or y-modulation mode.

HIGH-SPEED WIDE-AREA ANALYSIS BY ELECTRON PROBE

Yoshiaki Ono, C. H. Nielsen, Shojiro Tagata, and Yoshihiro Seo

Traditional analysis with the EPMA mainly utilizes extremely small probes for x-ray analysis of micro areas. Application of EPMA in two-dimensional analysis is confined to small areas due to limited electron probe scanning and problems with crystal defocusing, and is qualitative at best. Rapid accurate quantitative element analysis of a wide area (more than a few square millimeters) is very difficult.

JEOL has engineered a new system, and developed a new method of analysis, which makes high-speed wide-area analysis possible. The system, based on the conventional EPMA, has new features which render it particularly suitable for wide-area analysis. None of the traditional features of the EPMA is forfeited in its capabilities. The system accommodates a large sample, moves at very high speeds, acquires various data (e.g., x ray, BSE, SE, etc.), processes the data on line, and displays results of the two-dimensional analysis on a high-resolution color CRT or digital plotter.

System and Method

Figure 1 illustrates the system, which consists of the electron column, large specimen stage, x-ray spectrometers, x-ray counting system, computer, interface, data storage, data display, and so forth.

The electron optical system, basically the same as the EPMA, provides stable high probe currents. The specimen stage is designed to accommodate large and heavy samples (up to $100 \times 100 \times 20$ mm), rapid sample exchange achieved through the pre-evacuation chamber, and high-speed (5mm/s) axis scanning. The computer-controlled stage moves at minimum $1\mu\text{m}$ steps, and its movable range in the X and Y direction covers 80×80 mm.

The specimen chamber can be equipped with 5 wavelength-dispersive spectrometers (WDS), and one energy-dispersive spectrometer (EDS), secondary electron detector, backscattered electron detector, and so forth. The WDS is mainly used as an x-ray spectrometer for high-speed two-dimensional analysis. The WDS is particularly suitable for detecting trace element distributions in high-speed large-area analysis, because it provides better S/N ratio and wavelength resolution than the EDS, and has superior minimum detection sensitivity when high probe currents are possible. The annular, split-ring, backscattered-electron detector is capable of separating signals into pure topography images and pure composition images; the latter may be used to study distribution of mean atomic number in a wide area area of a sample.

In wide-area x-ray analysis with the WDS, the height of an analytical point (Z axis) must be adjusted precisely over the entire area of analysis. The system uses the optical microscope to measure the height of the sample surface at four corners of the area of analysis, then calculates the tilt of the surface, and continues to correct the sample height (Z axis) while analyzing the wide area. Stage reproducibility is approximately $1\mu\text{m}$, and backlash a few micrometers. When the distance between analytical points is less than a few micrometers, the system moves the sample only in one direction to collect information; when it is more than $10\mu\text{m}$, the system moves the sample in the reverse direction as well, neglecting backlash correction. The system employs gradual acceleration to start stage movement, and gradual speed reduction to stop the stage, in order to eliminate stage shift due to inertia. During acceleration and deceleration, the system continues to collect data. Minimum analysis time per point is 1 ms. Signals collected at each analytical point are processed by a computer, and stored in a two-dimensional array (maximum 1000×1000 points) on a hard

Authors Ono and Nielsen are at JEOL USA, Inc., 11 Dearborn Road, Peabody, MA 01960; authors Tagata and Seo are at JEOL LTD., 1418 Nakagami, Akishima, Tokyo 196, Japan.

disk. Characteristic x-ray intensities are then converted to element concentrations and displayed on either the color CRT or plotter in such forms as single-element concentration maps, or contour maps, according to the operator's research requirements.

Example

Figure 2 shows an example of a wide-area analysis of Mn in a slab of continuous cast steel. The area analyzed is 76×34 mm and consists of 380×210 analytical points. In this analysis, C, P, and CR are also measured. Total time for the map was approximately 80 min. X-ray intensities of each analytical point were stored on disk, converted to weight concentrations based on a calibration curve (obtained with standards), and displayed on the CRT based on a user-selected color scale. The original color photo of Fig. 2 shows that the highest concentration of Mn is more than 0.8% as opposed to the average concentration of 0.3%, and that Mn is segregated in the middle and forms a series of V-shaped zones. Wide-area element analysis of continuous cast steel is one of the crucial factors in studying the solidification process of iron and in determining optimum conditions for producing high-quality steel.

Figures 3 and 4 show distribution of Al and Fe in chromite and other minerals that constitute dunite in ultramafic rock.³ The area analyzed is 1.8×1.8 mm. Other elements, Cr and Mg, were analyzed at the same time. A total of 360×450 analytical points are displayed. Concentrations of both Al and Fe are converted to those of Al_2O_3 and FeO, and displayed on the color CRT. The concentration of Al_2O_3 in chromite is the lowest in the core and increases toward the rim, forming radially symmetric zoning. Concentration of FeO, also low in the core and high in the rim, is high along the crack running from the upper left to lower right. Distribution of Cr_2O_3 and MgO shows a reverse pattern of Al_2O_3 and FeO, respectively. The figures indicate that zoning of Al and Cr had been formed before the dunite was cooled, because diffusivity of Al and Cr in spinel is smaller than that of Mg and Fe^{2+} . The asymmetrical zoning of Fe and Mg also indicates that these elements migrated along the crack immediately before or during the cooling of the dunite. Distribution of Al_2O_3 is plotted in a contour map in Fig. 5. Studying uneven distribution of any element in minerals is one of the crucial factors in estimating the process of rock formation. The technique of wide-area two-dimensional analysis has substantially reduced time and labor required to measure element distribution in rocks.

Conclusion

The simple technique of wide-area mapping opens up new fields of two dimensional analysis, especially those dealing with critical distributions of light or trace elements. An established tool in the steel industry, the wide-area analyzer solves steel quality control and processing problems, and aids in the development of new specialty steels. Materials scientists use wide-area analysis in the study of growth kinetics and two-dimensional diffusion processes. The digital form of the data is ideally suited to image type manipulation, yielding useful information such as trace carbon equivalent maps, atomic ratio maps, three-dimensional contour maps, and modal analysis.

References

1. I. Taguchi et al., "Measurement of element and precipitate distribution in steel by computer-aided micro analyzer (CMA)," *Annual Meeting of Japan Institute of Metals*, 1981, 89-90.
2. Y. Ono and S. Tagata, "Newly developed wide area analysis with EPMA," *18th Meeting for Applied Spectrometry at Tokyo*, 1982, 182-183.
3. K. Ozawa, "Compositional zoning of spinel investigated by computer-aided micro analyzer (CMA)," *JEOL News* 22E (2): 19-24, 1984.

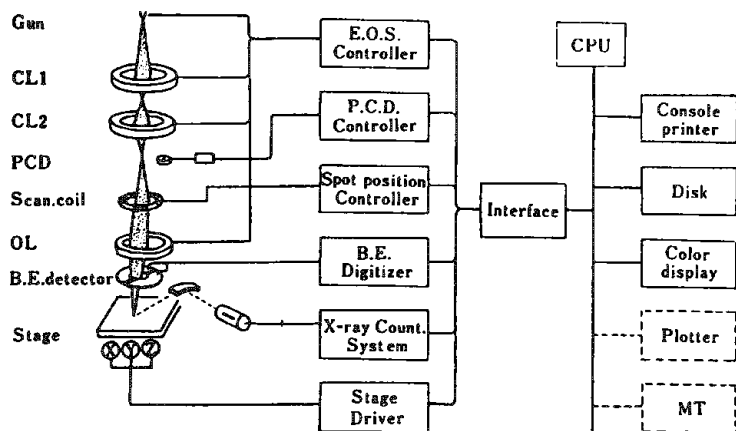


FIG. 1.--System diagram.

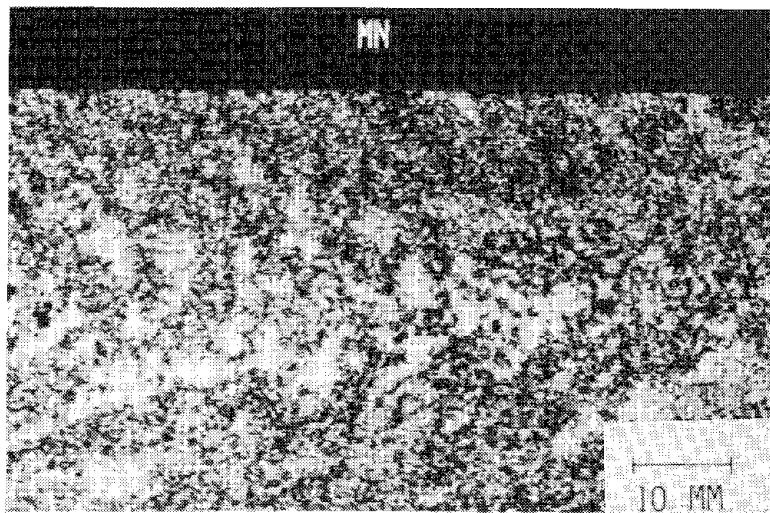
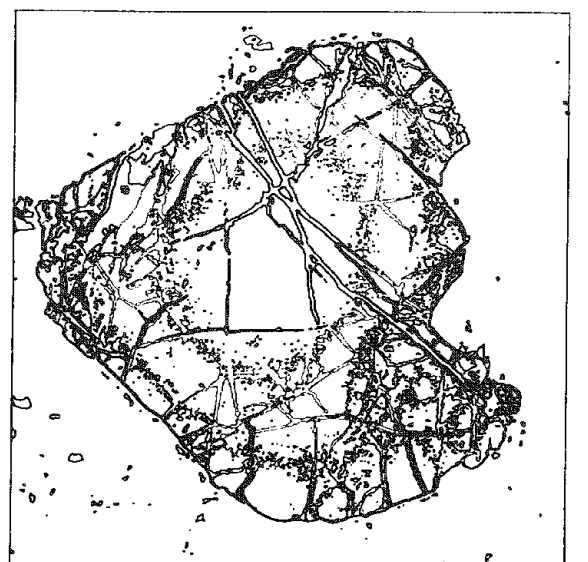


FIG. 2.--Mn distribution in continuous cast steel.



CONC. (WT. %)	AREA (%)	CHROMITE-AL2O3-	< AL >
13.500	9.68	PROBE SIZE: 5 * 4	CUM=UM
11.000	22.11	MEAS. AREA: 1800. * 1800.	CUM=UM
7.000	17.48		

AVERAGE CONC.: 6.488 WT. %

FIG. 5.--Al₂O₃ contour map.

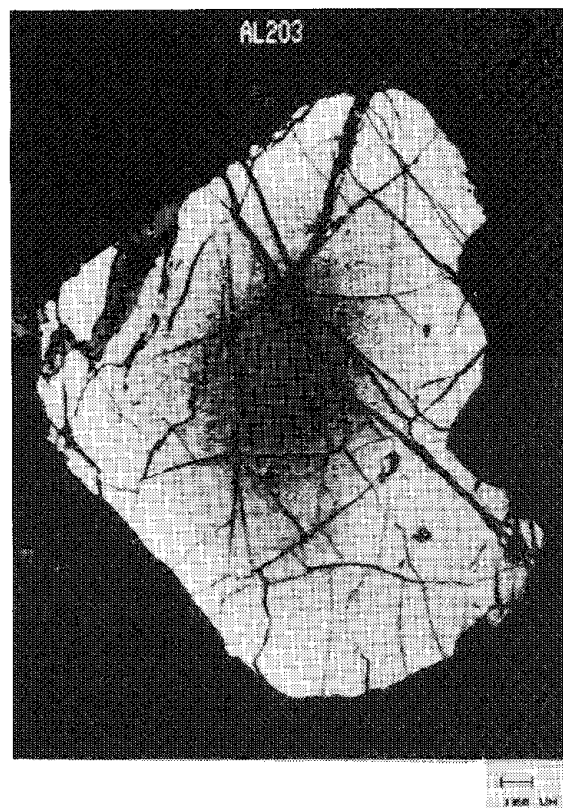


FIG. 3.--Al₂O₃ map.

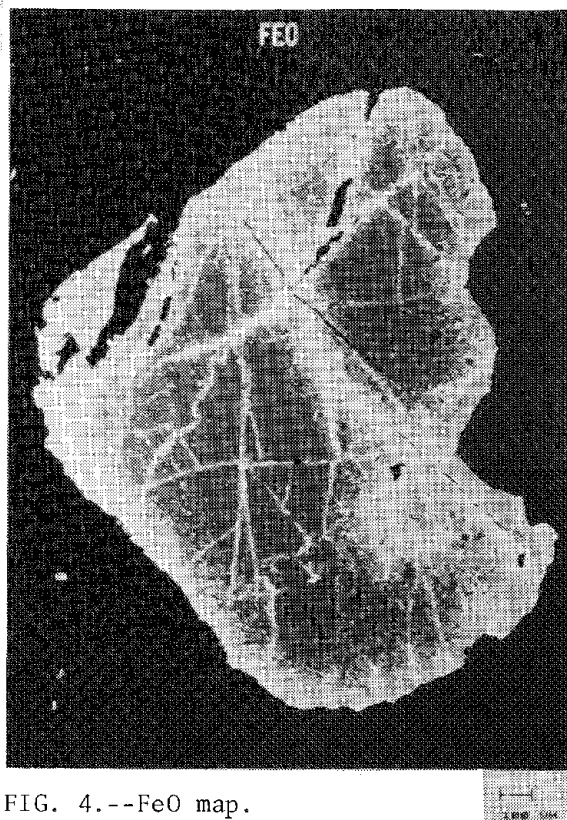


FIG. 4.--FeO map.

COMPUTERIZED ANALYSIS OF ELECTRON CHANNELING PATTERNS

S. H. Vale

Electron channeling patterns (ECP) are a well-established technique for obtaining crystallographic information from samples in the scanning electron microscope.¹ ECPs are commonly used for measurements of crystallographic texture² and material deformation,³ but taking measurements from photographs and subsequent interpretation is tedious and time consuming. This paper describes a computer program that performs basic interpretation and analysis of an ECP acquired directly onto the computer display screen.

Experimental

ECPs were obtained from a specimen of electropolished silicon examined at 25 kV in a JEOL 840 SEM. The computer was a Link Systems AN10000, a computer normally used for x-ray microanalysis, with a 16-bit word length, 20 MHz CPU, 128 kbyte memory, 256 kbytes of extended memory for intermediate image storage and processing, and a 512 × 512 pixel display. An interface is provided for digital control of an electron beam through 12-bit DACs and for reading the secondary electron signal through a 5MHz counter. With the SEM set up to acquire an ECP, control of the electron beam position was taken by the computer and the beam rastered over a point on the sample. The intensity of the signal at each beam position was stored in extended memory to 8-bit precision and also displayed on the computer screen.

Software

The ECP analysis program consists of routines for editing files of crystal structure data, calibration of the SEM, defining the band edges of collected ECPs, and analyzing them. Ancillary routines are also provided for plotting the band edges of any required ECP, stereographic projections and simple crystallographic calculations. Figure 1 shows an ECP plotted on the computer screen for titanium about the 121 zone axis.

A suite of programs have been developed to run on the AN10000 for general-purpose image collection, processing, and display. Figure 2 is a photograph of the computer display showing a contrast stretched ECP from silicon. The processed image data are stored in extended memory and can be re-displayed within the ECP analysis program. One can then define the edges of the ECP bands by moving a cross over the image on the display screen and selecting several points. A straight line is fitted to these points and the process is repeated for the other band edge (Fig. 3). The perpendicular distance between these lines is calculated and converted to a d-spacing on the basis of a calibration performed on a known specimen. The accuracy of this measurement is limited by the screen resolution and by the operator's subjective assessment of where the band edges are. One can overcome this limitation by performing a scan perpendicular to the direction of band to the full resolution of the DACs driving the electron beam (1 part in 4096). A profile across a silicon 220 band is shown in Fig. 4. Two cursor bars can be moved to select the positions on the profiles corresponding to the band edges. This measurement can be repeated at several positions on the band. This process is repeated for up to 10 individual bands from the same zone.

To proceed with the analysis of the ECP and if the sample can be identified, the details of the crystallographic data are entered from a file stored on disk. If the sample is one of several possibilities then each of these materials can be entered into the computer for comparison with the measured data. The analysis proceeds by comparing the list of measured band spacings and angles with those from reciprocal lattice sections from all the materials suggested for analysis. Due account is taken of any errors in measurement and calibration.

After analysis the solution with the best fit can be selected and displayed on top of the original ECP (Fig. 5). At this stage, allowance can be made for the possible 180° ambiguity in the assignment of Miller indices to each of the bands by examination of the

The author is with Link Systems Ltd., Halifax Road, High Wycombe, Bucks, England HP12 3SE.

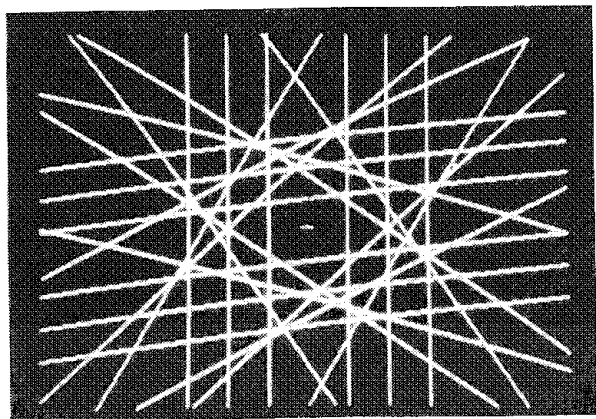


FIG. 1.--Computer-generated band edges of ECP for titanium about 121 zone axis.



FIG. 2.--Photograph of computer screen showing 111 zone axis ECP acquired from silicon; secondary electrons, 25 kV.

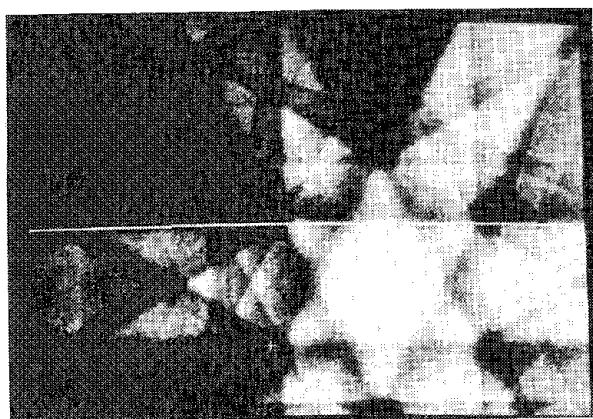


FIG. 3.--Defining ECP band edges by use of cursor.

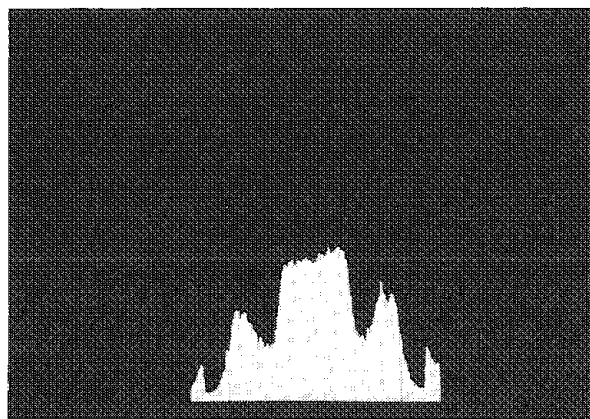


FIG. 4.--Profile across 220 band on silicon ECP.

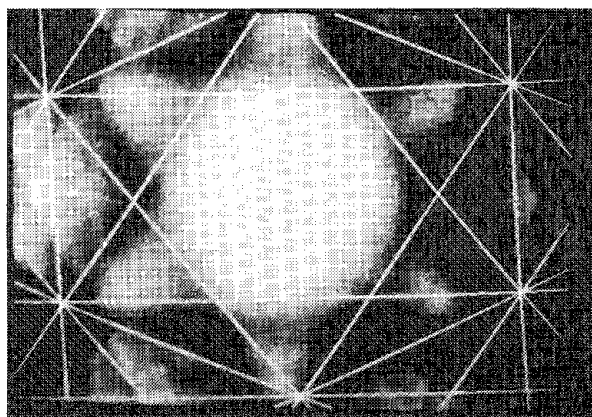


FIG. 5.--Overlaid theoretical and experimental ECPs from silicon after analysis.

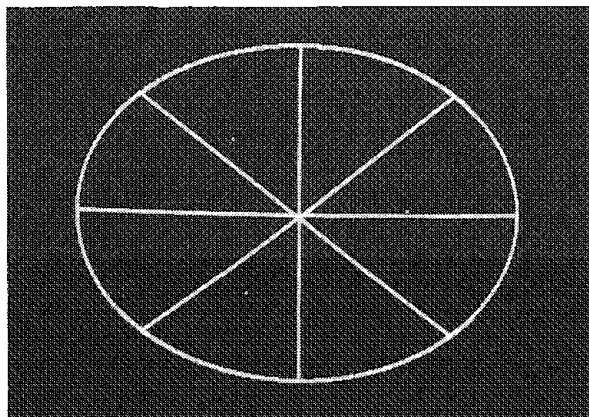


FIG. 6.--Stereographic projection showing 100 poles of sample in orientation given by ECP in Fig. 5 with respect to coordinate system of screen edges and electron beam.

alignment of the theoretical pattern with neighboring zone axes around the fitted zone. The orientation of the crystal is now defined by this ECP. A matrix describing this orientation with respect to a coordinate system based on the electron beam direction and the screen edges can be stored on disk. Further matrices could be stored on the same disk file after analysis of many ECPs obtained from a polycrystalline sample. A routine can then be run on this stored data to display the orientations in stereographic projection forming a texture map. The 001 poles of the orientation represented by the ECP in Fig. 5 are shown in the stereographic projection of Fig. 6.

Conclusions

The computer can aid the user of ECPs in several ways: data acquisition, image processing, interpretation of data, and presentation of results.

References

1. D. C. Joy et al., "Electron channelling patterns in the scanning electron microscope," *J. Appl. Phys.* 53: 251-280, 1982.
2. R. J. Matson and Y. S. Tsuo, "Complementary use of electron channelling and EBIC for analysis of polycrystalline semiconductor materials," *Microbeam Analysis--1984*, 93-96.
3. D. L. Davidson, "The quantification of deformation using electron channelling," *SEM/1983 III*, 1043-1050.

Digital Image Processing and Image Analysis

DEVELOPMENT OF AN AUTOMATED DIGITAL IMAGE ACQUISITION SYSTEM FOR AEM

E. B. Steel, R. L. Myklebust, and A. A. Bell

A VAX 11/730 computer was interfaced to a JEOL 200CX analytical electron microscope (AEM) for the purpose of producing and manipulating digital images from the microscope, and communicating in real time with a VAX 11/780.¹ This combination of computers allows fast acquisition and sophisticated manipulation of large image arrays. Other systems, dependent on microcomputers, are often memory limited and have relatively slow acquisition and computing times, which makes sophisticated real-time image analysis difficult or impossible. A block diagram of the overall system is shown in Fig. 1.

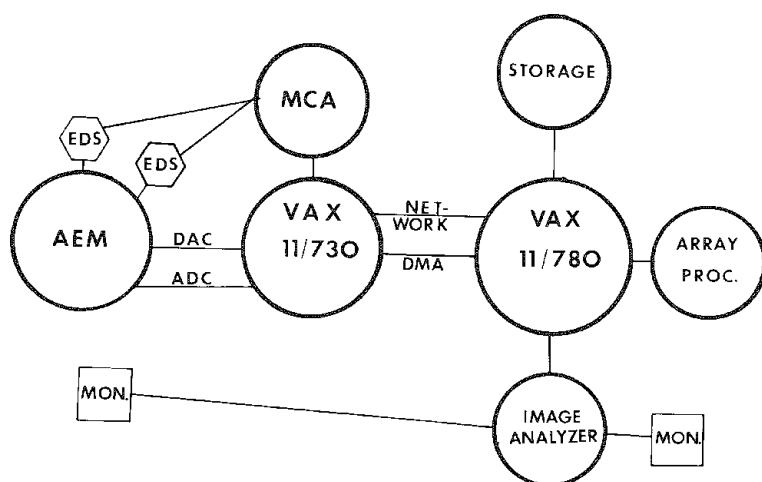


FIG. 1.--Block diagram of analytical electron microscope-multiple VAX system.

The 11/730 is used to control many functions of the AEM. The scanning coils (bright field and dark field) of the electron microscope are controlled by the 11/730 through digital-to-analog converters (DAC) and the output of the secondary-electron, transmitted-electron, and EELS spectrometer detectors on the microscope are input to the computer via analog-to-digital converters (ADC). The x-ray emissions from the specimen may be detected by use of two energy-dispersive x-ray spectrometers (EDS) (a zero-degree take-off angle ultrathin window EDS, and a high-take-off-angle beryllium window EDS) whose output is processed through a multiplexed multichannel analyzer (MCA) controlled by the 11/730. The 11/730 also controls the six magnetic lenses of the AEM through DAC

allowing the different modes of the AEM to be varied automatically. Additional controls for stepping motors to translate the specimen are planned.

A network and a direct memory access (DMA) channel link the VAX 11/730 to a VAX 11/780. the network communicates between the two computers at 19 200 baud; the DMA communicates at a more than 100 000 words/s. The VAX 11/780 is equipped with a DeAnza IP8500 image analysis system with six image planes, each containing 512 by 512 pixels with 8 bits per pixel. The image analyzer has two monitors, one at the AEM for viewing images during live-time experiments and another monitor in an office which is used for software development or viewing of archived images. An array processor on the 11/780 is used for accelerating computing times for complex algorithms.

The image-acquisition software controls the microscope so that either a scanning electron microscope (SEM) image, a scanning transmission electron microscope (STEM) image, or electron energy loss spectrometer (EELS) image can be obtained. The system allows the SEM, STEM or EELS, and x-ray signals to be collected concurrently or sequentially. Realistic image arrays up to 1024 by 1024 pixels at magnifications of 20× to 800 000× with each pixel having a resolution of 12 bits (4906 gray levels) can be acquired and manipulated. Typically, 512 × 512 pixel × 8 bit images are collected for the electron images and due to x-ray signal limitations, selected area or 64 × 64 pixel × 8 bit images are collected for EDS x-ray images.

The authors are with the Center for Analytical Chemistry, National Bureau of Standards, Gaithersburg, MD 20899.

The 11/730 is equipped with a 2Mbyte cpu and a 450Mbyte Winchester disk, and the 11/780 has a 5Mbyte cpu, various disk drives, and a magnetic tape drive for archival storage. This multiple-Vax configuration allows rapid x-ray spectra acquisition and image manipulation, and storage with almost no problems of memory or storage limitations.

The software for the system is written in a combination of Macro, Fortran, and LISP giving speed, flexibility, and computing power on a level currently unachievable by micro-computer-based systems.

Some early applications of the system were in analyses of air particulates, thin-film standards, asbestos, and several other mineral particulates, including the use of image analysis for particle finding, image comparing, electron diffraction analysis, magnification calibration, and film thickness measurement.

References

1. Certain commercial equipment, instruments, or materials are identified in this paper. Such identification does not imply that the materials or equipment identified are necessarily the best available for the purpose.

MICRO IMAGING: A LINK BETWEEN MICROSCOPY, IMAGE ANALYSIS, AND IMAGE PROCESSING

R. J. Lee, J. S. Walker, and J. J. McCarthy

This paper introduces a novel procedure that couples image analysis software with more traditional microscopy functions. Simple in concept, the procedure takes advantage of recently developed digital-scan generator technology in the TN-5500 microanalysis system. We believe that this procedure will accelerate the integration of computer-controlled electron microscopy (image analysis and image processing) with the more traditional visual microscopic observation.

Microscopy can be divided into three general activities. The first is probably best defined as Pan and Zoom. This activity requires a knowledge of the problem at hand and some ability to operate the instrument using functions such as: move the specimen, adjust the focus, vary the magnification to observe more or less detail, and so on. The second function is, in a broad sense, a processing function. This activity generally requires less knowledge of the problem and a greater skill and knowledge of the available signals (SEI, BSE, x ray, Auger, cathodoluminescence). The operator must know how to adjust the instrument in order to optimize the particular signal collection and display, how to enhance the collected signal, and so on. The third activity is often the most difficult: interpretation of the results from the second activity in terms of the entire process. Simply put: Is a "representative" micrograph real, and what does it mean?

In automatic image analysis (AIA), as it has been more broadly defined, the spatial distribution of any combination of available signals is quantified. In its simplified form, the size, shape, and composition of individual discrete particles are collected, classified, and collated. Information about the distribution of particle size or shape, the distribution of species by frequency, volume, or weight are produced in tabular, histogram, or other form.

These data, although extremely valuable, leave many microscopists wondering, "what happened to my micrograph?" How do I determine the texture, porosity, or chemical inhomogeneity associated with a particular group of features as I used to? In past usage of real-time analyzers, this qualitative information has been lost. In stored-image analysis (SIA), one attribute of a particle may be represented, for example morphology, but other attributes such as composition are not always simultaneously available. Also, if the zoom function is applied to increase the magnification of a stored digital image, only a limited 2× or 4× effective increase can be achieved.

Micro Imaging overcomes many of these problems by implementation of a computer-controlled pan and zoom, with the zoom triggered through a specific algorithm much like that used automatically by an experienced operator. The operator may observe a shape or composition that registers in his mind as being significant. He may not think of it as such, but he develops an algorithm which describes a set of procedures specific to his problem.

In Micro Imaging, the beam is scanned by the computer over the sample at some magnification, detecting features in sequence in the field. In a real-time version, for example, the magnification may be nominally 100×. Once a feature is located that meets some criterion described by a predetermined and computer-coded algorithm, the gain and offset of the scan are automatically adjusted so that a miniraster is centered about the feature. This approach is feasible in the TN-5500 because of the use of a 12-bit scan generator with separate 8-bit control of raster offset and size, which allows the computer to position the image raster anywhere in the normal field of view to one part in 256 and select a digital magnification of up to 128 times in the miniraster.

The signal produced by the miniraster is retained in image memory and is displayed on the TN-5500 CRT. The image collection mode can be varied, and the magnification, focus, contrast, and brightness dynamically adjusted. The operator views the image on a

Authors Lee and Walker are at U.S. Steel Technical Center, Monroeville, Pa.; author McCarthy is at Tracor Northern, Middleton, Wisc.

static display (nearly as valuable as a micrograph), then decides whether to store the image, spectra, and/or x-ray map on a disk for later retrieval. Once any of these operations is completed, the raster size and offset are reset to the initial conditions and the automated panning (i.e., image analysis operation) resumes.

At this point, the value of Micro Imaging to link image analysis is probably apparent. What about image processing? At first glance, the link is not as apparent. In optical microscopy and in TEM, image processing operations are directly used to enhance detail after the operator has optimized the microscope operating conditions. Image processing, therefore, is the enhancement of images collected under less than optimal conditions. In a sense, this is exactly the condition under which most micro images are collected. There is little doubt, for example, that an experienced operator, given the location of the feature, could tilt, rotate, and otherwise tweak the knobs to produce a better image than those collected with automatic pan and zoom. With image-processing functions, this tweaking can to a large extent be performed on a postcollection basis, using digital filters to enhance images collected in the micro imaging mode. Thus, image processing functions may find extensive application in what would otherwise be routine manual searching and imaging.

Application

The applications of this technique are extensive. For example, potassium and its compounds have a deleterious effect on the strength and stability of blast furnace coke. It is thus important to understand what potassium phases are present and whether volatilization and/or condensation reactions occur which lead to potassium recycling and accumulation. In combined AIA/Micro Imaging, the abundance, size, and average composition of all mineral phases are quantified as in conventional real-time AIA. Sample results are shown in Table 1. These results illustrate depletion of potassium and silicate at the bottom hot zone and enhancement of these elements higher in the burden. The interpretation of the raceway study will be reported elsewhere. Suffice it to say it is of interest to examine the potassium and silicate phases in detail to understand the probable reactions.

Conclusions

In summary, we have briefly described a new approach that combines automatic image analysis and image processing with more traditional visual microscopic evaluation. A specific illustration has been presented and the utility of this technique in other applications, such as the detection and analysis of minor or trace constituents in coal, ores, steel, or air particulate samples, is readily apparent.

STEM CALIBRATION BY ANALYSIS OF HOUGH TRANSFORMED IMAGES OF OPTICAL GRATING REPLICAS

D. S. Bright and E. B. Steel

A traditional method of calibrating the magnification of a scanning transmission electron microscope (STEM) is to measure the spacings of an optical diffraction grating replica.¹ Typically the spacings are measured along an intensity profile taken perpendicular to the lines of grating. A few linear-intensity profiles do not take into account the local non-linearities or bumps of the grating replica, and often multiple measurements on multiple images must be taken to average out these variations. The method presented here uses an algorithm that averages the grating spacings over the whole image rather than over a limited number of linear traces across the image. The accuracy of this algorithm is of the order of a tenth of a pixel for a given image, which is better than that needed for most applications.

Experimental

A 200CX JEOL analytical electron microscope was used in STEM mode, with digital image acquisition controlled by a PDP 11/23 computer.² The PDP 11/23 was linked to a VAX 11/780 equipped with a DeAnza IP8400 image processor with 512 by 512 pixel resolution. The VAX was used for image analysis and the image processor was used for viewing.

The JEOL 200CX has calibration adjustments for magnifications of 300 \times , 1000 \times , 10 000 \times , and 100 000 \times . Magnifications ranging from 3000 \times to 100 000 \times were tested because below 3000 \times the 512-pixel resolution was not sufficient to resolve the grating lines. This was not a limitation of the algorithm or of the microscope but only of the resolution chosen for this experiment.

The data represented here are from a replica of an optical line grating. The replica had been shadowed with tungsten to increase contrast. The STEM images of the replica appear as shaded lines (Fig. 1). Calibration of the STEM consists of measuring the spacings of these lines.

Image Analysis

The first step in analysis of the grating images was to take the gradient of the images (Fig. 2). The gradient operation emphasizes short-range changes in intensity and enhances the lines of shadowed gratings like this one. The lines were now adequately represented by the brightest 5% of the pixels in the entire gradient image. (By the gradient of an image, we mean an approximation to the magnitude of the gradient, calculated as the maximum of the absolute values of the differences of the horizontal or vertical neighboring pixels.³) The advantage of using the gradient can be seen if the intensity profiles of the gradient image and of the original image are compared.

The peaks of the intensity profiles (Figs. 1 and 2) vary noticeably in height due to the spottiness of the lines. This problem, as well as the above-mentioned bends in the lines on the replica, was overcome by using the Hough transform,⁴⁻⁵ which results in spacing measurements that are averaged over most of the image. Mathematically, the Hough transform maps lines into points (Fig. 3). In our images, this operation had the effect of mapping the grating lines into bright spots on a much less intense background. The Hough transform was applied to the binary image made by thresholding the gradient image (Fig. 2) to select the upper 5% of the bright pixels. The result, which is not a binary image, is shown in Fig. 4. For the purposes of measuring the line positions the intensity profile along the spots (line A-B) showed an even better peak-to-background ratio than the intensity profile in Fig. 2.

The horizontal position of any spot in the Hough-transformed image corresponded to the tilt θ of the corresponding line in the original image (Figs. 1 and 3). The analysis took advantage of this to identify the spots. Because the grating lines were parallel, the corresponding spots were on a vertical line (Fig. 4). The orientation of the grating

The authors are at the Center for Analytical Chemistry, National Bureau of Standards, Gaithersburg, MD 20899.

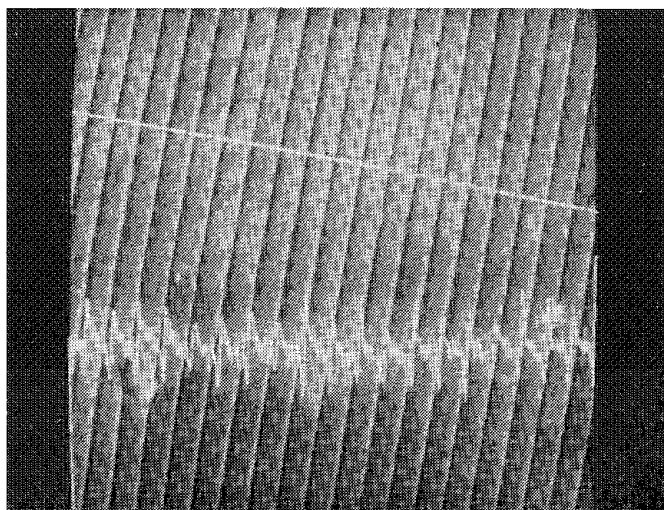


FIG. 1.--Original image with intensity profile along line (shown) perpendicular to replica lines.

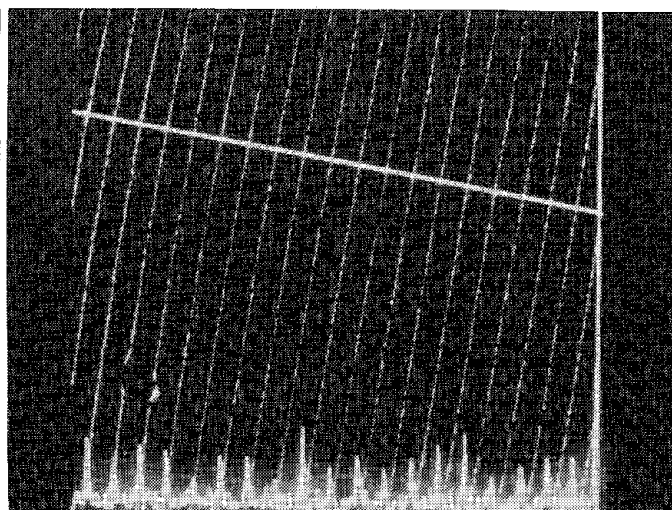
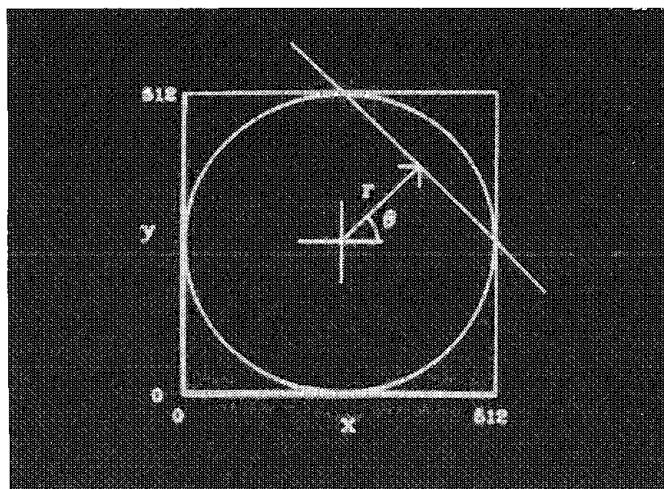
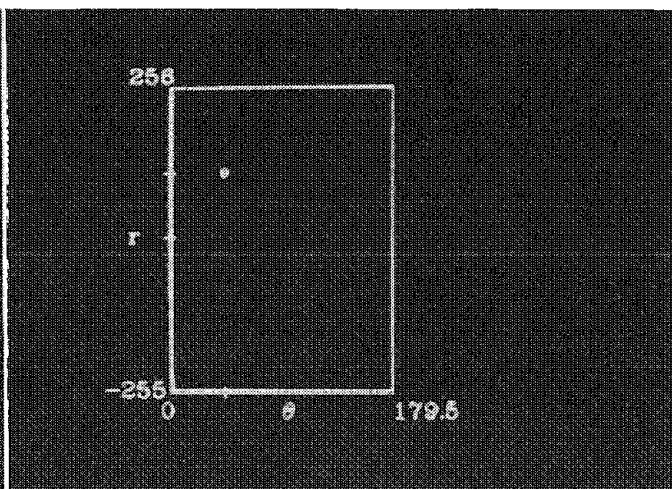


FIG. 2.--Gradient of Fig. 1; same location for intensity profile.



(a)



(b)

FIG. 3.--(a) Coordinate system of original image (Figs. 1 and 2) and typical line segment. Area within circle represents area of original image represented by Hough transform and thus area covered by our averaged spacing measurement. (b) Coordinate system of Hough transform (Fig. 4) showing location of spot representing typical line in (a).

did not affect the analysis but merely determined the position of the vertical lines. Grating orientation was important in calibrating the raster-scan aspect ratio of the microscope because the horizontal and vertical scan controls are adjusted separately.

The vertical position of any spot corresponded to the perpendicular distance r of the line from the image center (Fig. 3). Measurement of the average line spacing was then equivalent to measurement of the vertical spacing of the spots. This time, rather than using a vertical intensity profile, as shown in Fig. 4, we used an average of the pixel positions, weighted by intensity, for each entire spot.

The spots were located automatically, first by thresholding the Hough image to select pixels with 40-100% full intensity. These pixels adequately represented the spots and rejected the background (Fig. 4). The 40% threshold was not critical, due to the large signal-to-background ratio of the spots, and it worked on all of the images, regardless of magnification. The resulting image had spots on a vertical line that obviously corresponded to the grating lines. Other spots sometimes occurred that corresponded to image borders or to scratches.

Since the grating lines were parallel and evenly spaced, the algorithm searched for

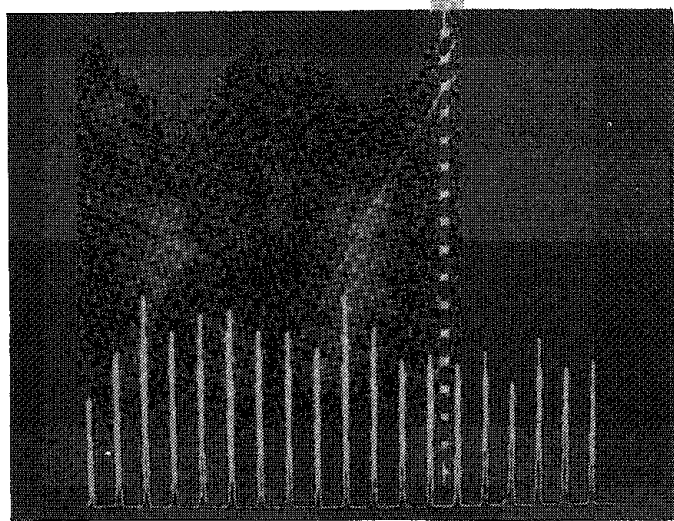


FIG. 4.--Hough transform of brightest 5% of pixels in Fig. 2 with intensity profile at bottom of picture taken along line A-B.

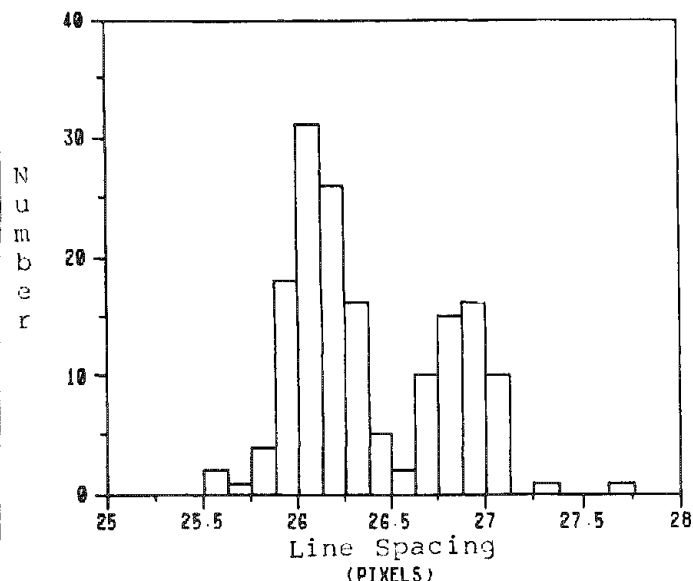


FIG. 5.--Histogram of grating replica line spacings for the nine 10 000 magnification images in Table 1, showing bimodal distribution due to digitization of slanted lines.

TABLE 1.--Summary of calibration data.

Nominal Magnification at STEM	Grating Replica Spacing in pixels (std. error)	Range of Mean Spacing in pixels (one per image)	Number of Spacings per image	Number of Images
-----	-----	-----	-----	--
5,000	10.07 (0.18)	9.99 - 10.26	22 - 49	9
10,000	26.38 (0.42)	26.10 - 26.77	16 - 18	9
30,000	79.0 (1.3)	77.0 - 80.4	2 - 6	13
50,000	130.7 (2.6)	125.9 - 133.3	2 - 3	11
60,000	155.7 (3.3)	149.5 - 157.9	2	11

three or more spots that were vertically and evenly spaced. The algorithm started with one spot that had two neighboring spots equally distant above and below it. This process defined an initial estimate of the spot spacing. The algorithm collected any other spots within this distance by an upward and downward search from the initial spot, until no spot appeared in the image at the required distance. For operations such as testing for equal spacing or searching for spots, the algorithm allowed a small error tolerance in spot position that was proportional to the initial estimate of the spot spacing. The line spacing was then calculated by averaging of the spacing of all the selected spots.

The averaged line spacing was needed to represent the measurement because of occurrences of multimodal spacing distributions caused by digitizing of the lines. Figure 5 shows the distribution of individual spacing measurements (the distance between two adjacent spots) from nine images taken at the same angle and magnification. The modality was shown to be a digitization artifact by reproduction of the same modality with synthetically (mathematically) produced lines. The mean value of these spacing distributions yielded the correct spacing. The modality was a function of angle: grid orientations with the lines orthogonal to or parallel to the microscope scans yielded unimodal spacing distributions, and other orientations yielded unimodal, bimodal, or trimodal distributions.

The averaged line spacing measurements in pixels over a range of magnifications and images taken during a six-month period are shown in Table 1. The standard error of the

line spacing and thus of the magnification measurement is less than 3% in all cases over a 6-month period. These data show that the system and algorithm are stable enough for routine use.

Conclusions

The Hough transform is useful in an accurate determination of the spacing between the lines of an optical diffraction grating replica as observed on a STEM. This algorithm is currently being used to calibrate the magnification of our STEM. The same method can be used for the same purpose on the TEM, SEM, and light microscope, or wherever a line-spacing magnification standard is used. The use of the Hough transform has the advantage of averaging the line spacings over the interior of the circle in Fig. 3(a), rather than along a few intensity profiles. Also, the Hough transform improves the signal-to-noise ratio of the line spacings and so makes the measurement less sensitive to image contrast. The algorithm yields reproducible and accurate results, and works without operator intervention for most of our images of shaded grating replicas.

References

1. C. E. Hall, *Introduction to Electron Microscopy*, New York: McGraw-Hill, 1953.
2. Certain commercial equipment, instruments, or materials are identified in this paper. Such identification does not imply that the materials or equipment identified are necessarily the best available for the purpose.
3. Azriel Rosenfeld and A. C. Kak, *Digital Picture Processing*, New York: Academic Press, 1982, vol. 2, pp. 121-126.
4. W. K. Pratt, *Digital Image Processing*, New York: Wiley, 1978, 523-525.
5. C. R. Dyer, "Gauge inspection using Hough transforms," *IEEE Trans. PAMI-5*: 621-623, 1983.

WAVELENGTH-DISPERSIVE TECHNIQUES FOR COMPOSITIONAL MAPPING IN ELECTRON-PROBE MICROANALYSIS

R. B. Marinenko, R. L. Myklebust, D. S. Bright, and D. E. Newbury

Digital compositional mapping is developing rapidly and is replacing conventional analog x-ray area scanning. Because of the high peak-to-background ratio of wavelength-dispersive spectrometers (WDS), compositional mapping is preferred to mapping with energy-dispersive spectrometry (EDS) for certain applications, especially when one is looking for low-concentration element distributions. Although commercial software from manufacturers of electron microprobes and SEM automation packages is available for acquiring digital maps by both EDS and WDS, only EDS has been used extensively.^{1,2} This situation has probably developed because there are fewer technical problems in obtaining EDS maps and because data from more elements can be acquired in parallel.

Digital WDS or EDS x-ray maps are preferred to conventional analog x-ray area scans because of the greater flexibility during analyses and the reliability of the final result, when long accumulation times are involved. By recording the x-ray data as true counts rather than a simple photograph, the data are preserved on disk or tape and made available for subsequent manipulation with advanced image processing algorithms, which ultimately leads to more information about the image.

This paper describes a study of problems encountered in acquiring and interpreting digital x-ray maps with WDS. The precautions needed to make the technique quantitative are discussed.

Instrumentation and Data Acquisition

The electron microprobe used in this work is equipped with three spectrometers, a standard Tracor Northern TN-2000 analyzer, and a TN-1310 automation system.* The PDP-11/34 computer is configured with 48K words of memory including memory management.

The WDS digital x-ray maps were accumulated with a modified Tracor Northern XIP program and the accompanying Tracor Northern WDS module. These programs, as originally supplied by the manufacturer, had acquired only dot maps for a given element. Above a given threshold value, the element had been assumed to be present and below, to be absent. No gray-level quantitative information had been stored. Because quantitative WDS x-ray maps were needed, the programs were modified to store the number of counts observed at each pixel location. The array data were stored in extended memory and then dumped by blocks on a floppy disk when the extended memory was full. The modified version can record 32×32 , 64×64 , or 128×128 pixel maps, and data from the three spectrometers can be acquired simultaneously. The maps are transferred from the floppy disks to a Digital Equipment Corp. VAX 11/780 computer, where the data are separated into individual maps for each spectrometer for display on an IP 8500 DeAnza Image Analysis System.

The time required to acquire a map depends on the size of the map and on the accumulation time for each pixel. High beam currents are generally used to improve count rates. The time per pixel for most pure elements with a high count rate is usually a few tenths of a second, whereas maps of low-concentration elements are sometimes taken at several seconds per pixel. These latter maps are often acquired in overnight runs of 10 h or more.

Discussion

With standards data and background corrections, k-ratios could be immediately calculated from the accumulated counts at each pixel. The resulting k-ratio maps could then be transferred to the VAX for quantitation at each pixel. Unfortunately this procedure is limited to maps taken at high magnification. At lower magnification defocusing effects,

The authors are at the Center for Analytical Chemistry, the National Bureau of Standards, Gaithersburg, MD 20899.

*Certain commercial equipment, instruments, or materials are identified in this paper to specify adequately the experimental procedure. Such identification does not imply recommendation or endorsement by the National Bureau of Standards, nor does it imply that the materials or equipment identified are necessarily the best available for the purpose.

which are different for each spectrometer, become evident and can cause errors as great as 50% relative. X-ray maps of chromium taken simultaneously with the three spectrometers (LiF crystals) on our instrument are presented in Fig. 1. The three maps to the left are original. When pseudo gray levels are used to display these maps, the three maps on the right are obtained. The wide gray bands are the regions of most intense x-ray detection. Spectrometer 1 is inclined, 2 and 3 are vertical. The line of focus is different for each spectrometer. At the 400 \times magnification used to record these maps, there is appreciable change in intensity across the surface of this homogeneous specimen. The number of accumulated counts per pixel varies from 7474 to 18 187 in map 1A. Rocking the crystal in conjunction with the scan can be used to correct defocusing mechanically, but such a procedure is only applicable to one spectrometer where the line of focus is set parallel to the scan line.

A study of homogeneous specimens was begun to elucidate the problems involved in x-ray mapping and to demonstrate a workable technique before more complex specimens were examined. A "standard map" procedure was used.³ In this procedure, a digital x-ray map of each of the standard elements is recorded with the respective spectrometer used for mapping the same element in the unknown specimen. After making background and dead-time corrections, pixels from the unknown specimen and standard are matched for a k-ratio calculation on each pixel. A modified version of the NBS data reduction program, FRAME 4, is used to calculate concentrations from the k-ratio at each pixel point, with a resulting concentration distribution. This procedure was used to analyze several of the NBS SRM 481 gold-silver alloys which were previously shown to be homogenous on the micrometer scale.^{5,6} In Table 1 the mean concentrations calculated from all 64 \times 64 pixels in each composition map of these SRM alloys are tabulated and compared to the certified values. The gold concentration is systematically low in these analyses because of a fundamental error in the data reduction (ZAF) calculations, not because of any imaging effect. The digital x-ray map for Ag L α x-ray emission from the silver standard and the respective calculated concentration maps for Ag L α in three of the alloys are in Fig. 2. The same pseudo-gray-level display technique has been applied to all four maps. Since the maps in 2B, C, and D are from homogeneous specimens, each composition map should be nearly homogeneous if the standard map procedure had, in fact, properly corrected for the defocusing effects. Note that these maps are considerably more homogeneous than the standard Ag L α map (Fig. 2a).

There are several considerations in the quantitative mapping procedure. Often the specimen and standard have blemishes such as voids, scratches, inclusions, or cracks. These blemishes cannot be always avoided or eliminated from the scanned area when working at 200-800 \times magnification. They show up vividly in the digital x-ray maps (Fig. 3). Even contamination build-up from a previous raster scan on the same specimen becomes evident in the map. This effect is visible in Fig. 3(b) (upper right), which was recorded after Fig. 3(a) (upper left) was completed. On the standard specimens these blemishes are data outliers and can be removed by smoothing techniques which are currently under development by one of the authors. Such smoothing was done for the gold-silver data cited above.

The size of the standard in a technique such as EPMA has traditionally not been a consideration. But when scanning at 200 or 400 \times magnification, often the standard is too small for the rastered area. A specimen must be at least 0.5 mm in each direction at 200 \times . Also, when taking separate maps on the standard and specimens, the time requirement for an analysis can increase significantly. That may not be quite as serious as it sounds since a substantially higher count rate is usually observed for the standard. The time per point can be therefore reduced when one is acquiring the standard map; time corrections can be made later with software.

Alternatively, to avoid the necessity of scanning standards for each map, a limited collection of maps can serve as the basis for modeling additional standards as needed. Techniques for modeling standard maps are currently under development.

References

1. J. J. McCarthy et al., "Acquisition, storage, and display of video and x-ray images," *Microbeam Analysis--1981*, 30-34.
2. P. J. Statham and M. Jones, "Elemental mapping using digital storage and colour display," *Scanning* 3: 168, 1980.

TABLE 1.-- Quantitative analysis of EPMA digital x-ray maps.
SRM 481 gold-silver alloys (concentrations in weight percent)

	Element	Alloy			
		Au80Ag20	Au60Ag40	Au40Ag60	Au20Ag80
Certified values	AuM α	80.05	60.05	40.03	22.43
	AgL α	19.96	39.92	59.93	77.58
X-ray maps modified FRAME*	AuM α	78.75	58.10	38.06	21.22
	AgL α	19.68	39.75	59.05	77.50

*Mean composition values calculated from all 64 \times 64 pixels in respective composition map.

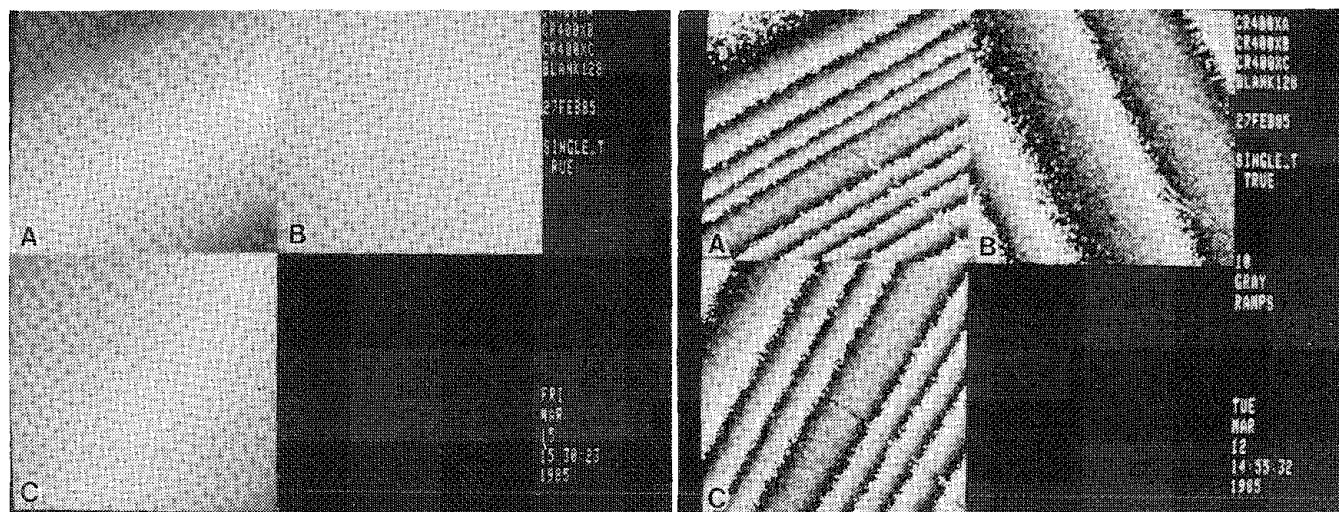


FIG. 1.--Digital x-ray maps of Cr K α line taken at 400 \times magnification, 20 kV, 128 \times 128 pixels, 0.5 s. A (upper left), inclined spectrometer 1; B (upper right), vertical spectrometer 2; C (lower left) vertical spectrometer 3. Maps at left are original, those on right are displayed with pseudo gray levels.

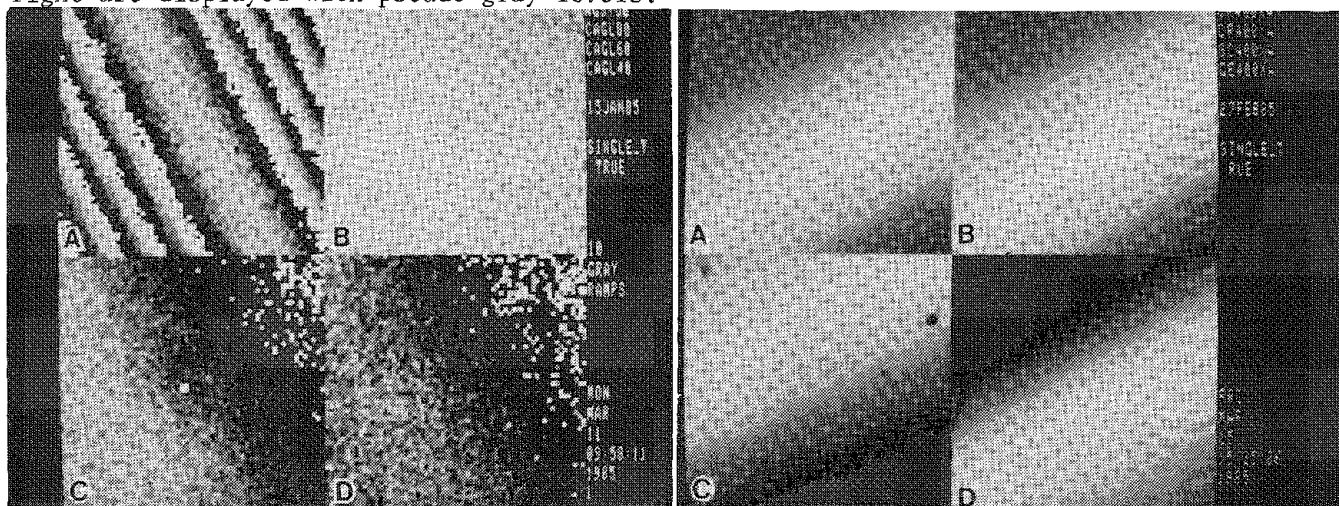


FIG. 2.--Digital x-ray map of silver standard. A (upper left), calculated Ag L α composition maps for B (upper right), Au²⁰Ag⁶⁰ alloy; C (lower left) Au⁴⁰Ag⁶⁰ alloy; D (lower right) Au⁶⁰Ag⁴⁰ alloy. All maps were taken at 400 \times magnification on vertical spectrometer 2 with Ag L α line, 20 kV, 64 \times 64 pixels, 1 s/pixel for alloys, 0.5 s/pixel for silver standard.

FIG. 4.--Digital x-ray maps taken with the inclined spectrometer at 400 magnification, 20 kV, and 128 \times 128 pixels. A (upper left), chromium; B (upper right), chromium taken after map in A was recorded; C (lower left), scandium; D (lower right), germanium. Blemishes such as scratches, voids, cracks, and contamination markings are visible in all maps.

3. R. L. Myklebust et al., *Microbeam Analysis--1985*, 101.
4. H. Yakowitz, R. L. Myklebust, and K. F. J. Heinrich, *FRAME: An On-Line Correction Procedure for Quantitative Electron Probe Microanalysis*, NBS Tech. Note 796, 1973.
5. K. F. J. Heinrich, R. L. Myklebust and S. D. Rasberry, *Preparation and Evaluation of SRM's 481 and 482 Gold-Silver and Gold-Copper Alloys for Microanalysis*, NBS Special Publication 260-28, 1971.
6. R. B. Marinenko, K. F. J. Heinrich, and F. C. Ruegg, *Micro-homogeneity Studies of NBS Standard Reference Materials, NBS Research Materials, and Other Related Samples*, NBS Special Publication 260-65, 1979.

AUTOMATED METHOD FOR ANALYZING IMAGES CONTAINING ELECTRON DIFFRACTION SPOTS

D. S. Bright and E. B. Steel

Electron diffraction patterns of polycrystalline substances are routinely obtained for small sample areas by use of the analytical electron microscope in the selected-area diffraction mode. These patterns typically appear in images on film that are analyzed manually.¹ Our diffraction images are digitized directly on the microscope with a television camera, or with a scanned diffracted electron beam. Sometimes, they are digitized later by optical scanning of a negative. Automated analysis of the digitized images yields basis vectors describing the single-crystal spot patterns.

Our applications often require the identification of a single particle or group of particles within an agglomerate of particles. In these cases, several particles of differing crystal type contribute to the diffraction image and yield several superimposed diffraction patterns. The particle of interest is oriented to a zone axis; the other particles are at random orientations. Thus the diffraction maxima from the particle of interest forms a regular array amid the less regularly positioned maxima from the other particles. Automated analysis of such images is often difficult because of overlapping diffraction images that yield complex combinations of rings, arrays of spots, and isolated spots.

The computer method presented here includes image processing to locate all of the spots in the image and an algorithm to select, from among these spots, the groups of spots that belong to regular arrays. Each array represents a single crystal and is described by a pair of basis vectors,¹ which is then used for compound identification by comparison with standard diffraction data.

As illustrated by the scan line in Fig. 1 or the mesh plot in Fig. 2, most of the diffraction maxima are spots or peaks consisting of a few pixels that are superimposed on diffraction rings on a large Gaussian-shaped background. The first step in processing such a diffraction image is to isolate the spots from the rings, the background, and the image of the beam stop. The isolation is accomplished by a two-dimensional top-hat filter² which, for the image in Fig. 1, is set for a spot radius of 1 pixel, a local background radius of 3 pixels, and a spot height above local background of 10 units (out of 255 full scale). This filter adequately isolates the spots from the other components in the image, as shown in Fig. 3.

The problem is to select, from all of the spots, a group or subset of spots that represents a single crystal and thus gives a pair of basis vectors. The basis vectors are two vectors of minimum length that subtend a minimum angle that describe the relative positions of a two-dimensional regular array of points. The coordinates of the spots in the top-hat-filtered image are first determined by an algorithm that segments the image into background pixels and spot pixels. Background pixels are set to zero intensity by the top-hat filter. Pixels of a single spot are contiguous with each other but not with pixels of other spots. The coordinates for each spot are the intensity-weighted averages of the pixel locations for each contiguous pixel group.

Given the spot positions, the algorithm selects a spot (somewhat arbitrarily from among the brighter spots that are near the center of the image) and examines the neighboring spots in an attempt to get an initial approximation for a pair of trial basis vectors. Each single trial basis vector must correspond to the spacing between three colinear, equally spaced spots that include the above selected spot. The details for selecting the trial pair of vectors will be published later. If a trial pair of basis vectors can be found, then the original spot probably belongs to a regular array of spots in the image.

The algorithm then starts again at the initially selected spot and, using the vectors, collects other spots belonging to the regular array by hopping from spot to spot throughout the image, thereby locating those spots which fit the basis vectors, until no more spots can be reached by moving along the vectors. The hops for one such process are shown by the arrows in Fig. 4. The collection process halts at any spot when no new neighboring

The authors are at the Center for Analytical Chemistry, National Bureau of Standards, Gaithersburg, MD 20899.

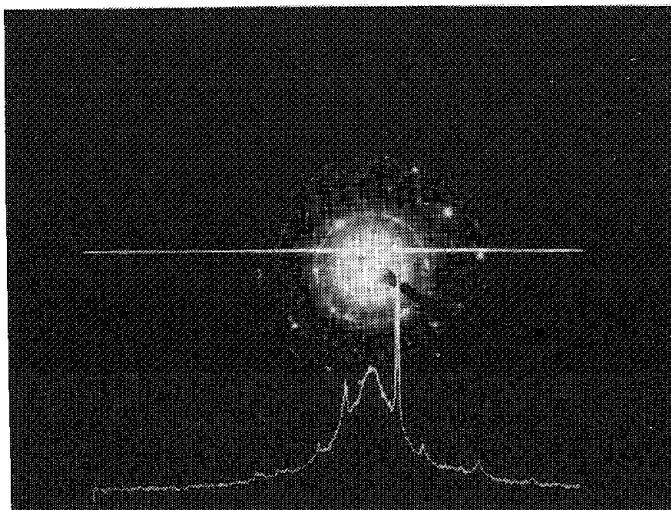


FIG. 1.--Original image with intensity profile taken horizontally across image just above beam center.

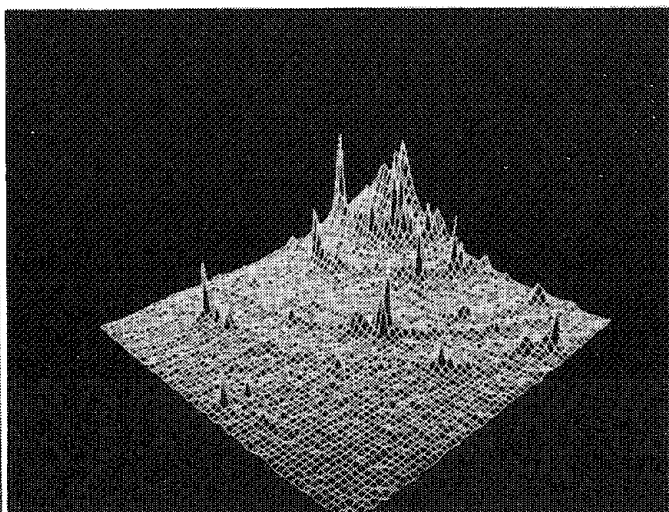


FIG. 2.--Mesh plot showing intensity as function for portion of original image just to the lower left of beam center.

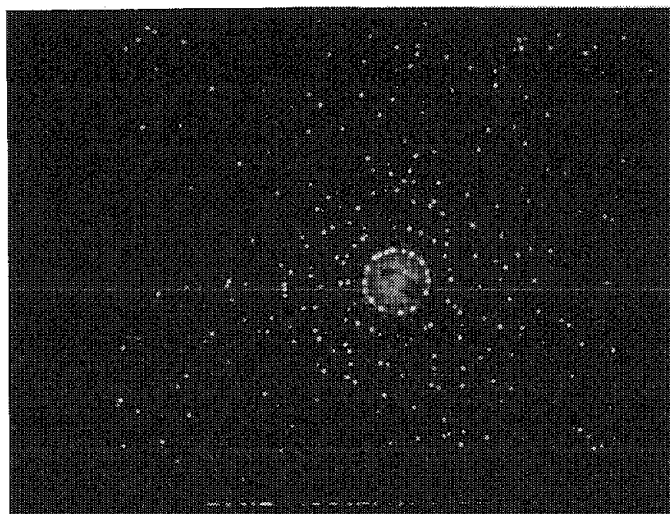


FIG. 3.--Top-hat-filtered image (dark background with the dimmer spots artificially brightened for display) superimposed on original image (Fig. 1).

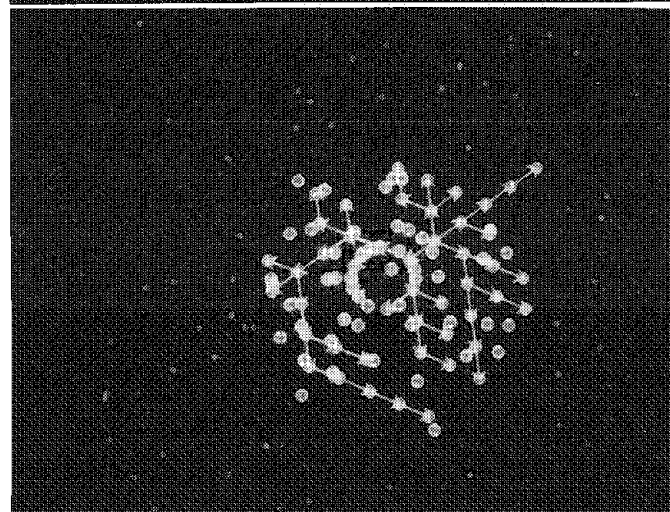


FIG. 4.--Automated array identification: brighter spots of Fig. 3 selected for analysis; 0 dots that belong to one regular array; \rightarrow search paths or "hops" used to find circled dots.

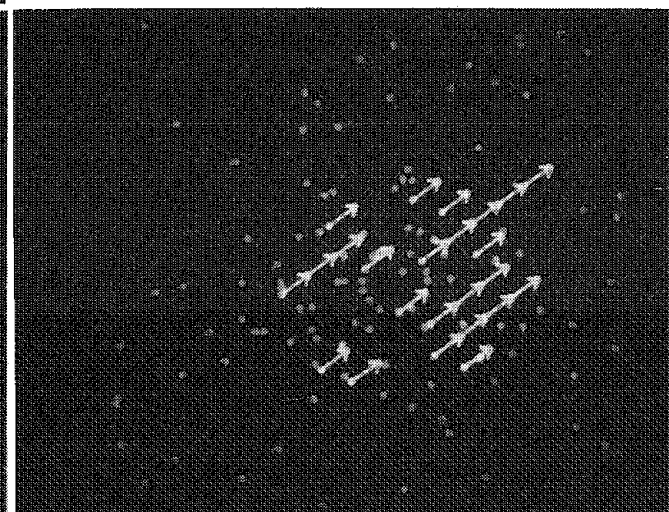


FIG. 5.--Refined array: all occurrences of one of the two basis vectors. After vectors are measured from image as differences in spot coordinates, they are averaged for final determination of basis vector.

spots can be reached by one hop in any direction allowed by the basis vectors. An error tolerance is built into the algorithm so that a spot, to be reachable, is allowed to be located within a small area of the image, rather than centered exactly on the tip of the vector.

The circled spots in Fig. 4 that have no associated arrow have been rejected by the algorithm as not lying in the array. The spots that are not circled are rejected by default, as these regions of the image were not reached from the initial spot by repeated applications of the basis vectors. In other images, the spots not selected by this process could be formed by electrons diffracted by another crystal and thus could be analyzed by re-application of the algorithm to them. However, in this image the spots were randomly spaced reflections of crystallites. The algorithm therefore halted after failing to find any other pair of basis vectors.

Once the spots have been selected, a more accurate determination of the basis vectors is calculated by averaging all of their occurrences between the selected spots. All the occurrences for one of the vectors used in Fig. 4 are shown in Fig. 5.

Conclusions

We have applied a computer method to the analysis of agglomerate particles that automates the analysis of spots in electron diffraction patterns. The method isolates the zone-axis diffraction pattern in a polycrystalline diffraction image by isolating the spots from other features of the image and then by selecting the spots that belong to a regular array. The method gives the basis vectors for the array that can then be used to identify the particle by comparison with standard diffraction data.

References

1. P. B. Hirsch et al., *Electron Microscopy of Thin Crystals*, London: Butterworths, 1965.
2. This reference describes one-dimensional top-hat-like filters: J. J. McCarthy and F. H. Schamber, "Least-squares fit with digital filter: A status report," in K. F. J. Heinrich et al., Eds., *Energy Dispersive X-ray Spectrometry*, NBS Special Publication 604, Washington: U.S. Department of Commerce, 1981.

7 Materials Analysis and Failure Analysis

ANALYSIS OF ATMOSPHERIC CORROSION PRODUCTS ON METALLIC COATINGS

J. J. Friel

Sheet steel coated with Al, Zn, or a combination of them is often used to resist atmospheric corrosion in applications involving outdoor exposure. The performance of Zn and Al-Zn alloy coatings in both atmospheric and laboratory tests has been previously reviewed by Friel and Townsend¹ and by Townsend and Zoccola.² The principal components of the atmosphere that react with these coatings are generally surmised to be SO₂ and NO_x gases in industrial environments and chlorides in marine environments, along with H₂O and CO₂ in both cases.

The analysis of corrosion products can provide information about these reactions but is hindered because of (1) limited mass, (2) interference from the substrate, and (3) lack of crystallinity. Previously Friel and Mehta³ examined various experimental techniques to analyze the corrosion products of Zn and Al coatings in an industrial atmosphere and found that amorphous sulfates of Al, Zn, and Fe were common. In this paper the study was extended to the marine environment, and a method of analysis was developed based on the SEM rather than the AEM.

Experimental

Panels of metallic-coated sheet steel were examined after 3 years of exposure to the marine atmosphere at Kure Beach, N.C., 25 m from the Atlantic Ocean. The panels are described in Table 1 along with original and present coating thicknesses determined metallographically. Samples were cut from the center of each panel. The skyward surface was examined in all samples, and the groundward side was examined in selected cases. The corrosion products were extracted from the metallic substrate on cellulose acetate and coated with about 20 nm of carbon. The acetate film with the particles on top was placed on a beryllium grid, and the acetate was dissolved in acetone leaving the carbon-coated corrosion products. The grid was then mounted on a carbon stub for scanning electron microscopy. The effect of this procedure is to eliminate interference from the substrate and minimize it from the surrounding grains. One sample of Al-Zn-coated sheet steel was mounted in cross section and polished by means of a lapping oil instead of water to preserve the interdendritic corrosion products within the metallic coating. These products were analyzed quantitatively for Al₂O₃, ZnO, and SO₃ with a JEOL 733 automated electron probe microanalyzer (EPMA). Water was included by difference. The EPMA was operated at 15 kV and 10 nA. The extraction replicas were examined with an Amray 1600 SEM, and selected samples were analyzed with a Philips EM400 AEM. The AEM was used to observe the smallest particles and to check for crystallinity. Even though crystallographic information is available from the AEM, the SEM is faster and yields more representative results. This improvement in confidence comes from the ability to examine more particles in a given period of time and also from the analysis of larger particles that make up the greatest volume of products on the surface. X-ray diffraction (XRD) was also carried out on coupons of the corroded sheet steel.

Results and Discussion

The results of SEM/EDS, AEM/EDS, and XRD analysis are given in Table 2. It can be seen that Al-sulfate is common on the coatings that contain Al, and this result is consistent with our earlier results in an industrial atmosphere.³ This phase is surely hydrated, but

The author is at the Homer Research Laboratories of Bethlehem Steel Corp., Bethlehem, PA 18016. The aid of Charles Santos is acknowledged for his sample preparation, and that of Linford Hahn and James Kerner for their assistance with the analyses.

the degree of hydration is not known. Selected area electron diffraction in the AEM confirmed that these particles are amorphous and thus are not detected by x-ray diffraction. However, XRD analysis is useful for compounds of metals with only light elements, such as $\text{Zn}_5(\text{CO}_3)_2(\text{OH})_6$. These elements are particularly difficult to confirm by energy-dispersive spectroscopy because only the metallic element appears in the spectrum and may be confounded with the pure metal. Unlike the Al-containing coatings, the Zn coating produced all crystalline products including Zn-sulfate; thus, XRD was the most informative technique. On the basis of all the data, a summary of the probable corrosion products forming on each of these coatings is given in Table 3.

In addition to the corrosion products, the surface of these coatings also contained NaCl, SiO_2 , and clay minerals, but these were easily identified. The remains of some marine microorganisms were also observed. The zinc coating was the only one on which chlorides were found. Evidence of small amounts of chlorine was present in some of the EDS spectra from all of the coatings, but individual chloride particles could not be located. However, the absence of chlorides may be due merely to dissolution in rainwater. The high concentration of sulfates, though, was a surprising finding. They would be expected in an industrial atmosphere, but not in a marine one. They occurred equally on the skyward and groundward sides and were highly adherent to the surface of the coating. In fact, they may provide protection from additional attack, although this possibility has not been demonstrated.

In an attempt to learn more about these compounds, the EPMA was used to analyze some of them found on the Al-Zn-coated steel. The microstructure of this coating consists of Al dendrites surrounding a Zn-rich interdendritic region. It is known that the Zn-rich area corrodes preferentially and the channels thus formed fill with corrosion products retarding further corrosion.² In the past it has been assumed that these products were zinc rich. However, our analyses show that Al-sulfate-hydrate containing various amounts of zinc is the principal interdendritic corrosion product. Examples of representative analyses are given below:

	wt %	±	Calculated Stoichiometry
Al_2O_3	50.5	1.7	$2\text{Al}_2\text{O}_3 \cdot \text{SO}_3 \cdot 7\text{H}_2\text{O}$
ZnO	0.7	0.05	
SO_3	18.7	1.6	
H_2O diff.	<u>30.1</u>		
TOTAL	100.0		
<hr/>			
Al_2O_3	66.7	1.9	$4\text{Al}_2\text{O}_3 \cdot \text{ZnO} \cdot \text{SO}_3 \cdot 4\text{H}_2\text{O}$
ZnO	13.7	1.3	
SO_3	8.4	0.8	
H_2O diff.	<u>11.2</u>		
TOTAL	100.0		

The analytical sensitivities given above are due to counting statistics alone and are 2σ values. Other uncertainties arising from the sample or within the instrument will increase these values. It is evident that the composition and extent of hydration is variable, but in each analysis, the calculated stoichiometry worked out closely to integral molar proportions of each component.

In addition to the samples exposed at the Kure Beach 25m lot, a sample of the Al-Zn coating exposed for three years 250 m from the ocean was also analyzed. The predominant corrosion product on this panel was once again Al-Zn-sulfate-hydrate. If sulfates are common as far as 250 m from the sea, the source of the sulfur is probably the atmosphere. These results demonstrate the significance of sulfur compounds in the atmosphere and imply that sulfur as well as chlorine must be considered when engineering a corrosion-resistant coating system for use in the marine atmosphere.

Conclusions

- Use of extraction replicas in the SEM or AEM permits qualitative analysis of atmospheric corrosion products on coated sheet steel.
- Metallographic polishing in lapping oil retains corrosion products for quantitative analysis with the EPMA.
- Sulfur is a significant factor in the process of atmospheric corrosion in the marine environment.

References

1. J. J. Friel and H. E. Townsend, "Corrosion resistance of zinc and zinc aluminum alloy coatings," *Sheet Metal Industries* 60: 506-507, 1983.
2. H. E. Townsend and J. C. Zoccola, "Atmospheric corrosion resistance of 55%Al-Zn-coated sheet steel: 13 year test results," *Materials Performance* 18: 13-20, 1979.
3. J. J. Friel and S. Mehta, "Industrial atmosphere corrosion products on metallic coatings," *Microbeam Analysis--1984*, 55-58.

TABLE 1.--Sample description.

Coating	Nominal composition	Coating thickness (μm)	
		1981	1984
Al-coated Type 2	Al	39	36
Galvanized	Zn	17	10
Galvalume*	Zn 55 Al 1.6 Si	32	28

*Galvalume Sheet Steel is Bethlehem Steel Corp.'s trademark for a product with the coating composition given above.

TABLE 2.--Analytical results and interpretation.

Technique	Al-coated	Zn-coated	Al-Zn-coated
SEM			
Results	Al,S	Zn,S; Zn	Al,Zn,S
Interpretation	Al-sulfate	Zn-sulfate Zn-(oxide, hydroxide, carbonate)	Al-Zn-sulfate
AEM			
Results	Al,S; Al	Zn	Al,S
Interpretation	Al-sulfate Al-hydroxide	Zn-(oxide, hydroxide, carbonate)	Al-sulfate Al-sulfate
XRD			
Results	$4\text{Al}_2\text{O}_3 \cdot \text{H}_2\text{O}$ $\text{Al}(\text{OH})_3$	$\text{Zn}_5(\text{CO}_3)_2(\text{OH})_6$ $\text{Zn}_5(\text{OH})_8\text{Cl}_2$ ZnSO_4 ZnO	$\text{Al}_2(\text{OH})_6 \cdot \text{H}_2\text{O}$ ZnO

TABLE 3.--Probable solid corrosion products.

Al-coated	Zn-coated	Al-Zn-coated
Al-sulfate-hydrate	$\text{Zn}_5(\text{CO}_3)_2(\text{OH})_6$ $\text{Zn}_5(\text{OH})_8\text{Cl}_2$	Al-Zn-sulfate-hydrate $\text{Al}_2(\text{OH})_6 \cdot \text{H}_2\text{O}$
$4\text{Al}_2\text{O}_3 \cdot \text{H}_2\text{O}$	ZnO	ZnO
$\text{Al}(\text{OH})_3$	ZnSO_4	

ELECTRON MICROPROBE DETERMINATION OF PHASE EQUILIBRIA IN THE Cu-As-Sn SYSTEM

J. F. Roeder and M. R. Notis

The Cu-As-Sn system is important in both archaeological and modern contexts. The majority of ancient Cu alloys with Sn and As are properly considered binary systems (Cu-As or Cu-Sn), whereas ternary Cu-As-Sn alloys might be expected, based on ore sources. However, some true ternary Cu-As-Sn alloy compositions have been found in artifacts.² Clearly, the effects of tin on arsenical copper of antiquity are not well understood. In the modern context, As is an important impurity in continuous copper smelting operations.³ Maes and de Stryker^{4,5} performed an extensive study of the Cu-As-Sn system and generated the only available equilibrium phase diagram. However, their techniques were restricted to thermal analysis, optical metallography, and limited x-ray work, so that tie lines were not determined for the system. In the present study, quantitative chemical analysis with an electron microprobe was used to determine tie-line end member compositions in various regions of the Cu-As-Sn system for two Cu-rich alloys isothermally transformed at 570 C. Quantitative electron metallography was used to check that the bulk compositions of the alloys were consistent with the tie-line results.

Experimental

Two 10g alloys with compositions Cu-2 wt% As-20 wt% Sn (alloy 1) and Cu-10 wt% As-2.5 wt% Sn (alloy 2) were melted at 1100 C under vacuum in sealed quartz ampoules and water quenched. Due to the high vapor pressure of arsenic over the melt, estimated to be as high as ~4 atm at 1100 C from available thermodynamic data,^{6,7} arsenic losses were expected. Alloy 1 was isothermally transformed at 570 C \pm 3 C for a total of 196 h. Alloy 2 was held at the same temperature for 100 h. After mounting and polishing, phase compositions of the transformed alloys were analyzed by point counting on a JEOL 733 electron microprobe operated at 20 kV accelerating voltage, 10 nA beam current, and 40° take-off angle, and equipped with a Tracor Northern TN2000 computer system. The ZAF correction technique was used to obtain composition in weight percent. Pure-element standards were used for Cu and Sn and a pure-NiAs standard was used for As. Bulk compositions were verified using the Image Processing Program available on the TN2000. This program calculated the area fraction for each phase present from color video images obtained at 300 \times magnification and generated from a backscattered electron (BSE) signal, smoothed by averaging nine nearest neighbors for each pixel in the video image (256 \times 256 pixels) and repainted into two colors. We determined the actual bulk composition by first converting area fraction to weight fraction (assuming a linear dependence of density on the experimentally determined compositions of the constituent phases) and then back calculating for the bulk composition.

Results and Discussion

BSE images of alloys 1 and 2 are shown in Figs. 1 and 2. The phases present in alloy 1 are: γ (light) + α (dark); in alloy 2: α (dark) + Cu₃As (light). Quantitative line profiles across various regions of the specimens revealed a high degree of homogeneity; thus, the alloy microstructures appear to be very near equilibrium. Both alloys were found to be near equilibrium after the specified holding times, but alloy 1, which contained considerably more Sn, took longer to equilibrate. After 100 h, alloy 1 contained a layer with higher Sn content than either phase at the α/γ particle interfaces and of varying thicknesses up to ~5 μ m. After an additional 96 h at 570 C, a homogeneous microstructure was obtained.

The authors are affiliated with the Department of Metallurgy and Materials Engineering, Lehigh University, Bethlehem, PA 18015. This project was supported by an INCO Fellowship.

TABLE 1.--Experimentally determined tie-line compositions.

Phase Boundary	Composition (wt%)		
	Cu	As	Sn
$\alpha/\alpha+\gamma$	85.32 \pm 2.04	2.40 \pm 0.54	12.28 \pm 0.93
$\gamma/\alpha+\gamma$	73.72 \pm 1.65	1.54 \pm 0.54	24.74 \pm 1.08
$\alpha/\alpha+\text{Cu}_3\text{As}$	91.23 \pm 2.46	7.19 \pm 0.65	1.59 \pm 0.15
$\text{Cu}_3\text{As}/\alpha+\text{Cu}_3\text{As}$	71.94 \pm 2.22	27.87 \pm 1.17	0.14 \pm 0.24

TABLE 2.--Original and experimentally determined bulk compositions.

Alloy	Composition originally weighed out (wt)			Experimentally determined (wt%)		
	Cu	As	Sn	Cu	As	Sn
1	77.99	1.99	20.03	78.2	1.9	20.0
2	87.51	10.01	2.48	88.9	9.7	1.4

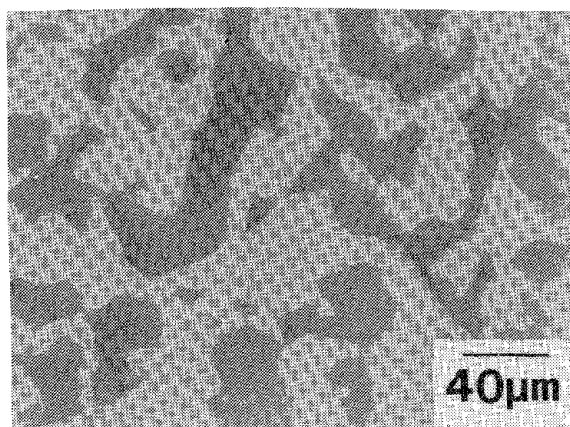


FIG. 1.--Backscattered electron image of Alloy 1 isothermally transformed at 570 C for 196 h.

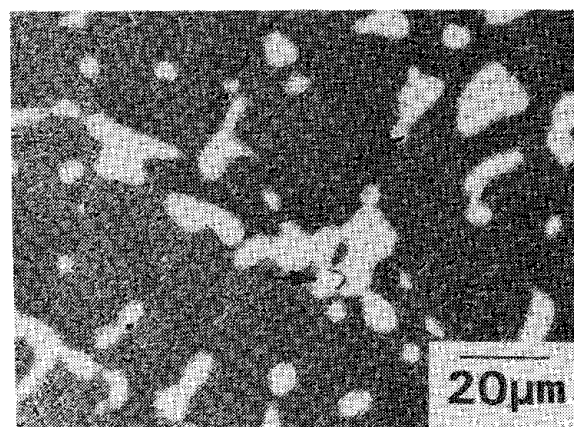


FIG. 2.--Backscattered electron image of Alloy 2 isothermally transformed at 570 C for 100 h. Arrow indicates SnO_2 inclusions.

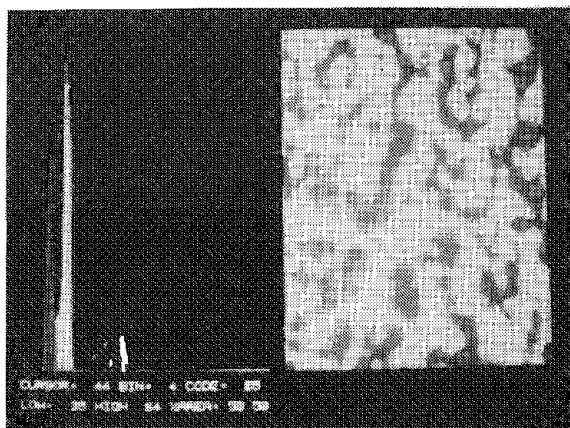


FIG. 3.--Digital image of Alloy 1 and histogram for digital image.

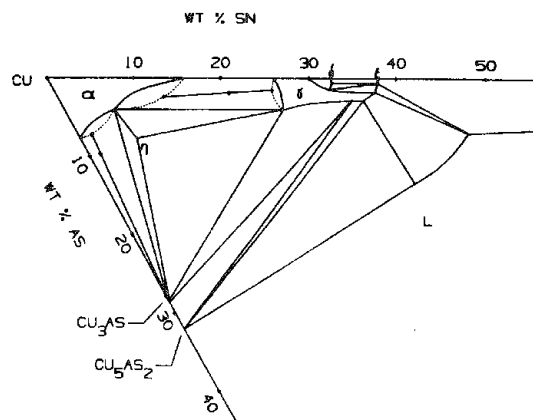


FIG. 4.--Isothermal section in Cu-rich corner of Cu-As-Sn system at 569 C (from Ref. 5).

This result indicates that Sn is the slow diffusing species, which is not surprising considering the large atomic size of Sn compared to As.

Figure 2 reveals the presence of cuboidal inclusions in alloy 2. These inclusions produced energy-dispersive x-ray spectra containing only Sn peaks and with a very small amount of Cu, probably from the matrix. We found the inclusions to be SnO_2 by quantitative analysis using the ZAF technique with a stoichiometric SnO_2 standard and computing oxygen by difference. These oxide inclusions, which probably resulted from a poor vacuum during melting, were assumed to have no effect on the metallic phase equilibria.

The experimentally determined tie-line end member compositions for each alloy are given in Table 1. Ten points were taken for each average and the errors represent deviations from the mean for a 99% confidence level. The bulk composition of another alloy, not reported here in detail, was analyzed both by the IPP package technique and by quantitative area scanning using a 6×6 grid matrix in an adjacent region of a specimen. The results agreed quite well: 67.3 wt% Cu-9.8 wt% As-22.9 wt% Sn by IPP vs 67.2 wt% Cu-10.6 wt% As-22.2 wt% Sn by quantitative area scanning. These results demonstrate the utility of the IPP approach to bulk composition determination in comparison with the more tedious area-scanning method.

Figure 3 shows a smoothed and repainted digital color image as well as the histogram for the color image of a representative area of alloy 1. As mentioned previously, the light phase is γ and the dark phase is α . The digital image in Fig. 3 was generated from the same area shown in Fig. 1. In all, five areas were analyzed for each alloy. These results also indicate a homogeneous microstructure. The experimentally determined bulk compositions and starting alloy compositions are given in Table 2. The results are in excellent agreement for alloy 1, but Sn losses from alloy 2 appear significant. This result was consistent with the presence of SnO inclusions. Surprisingly little arsenic was lost from either alloy.

All results for alloys 1 and 2 are shown in Fig. 4 superimposed on an isothermal section for 569 C redrawn on a computer graphic system. All of the pertinent phase boundaries except the $\alpha + \text{Cu}_3\text{As}/\text{Cu}_3\text{As}$ boundary appear to need correction. Although Maes and de Stryker^{4,5} investigated some 250 alloy compositions, very few of their alloys were located near the ends of the tie lines in the Cu-rich corner determined here to be at variance with their work. Given the present results, these boundaries were redrawn with dashed lines also shown in Fig. 4. The redrawn phase boundaries near the Cu corner are consistent with each other based on a rule of phase diagram construction⁸ which states that the boundaries of a single-phase region in the corner of a ternary phase diagram must both extend into either one or two phase regions. The redrawn $\gamma/(\alpha + \gamma)$ boundary places some question on the overall shape of the γ phase field in the ternary system. Finally, the bulk compositions of the two alloys fall on the independently determined tie-lines, which shows that the results from the IPP package are consistent with the point counting.

References

1. J. A. Charles, "Early arsenical bronzes: A metallurgical view," *Am. J. Archaeology* 71: 21-26, 1967.
2. E. R. Caley, "Chemical composition of ancient copper objects of South America," in W. J. Young, Ed., *Application of Science in Examination of Works of Art*, Boston: Museum of Fine Arts, 1970, 53-61.
3. M. Nagamori and P. J. Mackey, "Thermodynamics of copper converting: Part II. Distribution of Au, Ag, Pb, Zn, Ni, Se, Te, Bi, Sb and As between copper matte and slag in the Noranda process," *Met. Trans.* 9B: 567-579, 1978.
4. R. Maes and R. de Stryker, "The copper-tin-arsenic constitution diagram: Part I. Solidification reactions," *Trans. AIME* 236: 1328-1336, 1966.
5. R. Maes and R. de Stryker, "The copper-tin-arsenic constitution diagram: Part II. Reactions in the solid state," *Trans. AIME* 236: 1336-1341, 1966.
6. O. Kubaschewski and C. B. Alcock, *Metallurgical Thermochemistry*, New York: Pergamon Press, 1979, 358.
7. D. Lynch, "Activity of arsenic in copper," *Met. Trans.* 11B: 623-629, 1980.
8. F. N. Rhines, *Phase Diagrams in Metallurgy: Their Development and Applications*, New York: McGraw-Hill, 1956, 131.

METASTABLE PHASE FORMATION IN Ni-IMPLANTED Al: AN ANALYTICAL ELECTRON MICROSCOPE INVESTIGATION

D. M. Follstaedt and A. D. Romig Jr.

Ion implantation is being widely used to form metastable alloys in the near-surface region (~ 0.01 - $1.0 \mu\text{m}$) of metals.^{1,2} By athermal injection of ions with energies from a few keV up to several MeV, virtually any atomic species can be alloyed into any host metal, independently of many of the thermodynamic constraints that apply to thermal alloying processes. Implanted alloy microstructures are currently being extensively investigated in attempts to arrive at a more general understanding of the phases that are produced.³ The phase types include metastable solid solutions, amorphous phases, and second crystalline phases.

Al-Ni Alloys: Background

Alloys of Al and Ni have been shown to be a useful model system for the study of metastable phase formation with the techniques of ion implantation and ion irradiation as well as pulsed melting. This single-alloy system exhibits a number of metastable modifications to its equilibrium phase diagram, including the absence of equilibrium phases, and the formation of metastable solid solutions and an amorphous phase. Furthermore, the Al-Ni alloys can be studied over a wide concentration range by several ion-beam techniques,³ which allows the metastable features to be characterized as a function of concentration and type of ion beam process. Figure 1(a) shows the Al-rich portion of the Al-Ni equilibrium phase diagram as taken from Hansen.⁴ Studies of Ni-implanted $\langle 110 \rangle$ Al

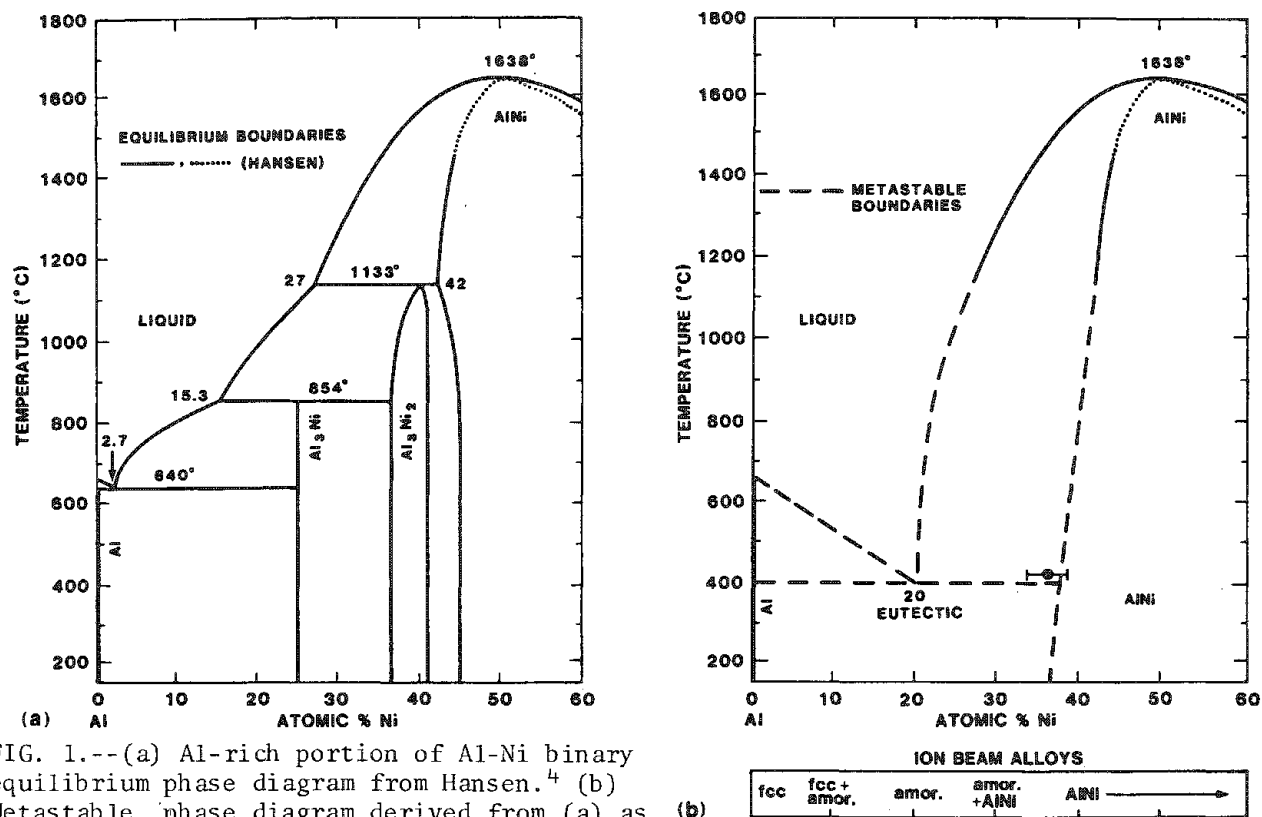


FIG. 1.--(a) Al-rich portion of Al-Ni binary equilibrium phase diagram from Hansen.⁴ (b) Metastable phase diagram derived from (a) as described elsewhere⁵ to account for microstructures observed after melt quenching. Bar graph at bottom shows phases observed in ion-beam alloys implanted at room temperature. Datum is composition of AlNi precipitates as determined in the present study.

The authors are at Sandia National Laboratories. This work was supported by the U.S. Department of Energy under Contract DE-AC04-76DP00789.

at concentrations up to 32 at.% Ni yielded the following microstructural observations:⁵ (1) the equilibrium phases Al_3Ni and Al_3Ni_2 do not form; (2) for <20 at.% Ni a two-phase alloy with fcc Al plus an amorphous phase forms; (3) for 20-25 at.% Ni, a single, amorphous phase forms; and (4) for 32 at.% Ni another two-phase mixture of the amorphous phase plus ordered bcc AlNi forms. Several other ion-beam treatments have also been used to produce metastable Al(Ni) alloys: ion-beam mixing of alternating Al/Ni layers,^{6,7} heavy-ion irradiation of the (pre-existing) compounds Al_3Ni , Al_3Ni_2 and AlNi,^{6,8,9} and Al implantation of Ni.¹⁰ These techniques produce essentially the same phases for the same overall composition as those discussed above for Ni-implanted Al. Taken with the observation of two-phase microstructures on either side of the pure amorphous phase, these results suggest that some measure of metastable thermodynamic equilibrium has been attained between fcc Al, the amorphous phase, and AlNi during the ion irradiations that produced many displacements for each alloy atom.³ All the ion-beam treatments were done at room temperature where vacancies are mobile in Al, which may have contributed to the equilibration.

Metastable Al-Ni alloys have also been produced by pulsed surface melting,^{5,11} and the resulting phases as a function of concentration show only minor differences from those produced by the ion-beam methods. A metastable phase diagram that accounts for the final phases observed after pulsed melting has been given earlier⁵ (Fig. 1b). The equilibrium phases Al_3Ni and Al_3Ni_2 were removed, and the liquid of the fcc Al and AlNi phases in Fig. 1(a) were extrapolated to lower temperatures to meet at a eutectic. The amorphous phase is identified with a quenched liquid near a eutectic concentration, and the curvature of the AlNi liquidus was therefore adjusted to intersect the fcc Al liquidus at 20 at.% Ni for which a single phase amorphous alloy was observed. Since the phases resulting after the ion irradiation treatments are the same as those produced by melt quenching, this diagram is also appropriate for the ion-beam alloys. The phases observed are those just above the eutectic temperature, with the qualification that the liquid phase becomes the amorphous phase, as indicated in the bar diagram at the bottom of Fig. 1(b). The part of the metastable phase diagram below the eutectic does not apply to either pulse surface melted or the ion beam-produced alloys since the eutectic reaction: liquid \rightarrow fcc Al + AlNi does not occur.

For a better description of the ion-implanted alloys with such a diagram, the composition ranges of the metastable crystalline phases need to be determined. Ion channeling analysis¹² has been used to obtain a substitutional concentration of 0.2 at.% Ni in the fcc Al lattice which, although small, exceeds the maximum equilibrium solid solubility by a factor of 10. In this paper we examine the lower limit on the Ni concentration needed to form AlNi in Ni-implanted Al by using energy-dispersive spectroscopy (EDS) with Al and Ni characteristic x rays in an analytical electron microscope (AEM).

Analysis of Al-32 at.% Ni

An alloy implanted with 32 at.% Ni was previously found to contain AlNi precipitates plus the amorphous phase,³ and was used here for AEM analysis of the AlNi phase. The polished <110> Al single-crystal sample was implanted with nominal fluences of 1.0×10^{17} Ni/cm² at 160 keV, 0.5×10^{17} Ni/cm² at 80 keV, and 0.5×10^{17} Ni/cm² at 40 keV, in that order. Rutherford-backscattering analysis showed that the Ni concentration peaked at 32 at.% within 15 nm of the surface, was ~30 at.% to a depth of 75 nm, decreased to 20 at.% at ~100 nm, and fell to zero at ~300 nm.¹¹ The measured Ni areal density was 2.8×10^{17} Ni/cm².

The microscopy was done with a JEOL 100 CX transmission electron microscope at 120 kV. The sample was electro-jet polished from the unimplanted side with a solution of 450 ml methanol, 50 ml 70% nitric acid and 30 ml H₂O at -70 C with a single-sided jet thinner.¹³ A bright field image showing the AlNi particles (50-300 nm in diameter) is shown in Fig. 2. The cross section schematic above the micrograph shows the depth-dependent microstructure deduced from our analysis. The particles are seen to be suspended on an aluminum oxide film which extends across the "hole" in the sample made by the electro-jet polishing. The electron diffraction pattern from a large area on the oxide film (area α in Fig. 2) shows a set of diffuse rings from the oxide and a sharp ring pattern which indexes to AlNi. In the thicker material (area β), the particles are also seen with the same areal number density as on the oxide film, $\sim 2 \times 10^8/\text{cm}^2$. The electron diffraction pattern from this more restricted area shows a diffuse ring from the amorphous metal phase with

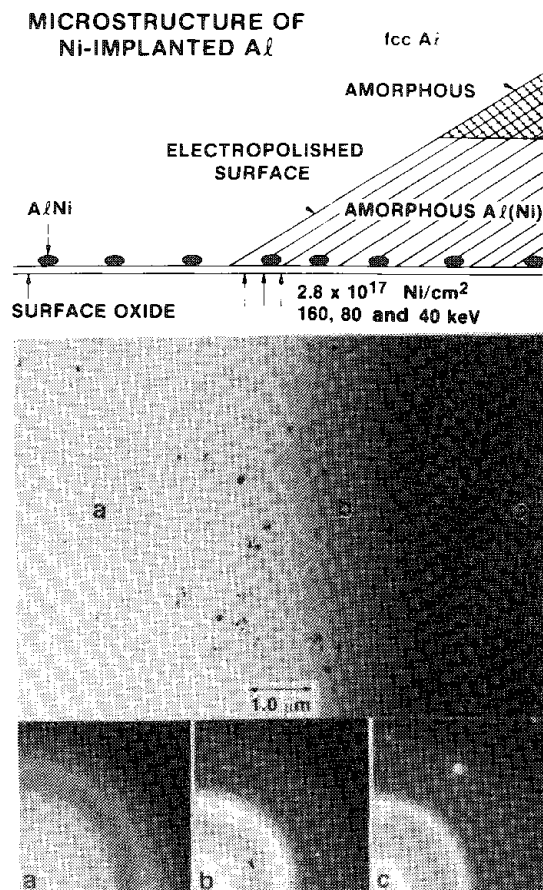


FIG. 2--Microstructure of Al(Ni) alloy used in this study as determined by TEM. Cross-section schematic shows depth-dependent microstructure as determined by examination of successively thicker regions (a-c) in bright-field micrograph below it. Diffraction patterns (a), (b), (c) are from correspondingly labeled areas on micrograph.

other alloys with <20 at.% Ni, we infer that this two-phase structure is present beneath the amorphous layer. The constant particle density and the suspension on the oxide film imply that the AlNi particles formed at the metal/oxide interface, which may have promoted their nucleation.

Because the AlNi particles are isolated on the oxide layer, we can measure their concentration ratio by EDS without having to account for effects due to the amorphous Al(Ni) phase. The EDS was done with a high take-off angle detector (72°). The microscope's anticontamination shield which surrounds the sample was cooled with liquid nitrogen, and the Be sample holder was cooled to -189°C . With the low sample temperature, carbon deposits were not observed on analyzed areas. The x rays were collected in the conventional TEM mode at 120 kV by use of the free lens control on the first condenser to obtain a spot size slightly smaller than the particle size. Monte Carlo modeling of electron trajectories showed that beam broadening ($< 10\text{ nm}$) for our sample thickness (see below) was not significant. The spectra were collected in pairs with 100s count times each. The beam was first placed on a particle to obtain a spectrum, and then a second spectrum was collected from the oxide film about 2-3 particle diameters away. Fifty such pairs of spectra were accumulated and summed to obtain two total spectra from the particles and from the oxide layer, which are shown in Fig. 3.

It is clear from the size of the Al peak in the oxide spectrum that one must correct for the influence of the oxide. Aluminum oxide is initially present on the Al surface

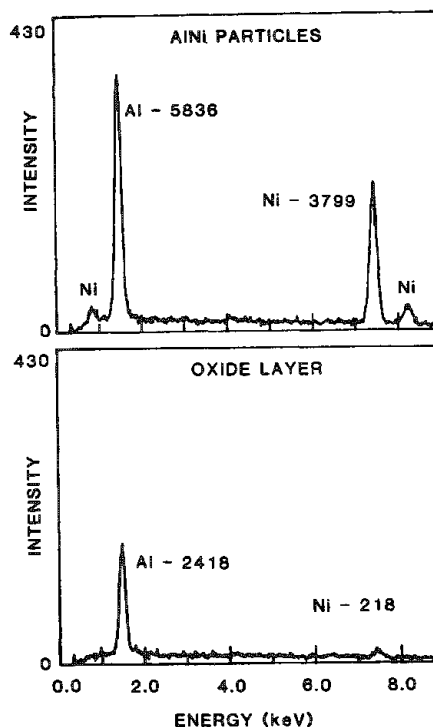


FIG. 3.--Cumulative EDS spectra from AlNi particles and from nearby areas of oxide layer on which particles were suspended.

several superimposed randomly oriented reflections from AlNi. A few weak (100) AlNi reflections (shown by arrows) are seen, indicating that some ordering of the Al and Ni atoms into their respective sublattices is present in this phase after the implantation. In the thickest areas (area c), crystalline fcc Al can be observed as indicated by the bright spot reflections in the third diffraction pattern. Based on the observation of two-phase (amorphous + fcc) microstructures in

before implantation. Because of the chemical affinity of Al for O, and oxide layer is probably present on the sample during the Ni implantation in our vacuum system ($\sim 10^{-6}$ Torr). Because the Ni is injected through the oxide layer during implantation, we believe that the particles are just beneath the oxide layer, as indicated schematically in Fig. 2. The metal-oxide interface may provide the nucleation site for the AlNi phase. Nuclear reaction analysis with a deuterium ion beam of Ni-implanted Al gave an O areal density equivalent to ~ 5 nm thickness of Al_2O_3 . From the ratio of Al counts in the two spectra in Fig. 3 and their electron transparency, we judge the particles to be also ~ 5 nm thick. The Monte Carlo modeling indicates that for this geometry and thicknesses, a simple subtraction of the counts in the oxide spectrum would yield the net signal from the particles. Calculation showed that for these thicknesses, corrections for x-ray absorption are not necessary. It is also possible that an oxide film has been deposited on the sample by electropolishing from the back side. Given the similar expected thickness of this film, the subtraction would also correct for it. Examination of individual spectra and of portions of the total accumulated spectra showed the same relative Al and Ni intensities, which indicates that any Ni redeposition was uniform; the low Ni counts from the oxide show that Ni was not incorporated into the oxide and that any Ni redeposition from the polishing solution was minimal.

The composition of the AlNi particles was determined by the standardless ratio technique, where the compositions are related to the measured x-ray intensities by

$$\frac{C_{\text{Al}}}{C_{\text{Ni}}} = k_{\text{AlNi}} \frac{I_{\text{Al}}}{I_{\text{Ni}}}$$

C_{Al} and C_{Ni} are the concentrations in weight percent and I_{Al} and I_{Ni} are the background-corrected x-ray intensities for Al and Ni, respectively, and k_{AlNi} is the sensitivity factor. The standardless ratio relationship is valid only if the thin film criterion, which requires that x-ray absorption not be significant, is not violated.¹⁴ Calculations showed that absorption effects were not significant for our analyzed thicknesses. The value of k_{AlNi} can be calculated from first principles or can be determined from homogeneous standards of known composition.¹⁴ For this work it was measured from standards because the energy of the Al $K\alpha$ line is low enough (1.48 keV) that it may be absorbed in the EDS x-ray detector (i.e., by the Be window, Au contact layer, Si dead layer, or film of carbonaceous contaminant). Hence, unless the detector efficiency is well known and these absorption effects can be quantified, an accurate value of k_{AlNi} cannot be calculated. Two other Ni-implanted alloys containing 17 ± 1 and 20 ± 1 at.% Ni, as determined by Rutherford backscattering,⁵ were used as standards to determine k_{AlNi} . The standards were less than 50 nm thick so that absorption effects did not affect the intensity ratio at the 5% level of significance. The experimentally determined value was $k_{\text{AlNi}} = 0.85 \pm 0.05$, where the error was determined by the uncertainty in Ni concentrations of the standards, and was consistent with first principles calculations. Assuming a 7.5 μm Be window, a 20 nm Au contact layer, a 0.3 μm Si dead layer, and no carbonaceous contaminant, the calculated value of $k_{\text{AlNi}} = 0.84$ was obtained; for a typical thickness of 0.3 μm C the value was 0.85.¹⁴ The calculated values are accurate to ± 0.04 ; hence the overall uncertainty in k_{AlNi} obtained by combining experimental and calculated results is probably less than this value. Thus knowing k_{AlNi} for our instrument, one can determine the composition of the unknown AlNi. The FWHM (full width at half maximum) Al $K\alpha$ and Ni $K\alpha$ background-corrected peak intensities are given in Fig. 3. After subtracting the contribution from the oxide layer, the resulting intensities from the 50 analyzed particles were $I_{\text{Ni}} = 3581 \pm 126$ and $I_{\text{Al}} = 3418 \pm 182$, where the error is $2/\sqrt{N}$ for N total counts in the two spectra. The calculated intensity ratio $I_{\text{Al}}/I_{\text{Ni}}$ then is 0.954 ± 0.061 . Combining the errors in $I_{\text{Al}}/I_{\text{Ni}}$ and k_{AlNi} through Gaussian quadrature, and allowing for 10% relative uncertainty in the subtraction procedure, one obtains for the composition of the AlNi particles produced by ion implantation $C_{\text{Ni}} = 36.5 \pm 2.5$ at.%.

Discussion

The AlNi particles are in contact with the amorphous phase containing a lower concentration of Ni, and thus we interpret the above concentration to be the minimum Ni concentration needed to form AlNi in an ion irradiation environment. From Fig. 1(a), we see

that the value is significantly less than the minimum equilibrium Ni concentration (45 at.% Ni) in AlNi at room temperature where the implantation was done. It is also less than the absolute minimum found in the equilibrium diagram, 42 at.% Ni, which occurs at 1133 C. This minimum occurs at the peritectic reaction below which liquid + AlNi transform to Al_3Ni_2 . In the absence of Al_3Ni_2 and Al_3Ni , we expect the AlNi phase field to be extended to lower Ni concentrations as shown in the metastable diagram of Fig. 1(b). We can further interpret the 36.5 ± 2.5 at.% Ni concentration as the AlNi concentration in equilibrium with the amorphous phase (quenched liquid) at approximately the eutectic temperature; however, this interpretation assumes complete equilibration between the AlNi and amorphous phases, which may not have been fully achieved. The value is in reasonable agreement with tangential extrapolation of the AlNi solidus from high temperatures, as shown in Fig. 1(b).

Our result is consistent with results obtained by ion irradiation of Al_3Ni_2 , which transformed to AlNi.⁸ The equilibrium AlNi lattice below 50 at.% Ni contains vacancies in the Ni sublattice of the B2 (CsCl) structure.¹⁵ The Al_3Ni_2 structure is obtained from that of AlNi by the further ordering of vacancies on certain planes; hence the transformation to the more disordered AlNi phase is not unexpected. Our minimum Ni concentration for AlNi extends to the Al-rich side of Al_3Ni_2 , and is consistent with this transformation.

Our observation of (100) AlNi reflections, the observations by others of retained order in irradiated AlNi,¹⁶ and the known structure of Al-rich AlNi¹⁵ indicate a high concentration of vacancies in the AlNi phase examined here. Assuming no Al atoms on the Ni sublattice, we calculate 21 at.% vacancies in the AlNi lattice, or 42% empty Ni sublattice sites for 36.5 at.% Ni.

Finally, the extent to which Fig. 1(b) applies to ion-beam-modified alloys remains to be fully determined. The metastable diagram was derived from liquid-quenched alloys, and ion-implanted alloys show some deviations from its predictions. For instance, implantation to 25 at.% produces a single amorphous phase, whereas liquid quenching gives AlNi precipitates in an amorphous matrix; the latter result is consistent with Fig. 1(b) and the former is not. Other studies also show that compound nucleation does not occur in ion-implanted alloys at the same concentration for which it occurs in melt-quenched alloys.¹⁷ Hence we place the minimum Ni concentration for AlNi produced by ion implantation on the metastable diagram obtained from melt-quenching studies with caution. Nonetheless, the metastable phase diagram for Al-Ni in Fig. 1(b) with the extended AlNi phase accounts for the phases observed in a wide range of ion beam alloys. The extent to which such metastable phase diagrams can account for the phases observed in other ion-implanted alloy systems remains to be established.

Summary

The work presented above demonstrates that AEM can be used to obtain the compositions of small precipitates in ion implanted metals. The EDS measurement establishes a lower limit of 36.5 ± 2.5 at.% for the Ni concentration needed to form AlNi in Ni-implanted Al, and probably in Al-Ni alloys formed by other ion beam methods also. This value is taken to be the minimum Ni concentration of the AlNi phase near the eutectic temperature in Fig. 1(b), with the caveat that the full equilibration of AlNi with the amorphous phase implied by use of Fig. 1(b) may not have been achieved.

References

1. B. M. Ullrich, Ed., Proc. Int'l. Conf. on Ion Beam Modification of Materials, *Nucl. Inst. and Meth.* B-7/8, 1985.
2. G. K. Hubler et al., Eds., *Ion Implantation and Ion Beam Processing of Materials*, New York: North-Holland, 1984, 117.
3. D. M. Follstaedt, in Ref. 1, p. 11.
4. M. Hansen, *Constitution of Binary Alloys*, New York: McGraw-Hill, 1958, 2d ed., 118.
5. D. M. Follstaedt and S. T. Picraux, in L. H. Bennett et al., Eds., *Alloy Phase Diagrams: Extended Abstracts*, Pittsburgh: Materials Research Society, 1984, 94.
6. L. S. Hung, M. Nastasi, J. Gyulai, and J. W. Mayer, *Appl. Phys. Lett.* 42: 672, 1983.

7. M. Nastasi, L. S. Hung, and J. W. Mayer, *Appl. Phys. Lett.* 43: 831, 1983.
8. M. Nastasi, L. S. Hung, H. H. Johnson, J. W. Mayer, and J. M. Williams, *J. Appl. Phys.* 57: 1050, 1985.
9. J. L. Brimhall, H. E. Kissinger, and L. A. Charlot, *Rad. Eff.* 77: 273, 1983; also Ref. 2, p. 163.
10. D. I. Potter, M. Ahmed, and S. Lamond, in Ref. 2, p. 117.
11. S. T. Picraux and D. M. Follstaedt, in J. M. Poate et al., Eds., *Surface Modification and Alloying: Aluminum*, New York: Plenum Press, 1983, 287.
12. S. T. Picraux, D. M. Follstaedt, J. A. Knapp, W. R. Wampler, and E. Rimini, in J. F. Gibbons et al., Eds., *Laser and Electron-Beam Solid Interactions and Materials Processing*, New York: North-Holland, 1981, 575.
13. J. H. McDonald, Sandia National Laboratories Report No. SAND81-0368, April 1981.
14. A. D. Romig Jr., Sandia National Laboratories Report No. SAND84-1422, October 1984.
15. P. Georgapoulos and J. B. Cohen, *Acta Met.* 29: 1535, 1981.
16. J. L. Brimhall and H. E. Kissinger, *Proc. Symp. High-temperature Ordered Inter-metallic Alloys*, Boston, 1984, to be published by North-Holland.
17. D. M. Follstaedt, J. A. Knapp, and P. S. Peercy, *J. Non-Crystalline Solids* 61/62: 23, 1984.

WELD METAL HOT-CRACKING OF HASTELLOY ALLOYS C-22 and C-276: A STUDY BY ANALYTICAL ELECTRON MICROSCOPY

M. J. Cieslak, A. D. Romig Jr., and T. J. Headley

Weld metal hot-cracking in multicomponent alloy systems is often the result of the formation of small volume fractions of nonequilibrium constituents along solidification grain boundaries. These constituents arise as a result of the segregation phenomenon accompanying weld solidification and often serve to extend the solidification temperature range well below the equilibrium solidus. The purpose of this study was to identify and characterize as to crystal structure and composition, by analytical electron microscopy (AEM), the phases associated with weld metal hot-cracking in Hastelloy alloys C-22 and C-276.

Background

Hastelloy C-22 and C-276 are nickel-base alloys designed for use in severely corrosive environments such as those encountered in the marine, petrochemical, pulp and paper, and chemical process industries. In the mill annealed condition, these alloys are single phase. Their crystal structure is face-centered cubic. They are solid-solution strengthened alloys not hardenable by aging treatments. The thermal expansion coefficient of these alloys is such that they are compatible materials for certain glass-sealed hermetic electrical connectors. In many applications, welding of such connectors to other components is required. As part of a larger investigation of the weldability¹ of solid-solution strengthened nickel-base alloys, this study describes the solidification and subsequent solid-state transformation behavior of Hastelloy C-22 and C-276 gas-tungsten-arc welds.

Experimental Procedure

Welding and Metallographic Specimen Preparation. The mill analyses of the alloys studied are given in Table 1. The base metal microstructure prior to welding was that characteristic of mill annealed material, i.e., single-phase austenitic. The susceptibility of each alloy to fusion zone hot-cracking during autogenous gas-tungsten-arc welding was quantified by the Varestraint Test.^{2,3} The welding parameters used were 100A, direct current, electrode negative, and 13.5 V machine voltage at a travel speed of 20 cm/min.

Subsequent to welding, metallographic specimens were removed from regions of the fusion zone containing hot-cracks. These specimens were mounted in epoxy and polished through 0.05 μm alumina. Microstructures were revealed by electroetching in a solution of 10% chromic acid. The specimens were then carbon coated and examined in a Hitachi S-520 SEM.

Analytical Electron Microscopy. The samples for AEM analysis were sliced from the bulk weld metal with a low-speed carbide saw and ground to a thickness of approximately 125 μm . Standard 3mm-diameter disks were cut from the thin sheet with a mechanical punch. Electron-transparent foils were produced by electrojet thinning at 15 V in a 10% perchloric acid in methanol solution at approximately -65 C. Following electrochemical thinning, the foils were placed in an ion mill to increase the amount of thin area and to remove any electrolyte residue. The thin foils were examined in a JEOL 100C AEM operated at 100 kV, equipped with a low take-off angle x-ray detector and a Tracor-Northern TN2000 multichannel analyzer.

Electron diffraction was used to identify uniquely each intermetallic phase prior to x-ray microanalysis. The phases were then analyzed with a focused beam in the STEM mode (nominal Gaussian beam diameter of 18 nm). The particles analyzed were all 0.5 to 1.0 μm in diameter. The nominal thickness of the foil at the points of analysis was 50 to 100 nm. Under these experimental conditions, the beam scattering volume was contained entirely within the phase with no contribution from the adjacent matrix.

The authors are at Sandia National Laboratories at Albuquerque, NM 87185.

TABLE 1.--Alloy compositions.

Element	Hastelloy C-22	Hastelloy C-276
Ni	56.96	55.58
Cr	21.22	15.83
Mo	13.43	15.56
Fe	3.17	5.44
W	3.29	3.93
Co	0.84	0.96
Mn	0.31	0.50
Si	< 0.02	0.03
V	0.14	0.18
C	0.006	0.003
S	< 0.002	0.002
P	0.010	0.014

TABLE 2.--Pertinent characteristic x-ray lines.

Line	E (keV)	Line	E (keV)
W M_{α}	1.78	Fe K_{β}	7.06
W M_{β}	1.84	W L_I	7.39
P K_{α}	2.02	Ni K_{α}	7.47 *
Mo L_I	2.02	Co K_{β}	7.65
Mo L_{α_1}	2.29	W L_{α}	8.40
Mo L_{β_1}	2.40	Ni K_{β}	8.91
Mo L_{β_2}	2.52	W L_{β_4}	9.52
Mo L_{γ}	2.62	W L_{β_1}	9.67
Cr K_{α}	5.41 *	W L_{β_3}	9.82
Cr K_{β}	5.95	W L_{β_2}	9.96
Fe K_{α}	6.40 *	W L_{γ}	11.28
Co K_{α}	6.93 *	Mo K_{α}	17.44 *
* Line(s) used in analysis.		Mo K_{β}	19.63

When the material being analyzed by energy dispersive x-ray analysis contains a large number of elements, the problem of x-ray line overlap must be addressed. The line overlap problem is intensified when one of the component elements is of high atomic number and may therefore have both characteristic K and L or L and M lines in the energy range of interest. Table 2 summarizes the pertinent characteristic x-ray lines for this study. The x-ray lines used for the chemical analysis have been indicated. Care must be taken when selecting regions of integration to minimize problems of line overlap. Two nonstandard procedures were used to obtain suitable integrated intensities to quantify the Co and W. The Fe K_{β} line interferes with the Co K_{α} line. The Fe K_{β} line was stripped from the Co K_{α} with an empirical procedure described elsewhere.⁴ The stripping procedure requires measuring the Fe K_{α} to K_{β} ratio at 100 kV from a pure Fe standard. With the obtained normalization constant the Fe K_{β} contribution to the (Co K_{α} + Fe K_{β}) in the unknown can be estimated from the measured Fe K_{α} intensity, allowing for a calculation of the true Co K_{α} intensity. For high-atomic-number materials, the M lines are generally not suitable due to x-ray absorption effects.⁵ Unfortunately, the W L_{α} line could not be used due to interference from the Co K_{β} and Ni K_{β} . However, the grouping of W $L_{\beta_1,2,3,4}$ lines occurred in a clean portion of the spectrum. The family of L_{β} lines was therefore used for the quantitative analysis.

The compositions were determined with the standardless ratio technique, where the compositions are related to the measured x-ray intensities by $C_x/C_{Ni} = k_{xNi}(I_x/I_{Ni})$, where $x = \text{Fe, Cr, Co, Mo, or W}$; C is composition in weight percent; I is the integrated x-ray intensity; and k_{xNi} is the Cliff-Lorimer sensitivity factor. The standardless ratio equation is valid only if the thin film criterion, which requires that x-ray absorption and fluorescence in the sample are negligible, is not violated.⁶ The values of the sensitivity factors k_{xNi} were determined from a well-homogenized sample of alloy C-276 with a well-known composition. The k factor determinations utilized the Co K_{α} stripping procedure. The $k_{W_{Ni}}$ was determined for the family of W L_{β} lines. It was not possible to integrate over the same relative portion of each x-ray line (e.g., Full Width at Half Maximum, FWHM) due to line overlap. However, no error is introduced into the analysis if the same integration windows are used for the experimental determination of k_{xNi} and for the analysis of the unknown. The effect of variable integration windows can be seen by a comparison of the experimental values of k_{xNi} to values of k_{xNi} calculated from first principles, as illustrated by W L_{β} and Co K_{α} in Table 3.⁷ It is believed that the differences in the experimentally determined and calculated sensitivity factors for W L_{β} and Co K_{α} arise from the inability to select the same relative portions of these peaks affected by overlap and ambiguous background. The compositions of the unknowns were

determined with the experimental values of k_{xNi} in the standard Sandia data reduction routine.⁷ X-ray absorption in these samples was not significant. At the 5% level of significance, the thin film criterion is violated only at a thickness exceeding 250 nm.⁶

TABLE 3.--Sensitivity factors k_{xNi} (at 100 kV).

Elemental Ratio	k_{xNi}	
	Experimental	Calculated ⁷
Cr/Ni	0.83 ± 0.02	0.85
Mo/Ni	3.41 ± 0.2	3.41
Fe/Ni	$0.95 \pm .03$	0.92
W(L_{β})/Ni	9.09 ± 0.6	2.80
Co/Ni	$1.62 \pm .08$	0.99

Results and Discussion

Weld samples examined in the SEM were observed to contain what appeared to be a single-phase constituent associated with hot cracks. Examples are shown in Figs. 1 and 2. In addition to the relatively large volume of constituent located along the crack path, smaller pockets can also be observed at scattered interdendritic regions in these micrographs. Weld metal hot-cracking in both alloys was always found to be associated with a solidification grain boundary constituent. Solidification grain boundaries are regions of increased weld metal segregation and as such are the most likely places for the formation of relatively large amounts of a nonequilibrium constituent.

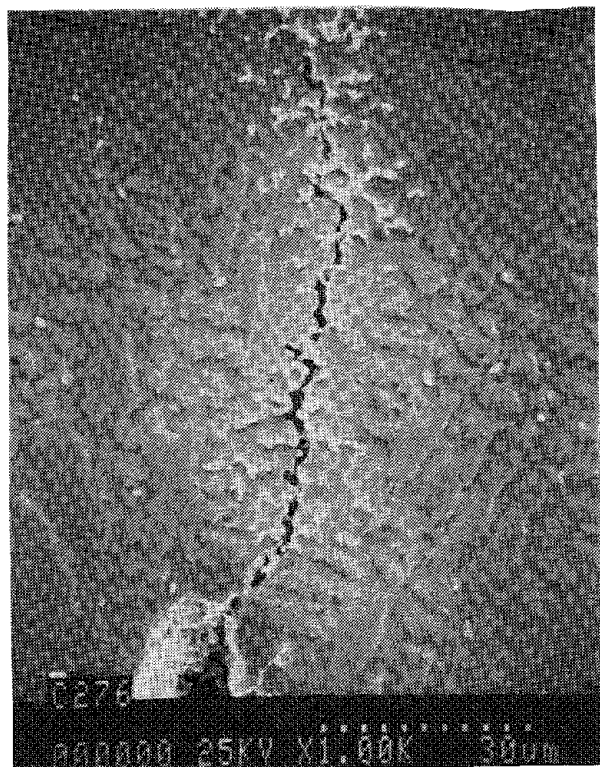


FIG. 1.--SEM micrograph of hot-cracked region in Hastelloy C-276 weld metal.

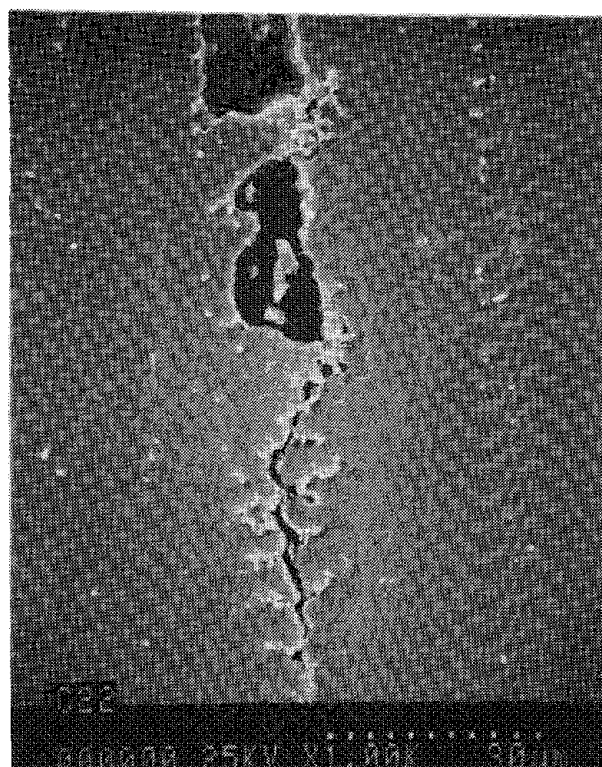


FIG. 2.--SEM micrograph of hot-cracked region in Hastelloy C-22 weld metal.

The welds were analyzed in the AEM to establish the structure and composition of the weld metal phases. The apparent single phase constituent associated with hot cracks was found to be a combination of two or more phases. In addition to the austenite matrix, both alloys contained topologically close-packed (TCP) phases. Alloy C-276 contained the P phase (orthorhombic: $a = 0.907$ nm, $b = 1.698$ nm, $c = 0.475$ nm) and the μ phase (hexagonal: $a = 0.476$ nm, $c = 2.591$ nm) in an austenitic matrix (FCC: $a = 0.352$ nm). Alloy C-22 contained the P phase, the μ phase, and the σ phase (tetragonal: $a = b = 0.908$ nm, $c = 0.475$ nm) in an austenitic matrix. Figures 3 and 4 show thin-foil micrographs, selected-area electron diffraction patterns, and STEM/EDS spectra from the various TCP phases found in this study.

It was observed during the AEM analysis that approximately equal amounts of μ phase and P phase existed in the weld metal of Alloy C-276. In Alloy C-22 weld metal approximately 80% of the TCP phase constituent is P phase and 20% is σ phase. Only trace amounts of μ phase were observed in the C-22 weld metal.

Table 4 lists the average concentration of each element in each phase. The values within the parentheses are the sample standard deviations. For comparison purposes, literature values are also included in this table, along with the method of data generation. As can be seen, a substantial amount of variation exists among the different data, but the trends in the present data, discussed below, were found to correlate with established phase diagrams.¹²⁻¹⁴ Some of the differences among the published data can be explained solely from a metallurgical viewpoint. The microstructures in the present study were produced during the solidification and cooling of weld metal, an inherently nonisothermal, nonequilibrium process. At least some of the TCP phases observed were formed directly from the liquid and not by solid-state diffusion processes. In addition to metallurgical differences, the current method of data acquisition was different from the other two studies. The microprobe data were obtained from extractions containing an unknown amount of M_6C carbide and will not be considered further. The Mo K α and the W L $\beta_{1,2,3,4}$ x-ray lines were used in the present analysis instead of the Mo L and W M lines used in the earlier investigation.¹¹

The similarity in composition of the various TCP phases required that the individual

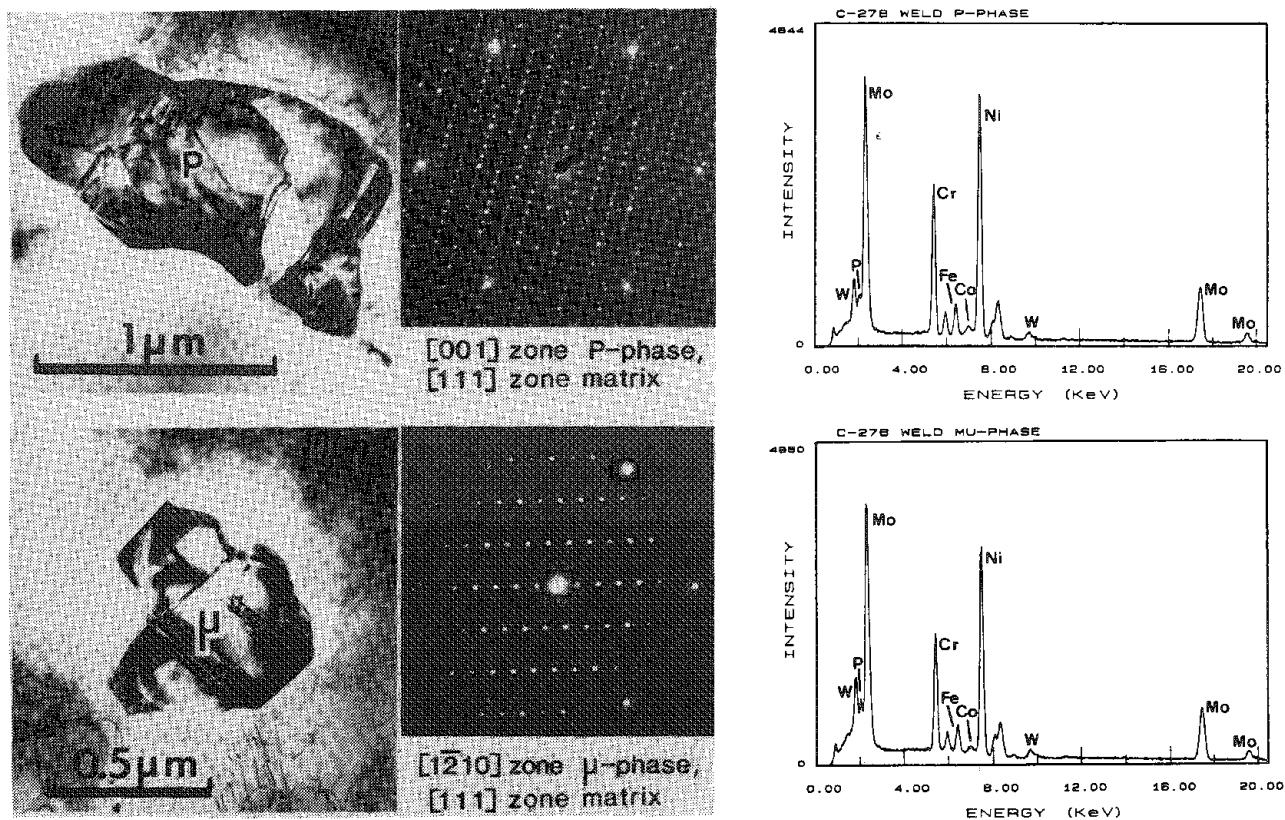


FIG. 3.--TEM micrograph, SAD pattern, and EDS spectrum from TCP phases found in Hastelloy C-276 weld metal.

chemistry data points be examined closely to determine trends between the compositions of the various phases. Histograms for the Cr, Mo, and W contents from a number of particles of the TCP phases and the remaining austenitic (γ) matrix are shown in Fig. 5. Several trends can be observed. Within Alloy C-276, the Cr content decreases in the following order: γ phase, P phase, μ phase. The Mo content of μ phase is greater than that of P phase. The W content of P phase and μ phase are approximately equal and both are higher than that of γ . Within Alloy C-22, the Cr content decreases in the following order: σ phase, P phase $\approx \gamma$, μ phase. The Mo content decreases in the following order: μ phase, P phase, σ phase. The W content decreases in the following order: μ phase, P phase, σ phase, γ . The Mo content of the remaining γ matrix was always less (Table 4) than for any of the TCP phases. In all cases the Fe content of the matrix was higher than that of the TCP phases. Co was not found to partition preferentially to any of the TCP phases. Small amounts of phosphorus were also found associated with the TCP phases. No attempt was made to quantify this element. The small weight fraction (Table 1) present in the bulk alloys made experimental determination of an appropriate sensitivity factor impossible.

Ternary Ni-Cr-Mo phase diagrams can be found in the literature for a limited number of temperatures.¹²⁻¹⁴ Figure 6 shows the Ni-Cr-Mo ternary diagrams recently determined by Raghavan et al.¹⁴ by AEM techniques. All of the phases observed in both weld metals are possible equilibrium phases in the Ni-Cr-Mo system.

The following observations can be made concerning these diagrams. The μ phase is not stable at near-solidus (1250 C) temperatures. At 1250 C, P phase is stabilized relative to σ phase by increasing the Mo content and decreasing the Cr content. The Ni contents of P and σ phase are approximately the same. The same chemistry relationship between P and σ phase exists at 850 C, except that in addition to P and σ phase, the μ phase exists, which is stabilized by higher Mo and lower Cr content than either of the other two phases.

It can also be shown that within the composition region of interest the following transformations must occur as the temperature falls from 1250 C to 850 C: $P \rightarrow \mu$ and $\sigma \rightarrow P$. As an example, an alloy of composition 50Ni-35Mo-15Cr (Pt. 1, Fig. 6) clearly resides within the $\gamma + P$ field at 1250 C. The same alloy is within the $\gamma + \mu$ field at 850 C, necessitating a $P \rightarrow \mu$ transformation. Similarly, an alloy of composition 50Ni-20Mo-30Cr (Pt. 2, Fig. 6), which lies clearly within the $\gamma + \sigma$ at 1250 C, exists within the $\gamma + P$ field at 850 C, requiring the transformation $\sigma \rightarrow P$. It can also be seen that the single phase μ field exists at 850 C in the same composition space that the P phase occupies at 1250 C. In addition, the lower Cr regions of single phase σ stability at 1250 C become regions of P stability at 850 C.

Bloom and Grant¹³ have determined the liquidus surface for the Ni-Cr-Mo system (Fig. 7). Although liquid/solid phase relationships were not determined explicitly, the authors suggested regions of specific solidification transformations. In the vicinity of 40-60% Ni, 20-40% Mo, and 10-30% Cr, the possible solidification phases are γ , P, and σ . In all cases, γ is the primary solidification phase with the TCP phases forming at the terminal stages of solidification. Specifically, the following solidification sequences can be inferred from their investigation: $L \rightarrow L + \gamma \rightarrow \gamma$ for Ni-rich alloys, $L \rightarrow L + \gamma \rightarrow L + \gamma + \sigma \rightarrow \gamma + \sigma$ for higher Cr, lower Mo compositions, and $L \rightarrow L + \gamma \rightarrow L + \gamma + P \rightarrow \gamma + P$ for higher Mo, lower Cr compositions. A crossover between P and σ solidification was suggested at approximately 20% Cr.

Proposed Solidification and Transformation Sequence

Before proposing a solidification sequence for Alloys C-276 and C-22, we must place them in the proper positions on the available Ni-Cr-Mo ternary diagrams. From a strictly theoretical standpoint, this is not possible as the alloys are not pure ternary systems. It is proposed that the remaining solute elements, in particular Fe and W, be treated as equivalents of certain of the major alloying elements. This proposal is similar to the Cr and Ni equivalent approach for austenitic stainless steel weld metal.¹⁵ The grouping of the various elements will be shown to be both reasonable from a physical metallurgy standpoint and consistent with the data generated in this study and other work.

The weight fraction of W is combined with the weight fraction of Mo to form a Mo equivalent, Mo_{eq} . Both Mo and W are BCC elements whose refractory nature suggests a similarity in bonding characteristics. The data in Table 4 indicate that W partitions to the TCP phases, the opposite behavior of Ni, which suggests that an equivalence in behavior between W and Ni does not exist. The table also shows that for Alloy C-22, in

TABLE 4.--Phase compositions--
weight percent.

Phase	Ni	Mo	Cr	W	Fe	Co
C-276						
μ	33.2(0.8)	40.9(0.8)	16.2(0.8)	6.3(1.6)	3.5(0.3)	1.0(0.5)
P	33.5(0.8)	39.7(1.8)	15.7(0.8)	6.5(1.6)	3.7(0.2)	0.8(0.4)
Matrix	57.0(2.3)	16.0(1.8)	16.3(0.4)	4.2(0.8)	5.6(0.3)	1.0(0.3)
Nominal	55.55	15.55	15.53	3.93	5.44	0.96
C-22						
μ	33.1(2.4)	38.7(0.2)	19.3(0.7)	6.3(1.1)	2.1(0.2)	0.6(0.2)
P	32.6(0.8)	37.4(1.0)	21.7(0.7)	6.3(1.1)	2.2(0.2)	0.9(0.4)
σ	34.5(0.8)	34.9(0.4)	23.4(1.3)	4.2(1.2)	2.2(0.1)	0.8(0.2)
Matrix	58.5(1.2)	12.7(0.8)	21.8(0.6)	2.0(0.7)	8.4(0.1)	0.8(0.2)
Nominal	56.96	13.43	21.22	3.28	8.17	0.84
Ref. 9: C-276 *						
μ (780°C)	42.8	24.5	18.7	6.7	6.1	1.3
μ (870°C)	50.8	19.5	20.0	2.4	6.7	0.6
μ (880°C)	44.8	22.4	16.8	9.2	5.8	1.0
Nominal	55.94	16.01	16.11	3.86	6.46	0.92
* Microprobe Analysis of Extracted Residue (traces of MoC included)						
Ref. 11: C-276 **						
μ	28.0(2.4)	49.5(2.2)	11.0(0.4)	7.5(2.8)	2.0(0.2)	1.5(0.1)
P	27.9	48.0	13.3	4.0	4.9	1.7
Nominal	57.0	15.5	15.06	3.76	6.4	2.16
** AEM/EDS Analysis						

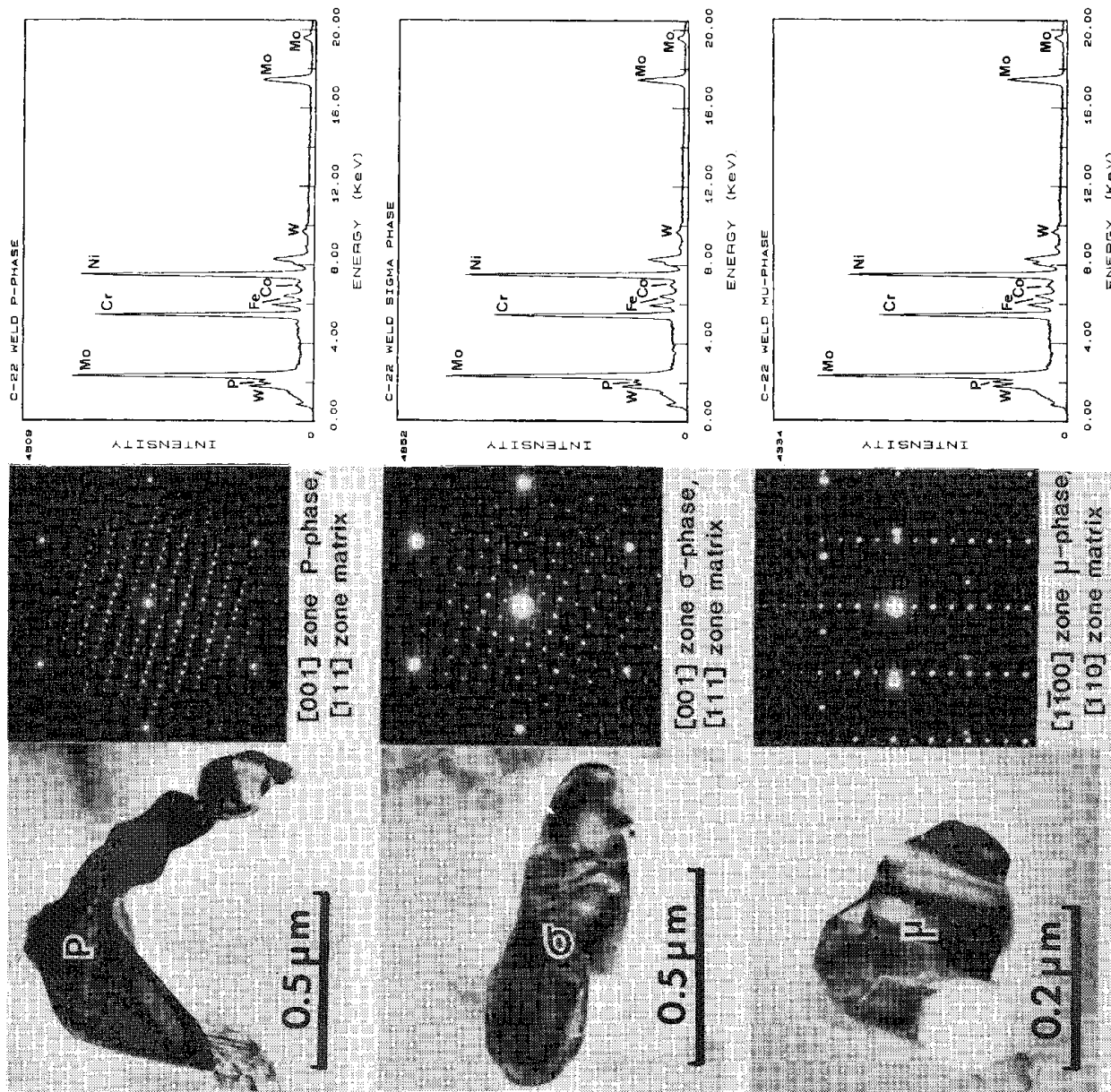
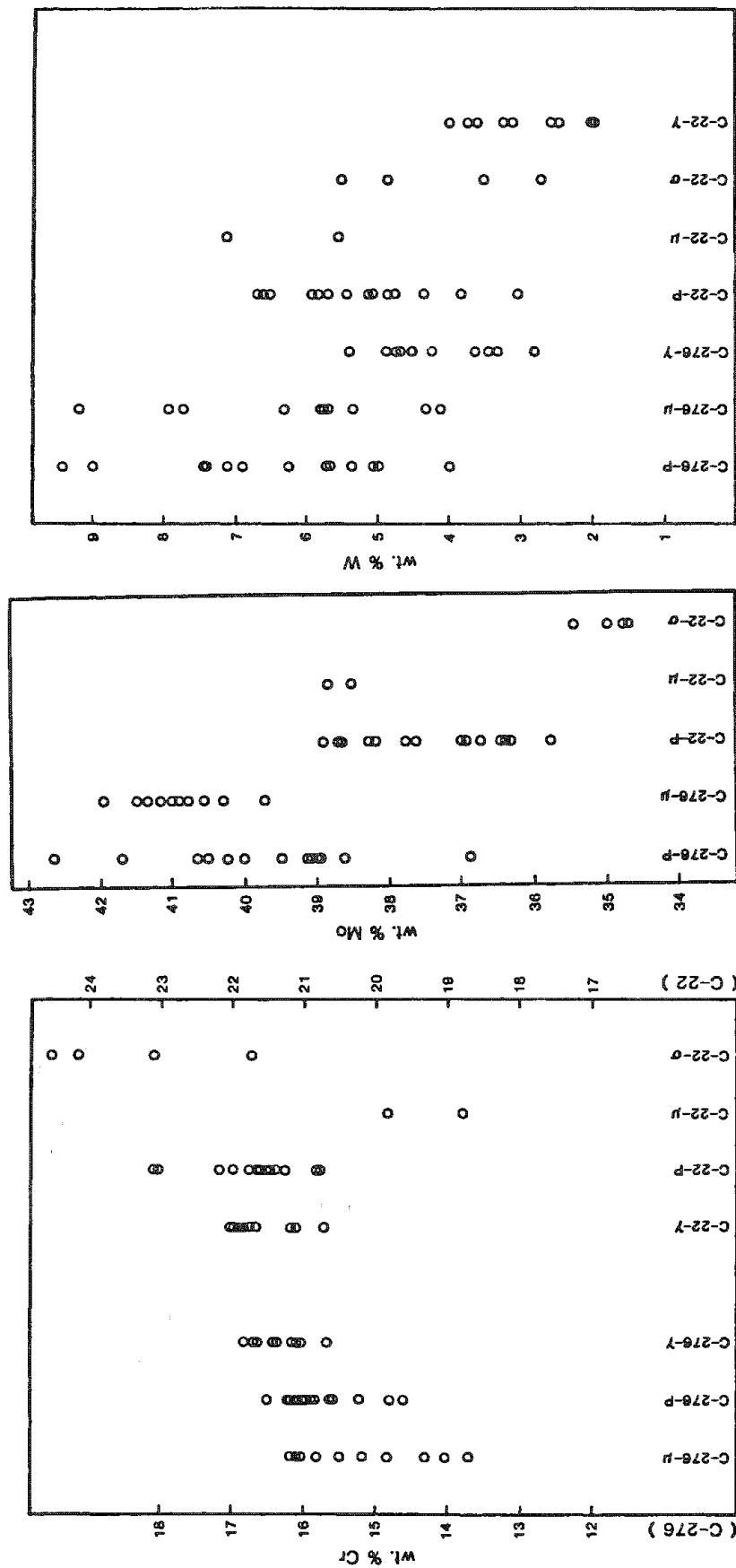


FIG. 4.--TEM micrograph, SAD pattern, and EDS spectrum from TCP phases found in Hatelloy C-22 weld metal.



(c)

(b)

(a)

FIG. 5.--Histograms of alloy content as determined by AEM for (a) Cr, (b) Mo, and (c) W in various phases found in weld metal examined.

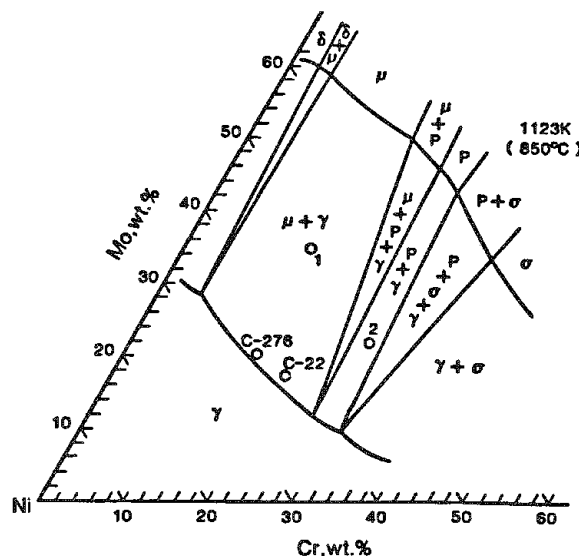
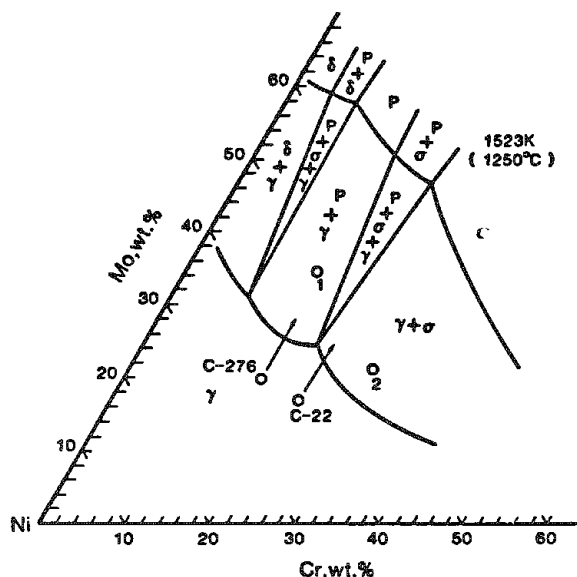


FIG. 6.--Isothermal sections of Ni-Cr-Mo ternary system, after Raghavan et al.¹⁴ (a) 1523K section at 1250 C, (b) 1123 K section at 850 C.

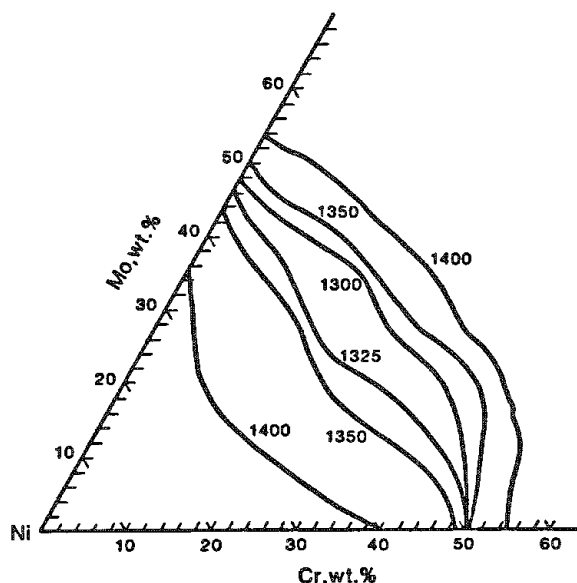


FIG. 7.--Liquidus isotherms for the region of interest in the Ni-Cr-Mo ternary system, after Bloom and Grant.¹³

which the P, μ , and σ phases exist, the W content of the σ phase is less than either of the other two TCP phases. σ phase is stabilized by increasing Cr content, whereas the P and μ phases are stabilized by increasing Mo content, which suggests a similarity in chemical behavior between Mo and W.

The Fe weight fraction is combined with the Ni weight fraction to form a Ni equivalent, Ni_{eq} . Within most of the high-temperature region under consideration, elemental Fe has the FCC structure, the same as Ni. In reviewing Table 4 again, we see that the Fe content of the residual austenite matrix is greater than that for all TCP phases examined in this study. This is the same partitioning effect shown by Ni and suggests a similarity in chemical behavior. It can also be shown within experimental error that the partitioning ratio for Fe, $\%Fe_{TCP}/\%Fe_{\gamma}$, is the same as the partitioning ratio for Ni, $\%Ni_{TCP}/\%Ni_{\gamma}$, when the compositions of all TCP phases are averaged together within a single alloy. The value of both partitioning ratios is approximately 0.6.

At the present time, it is assumed that all other alloying elements combine with Ni and Fe to form part of the Ni equivalent. In the present study, Co was found in approximately equivalent quantities in all phases, which suggests that it is relatively inert. Earlier AEM analysis¹¹ indicated that Co does not partition to the TCP phases, but remains preferentially in the matrix. This result supports the grouping of Co in the Ni equivalent. The Co content of the C-276 in the earlier study was approximately twice that in the present work and therefore any partitioning effect would have been easier to detect. The Cr equivalent, Cr_{eq} , is simply the alloy Cr content.

With these assumptions, an equivalent composition can be calculated from the mill analyses for both C-22 and C-276, and these compositions can then be positioned on the phase diagrams. The equivalent composition for the two alloys are given as follows:

C-276

$$\text{Ni}_{\text{eq}} = 64.68 \quad \text{Cr}_{\text{eq}} = 15.83 \quad \text{Mo}_{\text{eq}} = 19.49$$

C-22

$$\text{Ni}_{\text{eq}} = 62.06 \quad \text{Cr}_{\text{eq}} = 21.22 \quad \text{Mo}_{\text{eq}} = 16.72$$

These compositions have been plotted on the phase diagrams of Fig. 6 and represent a starting point for understanding the transformation behavior in these alloys.

The nonequilibrium behavior of weld solidification results in both segregation of alloying components and the formation of phases not expected in an equilibrium environment. Even under global nonequilibrium conditions, the phase diagram controls the solidification path. From a starting composition and liquidus temperature, an alloy solidifies by sliding down the liquidus/solidus gradient until either the liquid phase is completely transformed or until an invariant reaction is reached at which point the remaining liquid will solidify essentially isothermally.

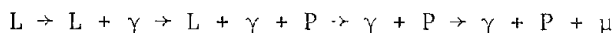
An examination of the liquidus surface (Fig. 7) reveals that in the composition region of interest, the liquidus isotherms are essentially normal to the Cr isopleths and decrease in temperature with decreasing Ni content. This result implies that solidification would occur at a constant Cr concentration and that Mo would segregate at the expense of Ni to final solidification volumes, promoting the solidification of the TCP phases.

Due to the lack of the appropriate solidus surface, the expected solidification path (arrows) for C-276 and C-22 are plotted on the 1250 C phase diagram (Fig. 6a). This is the closest available isothermal section to the solidus. The paths indicate that σ phase would be the expected TCP phase to solidify at the terminal stages of solidification in Alloy C-22. P phase would be expected to form at the terminal stages of solidification in Alloy C-276. This finding correlates well with the solidification reactions suggested by Bloom and Grant.¹³

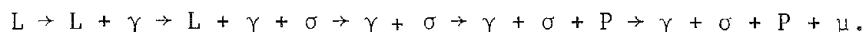
Subsequent transformation on cooling of the solidification TCP phases can be expected to occur by the mechanisms described earlier. That is, P phase can be expected to transform to μ phase and σ phase can be expected to transform to P phase. This result correlates well with the observed phases in each weld metal. The C-276 welds contain only P phase and μ phase. The C-22 welds contain predominantly σ phase and P phase. The trace amounts of μ phase in the C-22 weld metal are probably indications of the beginning of the transformation of the P phase to μ phase. The cooling rates in weld metal are rapid enough that complete transformation probably does not occur.

The overall transformation sequence which leads to the observed room temperature microstructures are proposed to occur as follows:

C-276



C-22



Summary

The proposed phase transformation sequences in Hastelloy C-22 and C-276 have been developed from existing phase diagram data, the application of basic solidification theory, and from extensive AEM phase analyses.

The TCP phases which form during weld metal solidification are P phase in Alloy C-276 and σ phase in Alloy C-22. Hot-cracking occurs during the solidification of these phases. The apparent single-phase constituents observed along hot cracks in the SEM micrographs are the room temperature remnants of both the solidification TCP phases (P in C-276, σ in C-22) and their subsequent transformation phases (μ in C-276, P and μ in C-22).

Conclusions

1. Only by AEM techniques can the solidification and transformation sequences in these welds be determined.
2. With the proper experimental approach, L β lines, in this case W L β , can be used for a quantitative AEM analysis.
3. The proposed transformation sequence for Hastelloy C-276 weld metal is
 $L \rightarrow L + \gamma \rightarrow L + \gamma + P \rightarrow \gamma + P \rightarrow \gamma + P + \mu$.
4. The proposed transformation sequence for Hastelloy C-22 weld metal is
 $L \rightarrow L + \gamma \rightarrow L + \gamma + \sigma \rightarrow \gamma + \sigma \rightarrow \gamma + \sigma + P \rightarrow \gamma + \sigma + P + \mu$.
5. The TCP phases associated with weld metal hot-cracking in Hastelloy C-276 and C-22 are P phase and σ phase, respectively.
6. Ni, Cr, and Mo equivalents can be used to predict the phase transformation sequence in Hastelloy C-276 and C-22.
7. The apparent (in SEM) single-phase constituents observed along weld metal hot cracks are actually a complex combination of TCP phases. These constituents are comprised of both remnants of solidification TCP phases (P in C-276, σ in C-22) and their subsequent solid-state transformation products.

References

1. M. J. Cieslak, unpublished research at Sandia National Laboratories, Albuquerque, NM, 1985.
2. W. F. Savage and C. D. Lundin, "The Varestraint test," *Welding Journal*, Oct. 1965, p. 433S.
3. W. F. Savage and C. D. Lundin, "Application of the Varestraint test to the study of weldability," *Welding Journal*, Nov. 1966, p. 497S.
4. A. D. Romig Jr., "Quantitative x-ray microanalysis of U-Nb alloys with the scanning transmission electron microscope," *Microbeam Analysis--1981*, 249.
5. A. D. Romig Jr., "Quantitative x-ray microanalysis of uranium alloys with the analytical electron microscope," *J. Microscopy*, 1984, p. 191.
6. J. I. Goldstein, J. L. Costley, G. W. Lorimer, and S. J. B. Reed, "Quantitative x-ray analysis in the electron microscope," *SEM/1977*, 315.
7. A. D. Romig Jr., "X-ray analysis in the analytical electron microscope," Sandia National Laboratories Report SAND82-2938, 1983.
8. R. B. Leonard, "Thermal stability of Hastelloy alloy C-276," *Corrosion*, May 1969, p. 222.
9. F. G. Hodge, "Effect of aging on the anodic behavior of Ni-Cr-Mo alloys," *Corrosion*, Oct. 1973, p. 375.
10. F. G. Hodge and R. W. Kirchner, "An improved Ni-Cr-Mo alloy for corrosion service," *Corrosion*, Aug. 1976, p. 332.
11. M. Raghavan, B. J. Berkowitz, and J. C. Scanlon, "Electron microscopic analysis of heterogeneous precipitates in Hastelloy C-276," *Metallurgical Transactions A*, June 1982, p. 979.
12. S. Rideout, W. D. Manly, E. L. Kamen, B. S. Lement, and P. A. Beck, "Intermediate phases in the ternary alloy systems of transition elements," *Trans. AIME (Journal of Metals)*, Oct. 1951, p. 872.
13. D. S. Bloom and N. J. Grant, "An investigation of the system formed by chromium, molybdenum, and nickel," *Trans. AIME (Journal of Metals)*, Feb. 1954, p. 261.
14. M. Raghavan, R. R. Mueller, G. A. Vaughn, and S. Floreen, "Determination of isothermal sections of nickel rich portion of Ni-Cr-Mo system by analytical electron microscopy," *Metallurgical Transactions A*, May 1984, p. 783.
15. A. L. Schaeffler, "Constitution diagram for stainless steel weld metal," *Metal Progress*, 1949, p. 680.

SURFACE CRYSTALLIZATION ON METALLIZED 94% ALUMINA CERAMICS

J. R. Hellmann, W. R. Sorsenson, M. J. Carr, and T. J. Headley

Fabrication of 94% alumina (Wesgo AL500:94% α - Al_2O_3 , balance SiO_2 - MgO - CaO glass) ceramic-to-metal seals involves metallization and nickel plating of the ceramic surface before brazing to the metal. To obtain a satisfactory joint, the metallized layer must be nickel plated for it to be wetted by the braze alloy.¹ The strength and hermeticity of these seals are occasionally compromised by formation of an acicular reaction product on the metallized surface of the ceramic prior to plating. This reaction phase is electrically nonconductive and inhibits uniform nickel plating. In this study we integrated a variety of electro-optical techniques to identify the structure and composition of this deleterious acicular phase and deduce how it forms. A means to retard its formation is suggested.

Experimental

A metallized slurry consisting of molybdenum, manganese, titanium subhydride, and an organic carrier of the proportions shown in Table 1 was screen printed onto a 94% alumina substrate, dried at 110 C for 2 h in air, then sintered at 1495 C for 45 min in wet hydrogen (dew point 30 C). Metallized surfaces were examined for the occurrence of the acicular phase using a JEOL 35C scanning electron microscope (SEM). Initial elemental analysis was performed using the x-ray mapping capabilities of the SEM on the as-metallized surfaces and on metallographic cross sections to reveal the depth of penetration of the acicular phase. A CAMECA MBX electron microprobe was employed to quantify the elemental species present in the reaction product. A number of acicular particles were scraped from the metallized surface and dispersed onto a holey carbon film for transmission electron microscopy. A JEOL 100 C scanning transmission electron microscope (STEM), equipped with an x-ray detector for energy dispersive spectroscopy (EDS), was employed for phase identification and elemental analysis. Controlled tilting experiments were performed using a JEOL 200CX transmission electron microscope (TEM) in conjunction with newly developed computerized search routines^{2,3} to permit real time crystallographic analysis and identification using existing JCPDS (Joint Committee on Powder Diffraction Standards) data files.

Results and Discussion

Initial SEM characterization revealed acicular features on the metallization layer which appear crystalline in nature (Fig. 1). Microprobe analysis indicated that the unknown phase contained primarily Al, Ti, and O. The background (metallization) consisted primarily of Mo, Al, Si, and Mn. The appearance of texture beneath the acicular features indicated the phase was relatively transparent to electrons and may actually entrain some of the metallized particles. This was interpreted as evidence that the unknown phase may have formed by crystallization from a semicontinuous glass phase surrounding the metallic particles during the metallization firing.

Bright-field transmission electron microscopy of the extracted fragments revealed two phases: a Mo-rich metallize constituent and the unknown phase (labeled X in Fig. 2). EDS analysis corroborated the microprobe results showing primarily Al and Ti in the unknown phase. Furthermore, the appearance of extinction contours in the unknown phase conformed its crystalline nature.

Electron diffraction patterns were obtained from several particles of the unknown phase to gather crystallographic information. The automated search scheme³ was employed to iden-

The authors are with Sandia National Laboratories, Albuquerque, NM 87185. They acknowledge the aid of P. F. Hlava for microprobe analyses and D. H. Huskisson for SEM analyses. This work was supported by the U.S. Department of Energy under contract DE-AC04-76DP00789.



FIG. 1.--SEM micrograph showing acicular reaction product on metallized surface.

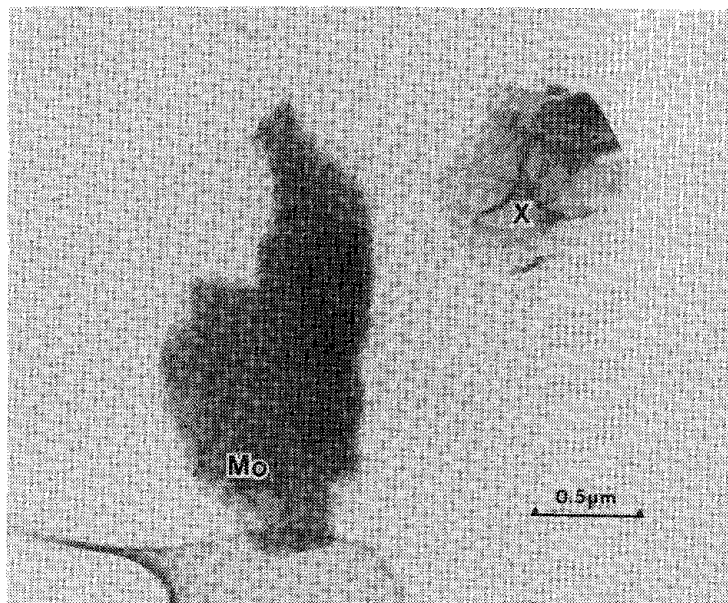


FIG. 2.--TEM brightfield image showing typical particles extracted from metallized surface.

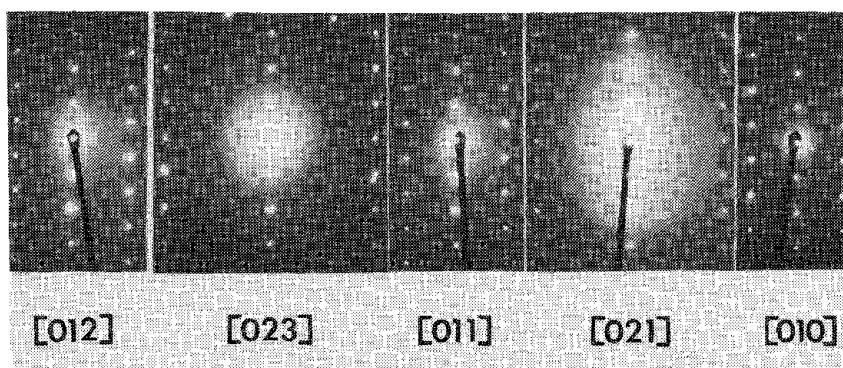


FIG. 3.--Symmetrical diffraction patterns obtained by controlled tilting about (200).

TABLE 1.--Composition of metallization slurry.

Component	Weight %
Mo	69
Mn	16
TiH _{2-x}	13-14
Si	0.8-1.0
Ca	<0.05
Al	<0.5

Organic carrier is a mixture of ester alcohol and ethyl cellulose.

TABLE 2.--JCPDS search/match results.

Best Matches
Al ₂ TiO ₅ , Ti ₃ O ₅
Considered, But Rejected
Ti ₉ O ₁₇ , Al ₂ O ₃ , TiH, Ti ₅ O ₉ , Ti ₃ Al, Ti ₂ Al
Obviously Wrong
16 other including Li ₂ TiO ₃ , Al ₁₄ B ₂ O ₉

tify a number of potential matches (Table 2) from the JCPDS file based on the chemical and structural information obtained from the EDS and diffraction analyses, respectively. Most of the tentative matches were eliminated on the basis that they contained certain light elements ($Z < 10$) which, although not detectable by EDS, were known to be absent from batch analyses of the starting materials or considered unlikely from a knowledge of the process history. Calculations based on single crystal data were made for the remaining candidates and compared with the experimental data to discriminate among those candidates. Two very good matches to our data emerged: Al_2TiO_5 (JCPDS#26-40) and Ti_3O_5 (JCPDS#9-309). Both possess the pseudobrookite (Fe_2TiO_5) structure and have such similar lattice parameters that electron diffraction patterns would be virtually indistinguishable for the same orientation. A controlled tilting experiment was performed in which several symmetrical zone axis patterns and the included angles were obtained (Fig. 3). Comparison of the experimentally measured angles with calculated values for both candidate compounds showed very good agreement with both, with the Ti_3O_5 fitting slightly better (Table 3).

We have concluded that the unknown phase is a solid solution of Ti_3O_5 and Al_2TiO_5 . Chemical analysis using data obtained from STEM-EDS and corrected for absorption effects with the standard Sandia thin film EDS reduction algorithm⁴ indicated that the R sites in this pseudobrookite structure [R_2TiO_5 ($\text{R}=\text{Al}, \text{Fe}, \text{Ti}$, etc.)] are occupied by aluminum and titanium on an approximately equal basis; a small amount of magnesium was also detected (Table 4). The presence of titanium on tri-valent R site corroborates the observed sensitivity of the formation of this compound to oxygen partial pressure (the occurrence of the acicular features on the metallized surfaces is enhanced at hydrogen dew points below 30 C). Phase equilibrium in the Ti-O system is quite complex⁵ and illustrates the multivalent character of the titanium cation. The oxidation state of titanium in the oxide can be dramatically altered by exposure to atmospheres of different oxygen potentials. The structure and composition of titanium oxides are strongly related to the oxidation state of the titanium ion and can be described as a homologous series of oxides characterized by a molecular formula $\text{Ti}_n\text{O}_{2n-1}$, where n is an integer ≤ 38 .⁶ The pseudobrookite form identified in this study (Ti_3O_5 ; $n = 3$) forms when a substantial fraction of the titanium is present in the tri-valent form. The presence of aluminum and a small quantity of magnesium in the compound is not surprising since both cations form pseudobrookite structures with titanium which are mutually soluble in each other.⁷

Summary and Conclusions

Real-time comparisons of electron diffraction data with existing JCPDS powder diffraction files, coupled with chemical analyses obtained from scanning transmission electron microscopy, permitted an unambiguous determination of the unknown phase which forms on the metallized surfaces of alumina ceramic during metallization sintering. The unknown phase has been identified as a crystalline substance, R_2TiO_5 ($\text{R} = \text{Al}^{+3}, \text{Ti}^{+3}$) possessing the pseudobrookite structure. Chemical analysis revealed that the tri-valent cation sites are nominally equally occupied by titanium and aluminum ions. The presence of a minor amount of magnesium in the compound suggests the compound may actually be a solid solution with another pseudobrookite form MgTi_2O_5 . The occurrence of the $(\text{Al}_{1-x}\text{Ti}_x)_2\text{TiO}_5$ phase is strongly related to the hydrogen dew point during metallization sintering, suggesting that the $\text{Ti}^{+4}:\text{Ti}^{+3}$ ratio may play a role in the formation and stabilization of this compound. Raising the metallization sintering atmosphere to a higher oxygen partial pressure (higher wet hydrogen dew point) should reduce the occurrence of this phase and improve the integrity of alumina ceramic-to-metal seals fabricated by metallizing and brazing.

References

1. W. H. Kohl, *Handbook of Materials and Techniques for Vacuum Devices*, New York: Reinhold, 1967, ch. 15.
2. M. J. Carr and W. F. Chambers, "RAD: A comprehensive software system for analytical electron microscopy," *Proc. 40th EMSA*, 1982, 744.
3. W. F. Chambers and M. J. Carr, "A search/match program for electron diffraction," *Analytical Electron Microscopy--1984*, 135.
4. A. D. Romig Jr., *X-Ray Microanalysis in the Analytical Electron Microscope*, Sandia National Laboratories Report SAND82-2938, Albuquerque, N.M., 1983.
5. P. Kofstad, *Nonstoichiometry, Diffusion, and Electrical Conductivity in Binary Metal*

Oxides, New York: Wiley, 1982, 137.

6. L. A. Bursill, B. G. Hyde, O. Terasaki, and D. Watanbe, *Phil. Mag.* 20: 347, 1969.

7. E. Kato, K. Daimon, J. Takahashi, R. Kato, and K. Hamano, "Fabrication of Al_2TiO_5 ceramics: II. Stabilization of Al_2TiO_5 with cation substitution," in *Report on the Research Laboratory of Engineering Materials*, Tokyo Institute of Technology, 9: 87, 1984.

TABLE 3.--Comparison between measured and calculated interzonal angles.

	[012] -- [023]	-- [011]	-- [021]	-- [010]
Measured:	7.8	9.5	9.9	11.3
Al_2TiO_5 :	7.5	8.8	9.9	10.6
Ti_3O_5 :	7.6	9.0	10.2	10.9

TABLE 4.--STEM EDS determination of cation concentrations in unknown crystalline phase X (in atomic %).

$$[\text{Al}] = 27.66 \pm 2.13^*$$

$$[\text{Ti}] = 69.37 \pm 3.10$$

$$[\text{Mg}] = 3.12 \pm 0.99$$

*95% confidence interval for n=6 measurements.

MATERIALS ANALYSIS OF FIBERGLASS-REINFORCED PLASTICS BY SCANNING ELECTRON MICROSCOPY

J. A. Davis and T. E. Laskowski

Fiberglass reinforced plastic (FRP) composites are being utilized in an ever-increasing number of applications. Over 40 000 different FRP products may now be found in such diverse areas as the transportation, construction, and electronics industries. The popularity of these composites (which are a mixture of glass fibers and, typically, one or more inorganic fillers in a plastic resin) is a reflection of their cost effectiveness and various favorable physical properties; e.g., strength, low density, etc. Effective utilization of FRP composites depends on an understanding of how these systems are constructed and why they perform as they do. To this end, a variety of techniques have been applied to the characterization of FRPs. Various dynamic and static physical testing methods, as well as x-ray radiographic and microscopic techniques have been utilized in the past.¹⁻³

In this laboratory, specific analytical methodologies have been developed to allow the thorough characterization of FRP materials by scanning electron microscope (SEM)/energy dispersive x-ray analysis (EDX) based techniques. A considerable part of this effort has been the development and implementation of suitable sample preparation methods which may be used to illustrate the features of interest without inducing artifacts.

Experimental

A thorough characterization of FRP composites by scanning electron microscopy frequently involves the examination of intact or fractured surfaces as well as polished cross sections. Surface views, which are typically obtained in a secondary-electron mode, provide overall topographic information on the composite. The corresponding cross-sectional studies, which are generally done with the aid of a backscattered electron detector, reveal the various internal features present and provide data on the orientation and distribution of sample constituents. Depending on the type of information required, one or all of the sample types mentioned above may be required to characterize a composite fully.

The initial preparation of an FRP composite for surface characterization in the SEM can be as simple as cutting a region of the sample that is small enough to fit physically into the instrument. The actual cutting is best done with a slow-speed saw to minimize sample damage. Fracture surfaces may be handled in a similar manner. The resulting materials are then secured to a sample mount with standard conductive paints.

Unlike samples for surface studies, the preparation of FRP cross sections requires a lengthy process to insure an end product of the highest quality. Entirely manual methods are available, but in our laboratory cross sections are prepared with the aid of a Struers Abrapol automatic polishing unit. This device is capable of simultaneously polishing up to twelve specimens to provide a mirror-like finish. The first step in the preparation of a FRP cross section is to embed the raw samples in a two-component epoxy system. After an appropriate curing time, these mounts are secured into a sample jig assembly and ground down on a cast-iron lapping wheel with successive slurries of silicon carbide grits suspended in water/detergent mixtures. This procedure is terminated after the use of 1000 grit particles. The samples are then polished with subsequent 6, 3, and 1 μm diamond pastes suspended in aqueous detergent. The final polishing step involves the use of 0.05 μm alumina particles on a nap cloth. The end product is a sample that reveals the internal morphologies of the composite and exhibits negligible surface relief. Further details on this procedure are available from the authors.

Prior to introduction into the SEM, all FRP samples are coated with a 20 to 30nm carbon film by the vacuum evaporation of carbon rods. Care must be taken during this process to minimize sample damage from thermal effects. A shutter device is typically used to shield the composite from the carbon rod assembly during initial heating (outgassing) of the rods.

The authors are at the Owens-Corning Fiberglass Technical Center, Granville, OH 43023.

Once this step has been completed and the shutter moved out of the direct line of sight between the sample and the carbon source, the rods are vaporized in short (approximately 5s) bursts to minimize heating effects. We have found it helpful to have a small section of Nuclepore polycarbonate membrane filter mounted next to the sample during the evaporation. Past experience has shown that if the coating process can be carried out without inducing disruption of the filter (e.g., cracking and warping), then the FRP will also be undisturbed. Failure to take due caution during carbon coating can result in pronounced changes in the surface topography of FRP materials. These phenomena may take the form of fiber/resin delaminations, as well as loss of fine detail on the resin itself. The introduction of such artifacts can lead to the false interpretation of subsequent SEM images and must be carefully avoided.

Once a fiberglass-reinforced plastic composite has been properly prepared, it is characterized by a JEOL JSM T-300 SEM. This instrument is equipped with a solid-state backscattered electron detector and a Tracor-Northern TN-2000 energy-dispersive x-ray analysis system. TN-1310 digital beam control electronics are also present in this unit and may be utilized for automated particle analysis.

Results and Discussion

An area of key interest in the development of fiberglass-reinforced plastic products is the relative degree of adhesion between the composite's organic resin system and the various inorganic materials present, particularly the glass fibers. The extent of bonding may be evaluated by an SEM examination of appropriate fracture surfaces. Typically, this type of work is performed at low accelerating voltages (e.g., 2-15 keV) to minimize electron beam penetration. This overall approach may be used to evaluate the role of glass/resin adhesion in such properties as composite strength, toughness, etc. In addition, a careful examination of the fracture surface of individual glass fibers may be used to determine the type of physical forces that the fiber was subjected to as it was broken. Figure 1 contains representative SEM photomicrographs of the fracture surface of two different FRP systems which had been designed to have a high and a low degree of fiber/resin adhesion, respectively. The strong fiber/resin bond present in the first sample is reflected by the intact interface between these materials (feature 1). Composites with lower degrees of adhesion exhibit clean separations between the resin and the individual glass fibers (feature 2).

The various internal features present in fiberglass-reinforced plastics may be characterized and documented by the examination of the sample in a polished cross-sectional form. Optimum contrast is provided through the use of a backscattered electron detector. The resulting image readily delineates individual glass fibers and, if present, inorganic filler particles, from the bulk plastic resin. Nominal accelerating voltages of 20-30 keV are required to insure reasonable signal levels.

Figure 2(a) contains a backscattered electron image of a cross section prepared from a fiberglass reinforced plastic material that contains only glass fibers and resin. Individual glass fibers (features 1 and 2) have shapes ranging from circles to ellipses depending on their orientation relative to the sample's polishing plane. A corresponding cross-sectional view of a more complex FRP composite is shown in Fig. 2(b). Here, various inorganic fillers are present (features 3 and 4) in addition to the glass fibers (5) and resin (6). If necessary, each of these species may be further characterized by EDX analyses to provide information on the inorganic constituents present.

Part of the value of cross-sectional studies lies in the ability to determine such parameters as particle size, loading, and geometry. Such information may be obtained by manual measurements from individual photomicrographs, but computer-based methods are available.⁴ We have found the digital beam control hardware and software which is integrated into our Tracor-Northern x-ray analysis system to provide the basis for an automated image analysis system that is very effective in characterizing FRPs. Programs are present to measure the size and orientation of the particles present, calculate area percentages, and relate these physical properties to the chemistry of the various materials present in the composite.

A conventional backscattered electron image of a cross section prepared from an FRP material which had been tensile loaded to the point of failure is shown in Fig. 3(a). Bundles of glass fibers (feature 1) as well as large filler particles (2) are evident in this photomicrograph. A stress-induced crack (3) is also prominent. The digitized equivalent of this image, as acquired by the Tracor-Northern digital beam control equipment is displayed in

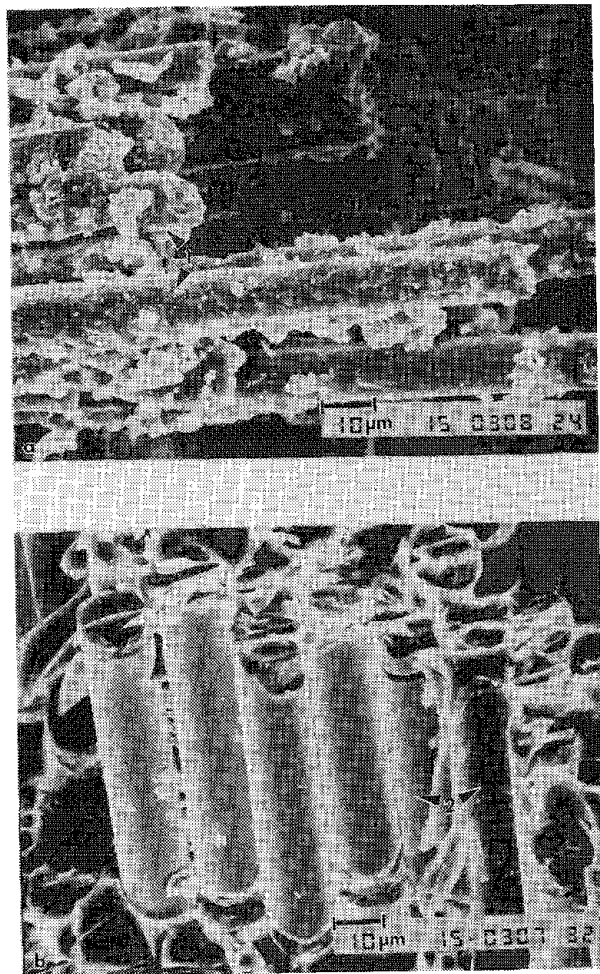


FIG. 1.--SEM photomicrographs of fracture surface prepared from FRP composites with (a) good and (b) poor fiber/resin adhesion. Note fibers well encapsulated in resin (feature 1) vs fibers relatively free of resin (feature 2).

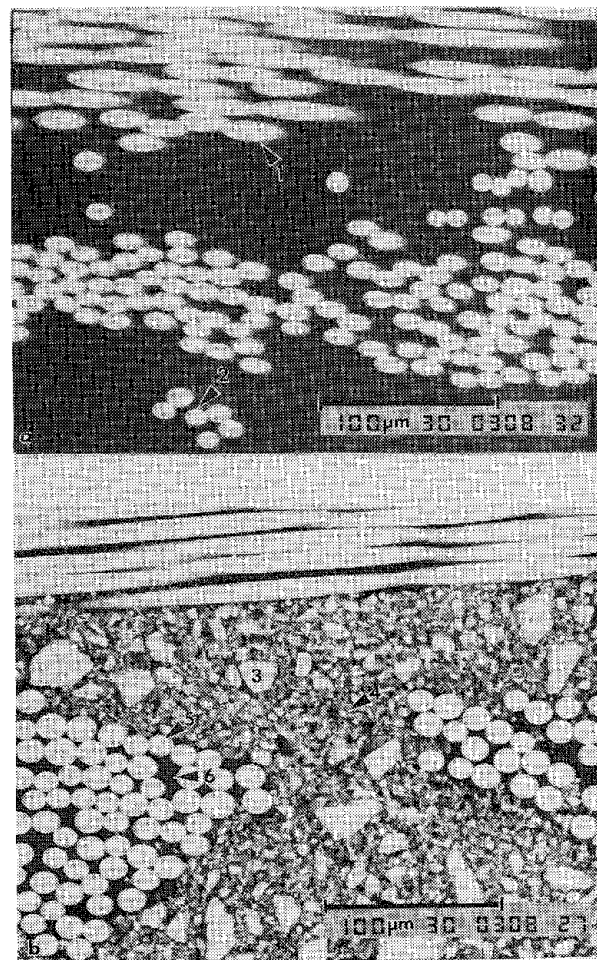


FIG. 2.--Cross-sectional view of (a) simple and (b) complex FRP systems. Shape of fibers (e.g., 1 and 2) is related to their orientation in composite. Complex FRP has numerous filler particles (3 and 4) as well as glass fibers (5) and resin (6).

Fig. 3(b). (A black-and-white representation of the actual color image is shown here.) One of the most useful image processing functions available with this system is one that generates a gray-level histogram of a backscattered electron image and then calculates area fractions for the various species present. An example of this capability is given in Fig. 3(c), which depicts a histogram derived from Fig. 3(b) as well as the area percentage calculated for one of the gray-level bins which corresponds to the resin present. Additional analyses of the gray levels shown here may be used to evaluate fully the resin, fiberglass, filler, and void content of this image.

Conclusions

Specific analytical methodologies have been described here for the proper preparation and SEM characterization of fiberglass reinforced plastic composites. Use of these techniques can lend insight into the physical properties and behavior of FRP materials.

References

1. J. C. Halpin, *Primer on Composite Materials: Analysis*, Lancaster, Pa: Technomic Publishers, 1984.
2. A. Blaga, "Examination of fracture surfaces by scanning electron microscopy," *J. Composite Materials* 1: 208-210, 1967.
3. C. H. Hilado, *Materials Technology Series: Glass Reinforced Polyester Systems*, Lancaster, Pa: Technomic Publishers, 1984, vol. 14.
4. J. J. McCarthy and P. R. Ferrera, "On-line processing of digital SEM images," *Microbeam Analysis--1982*, 118-120.

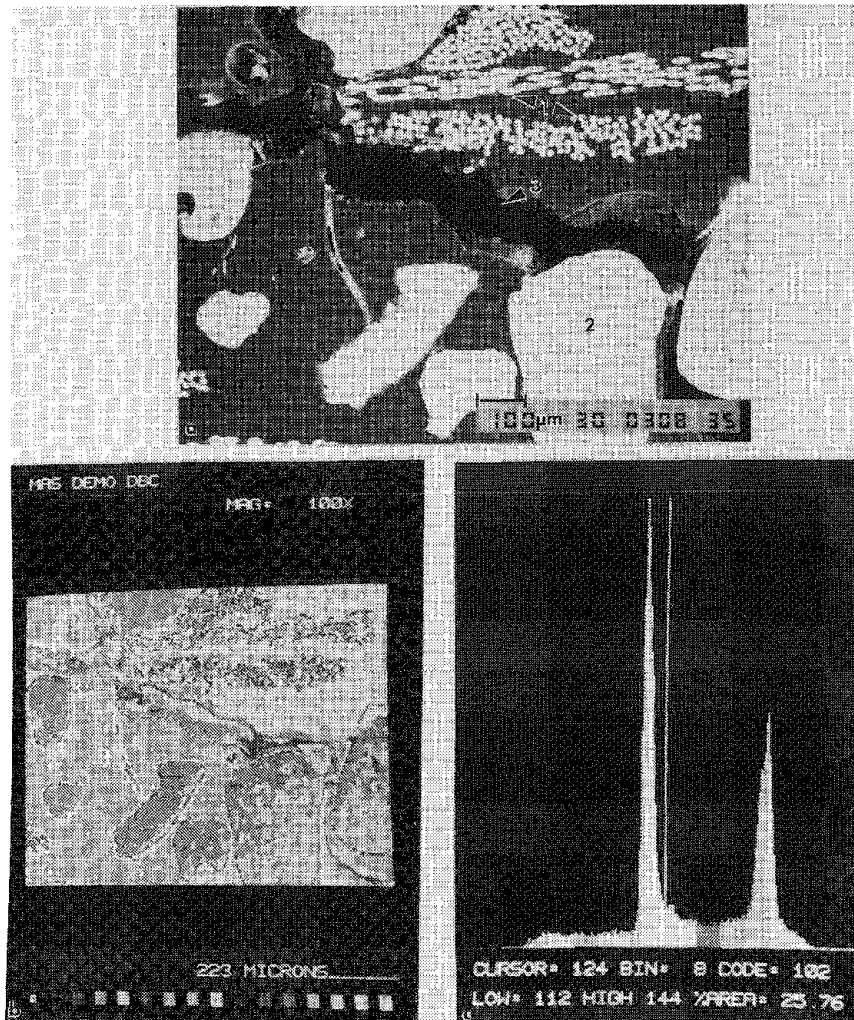


FIG. 3.--(a) Cross-sectional view of tensile-loaded FRP: glass fibers (1), filler particles (2), and stress-induced crack (3) are evident. (b) Digitized analog of (a). (c) Corresponding gray-scale histogram and area measurement.

MICROPROBE EXAMINATION OF NITROGEN AND/OR OXYGEN CONTAMINATION IN TITANIUM ALLOYS

J. E. Bohning

A materials problem concerning titanium alloys has been found for years in the form of apparent low-density inclusions. These defects have been metallographically characterized as being large apparent alpha phase grains showing much higher hardness than the surrounding matrix area and being highly embrittled. Work performed for a period of 14 years has shown the feasibility of analyzing this type of defect in titanium alloys for nitrogen and oxygen by the electron microprobe. The analyses described in this paper were performed at Teledyne Wah Chang Albany Corp. with a Hitachi XMA-5 electron microprobe. The techniques used in this type of materials analysis can be successfully used with currently available electron microprobes.

The low-density inclusions in titanium alloys have been previously labeled as Type I alpha-phase defects (oxygen and/or nitrogen stabilized).¹ The analyses of Type I alpha phase defects were performed for nitrogen and oxygen with a microprobe spectrometer equipped with a lead stearate pseudocrystal and a thin-window flow proportional detector. The detector gas was argon -10% methane (P-10). Several specific items in the analytical technique should be mentioned. First, the use of standards similar in composition to the defects analyzed have been found to be the best choice for the quantitative analysis of light elements.^{2,3} The particular standards used were Ti-19.6 wt.% N and Ti-31.2 Wt.% O. Second, the determination of background x-ray count intensities from the defect sample at the characteristic elemental wavelengths for nitrogen K α and oxygen K α x rays is essential for accurate quantitative electron probe microanalysis. In the case of nitrogen in titanium, there is a problem of x-ray peak overlaps. The wavelength of the N K α x-ray line is 31.6Å and the wavelength of the Ti L α x-ray line is 31.36Å. To establish a usable background count level for either N K α or O K α x rays from titanium alloy defects, the count total acquired from the sample matrix for the particular elemental x-ray line of interest is used as the background count level for the corresponding defect area. This technique is a practical method of establishing a background count level for N K α x rays being generated in a low nitrogen content level (<5.0 wt.% N) Type I alpha-phase defect in titanium alloy systems. Similar techniques have been used in the analysis of nitrogen and oxygen in zirconium alloy defects.³ The method of background determination described above has been shown by the author to be equivalent in accuracy to using off-peak wavelength measurements for N K α microanalysis in zirconium alloys where there is no problem with x-ray peak overlaps.

Two typical Type I alpha-phase defects in Ti-6Al-4V alloy were analyzed as described above for nitrogen and oxygen. The results of microprobe analyses for nitrogen and oxygen are given in Table 1 as first approximations of weight percentage content. These values

TABLE 1.--Calculated first approximations of weight % concentration of nitrogen and oxygen in Type 1 alpha phase defects in Ti-6Al-4V alloy.

Sample and Region of Analysis	Concentrations, %	
	N	O
Type I α -phase defect #1	5.86	-
Type I α -phase defect #2	-	1.85
Lower Limits of Detection	0.26	0.21

are called K-ratio percentages [(Net x-ray counts on the defect/Net x-ray counts on the standard) \times Elemental weight percentage content of the standard for the element analyzed]. Also included in the table are calculated lower limits of detection for nitrogen and

The author is at General Electric Co., Aircraft Engine Business Group, Cincinnati, OH 45215-6301.

oxygen in these specific defect samples. The lower limits of detection are calculated by standard statistical calculation techniques used for electron probe microanalysis.⁴

Detection of nitrogen and oxygen in the same two Type I alpha phase defects was successfully performed using a JEOL 733 electron microscope in February 1985.

In the past 14 years, electron microprobe analysis of nitrogen and/or oxygen has been successfully performed on 130 Type I alpha phase defects in titanium alloys. Of that total, 91 were found to be nitrogen stabilized, 17 were nitrogen (major element) and oxygen (minor element) stabilized, 20 were oxygen stabilized, and two were oxygen (major element) and nitrogen (minor element) stabilized. The consistent ability to obtain accurate and reliable results in the microprobe analysis of nitrogen and oxygen in titanium alloy defects demonstrates that, with care, the techniques described above are an acceptable method of characterization of a major material defect problem.

References

1. E. M. Grala, *Characterization of Alpha Segregation Defects in Ti-6Al-4V Alloy*, Technical Report AFML-TR-68-304, 1968, iii.
2. J. I. Goldstein et al., *Practical Scanning Electron Microscopy*, New York: Plenum Press, 1977, 3rd ed., 437.
3. J. E. Bohning, "Microprobe examination of nitrogen and oxygen contamination in zirconium alloys," *Microbeam Analysis--1979*, 114.
4. Ref. 2, p. 452.

8 Geological and Energy Applications

SEM MORPHOLOGIES REVEALED BY ATTACK OF THE STRUCTURE OF ENTREDICHO ORE (CIUDAD REAL, SPAIN)

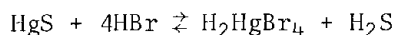
F. A. Calvo, J. M^a Guilemany, and J. M^a Gómez de Salazar

The structures left after leaching with hydrobromic acid for various times are discussed and the distribution of the several constituents is cleared up. The structures shown support the possibility of a hydrometallurgical process proposed for the beneficiation of mercury ore. They also give new data about the host rock, which also support our genetic hypothesis.

In other work¹ we have studied the nature and structure of the Entredicho ore, formed mainly by cinnabar (HgS) as the economic mineral and quartz as gangue (Fig. 1). In the same way the presence of intracrystalline native mercury in the cinnabar (Fig. 2) and in the quartz crystals is to be mentioned (Fig. 3).

The extractive metallurgy of the mercury from its sulfide ores is currently done by a pyrometallurgical process.² Mercury is obtained by condensation of its vapor. This process originates the formation of solid residues from the combustion and from the thermic decomposition of the inert constituents, similar to quartz and silicates phases,² and those joined with the mercury to form the so-called soots (hollines), which are difficult to treat.

Recent investigations allow the treatment of the mercury ores hydrometallurgically by leaching with hydrobromic acid in aqueous solution, as shown in the following reaction:



The precipitation of the mercury from its solution can be accomplished by various methods--cementation, electrolysis, or direct precipitation as mercury oxide (red oxide)--which are of industrial importance.

Methods and Procedures

Samples of minerals were obtained by brittle fracture (liquid air) and metallized with gold (200 Å) in order to test the massive mineralization of quartz by the cinnabar. Successive attacks at room temperature on the samples were done with aqueous concentrated periods of 5 min each. The chemical attack was interrupted by washing with acidulated water in hydrochloric acid. At the end of each period of leaching of the mercury, the samples were once more metallized with gold (200 Å), which implies that the cover of gold must be eliminated previous to the leaching with hydrobromic acid, by attack in aqueous solution of potassium cyanide for 10 min and further washing in alcohol.

Results

The leaching action of hydrobromic acid on the samples is shown in Figs. 4-6, which correspond to the attack in the same place for 5, 10, and 15 min, respectively. The final results show a skeleton of siliceous nature, formed mainly by idiomorphic quartz crystals (Fig. 7).

In an attempt to study the dissolution mechanism of mercury sulfide, an observation was made on the attack surfaces that confirms that the hydrobromic acid attacks preferentially the active surfaces of the mineral, which become the fracture planes of mercury sulfide (Fig. 8). Figure 9 shows the resulting structure of the attack of hydrobromic acid on cinnabar after 5 min; a magnified detail (Fig. 10) confirms that the action of the hydrobromic acid is principally on the previously mentioned sites.

The existence of other minor sulfide-like constituents, such as pyrite (FeS₂), in the ore made it necessary to study the effect of the leaching agent on it.

Figure 11 shows the resulting structure after a 5 min attack on a sample densely mineralized by cinnabar. If we study the same area after a second attack (10 min), we can

Authors Calvo and Gómez are at the Department of Metallurgy of the Complutense University of Madrid; author Guilemany is at the Department of Metallurgy of the University of Barcelona.

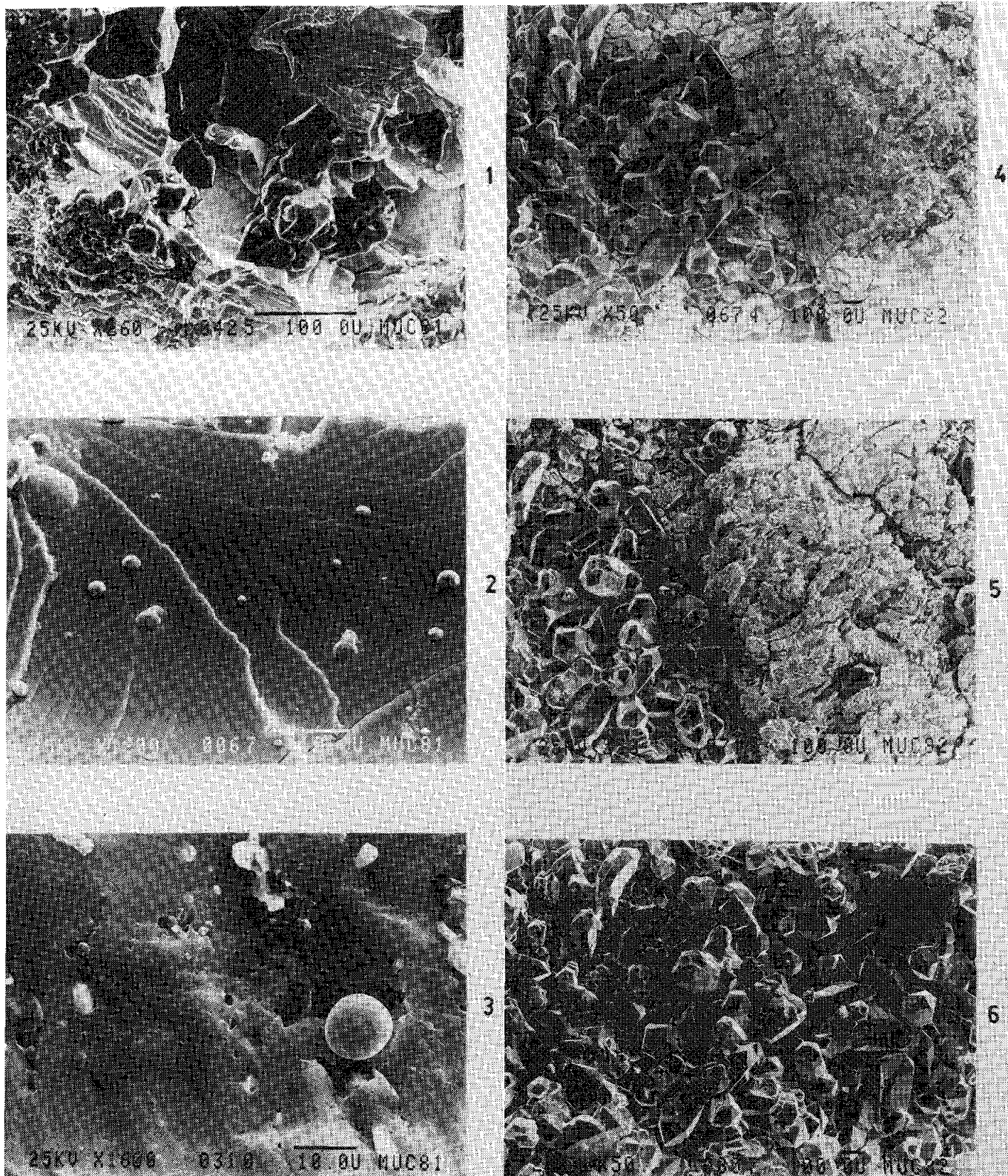


FIG. 1.--(SEM) Structure of Entredicho ore.
 FIG. 2.--(SEM) Native mercury into cinnabar.
 FIG. 3.--(SEM) Native mercury into quartz crystal.
 FIG. 4.--(SEM) Leaching of ore after 5 min.
 FIG. 5.--(SEM) Leaching of ore after 10 min.
 FIG. 6.--(SEM) Leaching of ore after 15 min.

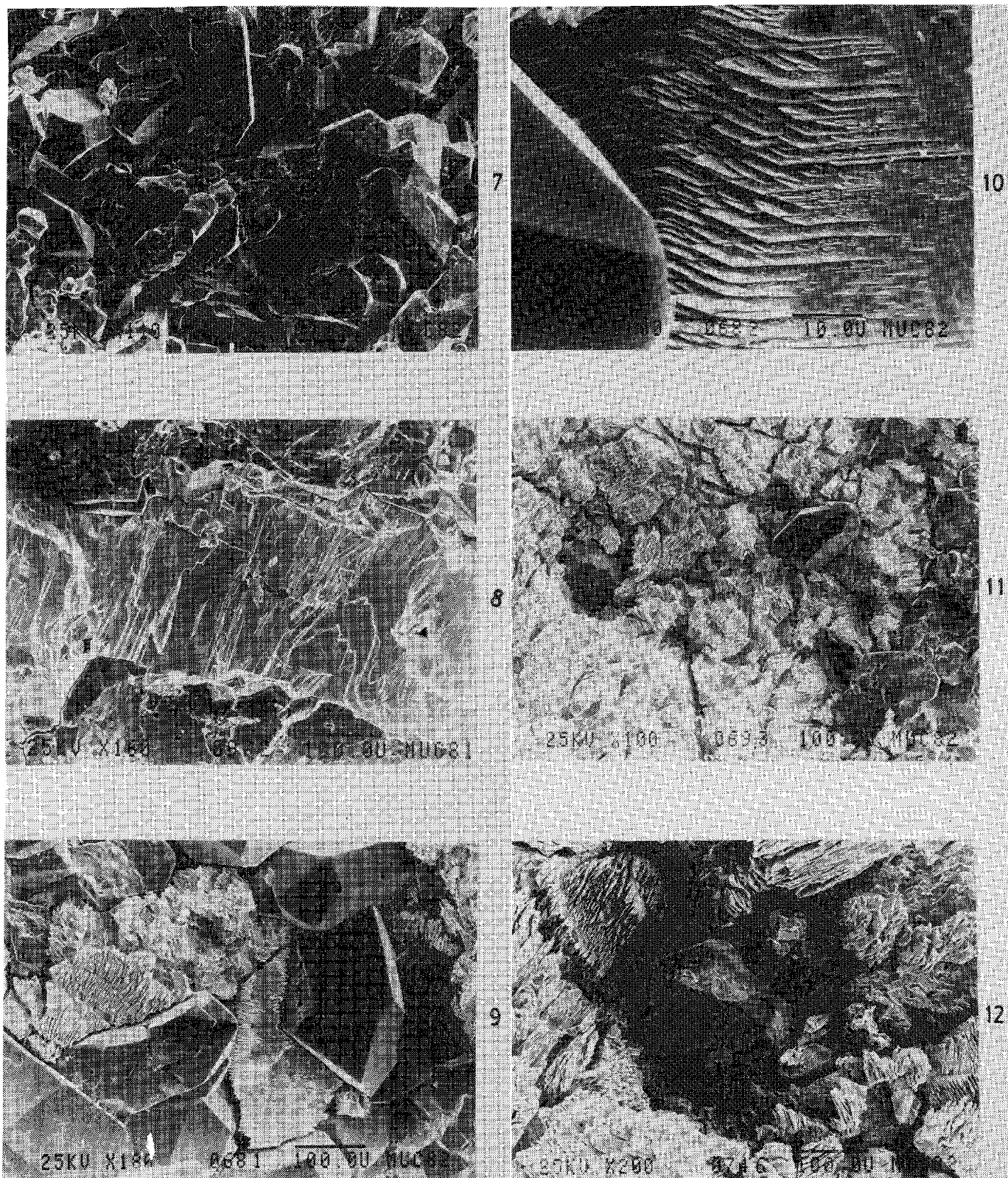


FIG. 7.--(SEM) Skeleton of siliceous nature, formed by idiomorphic quartz crystals.
 FIG. 8.--(SEM) Fracture surface (fibrous-lamellar) of cinnabar.
 FIG. 9.--(SEM) Structure of attack by hydrobromic acid on cinnabar after 5 min.
 FIG. 10.--(SEM) Magnified detail of Fig. 9.
 FIG. 11.--(SEM) Structure after 5min attack on sample densely mineralized by cinnabar.
 FIG. 12.--(SEM) Same area after second attack (total time, 10 min). Presence of pyrite on quartz crystal (A).

observe that a phase of different nature appears on the quartz crystals (Fig. 12a). EDS analysis shows that it is pyrite (FeS_2 , Fig. 13), not seen in Fig. 11.

After the third period of attack (a total time of 15 min) the cinnabar was totally leached but not the pyrite, and its surface appears unmodified (Fig. 14). The solvent action of hydrobromic acid is thus selective; cinnabar is easily demineralized and the other constituents of no economic interest are left unaltered. Of course the leaching process must be controlled, because a variation in the condition of pH or Eh could modify the speed of dissolution of cinnabar and could provoke the precipitation of the other mercury phases, similar to mercury oxibromide.

Figures 15 and 16 show a fine precipitate on the quartz crystals. EDS analysis indicates the presence of mercury bromide (Hg_2Br_2 , Table 1).

The recuperation of this phase is possible by attack with water at 70 C after dissolution of gold by potassium cyanide solution, as shown in Fig. 17, which is for the same area as Fig. 15.

The demineralization of the ore serves to show some structural facts of great interest: (a) porosity and permeability of the host rock; (b) the existence of a great number of nonidiomorphic quartz crystal or information processes that confirm the genesis hypothesis of its formation;³ (c) the presence of microcrystalline defects on the quartz crystals, and principally in the twin planes (Fig. 18), which also confirms that the presence of intracrystalline cinnabar and native mercury inside the quartz crystals is the consequence of its existence in vapor phase in the magmatic fluid, formed principally by molten cinnabar, that mineralized the host rock;⁴⁻⁶ and EDS analysis confirms the existence of the other phases of silicated nature, composed by aluminum and magnesium.

References

1. F. A. Calvo, J. Ma Guilemany, and J. Ma Gómez de Salazar, "Microstructure of Entredicho mercury ore, Ciudad Real, Spain," *Microbeam Analysis--1982*, 435-440.
2. J. D. Gilchrist, *Extraction Metallurgy*, New York: Pergamon Press, 1967.
3. F. F. Mackenzie and R. Gees, "Quartz synthesis at earth surface conditions," *Science* 6: 533-535, 1973.
4. F. A. Calvo, J. M. Guilemany, and J. M. Gómez de Salazar, "The contribution of SEM-EDX and EPMA to the study of the structure and genesis of Spanish mercury ores," *EUREM 1980/I*, 456-457.
5. F. A. Calvo, J. M. Guilemany, and J. M. Gómez de Salazar, "The application of SEM and XRM to the study of the structure and composition of Spanish mercury ores: A genesis hypothesis," *Scanning* 5: 32-38, 1983.
6. J. M. Gómez de Salazar, doctoral thesis, Complutense University of Madrid, 1982.

TABLE 1.--EDS analysis on mercury bromide phase.

SPECTRUM - CORR-ANAL3

20 EV/CH
200. SEC. ACQ. TIME

UNKNOWN ANALYSIS RESULTS

	CALIB.	MEAS.		
	ENERGY	ENERGY	CTS/SEC	PERCENT

1 BR (Z=35) K-ALPHA 1	11.922	11.922	22.51	2.1
2 BR (Z=35) K-ALPHA 2	11.876	11.876	11.67	4.5
BR (Z=35)			34.17	1.2
3 HG (Z=80) M-ALPHA 1	2.195	2.195	122.9	1.0
4 HG (Z=80) M-ALPHA 2	2.193	2.193	122.9	1.0
HG (Z=80)			245.8	0.4

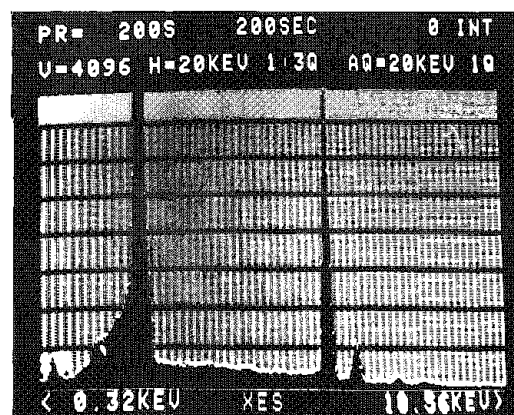


FIG. 13.--(EDS) Analysis of pyrite phase.

SPECTRUM CORR-ANAL3

JUNE 2, 1982

STANDARDLESS EDS ANALYSIS
(ZAF CORRECTIONS VIA MAGIC V)

ACCELERATING VOLTAGE	25.0 KEV	ELEMENT & LINE	WEIGHT PERCENT	ATOMIC PERCENT	PRECISION 2 SIGMA	K-RATIO	ITER
INCIDENCE ANGLE	90.0 DEGREES	BR KA	30.97	52.97	0.74	0.4051	
EFFECTIVE TAKE-OFF ANGLE	35.0 DEGREES	HG MA	69.03	47.03	0.55	0.5949	9
		TOTAL	100.00				

NORMALIZATION FACTOR: 0.833

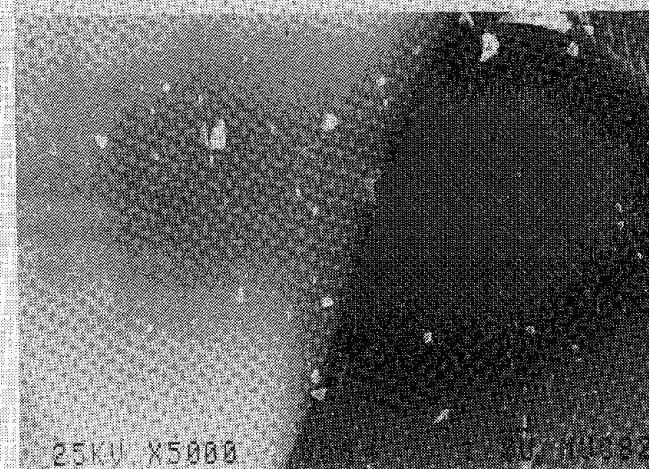
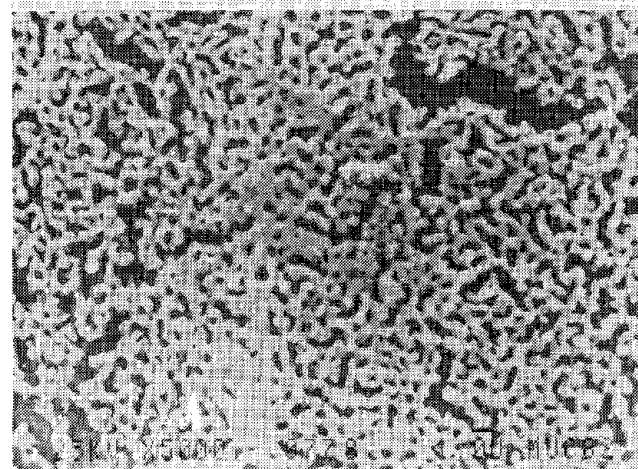
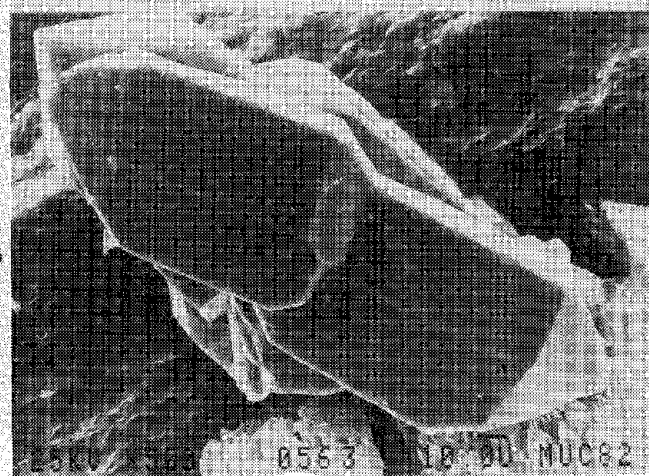
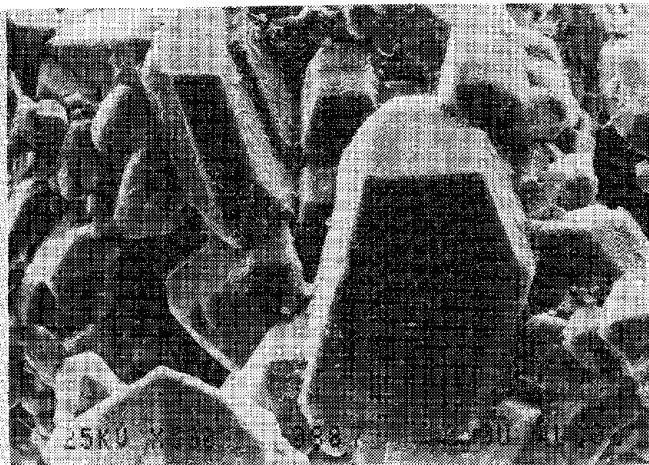
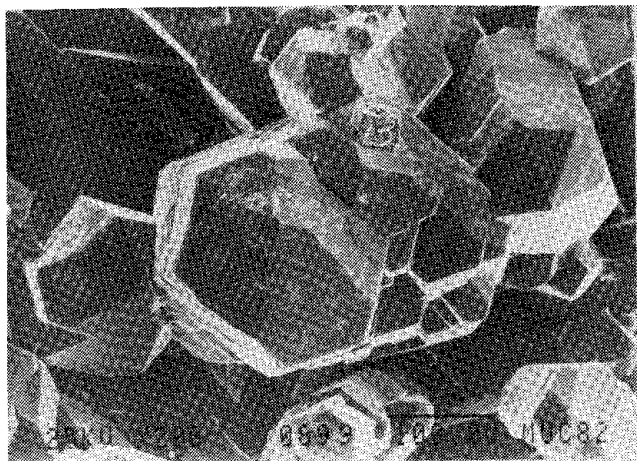


FIG. 14--(SEM) Area of Figs. 11 and 12 after 15min attack; pyrite phase is unaltered.
FIGS. 15 and 16.--(SEM) Mercury bromide on quartz crystals.

FIG. 17.--(SEM) Same area as Fig. 15, after attack with water at 70 C.

FIG. 18.--(SEM) (a) Idiomorphic quartz crystals (twinning); (b) detail of porosity in twin planes on quartz crystal.

Advanced Imaging Techniques

COMPOSITIONAL MAPPING OF THICK SPECIMENS

D. E. Newbury

Since the first demonstration of x-ray area scans obtained with the scanning electron microprobe of Cosslett and Duncumb, the use of the electron microprobe to produce two-dimensional elemental distribution maps has become a powerful adjunct to conventional fixed-probe analysis.¹⁻³ We are now at a significant point of change in the methodology for the recording and utilization of x-ray elemental mapping. Currently, most mapping is carried out by means of analog signal processing. X-ray signals detected with a wave-length-dispersive (WDS) or energy-dispersive (EDS) x-ray spectrometer are used to modulate the intensity of a cathode ray tube (CRT) scanned in synchronism with the specimen, and the resulting image is recorded photographically. Such an x-ray area-scan image when properly recorded is a powerful tool for solving practical problems, but the image is only qualitative in nature and conveys little quantitative information.

A new method of quantitative digital compositional mapping is now emerging.⁴⁻⁸ This method is opening new levels of utility and application for the familiar x-ray mapping technique. Furthermore, elemental mapping of bulk samples by electron-excited x rays is being augmented by other methods which obtain information not available in the x-ray signal. These associated methods include electron-excited Auger electron spectrometry to map surface constituents, and secondary-ion microscopy/microprobe analysis to map trace constituents, light elements, or isotope ratios.

X-ray Elemental Mapping

Analog Methods. The various analog methods for efficiently using the x-ray signal for mapping have been reviewed in detail by Heinrich.⁹ In the principal analog recording method, the "dot map," the beam is continuously scanned on both the specimen and the CRT. When an x-ray pulse is processed, the intensity on the CRT is set to a specific value for the duration of the pulse, typically 50-100 μ s after shaping. The scan speed is chosen so that the pulse duration produces a bright dot on the final photographic material. Each dot denotes the position of the scanned beam when an x-ray of a specific energy is detected. By building up a sufficient number of such events, the areal density of dots can be used to indicate the presence or absence of various constituents. Because of the poor efficiency with which characteristic x rays are generated compared to the electron signals used for conventional morphological imaging, it is generally not possible to form x-ray images with gray-scale information. To reduce the sensitivity to random noise, the brightness can be adjusted so that a single written dot does not expose the film, but two dots superimposed produce a dot in the final image. An example of the use of analog mapping near the practical lower limit of concentration, about 1 wt.%, is shown in Fig. 1, which shows a map of the zinc distribution at the grain boundaries of polycrystalline copper after diffusion-induced grain boundary migration (DIGM).¹⁰ To record this image, about 6 h of scanning time was required.

The chief technical limitations of the analog dot map are as follows.

(1) A severe limitation exists on displaying quantitative concentration variations. Each picture element in the recorded image can exist in only one of two states, bright ("on") or dark ("off"), a dynamic range of only 1 bit. Although the composition, and hence the x-ray signal, may vary from place to place within the scanned field, the recorded image can only register the presence of x rays, not the intensity. The number of dots per unit area is the main indication of concentration differences within the image.

(2) The analyst is unable to modify the x-ray information after recording in order to

The author is with the Center for Analytical Chemistry, National Bureau of Standards, Gaithersburg, MD 20899. He is grateful to his colleagues R. Marinenko, D. Bright, and R. Myklebust for their excellent efforts in developing quantitative compositional mapping, and D. Butrymowicz for the opportunity to apply the techniques to diffusion-induced grain boundary migration.

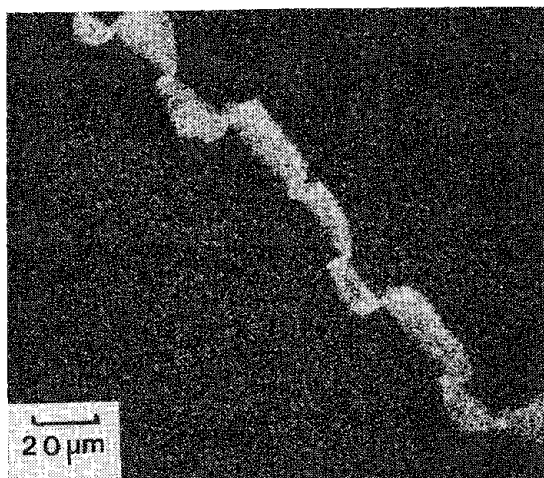


FIG. 1.--Conventional analog x-ray dot map of zinc at grain boundaries of polycrystalline copper. Accumulation time 6 h.

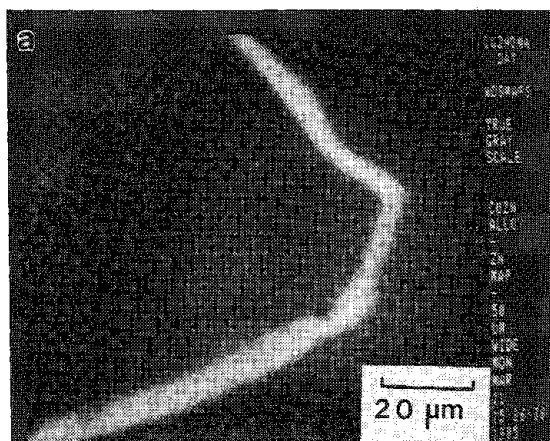


FIG. 2.--(a) Digitally recorded x-ray map (128 × 128 pixels) of zinc at grain boundaries of copper. Accumulation time 6 h. (b) Gamma contour processing of image (a).

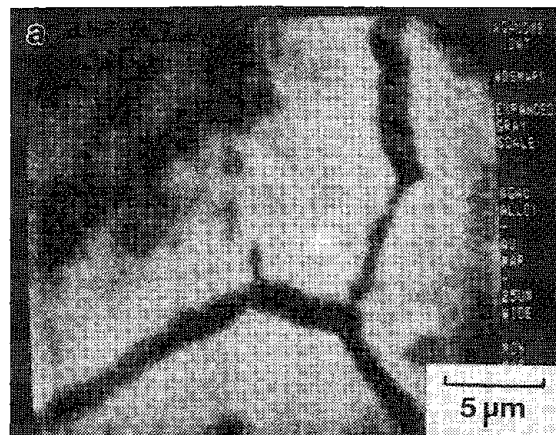
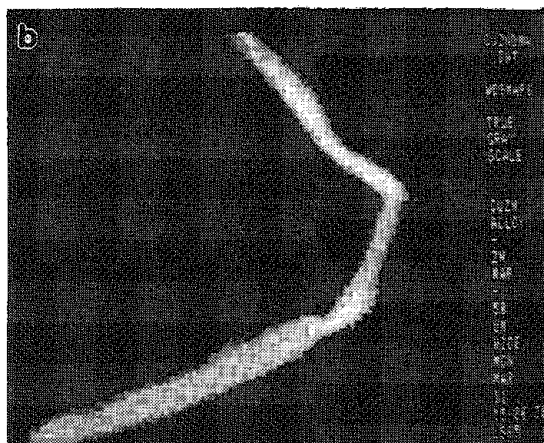


FIG. 3.--(a) Digitally recorded x-ray map (128 × 128 pixels) of gold distribution at grain boundaries of a silver gold alloy. Contrast was enhanced by subtraction of gold intensity from silver intensity. (b) Gamma contour processing of image (a).

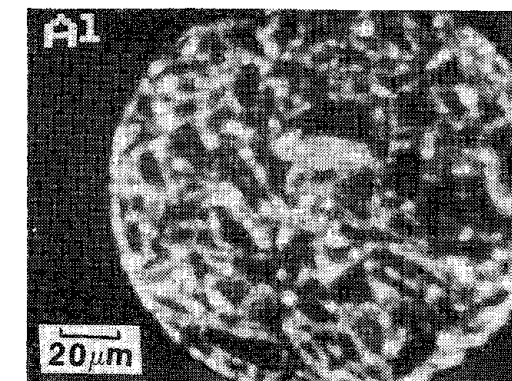


FIG. 4.--Digital ion microscope map of aluminum distribution in reaction-bonded silicon carbide. 512 × 512 pixels; accumulation time 10 s.

eliminate background or manipulate contrast, which is particularly limiting in the case of energy-dispersive maps where the peak-to-background signal is poor.

(3) Because the dynamic range is so small, it is difficult to see small concentration differences superimposed on a high concentration level. Further, practical limitations arise from the need for careful control of the recording CRT, particularly on very long exposures. The total count must be monitored carefully. Generally, 10^5 - 10^6 counts are needed for a high-quality map. If the scan is interrupted too soon, the image appears dark; if too many counts are accumulated, the image saturates.

Digital Methods. The advent of powerful laboratory computers dedicated to the electron microprobe has made the quantitative digital compositional map possible. Such computers are usually found in the form of an advanced multichannel analyzer capable of processing both EDS and WDS signals. In the digital method, the beam is stationed at a point for a certain dwell time, and the x-ray signal is integrated to produce a single-channel count with WDS, or a multichannel spectrum with EDS. The EDS spectrum may be processed to yield data on more than one element, and/or several WDS signals can be recorded in parallel if more than one spectrometer is available. A digital x-y grid of counts at each x-y scan location is stored in the computer for each x-ray signal.

The main advantage of the digital map is the flexibility which this method of recording brings to the x-ray data. The analyst avoids the possibility that the data will be unusable due to failure to establish the proper photographic conditions. The digital signal can be repeatedly read out of the computer storage and transformed into analog signals to modulate a CRT scanned with the x-y pattern of the data x-y grid. Thus, the photographic conditions can be adjusted until a satisfactory image of the qualitative x-ray area scan is obtained. An example of a digital x-ray map of zinc/copper DIGM in a region similar to Fig. 1 is shown in Fig. 2. Comparison of the two maps shows that the contrast of the digital map, which has been manipulated by background subtraction and gamma (output signal = input signal to a fractional power) processing is superior to the analog map. The digital map allows discrimination of three distinct compositional contours within the zinc-enriched grain boundary region. Much more important is the possibility that the stored data can be transformed to reveal low levels of contrast in the signal which would not be visible in a conventional analog recording. An example of the application of the digital equivalent of black-level suppression to enhance a limited contrast range of DIGM in the Au-Ag system is shown in Fig. 3.¹¹ In this case, the strong image contrast is produced by a decrease of 8 weight percent in the concentration of gold at the boundary against a general background of 35%.

The highest level of sophistication of a quantitative digital compositional map consists of performing a complete quantitative analysis at each pixel. Such a procedure requires that the intensity for each element of the unknown, the background, and the intensity for an appropriate standard be available for each pixel in order to calculate a k-value (intensity unknown/intensity standard) x-y grid. Because of the existence of wavelength spectrometer defocusing effects, the determination of an appropriate standard intensity throughout the scan field is not a trivial problem. Detailed techniques for calculating valid k-value matrices are described by Marinenko et al.⁷ If EDS data are used, the inherently poor peak-to-background (P/B) of the spectrometer necessitates the use of accurate background removal in order to calculate a k-value x-y grid. Once the k-value x-y grid is determined, matrix corrections must be applied at each point to determine quantitative compositional values. Since a large number of points must be calculated (16 384 for a 128×128 x-y grid, which is a very modest density), efficient methods of matrix correction calculation must be employed. These methods are also considered in a separate paper.⁸ Finally, when x-y grids of compositional values are calculated, a variety of image display techniques, including various transformations and color-display schemes, can be applied to enhance the visibility of the compositional differences.

For the purposes of mapping, EDS and WDS systems offer different advantages. The EDS map is practically free from defocusing effects, even at low magnifications with very large scan excursions of 1 mm or more, whereas defocusing is significant in WDS maps even at high magnifications of 1000 or more, especially when enhancement is used to expand contrast in the final image. However, WDS images can be used to display much lower values of concentration than EDS images, because of the higher P/B for WD spectrometry. Concentrations as low as 1000 ppm can be displayed with sufficient accumulation time.

Trace Imaging

Imaging at trace levels (parts per million by weight) by means of electron-excited x rays is eventually limited by spectrometer peak-to-background, system stability, or patience. Of these three, the third is often the most difficult to extend. Consequently, compositional mapping methods that can image at trace levels more rapidly are of increasing importance. The most successful of these methods is secondary-ion mass spectrometry (SIMS). The main character of the SIMS spectrum which lends itself to trace imaging is the extremely high peak-to-background which is available for many elements, often extending to $10^6/1$ or more. Two instrumental alternatives are available for mapping. The ion microprobe is based on focusing the primary ion beam, combined with a scanning system, to provide elemental distribution maps. The alternative of focusing the secondary ions is employed in the ion microscope, in which ion images are formed by a true optical process. In the ion microscope the images are viewed directly on a fluorescent screen and are not scanned but rather are formed continuously, following ion to electron to photon conversion. Digital recording of such continuous images is accomplished by means of a computer-controlled high-gain television camera or semiconductor array device. As an example of the performance of such a system, a map of the distribution of aluminum in reaction-bonded silicon carbide is shown in Fig. 4. The aluminum is present in this material as a trace constituent at a level of 100 ppm in the bulk, but the distribution map could still be obtained in only 10 s of ion bombardment due to the great efficiency of signal collection and recording in the ion microscope.

Surface Imaging

Electron-excited x rays integrate information over 1 μm or more of depth into the sample, and thus the technique cannot be thought of as surface characterization. The increasing interest in surfaces has led to the development of surface imaging techniques. Illustrative of these techniques are Auger mapping and SIMS imaging.

The electron-excited Auger technique is complementary to x-ray mapping, since the same distribution of inner-shell ionization events gives rise to Auger electrons as well as characteristic x rays. The x rays can escape the sample from a range of depths, but the Auger electrons cannot travel more than a few nanometers in the sample without losing their characteristic energy, and thus they carry surface information. The lateral resolution of the Auger signal is limited by the lateral spread of the beam electrons and subsequent backscattering, but in general it depends strongly on signals produced by the incident probe. The high background which arises from competing backscattering and secondary electron processes can limit the contrast sensitivity of this technique, even with digital processing.

SIMS imaging is also confined to the surface of a sample, since the range of secondary ions is also of the order of nanometers. However, the erosion of the sample by ion sputtering necessarily destroys the surface as it is imaged and integrates the image information over some range of depth. For highly sensitive species and with an efficient image collection system, the depth of material removed can be kept to a few atom layers. Since a series of images can be recorded as a function of sputtering time, a three-dimensional map of the specimen can be created by a combination of the information contained in several images.

References

1. V. E. Cosslett and P. Duncumb, *Nature* 177: 1172, 1956.
2. J. I. Goldstein et al., *Scanning Electron Microscopy and X-ray Microanalysis*, New York: Plenum, 1981, 299.
3. K. F. J. Heinrich, *Electron Beam X-ray Microanalysis*, New York: Van Nostrand, 1981, 515.
4. P. J. Statham and M. Jones, *Scanning* 3: 168, 1980.
5. J. J. McCarthy, G. S. Fritz, and R. J. Lee, *Microbeam Analysis--1981*, 30.
6. C. E. Fiori, C. R. Swyt, and K. E. Gorlen, *Microbeam Analysis--1984*, 179.
7. R. B. Marinenko, D. B. Bright, R. L. Myklebust, and D. E. Newbury, *Microbeam Analysis--1985*, 159.
8. R. L. Myklebust, R. B. Marinenko, D. B. Bright, and D. E. Newbury, *Microbeam Analysis--1985*, 101.

9. K. F. J. Heinrich, "Scanning electron probe microanalysis," in R. Barer and V. E. Cosslett, Eds., *Advanced Optical and Electron Microscopy*, London, Academic, 1975, 6, 275.
10. T. J. Piccone, D. B. Butrymowicz, D. E. Newbury, J. R. Manning, and J. W. Cahn, *Scripta Met.* 16: 839, 1982.
11. D. B. Butrymowicz, D. E. Newbury, D. Turnbull, and J. W. Cahn, *Scripta Met.* 18: 1005, 1984.

HIGH-RESOLUTION TOPOGRAPHIC AND ISOTOPIC IMAGING WITH A 40keV Ga⁺ SCANNING ION MICROPROBE

Riccardo Levi-Setti, Geoffrey Crow, and Y. L. Wang

A newly developed scanning ion microprobe (SIM) focuses 40-60keV Ga⁺ and In⁺ probes to spot sizes in the range 20-90 nm, with probe currents of 1.5-30 pA. With such probes, it is feasible to explore the useful sensitivity and lateral resolution limits of imaging secondary ion mass spectrometry (SIMS). High quality isotopic maps can still be obtained at the 20nm level of lateral resolution, for samples rich in elements of low ionization potential (for positive secondary ions) or high electron affinity (for negative secondary ions). In these conditions, submonolayer depth resolution can be achieved.

The practical utilization of ion probes at the pA current and 20nm spot size level for the purposes of SIMS microanalysis and mapping requires the use of a highly efficient secondary ion collection and transport system. For this capability in particular, and in terms of spatial resolution attained, our results improve on previous uses¹⁻³ of probes from liquid metal ion sources (LMIS), for SIMS imaging microanalysis.

Requirements for High-resolution SIMS Mapping

Careful optimization of many parameters affecting both the target sample and its retrieved image is required to attain high spatial resolution from highly destructive probes such as those extracted from LMIS in a SIM.^{4,5} This requirement holds for either topographic imaging in which the *ion-induced secondary* electron (ISE) or *ion* (ISI) signals are exploited,⁶ or for SIMS mapping. In fact, relevant aspects of the probe-target interaction and image acquisition system must be considered in order to achieve image resolution approaching the probe size.⁷

On one side, the total primary ion dose should be minimal to reduce the loss of surface detail due to sputter erosion of the sample using ISE or ISI imaging. Similarly, for surface SIMS imaging, it is desirable to limit the sampled depth to the intrinsic ISI escape depth, comparable to the thickness of one monolayer. At the same time optimal specimen sampling with a digital raster involves the scan of an area whose side is given by the product of the probe diameter times the number of picture elements (pixels) per frame, which thus defines an optimal magnification. The desired erosion depth and the scan area define a volume of material sputtered and in turn an overall tolerable dose of primary ion beam.

On another side, the conditions in which this dose is administered is important. In a digitally controlled raster scan coupled to a SIMS system, the dwell time per pixel must exceed the time of flight of the analyzed secondary ions to preserve synchronous image display. This requirement leads to a mass-dependent, minimum dwell-time condition. An upper bound on the dwell time per pixel also exists, imposed by the desirability of maintaining a monolayer O₂ coverage on the sample during a SIMS scan, to enhance the ISI yields,⁸ thus improving SIMS sensitivity and image statistics. Two conditions to satisfy this requirement, depending on whether or not O₂ replacement is available, are discussed in detail elsewhere.^{5,7}

With a carefully designed SIM and SIMS system coupled to a high-resolution image display, it has proved feasible to preserve the matching of beam spot size and image resolution to reach the 20nm level in either ISE, ISI, or SIMS images, with probe currents as low as 1 pA. Under these operating conditions, we approach the limits of SIMS lateral resolution set by the size of the collisional cascade initiated by the incident ions.⁹

Instrumentation

The high-resolution SIM (Fig. 1) was developed in a collaboration between the University of Chicago (UC) and Hughes Research Laboratories (HRL). The ion beam, extracted (thus far) from a Ga⁺ or In⁺ LMIS, is accelerated and focused by a two-lens column, with one crossover.

The authors are at the Enrico Fermi Institute and Department of Physics, The University of Chicago, Chicago, IL 60637. This work was supported by the National Science Foundation under Grant DMR-8007978 and partially by the Materials Research Laboratory at the University of Chicago.

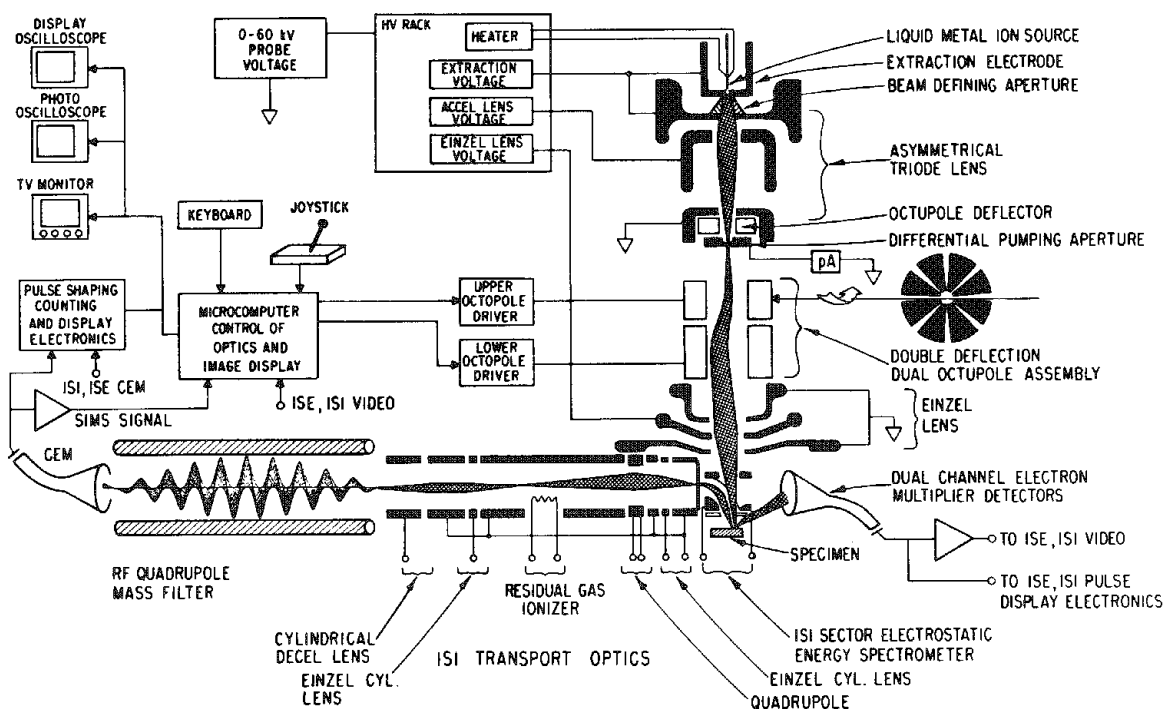


FIG. 1.--Schematics of UC-HRL scanning ion microprobe.

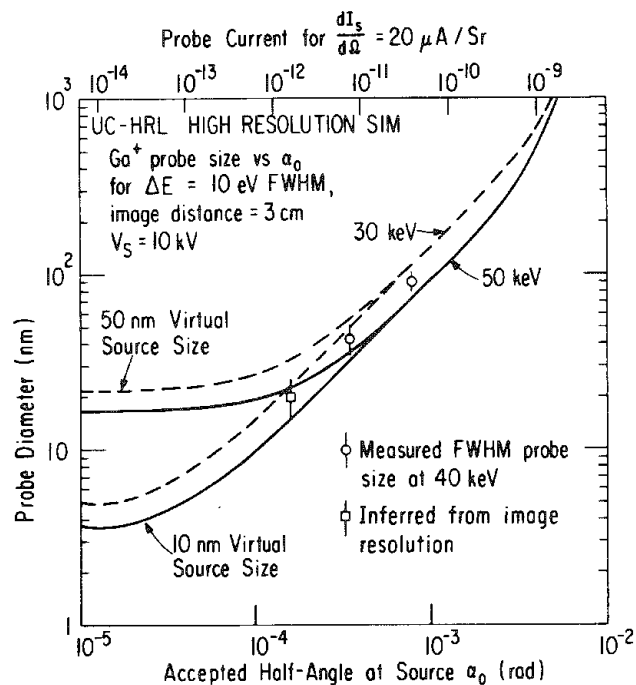


FIG. 2.--Calculated probe diameter d_p vs beam acceptance half-angle α_0 at the source for Ga-probe in UC-HRL SIM. Experimental points at three beam-defining apertures are shown.

and stigmator are controlled by a Z-80-based microprocessor. The raster size and dwell time per pixel can be varied over a wide range. All micrographs reproduced here contain 1024×1024 pixels/frame. For optimal imaging, such that contiguous pixels on the sample are mapped on the CRT, the size of the imaged area is 1024×1024 or $20 \times 20 \mu\text{m}^2$ at (for example) $d_p = 20 \text{ nm}$.

An optical aperture, placed in front of the LMIS defines the source acceptance half-angle α_0 , and in turn the final probe size d_p , in this chromatic-aberration-limited optical system (Fig. 2). The calculated performance of the column has been verified at three settings of α_0 , with aperture diameters of 25, 12.5, and 5 μm . From the Gaussian profile of grooves sputter-etched in Au-coated Si wafers, we have determined a d_p FWHM of 90 and 43 nm at α_0 values of 0.78 and 0.39 mr, respectively. For the smallest α_0 (0.16 mr), a probe size of $\sim 20 \text{ nm}$ was inferred from the observed image resolution. For a source current of 2 μA , the probe currents are 32, 8, and 1.6 pA for the three aperture settings, respectively. Departures from the chromatic-aberration-limited regime, due to the Gaussian image of the virtual source size, have not yet been observed, which implies that the latter must be smaller than $\sim 50 \text{ nm}$.

ISE and ISI topographic imaging is obtained from the signals collected by two channel electron multiplier detectors (CEM) overlooking the target region at a shallow angle. Individual CEM pulses are discriminated, amplified, shaped, and displayed with variable width and amplitude on a high-resolution CRT. The probe deflection system

A miniaturized ISI energy analyzer and transport system (2 cm deep) is coupled to an RF quadrupole mass filter for SIMS microanalysis (Fig. 1). The scheme is conceptually similar to that developed by Wittmaack.¹⁰ The positive or negative ISI are extracted from the target region by an accelerating potential of ± 100 V within a distance of a few millimeters. They are energy-analyzed by a 90° electrostatic prism and focused onto a slit that transmits ions within an energy window of ~ 10 eV. The center of the quadrupole is maintained at an offset potential of a few volts relative to the target potential. The SIMS CEM signal is processed in the same way as the ISE or ISI signals for pulse-mode image displays.

Microanalytical SIMS Capability of Ga⁺ and In⁺ Probes

A detailed analysis of the residual SIMS sensitivity at the present limits of lateral resolution (~ 20 μm) has been reported previously.⁷ From a sample of natural fluoroapatite of known composition, an overall detection efficiency for Ca⁴⁰⁺ of 1/250 sputtered atoms has been derived. The measured Ca⁴⁰⁺ ion yield observed for this sample is 2×10^4 cps/pA, for a 40keV Ga⁺ probe, and 1.4 times higher for an In⁺ probe. Both positive and negative ISI spectra have been found to agree substantially with those obtained with an O⁻ probe,¹¹ in a Cameca IMS 300 analyzer, although the dynamic range in our case is reduced by 2-3 decades relative to that available with the latter. Nevertheless, even without external O₂ enhancement, our ion yields are a factor of $\sim 10^3$ higher than those of the Cameca IMS 300, and still a factor of 10 higher than those of the Cameca IMS-3f.¹²

In addition to Ca in fluoroapatite, the highest yields for positive ISI, in the 10^4 cps/pA range, have been observed for the other elements of low ionization potential, the alkali in particular, in silicate minerals and glasses. Comparable yields for the negative ISI have been observed for the elements of high electron affinity, the halogens in particular, and oxygen. Among the elements of lowest sputtering yield, C⁻ and C₂⁻ in (for example) graphite for an In⁺ probe have ISI yields of $\sim 2 \times 10^2$ cps/pA. The ISI yields of oxygen-saturated pure metal surfaces under bombardment by a 9 keV In⁺ probe have been studied extensively by the Vienna group.^{13,14} With our 40keV Ga⁺ or In⁺ probe, we observe yields $\sim 10^3$ higher than those reported by the above authors for a variety of matrices. Al metalizations of integrated circuits have shown yields in the range 10^3 - 10^4 cps/pA, and Ti and Cu from a superconducting wire, $\sim 10^3$ cps/pA. Fe and Cr in stainless steel yield $\sim 10^3$ cps/pA with primary currents of ~ 1 -2 pA, but the yields are reduced to $\sim 2 \times 10^2$ cps/pA for currents above 10 pA. This effect may be related to the rate of surface O₂ depletion, in absence of O₂ flooding.

In summary, the relative yields of positive and negative ISI from Ga⁺ and In⁺ probes 20-50 nm in size, at 40 keV, are quite comparable to those of O⁻ probes. When coupled to a highly efficient SIMS system, they still provide ~ 4 decades of spectral sensitivity at currents of 1-10 pA in acquisition times $\lesssim 1$ h.

High-resolution Topographic and Isotopic Imaging

Topographic imaging plays an important role as a diagnostic tool for the optimization of a SIM focusing performance, prior to elemental mapping. The image quality obtainable with the UC-HRL SIM is illustrated in Fig. 3. Figures 3(a) and (b) are two views of the eye of the fruit fly (*Drosophila melanogaster*) with the ISE signal from a Ga⁺ probe of 1.6 pA. The image resolution, estimated at ~ 20 nm (from higher magnification images), is sufficient to reveal the "corneal nipple array" on the lens surface, which serves an anti-reflection role in the insect eye. This structure is rapidly eroded in subsequent scans at the magnification of Fig. 3(b). With a 10pA In⁺ beam, at this magnification, the lenses collapse during visual focusing. Figures 3(c) and (d) show two views of the SiO₂ skeletons of fossil diatoms. The field of view in Fig. 3(d) is 5 μm wide and the resolution limits of the SIM begin to be noticeable. However, the absence of truly sharp edges at high SIM magnification is also partly due to sputter erosion of the sample.

Meeting the requirements previously set forth concerning optimal, submonolayer SIMS mapping has made it possible to observe the interplanar distribution of intercalant in graphite (HOPG), intercalated with SbCl₅. Figures 4(a) and (b) refer to stage-4; Figs. 4(c) and (d) to stage-2 of intercalation. (The stage number corresponds to the number of graphite layers between each layer of intercalant.) The observed structures can be sharply mapped only in the first scan with a 1.6pA, 20nm Ga⁺ probe, but most detail is lost with an

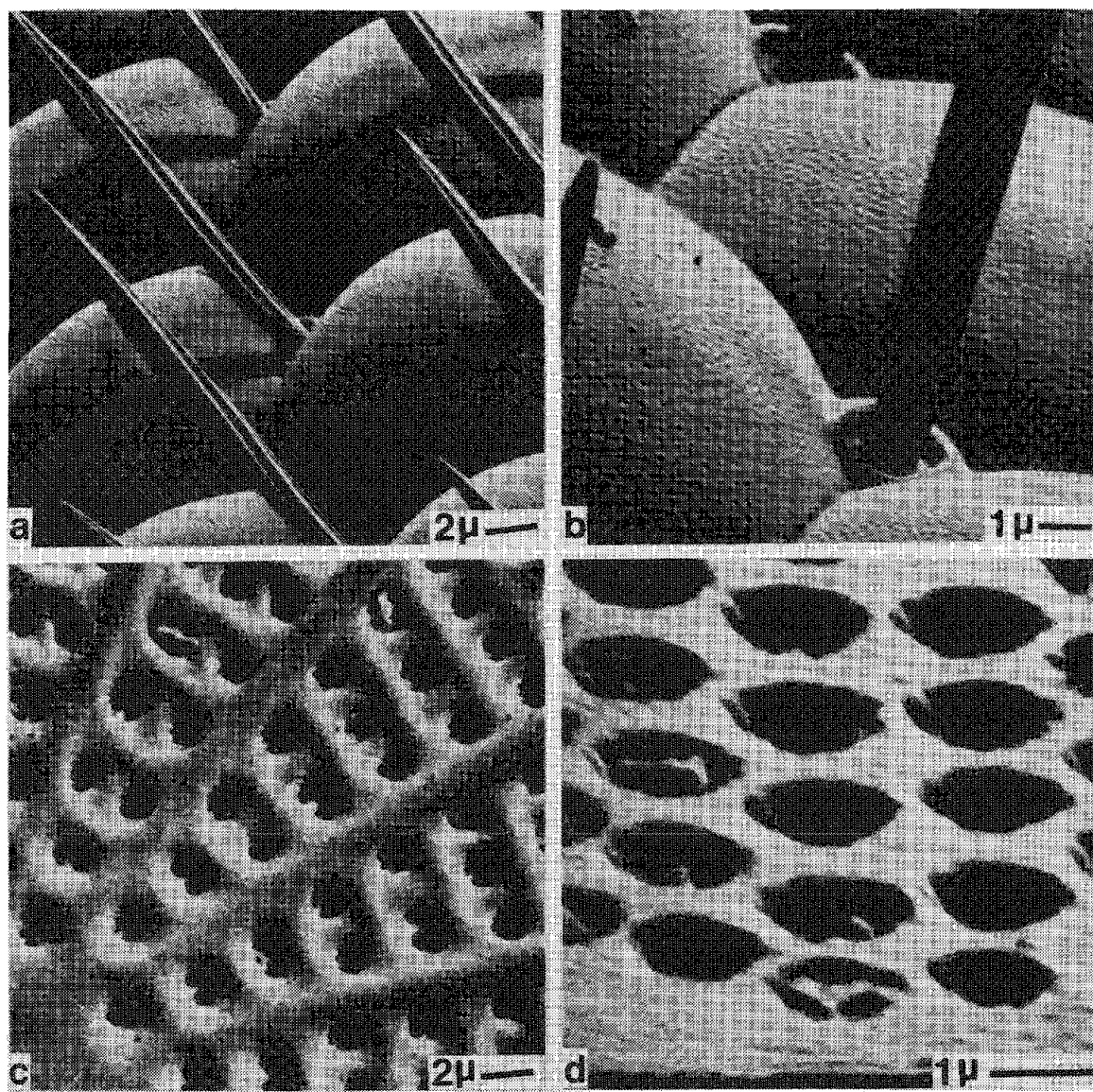


FIG. 3.--Topographic contrast in ISE and ISI images obtained with 40keV, 1.6pA Ga⁺ probe in 256s exposures: (a) and (b) details of the eye of *Drosophila melanogaster*, ISE signal; (c) and (d) fossil diatoms (SiO₂). ISE signal in (c), ISI signal in (d).

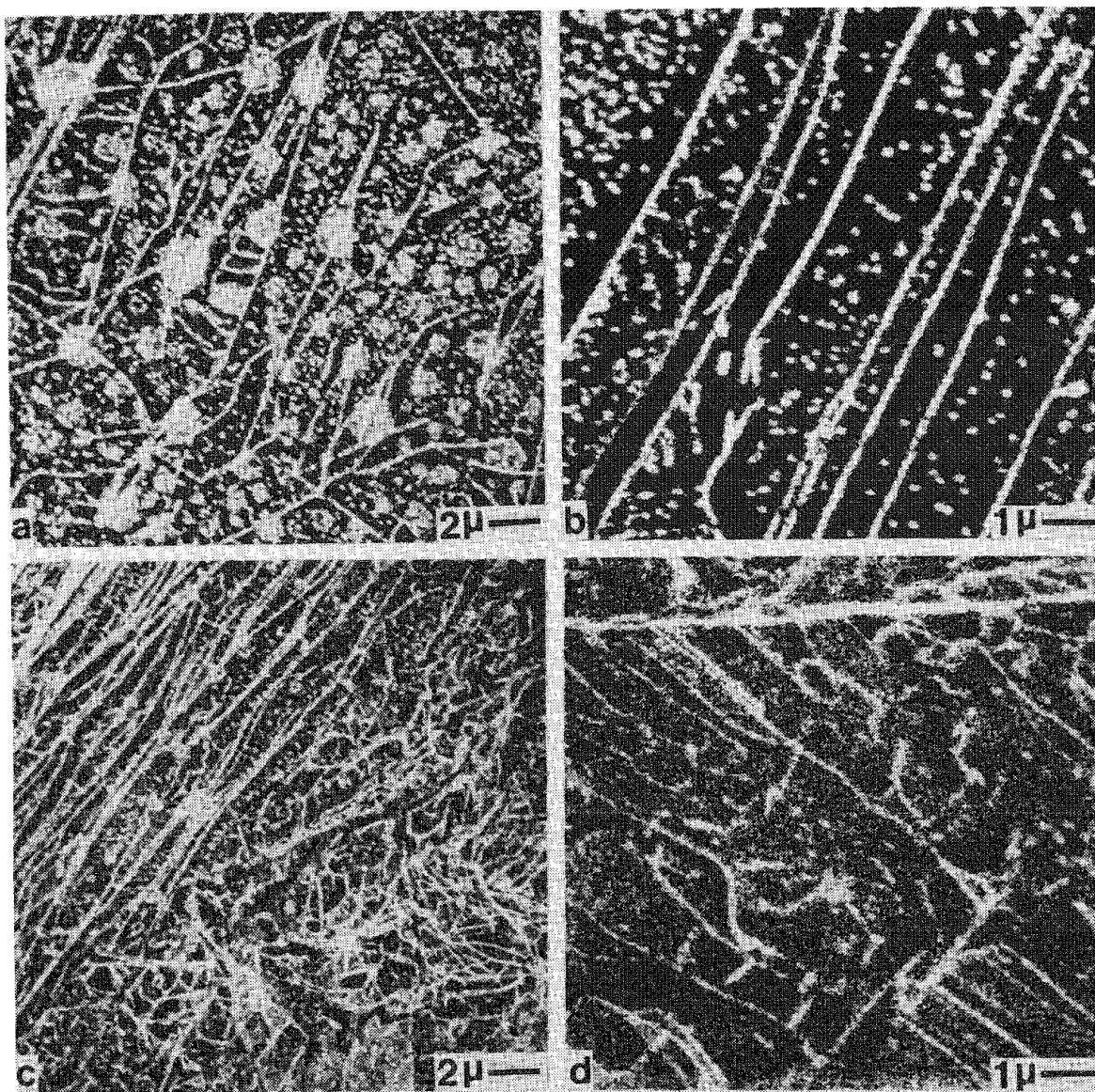


FIG. 4.-- Cl^{35} maps of freshly cleaved, SbCl_5 -intercalated, highly oriented pyrolytic graphite; 1.6pA, 40keV Ga^+ probe, 512s exposures. (a) Stage-4, 1.3×10^6 counts; (b) stage-4, 3.2×10^5 counts; (c) stage-2, 1.5×10^6 counts; (d) stage-2, 5.3×10^5 counts.

8pA scan due to the superposition of multilayer structure. The bead-like domains are interpreted¹⁵ as representing the intercalant structure predicted by Daumas-Herold,¹⁶ which has heretofore escaped direct observation. The line network is attributed to the migration and coalescence of intercalant domains along surface steps and stacking faults created during the cleavage of the samples.

FET structures in GaAs, observed with an 8pA, 45nm Ga⁺ probe, are shown in Fig. 5. The topography, enhanced by sputter erosion, is seen in Fig. 5(a). Figure 5(b) is a Ti⁴⁸⁺ map, outlining the Ti-W metallization of the gate areas. Differential Ga⁺ and Ga₂⁺ self-sputtering is observed in Figs. 5(c) and (d). The relative yields of resputtered Ga⁺ from the different target materials represented here (W for the gates, Au for the source and drain pads of the FETs, GaAs for the matrix), reflect the relative surface concentrations c(Ga) which are reached as an equilibrium between implant and sputtering rates. These concentrations depend on the sputtering yield Y of the target material and the projected range R_p and straggling σ_p of the probe ions in the target, as^{14 17}

$$c(\text{Ga}) = (\frac{1}{2}Y)[1 + \text{erf}(R_p/\sqrt{2}\sigma_p)]$$

In our case, since the ranges of the primary ions in W and Au are comparable, the observed Ga⁺ yields are determined by Y. For the monomer Ga⁺ as seen in Fig. 5(c), we observe relative intensities from W and Au consistent with the above, since Y for Au is expected to be much larger than for W. It is interesting that the emission of the dimer Ga₂⁺ does not always follow the behavior of the self-sputtered Ga⁺, as is seen in Fig. 5(d), which shows that Ga₂⁺ emission is totally absent for the W surfaces, quite the opposite of that of Ga⁺. This suggests that specific surface molecular effects are operative in this case, which deserve further investigation.

The highly differentiated silicate mineral structures of stone meteorites (chondrites) can be imaged with unprecedented detail with our microprobe. This class of primitive meteorites consists of aggregates of spheroidal bodies called chondrules, made up of crystalline grains of olivine and pyroxene, cemented by a glassy matrix as quenched melt droplets. Prior to accretion, the chondrules are thought of as having been exposed to the dusty environment of the early solar nebula, acquiring rim coatings whose composition and structure is still under active study.¹⁸

Figure 6 shows some elemental maps obtained for the Mezo-Madaras chondrite, from polished sections lightly coated with Au-Pd to prevent charging of the insulating sample. These maps were obtained with a 8pA, 45nm Ga⁺ probe. Figures 6(a) and (b) show Mg²⁴⁺ and Fe⁵⁶⁺ maps of the boundary of a chondrule. The Fe-rich rim appears as a vertical band coating the body of the chondrule containing olivine grains, also rimmed by a thin layer of Fe. Several other maps of the same region, not shown here, identify the dark areas of both Figs. 6(a) and (b) as rich in Na, K, and Al, components of glass. Figures 6(c) and (d) are maps of Na²³⁺ and Mg²⁴⁺ for an area of the interior of a chondrule, exhibiting radiating structures of olivine crystals embedded in glass.

Numerous other applications of high-resolution SIMS mapping are at present under investigation. Of particular relevance in the biomedical field is the feasibility of studying the dynamics of elemental absorption, exchange, and fixation in biological tissues with stable isotopes as tracers. This approach is being attempted with Ca⁴⁴ as label in the study of the growth and calcification of neonatal skull bone (calvaria).¹⁹ Shown in Figs. 6(a) and (b) are the distributions of Na²³⁺ and Ca⁴⁰⁺ on the surface of such bone. The latter is covered by a network of organic material very rich in Na and K, containing only a sparse distribution of Ca nucleation centers. A much richer Ca distribution for deeper layers is exposed by sequential sputter erosion. The Ca⁴⁴/Ca⁴⁰ ratio measured for unlabelled samples is consistent with the natural abundance ratio = 0.0215, which indicates an absence of molecular interferences. For bone cultured live, in vitro, in a Ca⁴⁴ medium, surface Ca⁴⁴/Ca⁴⁰ ratios as high as 0.58 have been measured. Figures 6(c) and (d) show maps for Na²³⁺ and Ca⁴⁴⁺ for one of these labelled samples. The Ca⁴⁴ distribution, which corresponds closely to that of Ca⁴⁰ (not shown here), shows the pathways and sites of active bone calcification.

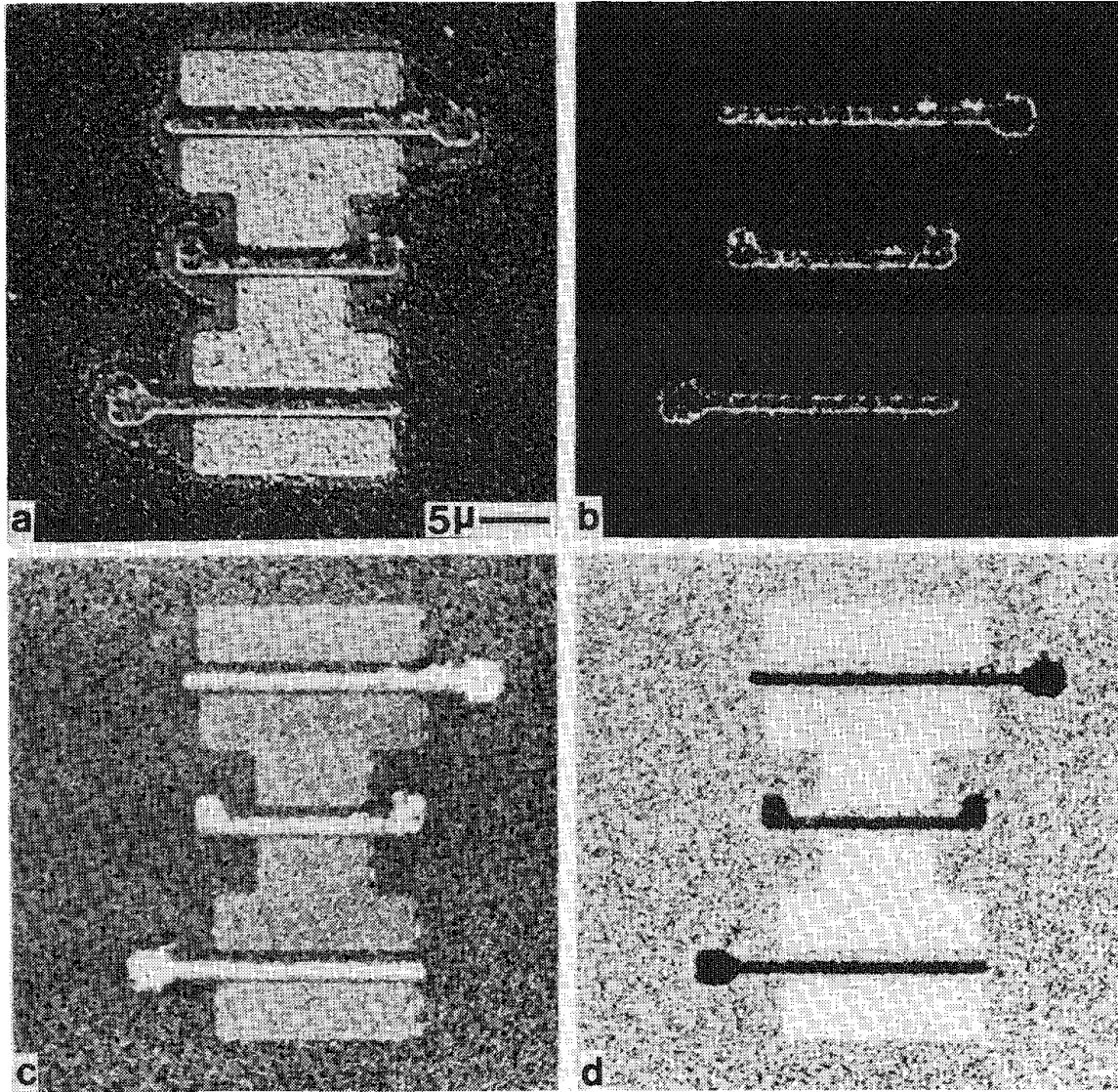


FIG. 5.--FET structures in GaAs. W metallizations cover gates; source and drain pads are coated with Au; 8pA, 40keV Ga⁺ probe. (a) ISI image after sputter erosion, 32s exposure; (b) Ti⁴⁸⁺ map, 512s exposure, 3600 counts; (c) Ga⁶⁹⁺ map, 256s exposure, 1.8×10^6 counts; (d) Ga₂¹³⁸⁺ map, 512s exposure, 3.8×10^5 counts.

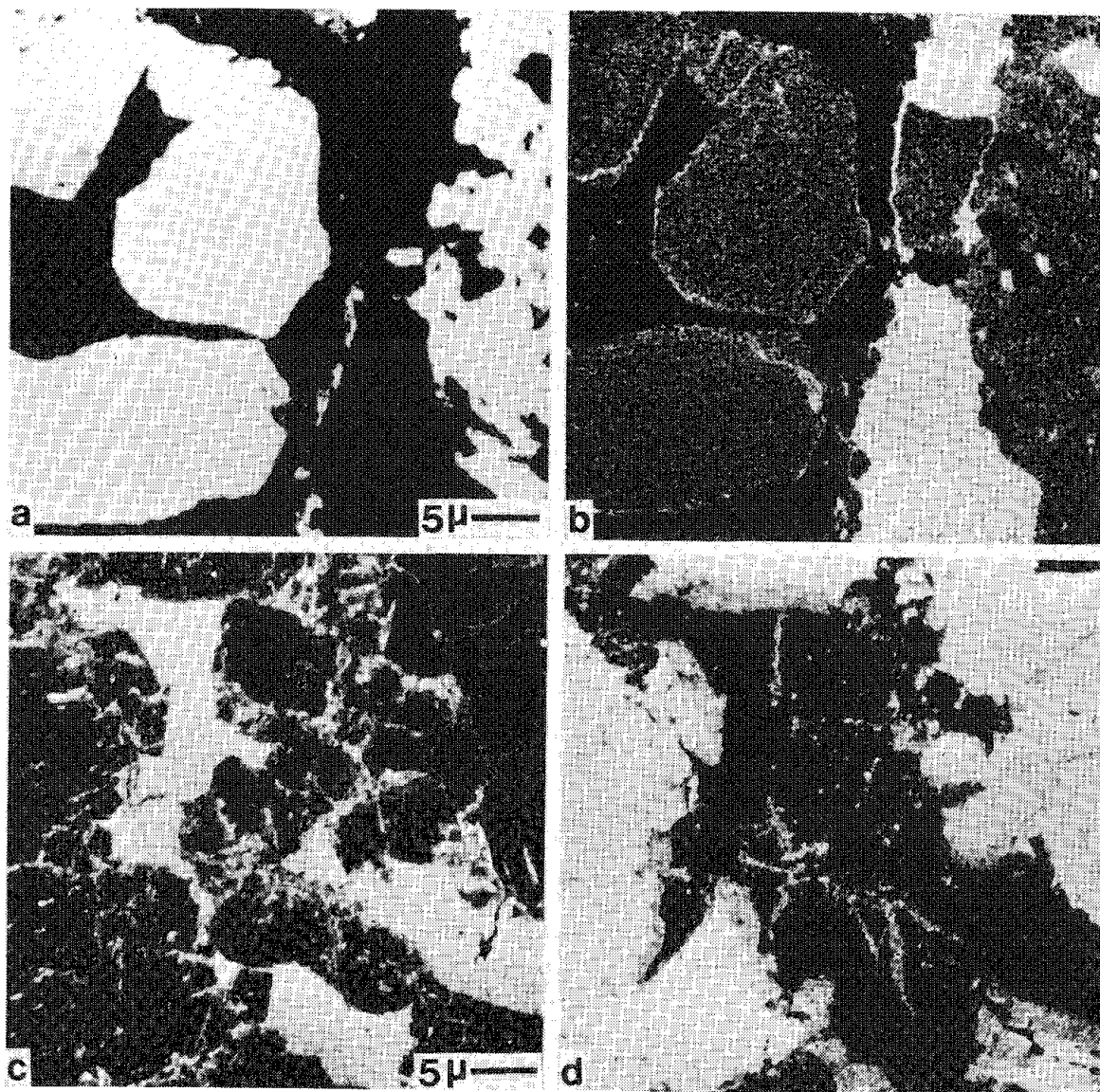


FIG. 6.--Elemental maps of polished section of Mezo-Madaras chondrite: 8pa, 40keV Ga⁺ probe. (a) Mg²⁴⁺, chondrule rim region, 256s exposure, 1.9×10^6 counts; (b) Fe⁵⁶⁺, same area as in (a); (c) Na²³⁺, chondrule interior, 512s exposure, 2.3×10^6 counts; (d) Mg²⁴⁺, same area as in (c), 512s exposure, 2.2×10^6 counts.

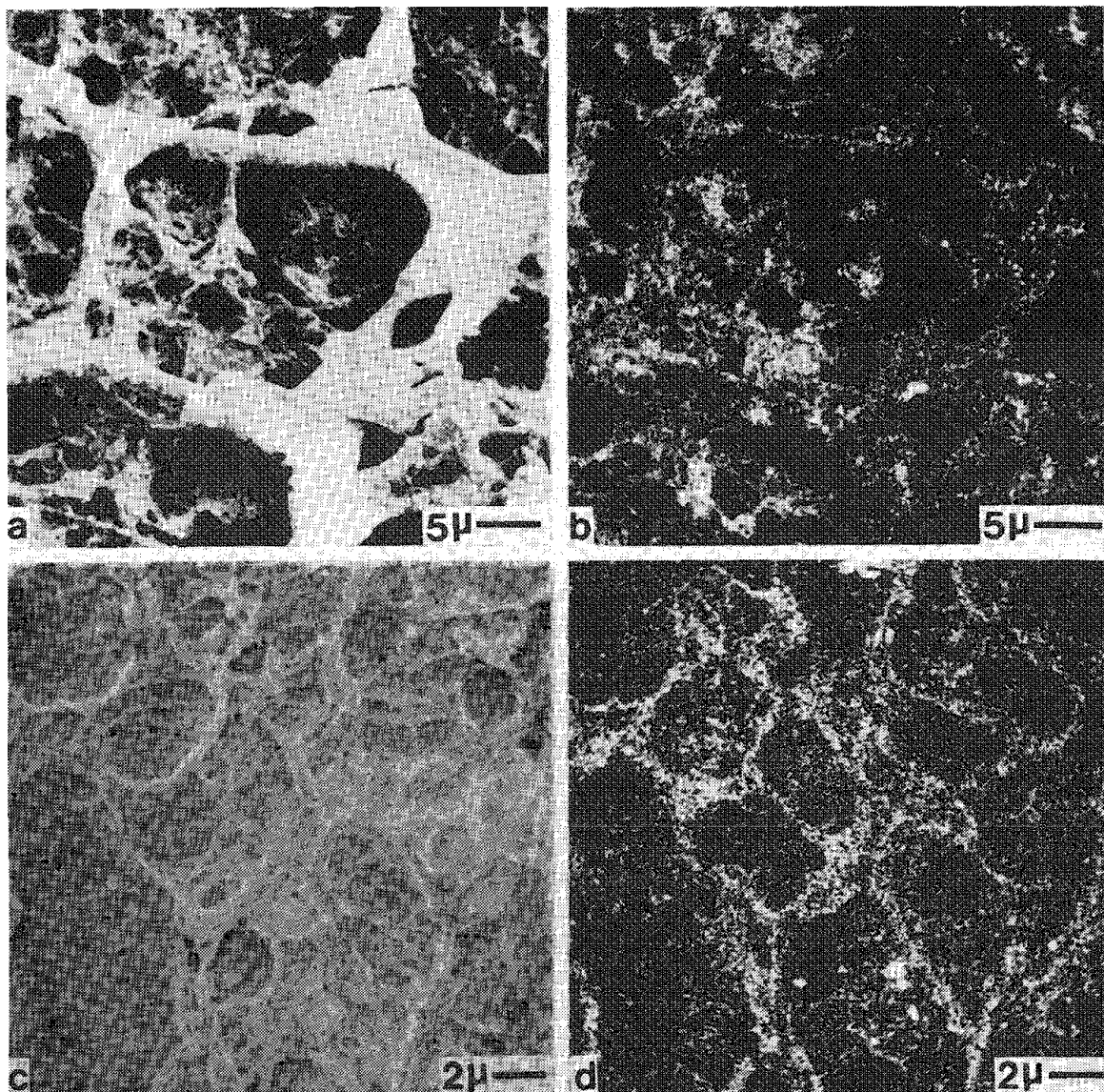


FIG. 7.--Elemental maps of skull bone of neonatal mouse. (a) Na^{23+} , 40keV, 8pa Ga^+ probe, 512s exposure, 2.8×10^6 counts; (b) Ca^{40+} , same area as in (a), 512s exposure, 1.3×10^5 counts, $\text{Ca}^{44}/\text{Ca}^{40} = 0.021$ for this normal bone; (c) Na^{23+} , 40keV, 1.6pA Ga^+ probe, 512s exposure, 3.4×10^6 counts, bone sample cultured live, in vitro, in Ca^{44} medium; (d) Ca^{44+} , same region as in (c), 512s exposure, 1.2×10^5 counts, $\text{Ca}^{44}/\text{Ca}^{40} = 0.55$ for area shown.

Conclusions

With careful design of the SIMS optics and optimal choice of operating parameters, exploitation for high-quality imaging microanalysis of Ga^+ and In^+ probes at the 20nm size, 1.6pA current level has been shown to be feasible. Although limiting in terms of spectral sensitivity, such high-resolution, low-intensity probes represent a most powerful tool for spatially resolved surface analysis and pave the way to a new generation of SIMS studies.

References

1. A. R. Bayly et al., "SIMS microanalysis with a gallium ion microprobe," *Nucl. Instr. Methods* 298: 375-382, 1983.
2. A. R. Bayly et al., "High resolution scanning secondary ion mass spectrometry (SIMS) using liquid metal field ionization sources," *SEM/83 I*, 23-29.
3. A. R. Waugh et al., "The application of liquid metal ion sources to SIMS," *Vacuum* 34: 103-106, 1984.
4. F. G. Rudenauer, "Liquid metal ion sources for scanning SIMS," in A. Benninghoven et al., Eds., *SIMS IV*, Springer-Verlag, 1984, 133-137.
5. R. Levi-Setti et al., "High spatial resolution SIMS with the UC-HRL scanning ion microprobe," *J. Physique* 45: C9-197-C9-205, 1984.
6. R. Levi-Setti, "Secondary electron and ion imaging in scanning ion microscopy," *SEM/83 I*, 1-22.
7. R. Levi-Setti et al., "Progress in high resolution scanning ion microscopy and SIMS imaging microanalysis," *SEM/85*, in press.
8. G. Blaise and M. Bernheim, "Adsorption of gases studied by secondary ion emission mass spectrometry," *Surface Science* 47: 324-343, 1975.
9. H. Liebl, "Ion probe microanalysis," *J. Physics* E8: 797-808, 1975.
10. K. Wittmaack, "Secondary ion mass spectrometry as a means of surface analysis," *Surface Science* 89: 668-700, 1979.
11. A. Lodding et al., "Secondary ion mass spectra of apatites," *Z. Naturforsch.* 33a: 697-708, 1978.
12. A. Lodding, private communication, April 1985.
13. F. G. Ruedenauer et al., "First results on a scanning ion microprobe equipped with an EHD-type Indium primary ion source," in A. Benninghoven et al., Eds., *SIMS III*, Springer-Verlag, 1982, 43-48.
14. H. Gnaser et al., "Application of a liquid metal ion source in ion microprobe analysis," H. O. Andren and H. Norden, Eds., *Proc. 29th Int. Field Emission Symp.*, Stockholm: Almqvist Wiksell Int., 1982, 401-408.
15. R. Levi-Setti et al., "High resolution scanning ion microprobe study of graphite and its intercalation compounds," *Bull. Am. Phys. Soc.* 30: 240, 1985.
16. N. Daumas and H. Herold, "Sur les relations entre la notion de stade et les mécanismes réactionnels dans les composés d'insertion du graphite," *C. R. Acad. Sci.* 268: C-373-C-375, 1969.
17. F. Schulz and K. Wittmaack, *Rad. Eff.* 29: 31, 1976.
18. Y. L. Wang et al., "High lateral resolution SIMS mapping of meteorite chondrule," *Nucl. Instr. Methods in Phys. Rev.* 1985 (in press).
19. D. Bushinsky et al., "High spatial resolution localization of a 44 Calcium label in neonatal mouse calvaria," Abstract, 7th Ann. Meeting Am. Soc. for Bone and Mineral Research, Washington, D.C., June 1985.

COMPUTER-AIDED COMPOSITIONAL MAPPING IN SCANNING ELECTRON COLUMN DEVICES

C. E. Fiori, R. D. Leapman, and K. E. Gorlen

This review paper is concerned with the acquisition, display, and interpretation of x-ray and/or electron energy loss images (maps) that can be obtained by a scanning electron column device, and how the modern digital computer can be applied in the process.

The Image Acquisition and Display System

In the conventional display system used on scanning electron column instruments we move the electron beam over the face of the recording oscilloscope in synchronism with the beam over the specimen surface. When a detector receives an increase in its signal from the specimen (e.g., brightfield, x rays, etc.) the beam on the recording oscilloscope is increased in brightness. Consequently, an "image" is "painted" onto the face of the display tube. The synchronous beams are displaced by imparting horizontal and vertical velocity components V_x and V_y . V_x is typically between 500-2000 times V_y . The direction in which the velocity component is greater is called the line direction and the other direction is called the frame direction. When the beam reaches the end of a line on the oscilloscope it is inhibited from producing light (blanked), moved to the beginning of the next line, and the scan repeated. The "conventional" display system has been used since the earliest days of scanning electron column devices since only simple analog electronic devices are required.

A method alternative to continuous beam rastering is discrete rastering accomplished with what is usually called a "digital scan generator." In this technique the x and y velocity components of the synchronous electron beams are not constant but remain zero for a finite period of time and then the beam is rapidly stepped to the next point. The displacements along the line direction are equal. When the end of the line is reached, the beam is moved back to the beginning of the line and displaced one step along the frame axis with the step size equal to the line step. Each point in the image at which the beam dwells is called a "pixel." Digital scan generators as used in scanning electron column devices typically use between 500 and 4000 pixels along the frame and line directions. The digital method of scan generation is very convenient for applications with the digital computer. Images contain an enormous amount of information and so mathematical manipulations involving images require the use of a computer. It can be expected that the digital technique will replace the "conventional" method in most future microscopes.

The application of an on-line and interactive computer results in a substantial improvement in several key capabilities of a scanning electron column. These capabilities derive mainly from the ability of the computer to record all the information generated and detected when the primary electron beam interacts with a location on the specimen. Consequently, beam-induced radiation damage is minimized (an important consideration in biological or polymer applications). The recorded information may be modified, and most important, combined, in a great variety of ways before presentation to the operator-analyst, which permits structure and/or analytical information to be seen in a micrograph where none could be seen before.

It was obvious from the beginning that the output from a scanning mode microscope could be directly digitized. Over the last several years there have been several reports of such work now that computers with sufficient memory, mass storage, and speeds have become available at an acceptable cost [see, for example, Refs. (1-10)]. Indeed, several commercial computer-based imaging products are now available that combine some of the features to be described below. What we discuss here is based on our experience in interfacing a laboratory grade minicomputer to an analytical electron microscope and an electron beam x-ray microanalyzer.

General Considerations for a Computer and Its Microscope Interface

We shall describe the advantages of an "on-line" and "interactive" computer. By "on-line" we mean that the computer does more than just record and process signals produced by

The authors are at the National Institutes of Health, Bethesda, MD 20205.

the microscope; it also actively controls how the signals are acquired. Once the analytical requirements have been specified by the operator the computer controls, for example, the position of the electron beam, the acquisition parameters for the x-ray spectrometers (EDS or WDS), and gain and integration times of the secondary or backscattered electron detectors. By "interactive" we mean that the computer returns an answer quickly enough to be useful in the analytical strategy of the operator. For example, if the operator requires an x-ray analysis the computer can process the acquired spectra to obtain atomic concentrations. Also, images may be processed by modifying or combining information content in such a way as to permit the operator to see features in the image that the unprocessed image did not reveal. The operator can utilize the results of such rapid calculations on data to decide whether a particular feature of a specimen should be further examined.

We need to clarify a possible confusion in terminology. An "image" ("micrograph," "picture," "area scan," etc.) of an "area" is obtained by scanning the primary electron beam over a usually rectangular area of the specimen and changing the intensity of the electron beam of the display oscilloscope (which is scanning in synchronism with the primary beam) by a signal derived from some component of the beam-specimen interaction process. Confusion can result when more than one type of signal (e.g., bright or darkfield, characteristic or continuous x ray, etc.) are recorded simultaneously. We can now obviously have different "images" of the same area all derived from the same raster scan. Consequently, it becomes necessary to specify which signal (or combination of signals) was used and the area scanned for each "image." Indeed, in some situations it is desirable to record more than one raster scan of the same area, for example, to provide a measure of differential mass loss. It is then necessary to identify the raster scan in addition to area and signal.

Considerations for the Microscope

Several features are desirable on a computerized scanning electron column; also, there are limitations of the microscope itself that must be recognized in the design of the interface.

When the computer has completed a task, control of the microscope electron beam should be returned automatically to the conventional sweep circuits so that an image can be viewed on the microscope display. While the computer is processing data the beam can be turned off to avoid unnecessary specimen irradiation. Devices that accomplish this action are referred to as beam blankers and typically consist of an electromagnetic or electrostatic deflector located above the first condenser lens. These devices should be designed so that the electron beam can be moved on or off the specimen in a few microseconds. When the beam is moved back on the specimen there should be no spatial hysteresis. Such beam blankers permit the use of a "pulsed tube" mode of operation in conjunction with the energy-dispersive detector.¹¹ Pulsed tube mode EDS can increase x-ray count rates by as much as a factor of four.

Long data acquisition times (many hours) are sometimes required because of the nature of the samples being analyzed and the physical processes involved. If standards are being used in a quantitative scheme significant periods of time might elapse between standard measurements. During these times it is possible that the current in the electron probe may change and some measure of this change is required. A device that can accomplish this task is a small insertable Faraday cup (a carbon slab will work just as well) located preferably just above the specimen or between the condenser and objective lenses after any beam limiting apertures. This device can also serve as a slow beam blanker with a response in the order of one second. Both the insertable Faraday cup and the fast beam blanker are examples of what might be called "premium" accessories. That is, they are not yet on the standard accessory list of all microscope manufacturers but can be had at the time of initial purchase by "special" request (i.e., before submission of a purchase order).

Computer control of the electron beam in the microscope is accomplished by the use of digital to analog converters (DACs). Due to noise and magnetic and electrical nonlinearities in the microscope scan coil circuits it is not meaningful to use DACs which convert more than 12 bits.¹² This conversion corresponds to a spatial resolution of one part in about four thousand.

To avoid electrical ground loops it is desirable to exclude the metal of the microscope column from any signal circuit. Consequently, coaxial-type vacuum feed throughs may have

to be converted to triaxial or other multiple-pin types. Examples of signal lines for which this modification may be required include the solid-state detectors for backscattered electrons and the induced specimen current signal feed through.

Considerations for the Computer

As is well known, the development of computer and related technology is proceeding at a staggering pace. As soon as a "state-of-the-art" device is announced it is superseded. However, when one has work to be done and a need for some device to do this work, one has to select the best equipment affordable and proceed. A lot of good work gets done with "outmoded" equipment and one can console oneself that producing results is more important than finding design errors for the manufacturer of the "latest" state-of-the-art gadget. The following paragraphs describe equipment that is available at reasonable cost at the time of writing (1985). It is a certainty that better devices will soon be available to do many of the things discussed and so we have attempted to be as general as possible.

Image processing requires large amounts of main memory and disk storage. Even a simple operation such as subtracting one $512 \times 512 \times 8$ bit image from another would require 512 kilobytes (KB) of main memory to hold the data. Many 16-bit minicomputers (the most ubiquitous variety at the time of writing) cannot be equipped with so much memory, and most of those which can must resort to address-mapping tricks to access all of it. This situation exists because the instructions of 16-bit processors usually produce 16-bit addresses, which allows only 65K words or bytes of data to be accessed. Given this constraint, it is necessary for programs to operate on images in small pieces which must be moved between disk and main memory or in and out of a programs addressable memory. Even with these restrictions a number of commercial products of great power exist at reasonable cost and performance. However, 32-bit computers with more than sufficient memory capability have recently become available at quite reasonable cost and speed; these devices are definitely more suitable for image processing.

Scanning a specimen in an SEM can produce a large quantity of data. For example, a 512×512 picture element scan of a specimen taken while data are being collected from EDS, backscattered, and secondary electron detectors would require several megabytes of disk storage for raw data. Depending on the nature of the various signals, different amounts and type of storage are required for the data. An absolute minimum amount of storage, at each pixel, in STEM applications would be 12 bits, which corresponds to a resolution of one part in 4096. Some signals might require two full 16-bit "words" to store the data at each pixel in the image. Usually these data will be stored on large capacity disk units with either removable or fixed media packs. The latter units are often called "Winchester" disks and are available at present for example with 474 megabyte capacity for a total hardware cost of \$15,000. Versions of 5-30 megabytes are available for several thousand dollars. These disks have an average access time of about 40 ms and can transfer or accept data at a rate of about a megabyte/s (i.e., about an image/s). These units are also used to store the "operating system" of the computer, user programs, and small data files. After the acquisition of only a few images, however, it becomes apparent that some form of main archival storage is required. Reel-to-reel 9 track tape drives (capable of storing of the order of 100 images) are excellent for this purpose but are expensive (\$15,000). Recently, "streaming" tape units and tape cartridges have become available at greatly reduced cost which are equally effective, and more convenient, for archiving purposes.

An EDS or WDS x-ray spectrum can be mathematically described by a vector (one-dimensional array). Similarly, an image may be described by a matrix (an M by N dimensional array). There is a computer accessory, generally called an array processor, which can speed up operations on vectors and matrices by several powers of ten. For example, a typical array processor can perform a complex fast Fourier transform of a 1024 point x-ray spectrum in several milliseconds. The present cost of an array processor is approximately \$5-15,000. However, an array processor can be tricky to program.

Displaying digital images involves much more than exhibiting processed data on a screen. One should be able to alter contrast or brightness, perform pseudo-coloring, annotate with arrows, text, and other graphical notation, superimpose graphs (line scans), outline areas of interest, zoom, pan, or combine several images. To have the central processor (CPU) of the main computer do these functions is slow and burdensome and difficult to program. The computer is unavailable for anything else while any of the above is being performed.

Commercial products are available that are usually called image-display systems. These systems have enough memory to store multiple 512×512 or $1024 \times 1024 \times 8$ -bit images and a

number of similarly sized several bit overlays for alphanumeric and graphical information. Eight bits (i.e., 256 "levels") is totally sufficient for display purposes even though the data displayed, for example, were acquired with 16 bits of resolution (65 000 "levels"). It is a trivial matter to "map" the "acquired" resolution into the "displayed" resolution to display all of the data or only certain parts of it. Output can be produced on a standard red-green-blue (RGB) color monitor, refreshed at 30 frames/s directly from the display system memory. The main computer is free to perform other tasks, such as data acquisition, while all of the above mentioned display functions are being performed on previously acquired images by the display system. The display system is also considerably faster at performing the above since special hardware is usually included to make the display truly interactive with the operator. One such piece of hardware is an extremely fast integer array processor which operates directly on the 8-bit image planes. This processor can, for example, add one image plane to another in less than one frame time (i.e., $1/3$ s). The cost of this "built-in" array processor is several thousand dollars.

The motivation for the use of color in the display systems of scanning electron microscopes is simple. The human observer can simultaneously distinguish no more than about 15-20 useful levels of monochrome light intensity, but the same observer (if not color blind) can distinguish 350 000 distinct colors. The latter figure is based on experiments where many pairs of colors are compared side by side by many viewers who are asked whether the colors are different. With a color display system it is also possible to "overlay" images by assigning each one to a particular color. The primary colors red, green, and blue are usually chosen for this purpose.

At present, the cost of an image display system is between \$15,000 and \$50,000.

Satellite Processors

Positioning the microscope electron beam, controlling the various detectors, and reading data from the A/D converters during data acquisition are time-consuming tasks that are uneconomical to perform with a minicomputer. There are at least two efficient ways to handle these tasks: build special-purpose hardware or program a satellite microprocessor (a microcomputer) to do this job. Special-purpose hardware permits faster acquisition of the various signals, but a programmable microprocessor is substantially more flexible. The satellite processor has a reasonable amount of its own memory (e.g., > 64 kilobytes) and a high-speed parallel link into the host computer. A typical transfer rate would be 150 kilobytes/s. The link is used to load the microprocessor with any one of a large number of possible data-acquisition programs, depending on the mode of operation desired. The microprocessor acquires data which are sent in large blocks over the link to the host computer where they are processed and/or stored. An example of this processing is the continuum and dead time correction of x-ray maps.

Fiori et al.¹³ have described an x-ray imaging method using the top-hat digital filter. The top-hat filter was first applied to energy dispersive x-ray spectra by Schamber.¹⁴ The algorithm is both simple and elegant; calculations can be performed very quickly by a computer. The latter point is extremely important since we require the calculations to be made on the fly at every pixel and within the pixel dwell time. Briefly stated, counts in a group of adjacent channels of a spectrum are "averaged" and the "average" assigned to the center channel of the group; the procedure is repeated at each channel as the filter is stepped through that part of the spectrum from which we wish to remove the continuum.

The effect of the averaging procedure is as follows. If the original spectrum is curved concave upward across the width of the filter centered on a particular channel, the average will be negative; if the curvature is convex the result is positive. The greater the curvature, the larger the value. The filtering operation has an effect on the spectrum similar to taking a smoothed second derivative.

In order for the filter to respond with the greatest measure to the curvature found in spectral peaks, and with the least measure to the curvature found in the spectral background, the width of the filter must be carefully chosen. For a detailed treatment of the subject, see Schamber and Statham.^{14,15} In general, we choose the width of the filter to be twice the full width at half the peak maximum amplitude (FWHM) of the x-ray peak being used for imaging, with the number of channels in the central section equal to the combined number of channels in the side sections (see Appendix). Using the above filter dimensions with a standard resolution EDS detector one can image the adjacent elements Mg, Al, and Si with negligible interference even when the adjacent element is the pure element and the

imaged element is present at zero concentration.

The final step in the application of the digital filter is to extract a quantity which will be assigned to the coordinates of each pixel to represent the characteristic intensity. We choose the sum of counts in the central section, since this quantity provides the highest peak-to-background ratio.

The Si(Li) detector amplifier system produces an output pulse that can be many tens of microseconds long for each processed x-ray photon. Consequently, deadtime losses are high and we can easily attain a condition where the amplifier cannot process the detected x-ray photons fast enough and the output count rate for the analyte *decreases* for an *increase* in total input count rate. If we spend the same time at each pixel during the acquisition of an image under high count-rate conditions several bizarre artifacts can occur. A particularly insidious artifact is that regions of a specimen that contain higher concentrations of analyte can appear darker in the image than regions that contain less. This problem and other contrast reversal problems can be avoided by a simple logic gate by which pixel dwell time is determined not by "real" time but rather by amplifier "live" time. An EDS image must be deadtime corrected if any quantitative use is to be made of it.

Proper background correction of electron energy loss images is even more important than for x-ray images but is beyond the scope of this paper. (For a detailed explanation see Refs. 8 and 9.)

A computer system such as described will undoubtedly be asked to perform many functions in the laboratory: support applications program development, monitor instrument operating conditions, acquire and process data, display results, and play "Zork" and "Pacman." It is frequently desired to perform several of these functions concurrently. To simplify this job it is desirable to use a multi-tasking/multi-user operating system that would allow data to be processed (a CPU intensive task) while acquiring new data (an I/O-intensive task) from the microscope(s).

Some Examples

It is a trivial matter, using the computer, to weight-average the value of a pixel in an image with its nearest neighbors and to do it for every pixel in the image. Such a procedure is usually referred to as "smoothing" an image. In general, the smoothing of images is the two-dimensional equivalent of smoothing an x-ray spectrum. And just as that tool has been considerably abused we can only expect the same with image smoothing. Smoothing produces artifacts. Under the right circumstances (easily achievable in SEM-STEM applications) smoothing can convert an image with "correct" but difficult-to-see information into an image with easy-to-see nonsense. However, under appropriate circumstances, smoothing can produce spectacular improvements in an image. Figure 1(a) is an "original" unsmoothed image. This image is a 512×512 pixel computer simulation using an accurate Poisson random noise generator.¹⁶ Each pixel in the "background" has a mean of 50 counts and the "object," located approximately in the middle of the micrograph, is a 50×50 pixel square with a mean of 52 counts per pixel. As can be seen from the figure the object is difficult to visualize. The contrast and brightness have been adjusted to produce the maximum visibility. Figure 1(b) is a 21×21 pixel "smooth" of Fig. 1(a). Again, the contrast and brightness have been adjusted to produce the maximum visibility of the object. The "power" of smoothing in this example is readily apparent.

Our last example is an analytical electron microscope examination of a single macrophage obtained from the lung of a victim of "black lung" disease. The intent of the study, from which this example was chosen, is to determine the number and composition of respirable particles taken up by individual macrophages by victims of this debilitating disease.

The diameter of the macrophage in the images was $12 \mu\text{m}$, the acceleration potential was 100 kV and the probe current was 1 nA. The elemental images each contain 128^2 pixels; the brightfield image contains 256^2 pixels.

Figure 2(a) is the brightfield image. The tissue was fixed in gluteraldehyde but unstained. Consequently, the contrast mechanism is weak. Figures 2(b) through (e) are x-ray images of the same area and have been continuum and dead-time corrected by the procedure described above. Pixel dwell time was 100 live-time milliseconds. These images are fully quantitative in that the intensity at each pixel is proportional to the elemental concentration. For display purposes the images are scaled with the lowest pixel value assigned to be full black and the highest pixel value assigned to be full white. The concentration can be read out by several procedures including "line scans" and "regional

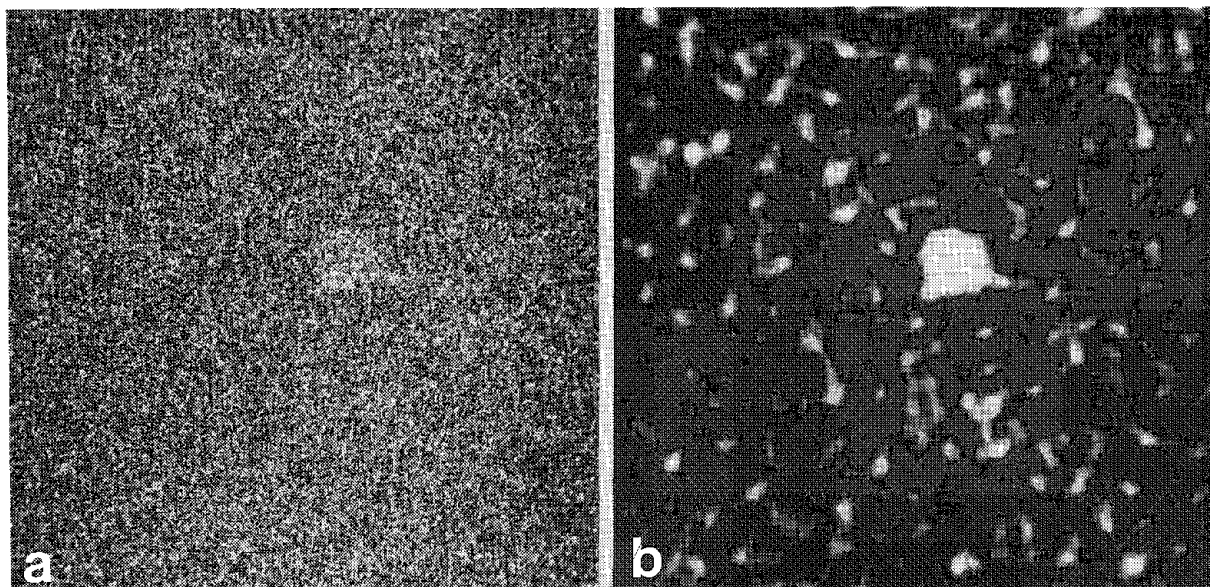


FIG. 1.--(a) "Original" unsmoothed image, 512×512 pixel computer simulation. Each pixel in "background" has mean of 50 counts and "object," located approximately in middle of micrograph, is 50×50 pixel square with mean of 52 counts per pixel. Contrast and brightness adjusted to produce maximum visibility of object. (b) 21×21 pixel "smooth" of (a); contrast and brightness adjusted for maximum visibility of object. note smoothing artifact.

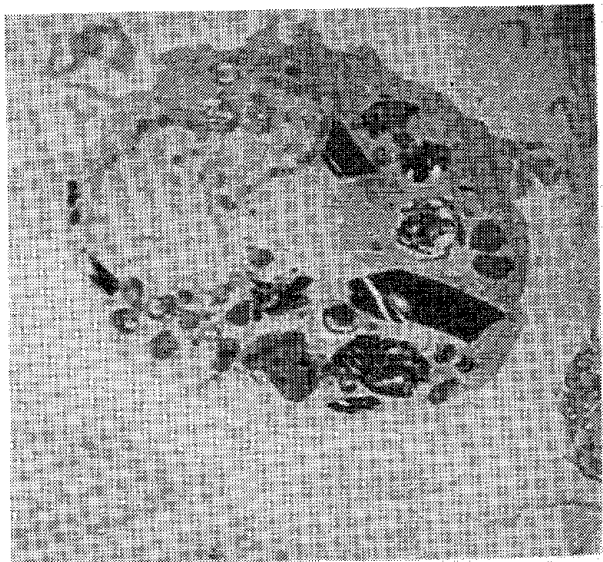
histograms."^{8,13} Figure 2(f) is a background-corrected electron energy loss image of the carbon K edge. The region of the image scanned is smaller than that of the x-ray images and emphasizes several essentially pure carbon (coal) particles. Note from the x-ray images the presence of sulfur in these particles, which shows that the particles are high-sulfur coal. The other particles are various silicates.

Conclusion

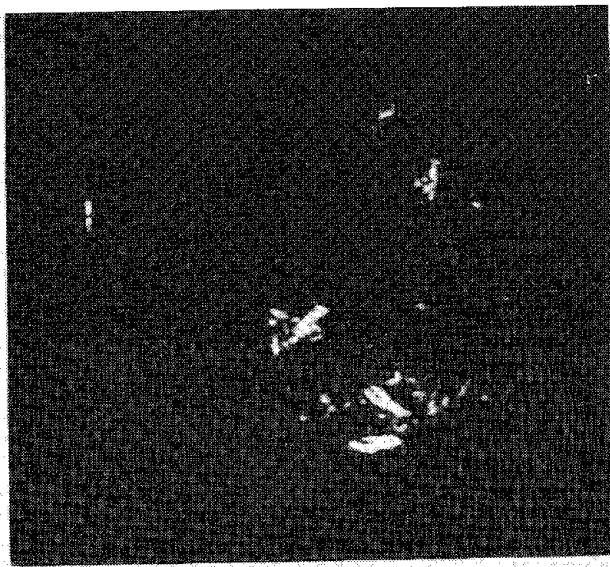
In this review paper we have described some of the more important considerations in interfacing a computer to a scanning electron column device. We included several examples showing a few powerful imaging and processing capabilities. In this latter regard only the surface was scratched. Using powerful image transform and stereology algorithms one can obtain vast amounts of information simply unavailable by any other means. And much of it can be done interactively while the operator is sitting at the microscope console.

[Opposite page:] FIG. 2.--(a) Brightfield image of single macrophage obtained from lung of victim of "black lung" disease. Diameter of macrophage in images is $12 \mu\text{m}$. (b) Continuum and deadtime-corrected aluminum $K\alpha$ image of same area as (a). (c) Continuum and deadtime-corrected silicon $K\alpha$ image of same area as (a). (d) Continuum and deadtime-corrected sulfur $K\alpha$ image of same area as (a). (e) Continuum and deadtime-corrected sulfur $K\alpha$ image of same area as (a). (f) Background-corrected electron energy loss image of carbon K edge. Region of image scanned is smaller than x-ray images and emphasizes several essentially pure carbon (coal) particles. Note (from x-ray images) presence of sulfur in particles, which indicates high-sulfur coal.

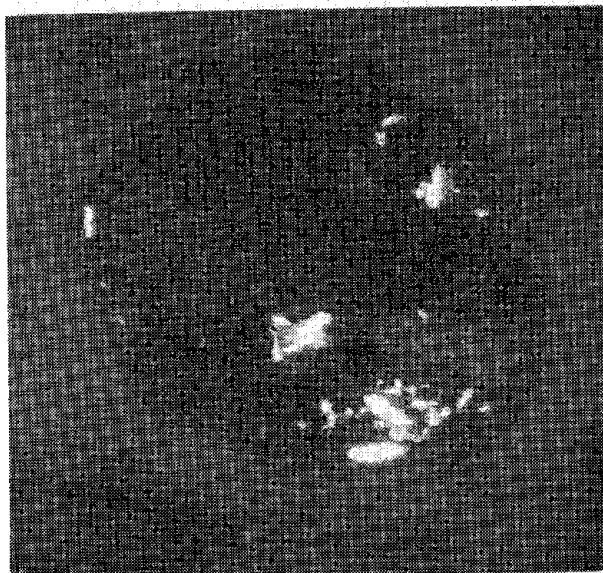
(a)



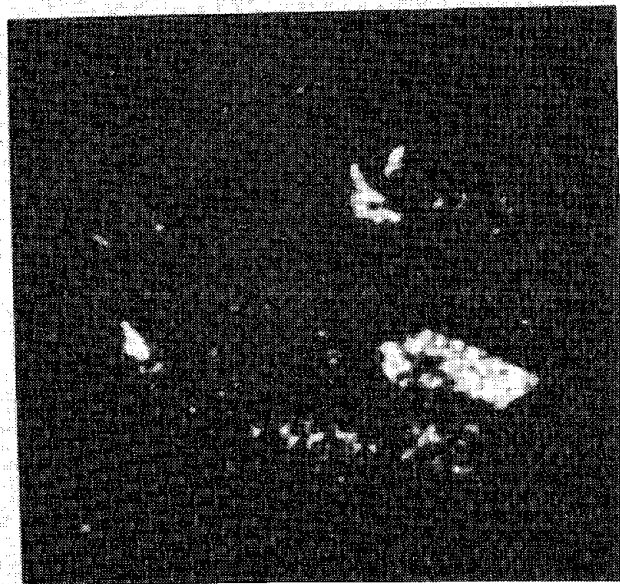
(b)



(c)



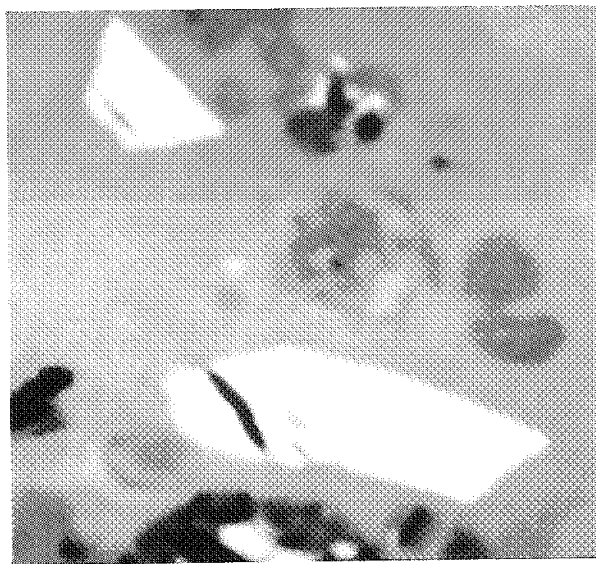
(d)



(e)



(f)



References

1. M. Strahm and J. Butler, *Proc. 37th EMSA*, 1979, 598.
2. M. Strahm and J. H. Butler, "Fast digital data acquisition and on-line processing system for an HB5 scanning transmission electron microscope," *Rev. Sci. Instr.* 52: 840-848, 1981.
3. J. Zubin and J. Wiggins, *Rev. Sci. Instr.* 51: 123, 1980.
4. R. Llimas et al., *SEM/1979 II*, 367.
5. A. Jones and K. Smith, *SEM/1978 I*, 13.
6. C. E. Fiori, K. E. Gorlen, and C. G. Gibson, "Comments on the computerization of an analytical electron microscope," *Proc. 40th EMSA*, 1982.
7. K. E. Gorlen, L. K. Barden, J. S. Del Priore, A. K. Kochhar, C. E. Fiori, C. G. Gibson, and R. D. Leapman, "A data acquisition system for an analytical electron microscope," *Proc. DECUS*, 1982.
8. K. E. Gorlen, L. K. Barden, J. S. Del Priore, C. E. Fiori, C. G. Gibson, and R. D. Leapman, "A computerized analytical electron microscope for elemental imaging," *Rev. Sci. Instr.* 55: 912, 1984.
9. R. D. Leapman, C. E. Fiori, K. E. Gorlen, C. G. Gibson, and C. R. Swyt, "Combined elemental and structural imaging in a computer-controlled analytical electron microscope," *Proc. 41st EMSA*, 1983, 10-13.
10. *Ultramicroscopy* 12: 281-292, 1984.
11. J. Jaklevic et al., *IEEE Trans. NS* 19: 392, 1972.
12. A. Jones and B. Unitt, *SEM/80 I*, 113.
13. C. E. Fiori, C. R. Swyt, and K. E. Gorlen, "Continuum correction of x-ray images in scanning electron column instruments," *Microbeam Analysis--1984*, 179-185.
14. F. H. Schamber, "A modification of the linear least-squares fitting method which provides continuum suppression," in T. G. Dzubay, Ed., *X-ray Fluorescence Analysis of Environmental Samples*, Ann Arbor, Mich.: Ann Arbor Science Publishers, 1977, 241.
15. P. J. Statham, "A comparative study of techniques for quantitative analysis of the x-ray spectra obtained with a Si(Li) detector," *X-ray Spect.* 5: 16-28, 1976.
16. T. Pun and J. Ellis, "Application of simulated Poisson processes in STEM imaging," *Signal* (in press).

MAPPING OF TRACE ELEMENTS WITH PHOTON MICROPROBES: X-RAY FLUORESCENCE WITH FOCUSED SYNCHROTRON RADIATION

A. L. Hanson, K. W. Jones, B. M. Gordon, J. G. Pounds, M. L. Rivers, and G. Schidlovsky

High-energy electron synchrotron storage rings provide copious quantities of polarized photons that make possible the mapping of many trace elements with sensitivities at the parts per billion (ppb) level with spatial resolutions in the micrometer range. The brightness of the x-ray ring of the National Synchrotron Light Source (NSLS), at present being commissioned, will be five orders of magnitude larger than that of the bremsstrahlung spectrum of state-of-the-art rotating anode tubes. We discuss mapping trace elements with a photon microprobe at present being constructed for use at the NSLS. This microprobe will have micrometer spatial resolution.

Brookhaven National Laboratory is commissioning the NSLS, an electron synchrotron storage ring dedicated only to the production of high-intensity x rays. This facility consists of two storage rings that will separately cover the vacuum ultraviolet (vuv) and x-ray regions of the electromagnetic spectrum. The larger 2.5GeV storage ring will provide a continuous spectrum of x rays with useful intensities up to an energy of approximately 20 keV. This storage ring is a high-current machine (500 mA design current) with bending magnets of 6.875m radii.

Figure 1 represents the energy spectrum of photons available on the high-energy ring. The typical beam line is positioned on a bending magnet and is labeled "arc source" in the figure. This curve is for the design electron current of 500 mA and a 1% energy bandwidth (through a monochromator). The other curves show spectra for the special cases in which multipole magnetic devices (wigglers) are inserted into straight sections of the storage ring to provide oscillations that enhance certain properties. For example, the high magnetic field of the superconducting wiggler will harden the x-ray spectrum to provide usable flux to 100 keV. The 24-pole REC wiggler using permanent magnet structures simply increases the flux by a factor of 24 over that of the arc source using a comparable magnetic field.

When used for x-ray fluorescence, synchrotron radiation provides a number of advantages over other fluorescence techniques utilizing charged particles and x-ray tubes. The broad and continuous spectrum of photons has sufficient intensity that a band of energies about a desired excitation energy may be selected with a monochromator. The combination of high brightness and polarization of the photons results in sensitivities in the 1-100ppb range for many elements with analysis times of 1 min or less. Elemental mapping is made possible by the low divergence of the photon beam which allows for x-ray focusing with mirrors at grazing angles.

Sensitivities for elemental analysis with x-ray fluorescence have been calculated¹ for focused x-ray beams, and a 30 μ m beam spot and intensities available from the NSLS. The calculations are shown in Figs. 2 and 3. The calculations were for trace elements in thin biological matrices (2 mg/cm² carbon) and thin geological matrices (3 mg/cm² USGS BCR-1), respectively. The calculations were based on the expected output from a scanning crystal spectrometer with 5s irradiating time. The discontinuity in the curves represents the required change of analyzing crystal. Sensitivities using a Si(Li) detector and 60s irradiation times are about a factor of 10 poorer due to inherently higher backgrounds.

Several experiments have been carried out at the Cornell High Energy Synchrotron Source (CHESS). The results of measurements of minimum detectable limits (MDLs) for thick biological samples in ambient air using the arc source (<20mA current) and a low

Authors Hanson, Jones, Gordon, Pounds, and Schidlovsky are at Brookhaven National Laboratory (Department of Applied Science), Upton, NY 11973; author River's permanent address is University of Chicago (Department of the Geophysical Sciences), Chicago, IL 60637. Development of the x-ray microprobe technology is supported by the Processes and Techniques Branch, Division of Chemical Sciences, Office of Basic Energy Sciences, U.S. Department of Energy under Contract DE-AC02-76CH00016; application to biomedical problems is supported by the NIH as a National Biotechnology Resource under Grant RR01838-02; application to problems in the Geosciences is supported by the National Science Foundation through a grant to the University of Chicago under Grant EAR-8313682.

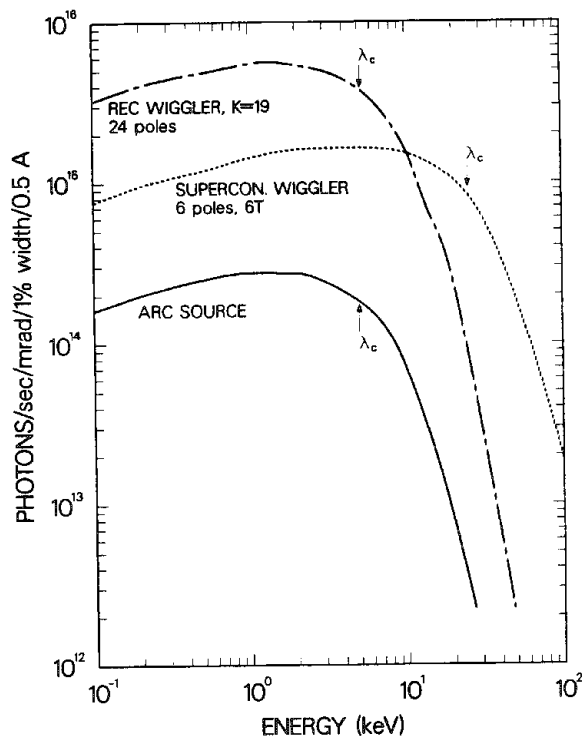


FIG. 1.--Photon energy spectrum for NSLS x-ray ring operating at 2.5 GeV. X-ray microprobe will be situated on arc source.

With a source-defining pinhole at the second phase focal point, no pinhole would be required at the third phase focal point. Ray tracing studies to determine fluxes transmitted through this system are in progress to determine the optimum optics and the available sensitivities.

Mapping trace elements with the microprobe will be performed by scanning a sample through the focused beam spot. Distributional maps of the trace elements in the samples can be made with minimum detectable limits on the order of those shown in Figs. 2 and 3. As noted, the beam line will be equipped with a monochromator to select a specific energy band from the incident x-ray beam. For x-ray fluorescence, monochromators with the largest available band passes will be implemented to maximize the photon flux. However, if a low-bandpass monochromator is used, with a sacrifice in sensitivity, the chemical states of the elements can be studied by measurements of the fine structure of the absorption or fluorescence around the elements' absorption edges.

X rays in the energy region available with the NSLS have a depth of penetration large enough for tomography, so the microprobe will permit the development of microtomography. The monochromatic x rays that will be available should improve the resolution obtainable with normal tomography. By measuring the fluoresced x rays, it will be possible to perform depth profiling of the trace elements. Similarly, the tomographic technique can be used in a transmission mode just above and below an absorption edge to provide a depth profile of the major and minor elements.

bandpass monochromator have been reported elsewhere.²⁻⁴ The MDLs, measured with a Si(Li) detector, were of the order of 200 ppb. These measurements scale within an order of magnitude with the calculations of Gordon.¹ More recent measurements with 3043keV x rays from the wiggler at CHESS have been made. These measurements emphasized analyses of geological samples with monochromated (low bandpass) x rays. Sufficient fluences of x rays were available for analyses with beam spots apertured to $100 \times 100 \mu\text{m}$.

The X-ray Microprobe

One beam line on the x-ray ring at the NSLS is dedicated to development and use of an x-ray microprobe for x-ray fluorescence analysis of trace elements. The design of the x-ray microprobe will utilize mirrors at grazing angles to the beam to demagnify the x rays ultimately to a 1-10 μm diameter beam spot. The present design of this microprobe includes a monochromator and a focusing platinum-coated ellipsoidal mirror. This mirror will provide an eight-fold demagnification with an energy limit of 17 keV. The final beam spot will be 20 to 30 μm in diameter. The final design of the beam line will use the focused 30 μm beam spot as the source image for further demagnification to 1-10 μm .

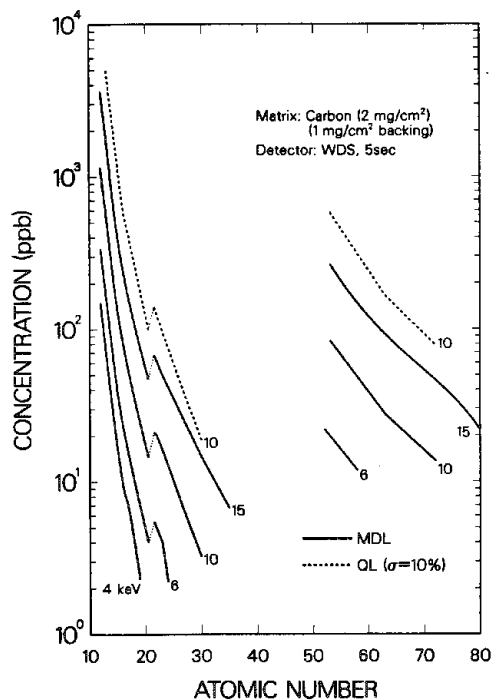


FIG. 2.--Sensitivity for trace element fluorescence analysis in thin biological matrix using 30 μ m beam spot. MDL is minimum detectable limit and QL is quantitation limit,⁵ where standard deviation is 10%. (From Ref. 1.)

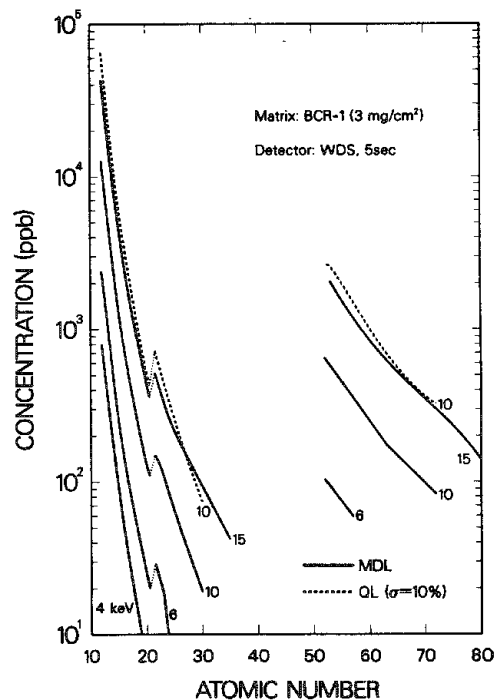


FIG. 3.--Sensitivity for trace element fluorescence analysis in thin geological matrix using 30 μ m beam spot. (From Ref. 1.)

References

1. B. M. Gordon and K. W. Jones, *Nucl. Instrum. Methods in Phys. Res.*, in press.
2. A. L. Hanson et al., *IEEE Trans. NS-30*: 1339-1342, 1983.
3. J. R. Chen et al., "Synchrotron x-ray fluorescence and extended x-ray absorption fine structure analysis," *SEM/1984 IV*, 1483-1500.
4. K. W. Jones et al., *Nucl. Instrum. Methods B3*: 225-231, 1984.
5. L. A. Currie, in T. Dzubay, Ed., *X-Ray Fluorescence Analysis of Environmental Samples*, Ann Arbor: Ann Arbor Science Publishers, 1977, 289.

Energy-dispersive X-ray Analysis

STATISTICS AND WISHFUL THINKING IN MICROBEAM AND IMAGE ANALYSIS

P. J. Statham

An earlier tutorial¹ established some concepts in statistics with particular reference to microanalysis and developed simple formulas for common applications. This paper extends the former treatment and places more emphasis on the deleterious efforts of statistics on techniques used in processing digital spectra, images, and analytical results. Many procedures that are quite plausible fail in practice through statistical disturbance, so it is useful to appreciate how that can occur.

Sources of Statistical Uncertainty

By "statistics" I mean the unavoidable random fluctuations which are the result of noise or probabilistic counting phenomena involved in the acquisitions of raw data. These fluctuations provide the ultimate limit to the precision of any derived parameter but are quite distinct from "experimental errors" involved in specimen preparation, instrumental distortion, theoretical formulation, and mistakes by the analyst, which tend to have a systematic effect. Thus, it is quite possible for an experiment to yield a precise, reproducible result that is wholly inaccurate.

To improve precision, we must reduce the "noise," which invariably involves extending the data acquisition time either directly, for example by increasing the preset time for x-ray spectrum acquisition, or indirectly by increasing the time constant for recursive frame averaging or integrating more individual frames in digital image acquisition.

With x-ray and electron signal measurement we are counting "quanta" produced by a certain dose on the specimen. Since, due to restrictions of solid angle or data storage for example, the signal may not be fully utilized, the final signal-to-noise ratio may be worse than dictated by statistics in the original source. In this case, the "detection quantum efficiency" $DQE < 1$ but the measurement technique can be varied to minimize the degradation.² If we are recording digital images from a scanning electron beam in a serial fashion, there is no inherent advantage in scanning fast because the signal-to-noise ratio is primarily limited by the total time the beam spends on any one area of the sample over the course of the acquisition. However, if the complete image is available at once, as in a transmission microscope for example, a TV camera can be used in conjunction with a phosphor screen to effect "parallel detection" which, given considerations of the camera conversion,² should still give a markedly better DQE than if the same image is scanned serially over a single detector. The concept of "parallel" and "serial" detection concerns how well the available signal is utilized. For example, although a WDS spectrometer can yield much higher data rates, the DQE of a solid-state EDS detector is higher because all photons falling within the detector solid angle are counted, not only those in a certain wavelength band.

The propagation of errors, from raw data to derived parameters, is quite straightforward provided results can be expressed in terms of data values that are "statistically independent." In x-ray spectra, that is usually possible provided the original integrals over discrete energy bands are available and the data have not been "background subtracted" prior to storage, for example. If a result depends on parameters that have been calculated with some data points in common then "cross correlation" has to be taken into account.¹

Feature Detection

Background Subtraction and Detection Limits. A detection limit value must always be calculated with reference to the exact technique that will be used to establish presence or absence of a peak because there is always a danger in misuse of published formulas. For example, in thin-foil analysis the MMF for element A in a matrix of B has been quoted³ as $3(2 I_B^A)^{1/2} (k_{AB} C_B / I_B)$, where I_B^A is "the continuum background for element A." Using the notation of Ref. 1, we see this formula results from using windows of equal

The author is at Link Systems Limited, Halifax Road, High Wycombe, Bucks., England HP12 3SE.

width for both background and peak determination ($W_p = W_b$) and defining a "counts per weight %" constant $\gamma = I_A/C_A = k_{AB}C_B/I_B$. This formula only applies if I_b is actually the *integral* counts in a background window equal in width to all those used for peak integration; if the background height in counts is used, the estimate of MMF is unduly optimistic. Furthermore, in background subtraction for EELS quantitation, it has been shown^{1,4,5} that the MMF can be considerably worse than predicted by previously quoted formulas that ignored the uncertainty introduced by fitting a gradient term before extrapolation beneath the ionization-loss edge.

Detection limits are often calculated assuming ideal conditions whereas in practice we find that

- (1) interference from nearby structures may prevent use of the same background fitting regions as used in the formula derivation;
- (2) systematic error due to imperfections in the background model may be larger than the statistical component; and
- (3) instrumental drift between experiments may occur so that background measurements may not be reproducible to within available statistical precision.

Detecting Objects. The same principles of detection can be applied to images where, instead of integrating over a number of channels, we use the eye to average intensity over an area equal in size to the expected object and compare it with that for neighboring areas of similar size.¹ For visibility, the difference in average intensity should be at least 5 times the standard deviation for a single average; an explicit example in x-ray imaging appears in Ref. 1. If we have a roughly uniform field of low-contrast (C) objects and the total count in the image is Q in equivalent quanta, then the number of features which can be resolved in one dimension is roughly, $0.2CQ^{1/2}$. With typical systems, the available pixel resolution often exceeds the intrinsic "statistical" resolution except for electron images acquired with total frame dwell of at least 1 s.⁶ The problem of pixel resolution and intrinsic "statistical" resolution in electron images is discussed further in Refs. 2 and 7.

In image analysis, one can sometimes separate objects from surrounding background by applying a threshold. Unfortunately, the threshold may be exceeded outside the object at noise excursions and the perimeter of the threshold result will also be ragged even though the original object is smooth. Ad hoc techniques such as eliminating small objects by "erosion" can be used to clean up the final image but at a loss to effective resolution. If possible, it is preferable to spend more time averaging the input signal prior to thresholding to maintain the fidelity of true image detail.

Smoothing. Both spectra and digital images can be "smoothed" by weighted local averaging of data points in an attempt to reveal detail obscured by noise.¹ Unfortunately, this procedure also transforms essentially broadband noise into low-frequency artifacts of the same size as the effective averaging domain. These "ripples" and "blobs" are often less satisfactory than the original noise because they give rise to detection of spurious features.

Resolving Features

Peak Overlap. Where peaks overlap, the effective local "background" is increased for each peak and this degrades detection limits.¹ Linear least-squares fitting techniques can be used to resolve overlaps provided peak shapes are known accurately; then the statistical error in fitted parameters can be estimated directly. Where instrumental drift or distortion is uncertain, nonlinear techniques can be used to adjust a series of parameters to optimize the fit to the data. Although such techniques guarantee a good fit, the derived parameters can be grossly inaccurate in certain circumstances.⁸⁻¹⁰ Whereas the nonlinear approach to equation solving is well defined and generally produces a unique solution, the presence of statistical noise in the data allows alternative solutions to offer just as good a fit as the correct parameterization for the noise-free case. Moreover, the formulas used to estimate the uncertainty in fitted parameters are only sensible if parameter results are close to the true values. The "chi-square" measure of "goodness of fit" is merely an index that describes how great the observed differences are relative to random statistical fluctuations at all the data points.¹ It does not measure the accuracy of fitted parameters, although it can be an indicator of bias in

fitted peak areas.¹¹

Deconvolution. Since spectra and images are normally the result of "convolution" of an input signal distribution by an "instrumented response function," the mathematical converse, "deconvolution," is well defined and normally involves frequency filtering in the Fourier domain to enhance high frequencies that have been attenuated by the instrumental response. Anyone who tries this procedure soon recognizes the problem introduced by statistical noise: the high-frequency content of the data is dominated by the noise component, so that deconvolution produces a result overwhelmed by enhanced noise. "Partial deconvolution" can be effected by an optimal least-squares technique¹² but the enhanced results exhibit spurious ripples which are most obvious in regions of background. However, the rms error of the restoration can still be calculated (Eq. 8, Ref. 12) and serves as a guide to the validity of enhanced features.

Interpreting Results

Concentration Differences. When statistical precision can be calculated from raw data, it is a straightforward matter to decide whether two results are significantly different. In the notation of Ref. 1, concentrations C_1 and C_2 are different (to 99.73% confidence) if

$$|C_1 - C_2| > 3(\sigma_1^2 + \sigma_2^2)^{1/2} \quad (1)$$

The calculation of standard deviations σ_1 and σ_2 in derived concentration may not be trivial. For example, in microbeam analysis, since concentration is roughly proportional to characteristic peak intensity, we might naively assume that (σ_1/C_1) would be equal to the relative standard deviation for net peak intensity of element 1. However, if concentrations are normalized to a total of 100% (as in thin-foil analysis), the data are "closed" and the uncertainty for one concentration value is affected by the concentration values of the other components in the sample.¹³ In the extreme single-element case, the result is always 100% whatever the uncertainty in the raw data!

The Error in the Error Estimate. A further complication arises if we attempt to include uncertainties in experimental and x-ray correction procedures into our estimate of σ_1 and σ_2 . Although we can do little to estimate likely imperfections in theory, we can estimate the standard deviation in a set of n results N_i by

$$s^2 = \frac{1}{n-1} \sum_{i=1}^n (N_i - \bar{N})^2 \quad (2)$$

where \bar{N} is the average over the set. This is an "unbiased" estimator and the formula is most often implemented on pocket calculators. However, s here is only an estimate of the true standard deviation σ single datum (which is generally less accurate than when calculated directly from the Poisson statistics of raw data). Since the variable

$$X = \sum_{i=1}^n (N_i - \bar{N})^2 / \sigma^2 \quad (3)$$

possesses a chi-square distribution with $n-1$ degrees of freedom, from tables we can find values X_1 and X_2 so that, with 90% confidence, $X_1 < X < X_2$. Since $s^2/\sigma^2 = X/(n-1)$, we can calculate the 90% confidence range for the ratio (s/σ) as a function of data points n . As suggested by Table 1, even if we use 10 results in Eq. (2) there is a 10% chance that the error in calculated standard deviation is greater than about 40%. Thus we have an additional uncertainty in the application of Eq. (1) to the testing of equality of two concentration values. Student's t distribution can be used in a more rigorous approach when σ is unknown and homogeneity is to be checked.¹⁴

Unexplained Sources of Error. If possible, it is helpful to use Eq. (2) to establish whether there are any unexplained sources of experimental error. For example, if

spectrum processing already provides peak intensities with standard deviation values calculated from Poisson statistics,¹ we can still repeat the same analysis many times and use Eq. (2) to give an alternate estimate for the standard deviation in a single intensity value. Subject to the limitations suggested by Table 1, if s exceeds the quoted spectrum processing value by a large margin, then it is worth looking for external sources of error (e.g., fluctuations in beam current, contamination, etc.).

TABLE 1.--90% confidence interval for ratio of estimated deviation s to true standard deviation σ as function of number of data n . In the long run, 9 out of 10 determinations of s fall within this fractional range of σ .

n	range
2	0.06 - 1.96
5	0.42 - 1.54
10	0.61 - 1.37
20	0.73 - 1.26
50	0.83 - 1.16
100	0.88 - 1.12
200	0.92 - 1.08

Elimination of Bad Data. Bearing in mind the above discussion, we can consider the problem of elimination of "bad" results. If we have a good estimate of the standard deviation it is tempting to eliminate data falling more than 3σ from the mean. If we have no good reason to explain exactly why a result should be eliminated it is unwise to throw it out on statistical grounds alone because it is precisely this type of result which determines the true experimental error. This practice can lead to undue optimism in terms of "error-bars" for published data and make it more difficult to establish corroborative evidence for a given theory. Where systematic bias could be involved, e.g., through use of different correction formulas, different sample preparation, or different geometries, elimination of results from one source cannot be based on statistics that only deal with random errors.

Conclusion

To summarize, here are some "morals" introduced by this paper and the earlier tutorial.¹

- (1) The more parameters one derives from a given data set, the worse their precision.
- (2) Do not use text book formulas unless all the terms are defined fully and their validity is proven.
- (3) "Chi-square" is not a measure of precision or accuracy.
- (4) A good fit to a parameterized expression does not imply that the parameters are good.
- (5) Using a finer sampling grid does not insure that finer detail will be observed.
- (6) Ad hoc processing is no substitute for better data.
- (7) The fewer the measurements made, the more complicated the calculation of statistical precision and the more vague the conclusion.
- (8) There is no such thing as a free lunch.

References

1. P. J. Statham, "Confidence in microanalysis: Lies, damned lies, or statistics?" *Microbeam Analysis--1982*, 1-7.
2. K. H. Herrmann and D. Krah1, "The detection quantum efficiency of electronic image recording systems," *J. Microscopy* 127: 17-28, 1982.
3. D. B. Williams et al., "Quantification of energy-dispersive spectra from thin-foil specimens," *Microbeam Analysis--1982*, 21-36.
4. R. F. Egerton, "A revised expression for signal/noise ratio in EELS," *Ultramicroscopy* 9: 387-390, 1982.

5. T. Pun et al., "Optimised acquisition parameters and statistical detection limit in quantitative EELS," *J. Microscopy* 135: 295-316, 1984.
6. P. J. Statham, "Interfacing of computers to a STEM," *Ultramicroscopy* 8: 309-320, 1982.
7. M. Van Heel, "Detection of objects in quantum-noise-limited images," *Ultramicroscopy* 8: 331-342, 1982.
8. P. J. Statham, "Pitfalls in linear and non-linear profile-fitting procedures for resolving severely-overlapped peaks," *X-ray Spectrom.* 7: 132, 1978.
9. F. H. Schamber, *Curve Fitting Techniques and Their Application to the Analysis of Energy Dispersive Spectra*, NBS Special Publ. 604 (Proc. Workshop EDXS, NBS, 1979), 1981, 193-231.
10. C. E. Fiori et al., "Sequential simplex: A procedure for resolving spectral interference in energy dispersive x-ray spectrometry," *ibid.*, 233-272.
11. P. R. Bevington, *Data Reduction and Error Analysis for the Physical Sciences*, New York: McGraw-Hill, 1969.
12. P. J. Statham, "Resolution enhancement of x-ray spectra," in D. R. Beaman et al., Eds., *Proc. 8th Int. Conf. X-Ray Optics and Microanalysis*, Midland, Mich.: Pendell Pub., 1980.
13. E. Johansson et al., "Minimising effects of closure on analytical data," *Anal. Chem.* 56: 1685-1688, 1984.
14. J. I. Goldstein et al., Eds., *Scanning Electron Microscopy and X-ray Microanalysis*, New York: Plenum, 1981, ch. 8.

Acceleration-based Microscopy and Microanalysis Techniques

DEVELOPMENT AND APPLICATION OF THE LOS ALAMOS NUCLEAR MICROPROBE: HARDWARE, SOFTWARE, AND CALIBRATION

T. M. Benjamin, P. S. Z. Rogers, C. J. Duffy, J. F. Conner, C. J. Maggiore, and
J. R. Tesmer

There is a great demand for spatially resolved quantitative trace element analyses of geologic samples. This class of samples is characteristically heterogeneous, fine grained, and compositionally complex. The Los Alamos nuclear microprobe has been developed for, and applied to, nondestructive in situ geochemical analysis, primarily by the proton-induced x-ray emission technique (PIXE). Characteristic x-ray spectra are acquired by bombardment with 1-200 nA beams of protons from the Los Alamos vertical Van de Graaff accelerator. Beam spot diameters of 10 μm are routine. After spectrum deconvolution, detection limits of approximately 5 ppm are obtained for an integrated charge of the order of 10 μC . Applications concomitant with development have included analyses of meteorites,^{1,2} including one potential sample of Mars,³ terrestrial oil shales,⁴ archaeological artifacts, and ore mineral samples.

Hardware

The Los Alamos nuclear microprobe system⁵ (Fig. 1) contains several special components. The vertical Van de Graaff accelerator is exceedingly versatile. Proton beams up to 20 μA , continuous, on the 24 in. Faraday cup are available over a range in energy from 1 to 6.5 MeV. Focused beams on target can exceed 200 nA. In addition, a wide variety of positive and negative particle beams can be utilized for low-Z element analysis by particle induced gamma ray emission (PIGE) and nuclear reaction analysis (NRA),⁶ and in Rutherford backscattering (RBS) analysis.⁵

The NbTi superconducting solenoid final lens is critical to the attainment of high current densities and micron scale spots. Unlike quadrupole final lenses, the solenoid can focus ion beams to submicron diameters while retaining a usable 200 pA/ μm^2 current density. Magnetic fields up to 80 kG can be produced by the solenoid. Ion optics considerations⁵ and the physical dimensions of the solenoid and liquid helium dewar constrain the position of the sample stage and the x-ray detectors (Fig. 2). The solenoid reduces the spot size defined by the selected Pt SEM aperture box (Fig. 1) by a factor of 10 when focused on target. The use of cooled SEM apertures simplifies spot size selection relative to a cooled microjaw slit system.

In addition to a Si(Li) x-ray detector, the sample chamber (Fig. 2) mounts two crystal x-ray spectrometers originally used on a MAC electron microprobe. Mounted horizontally rather than in the normal vertical orientation, due to solenoid-defined space constraints and a desire to maintain a take-off angle equal to that of the Si(Li) detector, these spectrometers have proved to be difficult to align. Further effort will solve this problem so that the high degree of x-ray wavelength discrimination characteristic of crystal x-ray spectrometers can be used on a PIXE nuclear microprobe system for the first time. Even with poor alignment, we have obtained peak-to-background ratios that are superior by more than an order of magnitude to those obtained with an electron microprobe. These spectrometers will radically improve the rare earth element (REE) detection limits compared to Si(Li) spectrum deconvolution results, to the benefit of many meteoritic and geochemical problems.

Near-term hardware additions will include precise current integration by RBS, secondary-electron suppression, and on-demand beam deflection to reduce bremsstrahlung, rapid 2D beam scanning, and secondary-electron imaging capability.

Software

The software developed at Los Alamos for deconvoluting and quantifying the Si(Li) PIXE data is based on calculations using fundamental parameters. When applied to the

Authors Benjamin, Rogers, and Duffy are in the Isotope and Nuclear Chemistry Division, Maggiore is in the Electronics Division, and Tesmer is in the Physics Division of the Los Alamos National Laboratory, Los Alamos, N. M.; author Conner is in the Physics Division, University of California, Davis, Calif.

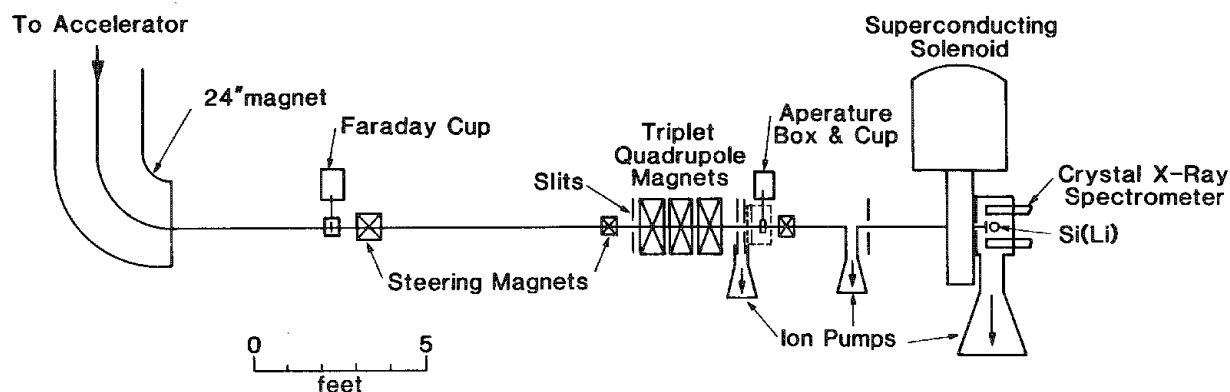


FIG. 1.--Los Alamos nuclear microprobe beam line schematic, side view.

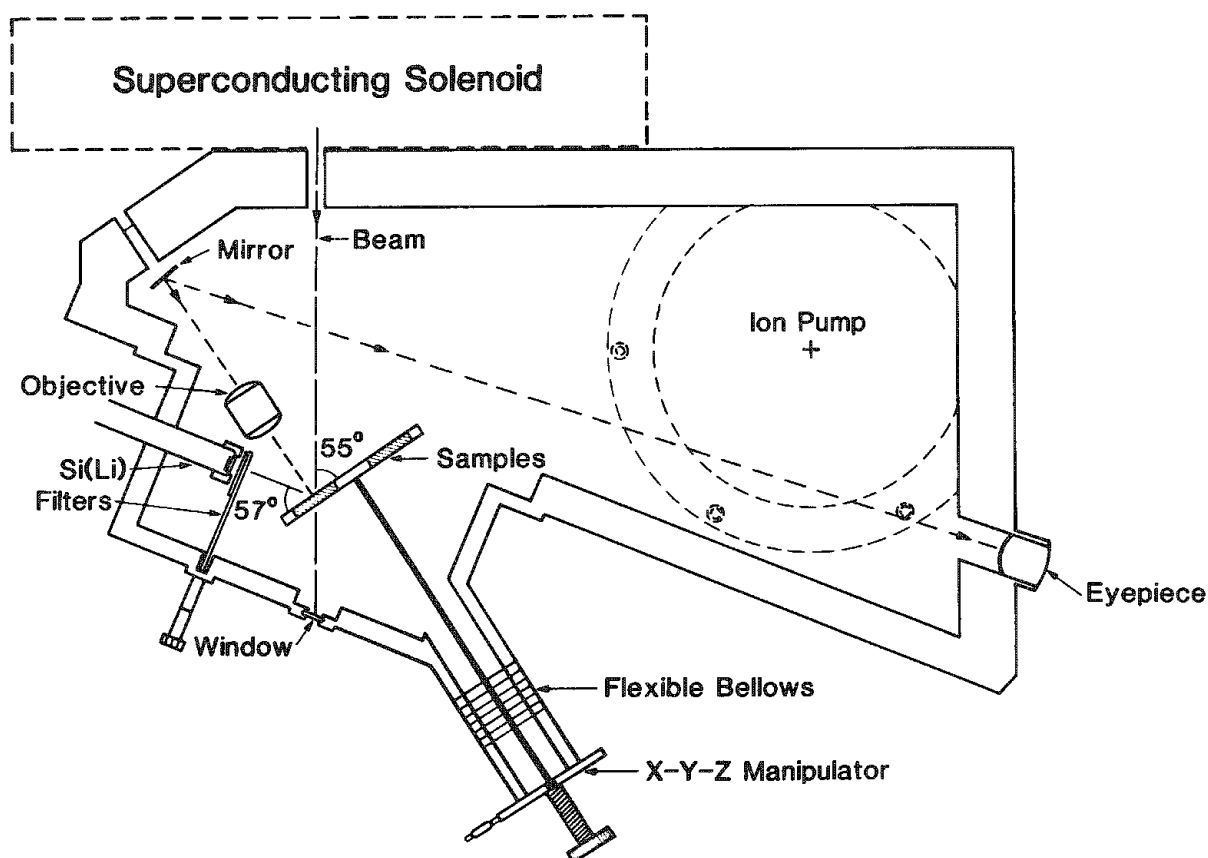


FIG. 2.--Los Alamos nuclear microprobe sample chamber, top view. Crystal x-ray spectrometers, not shown (see Fig. 1), are mounted above and below Si(Li) detector.

data, quantitative results are obtained by use of only one variable for each element, peak height. The electronic signal amplification gain and zero offset are determined in an energy calibration routine. Weighted-least-squares fitting of known elemental peaks in spectra from standards and the individual unknowns take into account the discrete x-ray lines in the data peak envelopes (for example, the α_1 and α_2 peaks in a $K\alpha$ envelope). The x-ray energy-dependent Gaussian peak half-width function is also calibrated from the same peaks used in the energy calibration. This function, a characteristic of the Si(Li) detector, appears extremely stable and reproducible. The sample spectra are then fit with discrete envelopes composed of the sum of the Gaussians for all the lines of each element. Because only one variable per multi-Gaussian envelope, characteristic of each element, is required in the fitting routine, many overlap problems can be quantitatively resolved while

excellent detection limits are maintained. In the case of REE data, severe overlap of the numerous closely spaced [relative to Si(Li) energy resolution] L-lines superimposed on a nonlinear bremsstrahlung background degrades the detection limits to roughly 100 ppm.

Essential to this method is knowledge of the relative intensities of every x-ray line for each element in that particular matrix, so that a single fitting parameter per element suffices. Also required are the relative intensities between lines of differing elements so that a known major element can be used as an internal standard for quantification of the abundance of all other elements in the spectrum. These relative intensities are calculated by numerical integration.⁷ As the samples are thick targets, the numerical integration includes the effects of decreasing beam energy (and the corresponding x-ray production cross sections) with depth and x-ray absorption in the sample. As an example, a 2.5MeV proton beam penetrates 50 μm into quartz but x rays from elements lighter than Ca, although produced at this depth, do not reach the detector (Na, 17 μm max.; Al, 37 μm max.; and Cl, 43 μm max.).

A truly typical spectrum is shown in Fig. 3. The sample, a meteoritic plagioclase that has been impact-shocked into a glass, was analyzed under the following conditions: 2.5MeV

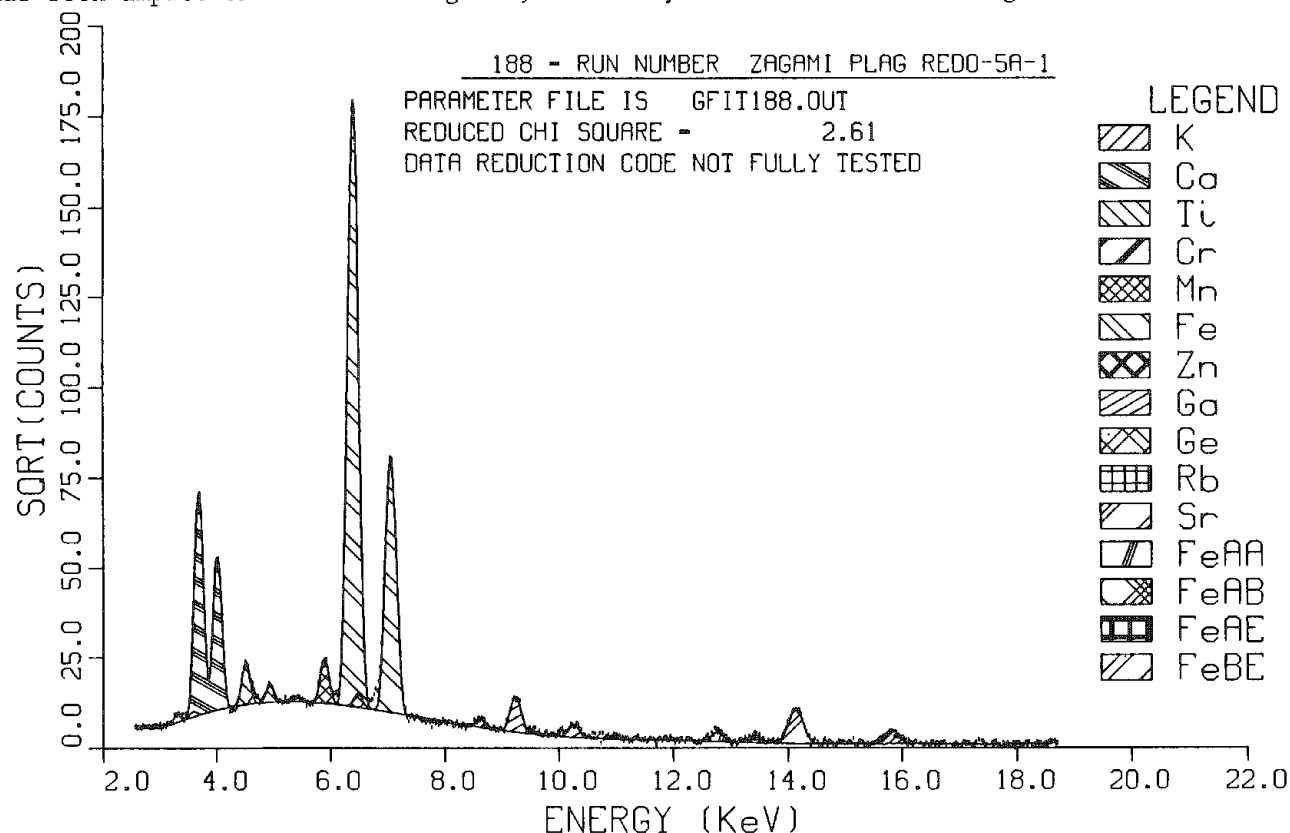


FIG. 3.--2.5 MeV PIXE spectrum and data deconvolution results for shocked plagioclase in Zagami meteorite. Concentrations given in Table 1.

protons, 9nA beam current, 10 μm spot, 6.8 μC integrated charge, x-ray filters consisting of 20.335 mg/cm^2 Be and 13.117 mg/cm^2 Al, and a numerical integration step size of 1.0 (1.0 = 10 keV). The elements given in the legend and tabulated in Table 1 were normalized to the electron microprobe value of 6.18 wt.% Ca through the relative intensity calculation. The x-ray filters were chosen to suppress the major elements such as Ca in order to minimize detector dead time. At this plot scale some of the peak areas are too small to exhibit the legend patterns. Also of note is the present lack of a detector efficiency correction. The efficiency calibration is in progress. The correction is negligible through Ga but could amount to 30 to 40% at Sr.

An enlarged portion of Fig. 3 is shown as Fig. 4. Considering that the peak positions and half-widths are determined by least-squares calibration and that the α/β ratios are calculated from fundamental parameters, the fit to Sr is very good. The sensitivity of the PIXE technique requires consideration of escape and pileup sum peaks. The Fe $K\alpha$

TABLE 1.--2.5MeV PIXE spectrum, Zagami plagioclase.

Element	Concentration (ppm)
K	3700 \pm 1400*
Ca	$\approx 6.18 \times 10^4$
Ti	534 \pm 35
Cr	13 \pm 7
Mn	131 \pm 8
Fe	7550 \pm 40
Zn	11 \pm 2
Ga	60 \pm 4
Ge	2 \pm 2
Rb	7 \pm 3
Sr	166 \pm 12
La	90 \pm 50
Ce	30 \pm 50

*Errors are 1 σ total uncertainty.

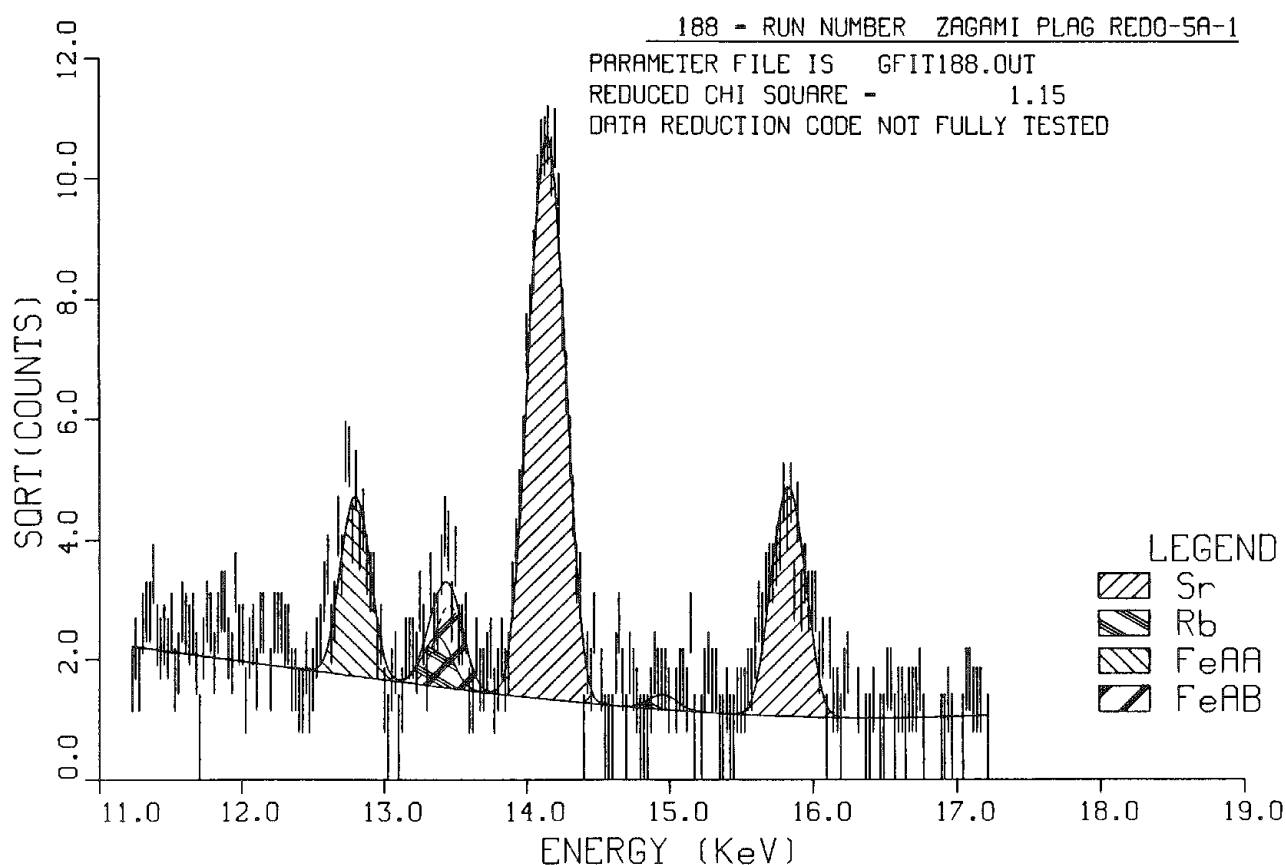


FIG. 4.--Enlarged portion of Fig. 3 showing excellent fit of relative intensity calculation to data.

sum peak is imperfectly fit although statistically the error is small. The Rb K α and Fe K α K β sum peak have a severe overlap. The sum peak proportionality systematics require the presence of some Rb to model the data adequately.

Development plans include addition of the x-ray fluorescence correction, Lorentzian intrinsic line widths, low-energy exponential tails, and bremsstrahlung modeling.

Calibration

Initial calibrations against known materials indicate an accuracy of the order of 10% when a major element is used as an internal standard. Precise current integration by RBS and new trace element standards, both synthetic and natural, permit precise intersample comparison. Calibration and software testing in progress include analyses of a suite of pure metals; simple alloys and minerals used as electron microprobe standards; and fused glasses of W-1, AGV-1, BCR-1, and BHVO-1 rock standards.

Sensitivity to variation in the beam energy (and therefore x-ray production cross sections), matrix, numerical integration step size, and beam-to-target and detector-to-target angles (55° and 57° , respectively) is being assessed by calculation.

Examples of the effect of matrix and numerical integration step size are given in Figs. 5 and 6. The two matrices, SiO_2 and Fe_3O_4 , encompass the mean atomic number of most geologic materials. The numerical integration step size is in units of 10 keV. In both Figs. 5 and 6 the curves are relative intensity calculations normalized to a 0.2 (that is, 2 keV) integration size. In Fig. 5 the x-ray energy dependence (plotted as atomic number

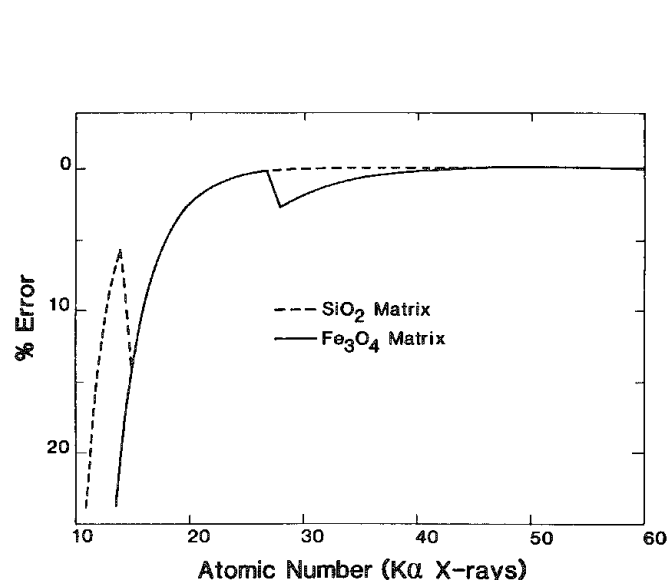


FIG. 5.--Percentage error as function of x-ray energy (plotted as atomic number for $K\alpha$ x rays) and matrix composition for numerical integration step size of 2.0 relative to step size of 0.2.

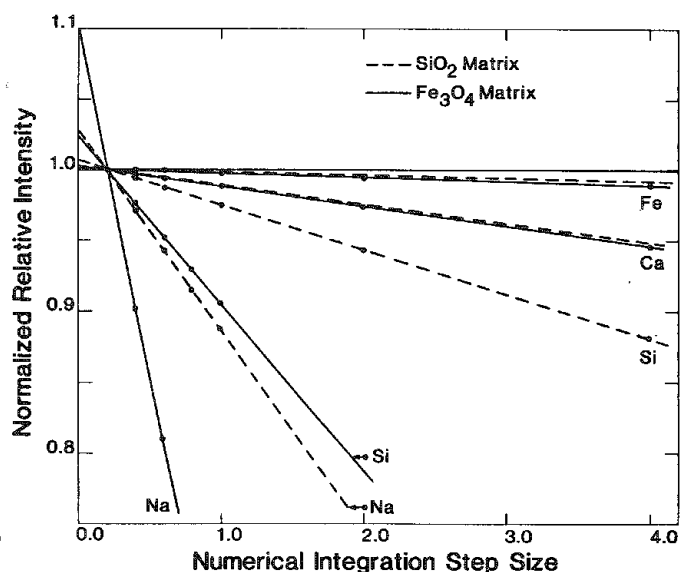


FIG. 6.--Deviations in relative intensities as function of step size and matrix composition normalized to step size of 0.2. Results for calcium and iron are nearly coincident and are displaced for clarity.

for $K\alpha$ x rays) vs the difference (error) in the relative intensities between a step size of 2.0 and a step size of 0.2 is shown. As expected, the larger step size yields poorer results but only for the softer x rays and at absorption edges. The difference is less than 5% for all elements heavier than Cl (for K-lines, and heavier than Rh for L-lines). Fortunately, the deviations due to step size are linear for reasonable ranges of step size (Fig. 6). This linearity allows, where necessary, extrapolation to zero step size. Again, the softer x rays are most affected and the matrix effects less significant for the higher atomic number elements. This type of analysis, when extended to other variables in the system will allow the details of the PIXE analysis technique to be tailored to the accuracy required by the particular problem.

Conclusion

The PIXE technique has proven to be a major advancement in in situ, nondestructive, spatially resolved trace element analysis. The Los Alamos nuclear microprobe is being developed and calibrated to produce rapid and comprehensive elemental analysis of complex geologic samples with a 5ppm detection limit.

References

1. T. M. Benjamin et al., "Microprobe analysis of rare earth element fractionation in meteoritic minerals," *Nuclear Instruments and Methods* B3: 677-680, 1984.
2. D. S. Woolum et al., "Trace element PIXE studies of Qinzhen (EH3) metal and sulfides," *Lunar and Planetary Science* 15(abs.): 935-936, 1984.
3. J. H. Jones et al., "The youngest meteorites: II. Trace element zoning in Zagami maskelynite," *Lunar and Planetary Science* 16(abs.), in press.
4. T. M. Benjamin et al., "The application of the Los Alamos nuclear microprobe to the characterization of trace element-mineral associations in geologic materials and solid wastes," *Nuclear Society, 5th Intern. Conf.*, Mayaguez, Puerto Rico, 1984 (in press).
5. C. J. Maggiore, "The nuclear microprobe-investigating surfaces with ions," *Los Alamos Science* 3: 27-45, 1982.
6. G. Amsel and W. A. Lanford, "Nuclear reaction techniques in materials analysis," *Annual Rev. in Nuclear Sci.* 34: 435-460, 1984.
7. P. S. Z. Rogers et al., "Geochemical applications of nuclear microprobes," *Nuclear Instruments and Methods* B3(231): 671-676, 1984.

MEASUREMENT OF THE CARBON CONTENT OF SILICATE GLASSES BY USE OF THE $^{12}\text{C}(\text{d},\text{p}_0)^{13}\text{C}$ REACTION

G. J. Fine, E. M. Stolper, M. H. Mendenhall, R. P. Livi, and T. A. Tombrello

Carbon dioxide is a significant dissolved component in a wide range of magmas and ubiquitous in gasses associated with volcanism.¹ This fact has motivated extensive study of the influence of CO_2 on the petrogenesis of many magma types.² Despite its importance, the absolute concentrations of dissolved C in silicate glasses quenched from these magmas are not well known. Standard carbon analysis techniques (e.g., gas manometry, quadrupole mass spectrometry, gas chromatography) have been applied to natural and synthetic C-bearing glasses,^{3,4} but a comparison of the results of these techniques shows wide discrepancies. These bulk analytic techniques are destructive and require relatively large samples; in addition, the effects of crystals, alteration phases, and C in bubbles (versus C dissolved in the glass) are often difficult to evaluate.

In recent years, several meso- to microbeam techniques have been applied to measurement of the C contents of natural and synthetic silicate glasses. These beam techniques have several advantages over bulk techniques. They are nondestructive, the beam may be aimed at specific sites in the sample to avoid some of the contaminants that complicate the interpretation of bulk analytic techniques, and sample homogeneity may be checked. We have developed a microbeam infrared spectroscopic technique for the quantitative measurement of C-bearing species dissolved in silicate glasses.⁵ With the state-of-the-art Fourier transform infrared spectrometers, the diameter of the analyzed spot can be as small as 10 μm . Detection limits depend on glass composition and thickness, but reliable analyses at the 1 ppm level are possible in some cases. Not all C-bearing species are detectable via infrared (e.g., graphite). This is often advantageous in that contaminants will not usually contribute to the infrared spectrum and, even if they do, they absorb at wavelengths different from the major dissolved species. However, infrared spectroscopy may also fail to detect forms of dissolved carbon that are of interest. Electron microprobe techniques have also been used for the qualitative analysis of low-level C in silicate glasses,⁶ but quantitative results are difficult to obtain for a variety of reasons, including the rapid attenuation of low-energy x rays and problems with surface contamination.⁷ More significant, sample currents required for the analysis of C result in mobility of sodium in these silicate glasses. Sodium is present in many geologically relevant glasses in relatively high concentrations. Since the mechanism of C dissolution in these glasses may be intimately associated with Na_2O ,⁵ electron microprobe techniques must be used with caution. Even if sodium mobility under the electron beam can be minimized, care must be taken to avoid mobilization of the carbon itself.

In this paper, we describe the use of the $^{12}\text{C}(\text{d},\text{p}_0)^{13}\text{C}$ nuclear reaction for the absolute measurement of dissolved C in a series of C-rich, synthetic silicate glasses. This beam technique avoids most of the problems encountered during analysis of low-level C contents by electron microprobe and by bulk analysis. It has been used previously for the analysis of C in metals,⁸ lunar samples,⁹ minerals,^{10,11} and meteorites.¹² Here we demonstrate the usefulness of the nuclear technique by the measurement of the C content of a variety of synthetic silicate glass standards.

Experimental Procedure

Glasses of four different compositions were synthesized and powdered: $\text{NaAlSi}_2\text{O}_6$, $\text{NaAlSi}_3\text{O}_8$, $\text{NaAlSi}_4\text{O}_{10}$, and a calcium aluminosilicate glass corresponding to approximately $\text{CaAl}_{0.8}\text{Si}_{2.9}\text{O}_8$. Adsorbed C was removed from the powders by heating in air at 850 C for 48 h. Carefully measured amounts of $\text{Ag}_2\text{C}_2\text{O}_4$ and silicate glass were then loaded into Pt capsules, which were subsequently sealed by arc welding. The capsules were run in a piston-cylinder apparatus at a variety of temperatures (1400-1625 C) and pressures (15-33 kbar) above the liquidus of each composition.⁵ Upon being heated, $\text{Ag}_2\text{C}_2\text{O}_4$ dissociates

Authors Fine and Stolper are at the Division of Geological and Planetary Sciences and authors Mendenhall, Livi, and Tombrello at the Division of Physics, Mathematics, and Astronomy, Caltech, Pasadena, CA 91125. (Division of Geological and Planetary Sciences Contribution No. 4200.)

to inert Ag and CO₂ that dissolves in the silicate liquid; the resultant melts were then quenched to glasses containing known amounts of dissolved C. No bubbles were present in the glasses. Due to both diffusion of C through the Pt capsules¹³ and possible C heterogeneities in the glasses, the absolute C contents at individual points in the glasses are estimated to be known within $\pm 10\%$. Glasses containing negligible C, for use as blanks, were synthesized at 1580 C under 1 atm of N₂. All of the glasses were doubly polished using a slurry of Al₂O₃ powder and water, mounted on tantalum holders with superglue, and coated with a $\sim 50\text{\AA}$ thick gold or gold-palladium layer.

The C analyses were performed by means of a collimated, 0.25mm², 1.4MeV deuteron beam from the Caltech EN tandem Van de Graaff accelerator and a 500mm² silicon detector placed at an angle of 160° to the beam. Samples were held under vacuum (10^{-7} Torr) with silicone-based diffusion oil and were in close proximity to an LN₂ coldfinger. The glasses luminesced under deuteron bombardment, which facilitated beam placement.

The principles of C analysis by nuclear reaction have been discussed previously.⁸⁻¹¹ Some features merit review. Deuterons impinging on the surface of the sample lose energy with increasing depth x as they penetrate the sample. At an energy ultimately determined by the cross section of the $^{12}\text{C}(d,p)^{13}\text{C}$ reaction, the deuterons no longer react to produce ^{13}C . Similarly, protons emitted by the reaction lose energy as they leave the glass; their ultimate energy as seen by the detector is determined both by the energy of the reactive deuteron and the characteristic stopping power $(dE/dx)_p$ of the glass as expressed by

$$E_p = E_{p\max} + 0.6(E_d - E_{d_0}) + \Delta x \sec 20^\circ (dE/dx)_p$$

where $E_{p\max}$ is the maximum proton energy, E_{d_0} is the deuteron energy at the surface, E_d is the deuteron energy at depth x , and 20° is the angle between incoming deuterons and outgoing protons. The highest energy deuterons (E_{d_0}) thus react at the surface of the glass; these reactions result in the highest energy protons ($E_{p\max}$) at the detector. The energetics of this relationship, shown schematically in Fig. 1, create the opportunity for

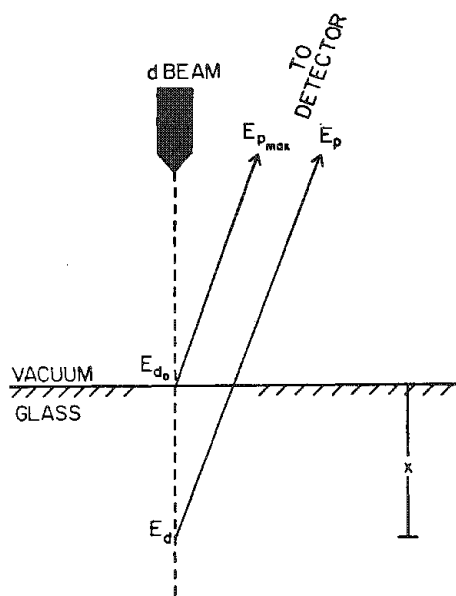


FIG. 1.--Representation of energetics of nuclear reaction as deuterons impinge on glass surface; $E_{d_0} > E_d$ and $E_{p\max} > E_p$. (After Filleux et al.⁹)

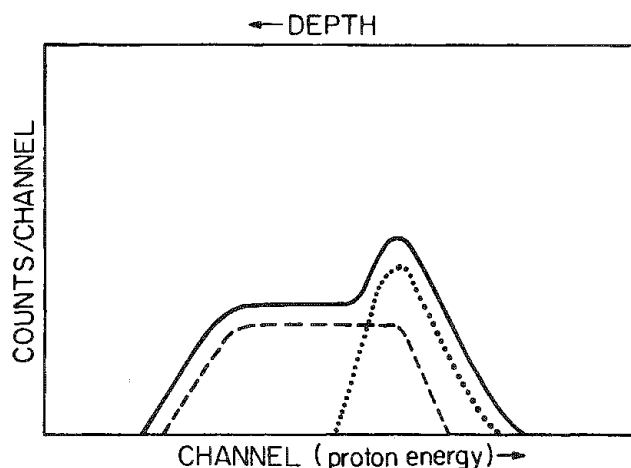


FIG. 2.--Idealized depiction of proton energy versus protons counted for thin surface layer (dotted), thick target (dashed), and thick target with thin surface contaminant layer (solid). (After Filleux et al.⁹)

depth versus concentration profiling by monitoring the number of protons emitted from a sample as a function of proton energy. The use of 1.4MeV deuterons, chosen for their large cross section, reduces the sensitivity of this method to surface contamination, but the spectra are clearly resolvable into a surface and volume component, shown

schematically in Fig. 2. The large reaction cross section allows us to reduce irradiation times to a mean of 10 min and minimizes radiation damage to the glasses.

Each glass spectrum was fit as a linear combination of the spectrum of a blank glass of the same composition (or SiO_2 glass) and of calcite (CaCO_3) from the Hilton deposit, San Diego, Calif., weighted by $(dE/dx)_p$.¹⁴ This fitting allowed calibration of the integrated intensity of the volume component versus C content. A spectrum of calcite was obtained after every 4 to 6 glass irradiations, to eliminate charge integration problems. We estimate the absolute accuracy of this method to be $\pm 5\%$ total C.

Results

Figure 3 shows the proton spectra for an $\text{NaAlSi}_3\text{O}_8$ glass containing 0.19 wt.% dissolved C. The peak due to the $^{12}\text{C}(d,p_0)^{13}\text{C}$ reaction is noted, as are peaks due to other resonant O reactions and Rutherford backscattering edges from the Na, Al, and Si in the glass. The increase in intensity of the C peak with increasing dissolved C content is shown in Fig. 4. Note that no surface component is visible in these spectra, which were

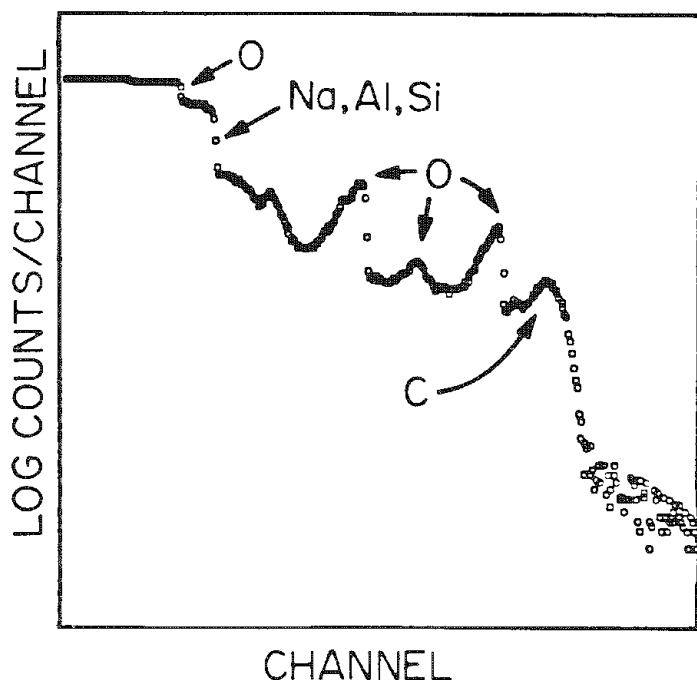


FIG. 3.--Proton spectrum of ABC-53. Resonant O reaction peaks and Rutherford backscattering edges due to Na, Al, and Si are noted. Irradiation time is approximately 10 min.

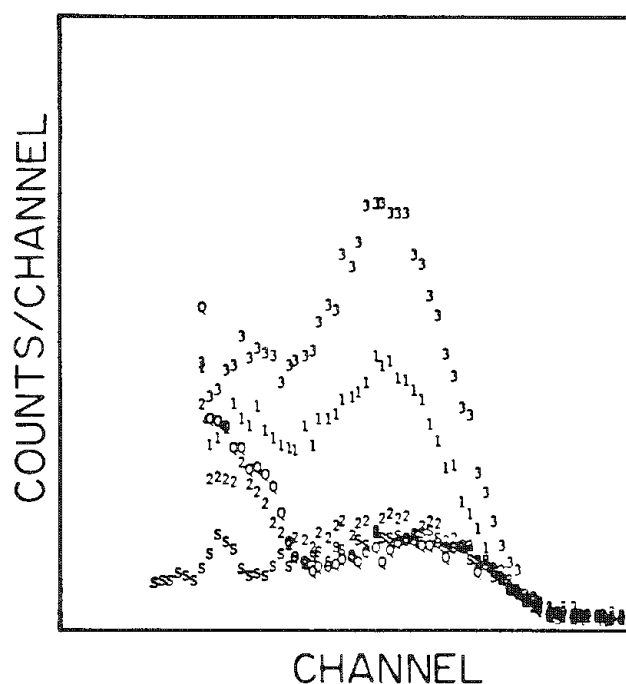


FIG. 4.--C reaction peaks for SiO_2 (Q), silicon (S), and $\text{NaAlSi}_2\text{O}_8$ glasses containing 0.085 (1), 0.049 (2), and 0.19 (3) wt.% dissolved C.

obtained during 10min runs. During 30min irradiations the surface component increases slightly in intensity with time, but no change is observed in the volume component, which implies no significant loss of C from the samples and confirms our ability to distinguish between these two components. The fit of a spectrum of $\text{NaAlSi}_2\text{O}_8$ glass as a linear combination of the spectra of CaCO_3 and SiO_2 glass is shown in Fig. 5.

Table 1 lists the C analysis of each glass accompanied by the amount of C originally loaded into each glass; the results are shown graphically in Fig. 6. In view of both the $\pm 10\%$ uncertainty in loaded C content and the $\pm 5\%$ uncertainty in the C analyses, the amount of loaded C is adequately reproduced. Analyses of these glasses and natural basaltic glasses containing <300 ppm C tend to be inadequate; preliminary work with glasses containing C at less than these levels has yielded inconsistent results. Our experience indicates that four factors are probably responsible: (a) a surface C film on the samples was not adequately removed before analysis; (b) these experiments were not performed under

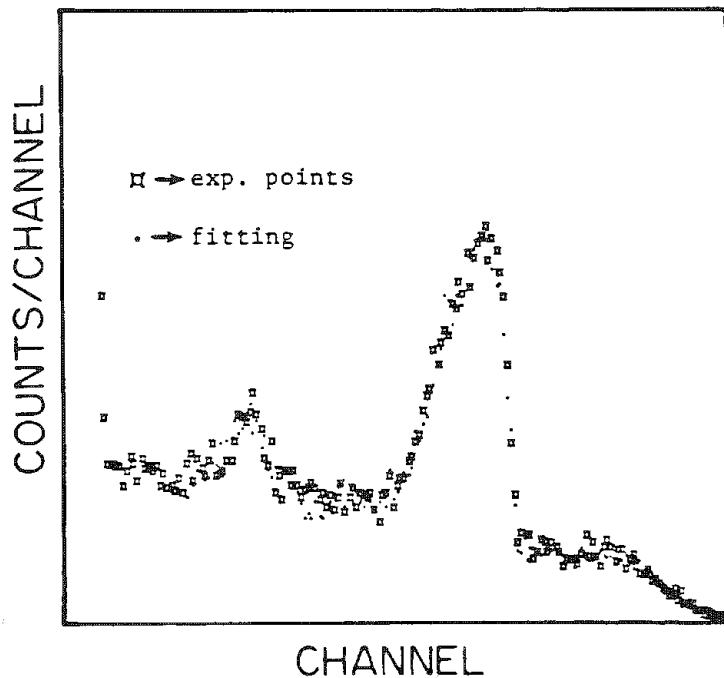


FIG. 5.-- $\text{NaAlSi}_3\text{O}_8 + \text{CO}_2$ glass spectrum fitted as linear combination of SiO_2 and CaCO_3 spectra.

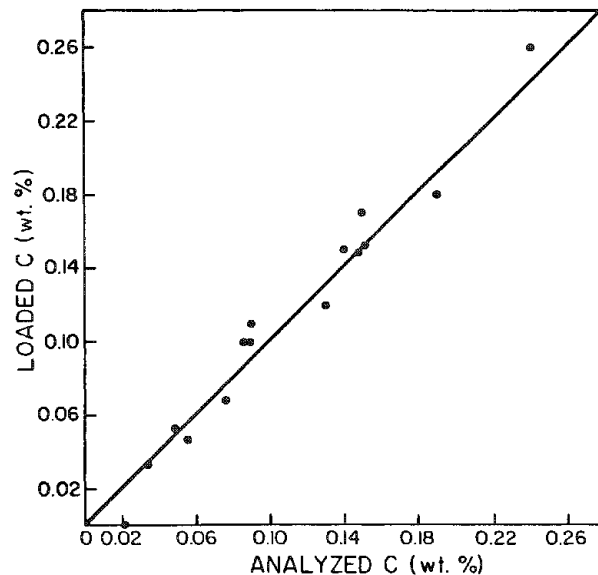


FIG. 6.--Analyzed C vs. loaded C for all glasses analyzed.

TABLE 1.--Results of C analyses.

Sample Number	Composition	C content (wt.%)	
		Loaded into capsule ^a	Analyzed ^b
ANC-9	$\text{CaAl}_{0.8}\text{Si}_{2.9}\text{O}_8$	0.033	0.034
ANC-10	$\text{CaAl}_{0.8}\text{Si}_{2.9}\text{O}_8$	0.17	0.15
ANC-11	$\text{CaAl}_{0.8}\text{Si}_{2.9}\text{O}_8$	0.10	0.089
JDC-111	$\text{NaAlSi}_2\text{O}_6$	0.047	0.055
JDC-112	$\text{NaAlSi}_2\text{O}_6$	0.15	0.15
JDC-116	$\text{NaAlSi}_2\text{O}_6$	0.15	0.15
ABC-53	$\text{NaAlSi}_3\text{O}_8$	0.18	0.19
ABC-54	$\text{NaAlSi}_3\text{O}_8$	0.10	0.085
ABC-55	$\text{NaAlSi}_3\text{O}_8$	0.053	0.049
ABC-58	$\text{NaAlSi}_3\text{O}_8$	0.11	0.090
ABC-62	$\text{NaAlSi}_3\text{O}_8$	0.26	0.24
ABC-63	$\text{NaAlSi}_3\text{O}_8$	0.00	0.021
ABC-64	$\text{NaAlSi}_3\text{O}_8$	0.21	0.21
NC-15	$\text{NaAlSi}_4\text{O}_{10}$	0.15	0.14
NC-17	$\text{NaAlSi}_4\text{O}_{10}$	0.068	0.076
NC-19	$\text{NaAlSi}_4\text{O}_{10}$	0.12	0.13

^a ±10% error assigned; ^b ±5% error assigned.

ultrahigh (10^{-9} Torr) vacuum, and observable surface contaminant C becomes significant relative to dissolved C at low levels of dissolved C, which makes deconvolution of the volume component in Fig. 2 quite difficult; (c) the presence of contaminant C in micro-cracks in the glass generated during polishing cannot be ruled out; and (d) our run times (10 min) were not long enough to eliminate inherent noise in the low-level C analyses. All four factors are easily eliminated⁹ and we are optimistic that this method is a useful technique for low-level C analyses in natural glasses.

Conclusions

The $^{12}\text{C}(\text{d},\text{p}_0)^{13}\text{C}$ nuclear reaction is a useful, nondestructive beam technique for the analysis of C in geologically relevant glasses. The method is unencumbered by many of the problems associated with other beam techniques, although more development of the procedure is necessary for adequate low-level (<300 ppm) C analyses. The use of collimated 100 μm diameter beam is eventually possible, accompanied by run times of reasonable length.

References

1. T. M. Gerlach, "Interpretation of volcanic gas data from tholeiitic and alkaline mafic lavas," *Bull. Volcanol.* 45: 235-244, 1985.
2. P. J. Wyllie, "Magmas and volatile components," *Am. Min.* 64: 469-500, 1979.
3. F. Pineau and M. Javoy, "Carbon isotopes and concentrations in midoceanic ridge basalts," *Earth Planet. Sci. Lett.* 62: 239-257, 1983.
4. J. R. Delaney, D. W. Muenow, and D. G. Graham, "Abundance and distribution of water, carbon, and sulfur in the glassy rims of submarine pillow basalts," *Geochim. Cosmochim. Acta* 42: 581-594, 1978.
5. G. Fine and E. Stolper, "The speciation of carbon dioxide in sodium aluminosilicate glasses," *Contrib. Mineral. Petrol.*, in press.
6. E. A. Mathez and J. R. Delaney, "The nature and distribution of carbon in submarine basalts and peridotite nodules," *Earth Planet. Sci. Lett.* 56: 217-232, 1981.
7. J. I. Goldstein et al., *Practical Scanning Electron Microscopy*, New York: Plenum Press, 1976.
8. J. A. Cookson, "The production and use of a nuclear microprobe of ions at meV energies," *Nuc. Inst. Meth.* 165: 477-508, 1979.
9. C. Filleux, T. A. Tombrello, and D. S. Burnett, "Direct measurement of surface carbon concentrations," *Proc. 8th Lunar Sci. Conf.*, 1977, 3755-3772.
10. G. Oberheuser, H. Kathrein, G. DeMortier, H. Gonska, and F. Freund, "Carbon in olivine single crystals analyzed by the $^{12}\text{C}(\text{d},\text{p})^{13}\text{C}$ method and by photoelectron spectroscopy," *Geochim. Cosmochim. Acta* 47: 1117-1129, 1983.
11. E. A. Mathez, J. D. Blacic, J. Beery, C. Maggiore, and M. Hollander, "Carbon in mantle minerals determined by nuclear reaction analysis," *Geophys. Res. Lett.* 11: 947-950, 1984.
12. D. Heymann, R. Vis, and C. van der Stap, "Carbon concentration mapping in a surface of the Allende meteorite," *Abst. 16th Lunar Sci. Conf.*, 1985, 348-349.
13. E. B. Watson, M. A. Sneeringer, and A. Ross, "Diffusion of dissolved carbonate in magmas: Experimental results and applications," *Earth Planet. Sci. Lett.* 61: 346-358, 1982.
14. H. H. Anderson and J. F. Ziegler, *Hydrogen Stopping Powers and Ranges in All Elements*, New York: Pergamon Press, 1977.

Surface Microanalysis—Auger Electron Spectroscopy

GRAIN BOUNDARY ANALYSIS TECHNIQUES FOR DUCTILE NICKEL-BASE ALLOYS

G. S. Was and J. R. Martin

Several Auger electron spectroscopy studies have been performed on the grain boundary segregation behavior of impurities in nickel-base and iron-nickel alloys.¹⁻⁶ In many cases, investigators report a scatter in the Auger measurements ranging from 5 to 30% of the average value. Recently, Briant¹ found that the variation in the segregation of phosphorus and antimony to grain boundaries in iron alloys is within about $\pm 30\%$ of the average value, but some boundaries had significantly different compositions both above and below the average. He considered several factors that could contribute to this variability, among them angular variations in the different grain boundary facets with respect to the cylindrical mirror analyzer, variations produced by the fracture process, variations that result from compositional banding in the matrix, and variations caused by nonequilibrium segregation. Another complicating factor is the presence of grain boundary precipitates whose composition differs significantly from the bulk. This factor requires a rethinking of the current practices used to report grain boundary chemistry. However, analysis of precipitate laden grain boundaries can reveal the nature of the fracture path, and in concert with STEM-EDS, the fractional coverage of the grain boundaries by precipitates.

However, before such measurements can be made, the grain boundaries must be exposed in a noncontaminating fashion. Although most iron-base alloys can be fractured intergranularly by impact loading following a hydrogen precharging operation, the task is considerably more difficult with austenitic stainless steels and nickel-base alloys. To fracture these alloys intergranularly, the sample must be strained at a very slow rate, e.g., 10^{-3} to 10^{-4} s^{-1} , in addition to having undergone a hydrogen precharging operation. However, the straining process must be conducted inside the vacuum chamber of the Auger electron spectrometer to prevent contamination of the newly created fracture surfaces. This paper focuses on the techniques used to fracture a ductile alloy in situ and to obtain information on impurity segregation, major alloying element redistribution, location of the fracture path, and coverage of grain boundaries by precipitates using Auger electron spectroscopy (AES) and energy-dispersive x-ray analysis via scanning transmission electron microscopy (STEM-EDS).

Material

High-purity heats of a Ni-Cr-Fe alloy were prepared with controlled additions of phosphorus and carbon. Four alloys were made covering all possible combinations of high C, low C, high P, and low P (Table 1). The 12mm-diameter ingots were swaged down to 3mm rod and solution-annealed at 1100 C for 20 min to dissolutionize any carbides that may have remained from the processing. The annealing recrystallized the alloys and produced a grain size of approximately 100 μm . The alloys were then subjected to heat treatments of 1, 10, or 100 h at 700 C to produce grain boundary carbides in the high-C alloys and grain boundary phosphorus segregation in the high-P alloys, and are described by the designations AFR45-A, -1, -10, etc.

In Situ Fracture

A slow extension rate fracture (SERF) stage⁷ shown in Figs. 1 and 2 is used to apply a tensile load to samples with a gage section 1.5 mm wide, 0.24 mm thick, and 9 mm long. A tensile load is applied to the sample by conversion of the rotational motion of a small electric motor to translational motion via a set of small ball bearings. Since electric motors appropriate for this type of application typically produce a torque of the order of 0.6 N-m, and the lever arm (distance between the centers of the motor shaft and reduction gear) is about 5.0 cm, the maximum force that may be applied to the sample is about 12 N. Hence, close control of the gage section thickness is required to insure that the net section stress exceeds the ultimate tensile strength of the alloy at the maximum applied load.

Author Was is with the Department of Nuclear Engineering, University of Michigan, Ann Arbor, MI 48109; author Martin is at the MIT Auger Laboratory, Cambridge, MA 02139.

TABLE 1.--Experimental alloy bulk composition.*

Alloy Designation	atomic %				
	Ni	Cr	Fe	C	P
AFR12	72.33	18.48	9.19	<.01	<.001
AFR45	72.19	18.26	9.48	<.01	.071
AFR46	72.50	18.03	9.31	.107	.065
AFR91	73.10	18.04	8.74	.124	<.001

*The Ni concentration is adjusted such that $X_{Ni} + X_{Cr} + X_{Fe} + X_C + X_P = 100.0$

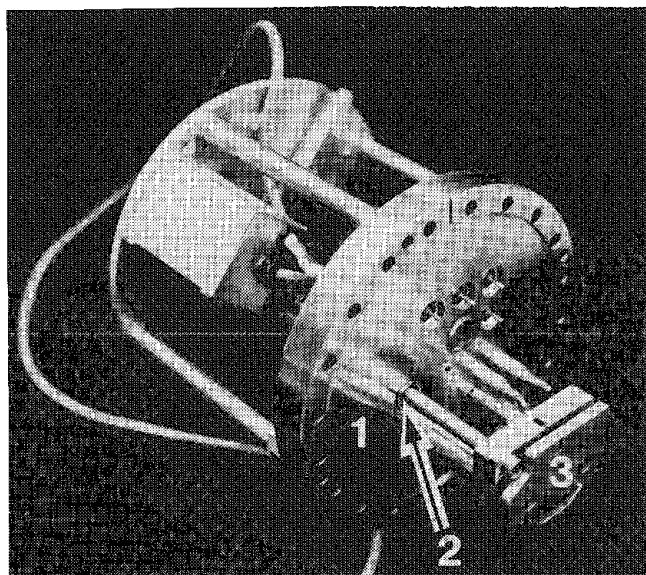


FIG. 1.--Slow extension rate fracture stage showing (1) vacuum flange, (2) mechanical feed through, (3) crosshead assembly.

high resolution. Data were collected with a 5kV focused electron beam with a current of 90 to 110 nA and approximately 1 μ m in diameter. On each sample, 3 to 5 grain boundary surfaces were selected on which 5 spot analyses were made. Each set of analyses was made on individual grain boundary facets to eliminate scatter due to inclusion of transgranular surfaces and also to study the variability between grain boundaries. An Auger survey (0-2000 eV) was made on one intergranular facet of each alloy heat treatment to insure that no other elements were present.

Data were collected using the Physical Electronics multiple technique analytical computer system (MACS) in a multiple-point, multiplex-analysis type mode. A five point analysis was made on each grain boundary measuring P, Cr, Ni, Fe, O, and C signals each time. The total analysis time for each five spot array was 10 min. This time was long enough to produce a reasonable signal-to-noise ratio of 20 (for phosphorus), but short enough to minimize contamination of in situ fracture surfaces with exposure time. Atomic percentages are calculated using standard sensitivity factors and mathematical methods supplied by PHI,⁸ specific to the instrumentation involved. In order to avoid ambiguities involved when applying this method to alloy systems, only atomic percent ratios are used. A total of 300 spot analyses were taken from 60 grain boundaries covering 10 material conditions.

In the presentation of Auger data, a common technique is to ratio the peak of the

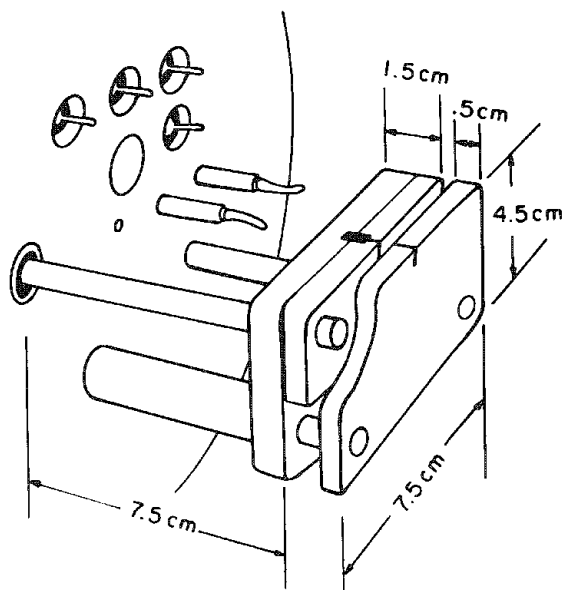


FIG. 2.--Slow extension rate fracture stage.

Sample preparation consists of charging with hydrogen in a solution of 1N H₂SO₄ + 2.0 mg NaAsO₂/l of solution at a current density of 10 mA/cm². Charging was conducted at either 21 C or 85 C for 72 or 24 h, respectively. At an extension rate of 10⁻⁴ cm/s, typical failure times are 3-6 min. Both hydrogen charging and slow straining are needed to produce intergranular fracture. Samples consistently yielded fracture surfaces that were better than 75% intergranular (Figs. 3 and 4).

Analysis Techniques

Fracture surfaces were analyzed in a Physical Electronics model PHI 590 Scanning Auger Microprobe (SAM) in a vacuum of better than 5×10^{-9} torr. This system is equipped with a vibration isolation stage to allow analysis at

high resolution. Data were collected with a 5kV focused electron beam with a current of 90 to 110 nA and approximately 1 μ m in diameter. On each sample, 3 to 5 grain boundary surfaces were selected on which 5 spot analyses were made. Each set of analyses was made on individual grain boundary facets to eliminate scatter due to inclusion of transgranular surfaces and also to study the variability between grain boundaries. An Auger survey (0-2000 eV) was made on one intergranular facet of each alloy heat treatment to insure that no other elements were present.

Data were collected using the Physical Electronics multiple technique analytical computer system (MACS) in a multiple-point, multiplex-analysis type mode. A five point analysis was made on each grain boundary measuring P, Cr, Ni, Fe, O, and C signals each time. The total analysis time for each five spot array was 10 min. This time was long enough to produce a reasonable signal-to-noise ratio of 20 (for phosphorus), but short enough to minimize contamination of in situ fracture surfaces with exposure time. Atomic percentages are calculated using standard sensitivity factors and mathematical methods supplied by PHI,⁸ specific to the instrumentation involved. In order to avoid ambiguities involved when applying this method to alloy systems, only atomic percent ratios are used. A total of 300 spot analyses were taken from 60 grain boundaries covering 10 material conditions.

In the presentation of Auger data, a common technique is to ratio the peak of the

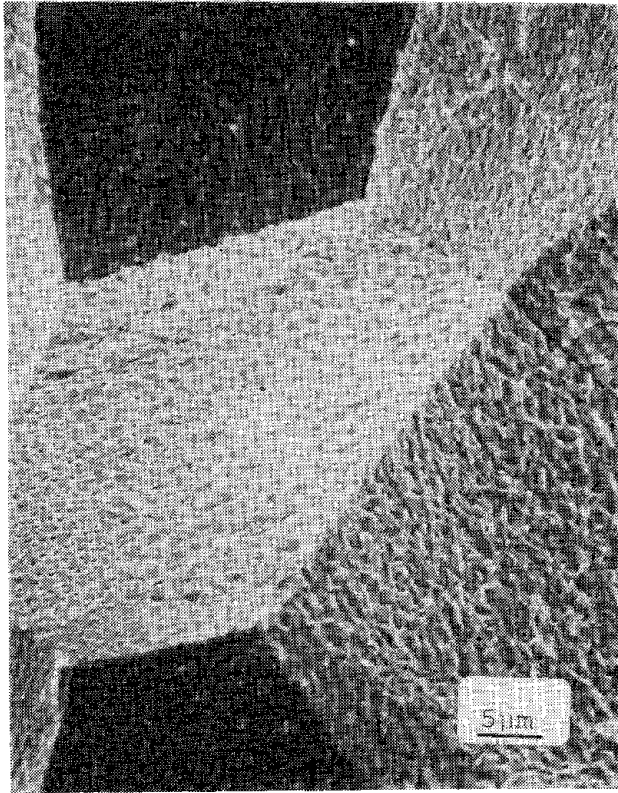


FIG. 3.--Fractograph of grain boundary surfaces in AFR46-100.

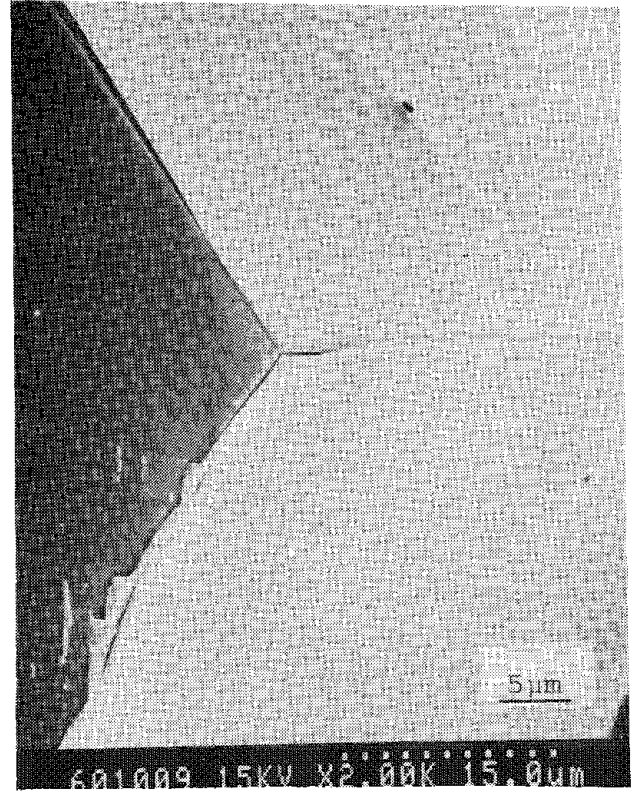


FIG. 4.--Fractograph of grain boundary surfaces in AFR45-A.

element of interest to that of a major alloying element. This method of data analysis circumvents the problem of converting Auger peaks to concentrations and yet can usually be used in a relative sense semiquantitatively to identify trends and large variations in segregation. The technique breaks down when heavy precipitation occurs at the grain boundary. Since intergranular fracture often occurs between precipitate and matrix, the concentration of the major alloying element used to normalize the signal may be much different in the matrix from that in the precipitate. In the case of Ni-Cr-Fe alloys used in this study, the bulk concentration is approximately 74.5 at% Ni, 16.5 at% Cr, and 9 at% Fe. However, STEM-EDS measurements of M_7C_3 carbides on grain boundary surfaces yield a composition of 96 at% Cr - 2 at% Ni - 2 at% Fe.⁹ Hence the ratio of x_j/x_{Ni} will yield vastly different results depending on the nature of the substrate. Therefore, the amount of P or Cr on the fracture surface is expressed as a ratio of the concentration of P or Cr to the sum of the concentrations of Ni + Cr + P. In these alloys, the atom fraction of iron on the fracture surface remains relatively constant and small for all heat treatments and need not be included in the denominator. Since the iron concentration varies from 2% in the carbides to only about 9% on the exposed matrix surface, significant changes are not expected. It is the variation in Ni, Cr, and P which is most important. The ratios of phosphorus and chromium to chromium + nickel + phosphorus are calculated as follows.

$$F_P = \frac{x_P}{x_{Cr} + x_{Ni} + x_P} \quad (1)$$

$$F_{Cr} = \frac{x_{Cr}}{x_{Cr} + x_{Ni} + x_P} \quad (2)$$

where x_j = atom fraction of element j on the fracture surface, and F_j = grain boundary surface ratio of element j. The standard deviation of each data group is calculated as a percentage of the mean value,

$$\sigma_j = \frac{\left[\frac{1}{N} \sum_{i=1}^N (F_j^i - \bar{F}_j)^2 \right]^{1/2}}{\bar{F}_j} \times 100 \quad (3)$$

where σ_j = normalized standard deviation = standard deviation/mean $\times 100$, \bar{F}_j = mean surface ratio of element j , and N = number of data points. Describing the standard deviation in this way allows intercomparison of the variations in measurements of different elements on different alloys and heat treatments.

Results

The chromium atom fraction ratios for each material condition for alloys AFR45 and AFR46 are shown in Fig. 5. Note the substantial difference between the scatter in these two alloys. Data from alloy AFR46 (high P, high C) have average normalized grain boundary standard deviations over 5 times as large as those from the high-P, low-C alloy. As the thermal treatment time increases, F_{Cr} rises from 0.21 after 1 h to 0.311 after 100 h. Data from alloy AFR91 heat treated for 100 h at 700 C are also given in Fig. 5 and agree well with the AFR46-100 data. Alloy AFR91 differs from AFR46 in that it is a high-C, low-P alloy and has no detectable phosphorus at the grain boundary.

The phosphorus atom fraction ratios for each material condition for alloys AFR45 and AFR46 are shown in Fig. 6. Although the presence of grain boundary carbides is responsible for the large variation in F_{Cr} between AFR45 and AFR46 in Fig. 5; i.e., note that σ_p is very similar in magnitude for the two alloys as shown in Fig. 6.

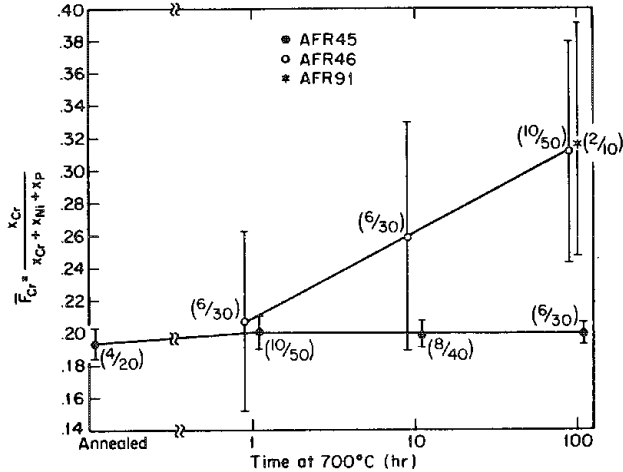


FIG. 5.--Chromium atom fraction ratio vs thermal treatment time at 700 C.

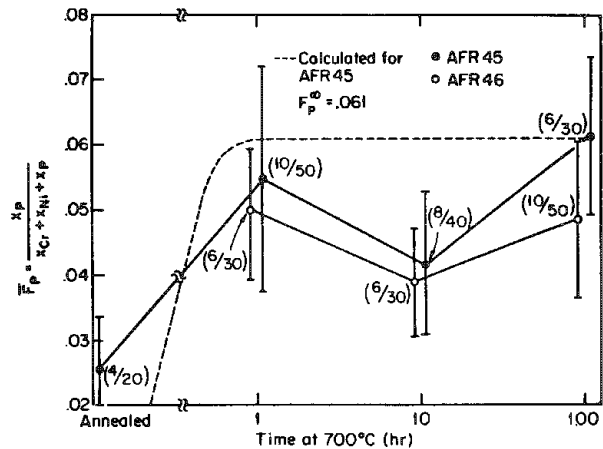


FIG. 6.--Phosphorus atom fraction ratio vs thermal treatment time at 700 C.

The complicated relationships between P, Cr, and Ni on the fracture surface can best be described using surface composition diagrams^{10,11} as shown in Figs. 7 and 8. In these figures, F_{Cr} , F_{Ni} , and F_P are plotted on a ternary phase diagram. The shaded region indicates the space encompassed by the data and the accompanying scatter. Note that for alloy AFR45, the error bars on the measured phosphorus (F_P) and chromium (F_{Cr}) levels are small for all heat treatments (Fig. 7). The data in Fig. 8 are from the carbon-containing alloy AFR46. Here there is a progression toward higher Cr levels with heat treatment, caused by the increasing Cr-rich carbide coverage of the fracture surface. The presence of carbides also causes a marked increase in the error bars. This method of data presentation includes the interrelationships between the main elements present on the fracture surface and the variations in their measurements.

Discussion

The effect of carbide precipitation on the measurement of Cr on the fracture surface is manifest in an increase in the value of F_{Cr} with thermal treatment time in the high C alloy (AFR46) and a significant increase in the scatter in F_{Cr} in alloy AFR46. The increase in F_{Cr} with thermal treatment time occurs due to lateral precipitate growth and hence an increasing coverage of the grain boundary. Since the Cr composition of the precipitate is significantly higher than that in the matrix, the value of F_{Cr} increases. The carbide coverage is shown in Fig. 3 in which the grain boundary surfaces appear rough

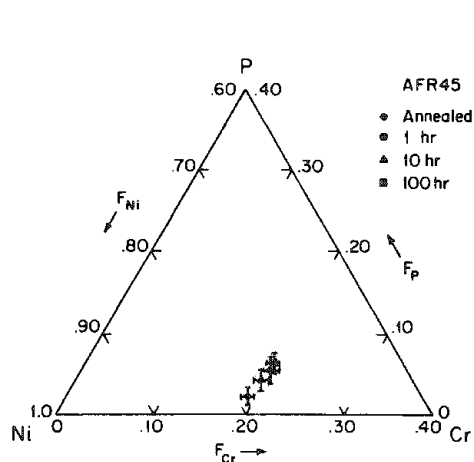


FIG. 7.--Ternary composition diagram for Cr, Ni, and P on grain boundary surfaces of AFR45.

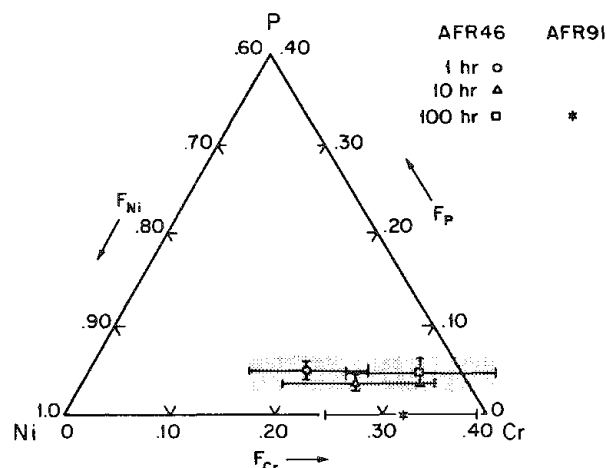


FIG. 8.--Ternary composition diagram for Cr, Ni, and P on grain boundary surfaces of AFR46.

as opposed to the smooth intercrystalline facets created by fracture of the low-C alloy (Fig. 4).

The second effect of grain boundary carbide precipitation is an increase in the scatter in F_{Cr} when analyses are made in spot mode. An increase in scatter of the measured quantity occurs when the analysis area is of the same size as the variation in surface chemistry (carbides or matrix). Hence, for carbides approximately $1\ \mu\text{m}$ in size (as measured by STEM), the analysis area could include carbide and matrix, carbide alone, or matrix alone. Since the Cr composition varies so significantly between carbide and matrix, the resulting analysis shows a high degree of fluctuation.

The variability in local Cr content due to the presence of $\sim 1\ \mu\text{m}$ -sized Cr_2C_3 carbides is shown in the Auger maps given in Fig. 9. The maps show Cr and Ni concentrations on the surface of the grain boundary of an AFR46-10 sample. Note that the Cr and Ni maps are strongly complementary, which shows that the concentrations trade off spatially, as discussed earlier. The spatial variations in the Ni and Cr maps are again on the order of $1\ \mu\text{m}$ in size. All the AFR46 samples show the same type of behavior in Cr and Ni.

In all cases, the maps of P were of uniform intensity and nearly featureless.¹² In addition, the P level does not appear to vary between the intercrystalline sites and the carbide-matrix sites. These results strongly suggest the existence of a fairly uniform layer of P on the grain boundary with variations arising from many of the same sources described by Briant,¹ with the addition of C and O contamination from the $\leq 5 \times 10^{-9}$ Torr vacuum used in this study.

From the analyses of the spatial distribution of Cr and P on the fracture surface, it can be deduced that fracture occurs along the carbide-matrix interface as opposed to through the carbides or some distance ($>10\ \text{\AA}$) into the matrix. Since P is not incorporated into the carbides, a fracture path that leads through the carbides would result in spatial inhomogeneities in the P maps similar to that found for Cr. That this is not the case suggests that the fracture surface must either be along the carbide-matrix interface or some distance into the matrix. However, recent measurements by Shinoda¹³ on P segregation in Fe-Ni-P confirm that the intergranular segregation extent of P is one monolayer and at most two monolayers ($\sim 5\ \text{\AA}$) thick. Hence, any fracture path deeper than 5 or $10\ \text{\AA}$ would show little or no P. On this basis we conclude that fracture proceeds along the carbide-matrix interface.

Given the location of the fracture path, an estimate can be made of the carbide coverage of the grain boundary. If we assume that the fracture path leaves half of the carbides on one half of the sample and the other half on the mate, then F_{Cr} on the exposed surface (defined by $x_{Cr}/(x_{Ni} + x_{Cr})$) is given by

$$F_{Cr}^{\text{surface}} = x_{Cr}^i [1 - (C/2)] + 0.98(C/2) \quad (4)$$

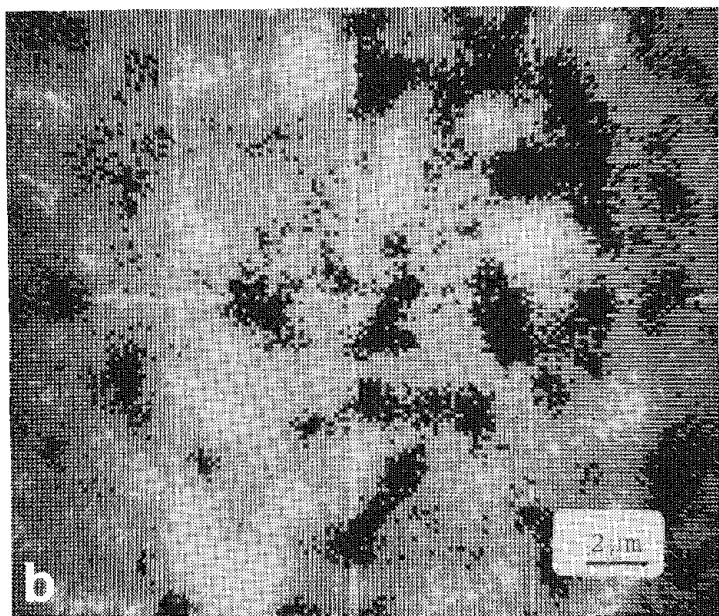
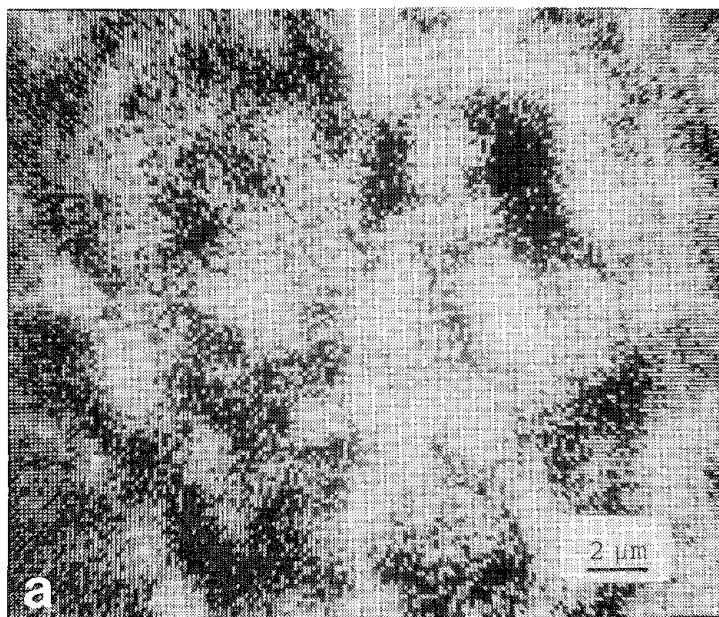


FIG. 9.--Auger maps of (a) Cr, (b) Ni on grain boundary surface of alloy AFR46-10.

is measured by AES and is found to range from 30% after 1 h at 700C to 46% after 100 h at 700 C.

References

1. C. L. Briant, *Acta Metall.* 31: 257-266, 1983.
2. R. R. de Avillez and P. R. Rios, *Scripta Metall.* 17: 677-680, 1983.
3. H. Erhart and M. Paju, *Scripta Metall.* 17: 171-174, 1983.
4. K. S. Shin and M. Meshi, *Acta Metall.* 31: 1559-1566, 1983.
5. R. A. Mulford, *Metall. Trans.* 14A: 865-870, 1983.
6. M. Guttman, P. Dumoulin, N. Tan-Tai, and P. Fontaine, *Corrosion* 37: 416-425, 1981.
7. G. S. Was, H. H. Tischner, and J. Martin, *J. Vac. Sci. & Techn.* 1A: 1477-1479, 1983.
8. L. E. Davis, N. C. MacDonald, P. W. Palmberg, G. E. Riach, and R. E. Weber, *Handbook of Auger Electron Spectroscopy*, Eden Prairie, Minn.: Physical Electronic Industries, 1976, 5.

where x_{Cr}^i is F_{Cr} for the matrix at the carbide-matrix interface, 0.98 is F_{Cr} for the carbide, and C is the fraction of the intact grain boundary covered with carbides (coverage). Hence, we can express the grain boundary surface coverage as a function of $F_{Cr}^{surface}$ as follows:

$$C = \frac{2}{(0.98 - x_{Cr}^i)} (F_{Cr}^{surface} - x_{Cr}^i) \quad (5)$$

Since chromium depletion occurs at the carbide-matrix interface, x_{Cr}^i is a function of time at 700 C, as measured by STEM-EDS, and is given in Table 2. Recall that x_{Cr}^i does not vary in the plane of the grain boundary or with proximity to the carbides. Solution of Eq. (5) using data from Table 2 yields grain boundary coverages of 30%, 40%, and 46% after 1, 10, and 100 h at 700 C, respectively.

Conclusions

Ductile nickel-base alloys can be fractured in situ by precharging with hydrogen and straining at a rate of 10^{-4} $cm \cdot s^{-1}$.

The presence of chromium rich carbide precipitates on grain boundaries of Ni-16Cr-9Fe results in a significant increase in the measured value of the Cr content on the fracture surface. An increase in the scatter in the measurements will occur when the analysis area is of the same size as the carbides. The scatter can be kept to a minimum by ratioing the element of interest to a sum of the elements appearing both in the matrix and in the carbide.

The fracture path is predominantly along the carbides or some distance into the matrix.

The fraction of the intact grain boundary surface covered with carbides

TABLE 2

Time at 700°C (hr)	F_{Cr}	x_{Cr}^{j**}	Coverage (%)
1	.218	.086	30
10	.269	.090	40
100	.327	.134	46

* Measured by AES

** Measured by STEM-EDS

9. G. S. Was and R. M. Kruger, *Acta Metall.* 33: 841-854, 1985.

10. G. D. Davis, T. S. Sun, J. S. Ahearn, and J. D. Venables, *J. Mater. Sci.* 17: 1807-1818, 1982.

11. G. D. David, S. P. Buchner, W. A. Beck, and N. E. Byer, *Appl. Surface Sci.* 15: 238-246, 1983.

12. G. S. Was and J. R. Martin, *Metall. Trans.* 16A: 349-359, 1985.

13. T. Shinoda, *Acta Metall.* 31: 2051-2062, 1983.

RECENT ADVANCES IN SURFACE ANALYSIS USING AUGER AND X-RAY PHOTOELECTRON SPECTROSCOPY

L. B. Church and G. E. McGuire

This paper reviews the major changes that have modified surface analysis over the past 4 years. The perspective of the observations is that of the user rather than the instrument manufacturer. Compared to mid-1981, a user of these analysis techniques can now expect to learn considerably more about the surface of a sample in a shorter time, even though no major scientific breakthroughs have occurred in the basic physics of Auger electron spectroscopy (AES) or x-ray photoelectron spectroscopy (XPS or ESCA).

Multichannel Detectors

Perhaps the most significant advance in instrumentation during the past 4 years has been the increased utilization of multichannel or position-sensitive detectors for electron spectrometers used in XPS. Compared to the former single detector, a multichannel array of detectors permits simultaneous acquisition of data at different energies. The net results are higher possible count rates because of increased electron throughput, superior energy resolution at the higher count rates, and shorter analysis times for both AES and XPS analyses. The multichannel detectors in use at present are usually solid-state position-sensitive detectors or an array of channels in a microchannel plate.

Smaller Areas of Excitation

Advances in the technology of electron optics continue to decrease the electron beam spot size and hence the effective area of excitation in AES. Current specifications on minimum beam spot size are now down to about 350 Å. However, a very important recent advance in XPS work has been the ability to concentrate the x-ray beam onto areas much smaller than was formerly possible.¹ Current specifications on small-spot-size XPS indicate areas of analysis as small as 0.15 mm, compared to 4 years ago when the effective area was 5 mm.² Both of these advances have contributed to improving the current status of AES and XPS analysis. This relationship is developed in the next sections, in which each technique is discussed separately.

XPS

Improved spatial resolution of XPS is the most significant change that has occurred in surface analysis during the past 4 years. One can achieve the smaller area of analysis either by concentrating the x-ray beam or by focusing the emitted electrons from a selected area into the energy analyzer. The first approach has been called the microprobe method; the latter is referred to as the selected-area method.³

The microprobe approach begins by focusing electrons on an anode. The x-ray flux is then focused and made monochromatic by a bent crystal. The x-ray flux that reaches the sample area is reduced by the low solid angle of collection on the crystal and the coefficient of reflection off the crystal, which results in a significantly reduced electron count rate unless the multichannel detector array is used.

At the present time, one can obtain an image map of the surface of the sample only by mechanically moving the sample. However, it is anticipated that scanning XPS, capable of producing both elemental and oxidation maps, will be available in the near future.⁴

The selected-area method bathes a large area of the sample with x rays. A multi-element electrostatic lens focuses the electrons from a small area onto the entrance of the electron analyzer. The result of using only a small fraction of the total available signal requires high-efficiency electron throughput to the detector, which is usually accomplished with the multichannel detectors and simultaneous counting of the signal. The results of the selected-area method are quite comparable to the microprobe method.⁵

AES

The major gains in AES have not been as dramatic as in XPS. As might be expected, commercial instruments strive to achieve the smallest area of electron beam excitation. By use of magnetic rather than electrostatic electron lenses, the minimum beam spot area has dropped by a factor of about 4 over the past 4 years. To compensate for the reduced numbers of emitted electrons when using the smaller spot size, it has been necessary to improve the efficiency of the electron energy analyzer.

The high rate of signal acquisition, combined with the ever-increasing rate of signal processing, data storage, data messaging, and display, have resulted in increase sample throughput in AES work. In fact the emphasis on sample analysis speed and turn-around is the hallmark of current AES marketing.

Conclusions

The increased inclusion of multiple-channel detectors has changed the capabilities of XPS analysis over the past 4 years. These detectors allow for a high efficiency of electron detection. The high-efficiency electron analyzers have altered XPS analysis by making it possible to analyze much smaller areas, either by limiting the area from which the electrons are analyzed or by concentrating the x rays onto a limited area. In AES analysis, the successful diminution of beam spot size and increased beam current density has resulted in faster sample throughput, which is important for jobs that require long periods of instrument time, such as depth profiling and elemental mapping.

References

1. M. Kelly, "More-powerful ESCA makes solving surface problems a lot easier," *Ind. Res. & Dev.* 26: 80-83, 1984.
2. *Model SSZ100 ESCA Spectrometer*, Surface Science Laboratories, Inc.
3. J. Cazaux, "How to improve spatial resolution in x-ray photoelectron and (x-ray induced) Auger electron spectroscopy," *SEM/1984* III, 1193-1202.
4. N. Gurker, M. F. Ebel, and M. Ebel, "Imaging XPS: A new technique," *Surf. and Interfaces* 5: 13-19, 1983.
5. *The PHI 5000 Series ESCA Systems*, Perkin-Elmer Physical Electronics Division.

Microbeam Analysis Techniques in the Study of Lunar, Meteorite, and Cosmic Dust Samples

MICROBEAM TECHNIQUES IN THE STUDY OF LUNAR ROCKS

Arden L. Albee

In January 1970 a unique gathering occurred. More than 500 scientists from nine countries gathered at Houston to present the first scientific results from the samples that three men had brought back from the surface of the Moon. The variety and sophistication of the techniques used in the study of these samples drew upon the expertise gained during the previous 25 years in the study of meteorites and of terrestrial petrology and mineralogy. The NASA sample investigator contract provided that no investigator was to divulge information prior to this gathering and that each investigator would submit his written report upon arrival at the conference.

As a result the 30 January 1970 issue of *Science* constituted a "blind test" of analytical techniques, since all of these studies were concentrated on a small set of samples, and so allowed ready comparison of the precision of the techniques. This comparison "validated" many of the emerging instrumental techniques for an audience of scientists that bridged many of the usual barriers among disciplines and scientific interest groups. Hence, this validation had an immediate and very wide distribution among a very vigorous group of scientists from many fields and from many institutions.

Included in the papers were results from about 30 electronprobe microanalysis laboratories in seven countries. These laboratories used different instruments and different correction schemes, but the close similarity of the results announced a new era in petrology and led to an immediate acceptance of electron probe analysis. For the first time each petrologist could have direct access to the chemical data that were required to test ideas that had developed over many years. This access has dramatically changed both the science and the teaching of petrology.

Attributes of Electron Probe Analysis for Petrology

The use and widespread availability of electron microprobe analyses has had an impact on various facets of petrology. The important attributes or capabilities of electron probe analyses for petrology can be categorized as follows:

- (1) accurate and low-cost analysis for major elements in silicates;
- (2) accurate analysis for major elements in opaque minerals;
- (3) analysis of μm spots in polished thin sections;
- (4) analysis for minor elements in major minerals;
- (5) analysis of rare minerals with major amounts of rare elements.

The lunar sample studies provide good illustrations of how these attributes have changed or have made possible a variety of studies on mineralogy, the partition of elements between phases, zoning in minerals, elemental mass balance between the minerals in rocks, experimental equilibria, diffusion couples, etc. This paper makes no attempt to summarize the results of electron probe studies on the lunar samples, since several excellent and detailed reviews already exist.¹⁻⁴

Accurate and Low-cost Analysis of Silicate Minerals. It is easy to overlook the importance of this attribute since it is not really related to the use of an electron microbeam. However, the ready availability of accurate analyses by means of the electron microprobe has, in itself, probably had the largest impact on petrology. Previously an analysis of a mineral from a rock required the painstaking separation and purification of 1-2 g of the mineral and a substantial wait before an analyst provided a "wet analysis" of dubious but indeterminable quality. Many published papers consisted essentially of a single such analysis, which would be highlighted as Table 1. A major field within petrology was the use of optical and simple x-ray properties to estimate the chemical composition of important rock-forming minerals such as the pyroxenes. Arbitrary classifications and names were formulated that were compatible with the precision of such estimates. Now petrologic papers, due to the current widespread use of the electron microprobe, simply

The author is at the Division of Geological and Planetary Sciences, California Institute of Technology, Pasadena, CA 91125.

state the composition of a mineral in the text, usually in terms of a detailed formula, and the arbitrary classifications are falling into disuse. Teaching the use of optical and x-ray properties to determine chemical composition, once a major part of petrology courses, is now greatly de-emphasized.

The typical electron probe analysis is also more accurate than the typical "wet chemical analysis" and, by its very nature, the user-analyst has at least some idea of the precision and can determine the completeness of the analysis. Since the lunar samples contain no ferric iron and no OH, the accuracy and precision of the microprobe analyses could be played against the stoichiometry of the silicate phases. Studies of this sort demonstrated the occurrence of trivalent Ti and divalent Cr in the lunar pyroxene and of vacancies in the plagioclase.

Accurate Analysis of Major Elements in Opaque Minerals. In the past petrologists made extensive use of optical properties in transmitted light to study the silicate minerals, but the opaque minerals were studied mostly by a relatively few specialists using polished sections and special microscopes. Accurate analyses of opaque minerals were rare and mostly incomplete. By contrast electronprobe analysis was not only accurate, but a "complete" analysis could be readily assured by scanning of the entire spectrum. Even the initial results from the Apollo 11 samples reported the finding of rare and new opaque minerals. Since probe analyses of rocks are best done on polished thin sections, the petrologist turned to combined transmitted-reflecting light microscopes and began to study the silicate minerals and the opaque minerals on an equal basis. It became clear that the opaque minerals presented their own complexities and answers and that the crystallization history of both silicate and opaque minerals was intimately comingled.

Analysis of 1 μ m Spots in a Polished Thin Section. The capability to analyze a particular very small volume, one that can be selected by microscopic examination, is the primary attribute of microbeam analysis. It makes possible precise determination of the homogeneity of individual grains, the grain-to-grain differences in composition, systematic zoning of composition, and of the composition of inclusions. Since each analysis of a mineral has stoichiometric constraints, detailed comparison of the composition of adjacent spots can provide tests of the accuracy and precision of the analyses, including freedom from inclusions of other material.

The pyroxenes in many of the lunar basalts are spectacularly zoned. Some display a sector zoning related to different growth rates on different faces. The pyroxenes in most samples display radial zoning and the pattern differs in different samples depending on the cooling rate. Many samples contain augite, orthopyroxene, and pigeonite; each of these pyroxene phases display systematic zoning. Complex exsolution textures are displayed in the pyroxenes of the highlands rocks and electron microprobe analyses have been used to gain an understanding of the subsolidus cooling history.

Minor Elements in Major Minerals. During the earlier part of the lunar studies the petrologists tended to be somewhat skeptical of their own analyses of minor elements in the major phases. However, several studies have demonstrated the capability to analyze minor elements with considerable precision in the major rock-forming minerals. Fe and Mg in plagioclase and Ca, Mn, Cr, Ti, and Al in pyroxene occur in abundances of less than 0.5% by weight. Nevertheless, microprobe analyses have been shown to be precise enough so that variation in the abundance of these elements has been used to understand differences in oxidation state and in cooling rates during crystallization of the melt. The partitioning of Zr between spinel and ilmenite has been calibrated as a function of temperature and measurements at levels lower than 0.5% have been used to determine the subsolidus cooling rates of lunar rocks.

Analysis of Major Amounts of Rare Elements in Minor Minerals. Many rare elements are "incompatible" with the major rock-forming minerals because they have abnormal ionic radii or charge relative to their radius. Such elements are concentrated within a rock in very minor amounts of certain minerals, many of them quite rare. More than 99% of an element may be concentrated as a major element in tiny grains of a phase that makes up less than 1% of the rock. P in the lunar rocks is concentrated in two calcium phosphates, apatite and whitlockite. The rare earth element content of each of these phases is typically high enough to measure with the electron microprobe, but Y and REE are much more highly concentrated in whitlockite than in apatite. Zr, Nb, U, Th, and Hf, along with Y and REE, are

typically concentrated in tiny grains of quite unusual minerals. In several samples it has been possible to calculate a "microprobe age" by analyzing the U, Th, and Pb and assuming that the Pb in the mineral is totally derived by radioactive decay of U and Th.

Crystallization of Basaltic Melts. Use of these important capabilities of the electron probe has revealed the complexities of the crystallization of the lunar mare basalts. The major silicate minerals that crystallize early--pyroxene, olivine, and plagioclase--are complex solid solutions and their compositions vary continuously with the temperature of equilibrium. However, crystallization with falling temperature proceeds rapidly enough so that the earlier crystallized material has no time to re-equilibrate with the surrounding melt. Instead the mineral becomes zoned, with each successive new layer representing equilibrium crystallization at successively lower temperatures. The partition of minor elements between crystal and melt is also related to temperature. Detailed study of the zoning reveals details of the crystallization history including cooling rate, interruptions in cooling rate, differing degrees of equilibration with the melt by the various minerals, changes in pressure, indication of the oxidation state, variation in the fugacity of volatiles, etc. The major rock-forming minerals have sites in their crystal structures that accommodate most of the major elements, but other elements remain in the melt until their concentration is high enough to stabilize a phase of their own or until a phase crystallizes that can accommodate them. The residual melt concentrates in the interstices between the crystals of the major minerals and results in small pockets high in unusual minerals and rarer elements. Even after the close of melt crystallization solid-state equilibration between certain phases, such as sulfides, may occur at the elevated subsolidus temperatures as the rock continues to cool. The microprobe makes it possible to understand these processes and to understand how each element is accommodated during the crystallization process. One does not really understand a rock until one understands the distribution of each element in each phase of the rock. The capabilities of the electron probe make it possible to determine the concentration of the elements in the various phases and the abundance and average composition of the mineral phases can be determined by point counting with the electron probe.

Improvements in Electronprobe Microanalysis

The intense competition to obtain significant new results, the financial support provided by NASA, and the very nature of the problems faced by the lunar sample scientists helped to accelerate improvements in electronprobe analysis. Developments in the following areas can be traced through papers in the proceedings of the annual Lunar Science Conferences:

- (1) development of well-characterized and shared standards;
- (2) development of analytical correction techniques for all elements and all types of minerals, replacing the use of working curves;
- (3) development of the use of the automated electron probe in an interactive manner with on-line data reduction;
- (4) use of energy-dispersive analysis and development of quantitative correction procedures for the method;
- (5) procedures for the analysis of very small particles;
- (6) procedures of defocused-beam analysis for the analysis of particulate material;
- (7) procedures for point-count techniques using the automated probe to identify the phases, their abundance, and their average composition in thin sections of particulate material;
- (8) techniques for using the microprobe to analyze diffusion profiles.

Conclusions

The interaction between electron probe microanalysis and the lunar sample studies was mutually beneficial. The lunar samples could not have been characterized so completely without the electron probe and the results of the analyses of the lunar samples proved that the electron probe was a necessary and reliable instrument for petrologic and geochemical studies.

References

1. J. W. Frondel, *Lunar Mineralogy*, New York: Wiley-Interscience, 1975.
2. J. J. Papike, F. N. Hodges, A. E. Bence, Maryellen Cameron, and J. M. Rhodes. "Mare basalts: Crystal chemistry, mineralogy, and petrology," *Rev. Geophysics Space Physics* 14: 475-540, 1976.
3. J. V. Smith, "Lunar mineralogy: A heavenly detective story (Presidential address): Part I," *Am. Mineral.* 59: 231-243, 1974.
4. J. V. Smith and I. M. Steele, "Lunar mineralogy: A heavenly detective story: Part II," *Am. Mineral.* 61: 1059-1116, 1976.

ANALYTICAL ELECTRON MICROSCOPY AND MICROBEAM ANALYSIS OF METALLIC PHASES IN EXTRATERRESTRIAL MATERIALS

J. I. Goldstein, D. B. Williams, and K. B. Reuter

Metallic phases are present in most meteoritic and lunar samples. An understanding of the structure and composition of the metallic phases can lead to determination of the thermal history of the extraterrestrial material. This paper discusses the use of various electron-optical techniques, namely electron probe microanalysis (EPMA), transmission electron microscopy (TEM), and analytical electron microscopy (AEM), to determine the structure and composition of these metallic phases. The discussion will consist of two parts: high-temperature and low-temperature phase transformations. The high-temperature transformations occur above ~ 500 C and the resultant structures can be observed optically and the phase compositions measured with EPMA. The low-temperature transformations occur below ~ 500 C. The resultant structures can be observed and the phase compositions measured with AEM. We emphasize low-temperature transformations because of current interest and the number of unexplained transformations that remain under study.

High-temperature Phase Transformations

The metallic phases of meteorites and lunar samples are mainly iron and nickel (5 to 60 wt%) with small amounts of cobalt, phosphorus, sulfur, and carbon. The iron meteorites developed a characteristic Widmannstätten microstructure during slow cooling, over tens of thousands of years, in their parent bodies. Figure 1 shows Widmannstätten plates of low Ni ferrite, α (bcc), which precipitated in the high Ni austenite matrix, γ (fcc), during cooling of the meteorite. Almost all iron meteorite samples were single-crystal γ before the Widmannstätten pattern formed (< 800 C). The α phase is often termed 'kamacite' and the γ phase is termed 'taenite' in the meteorite literature. In the retained taenite (γ) regions in between the kamacite (α) plates, further transformations occur (the darker regions in Fig. 1). The term 'plessite' is often used to describe these transformed regions and usually refers to a fine scale mixture of α and γ of varying compositions. This meteoritic terminology will be used interchangeably with the metallurgical terms α and γ .

An EPMA trace for Ni taken at right angles to the α growth front is illustrated in Fig. 2 for the Grant meteorite. Such a Ni profile with major Ni gradients in the γ is characteristic of all iron meteorites and shows that the meteorite is not in total equilibrium at its final growth temperature. The observed diffusion profiles may be explained by the nucleation and diffusion-controlled growth of ferrite, α , when homogeneous parent γ is slowly cooled into the two-phase $\alpha + \gamma$ region of the Fe-Ni equilibrium diagram¹ (Fig. 3). As the meteorite cools to about 500 C, the Ni content of the α and γ phases increases and the amount of α increases as the amount of γ decreases. Since the rate of diffusion of Ni at any temperature is about $100\times$ faster in bcc α than in fcc γ , Ni gradients in α are much flatter than the gradients in γ , as was shown in Fig. 2. Assuming that at any stage of growth, local equilibrium is maintained at the α/γ interface, one can understand how these Ni gradients developed. From the phase diagram of Fig. 3 and considering a typical bulk composition of $\sim 10\%$ Ni, it is clear that Ni will be rejected by the growing α and pass into the residual γ . Because of the slow rates of diffusion, the Ni gradient builds up in the γ near the α/γ interface as the temperature decreases. Although iron meteorites cooled over a period of tens of thousands of years, total equilibrium was not achieved.

Figure 4 shows an optical micrograph of the γ phase near an α/γ boundary in the Edmon-ton meteorite. The γ varies from 15 to 50 wt% Ni along the M-shaped composition profile (Fig. 2). Region K is the α (kamacite) phase adjacent to the α/γ interface. By using a combination of optical microscopy and the EPMA, one can show that region CTI (clear taenite I) is single phase γ , > 40 wt% Ni; region CZ is a dark etching region termed the 'cloudy

The authors are at Lehigh University (Department of Metallurgy and Materials Engineering), Bethlehem, PA 18015. The support of NASA Grant NAG 9-45 is gratefully acknowledged.

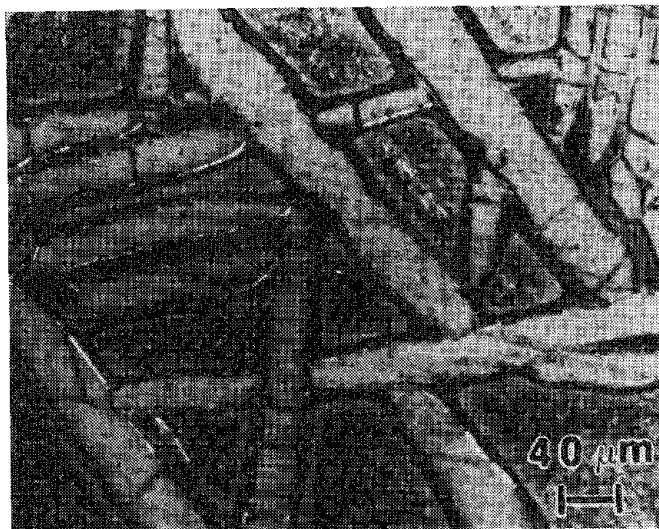


FIG. 1.--Optical micrograph of Widmannstätten pattern in Dayton meteorite. Light regions are kamacite (α). Dark regions are retained taenite (γ), also known as plessite.

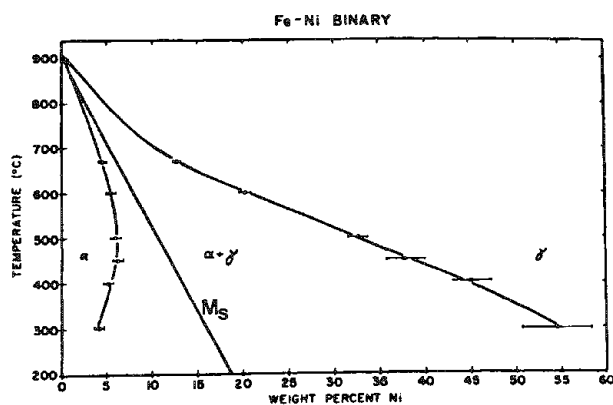


FIG. 3.--Fe-Ni equilibrium phase diagram experimentally determined down to 300 C. M_S refers to martensite start temperature.¹

zone' with submicroscopic structure and a bulk composition range of 30 to 40 wt% Ni, region CT2 (clear taenite II) is 25-30 wt% Ni, and region M has a martensitic structure and a composition range of 15-25 wt% Ni. In the latter region, the γ has cooled below the M_S curve (Fig. 3) and transformed to martensite (α_2). In some meteorites where Ni contents < 15 wt% Ni have formed in the central region of the M-shaped profile, a micro-Widmannstätten structure is also observed. Massalski² has discussed the mechanisms for the formation of these various plessite structures. Since these structures are generally formed below 500 C, we shall discuss the origin of these regions in the second part of the paper.

Assuming that equilibrium at the α/γ interface is maintained during cooling, one can

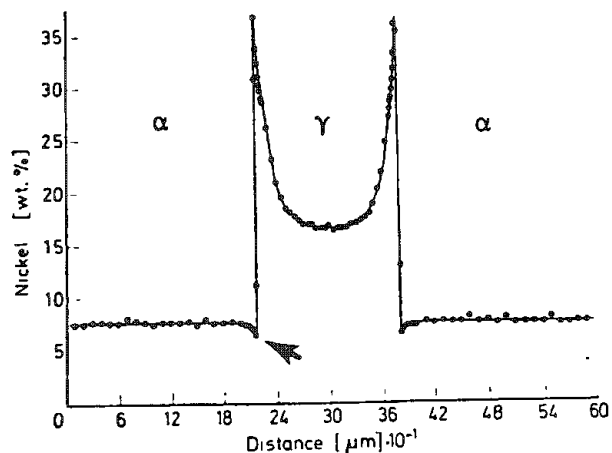


FIG. 2.--Ni concentration gradient across kamacite (α)-taenite (γ)-kamacite (α) area in Grant meteorite taken with EPMA. Arrow shows Ni depletion in α at α/γ interface known as Agrell effect.

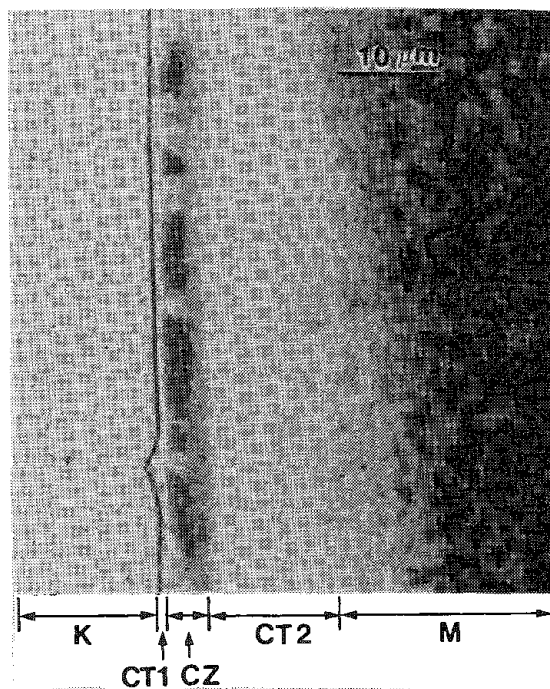


FIG. 4.--Optical micrograph of retained taenite (γ) near α/γ boundary in Edmonton meteorite. Region K is kamacite (α), region CT1 is clear taenite I, region CZ is cloudy zone, region CT2 is clear taenite II and region M is martensite.

use the measured Ni content of γ at the interface to determine the lowest temperature of cooling. For example in Grant, Fig. 2, the maximum Ni content in γ at the α/γ interface is ~ 38 wt% Ni and according to the phase diagram, Fig. 3, the lowest cooling temperature is approximately 450 C. As discussed in the next section the EPMA has limited resolution for measuring boundary compositions where a chemical gradient is present within $1\text{ }\mu\text{m}$ of the boundary interface. In the case of Grant, the boundary Ni content is much higher and the lowest cooling temperature is actually below 300 C.

In reheated metallic phases of meteorites and lunar samples, however, measurements of the composition of α and γ have led to the determination of final equilibration temperatures. Metallic $\alpha + \gamma$ specimens have been studied in Apollo 14 and 16 soils.^{3,4} Equilibration temperatures of ~ 550 -700 C were deduced from the α and γ interface compositions and the appropriate phase diagrams. Figure 5 shows a Ni concentration gradient measured across a γ (taenite) phase in Apollo 16 particle F5-16.⁴ In addition to obtaining a final cooling temperature from α/γ equilibrium, researchers have also used the presence of phosphide $(\text{FeNi})_3\text{P}$ in the metal to determine phosphide, α and γ equilibration temperatures using the Fe-Ni-P phase diagram.^{5,6}

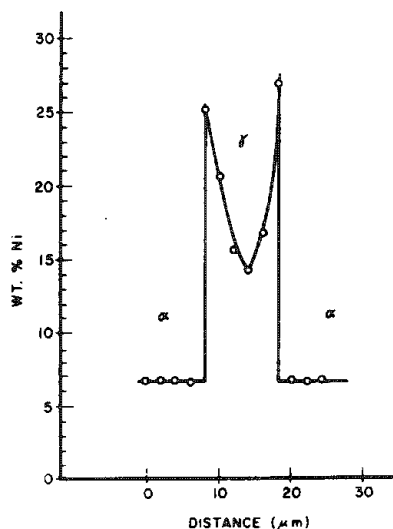


FIG. 5.--Ni concentration gradient across taenite (γ) phase in lunar particle F5-16 by EPMA.⁴

Romig and Goldstein¹ using x-ray microanalysis in thin foil samples in the AEM. The samples were quenched into the martensite region, then reheated at 300-500 C, which caused the transformation to $\alpha + \gamma$. Therefore the resultant diagram down to 300 C is not pertinent to all transformations in slow-cooled meteorites except to indicate that the equilibrium phases from martensite decomposition are a mixture of $\alpha + \gamma$.

A comparison of the resolution improvement in using AEM is shown in Fig. 6, which shows details of the composition profile across the α/γ interface in the Carlton meteorite by (a) AEM and (b) EPMA.¹⁴ With AEM the apparent interface concentration is higher, the change in concentration is more discrete, and there is evidence for compositional variations in region 2 (the cloudy zone). We shall now discuss the submicron structure and chemistry of each of the regions in Fig. 4 using the detailed information available from the TEM and AEM.

It has been demonstrated in the past few years that clear taenite I, the first zone observed next to the α -kamacite phase (Fig. 4), is ordered FeNi (γ').¹⁵ Scott and Clarke¹⁶ observed optical anisotropy in over 40 meteorites in all meteorite groups, and

Computer simulation models⁷⁻⁹ of the growth of α during cooling have been developed. The major unknown in such models is the cooling rate of the parent body. Calculations of cooling rates have yielded values of 1 - $100\text{ C}/10^6$ years.^{10,11} Recent experimental work by Narayan and Goldstein¹² has shown that α can be grown in slow-cooled FeNi alloys only if P is present, and the rate of growth is faster than that predicted by previous computer simulation models. A re-examination of the Fe-Ni-P diffusivities yielded much larger values than previously used. Calculations for various iron meteorites using the newly measured diffusivities yield cooling rates of 1 - $100\text{ C}/10^4$ years, two orders of magnitude faster than rates from previous models.

The Low-temperature Phase Transformations

Below ~ 500 C the transformations in Fe-Ni meteorites occur on a scale of $< \sim 1\text{ }\mu\text{m}$ and so are beneath the resolution limit of a typical optical microscope and the EPMA. Therefore, both microstructure and microchemistry are only accessible through higher resolution TEM and AEM techniques.

The conventional Fe-Ni or Fe-Ni-P phase diagram below 500 C shows the same regions as the higher temperature diagram (Fig. 3); namely, α , $\alpha + \gamma$ regions, and γ regions, and the M_s line. The prediction of Agrell¹³ that the $\alpha/(\alpha + \gamma)$ solvus line was retrograde was demonstrated experimentally by

concluded that the entire clear taenite I zone was ordered FeNi. However, optical microscopy cannot spatially resolve the exact extent of the ordered domains or observe details of the interface between domains. With the increased resolution and structural information available in the TEM, Mehta et al.¹⁷ observed individual domains and antiphase boundaries in the Estherville meteorite.

Ordered FeNi, also known as tetrataenite, has the LI_0 superstructure with the ordered planes in one of three $\langle 002 \rangle$ orthogonal directions (i.e., three variants of γ' exist). When clear taenite I is tilted close to a $\langle 111 \rangle_\gamma$ orientation the three variants diffract simultaneously. Each superlattice reflection can be imaged by centered dark-field (CDF) techniques. By overlaying the images of each variant, the ordered domains can be seen to fill the clear taenite I zone (Fig. 7). Microanalysis across this same zone shows a decrease in Ni content from 52 wt% Ni at the α/γ interface to 45 wt% Ni at the cloudy zone interface.¹⁸

Also observed throughout the clear taenite I zone are antiphase boundaries (APBs). APBs are planar defects which correspond to regions of local disorder. They appear as dark, wavy lines (Fig. 7). As the Ni content decreases away from the stoichiometric 50/50 composition one should observe more APBs and/or some disordered regions. Under equilibrium conditions one also expects the largest domains to be in the highest Ni region next to the kamacite (since this region will start to order first during cooling), decreasing in size as the cloudy zone is approached. From Fig. 7 it is clear that there is indeed a domain size trend through the clear taenite I; the largest domains are near the α/γ interface and the smallest near the cloudy zone. Thus, the decrease in the degree of order across clear taenite I, as dictated by the Ni content decrease, is manifest in the microstructure through an increase in the number of APBs. The ordered domain size has been reported to range from 15 to 650 nm.^{18,20}

The zone adjacent to clear taenite I is the cloudy zone, so named because of its appearance in the optical microscope after etching (CZ in Fig. 4). Its bulk composition is ~ 30 -40 wt% Ni. TEM imaging first performed by Scott²¹ revealed that the cloudy zone consisted of two phases forming a honeycomb structure (Fig. 8). The identity of these two phases, however, is still not clear. Scott²¹ first proposed single crystals of α interpenetrating single crystals of γ . Lin et al.²² supported this proposal with convergent-beam electron diffraction (CBED) patterns from ~ 20 individual cells in the Carlton meteorite. Albertsen and coworkers,^{20,23} on the other hand, reported γ -taenite and γ' -ordered FeNi as the two constituents of the cloudy zone in a number of IIIA, IIIC, IIID, and IA meteorites. Recently, the cloudy zone of Estherville has been examined by microanalysis and microdiffraction from the same area.^{19,24} The globular phase (bright in Fig. 8) was identified as ordered FeNi containing ~ 50 wt% Ni. The honeycomb (dark phase) contained ~ 16 wt% Ni. According to the phase diagram in Fig. 3, 16 wt% Ni at an equilibrating temperature of ~ 200 C is martensite, α_2 . Therefore, the cloudy zone in Estherville was concluded to be γ' -FeNi and α_2 -martensite. This discrepancy in the nature of the cloudy zone remains to be resolved. What is also obvious in Fig. 8 is the decrease in the dimensions of both the phases in the honeycomb structure as the Ni composition decreases towards the clear taenite II region. This result is consistent with the AEM and EPMA data (Fig. 6) but not consistent with proposals that the cloudy zone arises through spinodal decomposition.²⁰ If spinodal decomposition occurred the spinodal wavelength would be a minimum in the middle of the required miscibility gap, and a maximum at either extreme.²⁵ This effect is not observed in any microstructure of the cloudy zone.

Clear taenite II, the zone next to the cloudy zone (Figs. 4 and 8) is generally thought to be fcc γ containing ~ 25 to 30 wt% Ni.¹³ No detailed structural or chemical investigations have been performed. It remains a mystery how γ of this composition can remain untransformed when Ni-rich and Ni-poorer regions on either side have transformed to two-phase mixtures, unless an eutectoid reaction is postulated.²⁶

Martensite is the next zone (M in Fig. 4) and it contains ~ 15 to 25 wt% Ni. TEM imaging has revealed the presence of both lath and lenticular martensite in the same meteorite.²² Lenticular martensite forms at higher Ni contents consistent with its presence near the clear taenite II interface. The decomposition of martensite occurs by the transformation $\alpha_2 \rightarrow \alpha + \gamma$ (termed Type III plessite by Massalski²). Fine γ rods ~ 20 -30 nm wide are found in an α matrix with either a Kurdjumov-Sachs or Nishiyama-Wasserman orientation relationship (Fig. 9). The identification of α and γ was confirmed by AEM microanalysis.¹⁴ The highest Ni content of γ rods was 42 wt% and the lowest Ni

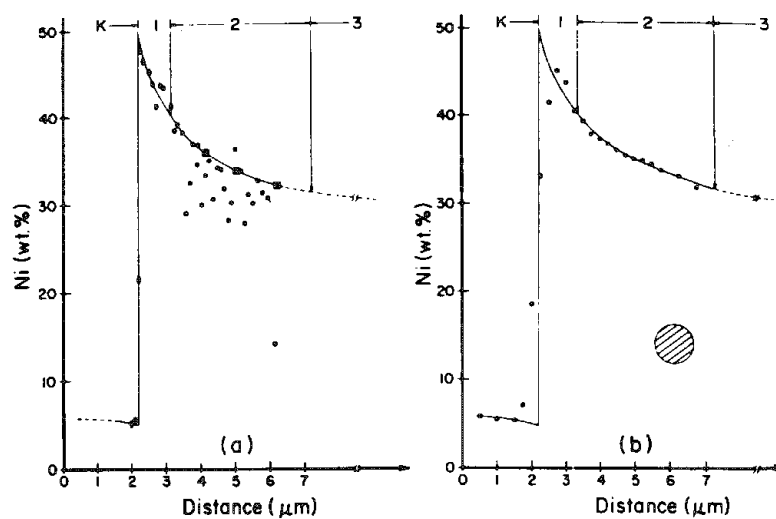


FIG. 6.--Ni concentration gradient across kamacite (α)/taenite (γ) interface in Carlton meteorite by (a) AEM and (b) EPMA. Circles below plotted data indicate x-ray spatial resolution of each technique. K refers to kamacite (α), 1 to clear taenite I, 2 to cloudy zone, 3 to clear taenite II.

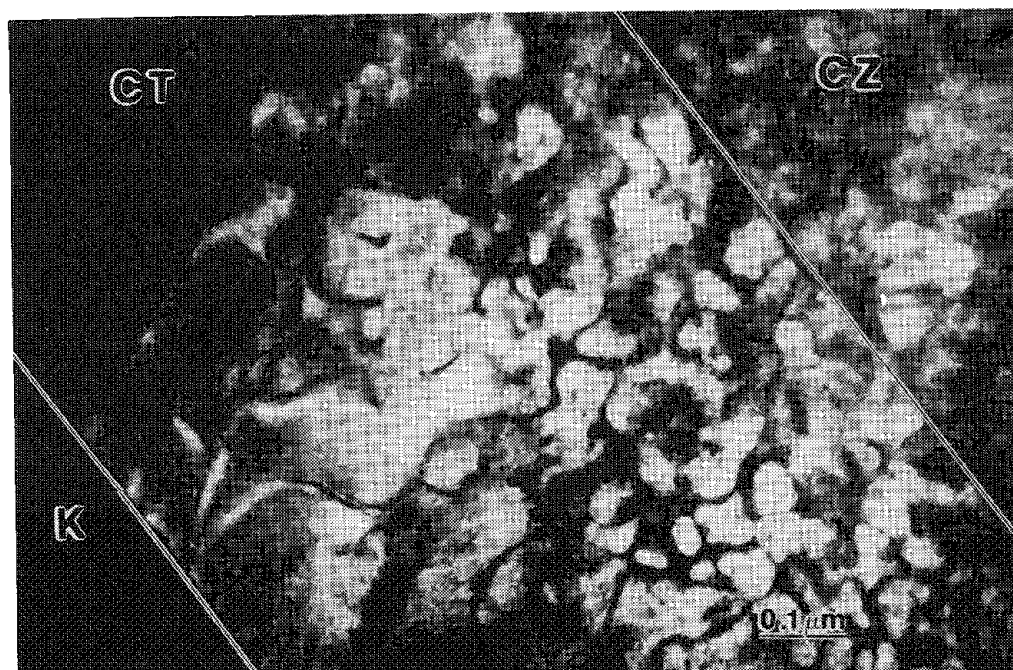


FIG. 7.--TEM micrograph of clear taenite I showing 3 variants of ordered phase in Dayton meteorite.

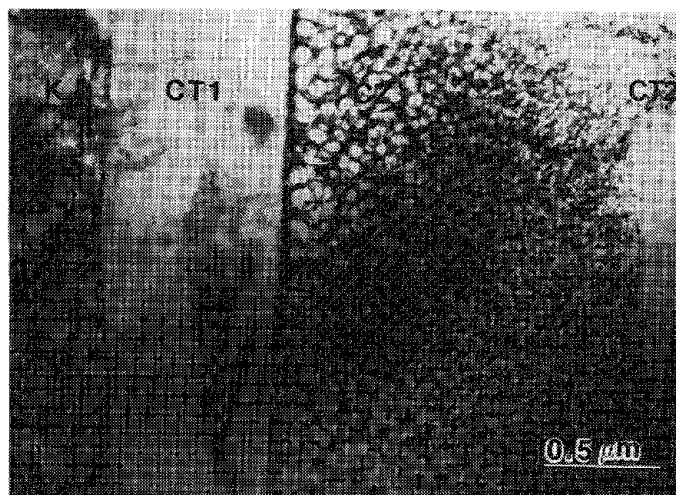


FIG. 8.--TEM micrograph showing structure across α/γ interface in Tazewell meteorite. Cloudy zone (CZ) is 2-phase honeycomb structure bordered by clear taenite I (CT1) on one side and clear taenite II (CT2) on the other.

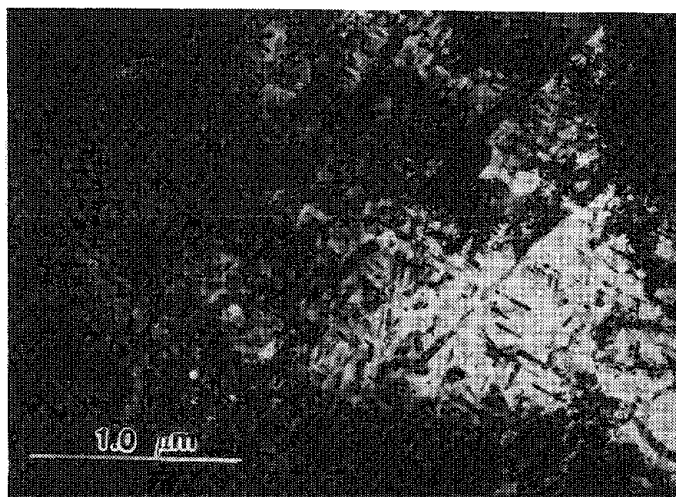


FIG. 9.--TEM micrograph of decomposed martensite in Carlton meteorite. Small, dark rods are γ ; lighter colored matrix is α .

content in α 9.8 wt%. (This is higher than typical α concentrations because of a strong Ni x-ray signal from the surrounding Ni-rich γ .) As shown in Fig. 3, α_2 forms between 350 and 100 C for Ni contents between 15 and 25 wt% Ni. The subsequent decomposition of high Ni martensite (25 wt% Ni) occurs below ~ 100 C. The small γ size is consistent with exsolution at low temperatures and slow cooling rates.¹²

Finally, in the interior region of plessite in the < 15 wt% Ni region, a coarse duplex $\alpha + \gamma$ mixture is observed. Rods of γ , 30-200 nm in width, are found in an α matrix with a Kurdjumov-Sachs orientation relationship. This duplex structure is nothing more than a coarser version of the fine scale decomposition discussed above (Fig. 9).¹⁴ The γ rods are larger than those observed in the decomposed martensite, consistent with a higher M_s (350 C) giving increased diffusion of Ni in the martensite after it forms. AEM microanalysis was also carried out on the coarse α and γ phases.¹⁴ The Ni concentration of the γ was always above 20 wt% Ni; the highest was ~ 43 wt% Ni.¹³ The Ni content in the α was measured more accurately at 3 wt% Ni because the coarse nature of the duplex $\alpha + \gamma$ permits microanalysis without interference from the surrounding matrix. The low Ni concentration indicates that the α/γ equilibrium was maintained to temperatures of ≤ 200 C. Because the γ rods in the duplex region have different crystal orientations from

the parent γ , it can be deduced that this duplex $\alpha + \gamma$ must also have arisen from Type III plessite. According to the behavior of the higher Ni plessite regions, it would be expected that those γ rods might also be ordered (i.e., γ'). No evidence for this has been found, although no one has looked for the evidence since Lin et al.'s original studies.¹⁴

In addition to the detailed work on iron meteorites similar studies of submicron metal particles in lunar materials have also been carried out.²⁷ The metal particles were α -Fe and Fe-Ni, of meteoritic origin containing 17 to 57 wt% Ni.

Problems to Be Solved

The high-temperature phase transformations are well understood. Major problems remain with the low-temperature transformations. In particular, (a) determination of the constituents of the cloudy zone, (b) understanding the role of clear taenite II, and (c) the development of a phase diagram that successfully describes the observed phases and their composition have yet to be achieved.

References

1. A. D. Romig Jr. and J. I. Goldstein, *Met. Trans.* 11A: 1151, 1980.
2. T. B. Massalski et al., *Geochim. Cosmochim. Acta* 30: 649, 1966.
3. H. J. Axon and J. I. Goldstein, *Earth Plan. Sci. Lett.* 16: 439, 1972.
4. J. I. Goldstein and H. J. Axon, *Proc. 4th Lunar Sci. Conf.* (suppl. 4 *Geochim. Cosmochim. Acta*) 1: 751, 1973.
5. J. I. Goldstein et al., *Earth Plan. Sci. Lett.* 28: 217, 1975.
6. R. H. Hewins and J. I. Goldstein, *Proc. 8th Lunar Sci. Conf.*, 1977, 1625.
7. J. A. Wood, *Icarus* 3: 429, 1964.
8. J. I. Goldstein and R. E. Ogilvie, *Geochim. Cosmochim. Acta* 29: 893, 1965.
9. A. E. Moren and J. I. Goldstein, *Earth Plan. Sci. Lett.* 43: 182, 1979.
10. J. I. Goldstein and J. M. Short, *Geochim. Cosmochim. Acta* 31: 1733, 1967.
11. J. Willis and J. T. Wasson, *Earth Planet. Sci. Lett.* 40: 141, 1978.
12. C. Narayan and J. I. Goldstein, *Geochim. Cosmochim. Acta* 49: 397, 1985.
13. S. O. Agrell et al., *Nature* 198: 349, 1963.
14. L. S. Lin et al., *Geochim. Cosmochim. Acta* 41: 1861, 1977.
15. J. R. Petersen et al., *Phys. Letters* 62A: 192, 1977.
16. E. R. D. Scott and R. S. Clarke Jr., *Nature* 281: 360, 1979.
17. S. Mehta et al., *Nature* 284: 151, 1980.
18. K. B. Reuter, M. S. Thesis, Lehigh University, 1984.
19. K. B. Reuter et al., *Analytical Electron Microscopy--1984*, 177.
20. J. F. Albertsen et al., *Phys. Scripta* 27: 314, 1983.
21. E. R. D. Scott, *Geochim. Cosmochim. Acta* 37: 2283, 1973.
22. L. S. Lin et al., *Geochim. Cosmochim. Acta* 43: 725, 1979.
23. J. F. Albertsen et al., *Phys. Scripta* 22: 171, 1983.
24. P. M. Novotny, M. S. Thesis, Lehigh University, 1981.
25. J. W. Cahn, *Trans. Met. Soc. AIME* 242: 166, 1968.
26. P. L. Rossiter and R. A. Jago, *Proc. Mat. Res. Soc. Symp.*, Elsevier, 21: 407, 1984.
27. S. Mehta and J. I. Goldstein, *Proc. 10th Lunar Plant. Sci. Conf.*, 1979, 1507.

ORIGINS OF Ca-, Al-RICH INCLUSIONS IN THE ALLENDE METEORITE

Lawrence Grossman

The Allende meteorite and other Type 3 carbonaceous chondrites contain abundant, large inclusions that contain such Ca-, Al-, Ti-rich minerals as melilite [$\text{Ca}_2(\text{Al,Mg})(\text{Si,Al})_2\text{O}_7$], spinel (MgAl_2O_4), perovskite (CaTiO_3), and hibonite ($\text{CaAl}_{12}\text{O}_{19}$). Because these phases are predicted by equilibrium thermodynamic calculations to be among the first to condense from a cooling gas of solar composition, these inclusions are thought by many workers to have formed in the solar nebula by very high temperature vapor-condensed phase reactions prior to planet formation.¹ The electron microprobe and scanning electron microscope have played a prominent role in the elucidation of the origin of these objects. Some examples are the subject of this brief report.

One group of these inclusions, the Type B's, are centimeter-sized, near-spherical, compact objects whose primary phase assemblages are rich in spinel, melilite, anorthite ($\text{CaAl}_2\text{Si}_2\text{O}_8$), and fassaite, a Ca-, Mg-clinopyroxene rich in Ti and Al. In some of these inclusions, elongated crystals of melilite terminate at and project inward from the inclusion rim, which suggests that they nucleated on the rim and grew inward. The fact that the other ends of the shortest melilite crystals abut against and terminate at the sides of neighboring longer crystals implies that they interfered with one another during growth. From these observations, MacPherson and Grossman² argued that these inclusions did not form by aggregation of separate grains that condensed independently in space. Melilite is a solid solution between gehlenite, Ge ($\text{Ca}_2\text{Al}_2\text{SiO}_7$), and åkermanite, Åk ($\text{Ca}_2\text{MgSi}_2\text{O}_7$). When all but the most magnesian melilite crystallizes from silicate melts at high temperature, it is relatively Ge-rich. With falling temperature, it exchanges with the liquid and becomes progressively more Åk-rich. In support of their interpretation, MacPherson and Grossman² used the electron microprobe to show that the elongated melilite crystals become progressively enriched in Åk along their lengths away from the inclusion margin, which implies that they nucleated there and grew inward with falling temperature. This observation, together with the compact texture and spherical shapes of these inclusions, is entirely consistent with crystallization of free-floating liquid droplets in response to radiative cooling from their outer surfaces.

That Type B inclusions were once molten was further indicated by the work of Stolper et al.³ who used thermodynamic data to compute the temperature dependence of the equilibrium constant for the reaction of diopside ($\text{CaMgSi}_2\text{O}_6$) with Ge to form Åk and $\text{CaAl}_2\text{SiO}_6$, where diopside and $\text{CaAl}_2\text{SiO}_6$ are known components in the fassaitic pyroxene of Type B inclusions. They also analyzed adjacent melilite and fassaite crystals, melilite crystals enclosed by fassaite, and fassaite enclosed by melilite. When the compositions of adjacent spots in these coexisting phases in all three textural settings were compared with the above calculations, equilibration temperatures of 1100-1400 C were indicated for four Type B inclusions. These temperatures are above the solidus temperatures, 1100-1200 C, for these compositions, which implies that pyroxene and melilite last equilibrated their compositions with one another when the inclusions were in a partially molten state. Most of these temperatures are also in excess of 1175 C, the temperature at which solid assemblages of these compositions are predicted to condense from the solar nebula at 10^{-3} atm total pressure. Because this is generally regarded as an upper limit to the pressure in those parts of the cloud that gave rise to meteoritic material, 1175 C would be the upper limit to the condensation temperature

Lawrence Grossman is at the Department of the Geophysical Sciences and Enrico Fermi Institute, The University of Chicago, 5734 South Ellis Avenue, Chicago, IL 60637. Support from the National Aeronautics and Space Administration through grant NAG 9-54 and from the National Science Foundation through grant EAR-8218154 is acknowledged.

of pyroxene-bearing, solid assemblages. This is further evidence that these inclusions did not form by direct condensation of solids from the nebular gas. Nor could they have formed by solidification of liquid droplets that condensed metastably instead of solids, as advocated by Blander and Fuchs.⁴ Rather, the inclusions must be solidification products of melts formed by re-heating of condensed material.

When a liquid of Type B composition is cooled, the crystallization sequence is spinel, melilite, anorthite, and fassaite at equilibrium and the melilite becomes progressively more $\text{\AA}k$ -rich. MacPherson et al.⁵ showed experimentally that cooling rates of 0.5-20 C/h cause suppression of anorthite precipitation, leading to crystallization of fassaite before anorthite. The onset of fassaite solidification without simultaneous anorthite precipitation causes the Al/Mg ratio of the melt to rise sharply and, with continued cooling, the crystallizing melilite grows richer in Ge, the opposite of the equilibrium situation. When anorthite finally does appear, the Al/Mg ratio of the liquid falls and the co-crystallizing melilite becomes more $\text{\AA}k$ -rich with falling temperature again. MacPherson et al.⁵ showed that restricted portions of many melilite crystals in Type B inclusions are reversely zoned; i.e., they become more Ge-rich with increasing distance from the centers of the crystals before returning to the normal situation, increasing $\text{\AA}k$ with distance, in the outermost reaches of the same crystals. The innermost edges of the reversely zoned portions usually coincide with the innermost edges of zones of the melilite crystals that contain many tiny fassaite inclusions. The reverse zoning of melilite thus seems to begin with the onset of fassaite crystallization, just as would be expected at cooling rates between 0.5 and 20 C/h. Such cooling rates are orders of magnitude slower than expected from radiative cooling of droplets of this size and composition in the nebular gas. Instead, it is likely that the droplets had the same temperature and cooled at the same rate as their surrounding gas. Since the cooling time of the solar nebula is thought to be of the order of 10^4 years, however, these inclusions were probably inside small hot regions that may have existed within the larger and cooler nebular cloud and that cooled more rapidly than the nebula as a whole.

Another group of Ca-, Al-rich inclusions in Allende have a primary phase assemblage consisting only of melilite, spinel, perovskite, and hibonite. They are up to 2-3 cm in size and have highly irregular shapes and nodular structures. Because these so-called "fluffy" Type A inclusions are so porous, fine-grained secondary alteration products, formed by relatively low-temperature reactions between the primary phase assemblages of the inclusions and the nebular gas, are far more abundant than in the much more compact Type B's. Their highly irregular, nonspherical shapes argue against their having been totally molten. Furthermore, Beckett and Grossman⁶ showed that when melts having the compositions of fluffy Type A inclusions are cooled at equilibrium, anorthite, a phase not found in these inclusions, crystallizes; but hibonite, which is found, does not. An important clue to the origin of these objects is the presence of reversely zoned melilite. Recall that co-crystallization of a phase with a high Mg/Al ratio like fassaite is responsible for this effect in Type B inclusions, but neither fassaite nor any other such phase is present in fluffy Type A inclusions. Condensation calculations shown by MacPherson and Grossman⁷ predict that when solid melilite condenses from a gas of solar composition, it is pure Ge at high temperature and becomes more $\text{\AA}k$ -rich as the temperature falls at all total pressures considered. With decreasing total pressure, however, the temperature of appearance of melilite decreases as does the temperature at which any particular $\text{\AA}k$ content becomes stable. Thus, melilite crystals whose rims are more Ge-rich than their cores would be expected during condensation from the solar nebular gas if the crystals continued to grow during periods of declining pressure, whether or not the temperature was also falling. MacPherson and Grossman⁷ pointed out that a melilite grain observed to be zoned in composition from a core of $\text{\AA}k$ 22 to a rim of $\text{\AA}k$ 8 could have formed by initial condensation at ~ 1458 K and 10^{-3} atm total pressure, followed by continued growth either during a drop in pressure to $\sim 7 \times 10^{-4}$ atm at constant temperature or during a drop in pressure to $\sim 4 \times 10^{-4}$ atm accompanied by a temperature decrease of 20° , for example. If, on the other hand, Mg were preferentially volatilized relative to Al during growth of melilite from liquids of this composition, reverse zoning might have been produced but so also would resorption of spinel, for which there is no petrographic evidence. Thus, fluffy Type A inclusions probably contain grains that condensed as solids directly from the solar nebular gas.

References

1. L. Grossman, "Refractory inclusions in the Allende meteorite," *Ann. Rev. Earth Planet. Sci.* 8: 559-608, 1980.
2. G. J. MacPherson and L. Grossman, "A once-molten, coarse-grained, Ca-rich inclusion in Allende," *Earth Planet. Sci. Lett.* 52: 16-24, 1981.
3. E. Stolper et al., "Thermometry of Ca-Al-rich inclusions," *Lunar Planet. Sci.* 16: 1985, in press.
4. M. Blander and L. H. Fuchs, "Calcium-aluminum-rich inclusions in the Allende meteorite: Evidence for a liquid origin," *Geochim. Cosmochim. Acta* 39: 1605-1619, 1975.
5. G. J. MacPherson et al., "The origin and significance of reverse zoning in melilite from Allende Type B inclusions," *J. Geol.* 92: 289-305, 1984.
6. J. R. Beckett and L. Grossman, "Melting experiments on Allende coarse-grained inclusion compositions," *Lunar Planet. Sci.* 13: 31-32, 1982.
7. G. J. MacPherson and L. Grossman, "'Fluffy' Type A Ca-, Al-rich inclusions in the Allende meteorite," *Geochim. Cosmochim. Acta* 48: 29-46, 1984.

ELECTRON MICROBEAM ANALYSIS OF COSMIC DUST

D. E. Brownlee

Most of the information on meteoritic materials has come from the analysis of conventional meteorites, centimeter and larger bodies that entered the atmosphere and were found on the surface of the Earth. During the past decade valuable and complementary information has also come from the study of the millimeter and smaller particles that are often referred to as cosmic dust. Because the dust particles are small, electron-beam techniques have played a crucial role in their analysis. Most of the particles are too small for detailed study by optical microscopy and even basic classification must be done by EM techniques. The microprobe, SEM, and TEM/STEM techniques are extensively used in the study of these particles.

The small particles are important to extraterrestrial material research because the most friable and perhaps most common materials in space can only survive hypervelocity entry into the Earth's atmosphere in the form of small objects.¹ The peak ram pressure on sub-millimeter meteoroids decelerating in the atmosphere is orders of magnitude smaller than that which must be survived by the larger objects that become conventional meteorites. This strength-selection effect partly explains why conventional meteorites are all rather strong solid rocks, whereas some of the collected dust particles are exceedingly porous and fragile. Fragile materials are of particular interest because debris from comets is known to be weak. Observation of the disintegration of cometary meteoroids at the top of the atmosphere indicates that many cometary particles have strengths of 10^{-5} dyne cm^{-2} or less. Comets are well-preserved relics of the early solar system and laboratory analysis of cometary materials should provide fundamental insights into the processes and environments that existed at the time and location where comets formed.

Extraterrestrial dust of both cometary and asteroidal origin is accreted by the Earth at a rate of 300 gs^{-1} , with the bulk of the mass being in the 0.1-1.0mm size range. Most particles are debris from comets and asteroids and they survive as free particles for only 10 000 years following liberation from their parent bodies. The flux of 10 and 100 μm particles is $1 \text{ m}^{-2}\text{day}^{-1}$ and $1 \text{ m}^{-2}\text{year}^{-1}$, respectively. Most of the particles smaller than 50 μm do not melt during atmospheric entry and are called micrometeorites. Micrometeorites of 10 μm size are found in the stratosphere at a density of 10^{-3} m^{-3} and they are routinely collected with impactors mounted on U-2 aircraft.² Particles larger than 100 μm usually melt during atmospheric entry and are too rare to be collected in the atmosphere. These meteor ablation spheres or "cosmic spheres" are recovered from deep-sea sediments and Greenland ice.

Meteor Ablation Spheres

The recovered meteor ablation spherules range in size up to 2 mm, although the typical samples used for EM studies are only a few hundred microns in size.³ Most of the spheres totally melted in the atmosphere, but a few percent of the particles contain some relic mineral grains that survived atmospheric heating without chemical alteration. The most common relic grains are forsterite and enstatite, and high-sensitivity microprobe analysis has shown that the minor element abundances (Cr, Mn, Al, Ti, and Ni) in the forsterite grains are uniquely different from those in most terrestrial and extraterrestrial olivines, but fairly closely match the composition of a subset of C2 carbonaceous chondrite meteorites.⁴ Many of the relic grains contain micron blobs of FeNi alloy. When relic sulfides are found they generally contain the moderate Ni contents that are typical of sulfides in unequilibrated meteorites.

The totally melted and recrystallized spheres are found as two basic types, stony and "iron." The stony spheres are composed of micron-sized grains of olivine and magnetite embedded in glass. The Fe content of the olivine is close to chondritic and is higher than that in the relic grains. The iron spheres are composed primarily of magnetite and wustite but they often contain a core of FeNi alloy or a single micron-sized nugget of Pt group metals. The Pt nuggets are produced by concentration during oxidation of a molten

The author is at the University of Washington (Astronomy Department), Seattle, WA 98195.

droplet of meteoritic metal.⁵ Many stony spheres have been analyzed by broad-beam microprobe analysis to determine the elemental composition of the original unmelted materials. The analyses were done on polished sections of sphere cores that contained pristine glass, an indicator that shows that the material was not chemically altered by chemical weathering. The abundances of Si, Mg, Al, Ca, Ti, Fe, and Mn in 300 analyzed spheres indicate that at least 85% of the spheres are compositionally related to C1 or C2 meteorites and distinct from other meteorite classes. Their compositions are chondritic and quite distinct from terrestrial materials. The elements Cr, S, Na, and Ni were analyzed but they are generally depleted from chondritic abundances by varying degrees due either to vaporization or loss of a siderophile-rich phase during atmospheric entry. There is strong evidence that the metal that formed the iron spheres separated from the stony spheres during the entry process. At least some of the metal was formed by in situ reduction.

The study of meteor ablation spheres has provided unique information on the nature of the millimeter meteoroids that constitute the bulk of the extraterrestrial material falling to Earth in a typical year. Although the particles are severely altered by atmospheric entry, it is clear that the most common precursor materials are related in elemental composition and forsterite minor element composition to the most carbon and volatile-rich meteorites. It is ironic that this match is made with refractory-element abundances because the volatile elements are lost during atmospheric heating. The best match is with C2 meteorites, although this does not mean that the spheres are actually produced by actual C2 meteorites, but rather, that they are produced by primitive materials with C2 elemental composition.

Stratospheric Micrometeorites

The typical micrometeorite available for study is only 10 μm in size, but these small particles are extremely important because they were not strongly heated during atmospheric entry. Although it has not been proven, it is likely that the micrometeorites are small samples of the larger particles that produce the cosmic spheres. The discovery of cosmic-ray tracks in micrometeorites proves that some particles were not heated to the track annealing temperature of 600 C.⁶ The tracks are randomly oriented linear defects that were originally found in these samples by dark-field TEM imaging. The densities range beyond $5 \times 10^{10} \text{ cm}^{-2}$. Ideally, particles selected for detailed analysis should be restricted to track-rich particles because those without tracks may have been strongly heated. Unfortunately, tracks were only recently found in micrometeorites, and at any rate testing for tracks is fairly involved because it requires mounting at least a small fraction of a particle on a TEM grid.

The collected particles have diverse properties, which implies that they may have come from a significant number of parent bodies. A common property of a majority of the samples is that they have a chondritic elemental composition for the elements abundant enough to be analyzed by EDX. Many particles have been quantitatively analyzed by use of the particle ZAF reduction program of Armstrong and Buseck,⁷ and abundance histograms center on chondritic (solar) compositions with a typical spread of a factor of two. The dispersion in composition is larger than in the cosmic spheres, probably because the spheres are much larger and represent a better sampling of the bulk composition of the parent material. The micrometeorite compositions are actually more chondritic than comparably sized volumes of meteorites. No mineral has chondritic elemental composition and the particles must be very fine-grained to match this composition for a large number of elements. Many of the particles that do not feature chondritic composition are single-mineral grains (usually olivine, pyroxene, or pyrrhite) that have fine-grained chondritic material adhering to their surfaces. These single-mineral grains were originally embedded in chondritic material.

Most of the chondritic particles are aggregates of grains ranging in size from $< 10 \text{ nm}$ to $> 1 \mu\text{m}$, but there is diversity among particles in both the structure and mineralogy of the aggregates. Two distinct types are porous aggregates composed of anhydrous minerals, and relatively nonporous particles containing hydrated silicates. The particles are routinely studied in the SEM, but because they are so fine-grained, in-depth investigation requires TEM/STEM analysis of carefully crushed grains mounted on TEM films. Morphology is obtained by secondary, backscattered, and transmission imaging; and structure is determined by selected area and convergent-beam diffraction, as well as lattice-fringe imaging. Composition is determined by EDX and EELs.

The hydrated micrometeorites are the particles that can be most closely associated with a particular meteorite type. In general, they are similar to C1 and C2 meteorites and in some cases they probably came from the same parent bodies as these meteorites. The C1 and C2 meteorites had a warm, damp period early in their histories that produced significant alteration by aqueous processes and may have produced most of the layer lattice silicates in the samples. The carbonates and distinctive magnetite grains in the dust particles are consistent with such an origin. In detail, however, the layer silicates in some of the hydrated particles that have been studied are uniquely different from those found in C1 and C2 meteorites. These reported differences include smectite and kaolinite.

A totally unique finding in a hydrated particle is the discovery by Tomeoka and Buseck of low-Ni pentlandite (Fe_9S_8).⁸ Pentlandite is fairly common in carbonaceous chondrites but it has never been found in meteorites or natural terrestrial samples in its low-Ni form. Low-Ni pentlandite has been synthesized by vapor deposition at temperatures below 200 C.

The micrometeorites that most closely resemble structural models for weak cometary materials are the chondritic porous aggregates, or CPAs. The CPAs are the most porous and fragile meteoritic materials. They are loose aggregates of rounded submicron grains that are weakly attached to form a porous "cluster-of-grapes" structure that can have a porosity in excess of 50%. The individual submicron grains have widely differing compositions and they obviously did not form in equilibrium with each other. Some of the individual grains are single minerals, usually silicates or sulfides, but many of the "grains" are themselves microaggregates of 10-100nm crystalline grains embedded in a carbonaceous matrix. Analysis of these fine-grained heterogeneous particles is a very challenging problem even in a modern analytical TEM. The CPAs have elemental compositions like carbonaceous chondrites but their anhydrous mineralogy and porous morphology are distinct from all other extraterrestrial materials. There is a strong likelihood that the CPAs are comet dust. It is conceivable that hydrous alteration of CPA material in a warm, damp parent body could produce the hydrous micrometeorites or the C1 and C2 meteorites.⁹

TEM evidence indicates that two minor phases in CPAs are preserved vapor-phase products. One is epsilon FeNi carbide¹⁰⁻¹¹ and the other is enstatite with distinctive whisker morphology.¹¹ The carbide has been produced synthetically by catalytic Fischer-Tropsch reactions of CO on grain surfaces, but it has previously never been seen in natural systems. Fischer-Tropsch reactions have long been proposed by Anders to be an important mode of formation of carbon compounds in meteorites. The enstatite whiskers are found as small rods, plates, and ribbons embedded in the CPAs. Some of the whiskers have axial screw dislocations and are perfect natural analogs to synthetic whiskers formed in the laboratory by direct vapor to solid growth.

Conclusions

Electron-beam techniques have provided a wealth of detailed information about the smallest meteoritic materials. Two decades ago meaningful study of these particles would not have been possible because of the lack of SEM/EDX and analytical and high-resolution EM capabilities. Research has relied heavily on EM techniques because this is often the only approach for extracting data from the particles at the size range where most of the information is contained. Because each extraterrestrial particle is really an individual meteorite, each with its own unique history,¹³ any non-EM analysis such as mass spectroscopy must be preceded by a fairly detailed EM study, otherwise the fundamental character of the sample could not be known. As a result, many of the investigations currently under way involve quite an extensive set of analytical procedures, all done on all or part of a single 10 μm -sized particle. These other analytical techniques include PIXIE, neutron activation, XRF, IR, and Raman spectroscopy, and solid source, rare-gas, and ion-probe (SIMS) mass spectroscopy. In addition to providing valuable information about extraterrestrial particles, these investigations are developing techniques for extracting detailed information from unique particles¹⁴ that must be studied individually.

References

1. D. E. Brownlee, "Cosmic dust: Collection and research," *Ann. Rev. Earth Planet. Sci.* 13: 189-215, 1985.
2. P. Fraundorf, D. E. Brownlee, and R. M. Walker, "Laboratory studies of interplanetary dust," in L. L. Wilkening, Ed., *Comets*, University of Arizona Press, 1982, 383-407.

3. D. E. Brownlee, "Extraterrestrial components in deep sea sediments," in C. Emiliani, Ed., *The Sea*, New York: Wiley, 1981, vol. 7, 733-762.
4. I. Steele, J. V. Smith, and D. E. Brownlee, "Minor element signature of relic olivine grains in deep sea particles," *Nature* 313: 297-299, 1985.
5. D. E. Brownlee, B. A. Bates, and M. Wheelock, "Extraterrestrial platinum group nuggets in deep sea sediments," *Nature* 309: 693-695, 1984.
6. J. P. Bradley, D. E. Brownlee, and P. Fraundorf, "Discovery of nuclear tracts in interplanetary dust," *Science* 226: 1432-1434, 1984.
7. J. T. Armstrong and P. R. Buseck, "Quantitative chemical analysis of individual microparticles using the electron microprobe: Theoretical," *Anal. Chem.* 47: 2178-2192, 1975.
8. K. Tomeoka and P. R. Buseck, "Transmission electron microscopy of low-Ca: A hydrated interplanetary dust particle," *Earth Planet. Sci. Lett.* 699: 243-254, 1984.
9. F. J. M. Rietmeijer, "On the continuum between chondritic interplanetary dust and Ci and Cm carbonaceous chondrites: A petrological approach," *Lunar and Planetary Science* 16: 698-699, 1985.
10. R. Christoffersen and P. R. Buseck, "Epsilon carbide: A low temperature component of interplanetary dust particles," *Science* 222: 1327-1329, 1983.
11. J. P. Bradley, D. E. Brownlee, and P. Fraundorf, "Carbon compounds in interplanetary dust: Evidence for formation by heterogeneous catalysis," *Science* 223: 56-58, 1984.
12. J. P. Bradley, D. E. Brownlee, and D. E. Veblen, "Pyroxene whiskers and platelets in interplanetary dust: Evidence of vapor phase growth," *Nature* 301: 473-477, 1983.
13. P. Fraundorf, "Interplanetary dust in the transmission electron microscope," *Geochim. Cosmochim. Acta* 45: 915-943, 1981.
14. S. A. Sandford and R. M. Walker, "Laboratory IR transmission spectra of individual interplanetary dust particles from 2.5 to 25 microns," *Ap. J.* 291: 838-851, 1985.

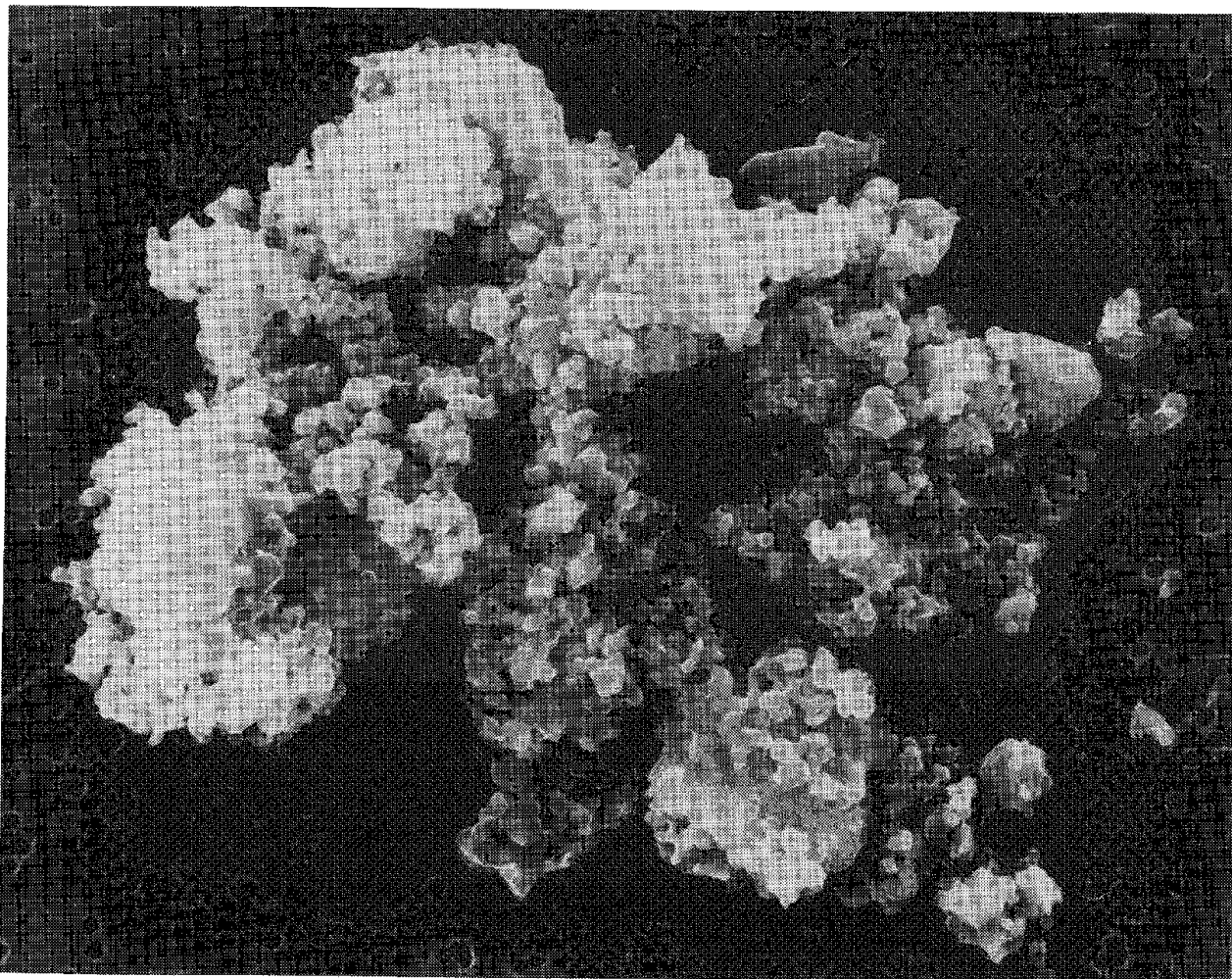


FIG. 1.--Ten-micron-long chondritic porous aggregate micrometeorite.

ISOTOPIC ANALYSES OF EXTRATERRESTRIAL MATERIALS WITH THE ION MICROPROBE

J. T. Armstrong and I. D. Hutcheon

The ion microprobe has enabled detailed, in situ isotopic studies of microvolumes of material in extraterrestrial samples such as meteorites and cosmic dust. These data, correlated with petrographic studies of the same specimens utilizing electron microbeam analysis, have helped to identify the oldest preserved material from our solar system and elucidate some of the complicated chemical and isotopic processes that occurred during early solar system history involving formation of the first solid phases.

Coincident with the return of the first lunar samples and first investigations of the immensely important, newly fallen Allende and Murchison meteorites were the installations of the first generation of commercial ion microprobe mass analyzers. It was not surprising that these instruments were soon applied to the study of lunar and meteoritic materials. The early results of these studies were promising; however, widespread use of the ion microprobe for the precise isotopic and chemical analyses necessary in such applications required extensive instrumental and analytical improvements. Some of the instrument manufacturers and several laboratories have concentrated on making such improvements, a second generation of high mass and spatial resolution ion microprobes with high ion transmission efficiency have been developed, and for the last 6-8 years the ion microprobe has been shown to be an important tool in the characterization of extraterrestrial materials. Indeed, of the four active ion microprobe laboratories situated in university geoscience departments in the United States, three have dedicated most of their research efforts to the study of meteorite and cosmic-dust samples.

The ability of the ion microprobe to perform in situ analyses of microvolumes of material for light elements and trace elements has made it an important complementary technique to electron microbeam analysis. However, it is the ability of the ion microprobe to perform relatively high-precision, in situ isotopic analyses of microvolumes of material ($2\sigma = 0.1\%$ in favorable cases), a capability so far unique to this microbeam technique, that has resulted in the widest range of applications in the study of meteorite and cosmic-dust samples.

Although ion microprobe isotopic analysis typically has not as good a precision as is obtained by thermal ionization mass spectrometry following chemical separation and concentration from bulk samples, its in situ microanalytical abilities make it an extremely valuable adjunct to conventional mass spectrometric determinations. The ability to perform in situ analyses in polished sections enables correlation of isotopic information with the textural and chemical information obtained on the same spots by electron microscopy and microbeam analysis, and thus permits correlation of isotopic systematics with the observed petrography of the samples, determination of isotopic variations across zoned crystals and across grain boundaries, and determination of isotopic microheterogeneities both laterally (with spatial resolution of $\sim 1 \mu\text{m}$) and in depth (with resolution of $\sim 100 \text{ \AA}$). Such information typically cannot be obtained from conventional mass spectrometric analysis. Furthermore, with ion microprobe analysis one can avoid areas containing included phases or alteration, which permits analysis of precisely the pure phase intended. Even when the most sophisticated microsurgery techniques are utilized (e.g., Refs. 1 and 2), it is difficult to achieve with conventional mass spectrometry the extremely low levels of contamination routinely obtained in careful ion microprobe analysis.

This paper reviews some of the significant recent scientific results obtained on meteorite and cosmic-dust samples by isotopic and chemical analysis with the ion microprobe. It is by no means an exhaustive review of the literature, which is growing at an increasingly accelerating pace. There have been reviews of applications of ion microprobe analysis of geological materials that include reviews of the early work on extraterrestrial materials (e.g., Refs. 3 and 4). A comprehensive bibliography of SIMS and ion microprobe analysis including applications to extraterrestrial materials has appeared previously in these volumes.^{5,6}

The authors are at the California Institute of Technology, Division of Geological and Planetary Sciences, Pasadena, CA 91125. This work was supported by funds from the National Aeronautics and Space Administration through grant NAG 9-43. [Division contribution #4218(515).]

Al-Mg Isotopic Systematics

Carbonaceous chondrite meteorites such as the Allende and Murchison falls of 1969 contain rounded whitish inclusions from < 1 mm to > 1 cm in diameter that are largely composed of phases rich in calcium and aluminum. A number of the minerals present in these Ca-, Al-rich inclusions (CAI) are the same as those predicted from equilibrium thermodynamic calculations to be among the first solid phases to have initially condensed from the cooling solar nebula (e.g., Refs. 7 and 8). Since these inclusions are contained in matrices that are thought never to have been heated to any significant degree, some CAI may have remained unaltered since their formation some 4.5 billion years ago and contain, locked up within them, information regarding the chemical processes and isotopic compositions of the early solar nebula. Mass spectrometric studies of mineral separates (of mass varying from micrograms to milligrams) from these inclusions revealed large isotopic anomalies in the isotopic composition of elements such as oxygen and magnesium, isotopic compositions that had not been found in any other meteorite samples nor in any natural terrestrial material (e.g., Refs. 9 and 10). These results dispelled the widely held notion that the early solar system was isotopically homogeneous; a variety of nuclear and fractionation mechanisms have been proposed to explain these anomalies, including injection of debris from neighboring supernova events into the early solar system, mixing of large amounts of interstellar dust, an early T-Tauri phase of our sun producing huge energetic neutron fluxes that induced nuclear reactions, etc.

Among the most studied of these isotopic anomalies is an excess of ^{26}Mg observed in a number of Al-rich, Mg-poor phases in CAI. In many instances ^{26}Mg appears to be correlated with Al/Mg so that measurements of $^{26}\text{Mg}/^{24}\text{Mg}$ vs $^{27}\text{Al}/^{24}\text{Mg}$ for the various mineral phases in an inclusion fall on linear arrays (e.g., Fig. 1). Such ^{26}Mg excesses ($^{26}\text{Mg}^*$) have been interpreted as due to the in situ decay of the short-lived isotope ^{26}Al ($t_{1/2} = 7.2 \times 10^5$ y) that was incorporated with normal Al at the time that CAI were formed, which implies that ^{26}Al was produced in one or more nucleosynthetic events occurring near the solar nebula less than a few million years before CAI formation.^{10,11} From the slopes of a number of these linear arrays measured in different inclusions it was estimated that, for at least a reasonable subset of CAI, approximately 50 ppm of the Al originally incorporated in the inclusions was live ^{26}Al —a surprisingly large amount for influx of short-lived radioactive material from an extra-solar component and a concentration that would provide a major heat source for early solar system processes.^{2,11,12}

The early studies of Al-Mg systematics in CAI were performed by thermal ionization mass spectrometry; however, increasingly, recent studies of these systematics are performed with the ion microprobe (e.g., Refs. 13 and 14). Use of the ion microprobe permits analysis of phases in CAI too small or too rare to concentrate for conventional measurements. It also enables analysis of isotopic variations within individual crystals and avoidance of Mg-rich alteration areas. As a result, Mg isotopic measurements have been made of areas of much higher Al/Mg and much greater $^{26}\text{Mg}^*$ than had been possible with thermal ionization mass spectrometry. For example, a recent ion microprobe study of a phase in a Ca-, Al-rich clast from the Dhajala meteorite with $^{27}\text{Al}/^{24}\text{Mg}$ of $\sim 16\,000$ yielded an almost 100% $^{26}\text{Mg}^*$ ($^{26}\text{Mg}/^{24}\text{Mg} = 0.275$ compared to the terrestrial value of 0.1398).¹⁵ Furthermore, the much shorter sample preparation and analysis times possible with the ion microprobe have enabled collection of more than an order of magnitude more data than obtained with conventional mass spectrometry.

Ion microprobe studies have demonstrated that Al-Mg systematics in CAI are very complicated and do not correspond to a simple model of in situ decay of ^{26}Al , at a constant initial concentration relative to ^{27}Al in CAI, without subsequent alteration. The complications, as outlined below, include (1) the absence of very low level of $^{26}\text{Mg}^*$ in some Al-rich, Mg-poor phases in CAI thought to have been the very first to have condensed, (2) the variability in $^{26}\text{Mg}^*/^{27}\text{Al}$ in a given phase from CAI to CAI (even when the inclusions are petrographically similar), and (3) the occasional variability in $^{26}\text{Mg}^*/^{27}\text{Al}$ in a given phase within an individual CAI.

Thermodynamic calculations predict that corundum (Al_2O_3) would be the first major element phase to condense from the solar nebula.⁷ This mineral occurs but rarely in CAI (much too rare to concentrate for conventional mass spectrometry), but has been identified and isotopically analyzed in two inclusions.^{16,17} Despite the corundum having extremely high Al/Mg ratios (> 20 000), either no $^{26}\text{Mg}^*$ or very low levels of $^{26}\text{Mg}^*$ ($^{26}\text{Mg}^*/^{27}\text{Al} < 1 \times 10^{-6}$) were measured.

The second most refractory major-element phase found in CAI is hibonite ($\text{CaAl}_{12}\text{O}_{19}$). This mineral occurs in CAI much more commonly than corundum, but is still relatively rare and very fine grained. A number of ion microprobe studies have been performed on this phase, with variable results (e.g., Refs. 13 and 15-19). In some CAI, the $^{26}\text{Mg}^*/^{27}\text{Al}$ for hibonite is 5×10^{-5} ,^{18,19} but in other CAI hibonites have $^{26}\text{Mg}^*/^{27}\text{Al} < 1 \times 10^{-5}$ or no detectable $^{26}\text{Mg}^*$ at all.¹⁵⁻¹⁷ In a few inclusions, low levels of $^{26}\text{Mg}^*$ are measured in hibonite, but the amounts of the excess are not correlated with the Al/Mg.¹³

The $^{26}\text{Mg}^*/^{27}\text{Al}$ may be different in hibonites from CAI of similar petrography. For example, the two CAI studied to date containing hibonite/corundum assemblages have hibonites with considerably different levels of $^{26}\text{Mg}^*$. Even in CAI with hibonites having $^{26}\text{Mg}^*/^{27}\text{Al}$ of 5×10^{-5} , other primary, Al-rich, Mg-poor phases may be depleted in $^{26}\text{Mg}^*$. For example, we have recently studied the Mg isotopic systematics of two similar hibonite-containing CAI from the Leoville meteorite.¹⁹ In one, the minerals hibonite and melilite ($\text{Ca}_2\text{Al}_2\text{Si}_2\text{O}_7\text{-Ca}_2\text{MgSi}_2\text{O}_7$) have $^{26}\text{Mg}^*/^{27}\text{Al}$ of 5×10^{-5} and coexisting anorthite ($\text{CaAl}_2\text{Si}_2\text{O}_8$) has $^{26}\text{Mg}^*/^{27}\text{Al}$ of 3×10^{-5} . In the other, hibonite has $^{26}\text{Mg}^*/^{27}\text{Al} < 1.5 \times 10^{-5}$.

The mineral in CAI most studied for $^{26}\text{Mg}^*$, both with conventional mass spectrometry and with the ion microprobe, is anorthite ($\text{CaAl}_2\text{Si}_2\text{O}_8$). It is abundant in many CAI and is sometimes relatively coarse grained. Analyses of this mineral provided the original determination of $^{26}\text{Mg}^*$ due to ^{26}Al decay. Subsequent ion microprobe studies, though confirming that often all anorthites of varying Mg contents from individual CAI lie on a linear array with $^{26}\text{Mg}^*/^{27}\text{Al} = 5 \times 10^{-5}$, demonstrate that in numerous other cases their systematics are much more complicated (e.g., Refs. 13, 14, 20, 21).

Comparative studies of CAI combining electron beam microanalysis with ion microprobe determinations have suggested that one particular petrographic type of CAI (type B1) is likely to have normal Mg isotopic systematics for plagioclase, and other types are likely to have smaller $^{26}\text{Mg}^*$.^{13,14} In some of the latter cases, $^{26}\text{Mg}^*/^{27}\text{Al}$ for plagioclase has not a unique value but sometimes scatters over a fairly wide range.¹³ It is surprising that some of the inclusions showing noncorrelated variations appear from their texture originally to have been totally molten, which should have homogenized the original $^{26}\text{Al}/^{27}\text{Al}$ throughout the inclusion. In these inclusions, variation in $^{26}\text{Mg}^*/^{27}\text{Al}$ can be readily explained only by variable alteration after decay of some or all of the original ^{26}Al .

Even some of the CAI of the petrographic type that show the least signs of disturbance of Mg isotopic systematics can have complicated $^{26}\text{Mg}^*$ in their anorthite. Recently, we have undertaken a series of detailed petrographic and isotopic studies of WA, a coarse-grained type B1 CAI from Allende which exhibits some of the largest $^{26}\text{Mg}^*$ thus far reported.^{14,20,21} Mg isotopic analyses of the various phases in WA by thermal ionization mass spectrometry provided the first experimental evidence that $^{26}\text{Mg}^*$ in CAI correspond to a simple isochron consistent with formation from in situ decay of live ^{26}Al originally present at a level of $^{26}\text{Al}/^{27}\text{Al} = 5 \times 10^{-5}$.^{2,11}

The ion microprobe reexamination of WA shows that the Mg isotopic systematics are not nearly as straightforward as indicated by the original determinations. The interiors of about half of the anorthite crystals studied with the ion microprobe (with $^{27}\text{Al}/^{24}\text{Mg}$ ranging from 170 to 780) had $^{26}\text{Mg}^*$ corresponding to $^{26}\text{Mg}^*/^{27}\text{Al} = 5 \times 10^{-5}$ (Fig. 1). (The Mg isotopic compositions of spinel, fassaite, and melilite from WA also lie on this array.) However, the interiors of the other half of the anorthite crystals do not fall on this array. Instead, a plot of $^{26}\text{Mg}/^{24}\text{Mg}$ vs $^{27}\text{Al}/^{24}\text{Mg}$ for these crystals (with $^{27}\text{Al}/^{24}\text{Mg}$ ranging from 60 to 1300) generally fall on a straight line with a slope corresponding to $^{26}\text{Mg}^*/^{27}\text{Al} = 3.1 \times 10^{-5}$ and an intercept corresponding to an initial $^{26}\text{Mg}/^{24}\text{Mg} = 0.1444$, enriched in ^{26}Mg by 3.3% relative to normal (Fig. 2). A few crystals have interior portions with $^{26}\text{Mg}^*/^{27}\text{Al}$ lying on each of the arrays. Furthermore, the rims of all of the anorthite crystals studied had depleted $^{26}\text{Mg}^*/^{27}\text{Al}$ relative to the interior (Fig. 3), regardless to which $^{26}\text{Mg}^*/^{27}\text{Al}$ the interior corresponded or to which phase the anorthite was adjacent.

No one mechanism can be readily invoked to explain all the complicated Mg isotopic variations uncovered by ion microprobe investigations. In some inclusions, the absence of $^{26}\text{Mg}^*$, particularly in phases with very low levels of Mg, could be due to total Mg remobilization after the complete decay of ^{26}Al . Variations in Mg isotopic systematics across individual mineral grains as observed in WA can most easily be explained as due to a secondary alteration event involving loss of either total Mg or $^{26}\text{Mg}^*$ from grain boundaries. The existence of two sets of Mg isotope linear arrays within the same inclusion, one with a

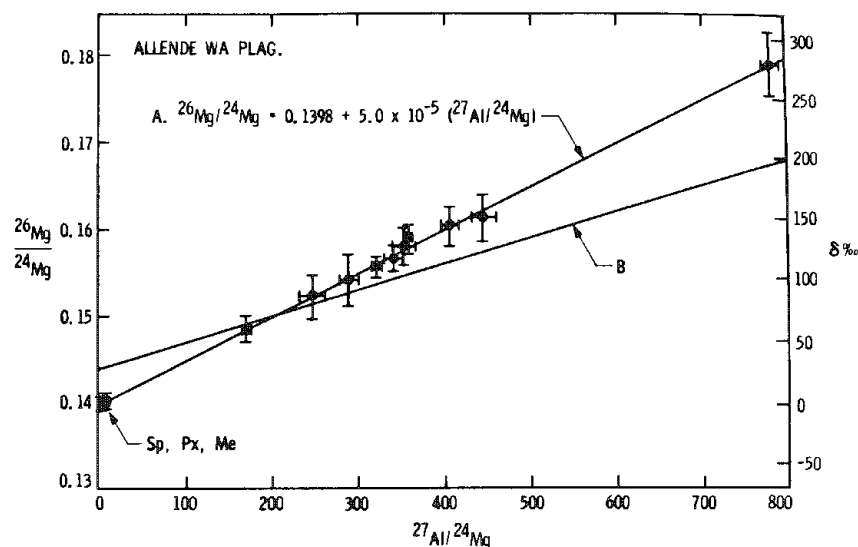


FIG. 1.--Plot of $^{27}\text{Al}/^{24}\text{Mg}$ for crystals from Allende CAI WA consistent with isochron originally determined by Lee et al.¹¹ All spinels, pyroxenes, and melilites but only about half of the anorthite crystals analyzed from WA lie on this array. Error bars are $\pm 2\sigma_m$ and include measurement uncertainties in corrections for fractionation and relative ion yields.

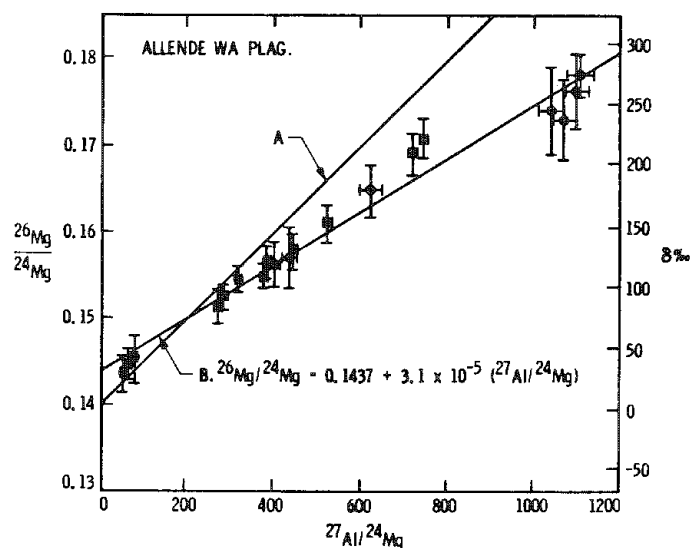


FIG. 2.--Plot of $^{27}\text{Al}/^{24}\text{Mg}$ for anorthite crystals in WA consistent with linear array of lesser slope and greater intercept than isochron measured by Lee et al.¹¹ Ion microprobe measurements suggest that about half of anorthite crystals in WA fall on this lesser sloped array.

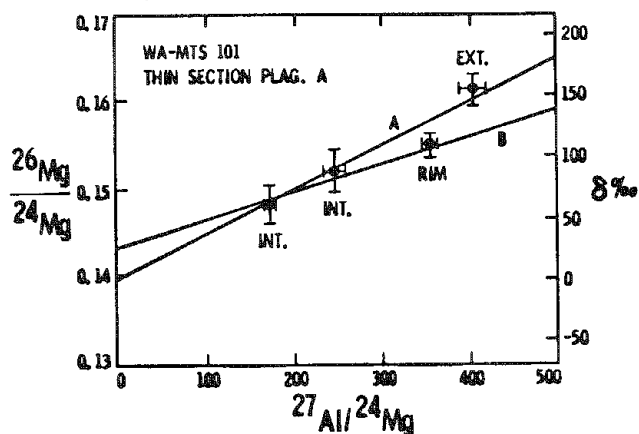


FIG. 3.--Plot of $^{27}\text{Al}/^{24}\text{Mg}$ for individual anorthite grain from WA. Data from interior and exterior portions of crystal lie on linear array; outer portion of crystal, in contact with melilite, is depleted in $^{26}\text{Mg}^*$ and lies below array. Depletion of $^{26}\text{Mg}^*$ at edges of anorthite crystals is common in WA, regardless of neighboring phase.

lesser slope and higher intercept, could be explained by a partial or total reequilibration of Mg isotopes in a portion of the crystals occurring after at least partial decay of ^{26}Al . If the two arrays in the inclusion WA correspond to real isochrons, then the results are consistent with a secondary event occurring at least 500 000 years after initial formation, at which time material with $^{27}\text{Al}/^{24}\text{Mg} = 160$ became partially or totally isotopically rehomogenized.²⁰ Indeed, there is some petrographic evidence in the WA inclusion that both alteration and rehomogenization may have occurred.²⁰

However, Mg isotopic variations observed in a number of studies, such as variation of $^{26}\text{Mg}^*/^{27}\text{Al}$ between inclusions that appear petrographically identical and absence of $^{26}\text{Mg}^*$ in primary refractory phases that do not appear to be altered, are hard to explain by alteration mechanisms. Two possible explanations for such variations are that the various crystals comprising the CAI may have formed over a long period of time before mixing and aggregation into CAI or, perhaps more likely, that the crystals formed in different regions of an isotopically heterogeneous solar nebula before aggregation.¹³ Either of these mechanisms requires an absence of isotopic equilibration during or after CAI formation--a serious problem for inclusions that appear to have been partially or totally molten during their formation. Clearly, a total understanding of Mg isotopic systematics in CAI does not currently exist. The degree of lack of understanding has been dramatically demonstrated by the results of the ion microprobe investigations performed to date. Improving the understanding will require continued carefully designed correlated studies involving electron and ion microbeam analysis.

Search for Excess ^{41}K and Other Isotopic Anomalies in CAI

The existence of $^{26}\text{Mg}^*$ in CAI from decay of ^{26}Al places an upper limit on the timescale between injection of fresh nucleosynthetic material and formation of the first solid material in the solar system of $\sim 8 \times 10^6$ years, but the lower limit of this interval is poorly constrained. The radioactive nuclide ^{41}Ca , which decays to ^{41}K with a half life of 110 000 years, could provide a sensitive indicator of the minimum time interval. Phases exist in CAI that are rich in Ca and very poor in K. However, the extremely high ratio of Ca/K required to look for $^{41}\text{K}^*$ and the abundant presence of K-rich alteration phases in CAI have made it difficult to search for evidence of live ^{41}Ca with conventional mass spectrometry.

We have conducted a series of studies using ion microprobe analysis to determine whether there is any evidence of $^{41}\text{K}^*$ in CAI.²²⁻²⁴ These experiments are very difficult to perform because of the extremely low concentrations of K involved, and estimates of the maximum possible $^{41}\text{K}^*$ have steadily decreased with experience. These studies have involved measurement of the isotopic composition of K at the ppb level. Count rates of $^{41}\text{K}^+$ are < 0.5 cps with $^{41}\text{K}^{++} < 0.1$ cps. The measurement is complicated by the presence of unresolvable interferences of the type $^{40}\text{Ca}^{42}\text{Ca}^{++}$ at the $^{41}\text{K}^+$ mass. The relative abundances of such interferences are strongly matrix dependent, varying by over an order of magnitude depending on the mineral phase.²⁴ Correction requires concurrent measurement of extremely low-level species such as $^{40}\text{Ca}^{43}\text{Ca}^{++}$. The newest data indicate that in the fassaite samples in CAI studied for $^{41}\text{K}^*$, 80% of the mass 41 signal is due to the $^{40}\text{Ca}^{42}\text{Ca}^{++}$ interference.

After correcting for background and estimated isobaric interferences, the results in fassaites from two type B1 CAI show variable excesses of up to 350%. It is as yet unclear whether these excesses are linearly correlated with $^{40}\text{Ca}/^{39}\text{K}$ and due to ^{41}Ca decay, or whether they are due to other interferences such as $^{26}\text{Mg}^{56}\text{Fe}^{++}$ (currently under investigation). The data taken as a whole place a strict upper limit of $^{41}\text{K}^*/^{40}\text{Ca} < 8 \pm 3 \times 10^{-9}$. This represents an upper limit of the possible amount of ^{41}Ca present at the time of CAI formation. Clearly ^{41}Ca was not nearly as abundant as ^{26}Al (< 1 ppb vs ~ 5 ppm in these CAI). Given reasonable estimates of the ^{41}Ca production rate in nucleosynthetic processes, its near or total absence in CAI requires either that $^{41}\text{K}^*$ was lost during subsequent CAI metamorphism or that the time interval between ^{41}Ca production and CAI formation was $\sim 2 \times 10^6$ years, a time fully compatible with that estimated from ^{26}Al .

Currently work is under way in a number of laboratories to search for daughter products of other short-lived radionuclides to constrain further the time scales involved in early solar-system formation (e.g., Refs. 25 and 26). In addition, a number of studies have been performed with the ion microprobe to identify isotopic anomalies in CAI not associated with decay of specific short-lived radionuclides (e.g., Refs. 14, 17, and 27-30). These studies have indicated that certain small phases contain extremely large anomalies--much larger

than measured by conventional mass spectrometry. For example, magnesium in hibonite and spinel from a CAI in the Murchison meteorite was found to be mass fractionated from 2.5% to 35.0% per mass unit,²⁸ and Ti in hibonite from a CAI in the Murray meteorite was found to have a 10% excess in ⁵⁰Ti.³⁰ Such variations provide added weight to the feeling that the early solar nebula was isotopically very heterogeneous on a fairly fine scale during CAI formation. It is quite possible that ubiquitous, low-level isotopic anomalies observed in CAI by conventional mass spectrometry for elements such as Ca and Ti may be due to fine-grained isolated phases having much larger anomalies. It is only by the fine-scale measurements enabled by ion microprobe techniques that the magnitude and frequency of these effects can be determined.

Isotopic Analyses of Fremdlinge: Some of the Oddest and Oldest Material in Meteorites

Among the most exotic and least understood objects found in meteorite CAI are "Fremdlinge" (strangers)--complex aggregates of metal grains, sulfides, phosphates, oxides, and silicates that have high concentrations (often several percent or more) of refractory siderophile elements such as Pt, Ir, Os, Re, and Ru.³¹ The large compositional variability among Fremdlinge and enigmatic nature of individual Fremdlinge, with coexisting refractory-rich and volatile-rich, highly reduced and highly oxidized phases, have prevented a clear understanding of their origin. Origins as diverse as aggregation of pre-solar material from outside of the solar system and alteration of existing CAI have been proposed. We have recently undertaken a series of petrographic studies of these objects, which typically are 10-30 μm and rarely > 100 μm in diameter, in order to help understand how they were formed.³²⁻³⁴ These studies provide strong evidence that Fremdlinge existed as solids before solidification of any of the major element phases in CAI (e.g., Fig. 4), which would make Fremdlinge the oldest identifiable preserved material found in the solar system. These studies have also identified a particularly well-preserved "Ur-Fremdling" (Fig. 5) whose petrography indicates that among the first phases to aggregate to form Fremdlinge were low-temperature oxidized minerals along with high-temperature Pt-group metal nuggets.³² These studies suggested complicated mechanisms by which Fremdlinge could have formed in the solar nebula; however, just on the basis of petrography, an extrasolar source for Fremdlinge could not be ruled out.

To determine whether Fremdlinge were formed inside or outside of the solar system, we have initiated a series of isotopic investigations of these objects using the ion microprobe.³⁵ If Fremdlinge were formed outside of the solar system and contain relic grains from an exploding star, large isotopic differences from solar-system materials would be expected for a number of elements, particularly for those with high atomic number (or very low atomic number). Isotopic measurements of Fremdlinge are complicated by the small grain size of the individual phases (typically < 1 to 10 μm), complex intergrowth, and isotopic interferences encountered. Our studies to date have included high mass and spatial resolution determinations of the isotopic compositions of Mg, Ca, Fe, Mo, Ru, and W in selected phases from Fremdlinge. Measurement precisions have ranged from 0.1-1% 2σ , depending on the element and grain size. No isotopic anomalies, except for a very small mass-dependent fractionation of Mo in one sample, have been observed. The absence of large (percent level) isotopic variations, even for the high-Z elements Mo, Ru, and W, strongly suggest that Fremdlinge were originated within the solar system.

With the demonstration that Fremdlinge were formed in our solar system, the phase assemblages they contain provide a series of thermometers and oxygen partial pressure barometers for early solar system processes.³²⁻³⁴ The proposed formation mechanisms for Fremdlinge³²⁻³⁴ require that neighboring parcels of the early solar nebula differed dramatically in temperature and oxygen partial pressure, and that the nebula was turbulent enough to enable intimate mixing of phases formed under considerably different conditions. This assumption underscores the complexity of early solar nebula processes. In addition, the nature and degree of reaction of phases within Fremdlinge and between Fremdlinge and their surrounding CAI host minerals provide strong constraints regarding the maximum temperatures of formation and minimum cooling rates of CAI.³²⁻³⁴ Studies utilizing combined electron and ion microbeam analysis are in progress to unravel what these oldest survivors can tell us of early solar system formation processes.

Isotopic Analysis of Interplanetary Dust Particles

Recently extensive efforts have been made by several laboratories to characterize particles collected by high-altitude aircraft from the stratosphere. It is generally

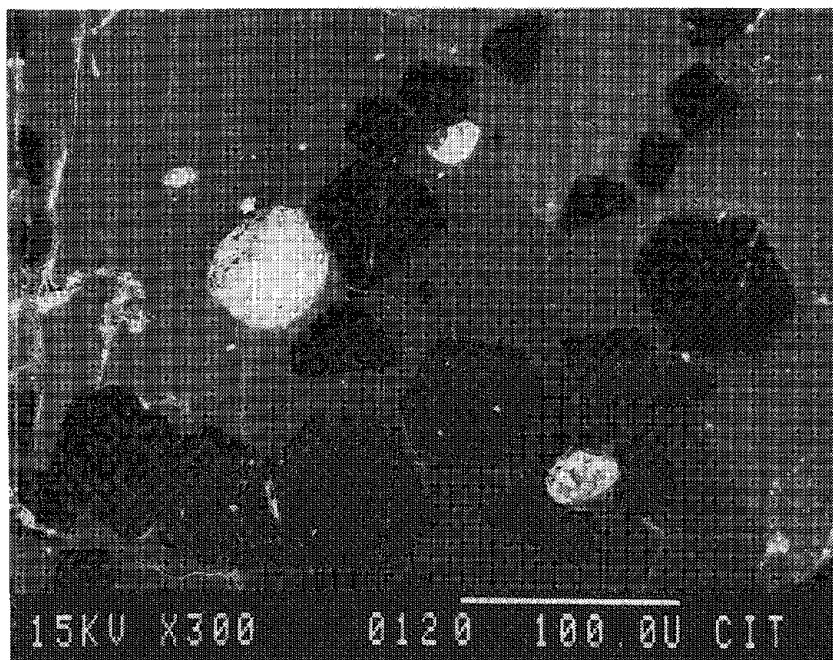


FIG. 4.--Backscattered electron image of small Fremdlinge (bright white areas) associated with spinel (black crystals) and melilite (light gray areas) in Allende CAI Ts-34.³² The Fremdlinge are commonly found to be partially enclosed in embayed areas in spinel. Since it is unlikely for a variety of reasons (discussed in Ref. 32) that Fremdlinge formed by replacing spinel, this occurrence strongly suggests that Fremdlinge were already solids during spinel crystallization and spinels grew around them. Since spinel is first major-element phase to have crystallized in this type of inclusion, Fremdlinge must be oldest solid components of these CAI. This spinel/Fremdling texture is a very common feature observed in many CAI. Scale bar is 100 μm .

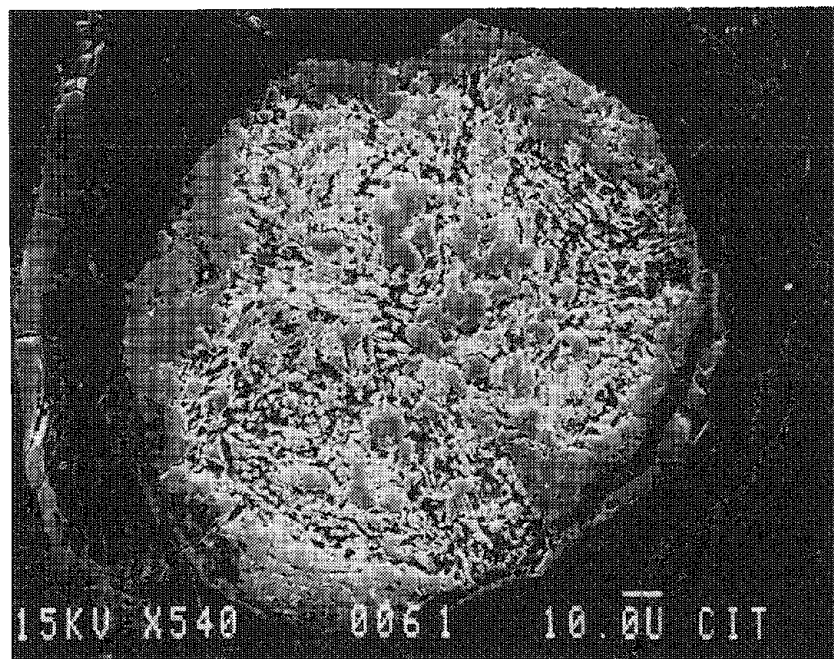


FIG. 5.--Secondary-electron image of "Ur-Fremdling" Willy from Allende CAI 5241.³² Fremdling is composed of fluffy core, surrounded by compact mantle and dense rim. Core is composed dominantly of V-rich magnetite, Ni-Fe metal containing Pt, Fe-sulfide, Os-Ru metal nuggets, and schmelite (CaWO_4). Mantle is composed largely of V-rich magnetite and Cl-apatite. Rim is composed of V-rich fassaite and V-rich spinel. This Fremdling is thought to be best-preserved, least-altered object of its kind described to date and a precursor of the more altered Fremdlinge commonly found in CAI.³²⁻³⁴ Scale bar is 10 μm .

believed that a large component of these particles are primitive material of extraterrestrial origin. Some of these particles may be cometary debris and may represent a component of dust collected from the interstellar medium. Several laboratories have conducted ion microprobe investigations of the isotopic compositions of light elements, such as H and C, in individual interplanetary dust particles (IDP) or components of IDP (e.g., Refs. 36-38). Spectacular anomalies have been reported. For example, enrichments in deuterium as high as 260% relative to terrestrial standards have been reported.³⁸ No natural terrestrial materials have anywhere near such enrichments, which indicates that these IDP are indeed extraterrestrial. Ion microprobe analyses of selected components in meteorites (e.g., Refs. 39 and 40) have confirmed bulk mass spectrometric determinations

that high deuterium excesses (> 500%) exist in certain meteorites as well. Future ion microprobe studies may help determine the nature of the carriers of such light element anomalies in IDP and meteorites and whether they are related.

Summary

The ion microprobe has enabled isolation of carriers of large isotopic anomalies in meteorite and cosmic dust particles. It has shown the degree of variability and complexity of Mg isotopic systematics within CAI, and has helped to relate disturbed Mg isotopic systematics with observed petrographic features. Ion microprobe measurements have placed strict upper limits on the amount of ^{41}Ca present during CAI formation and may help fix the minimum time between injection of nucleosynthetic material and condensation of the first solid materials. Isotopic analyses of the exotic Fremdlinge indicate that they were formed in the solar nebula, which would make them the oldest identifiable preserved objects in the solar system. Clearly the ion microprobe, with its in situ analytical abilities and relatively short sample preparation and analysis times, has shown itself to be an extremely important complementary technique to conventional mass spectrometry for the isotopic characterization of extraterrestrial materials.

References

1. D. A. Papanastassiou and G. J. Wasserburg, "Microchrons: The ^{87}Rb - ^{87}Sr dating of microscopic samples," in R. Ridings and R. B. Merrill, Eds., *Proc. 12th Lunar Sci. Conf.*, New York: Pergamon Press, 1981, 1027-1038.
2. T. Lee et al., "Mg and Ca isotopic study of individual microscopic crystals from the Allende meteorite by the direct loading technique," *Geochim. Cosmochim. Acta* 41: 1473-1485, 1977.
3. J. F. Lovering, "Application of SIMS microanalysis techniques to trace element and isotopic studies in geochemistry and cosmochemistry," in *Workshop on Secondary Ion Mass Spectrometry (SIMS) and Ion Microprobe Mass Analysis*, NBS Spec. Pub. 427, Washington: U.S. Government Printing Office, 1975, 135-178.
4. N. Shimizu and S. R. Hart, "Applications of secondary ion mass spectrometry to geochemistry and cosmochemistry," *Annual Rev. Earth Planet. Sci.* 10: 483-526, 1982.
5. Shaiw-Yih Yin, "Eighteen years of secondary ion mass spectrometry: A bibliography of SIMS, 1958-1975," *Microbeam Analysis--1980*, 289-311.
6. Shaiw-Yih Yin, "Recent developments in secondary ion mass spectrometry: A bibliography of SIMS, 1976-1980," *Microbeam Analysis--1981*, 342-378.
7. L. Grossman, "Refractory inclusions in the Allende meteorite," *Annual Rev. Earth Planet. Sci.* 8: 559-608, 1980.
8. L. Grossman, "Origins of Ca-, Al-rich inclusions in the Allende meteorite," *Microbeam Analysis--1985*, 266.
9. R. N. Clayton and T. K. Mayeda, "Correlated oxygen and magnesium isotopic anomalies in Allende inclusions: I. Oxygen," *Geophys. Res. Lett.* 4: 295-298, 1977.
10. G. J. Wasserburg and D. A. Papanastassiou, "Some short-lived nuclides in the early solar system: A connection with the placental ISM," in C. A. Barnes et al., Eds., *Essays on Nuclear Astrophysics*, Cambridge: Cambridge University Press, 1982, 77-140.
11. T. Lee et al., " ^{26}Al in the early solar system: Fossil or fuel?" *Astrophys. J. Lett.* 211: L107-L110, 1977.
12. G. J. Wasserburg and D. A. Papanastassiou, "Correlated oxygen and magnesium isotopic anomalies in Allende inclusions: II. Magnesium," *Geophys. Res. Lett.* 4: 299-302, 1977.
13. I. D. Hutcheon, "Ion probe magnesium isotopic measurements of Allende inclusions," in L. A. Curie, Ed., *Nuclear and Chemical Dating Techniques: Interpreting the Environmental Record*, Amer. Chem. Soc. Symposium Series No. 176, 1982, 95-128.
14. J. C. Huneke et al., "FUN with PANURGE: High mass resolution ion microprobe measurements of Mg in Allende inclusions," *Geochim. Cosmochim. Acta* 47: 1635-1650, 1983.
15. R. W. Hinton and A. Bischoff, "Ion microprobe magnesium isotope analysis of plagioclase and hibonite from ordinary chondrites," *Nature* 308: 169-172, 1984.
16. M. Bar-Matthews et al., "A corundum-rich inclusion in the Murchison carbonaceous chondrite," *Geochim. Cosmochim. Acta* 46: 31-41, 1982.
17. R. W. Hinton et al., "Magnesium and calcium isotopes in hibonite-bearing CAIs,"

Meteoritics 19: 240-241, 1984.

18. I. D. Hutcheon et al., "A Mg isotope study of hibonite-bearing Murchison inclusions," *Meteoritics* 15: 306-307, 1980.

19. I. D. Hutcheon et al., "Mg isotopic studies of Leoville 'compact' type A CAI," *Meteoritics* 19: 244-245, 1984.

20. J. T. Armstrong and G. J. Wasserburg, "Mg isotopic systematics in the Allende inclusion WA: PANURGE takes a second look," in *Lunar and Planet. Sci. XIV*, Houston: Lunar and Planetary Inst., 1983, 11-12.

21. J. T. Armstrong et al., "Disturbed isotopic systematics in Allende CAI," in *Lunar and Planet. Sci. XV*, Houston: Lunar and Planetary Inst., 1984, 15-16.

22. J. C. Huneke et al., " ^{41}K and ^{26}Mg in an Allende inclusion and a hint of ^{41}Ca in the early solar system," in *Lunar and Planet. Sci. XII*, Houston: Lunar and Planetary Inst., 1981, 482-484.

23. I. D. Hutcheon et al., "Excess ^{41}K in Allende CAI: Confirmation of a hint," in *Lunar and Planet. Sci. XV*, Houston: Lunar and Planetary Inst., 1984, 387-388.

24. I. D. Hutcheon et al., "Excess ^{41}K in Allende CAI: A hint re-examined," *Meteoritics* 19: 243-244, 1984.

25. R. W. Hinton et al., "search for ^{60}Fe in meteorites using the ion probe micro-analyser," in *Lunar and Planet. Sci. XV*, Houston: Lunar and Planetary Inst., 1984, 365-366.

26. D. E. Scatena-Wachel et al., "Preliminary ion microprobe study of chromium isotopes in Orgueil," in *Lunar and Planet. Sci. XV*, Houston: Lunar and Planetary Inst., 1984, 718-719.

27. R. N. Clayton et al., "New 'FUN' inclusions from Allende," in *Lunar and Planet. Sci. XIV*, Houston: Lunar and Planetary Inst., 1983, 122-123.

28. I. D. Hutcheon et al., "Extreme Mg fractionation and evidence of Ti isotopic variations in Murchison refractory inclusions," in *Lunar and Planet. Sci. XIV*, Houston: Lunar and Planetary Inst., 1983, 339-340.

29. R. W. Hinton et al., "Ion microprobe measurement of calcium and magnesium isotopic mass fractionation in refractory inclusions," in *Lunar and Planet. Sci. XVI*, Houston: Lunar and Planetary Inst., 1985, 354-355.

30. A. J. Fahey et al., "Ion probe measurements reveal large Ti isotopic effects in CM hibonites," in *Lunar and Planet. Sci. XVI*, Houston: Lunar and Planetary Inst., 1985, 229-230.

31. A. El Goresy et al., "Fremdlinge and their noble relatives," in R. B. Merrill, Ed., *Proc. 9th Lunar Sci. Conf.*, New York: Pergamon Press, 1978, 1279-1303.

32. J. T. Armstrong et al., "Willy: A prize noble Ur-Fremdling: Its history and implications for the formation of Fremdlinge and CAI," *Geochim. Cosmochim. Acta* 49: 1001-1022, 1985.

33. J. T. Armstrong et al., "Fremdlinge in Leoville and Allende CAI: Clues to post-formation cooling and alteration," *Meteoritics* 19: 186-187, 1984.

34. J. T. Armstrong et al., "Zelda revealed," in *Lunar and Planet. Sci. XVI*, Houston: Lunar and Planetary Inst., 1985, 15-16.

35. I. D. Hutcheon et al., "Isotopic studies of Mg, Ca, Fe, Mo, and Ru in Fremdlinge," in *Lunar and Planet. Sci. XVI*, Houston: Lunar and Planetary Inst., 1985, 384-385.

36. E. Zinner et al., "Laboratory measurements of D/H ratios in interplanetary dust," *Nature* 305: 119-121, 1983.

37. E. Zinner and K. D. McKeegan, "Ion probe measurements of hydrogen and carbon isotopes in interplanetary dust," in *Lunar and Planet. Sci. XV*, Houston: Lunar and Planetary Inst., 1984, 961-962.

38. K. D. McKeegan et al., "D/H ratios in interplanetary dust and their relationship to IR, Raman, and EDX observations," *Meteoritics* 19: 269-270, 1984.

39. R. W. Hinton et al., "Ion microprobe measurement of D/H ratios in meteorites," in *Lunar and Planet. Sci. XIV*, Houston: Lunar and Planetary Inst., 1983, 313-314.

40. K. D. McKeegan and E. Zinner, "On the distribution of excess deuterium in Renazzo and Semarkona: An ion microprobe study," in *Lunar and Planet. Sci. XV*, Houston: Lunar and Planetary Inst., 1984, 534-535.

MATRICES OF CHONDRITES AS THE RECORDS OF PRE-SOLAR AND EARLY-SOLAR SYSTEM

Hiroko Nagahara

Chondrites are one of the most primitive materials in the solar system. Chondrites consist of chondrules, Ca- and Al-rich inclusions in carbonaceous chondrites, mineral fragments (both silicates and non-silicates), and "lithic-fragments." The origin of chondrules has been long discussed and it has been recently revealed that chondrules were formed from pre-existing minerals through incomplete or complete melting.^{1,2} Contrary to intensive studies on chondrules, other components have not been well studied. Detailed petrological study aided by the scanning electron microscope (SEM) with energy-dispersive spectrometer (EDS) on the matrices of primitive chondrites shows that the matrix materials are extremely primitive keeping the records of processes that took place in the early solar system. Mineral assemblages and formation sequence of materials in chondrites of various chemical groups reflect the various chemical conditions of the place of chondrite formation of these groups.

Experimental

Fine-grained matrices are defined to be silicate, metal, sulfide, and amorphous materials less than 10 μm in size, which occupy the interstitial part of chondrules, inclusions, and fragments (Fig. 1). Because of fine grain size, they are black and opaque under transparent light of microscope and show rough surface under reflected light. Using SEM, we can observe the complex aggregation and occurrence of matrix materials. Recent progress in EDS techniques makes it possible to provide reliable analytical data that are useful for fine-grained materials and unknown phases. The system used in the present study is JEOL T-200 SEM equipped with LINK-SYSTEM Si(Li) detector and JEOL JCXA-733 microprobe.

Type 3 Ordinary Chondrites

Detailed petrological study on the matrices of Semarkona (subgroup 3.0),³ Krymka (3.0), Chainpur (3.4), Sharps (3.4), ALH-77015 (3.5), Khohar (3.7), Tieschitz (3.6), ALH-77278 (3.6), and ALH-77299 (3.7) were given by Nagahara.⁴ Major conclusions are as follows: (1) Minerals encountered are olivine, low-Ca pyroxene, high-Ca pyroxene, albitic plagioclase, Fe-Ni metal, troilite, magnetite, Mg-Al spinel, and chromite, which are found within chondrules. Most primitive Semarkona has fluffy fragments mainly composed of Si, Fe, and Mg with small amounts of Al, Ca, and Na which are probably amorphous or mixtures of very fine-grained materials (Fig. 2). (2) The most significant feature is an extremely wide range of olivine composition (Fo99-9 for chondrites investigated) and magnesian nature of pyroxene (mostly Mg/(Mg + Fe) ratio, (Mg#) > 0.8). (3) There are often present composite grains showing formational sequence (Fig. 3). The sequence estimated is high-Ca px, forsterite, enstatite, intermediate ol (Fo50), ferrous ol (Fo < 50), and albite in decreasing order. This sequence agrees well with that predicted in the "equilibrium condensation sequence" from the gas of solar system composition by thermochemical calculations⁵ suggestive of these minerals being condensates and reaction products with the gas at wide temperature range. (4) The presence of olivine more ferrous than Fo50 requires the presence of free SiO₂ or high activity of SiO₂ in the gas. A possible explanation for this is fractional condensation probably of Mg and/or Fe to increase SiO₂ activity in the residual gas at low temperatures. Another possibility is that the gas/dust fractionation occurred prior to heating of the solar nebula where gas and dust originated in an interstellar cloud.⁶ In the latter case, original bulk chemical composition was different from that of the solar system, and the increase of SiO₂ activity in the gas was an inevitable result of a different condensation path in the restricted area of the nebula.

The author is at University of Tokyo (Geological Institute), Hongo, Tokyo 113, Japan.

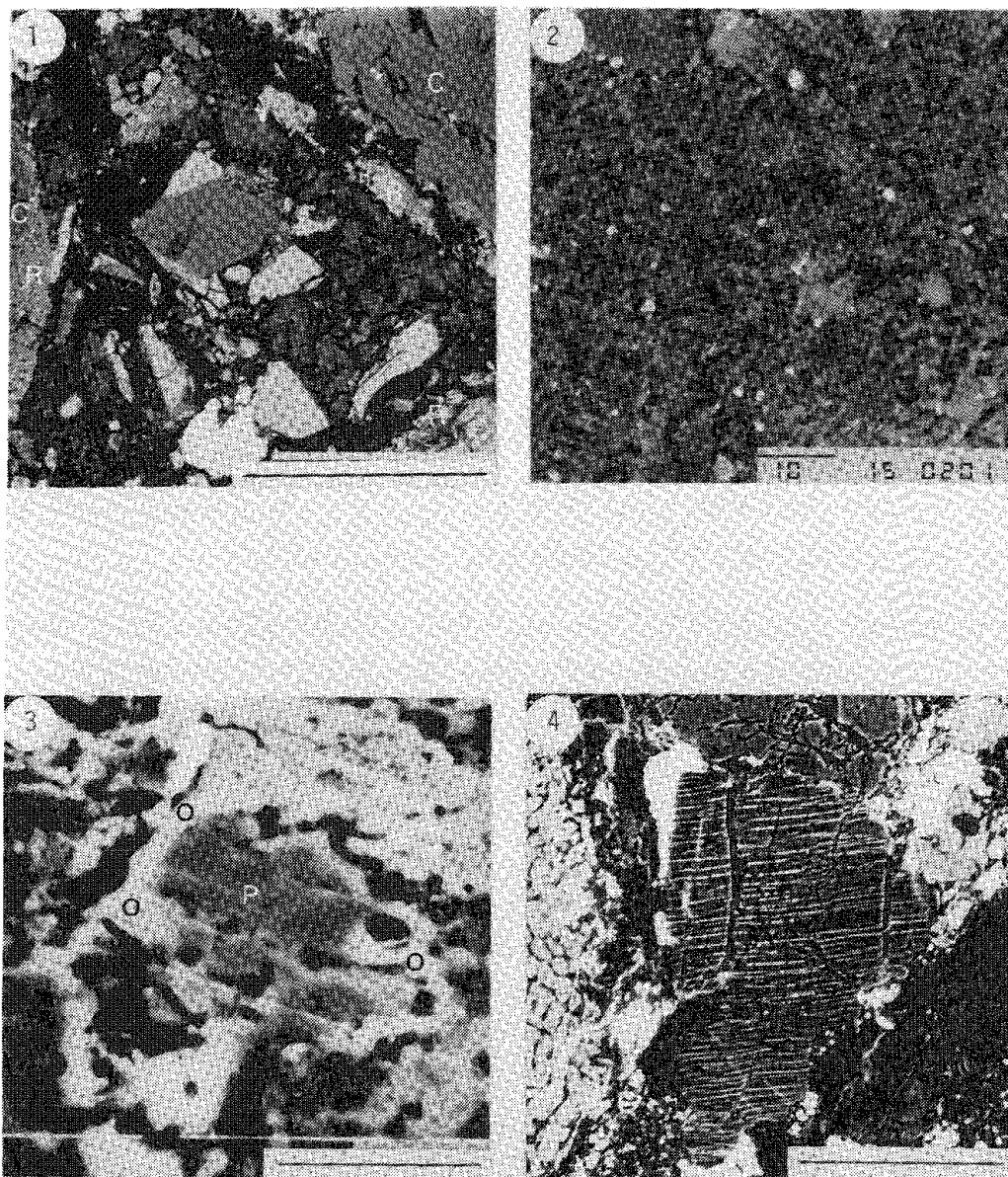


FIG. 1.--Tieschitz chondrite. Matrix is exceptionally coarse grained. Minerals, amorphous materials, and aggregates of very fine-grained materials occupy interstices of three chondrules (c) with well-developed chondrule rim (r). Scale bar 100 μm .

FIG. 2.--Extremely fine-grained Semarkona matrix. Matrix is mostly fluffy particles that are mixtures of several phases. Scale bar 10 μm .

FIG. 3.--Composite grain in Chainpur chondrite. Fo20 olivine (o) surrounds En92 pyroxene (p). Scale bar 10 μm .

FIG. 4.--Large olivine grain with lamellae of metallic iron in Yamato-691 E chondrite. Back-scattered electron image. Scale bar 500 μm .

Enstatite Chondrites

Enstatite (E) chondrites are known to be an extremely reduced clan of chondrites consisting of enstatite, SiO_2 minerals, metallic Fe-Ni, and troilite with subordinate sulfides and phosphides. Though most E chondrites are severely heated and equilibrated, only Qingzhen and Yamato-691 belong to type 3 and can provide information on precursors and pre-accretionary chemical processes in E chondrite environments. SEM observations on matrix minerals and also chondrule minerals reveal that multistage reduction occurred for the formation of E chondrites. Matrix minerals are low-Ca pyroxene (Mg# 0.99-0.91), olivine (Fo 99-88), albite, SiO_2 , Fe-Ni metal, troilite, and Mg-sulfide (ninningerite). Matrix pyroxene is richer in FeO than chondrule pyroxene (Mg# 0.99-0.95). Olivine and pyroxene in chondrules contain numerous reduced metal blebs and often show Mg-enrichment toward margin of grains showing reduction during chondrule formation. In addition to matrix FeO-bearing olivine and pyroxene, there are exceptionally iron-rich olivine and pyroxene fragments. Large olivine fragments with abundant lamellae of metallic iron are found being opaque under transparent light and observable only with SEM (Fig. 4). This shows that FeO-bearing pyroxene was reduced before incorporation into chondrite. Fe-rich pyroxene fragment always coexist with SiO_2 which was not highly reduced before incorporation into chondrite. These findings show that E chondrites originally contained FeO-bearing silicates, some of which were reduced though some were not. Olivine is abundant in these chondrites but scarce or absent in others, and contents of FeO in olivine and pyroxene in chondrules, matrices, and fragments decrease with the progress of equilibration. This change corresponds to the fact that the highly disequilibrium assemblage of type 3 E chondrites, forsterite-enstatite-metallic iron- SiO_2 -ferrous olivine and pyroxene, changes into equilibrium assemblage of type 4 or 5 chondrites, enstatite- SiO_2 -metallic iron. On the analogy of O chondrites, matrix minerals in E chondrites should have been formed through condensation from and reaction with nebular gas. Mineral assemblage of the E chondrite matrix was achieved by neither condensation nor fractional condensation from the gas of solar system composition. They can be formed under high (> 1.2) C/O ratio⁷ which might be achieved by gas/dust fractionation before formation of solar nebula.⁶

Conclusions

The results show highly primitive nature of matrix materials and that the matrix minerals in chondrites of different chemical groups were formed at places of different gas/solid composition in the solar nebula. There is another possibility that all of matrix materials originated in the interstellar materials.⁸ In order to clarify this problem, further investigation combined with isotopic measurement of matrix materials is required.

References

1. H. Nagahara, "Evidence for secondary origin of chondrules," *Nature* 292: 135-136, 1981.
2. H. Nagahara, "Chondrules formed through incomplete melting of the pre-existing mineral clusters and the origin of chondrules," in E. King, Ed., *Chondrules and Their Origins*, Houston: Lunar Planet. Inst., 1983, 211.
3. D. W. Sears et al., "Measuring metamorphic history of unequilibrated ordinary chondrites," *Nature* 287: 791-795, 1980.
4. H. Nagahara, "Matrices of type 3 ordinary chondrites-primitive nebular records," *Geochim. Cosmochim. Acta* 48: 2581-2595, 1983.
5. L. Grossman, "Early chemical history of the solar system," *Rev. Geophys. Planet. Phys.* 12: 71-101, 1974.
6. J. W. Larimer and H. A. Bartholomay, "Gas-dust fractionation and the origin of chondritic meteorites," *Lunar Planet. Sci.* 14: 423, 1983.
7. J. W. Larimer and M. Bartholomay, "The role of carbon and oxygen in cosmic gases: Some implications to the chemistry and mineralogy of enstatite chondrites," *Geochim. Cosmochim. Acta* 43: 1455-1466, 1983.
8. J. A. Wood, "Meteoritic constraints on processes in the solar nebula," in D. C. Black, Ed., *Protostar and Planets II*, Tucson: University of Arizona Press (in press).

PROTON MICROPROBE ANALYSIS OF MASKELYNITE IN THE ZAGAMI METEORITE

J. H. Jones, T. M. Benjamin, C. M. Maggiore, P. S. Z. Rogers, C. J. Duffy, Mark Hollander, and James Conner

The shergottites are a group of young basaltic meteorites which may be samples of the planet Mars.¹ Although the shergottites are clearly young ($\leq 1.3 \times 10^9$ years), their exact ages are the subject of controversy. In particular it is not clear whether the $\sim 180 \times 10^6$ year Rb-Sr and Sm-Nd isochrons of Zagami (one member of the shergottite group) represent an igneous or metamorphic age.² If the 180 m.y. event is igneous, the shergottites are the youngest meteorites yet discovered.

We have argued previously that the preservation of major, minor, and trace element zoning in the major mineral phases of Zagami and other shergottites implies that the Rb-Sr and Sm-Nd ages are igneous.³ Otherwise, we would expect that the same processes which allowed metamorphic isotopic equilibration would have erased the traces of an earlier igneous history.

Here we reiterate our earlier conclusion and present new proton microprobe data for Zagami maskelynite. Table 1 shows representative core and rim analyses of a single maskelynite grain. Of the eight elements reported, only K, Rb, and Sr are equivocal--all others appear strongly zoned. Sr is probably unzoned because the bulk partition coefficient of Sr was near unity during the crystallization of the Zagami magma; alkali elements such as Na, K, and Rb are known to be zoned from other studies.⁴

In summary, it appears that Zagami is a very young igneous rock. The ubiquity of chemical zoning implies that metamorphism has not reset the Rb-Sr and Sm-Nd systems. The recent and complex igneous history of Zagami reinforces the hypothesis that the shergottites are martian.

TABLE 1.--Trace and minor elements in Zagami maskelynite.

	<u>CORE</u>	<u>RIM</u>
K	1860 \pm 790	3700 \pm 1400
Ti	324 \pm 19	534 \pm 35
Mn	46 \pm 4	130 \pm 8
Fe	3812 \pm 17	7546 \pm 37
Zn	6 \pm 1	11 \pm 2
Ga	38 \pm 2	60 \pm 4
Rb	3 \pm 1.5	7 \pm 3
Sr	134 \pm 7	166 \pm 12
All Concentrations in ppm		

Author Jones is at the Lunar and Planetary Laboratory of the University of Arizona, Tucson, AZ 85721. Authors Benjamin, Maggiore, Rogers, Duffy, and Hollander are in the Isotopic and Nuclear Chemistry Division of Los Alamos National Laboratory, Los Alamos, NM 87545. Author Conner is at the Department of Physics of the University of California at Davis, Davis, CA 95616.

References

1. D. D. Bogard and P. Johnson, "Martian gases in an Antarctic meteorite?" *Science* 221: 651-654, 1983.
2. C.-Y. Shih, L. E. Nyquist, D. D. Bogard, G. A. McKay, J. L. Wooden, B. M. Bansal, and H. Wiesmann, "Chronology and petrogenesis of young achondrites, Shergotty, Zagami, and ALHA77005: Late magmatism on a geologically active planet," *Geochim. Cosmochim. Acta* 46: 2323-2344, 1982.
3. J. H. Jones, T. M. Benjamin, M. Hollander, and J. Conner, "The youngest meteorites: II. Trace element zoning in Zagami maskelynite," *Lunar and Planetary Science* XVI: 410-411, 1985.
4. E. M. Stolper and H. Y. McSween, "Petrology and origin of the shergottite meteorites," *Geochim. Cosmochim. Acta* 43: 1475-1498, 1979.

PENWELL: UNUSUAL METEORITIC MATERIAL

Jim Clark, C. B. Moore, and C. F. Lewis

Penwell, a 543g meteorite, was found in the Spring of 1981 near Penwell, Ector County, Texas (31°45'13" N, 102°29'33" W). This location is approximately two miles SE of the Odessa Crater, leading immediately to the question of whether or not Penwell is an inclusion from the Odessa iron meteorite. Although exhibiting the basic texture and characteristics of a mesosiderite, Penwell is unusual in that it contains a large concentration of cliftonitic graphite.

Sample Description and Analytical Procedures

A polished thin section of Penwell was photographed by reflected and transmitted light simultaneously (Fig. 1). The white areas are silicates, the light-gray areas are metal phases, and the black areas represent both the graphite and oxides of Fe-Ni. All the silicate grains were identified by qualitative EDS spectra, after which a modal analysis consisting of over 16 000 points was performed on the section. The results show the surface area to be comprised of 20% silicates and 21% metal phases (kamacite, schreibersite, and very rare taenite); the remaining 59% is divided between graphite and oxidized metal in an approximate ratio of 3:2. The silicates consist of 34% clinopyroxene, 16% orthopyroxene, 29% olivine, and 20% plagioclase. Various other phases observed in minor amounts include chromite, magnetite, sphalerite, and troilite. Numerous grains of SiO₂

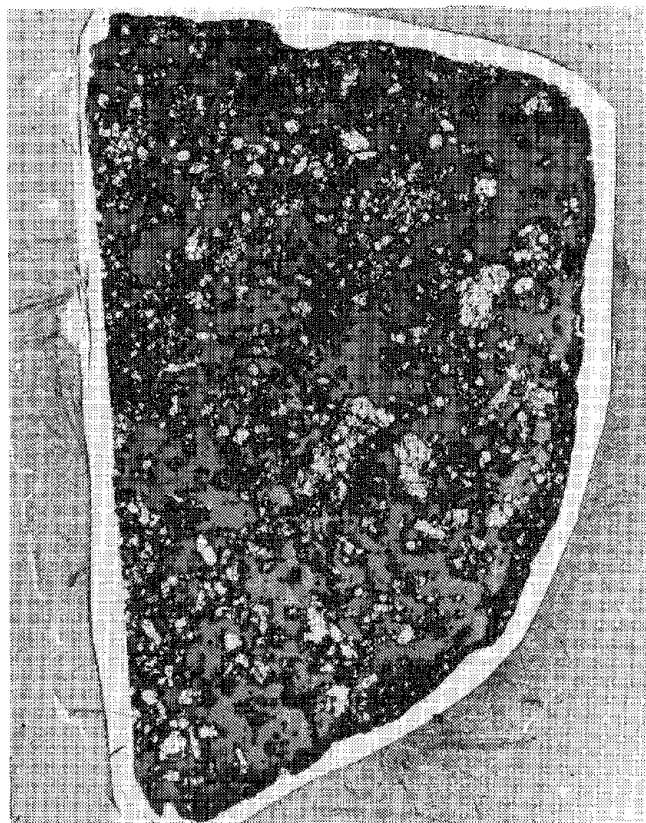


FIG. 1.--Thin section of Penwell photographed with reflected and transmitted light simultaneously.

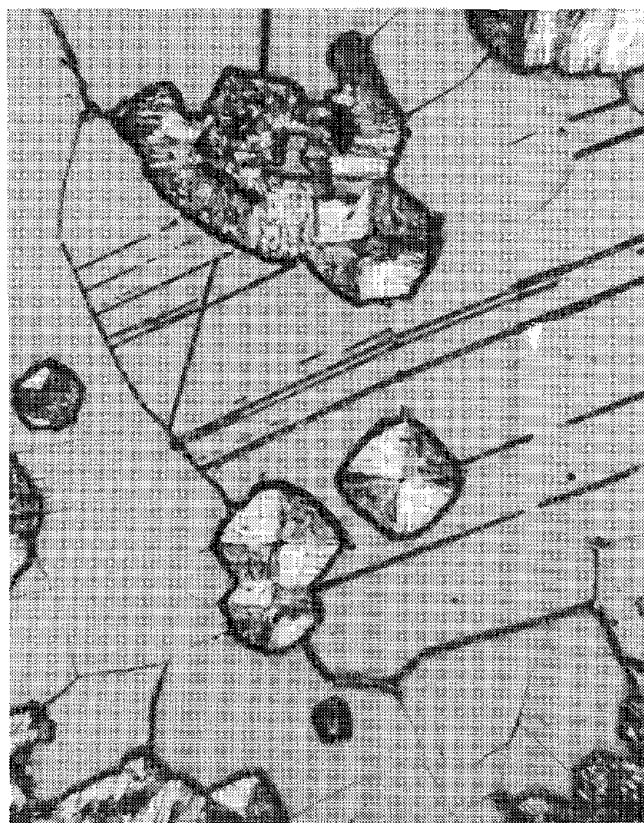


FIG. 2.--Cliftonite crystals in polarized reflected light.

Author Clark is with the Department of Chemistry, and authors Moore and Lewis are with The Center for Meteorite Studies, Arizona State University, Tempe, AZ 85287.



FIG. 3.--Backscattered-electron image of cliftonite crystals in various orientations.

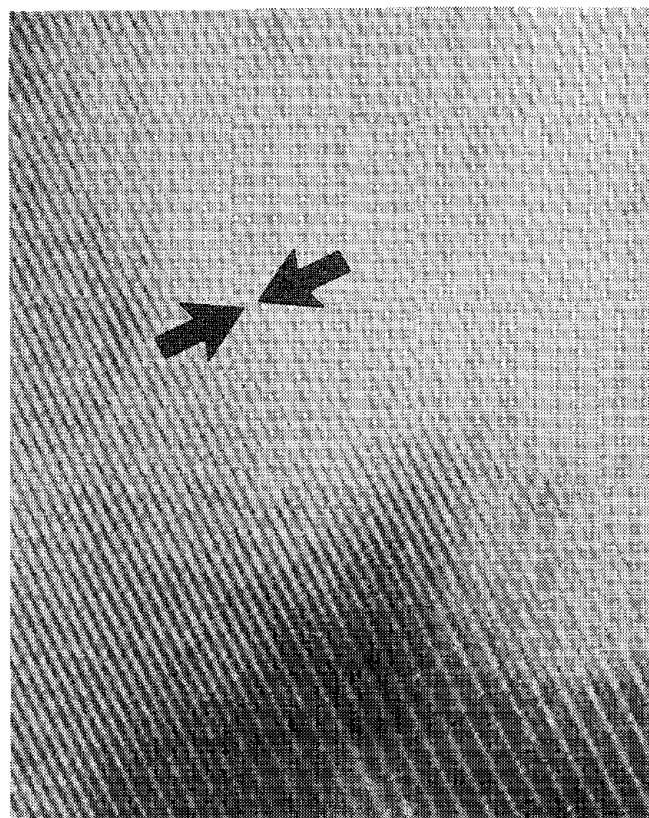


FIG. 4.--HRTEM image of cliftonite, d-spacing = 3.66 Å.

were observed in the section but are presumed to be an artifact of weathering, as they are all located within 0.5 mm of the outer surface.

Analyses of the major components in Penwell are given in Table 1. At least 15 separate points were averaged for each of the metal phases, and the average of at least 20 separate grains is given for each of the other minerals. Only the plagioclase, taenite, and schreibersite exhibit any significant variation in composition; all other phases are basically homogeneous throughout the section.

All analyses were performed on a Cameca MS-46 electron microprobe using a Tracor-Northern TN-2000 energy-dispersive analyzer. The microprobe was operated at 15 keV, with a specimen current of 20 nA as measured on Cu metal. A ZAF matrix correction scheme was employed for the metal analyses; Bence-Albee was used for all other phases.

Cliftonite in Penwell

Analyses performed with a LECO IR-12 gas chromatographic carbon analyzer show Penwell to contain 20.1% carbon by weight. Some of the carbon has the appearance of being ultra-fine-grained graphite, but the majority of the carbon is present in the form of cliftonite. Typical cliftonite crystals photographed in polarized reflected light are shown in Fig. 2; a JEOL JSM-35 scanning electron microscope was used to produce Fig. 3, a back-scattered-electron image that shows several crystals in various orientations. In both figures the crystals are situated in a field of kamacite. Discrete cliftonite crystals in Penwell are typically 10-200 μm .

A small amount of cliftonite was extracted from Penwell for observation on a JEOL 100-B transmission electron microscope. Figure 4 shows the cliftonite to have a d-spacing of 3.66 Å, which is intermediate in the range of spacings exhibited by various forms of graphite.

TABLE 1.--Electron microprobe analyses of Penwell.

	Olivine	Orthopyroxene	Clinopyroxene	Plagioclase	Chromite
Na ₂ O	n.d.	--	0.89	9.26	n.d.
MgO	52.93	34.61	18.05	--	9.59
Al ₂ O ₃	n.d.	0.34	0.83	21.06	2.26
SiO ₂	41.43	57.48	54.20	65.73	0.32
K ₂ O	n.d.	n.d.	n.d.	0.65	n.d.
CaO	n.d.	1.14	21.48	2.45	0.17
TiO ₂	n.d.	0.30	0.67	0.07	0.67
Cr ₂ O ₃	n.d.	0.25	1.16	n.d.	66.71
MnO	0.24	0.31	0.27	0.01	1.68
FeO	5.17	4.77	1.89	0.15	15.66
ZnO	n.d.	n.d.	n.d.	n.d.	2.40
Total	99.77	99.20	99.44	99.38	99.46
Mole % (Range)	% Fa = 5.2 (4.5 - 5.7)	% Fs = 7.0 (6.5 - 7.5)	% Fs = 3.1 (2.7 - 3.6)	% An = 11.7 (7.9 - 14.9)	

	Kamacite	Taenite	Schreibersite
Fe	92.73	54.94	43.30
Ni	6.68	44.95	41.40
P	n.d.	n.d.	15.00
Total	99.41	99.89	99.70
% Ni Range	(6.3 - 7.2)	(25.9 - 54.1)	(31.3 - 52.5)

n.d. = not determined.

TABLE 2.--Comparison of Penwell to Odessa silicate inclusions.

	Penwell	Odessa ²
Olivine (% Fa)	5.2	3.5
Orthopyroxene (% Fs)	7.0	6.5
Clinopyroxene (% Fs)	3.1	2.7
Plagioclase (% An)	11.7	9.2
Kamacite (% Ni)	6.7	4.5 (Inclusions) 6.3 (Matrix)

Origin of Penwell

Brett and Higgins have proposed that cliftonite is formed through the thermal decomposition of cohenite.¹ Calculations show that this mechanism requires a kamacite:graphite volume ratio of approximately 4:1. The disproportionate abundance of cliftonite in Penwell would indicate that in order for this model to hold, an original kamacite-rich portion of the meteorite parent body is required to provide a proper material balance. Due to the close proximity of the Penwell find to Odessa Crater, the Odessa iron is the most likely candidate for such a parent body. A comparison between various minerals in

Penwell and those from Odessa silicate inclusions is given in Table 2. The values from Penwell place it in the category of Odessa-type silicate inclusions as classified by Bunch et al.,² yet these data are not sufficient to determine unequivocally whether or not Powell is an inclusion from the Odessa iron. Further research is needed to resolve this problem.

References

1. R. Brett and G. T. Higgins, "Cliftonite in meteorites: A proposed origin," *Science* 156: 819-820, 1967.
2. T. E. Bunch and K. Keil, "Mineralogy and petrology of silicate inclusions in iron meteorites," *Contrib. Mineral. Petrol.* 25: 297-340, 1970.

MICROBEAM ANALYSES OF STRATOSPHERIC PARTICLES

I. D. R. Mackinnon, F. J. M. Rietmeijer, D. S. McKay, and M. E. Zolensky

Collections of solid particles from the Earth's stratosphere by high-flying aircraft have been reported since 1965,¹ with the initial primary objective of understanding the nature of the aerosol layer that occurs in the lower stratosphere. With the advent of efficient collection procedures² and sophisticated electron- and ion-beam techniques,³ the primary aim of current stratospheric collections has been to study specific particle types that are extraterrestrial in origin and have survived atmospheric entry processes.⁴ The collection program provided by NASA at Johnson Space Center (JSC) has conducted many flights over the past 4 years and retrieved a total of 99 collection surfaces (flags) suitable for detailed study. Most of these collections are part of dedicated flights and have occurred during volcanically quiescent periods, although solid particles from the El Chichón eruptions have also been collected.⁵ Over 800 individual particles (or representative samples from larger aggregates) have been picked from these flags, examined in a preliminary fashion by SEM and EDS, and cataloged⁶ in a manner suitable for selection and study by the wider scientific community.

The curation and cataloging of all particle types retrieved through the JSC program provides a unique opportunity to study not only the more exciting and (for NASA) important extraterrestrial particles, but also the natural and anthropogenic fractions of solid particles in the stratosphere over various periods of time. A wide range of particles have been studied in detail at JSC using electron beam techniques including AEM, SEM/EDS EELS, backscattered imaging, and quantitative bulk chemical analysis. Some particles, particularly the chondritic porous (CP) aggregates, present a considerable challenge to the analyst as they may contain many thousands of individual particles (of unknown mineralogy) ranging in size down to less than 15 nm. We present below a few typical examples of our studies on both extraterrestrial and terrestrial particles collected from the stratosphere.

Experimental

General procedures for sample preparation of CP aggregates for AEM analysis have been outlined by Bradley and Brownlee,⁷ except that a thick carbon film was used in addition to a holey carbon film supported by Cu mesh grids. Most aggregates studied at JSC are mounted only on holey carbon films supported by Be (150-mesh) grids and washed in situ with hexane. Silicone oil is used on the collector plates and is removed from particle surfaces by gentle washing with hexane. For all particles, conductive surface coatings (e.g., Au, Au/Pd, or C) are not applied in order to minimize the possibility of contamination during the coating process⁸ or the production of spurious artifacts in SEM images.⁹ Unfortunately, for spherical particles, the lack of a conductive surface coating increases the likelihood of charge build up and consequent loss of the particle. Charge build up is a significant problem for SEM imaging at operating voltages between 10 and 20 kV. We have found that charge build up on nonconducting particles (e.g., Al₂O₃ spheres) can be minimized when higher voltages are used (e.g., 40 kV).

Most analytical data have been obtained on a JEOL 100CX AEM with a PGT System IV EDS and a Gatan EELS attached. The microscope column has been modified to reduce spectral contamination of EDS analyses following the procedures of Allard and Blake.¹⁰ Additional improvements to the reduction of spurious x rays have included the use of a modified single tilt, carbon bulk specimen holder suitable for TEM studies. A significant improvement in the "in hole" count after these modifications can be seen in the EDS spectra

Authors Rietmeijer, McKay, and Zolensky are with the Solar System Exploration Division, Johnson Space Center; author Mackinnon is with the Department of Geology, University of New Mexico, Albuquerque, NM 87131, and Microbeam Inc. Technical support from A. M. Isaacs, F. Rietmeijer-Engelsman, and G. A. Robinson is appreciated. This work has been supported by NASA contracts NAS9-16768, NAS9-17005, and T-9077K to Microbeam Inc., as well as through postdoctoral awards to FJMR and MEZ from the National Research Council.

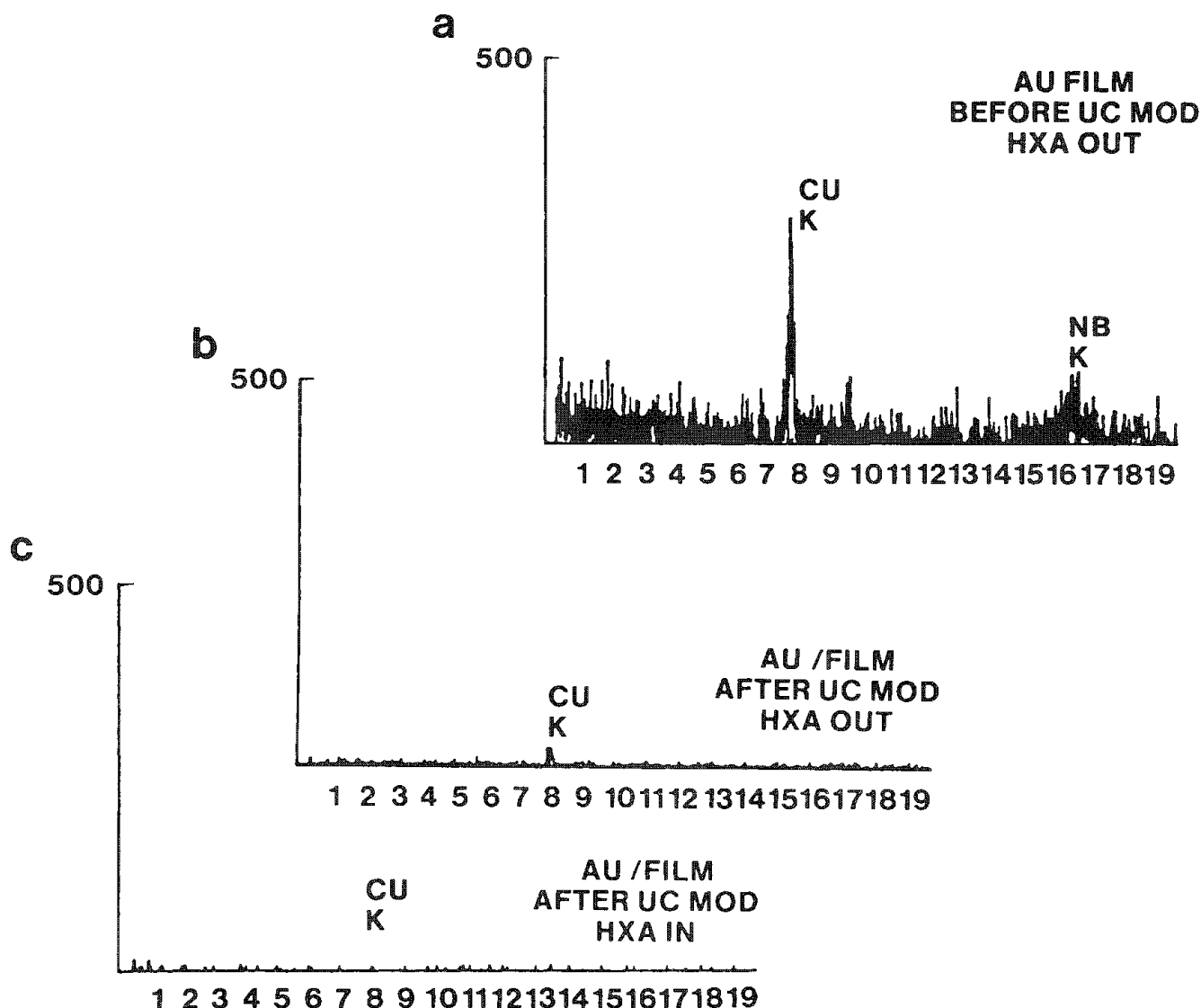


FIG. 1.--In-hole x-ray spectra for JEOL 100CX AEM (a) before modification, (b) after upper-column modification, (c) after all modifications.

shown in Fig. 1. Figure 1(a) shows a spectrum obtained before any column modifications to the AEM for a minimum beam size ~ 10 nm (STEM mode), a hole size < 1 μm , and a counting time of 500 s. Spectra taken under the same conditions (shown at the same scale) after upper column modifications, and after all modifications have been made, are shown in Figs. 1(b) and 1(c), respectively.

Observations

CP aggregates have been studied in detail by a number of techniques and noble gas,¹¹ isotopic,¹² bulk chemical,¹³ and mineralogical^{4,14,15} data provide strong evidence for an extraterrestrial origin. Figure 2 shows an unusual carbon-rich particle which occurs in a large ($\sim 60 \mu\text{m}$) CP aggregate identified as W7029*A. This particle is relatively large ($\sim 0.3 \times 0.5 \mu\text{m}$) compared to many others which occur in this aggregate, and has a smooth and coherent texture; and windowless EDS and EELS analysis indicates that only carbon is present. Interplanar spacings from an SAED pattern of the carbon particle (Fig. 2a, inset) do not correspond to spacings commonly observed in graphitized or partially graphitized carbons. However, high-resolution images from the rim of this grain (arrowed, Fig. 2a; Fig. 2c) show distinct lattice fringes of 0.34 nm, which agree well with the typical d_{002} basal spacing of graphite. Graphitized carbons are observed in this CP aggregate,¹⁶ but usually as discrete clusters of individual grains showing measurable SAED patterns and

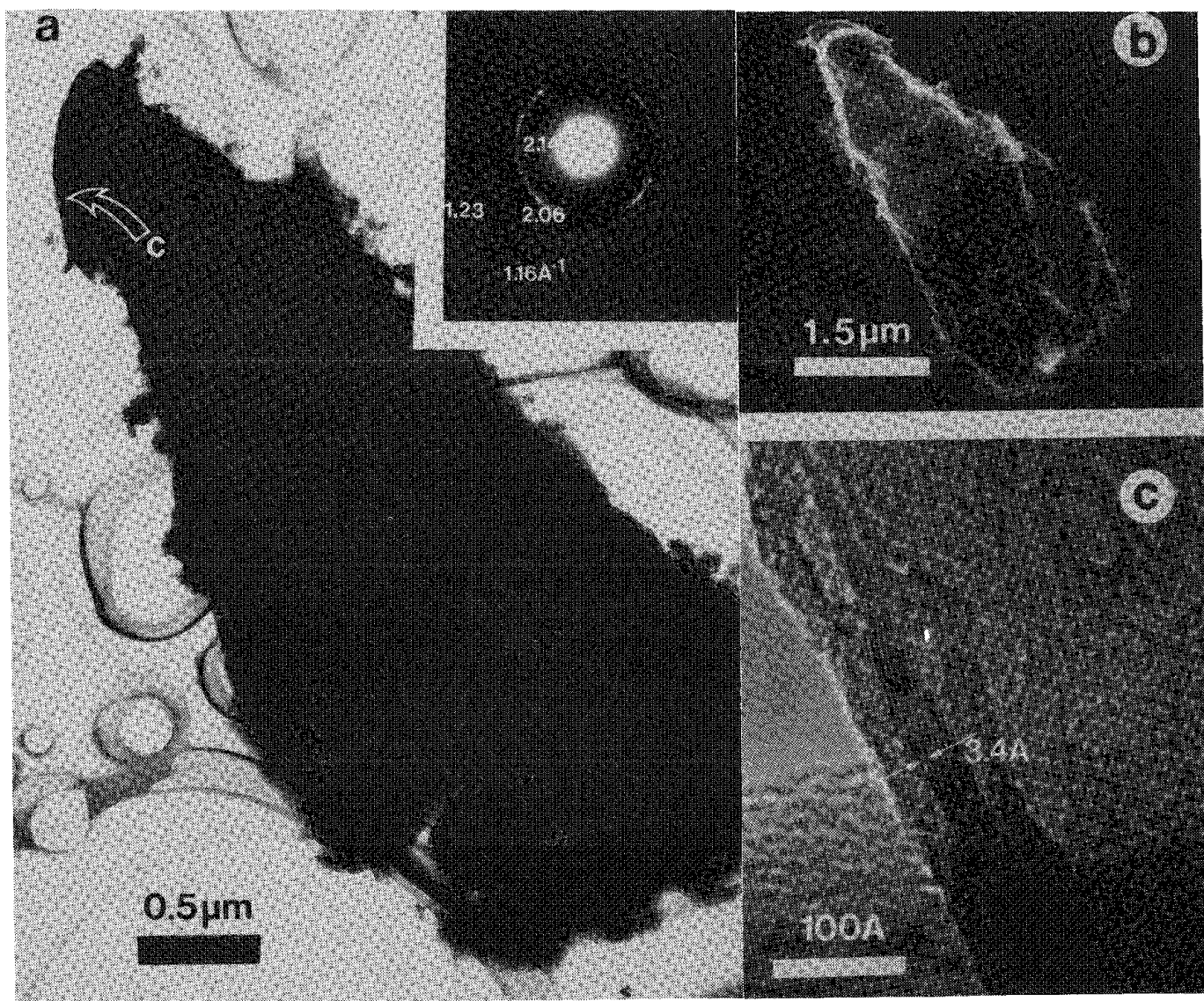


FIG. 2.--Unusual carbon-rich particle from interplanetary CP aggregate: (a) conventional TEM image with SAED pattern (inset), (b) complementary SEM image showing smooth surface texture, (c) HREM image of grain rim showing 0.34nm lattice fringes.

grain sizes up to 50 nm. The carbon grain shown in Fig. 2 may be an example of precursor carbon (or hydrocarbon) material that has begun to undergo graphitization at the grain rims due to an increase in temperature and/or the presence of a catalyst^{16,17} prior to collection in the stratosphere.

The bulk of anthropogenic particles collected from the stratosphere are aluminum-rich and show a range of morphologies and limited compositional variation.¹⁸ An interesting subset of aluminum-rich particles include Al metal and Al₂O₃ spheres which are shown to be exhaust from solid-fuel rocket motors.^{2,19,20} Another abundant particle is termed an aluminum-prime particle because it contains not only a high proportion of Al, but also a significant amount of other high-atomic-number (Z) elements. A typical example of an aluminum-prime particle is shown in Fig. 3, and the corresponding bulk EDS analysis is shown in Fig. 4. Backscattered imaging from this particle shows that the high-Z elements are not homogeneously distributed throughout the aggregate. Chemical data inferred from backscattered imaging for a wide range of Al-prime particles, as well as morphological characteristics, suggest that some Al-prime particles are ablation products from solid-fuel rockets or coatings of spacecraft.

Spherical particles comprise almost a third of the cataloged stratospheric collection at JSC¹⁸ and many can be considered ablation products from earth-crossing meteors. This is the case for predominantly Fe-Ni-S and Fe-Ni spheres, which show a size range, morphology, and composition similar to spheres observed on meteorite fusion crusts.²² In cases where fusion crust spheres are broken open, it appears that some spheres are hollow,²² which suggests that some ablation products that remain in the stratosphere for collection may also be hollow. Further support for the presence of hollow spheres in the stratosphere is provided by detailed studies of spheres from ice cores in Greenland and from the remains of an iron meteorite shower in Siberia.²³ A hollow morphology would considerably affect bulk density and may influence the relative settling rate for this type of particle. For example, a 10 μm -diameter sphere with density 2.5 g.cm⁻³ may reside in the aerosol layer for at least 20 days, if it were to settle from 35 km to a collection altitude of 18 km.²⁴ Hollow spheres of the same diameter but lower density (e.g., an estimated value of 0.1 g.cm⁻³) may take up to 140 days to settle through the same column height in the lower stratosphere.

The JSC dust collection has also been a valuable resource for the study of volcanic ash clouds and their influence on the lower stratosphere. The eruptions of El Chichón volcano in Mexico injected large volumes of ash into the stratosphere through March and April 1982.⁵ The resulting cloud which circled the Earth was subsequently sampled through the NASA Cosmic Dust Program over a range of latitudes and at regular time intervals. An example of the volcanic ash still in the stratospheric cloud in May 1982 is shown in Fig. 5. The particles show typical shard morphologies and are as large as 10 μm . Smaller particles also adhere to large grains and appear to predominate in samples taken later in 1982. A comparison of grain size and morphology with sampling interval has also provided experimental confirmation of the average settling rate for ash particles in the stratosphere.²⁵

Summary

A wide range of particle types 2-60 μm in size have been collected from the lower stratosphere by high-flying aircraft. A significant proportion of these particles are extraterrestrial in origin and the CP aggregates are among the most complex in terms of grain size, morphology, and mineralogy. All these stratospheric particles require electron-beam techniques for reliable characterization. An understanding of all particle types within the stratosphere provides a sound basis for the identification and interpretation of extraterrestrial particles and their provenance. Knowledge of the temporal and spatial distribution of specific particle types,²⁰ as well as the interactions of solid particles with aerosols,²⁴ also provide a firm experimental basis for the development of reliable stratospheric models.

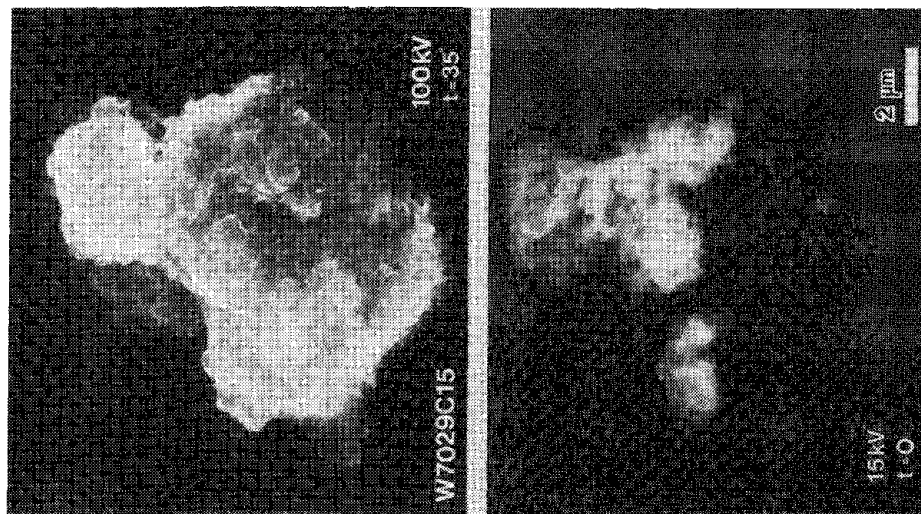


FIG. 3.--(a) SEM and (b) back-scattered image of typical Al-prime particle.

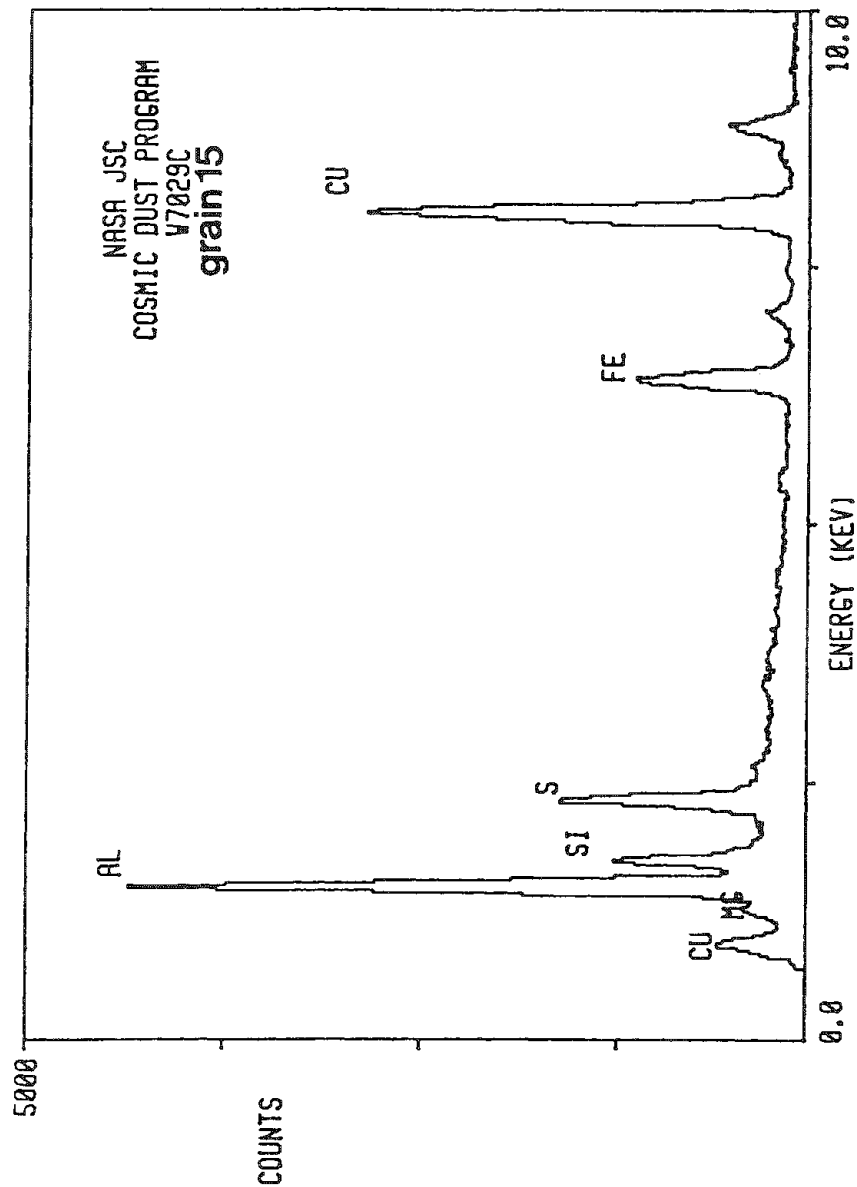


FIG. 4.--Bulk EDS x-ray spectra for particle shown in Fig. 3. Cu peak is not due to spurious column x rays.

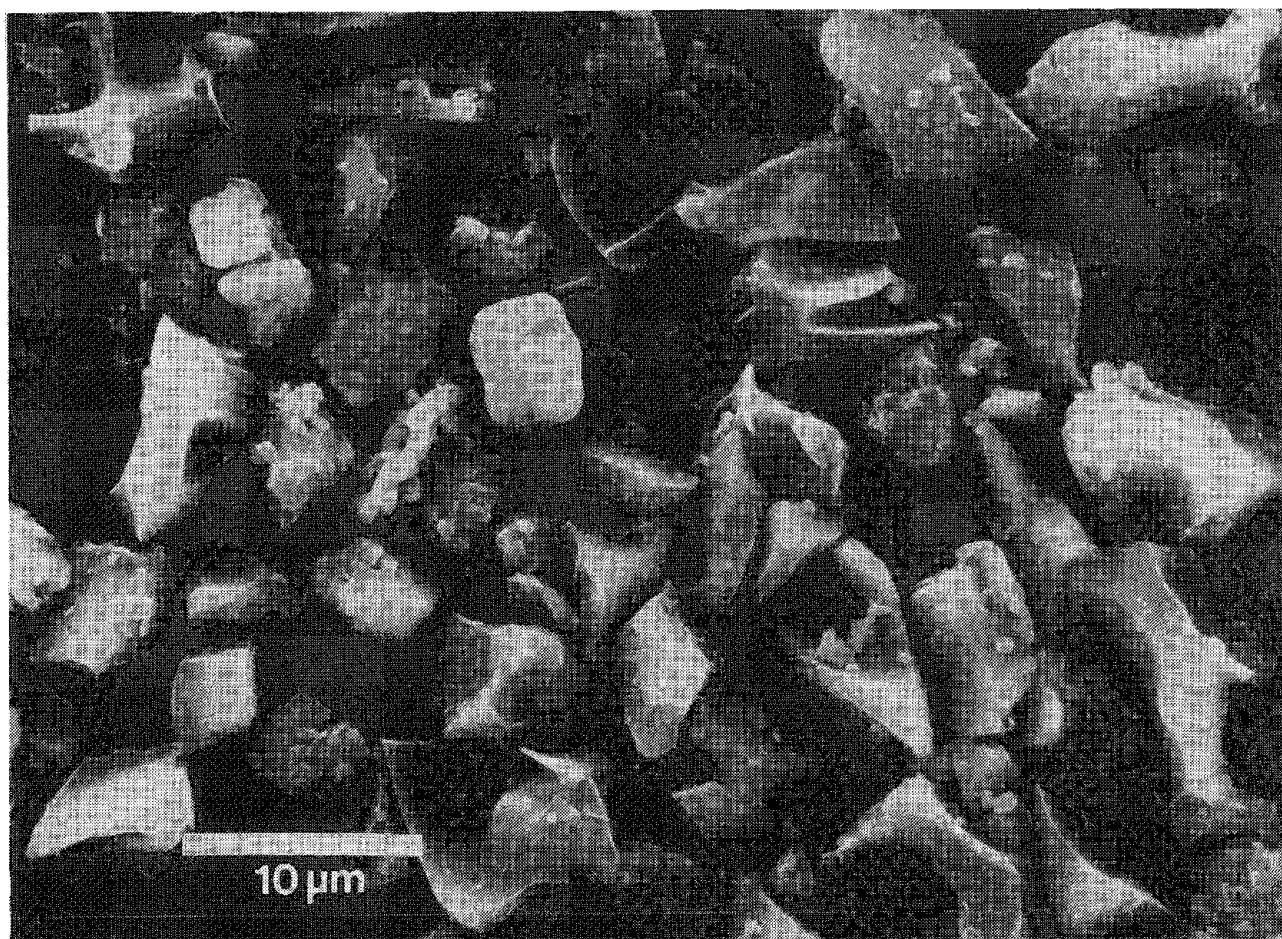
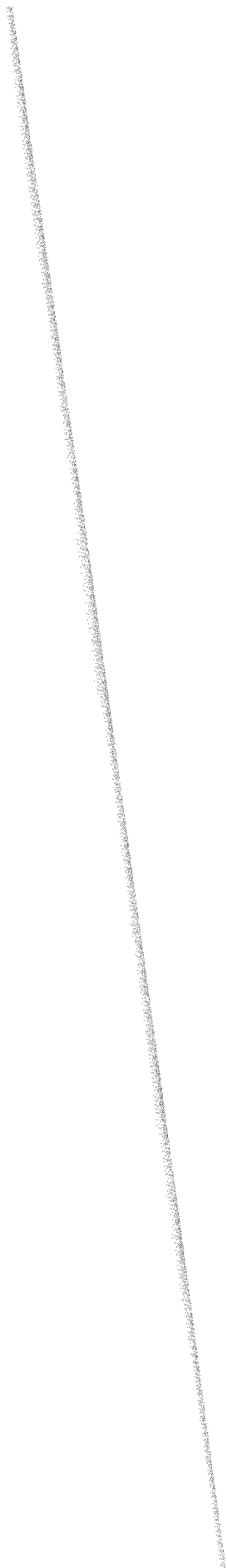


FIG. 5.--Low-magnification SEM image of El Chichón volcanic ash collected from stratosphere.

References

1. S. C. Mossop, "Stratospheric particles at 20km altitude," *Geochim. Cosmochim. Acta* 29: 201-207, 1965.
2. D. E. Brownlee, G. V. Ferry, and D. A. Tomandl, "Stratospheric aluminum oxide," *Science* 191: 1270-1271, 1976.
3. T. M. Esat, D. E. Brownlee, D. A. Papanastassiou, and G. J. Wasserburg, "The Mg isotopic composition of interplanetary dust particles," *Science* 206: 190-191, 1979.
4. J. P. Bradley, D. E. Brownlee, and P. Fraundorf, "Discovery of nuclear tracks in interplanetary dust," *Science* 226: 143-1434, 1984.
5. J. L. Gooding, U. S. Clanton, E. M. Gabel, and J. L. Warren, "El Chichón volcanic ash in the stratosphere: Particle abundances and size distributions after the 1982 eruption," *Geophys. Res. Lett.* 10: 1033-1036, 1983.
6. U. S. Clanton, C. B. Dardano, E. M. Gabel, J. L. Gooding, A. M. Isaacs, I. D. R. Mackinnon, D. S. McKay, G. A. Nace, and J. L. Warren, *Cosmic Dust Catalog*, NASA JSC Curatorial Branch Pub. 62, 1982.
7. J. P. Bradley and D. E. Brownlee, "Microanalyses of dispersed interplanetary dust particles," *Microbeam Analysis--1983*, 187-190.
8. F. J. M. Rietmeijer, "A poorly graphitized carbon contaminant in studies of extraterrestrial materials," *Meteoritics* 20: 43-48, 1985.
9. C. Beaton and B. Filshie, "Stereoscopic examination of the fine structure of some metal coatings used for scanning electron microscopy," *JEOL News* 20E: 23-27, 1982.
10. L. F. Allard and D. F. Blake, "The practice of modifying an analytical electron microscope to produce clean x-ray spectra," *Microbeam Analysis--1982*, 8-20.
11. B. Hudson, G. J. Flynn, P. Fraundorf, C. M. Hohenberg, and J. Schirck, "Noble gases in stratospheric dust particles: Confirmation of extraterrestrial origin," *Science* 211: 383-386, 1981.

12. E. Zinner, K. D. McKeegan, and R. M. Walker, "Laboratory measurements of D/H ratios in interplanetary dust," *Nature* 305: 119-121, 1983.
13. P. Fraundorf, D. E. Brownlee, and R. M. Walker, "Laboratory studies of interplanetary dust," in L. L. Wilkening, Ed., *Comets*, Tucson: University of Arizona Press, 1982, 383-412.
14. J. P. Bradley, D. E. Brownlee, and D. R. Veblen, "Pyroxene whiskers and platelets in interplanetary dust: Evidence for vapor phase growth," *Nature* 301: 473-477, 1983.
15. I. D. R. Mackinnon and F. J. M. Rietmeijer, "Bismuth in interplanetary dust," *Nature* 311: 135-137, 1984.
16. F. J. M. Rietmeijer and I. D. R. Mackinnon, "A new cosmo thermometer for primitive extraterrestrial materials: Poorly graphitized carbon," *Nature*, in press.
17. A. Oja and H. Marsh, "Phenomena of catalytic graphitization," *J. Mat. Sci.* 17: 309-322, 1982.
18. I. D. R. Mackinnon, G. A. Nace, A. M. Isaacs, and D. S. McKay, "Classification of the JSC stratospheric dust collection," *J. Geophys. Res.* 87: A413-A421, 1982.
19. L. D. Strand, J. M. Bowyer, G. Varsi, E. G. Laue, and R. Gaudlin, "Characterization of the exhaust particulates in the ground cloud and high altitude plume of large solid propellant booster rockets," *AIAA 18th Aerospace Sci. Meet.*, Pasadena, Calif., 1980, 1-15.
20. M. E. Zolensky and I. D. R. Mackinnon, "Accurate stratospheric particle size distribution from a flat-plate collection surface," *J. Geophys. Res.*, in press.
21. I. D. R. Mackinnon, D. S. McKay, G. A. Nace, and A. M. Isaacs, "Al-prime particles in the cosmic dust collection: Debris or not debris?" *Meteoritics* 17: 245, 1982.
22. F. J. M. Rietmeijer and I. D. R. Mackinnon, "Melting, ablation and vapor phase condensation during atmospheric passage of the Bjurbole meteorite," *J. Geophys. Res.* 89: B597-B604, 1984.
23. F. W. Wright, P. W. Hodge and C. C. Langway Jr., "Studies of particles for extraterrestrial origin," *J. Geophys. Res.* 68: 5575-5587, 1963.
24. I. D. R. Mackinnon and D. W. Mogk, "Surface sulfur measurements on stratospheric particles," *Geophys. Res. Lett.* 12: 93-96, 1985.
25. I. D. R. Mackinnon, J. L. Gooding, D. S. McKay, and U. S. Clanton, "The El Chichón stratospheric cloud: Solid particulates and settling rates," *J. Volcanol. and Geotherm. Res.* 23: 125-146, 1984.



Microanalysis Mass Spectrometry—Laser and Ion Microprobes

QUANTITATIVE LASER MICROPROBE MASS SPECTROMETRY: POTENTIAL AND CONSTRAINTS

Thad Mauney

Laser microprobe mass spectrometric analysis (LAMMA) provides a probe of elemental and molecular composition at the micron spatial scale, with analytical sensitivity to as few as a thousand atoms in the excited volume. Such sensitivity and spatial resolution combine with the wealth of information provided by a mass spectrum to provide an excellent tool for investigation of scarce or high-value samples, micron-sized particulate samples, and biomedical specimens with important microscopic features. The information required in each investigation is specific to the context, but it is generally true that quantitative information is an important adjunct to qualitative spectral information, if not an essential part of the investigation.

LAMMA has been proven as a qualitative tool, and has shown some promise as a quantitative tool; however, the hopes of early investigators for straightforward quantitative protocols have not generally been fulfilled. Several workers have presented straight-line calibration curves spanning several orders of magnitude in concentration.¹⁻³ These curves have been supplemented by estimates of relative sensitivity coefficients (RSFs) for the several elements in various matrices,^{2,4} and correction equations for the ionization conditions have been developed, based on the local thermal equilibrium approach.³⁻⁵ In actual practice, these approaches to quantitation have not proved useful if extended outside the narrow set of samples for which they were developed, and it is not yet standard practice to calibrate an instrument and then quantitate an unknown sample.

An excellent demonstration of quantitative technique was presented by Schroeder et al. in analysis of retinal tissue.^{6,7} By meticulously incorporating isotopic dilution standards into the samples analyzed and exacting stringent controls on the analytical conditions, they were able to determine the concentrations and concentration ratios of metabolically important alkali ions with micron spatial resolution. Development of the requisite standards and protocols required investment of several years of work; even so, these standards and protocols cannot be directly generalized to other samples or elements.

The author's experience is that although the instrument can yield suitably reproducible spectral intensity data for selected samples and conditions, subtle changes in conditions can result in radical changes in signal and alter both absolute and relative intensities. Further, significant random and bias errors are introduced into the results without warning. The result is that the temptation to make quantitative comparisons is great, but thoughtful examination of the data from week to week forces one to the realization that not enough is yet known about the measurement event to justify hasty interpretations.

Wieser, Wurster, and Wechsung have published an excellent discussion of the approaches to quantitation, and the considerations required in each approach,³ but have left open the problem of bringing the various approaches to practical fruition. The present paper explores the many aspects of the instrument and the physical and chemical processes involved in each LAMMA measurement, and is intended to provide portions of groundwork from which the techniques for quantitative LAMMA analysis can be based.

Numerous aspects of the analytical process can be identified as influencing recorded signal intensity, and thus as being important to quantification. Each of these aspects is subject to scientific characterization: if the causes for instrumental nonquantitativeness can be understood, they can largely be controlled. This paper lists several of these sources of measurement error and concludes with a list of suggestions for the basis of quantitative analytical protocols.

Sample Variability

Point-to-point variation in composition of the sample must affect the resultant

The author is with GeoResearch, Inc., 2815 Montana Avenue, Billings, MT 59101. This work was conducted at the University of Antwerp (UIA), B-2510 Wilrijk, Belgium, with support through grant 80/85-10 from the Belgian Interministerial Commission on Science Policy. The author thanks Fred Adams of the UIA for his continuing discussions on this work.

signal, for this is often the matter of interest in microanalysis. This variation may also arise from unexpected or random sources and result in measurement error. The volume analyzed varies with sample thickness or particle volume. With vapor-deposited carbon films, relative standard deviation in signal intensity around 5% could readily be achieved. In contrast, fine carbon particles yielded signals varying over several orders of magnitude due to their variation in size and their clumping together.

Another source of variation is random distribution of analyte atoms or molecules in a homogeneous medium. In noncrystalline materials without cooperativity or repulsion, trace constituents are approximately Poisson distributed over the volume elements; if the detection limit approaches a few tens or hundreds of atoms in the analyzed volume, the variance can become several percent of the signal (see, for example, Ref. 8).

Energy Deposition in the Sample

Mean energy available to the sample molecules is the time integral of laser intensity, less reflection and transmission losses, divided by the number of excited molecules. Intensity, transmittance, and reflectance are not constant over time or space, nor from sample to sample. This energy is partitioned into vaporization, ionization, and expansion. Both the volume analyzed and the ionization efficiency vary if the energy deposited varies. There is some inevitable variation in laser intensity. There is also large potential for variation in energy deposition if the laser is not reproducibly focused. For example, much of Surkyn's difficulty in achieving low standard deviations in measurements on NBS research-material glass-sphere standards⁴ probably arose from the difficulty of defining a true focus condition on a transparent sphere with a diameter of the order of the beam diameter. Surkyn also found that even the gross appearance of the spectra depended on the position of laser focus as well as on laser intensity.

Ion-formation Processes

Ideally, ions would be formed in concentrations approaching a local thermal equilibrium, and then detected with equal efficiency. Unfortunately, chemical and physical effects override this simplicity. It has been shown that different ionic species may be extracted with different kinetic energies.^{9,10} For example, for TiO₂ film, the median kinetic energies for some species were:

Ion	Kinetic Energy (eV)
Ti ⁺	-40
TiO ⁺	-75
Ti ₂ O ₂ ⁺	-90

These differences suggest formation of these species in different regions of the plasma plume. These regions presumably differ in temperature and stoichiometry, so that relative signal intensity depends on the chemistry of the entire plasma cloud, as well as on sample composition.

Denoyer observed transfer of O from aluminum and silicon oxides to reduced sulfur species, forming SO₄⁻; ¹¹ but in selected matrices, Bruynseels has been able to discriminate between oxidation states of sulfur.¹² Combination ions formed from physically separated sample components have been observed in carbon films¹³ and in metal films.¹⁴

In some cases, ions may also decay. Rosmarinowski and Hillenkemp¹⁵ have reported metastable decomposition of C_n⁻ to neutrals. Though only small fractions decayed in that case, spectral intensities can be influenced by decay during the 20-50 μs of flight time.

Even a correctly focused laser beam does not illuminate a disk with uniform intensity. Ideally, the beam tends toward a Gaussian profile.¹⁶ The center of the beam may produce "plasma mode" ionization; the fringes are intense enough to result in "laser desorption" ionization. In analyzing soot particles for polycyclic aromatic hydrocarbons, on its most intense setting, the laser beam could ionize particles as far as 10 μm from its center.¹⁷ Ions formed in the fringe necessarily experience different chemical and thermal conditions from those formed in the beam center, and may have different kinetic energy.

The sodium and potassium peaks arising from impurity in carbon film substrates were found to have delayed shoulders (Fig. 1).¹⁸ These delayed ions had kinetic energies between +3 and -17 eV, whereas the main peak had kinetic energy centered less than -17 eV. The delay must derive from late formation since arrival time is corrected for kinetic energy.

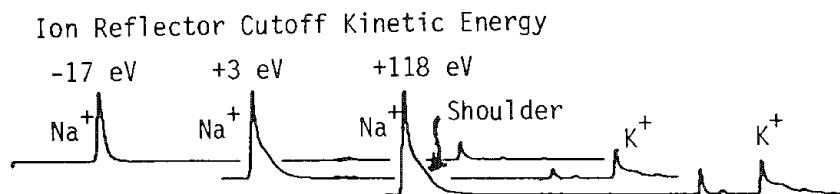


FIG. 1.--Shoulder on Na^+ and K^+ peaks. Cutoff kinetic energy is expressed as equivalent initial kinetic energy relative to a grounded sample.

These delayed ions of near-zero initial kinetic energy may derive from thermal ionization of the fringe zone of the laser beam, which is still intense enough to produce a puckered halo in the carbon foil.

Extraction

Because the extracting electrostatic field is formed over a gap of only about 6 mm, homogeneity of this field depends on the symmetry of the surfaces of the sample and holder. Edge effects from the sample holder can radically influence signal strength.¹⁸ A 40-fold reduction in signal intensity was observed in moving from the center to the edge of a specimen of vapor deposited carbon film 25 nm thick (Fig. 2). A new sample holder was machined with no o-ring groove and a sharper edge. The new sample holder resulted in more uniform response over the central portion of the sample, as also shown in Fig. 2, but very close to the edge roughly similar attenuation occurred. Presumably the nonuniform field near the step at the sample holder edge causes the ion packet to travel off the spectrometer axis. The magnitude of this effect is not equal for all ions in a spectrum and so relative intensities also are perturbed.

One can minimize the spectral effects of ion extraction by selecting the central portion of the sample, and by selecting or preparing a sample holder with very sharp and uniform edges. In the case of 'reflecting geometry' instruments such as LAMMA 1000 and LIMA, the problem should be minor for flat smooth specimens, but could be quite important for irregular samples. The specimen may yield a measurable spectrum, but its relative and absolute intensities would not necessarily be comparable to other specimens or locations on the same specimen.

Transmission

The ion lens that serves to collimate the ion beam and thereby improves the transmittance of the spectrometer is inevitably subject to chromatic aberration--dependence of the focal length on ion kinetic energy.

In a system employing such ion lenses, two sources of measurement variability arise: lens aberration and focusing errors. Ion lenses are recognized as having far worse spherical and chromatic aberration than have optical lenses.

Chromatic aberration in the ion lens is capable of truncating the ion kinetic energy distribution of ions extracted from the laser plasma. The extent to which this effect occurs depends on the effective energy bandpass of the ion optical system (Fig. 3).

Degradation of spectral information due to incorrect selection of the ion lens potential is readily observed. As an example, Fig. 4 shows averages of ten spectra of oil shale retort soot obtained at two lens potentials. The lens potential at 1980 V eliminated the peak above $m/e = 250$, which were assigned as polycyclic aromatic hydrocarbon molecular ions, yet these ions were consistently present in the spectra obtained at a lens potential of 1930 V.

The chromatic aberration of the ion lens limits the kinetic energy band of the ions detected, but in practice the limits may be sufficiently broad so that most ions extracted from the source are transmitted. If the ion lens potential is not optimized for the actual distribution of kinetic energies of ions extracted, signal strength is lost. If the energy passband lies off the center of the actual distribution, and its location is not determined, then undetermined errors in relative signal intensity may result from the filtering effect.

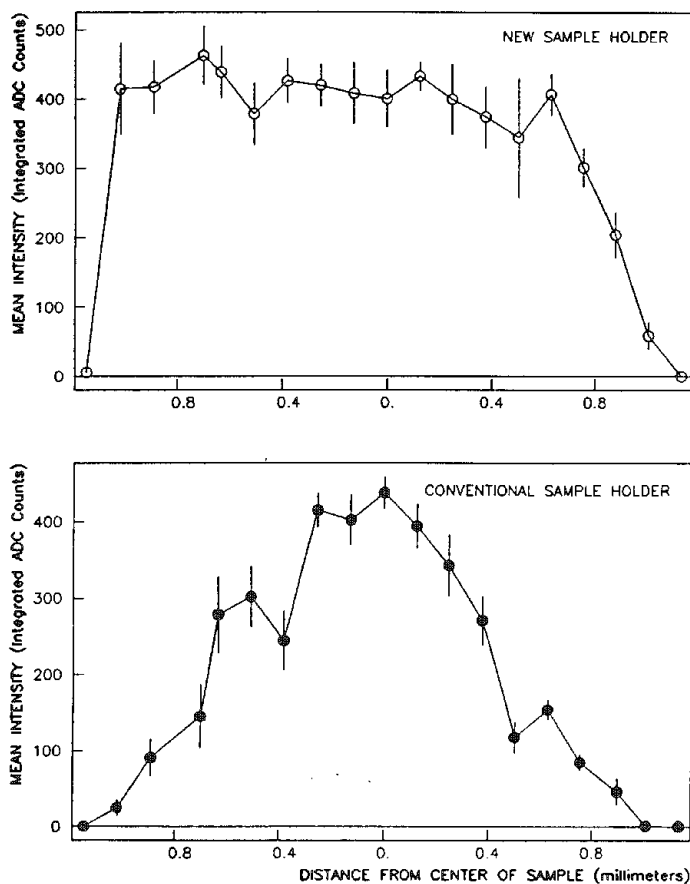


FIG. 2.--Effect of lateral sample position on signal intensity. Intensities are means of ten measurements at each point in line across entire accessible portion of carbon film specimen.

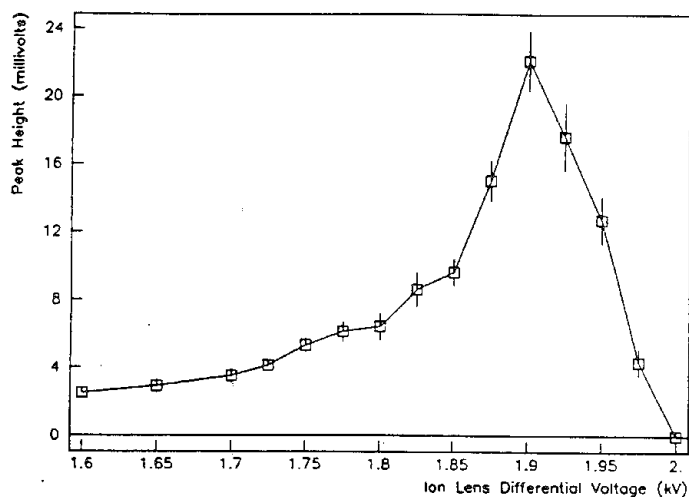


FIG. 3.--Effect of ion lens potential on intensity of $m/e = 24$ peak in negative ion spectra of carbon, measured at 3000 V accelerating potential and -110 V reflector potential. Each point represents mean of ten measurements.

Detection

An electron multiplier is an excellent but nonideal ion detector. Three sources of variation arise in detection: arrival shot noise, amplification shot noise, and conversion efficiency.

- Ion arrival is approximately a Poisson-distributed random process. At a conversion gain of 10^6 , a single ion arrival results in a pulse giving about 4 integrated counts in the transient recorder (Biomation 8100). Therefore, the smallest detected peaks can derive from only a few ion arrivals and have the attendant Poisson statistics: standard deviation equals square root of the mean.

- Amplification is not a deterministic process, but is itself a stochastic process. Additional variance is thus introduced, though smaller than that due to arrival statistics.

- Cathode conversion efficiency is not uniform, nor is it a simple function of ionic mass. In SIMS, Rudat showed differences in electron yield between ions of adjacent mass as great as between ions of widely different mass.¹⁹ With lower ion kinetic energy, LAMMA may have greater susceptibility to conversion efficiency discrimination than SIMS, but this property has not yet been quantified.

Spectrum Recording and Integration

Errors in analog-to-digital conversions are inherent in high-speed transient recorders, and Simons documented the degradation of precision by these electronic effects.²⁰ As superior transient recorders are developed, this difficulty will diminish, but it will still remain a significant consideration in quantitative analysis.

Computer integration of spectral peaks is another potential source of error: small peaks are significantly influenced by baseline estimates, and overlapping peaks are affected by the peak-splitting algorithm. In writing programs for LAMMA spectrum processing, one must adjust the algorithm carefully to the spectra; subsections must be sometimes integrated separately. For reliable integration the parameters may require adjustment for the spectral region and samples of interest in a series of experiments.

Conclusions

It is certainly possible to make quantitative LAMMA measurements if the instrument limitations and chemical and physical

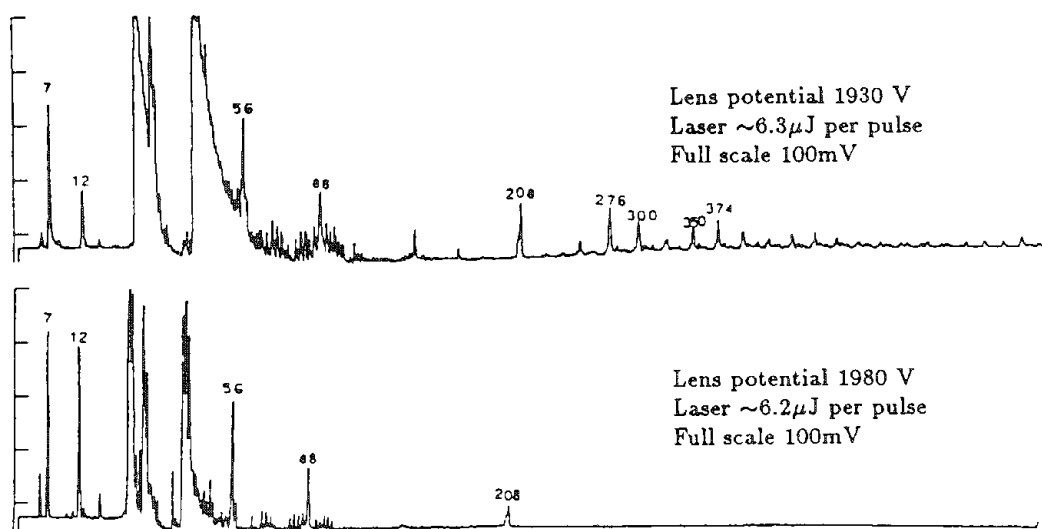


FIG. 4.--Mass spectra of oil shale retort soot acquired at different ion lens voltage settings, showing selective attenuation of peaks.

effects are acknowledged and carefully handled. The preceding discussion has centered on several of the intrinsic sources of measurement error. To minimize these errors, some suggestions are offered to aid in achieving accurate quantitation:

- work above 100 detected atoms to minimize shot noise
- test the sample and holder for lateral uniformity
- ground the sample as in electron microscopy to stabilize kinetic energy
- optimize ion lens and reflector often, and for each critical sample
- make laser intensity plots on the sample or a surrogate
- follow rigorous laser alignment protocol including temperature control of the laser chamber
- make interlaboratory comparisons of laser power meters
- follow rigorous focusing procedure
- utilize beam profile diagnostics if instruments are available
- develop and follow a rigid protocol for selection of spots to analyze
- predefine experimental procedures and limits for data acceptance
- average spectra if possible
- use isotopic dilution standards if possible
- test that internal standards represent the analyzed element or compounds in spatial distribution, ionization efficiency, and in transmittance, by making laser intensity and ion kinetic energy plots
- control integration as well as possible by examining graphs of selected spectra bit by bit
- shift baseline offset automatically and randomly from shot to shot to average out recorder effects.

There is every reason to expect that the science of routine quantitative LAMMA analysis will develop to reasonable success within the next few years. This development will entail exactly the same kind of effort that has been applied to SSMS, SIMS, AA, etc., although quite different considerations will result. As important as the actual achievement of quantitative accuracy will be the necessary fundamental studies into the processes involved in LAMMA measurement, including the light-matter interactions and the plasma chemistry and physics. Better measurements and possibly new analytical techniques will result.

Quantitative LAMMA measurement will not be the result of any single trick, technique, or method, nor of some special standard. Rather, reliable quantitation will be the consequence of persistent adherence to all the necessary procedures, so that the many sources of variability are simultaneously controlled.

References

1. R. Wechsung et al. *Microscopica Acta* Suppl. 2: 281-296, 1978.
2. R. Kaufman, *Microbeam Analysis--1982*, 341-348.

3. P. Wieser, R. Wurster, and R. Wechsung, *Proc Second LAMMA Workshop*, Borstel, Federal Republic of Germany (Leybold-Heraeus), 1984, 29-48.
4. P. Surkyn and Fred Adams, *J. Trace and Microprobe Tech.* 1: 79-114, 1983.
5. U. Haas, P. Wieser, and R. Wurster, *Fresenius Z. anal. Chem.* 308: 270-273, 1981.
6. W. H. Schroeder and G. L. Fain, *Nature* 309: 1984.
7. W. H. Schroeder, *Fresenius Z. anal. Chem.* 308: 212-217, 1982.
8. Emmanuel Parzen, *Stochastic Processes*, San Francisco: Holden-Day, 1962.
9. Thad Mauney and Fred Adams, *Intl. J. Mass Spectrom. & Ion Proc.* 59: 103-119, 1984.
10. Eric Michiels, Thad Mauney, Fred Adams, and Renaat Gijbels, *ibid.*, 61: 231-242, 1984.
11. Eric Denoyer, doctoral dissertation, Colorado State University, 1984.
12. F. Bruynseels and R. E. Van Grieken, *Anal. Chem.* 56: 871-873, 1984.
13. F. Bruynseels, personal communication.
14. R. Wurster, U. Haas, and P. Wieser, *Fresenius Z. anal. Chem.* 308: 206-211, 1981.
15. J. Rosmarinowski et al., Ref. 3, pp. 7-8.
16. H. Kogelnik and T. Li, *Proc. IEEE* 54: 1312-1329, 1966.
17. Thad Mauney, Fred Adams, and M. R. Sine, *Sci. Total Environ.* 36: 215-224, 1984.
18. Thad Mauney, doctoral dissertation, Colorado State University, 1984.
19. M. A. Rudat and G. R. Morrison, *Intl. J. Mass Spectrom. and Ion Phys.* 27: 249-261, 1978.
20. D. S. Simons, *ibid.*, 55: 15-30, 1984.

MASS SPECTROMETRIC IDENTIFICATION OF INORGANIC SUBSTANCES BY LASER MICROPROBE MASS ANALYSIS

J. Dennemont and J. C. Landry

Laser microprobe mass analysis (LAMMA) is a technique that allows the rapid analysis of nonvolatile organic and of inorganic compounds. A schematic representation of the LAMMA principle is given in Fig. 1.

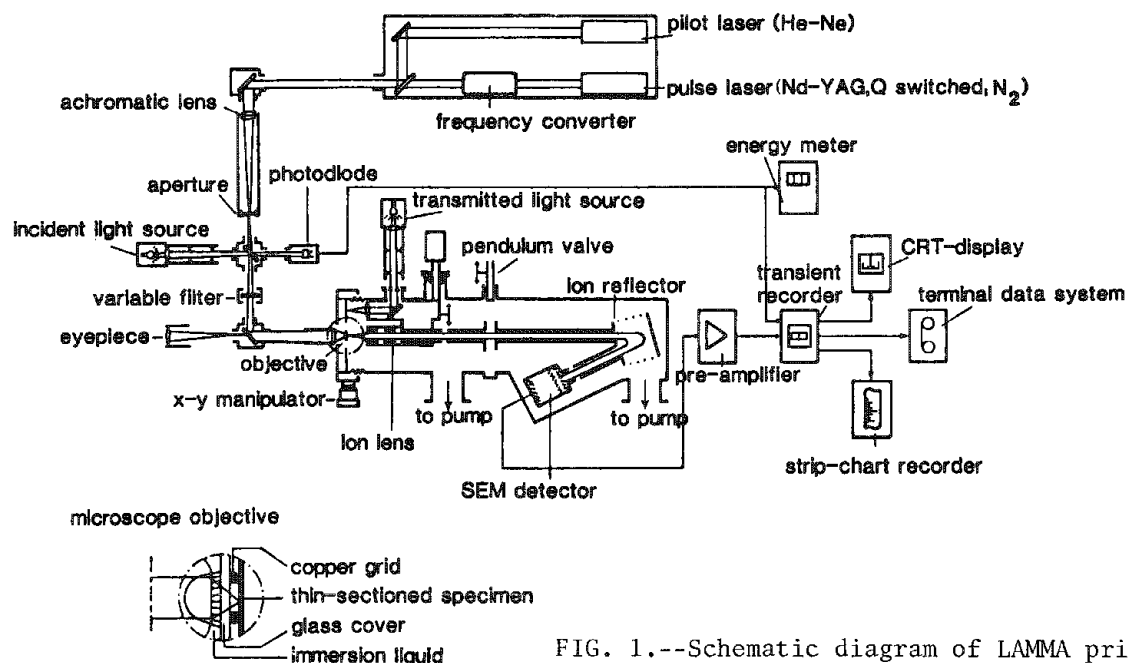


FIG. 1.--Schematic diagram of LAMMA principle.

The pulsed Nd-YAG laser (Q-switched, frequency quadrupled, wavelength 265 nm, pulse duration 15 ns) and the co-aligned He-Ne laser are focused on the sample by means of an optical microscope. The sampled volume is about $1 \mu\text{m}^3$ and the detection limit is in the ppm range. The ions formed are analyzed in a time-of-flight mass spectrometer, in which both positive and negative spectra can be recorded.

Due to the high sensitivity and lateral resolution of the instrument the technique has found applications in quite different fields. In the context of our work, for example, we frequently make use of this technique in industrial toxicology, criminology, general chemistry, environmental pollution, and several other disciplines.

At present we are mostly concerned with the analysis of inorganic substances. Our studies have led us to the conclusion that the interpretation of LAMMA spectra is straightforward only from the point of view of elemental analysis. In all other cases no satisfactory interpretation is possible unless one has a prior knowledge of the mechanism of ion formation during laser-induced ionization.

We have therefore undertaken a systematic study of the behavior of the nitrates, carbonates, sulfates, and halides of groups I and II of the periodic table; the nitrites and sulfites of some members of group I and the chlorides of Cr, Mn, Fe, Co, Ni, Cu, Zn, Ag, Cd, and Hg. In this paper we discuss the LAMMA spectra obtained for these inorganic salts with particular reference to the nitrates.

Figures 2 and 3 show the LAMMA spectra obtained for sodium and potassium nitrate, respectively. The first observation is that ion species are formed with m/z values much greater than that of the molecular ion. In both cases and indeed for all members of the group the same ion species are obtained. In the positive spectra the cations are easily identified. The presence of Na_2O^+ (m/z 62) and Na_2O_2^+ (m/z 78) in the positive spectrum

The authors are with the Service Cantonal d'Ecotoxicologie, C. P. 109, CH-1211 Geneva 4, Switzerland.

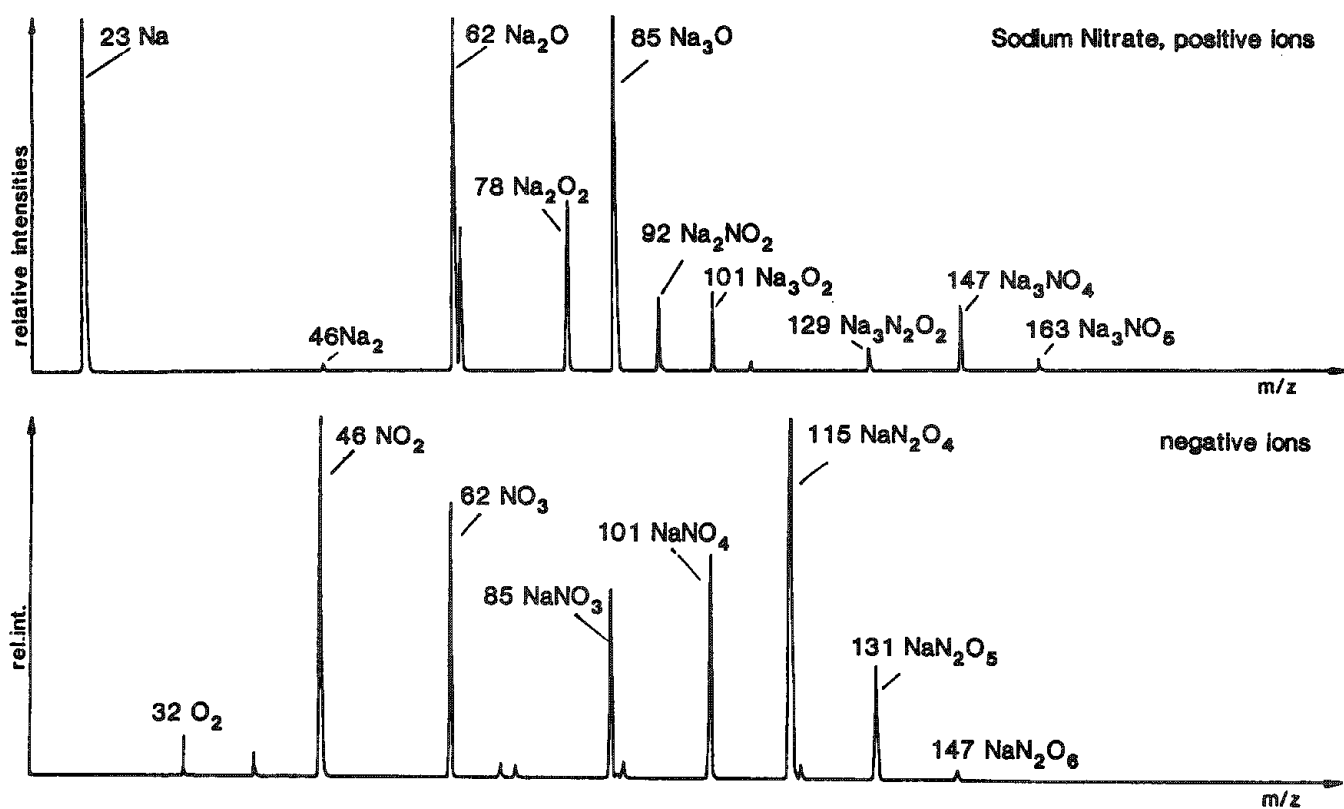


FIG. 2.--LAMMA positive and negative spectra of NaNO₃.

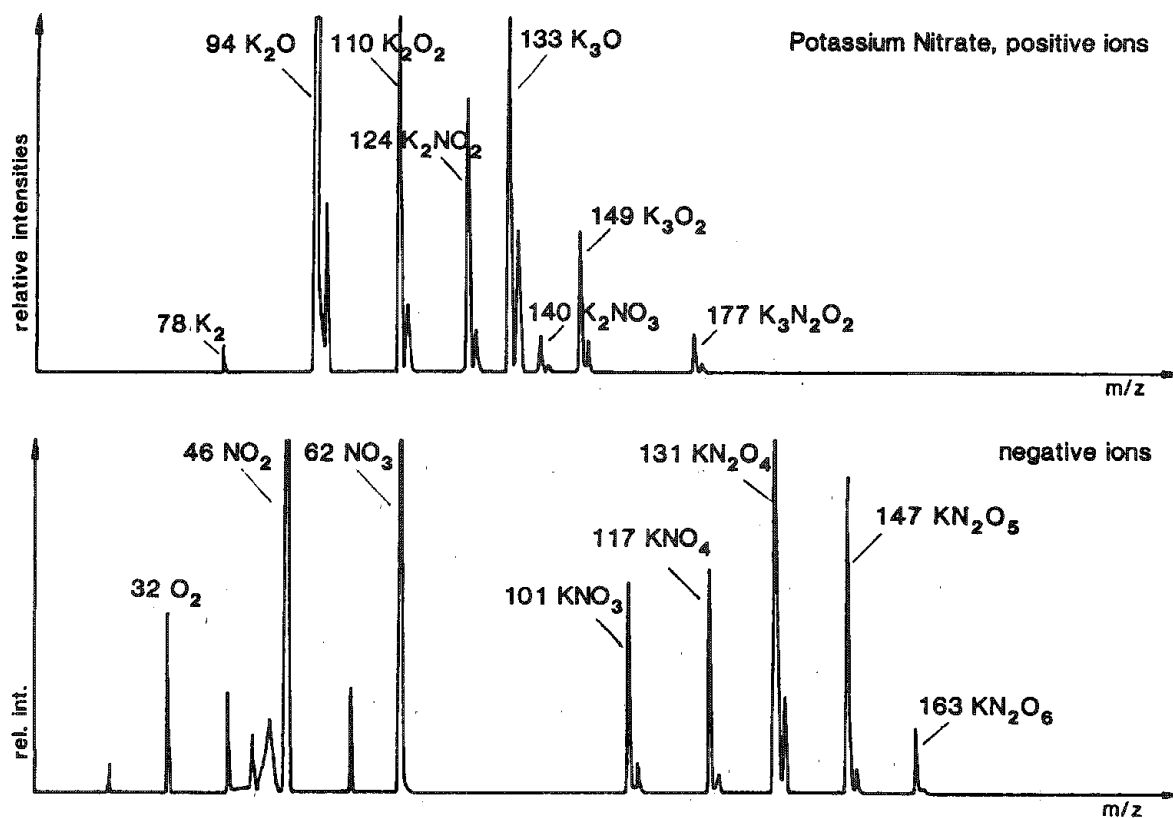
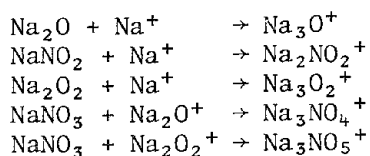


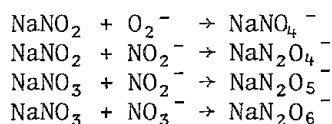
FIG. 3.--LAMMA positive and negative spectra of KNO₃.

and that of NO_2^- (m/z 46) and NO_3^- (m/z 62) in the negative spectrum of Fig. 2 indicate that these ions are formed by thermal decomposition of the parent molecule. The other peaks are presumed to be formed by ion-molecule interactions as indicated below:

For the positive ions



For the negative ions



As can be seen from Figs. 2 and 3 the same ion species are formed and the characteristic ions of the nitrates appear in the negative spectra. Table 1 shows the relative intensities of the nitrates; MN_2O_4^- is the most intense ion.

TABLE 1.--Relative intensities of characteristic ions of nitrates. MN_2O_4^- is the most intense ion in the negative mode. (M is the cation.)

Negative Ions

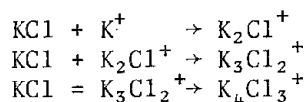
	O	OH	O ₂	NO ₂	NO ₃	M	MO	MNO ₂	MNO ₃	MNO ₄	MN ₂ O ₄	MN ₂ O ₅	MN ₂ O ₆
Lithium	+++	++	+	+++	+++				2,0	0,9	3,2	2,6	1,0
Sodium	+++	++	+	+++	++				1,7	2,0	9,1	1,0	0,1
Potassium	+++	+	+	+++	+++				0,6	0,7	4,0	1,0	0,2
Rubidium	+++	+	+	+++	++				0,3	0,4	2,1	1,0	0,2
Caesium	+++	+	+	+++	+++	1,7	0,4	0,1	0,3	1,0	60,0	1,0	

Positive Ions

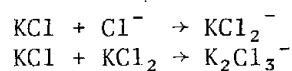
	M	M ₂	M ₂ O	M ₂ O ₂	M ₃ O	M ₃ O ₃	M ₂ NO ₂	M ₂ NO ₃	M ₃ NO ₂	M ₃ (NO) ₂	M ₃ NO ₄	M ₃ NO ₅	M ₅ NO ₃
Lithium	3,2	~ 0	1,8		7,2	~ 0	0,4 or (Li ₄ O ₂)	0,4	1 or (Li ₅ O ₂)				0,1
Sodium	>>20	0,5	20	5,3	15	1	2,1	~ 0		0,5	0,6	~ 0	
Potassium	>>10	0,6	>>10	5,5	3,8	1	4,0	0,8		0,6			
Rubidium	20	0,6	9,7	3,7	1	0,2	1,4			~ 0			
Caesium	>>10	0,1	>5	0,9	1	0,1	0,7	0,1		0,4			

Figure 4 shows the type of cluster ions obtained for potassium chloride. Here again the cluster ions are accounted for according to the following interactions:

For the positive ions



For the positive ions

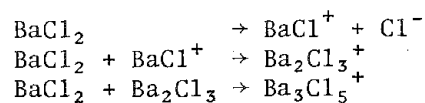


For all halides of group I the cluster ions formed are of the type $[\text{M}_{n+1} \text{X}_n]^+$ and $[\text{M}_n \text{X}_{n-1}]^-$ where M is the salt cation and X the salt anion.

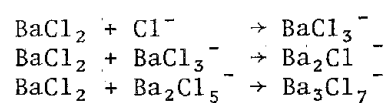
The situation for the halides of group II is quite different. The cluster ions formed are of the type $[\text{M}_n \text{X}_{2n-1}]^+$ and $[\text{M}_n \text{X}_{2n+1}]^-$.

For example, for BaCl_2 the ions are formed in the following way:

In the positive mode



In the negative mode



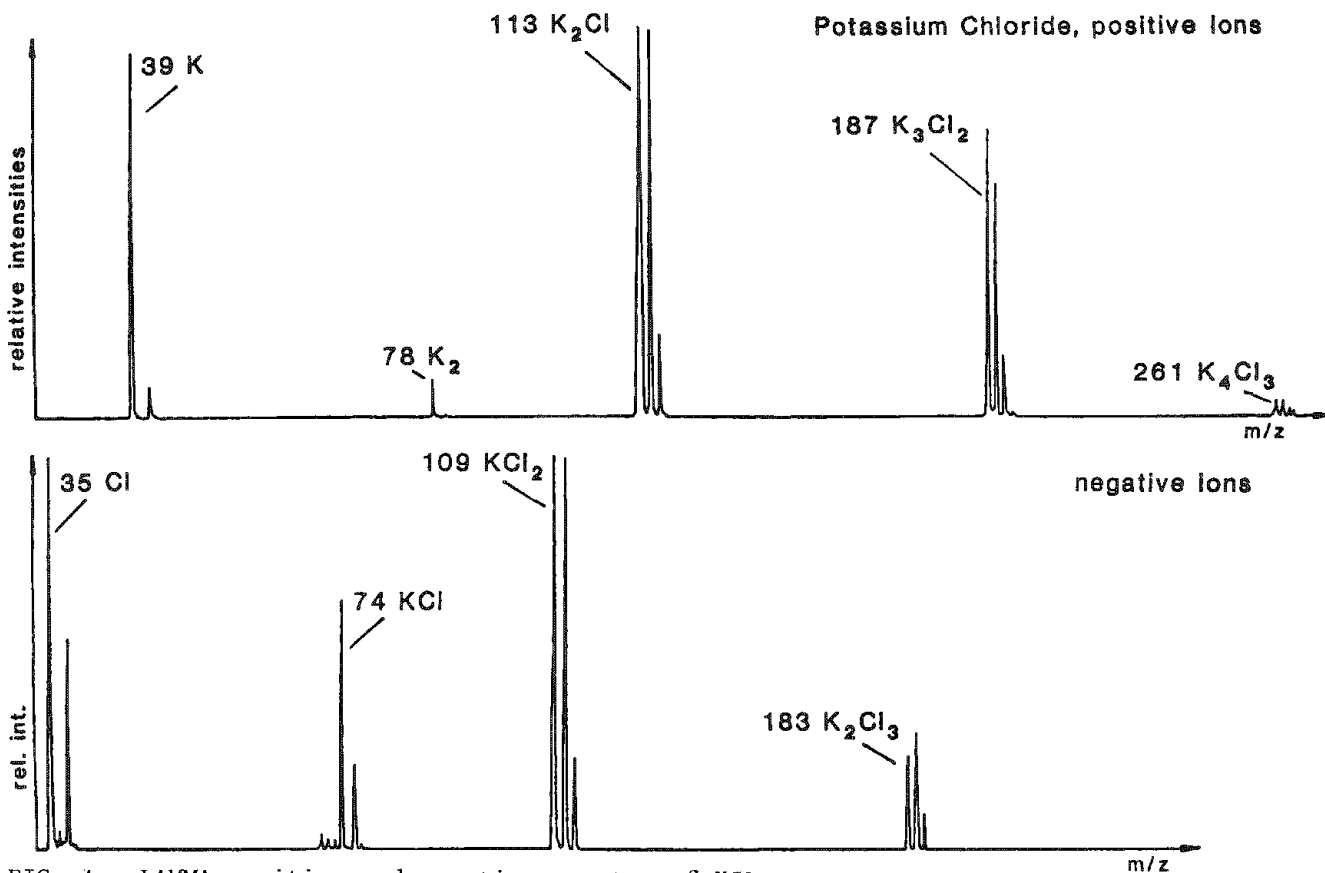


FIG. 4.--LAMMA positive and negative spectra of KCl.

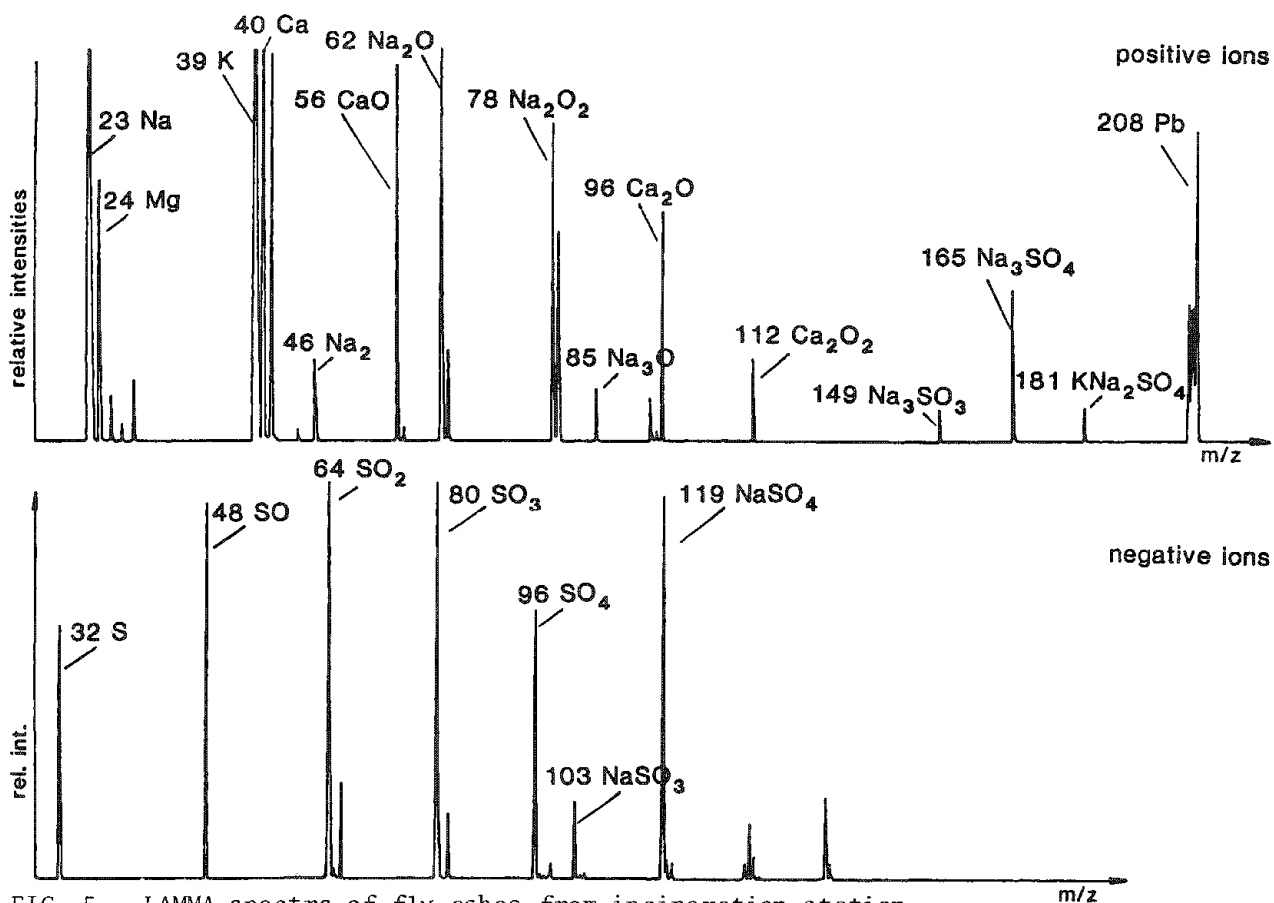


FIG. 5.--LAMMA spectra of fly ashes from incineration station.

We have yet a different picture for the halides of the transition elements.

CuCl and AgCl with one s electron in their outer orbital behave in the same way as the halides of group IA. ZnCl_2 , CdCl_2 , and HgCl_2 with two s electrons in their outer orbital behave in a similar way to the halides of group IIA.

The chlorides of Cr, Mn, Fe, Co, and Ni behave in a different way; the ions obtained for FeCl_2 are given below:

Positive ions

Fe^+ , FeCl^+ , Fe_2^+ , Fe_2Cl^+ , Fe_2Cl_2^+ , Fe_2Cl_3^+ , Fe_3Cl_3^+

Negative ions

FeCl_2^- , FeCl_3^- , FeCl_4^- , FeCl_5^- , Fe_2Cl_4^- , Fe_2Cl_5^- , Fe_2Cl_6^- , Fe_3Cl_7^-

Here again the formation of these ions can be explained on the basis of ion-molecule interactions with due regard to the variable valencies of the transition elements.

Examples are available showing how a knowledge of the mechanism of ion formation can help in the elucidation of unknown spectra.

QUANTIFICATION AND APPLICATIONS OF LASER-PROBE MICROANALYSIS

M. J. Southon, Andy Harris, Valerie Kohler, S. J. Mullock, and E. R. Wallach

This paper reports work with a LIMA (Laser Ionization Mass Analyzer)¹⁻³ manufactured by Cambridge Mass Spectrometry Ltd. Factors affecting the reproducibility of LIMA microanalysis are discussed and progress with both experimental and theoretical procedures for the quantification of LIMA data are reported. The wide range of important applications of LIMA laser-probe microanalysis in materials science is illustrated by reference to studies of the distribution of boron near brazed joints in nickel-superalloy turbine-blades; contamination responsible for the discoloration of titanium nitride coatings on steel; the nature of hard, erosive particles in coal dust used as a fluid fuel; and a trace segregant inhibiting the formation of Nb₃Sn in a superconducting filamentary composite wire, and of an isotopic-mass effect on diffusion of tin in this material.

Quantification of LIMA Results

The results obtained from successive LIMA mass-spectra typically show a significant scatter in the absolute ion yields, even for a completely homogeneous sample—an observation generally attributable to variation in the proportion of laser power actually absorbed by the specimen. However, by considering the relative ion yields of different elements or isotopes one can substantially reduce this scatter and obtain estimates of the scatter (1σ) in the measured ratios of major elements of less than 10%. A further complication is introduced by the inherent variability of about 2-3% (1σ) in the actual laser power from shot to shot, which implies that averaging of several spectra may lead to an overestimate of the scatter, since spectra are obtained at slightly differing powers, which will cause variations in both absolute and relative ion yields. It is hoped that the recent development of a laser-energy monitor will allow more meaningful averaging and hence further reduce the scatter.

It has also been found experimentally that reproducibility depends on the analytical conditions used; it is particularly influenced by the laser power, and apparently also depends on the ionization potentials of the elements under consideration. For example, in the analysis of a boron-containing Ni/Cr metallic glass of known composition, the spread of the experimentally obtained correction factors (actual, divided by measured, elemental ratios) changed from a 1σ value of about 100% at a relatively low laser power to about 50% at a power about 2.5 times greater for B/Ni; whereas for Cr/Ni, elements of more comparable ionization potentials, the correction factors were found to have a spread of less than 20% at all laser powers. These results were obtained prior to the development of the energy monitor and, as explained above, are thus less than the optimum.

Since the absolute ion yields show a large scatter, any attempt to quantify the LIMA results must involve relative ion yields. There are two possible approaches, as discussed by Kaufmann:⁴ a "working-curve" approach (as used in SIMS) and a more fundamental, theoretical approach. The former involves the use of a standard of known composition to produce graphs of the variation of one correction factor either with another (as shown in Fig. 1 for Ca/Si and Al/Si plotted against O/Si for a glass) or with laser power. The theoretical approach involves modeling the ionization processes in the laser-produced plasma. At present the Local Thermodynamic Equilibrium (LTE) model seems to be the most promising.⁴⁻⁶

The LTE model allows the calculation of the ratio of ions to neutral species in the plasma from the well-known Saha equation.^{4,5} This ratio can then be used to calculate the ratio of ions in the plasma to the original concentration of an element in the specimen. LTE has been used to calculate the plasma conditions (electron temperature and density) pertaining at various positions on the working curve of Fig. 1 (Table 1), which can then

The authors are at the Department of Metallurgy and Materials Science, University of Cambridge, Cambridge, England CB2 3QZ. They are grateful to their colleagues C. Ross for her work on superconductors, and J. E. Evetts and S. C. R. Barton for advice and the supply of samples; and to I. Bucklow of the Welding Institute and R. B. Newbury of the Tube Investments Research Laboratories for their cooperation and the provision of samples.

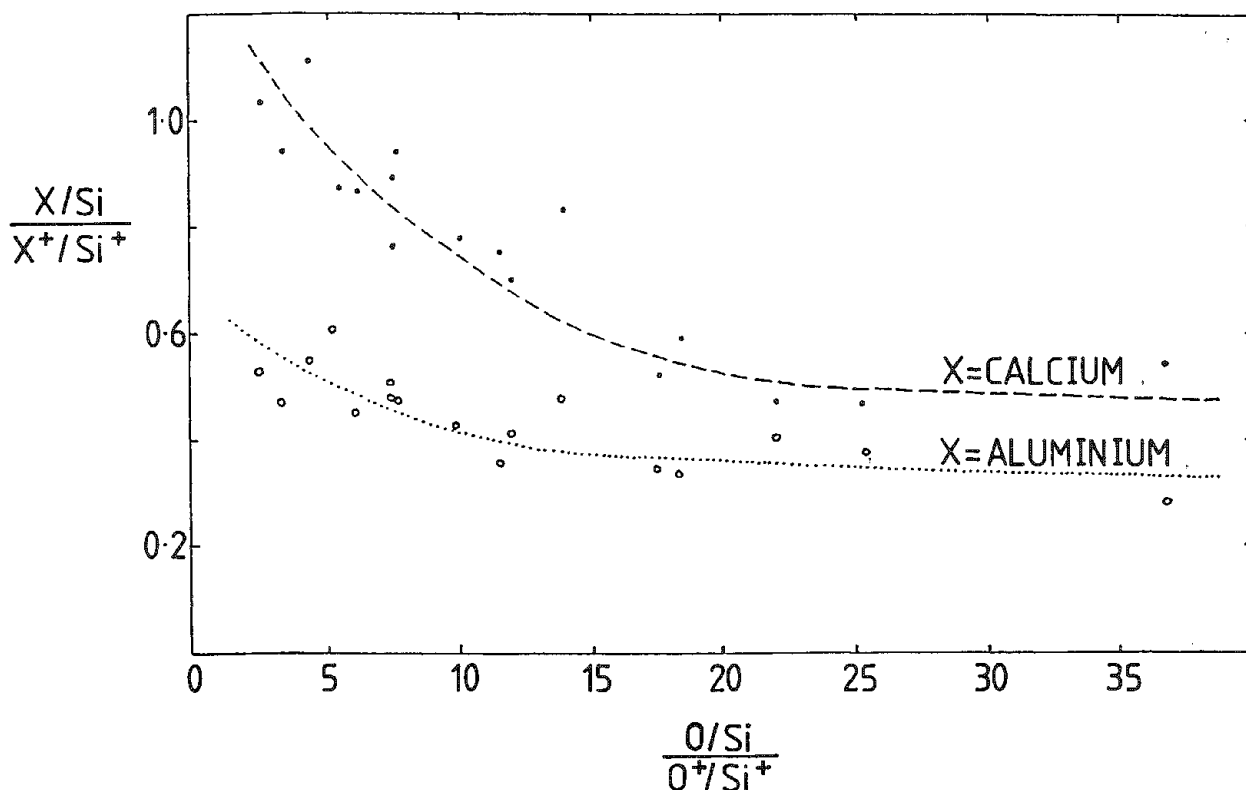


FIG. 1.--Variation of experimentally determined elemental-ratio correction factors for Al/Si and Ca/Si with that for O/Si in a glass.

TABLE 1.--Plasma conditions derived by LTE model from Fig. 1.

Correction-factor for O/Si	Correction-factor for Ca/Si	Temperature (K)	Electron Density (cm ⁻³)
5	0.95	17000	10 ¹⁹
10	0.8	16000	3x10 ¹⁹
15	0.7	15000	5x10 ¹⁹
20	0.63	14250	5x10 ¹⁹
25	0.55	13500	7x10 ¹⁹
30	0.48	13000	10 ²⁰
35	0.45	12500	2x10 ²⁰
40	0.4	12000	3x10 ²⁰

be used to find theoretical correction factors for any other element. The temperatures thus determined are higher than those found by Kaufmann⁴ (in the range 12 000-17 000 K opposed to 8-12 000 K), probably as a result of differences in laser optics between LIMA and LAMMA (the instrument used by Kaufmann). Kaufmann's assumption that the ion yield is much lower than the neutral yield in the plasma does not seem justified at the higher temperatures apparently produced during the LIMA analysis. The LTE model can also be used to predict the behavior of elemental sensitivities with changing power; in particular, it predicts a trend toward more uniform and constant sensitivities at higher powers, as has been determined experimentally elsewhere⁷

Applications

LIMA has several important features, such as sensitivity to all the elements of the periodic table with isotopic discrimination, the ability to analyze a very wide variety of specimens, good lateral and depth resolution (typically 1-3 μ m laterally and about 0.2 μ m in depth), and good trace sensitivity (of the order of a few ppm). In the following

section, selected LIMA studies are described in order to illustrate the scope and some of the advantages of LIMA as an analytical instrument in materials science.

The analysis of light elements is important in the study of the fabrication of turbine blades from oxide-dispersion-strengthened nickel-based superalloys, where the necessity to maintain the columnar microstructure precludes the use of welding as a fabrication technique; instead, brazing is used, with a Ni/Cr metallic glass foil as an interlayer. The properties of this foil are closely controlled by adjustment of the boron content, and LIMA has been used to study the distribution of the boron after the brazing. It was found that the boron had almost completely diffused out of the foil matrix (the original boron content of about 15% was reduced to less than 0.2%) and was instead segregated to the foil-superalloy interfaces and to the grain boundaries in the now crystallized foil, and to a lesser extent had diffused outward into the superalloy, producing a boron content of about 0.5%. These results are in agreement with data from scanning-SIMS, and have implications for the possible embrittlement of the material.

A further light-element application involved the use of LIMA to analyze the composition of two nitrided layers on steel. These coatings consist of nonstoichiometric titanium nitride, and are hard and wear resistant; they are typically used on bearing and cutting tools. The coating is sputtered onto the steel, with a bias voltage applied in order to refine the microstructure of the coating from a coarse columnar to a fine microcrystalline. Occasionally during this processing the golden color of the sputtered film turns black for no apparent reason. Compositional analyses carried out by LIMA on these layers showed a significant level of contamination of the black coating throughout its thickness, in contrast to the clean profile obtained from the gold-colored coating. Two representative spectra are shown in Figs. 2 and 3. The black coating contaminants were primarily K and Ca, with small amounts of O, C, and Na, elements typically found on the surface of improperly cleaned substrates.

An example of a problem where the nature of the specimen precluded the use of other analytical techniques involved a study of coal dust. Finely ground coal dust has the advantage that it may be transported in pipes as a fluid. However, the distribution system is subject to erosive wear, both by relatively soft particles of coal and by other mineral particles, such as quartz, which are associated with the coal, unless special efforts are made to exclude them. In an assessment of the likely wear rate the hardness of these particles makes them important despite their relatively low concentration. LIMA is ideally suited to the identification of such particles, which may be roughly sorted by eye into various categories of color and shape under an optical microscope. In particular, repeated laser shots have been used to penetrate the black coating of carbon, which often disguises a much harder alumino-silicate.

A further important feature of LIMA is the ability to discriminate between isotopes of an element while providing a microanalysis, as illustrated by the following example. Superconducting wire is now regularly used in applications requiring high magnetic fields of high stability. Of the superconducting materials used commercially, Nb_3Sn has the highest critical field at a given temperature and therefore potentially the best performance. However, it is too brittle to be drawn into wire in the conventional manner; instead, a composite wire of bronze and niobium is fabricated and then a heat treatment is used to grow the Nb_3Sn layers that will eventually carry the current (Fig. 4). The tin to form new Nb_3Sn diffuses from the bronze through the Nb_3Sn layer already formed to form a new superconductor. During this process the relatively narrow bronze channels near the center of the composite wire become severely depleted in tin. Diffusion from the outer bronze jacket is necessary to maintain the growth of Nb_3Sn . Analysis with the laser microprobe has been used to investigate two aspects of this diffusion process.

The outer filaments of niobium in the outer bundles are found to be incompletely reacted, unlike the central filaments, even though the tin should be most readily available there. It is known that the presence of phosphorus inhibits the Nb_3Sn growth and appropriate steps are taken to achieve low levels of phosphorus in the bronze used. However, it has been suggested that phosphorus may be gettered at the outer interfaces as the tin diffused in toward the center of the wire.⁸ LIMA analysis of the bulk bronze shows no phosphorus peak at normal instrumental sensitivities, whereas at the edge of the outer bundles a phosphorus peak appears clearly.

The lateral resolution of LIMA makes it possible to measure the tin concentrations in the bronze and in the Nb_3Sn separately: it is significant that an enrichment in the low-

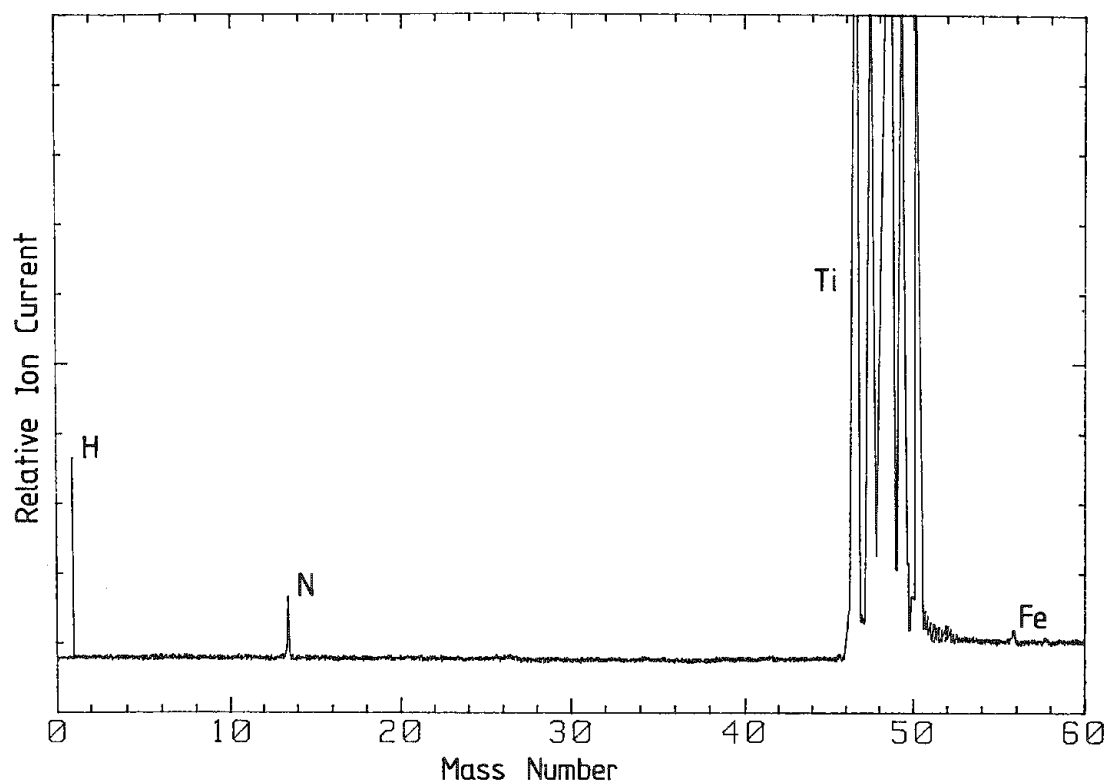


FIG. 2.--Positive-ion mass spectrum of gold-colored Ti-N layer.

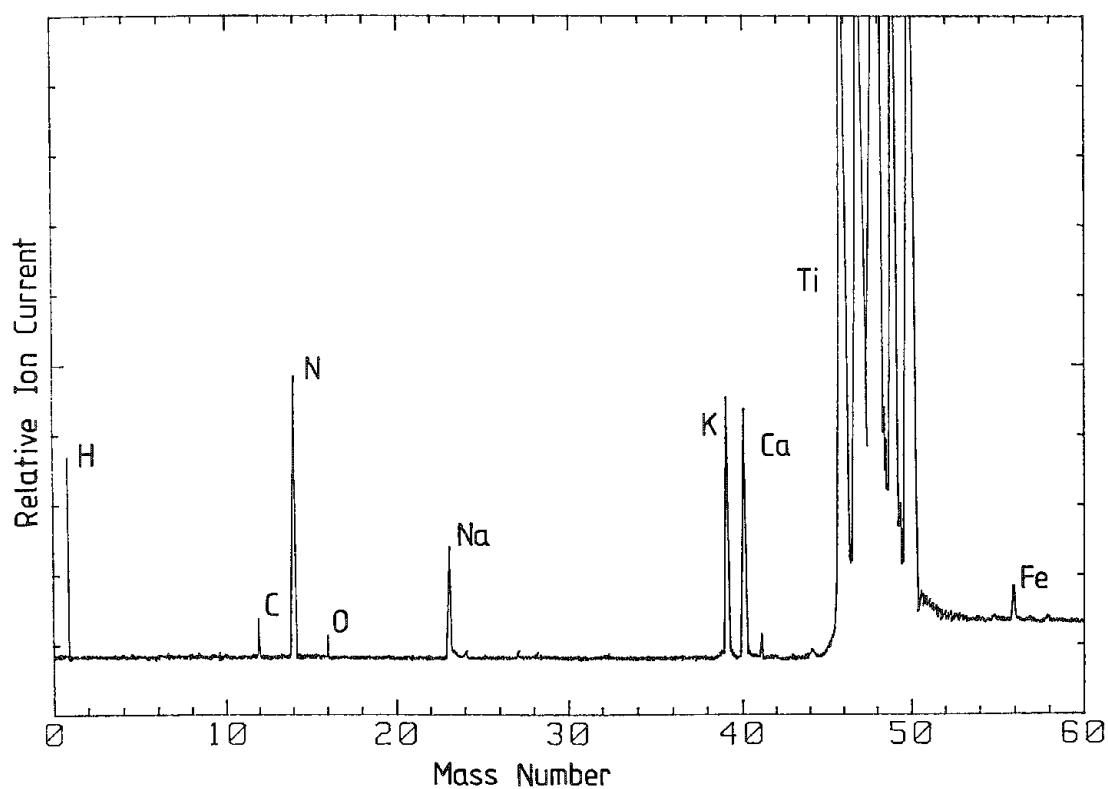


FIG. 3.--Positive-ion mass spectrum of contaminated black Ti-N layer.

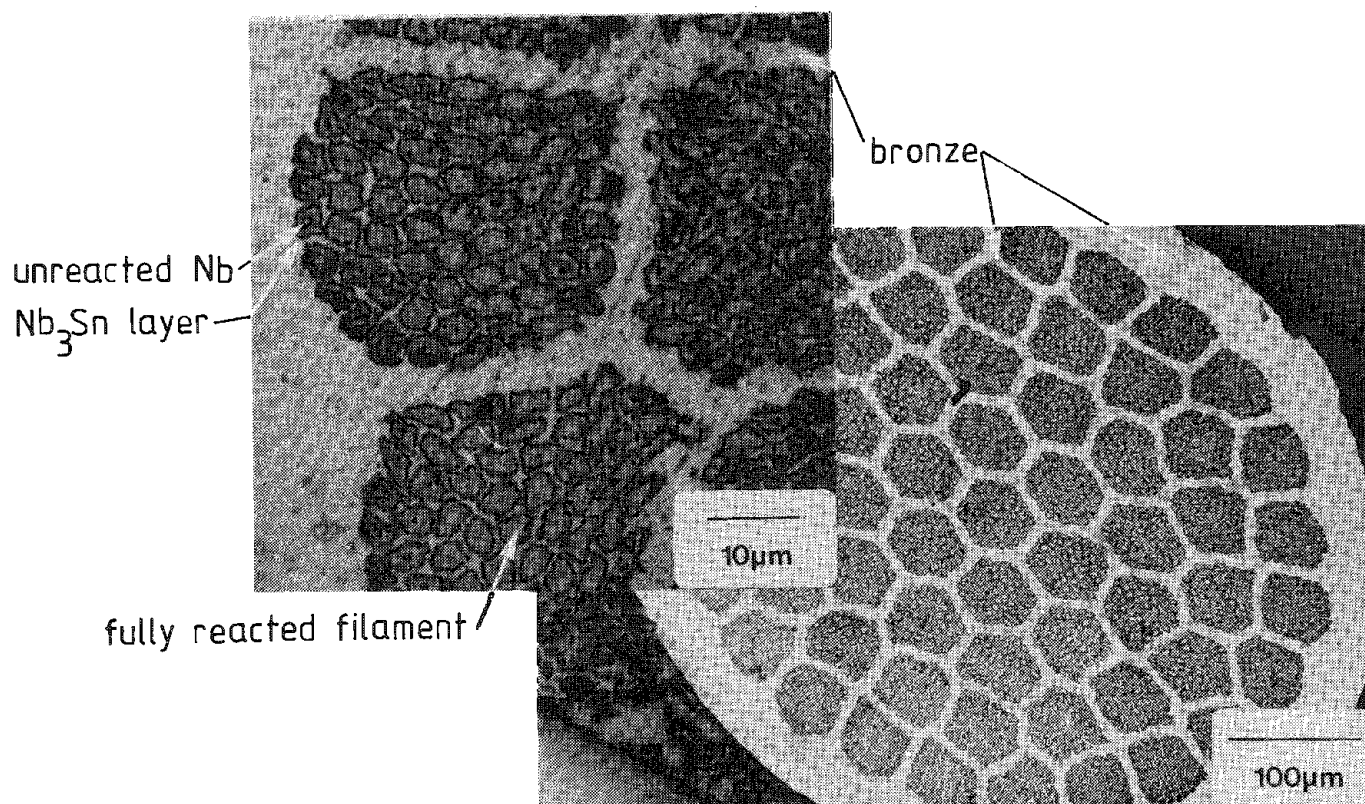


FIG. 4.--Optical micrograph of multifilamentary superconducting wire.

mass isotopes of tin was found in the Nb₃Sn layer. Apart from its academic interest as an example of an isotopic mass effect in diffusion, this observation is of potential practical importance since the superconducting critical field is approximately proportional to isotopic mass.

Conclusion

Basic work on the reproducibility and quantification of LIMA laser-probe microanalysis and its application to a variety of practical problems has demonstrated the power and versatility of this relatively new technique as an important addition to microanalytical capability in materials science.

References

1. C. A. Evans Jr. et al., *Microbeam Analysis--1983*, 101-105.
2. Trevor Dingle and B. W. Griffiths, *Microbeam Analysis--1984*, 23.
3. M. J. Southon et al., *Vacuum* 34: 903, 1984.
4. R. Kaufmann, *Microbeam Analysis--1982*, 341-358.
5. C. A. Andersen and J. R. Hinthorne, *Anal. Chem.* 45: 1421, 1973.
6. P. K. Carroll and E. T. Kennedy, *Contemp. Phys.* 22: 61, 1981.
7. Trevor Dingle and B. W. Griffiths, *Microbeam Analysis--1985*, 315.
8. J. E. Evetts, private communication.

EXAMPLES OF QUANTIFICATION IN LASER IONIZATION MASS ANALYSIS

Trevor Dingle and B. W. Griffiths

Laser ionization mass analysis (LIMA) is essentially a semiquantitative microanalytical tool at present. The laser-solid interaction is not sufficiently understood yet to allow a comprehensive model to give an absolute calibration of unknown samples from LIMA results. Instead, calibration must rely on internal standard reference specimens which, ideally, have chemical, optical, and thermal properties similar to those of the unknown sample, and are analyzed at the same laser power density.

In this paper we describe some LIMA results we obtained using NBS glass reference samples in the determination of nitrogen and carbon levels in silicate glasses. In addition we include supportive data from single-crystal calcite, which indicates that the calibration coefficients generated from the reference glass may have applications in more general systems. These results illustrate the potential of LIMA as a quantitative technique, since the determination of trace impurities on a microanalytical scale, particularly low-atomic-number elements, in such bulk insulating materials is a difficult problem for other analytical techniques.

The Detection of Carbon and Nitrogen in Silicate Glasses

This was a typical analysis in which unknown glass samples were supplied and we were asked to measure the carbon and nitrogen levels. Initially we knew only that the glasses were silicates, so that it was interesting to determine their matrix compositions. We used a glass standard to determine elemental relative sensitivity factors. The ion yield of a particular species in the laser microprobe is a strong function of power and of its ionization potential (I_p). Figure 1 shows an idealized view of this behavior.

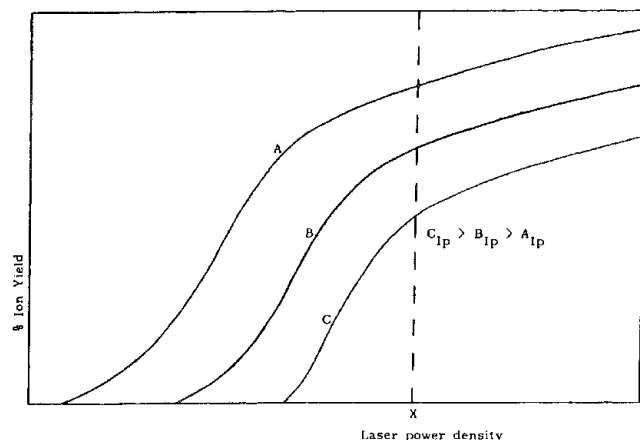


FIG. 1.--Percentage ion yield vs laser power density.

Since laser power is a relatively poorly controlled parameter, it is clear that one should operate the system in a region above a power density X (see Fig. 1) if possible. The element most difficult to ionize in the glasses to be analyzed was oxygen, and so the technique used was to obtain successive spectra of the glass at increasing laser power until the height of the oxygen peak was no longer increasing with respect to the other peaks present. The laser power density was then noted and used for all the ensuing measurements. The actual energy delivered to the sample was $\sim 100 \mu$ joules of 266nm radiation. If all of it were to arrive in the focal spot, it would give a power density of the order $10^{13} \text{ W cm}^{-2}$. In practice it is true that much of the energy is reflected by the sample or absorbed and

scattered by the microplasma generated in front of the sample.

Having established analytical conditions, five consecutive spectra were recorded from a standard glass and the relevant peak areas integrated and averaged with the help of the microcomputer attached to the instrument. From the known composition of the glass, relative sensitivity factors for the major elements present were then derived (Table 1). A typical spectrum is shown in Fig. 2.

It is interesting to note that if relative sensitivity factors are plotted against ionization potentials, in general the sensitivity factors do decrease as the ionization potentials increase and a smooth curve can be drawn between the points. However, there are anomalies, for example calcium.

The authors are at Cambridge Mass Spectrometry Ltd., Cambridge Science Park, Milton Road, Cambridge, England CB4 4BH.

TABLE 1.--The observed sensitivity of LIMA to various elements normalized to the sensitivity to silicon in a silica glass standard.

Element	Ca	O	Si	Al	Na
Relative Sensitivity	0.6	0.4	1.0	1.8	3.6

It is clear that factors other than ionization potential are relevant; at present work is in progress to try and elucidate this area. One particular factor that does seem to explain our observed results is the ratio of ionic radius to mass for the ions.

A typical survey spectrum over the mass range of interest on one of the unknown glass samples is shown in Fig. 3. The areas under selected peaks are measured on the computer system used in the LIMA-2A machine and plotted on the spectrum. The predicted matrix composition for the unknown glass samples is shown in Table 2, along with the composition obtained subsequently by other analytical methods.

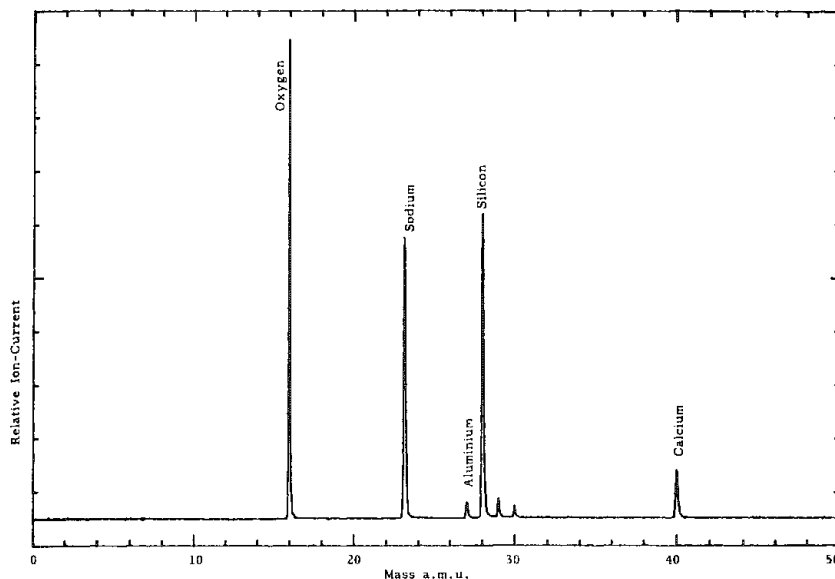


FIG. 2.--NBS glass sample bulk composition.

TABLE 2

Element	% LIMA	% given
O	64	60
Na	9	8.7
Mg	2	2.9
Si	22	23.7
Ca	3	4.6

The LIMA results are averages of five shots and are given to the nearest unity percentage, and are based upon integrated peak areas. The LIMA results used typically had a standard deviation of 7%. In terms of accuracy it seems reasonable to say that LIMA should yield bulk compositions, to within approximately 10% for major constituents and 30% for minor constituents if a known standard is used with this type of glass sample.

Trace element analysis on two unknown glass samples was then performed. Figures 4 and 5 show typical spectra produced on one sample. The main elements O, Na, Mg, Al, Si, and Ca are revealed as well as trace elements H, Li, B, C, N, S, Ti, K, Fe, Mn, Sr, Y, Zr, V, and Cl. Using the integrated peak areas and the relative elemental sensitivity factors obtained from glass standards, we obtained relative percentages (Table 3). In practice, if used with care, a plot of relative sensitivity factors against elemental ionization efficiency can be used to predict the relative sensitivity of an element not present in the standard.

The third column of Table 3 assumes that the abundance of ^{42}Ca is 0.0064 of the value of Ca^{40} , and referring to Table 2 we predict that we would expect 192 ppm of ^{42}Ca . Thus the calcium isotope is used as the standard to obtain the values of carbon and nitrogen. Any ambiguity due to surface deposits was minimized by pulsing into the sample. In addition, the contribution of Mg^{++} to the C^{12} peak and Si^{++} to the N^{14} peak were subtracted out of these results.

A similar determination was performed on another glass sample. In this, the main elements O, Na, Mg, Al, Si, and Ca were again revealed as well as trace elements H, Li, C, N, S, Cl, K, Ti, and Fe. The results, obtained by the same procedure as before, are also tabulated in Table 3. All the trace element determination results are an average of a number of LIMA shots and the standard deviation to mean was better than 9%.

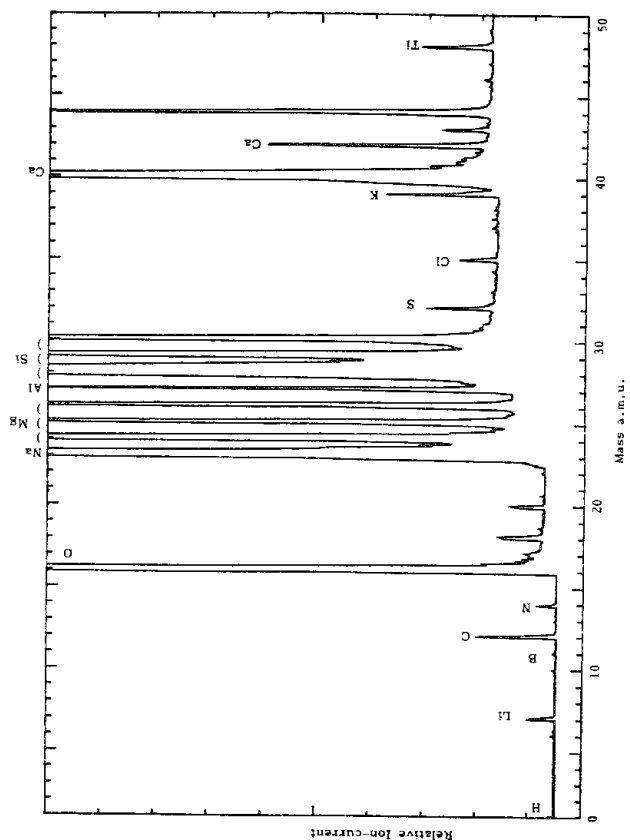


FIG. 4.--Unknown glass samples: trace elements.

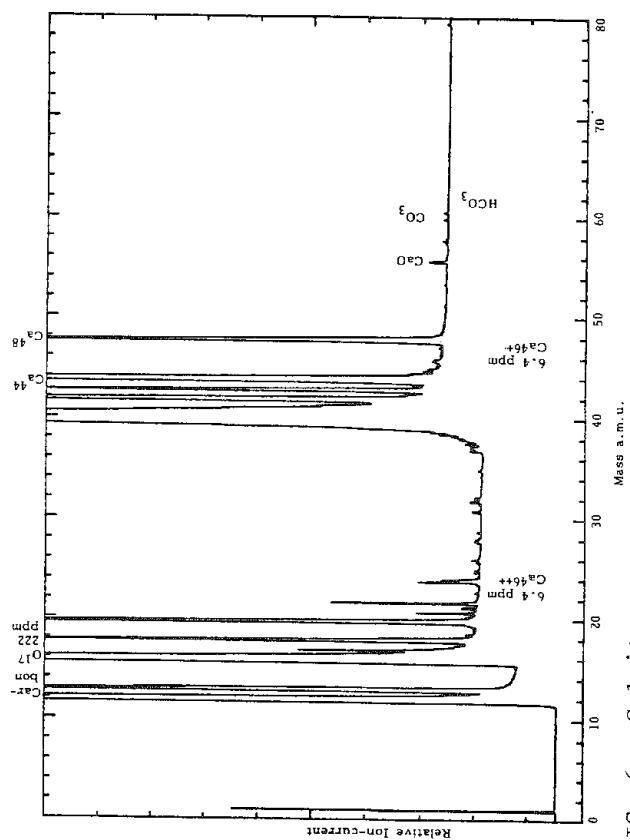


FIG. 6.--Calcite.

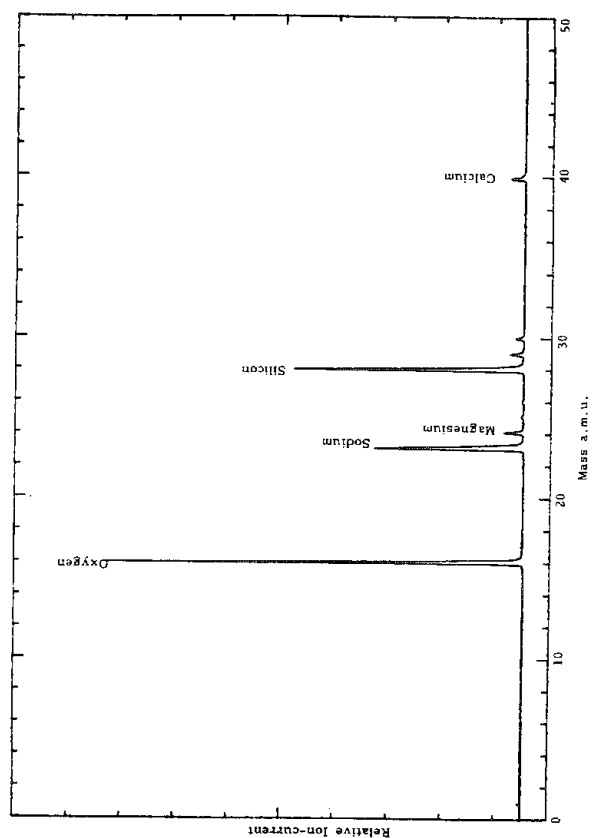


FIG. 3.--Unknown glass sample bulk composition.

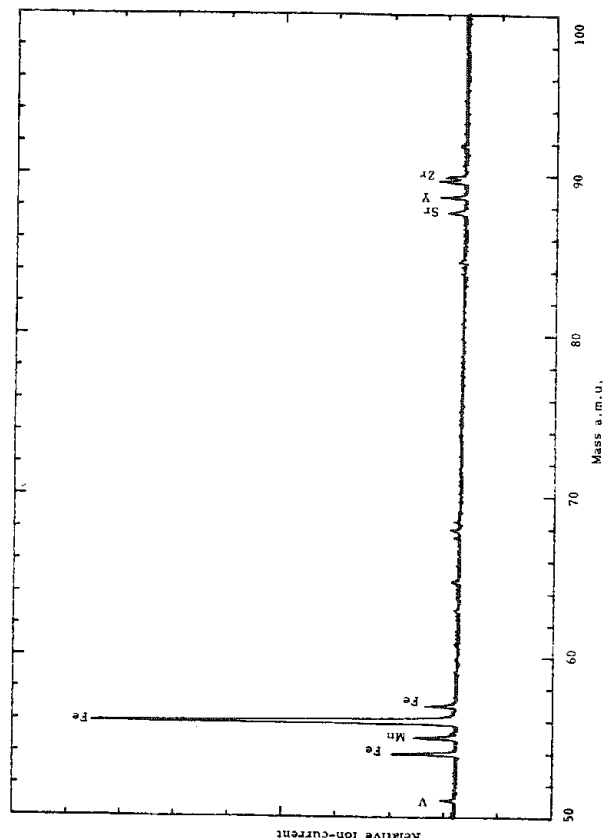


FIG. 5. Unknown glass sample: trace elements.

TABLE 3

Isotope	Relative %	LIMA ppm	Given ppm
Sample 1			
^{12}C	28.5	83	100
^{14}N	5.5	16	15 - 30
^{42}Ca	66	192	-
Sample 2			
^{12}C	27	94	100
^{14}N	18	63	50
^{42}Ca	55	192	-

The Analysis of Calcite

The calcite (CaCO_3) single crystal was in fact an optical component selected for its ultraviolet light transmission. In general, we use a laser wavelength of 266 nm in LIMA-2A and were still able to couple in its power effectively to vaporize and ionize a sample that transmits this light wavelength. The results obtained by integration of the areas under peaks to obtain the percentage of major constituents are shown in Table 4.

TABLE 4

Element	Ca%	C%	O%
Measurement 1	13.95	38.2	47.85
Measurement 2	17.98	22.98	59.04
Measurement 3	42.87	18.57	38.56
Measurement 4	15.45	28.84	55.71
Measurement 5	26.2	24.82	48.98

TABLE 5

	Ca%	C%	O%
Experimental mean values	23.3	26.68	50.03
True composition	20	20	60

As the sample is stoichiometric (that is, it contains 20% Ca, 20% C and 60% O), it is interesting to compare the mean values obtained from LIMA (Table 5).

The relative sensitivity factors generated from these measurements are shown in Table 6 normalized to carbon. Also shown in Table 6 are the calibration coefficients generated from our glass measurements renormalized to carbon.

TABLE 6

Element	Ca	C	O
Relative sensitivity factor normalized to carbon	0.87	1	0.62
Relative sensitivity factor from glass normalized to carbon	1.07	1	0.73
% difference	-18.7	0	-15

analyzer used in LIMA can compensate adequately for the large spreads in ion energy produced under such conditions.

Figure 6 shows a typical high-sensitivity spectrum from the calcite sample. The abundance sensitivity of the LIMA technique (that is, in simple terms, the ability to detect a small peak close to a large peak) is demonstrated. For example, the Ca^{46} is approximately 6 ppm, whereas the Ca^{44} and Ca^{48} are present at approximately the 4395ppm and 369ppm levels, respectively. More impressive, O^{17} present at 222 ppm is resolved next to the main 60% O^{16} peak.

Summary

It has been demonstrated that use of a suitable standard enables LIMA analysis to be quantified to accuracies of about 10%. Trace levels can also be determined to around a factor of 2 at the 100ppm level. In some circumstances, unknown calibration coefficients have been successfully inferred from plots of known data against ionization potential. Finally, we tentatively suggest that relative sensitivity factors can be successfully used in systems physically different from that in which they were generated.

Overall, the above preliminary study demonstrated that LIMA can, based on a standard, obtain matrix composition to within 10% on major and 30% on minor constituents and that standard deviations to mean in reproducibility can be better than 9%. The results obtained on the two glass samples were well within the typical χ^2 accuracy expected for detecting trace elements.

A COMPARISON OF TWO TRANSIENT RECORDERS FOR USE WITH THE LASER MICROPROBE MASS ANALYZER

R. A. Fletcher and D. S. Simons

In the Laser Microprobe Mass Analyzer (LAMMA),¹ a transient waveform recorder is used to capture the mass spectrum produced in a time-of-flight mass spectrometer from a single pulsed ionization event. The recorder has the characteristics of a digital oscilloscope. It incorporates a fast analog-to-digital converter combined with a large memory for storage of the digitized waveform. The transient recorder is the key component that permits high sensitivity to be achieved simultaneously for multiple elements in the LAMMA.

The recorder originally supplied with the LAMMA instrument has an A/D converter with a maximum digitization rate of 100 MHz, bandwidth of 25 MHz, a nominal resolution of 8 bits, and a memory capacity of 2048 locations (2 Kbytes).² The full mass range of elemental ions is dispersed over a time interval of about 70 μ s under standard operating conditions. Therefore, only a small portion of the mass spectrum (approximately 20 μ s) can be stored at the maximum digitization rate.

Slower digitization rates can be selected, but they reduce the density of data points that define individual peaks in the mass spectrum.

Recently, a new generation of transient waveform digitizers has become available that offers modular design based on the CAMAC standard, improved dynamic performance, and expanded memory. The purpose of this article is to evaluate one of these new recorders and to compare its performance to that of the original recorder for use in the LAMMA instrument.

Experiment

The new transient waveform recording system has the following characteristics. There are two independent recording channels, each with a full-scale sensitivity range adjustable between 50 mV and 2.5 V. Each channel has a maximum digitization rate of 100 MHz, bandwidth of > 100 MHz, a nominal amplitude resolution of 8 bits, and a memory capacity of 32 768 storage locations (32 Kbytes). Because the major difference in specifications between the original and the newer transient recorders is in memory size, we refer to them as 2Kb and 32Kb recorders for the remainder of this paper.

The first experiment involved analyzing missing output codes in the A/D converter using the histogram test.³ In this test, a full-scale sine wave of known frequency is sampled by each transient recorder and the digitized waveform level is collected over many cycles. A histogram is then produced that gives the relative probability of occurrence of the 256 amplitudes. The results of the histogram test for the 32Kb recorder are presented in Fig. 1 for (a) 100 kHz, (b) 1 MHz, and (c) 10 MHz input frequency. Both 2Kb and 32Kb recorders have an increase in lost codes for increasing slew rates, but in the 2Kb recorder approximately 90% of the codes are missing for the 10MHz input.² The 32Kb recorder is missing less than 10% of the codes at this frequency. This result implies a dynamic amplitude resolution of more than 7 bits, whereas the 2Kb recorder has been shown to have only 4-bit resolution under the same conditions.² The rise time of mass peaks obtained on the LAMMA have nearly a 10MHz slew rate and missing codes in the transient recorder translate to loss of precision for peak height and isotopic ratio measurements on the instrument.² The conclusion is that the 32Kb recorder should be able to digitize the pulse waveforms that make up the mass spectrum of the LAMMA more accurately.

In the three experiments to follow, the two recorders were made to collect in a simultaneous manner the waveform produced by the ion detector in the LAMMA 500. The sample used in this comparative study was a sputtered glass film containing oxides of 10 elements (similar to a zircon) at various weight percentages which produce positive-ion mass spectra with m/z values ranging from 1 to 270.

One can expand the dynamic range for recording a spectrum by utilizing two independent channels of the 32Kb transient recorder operating with different gain settings. The digitization rate was 10 ns/sample and only 8192 bytes of data (approximately 80 μ s) per

The authors are in the Center for Analytical Chemistry at the National Bureau of Standards, Gaithersburg, MD 20899.

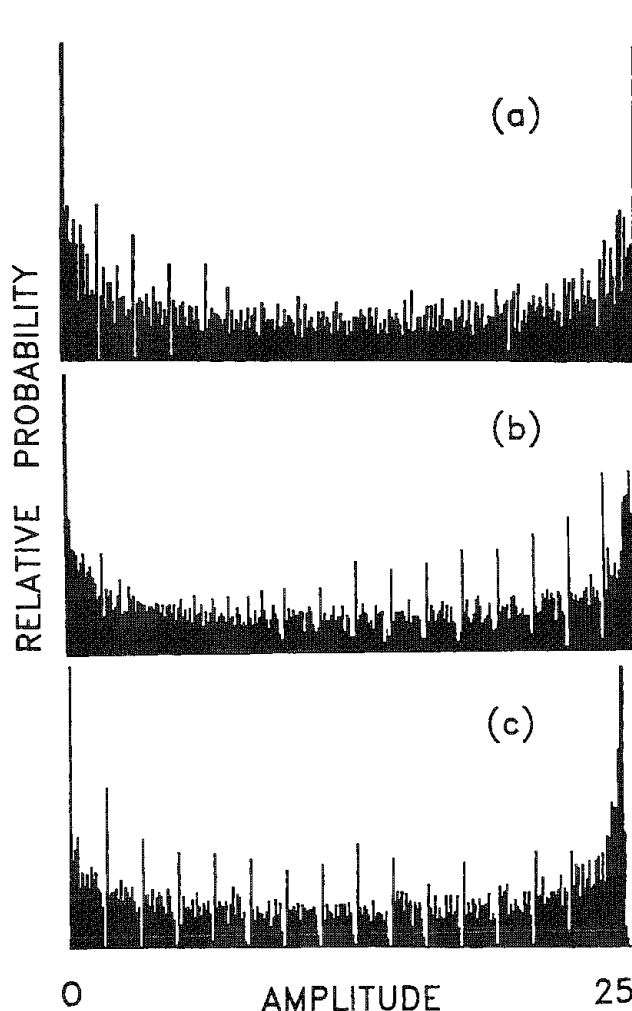


FIG. 1.--Histogram test results for 32Kb transient recorder: (a) 100 kHz, (b) 1 MHz, (c) 10 MHz sine wave input.

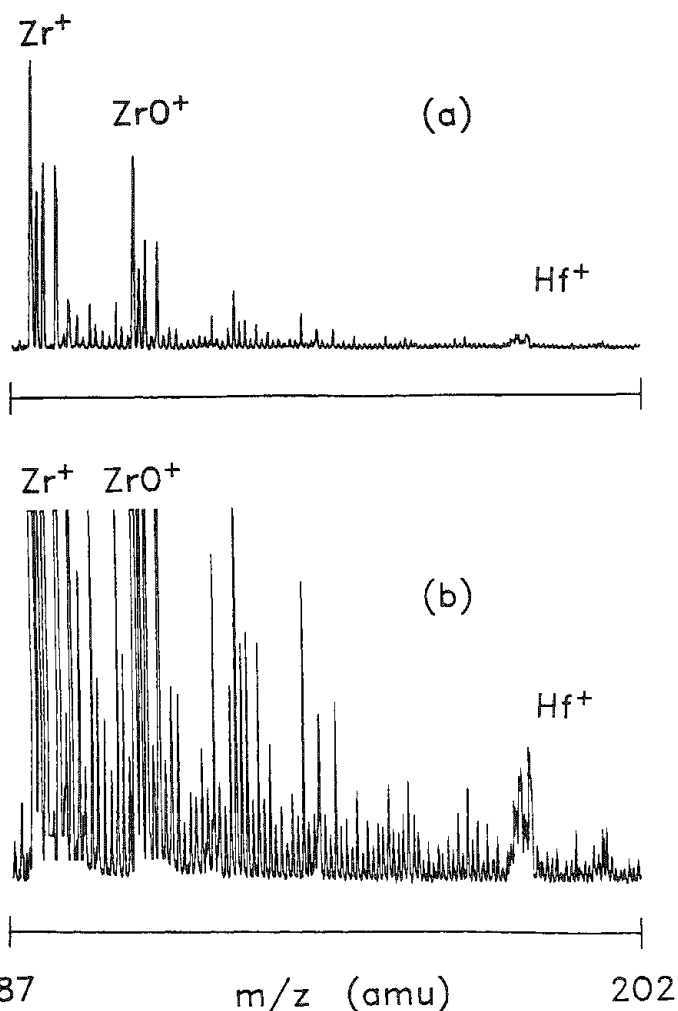


FIG. 2.--Same mass spectrum sampled by two 32Kb recorder channels operating in parallel: 1 V full-scale sensitivity, (b) 0.1 V sensitivity.

channel were saved. Figure 2 shows a 2 Kbyte portion of the mass spectrum recorded simultaneously by the two channels. Spectrum (a) collected at 1 V full scale shows the isotopes of Zr^+ and ZrO^+ with only a small indication of the presence of Hf^+ for the glass sample. (Zr is present with approximately 15 times the abundance of Hf.) Figure 2(b) shows the same spectrum at 10 \times gain in sensitivity. The Hf^+ peaks are clearly present; the Zr^+ and ZrO^+ species are off scale.

The main advantage of the 32Kb transient recorder is that a very large portion of the mass range can be recorded at the maximum digitization rate of 100 MHz. With the use of only the 8 Kb memory fraction and the highest digitization rate, spectra containing all the elements from hydrogen to uranium (actual mass of m/z 0 to 367) can be recorded from a single laser ionization event. The upper limit can be increased to $m/z > 5000$ when the entire 32 Kbytes of memory are used. The larger memory should be useful for those doing molecular organic LAMMA analysis, where m/z can be quite large. The 2Kb recorder must have a digitization rate of 20 MHz (50 ns between samples) to gather the full elemental mass range (m/z 1 to 300). A spectrum from the zircon glass film was recorded simultaneously at the same input sensitivity by the 2Kb recorder operated at a digitization rate of 20 MHz and by the 32Kb recorder at 100 MHz. Figure 3 shows a comparison of the spectra from the two recorders over a limited mass range. The five times longer time between samples of the 2Kb recorder shown in Fig. 3(a) results in very poor peak shape (due to the lack of point density), often with only one data point per peak, and can lead to large errors in peak amplitude measurements. Compare m/z 79, 83, and 84 on both frames of Fig. 3 to see an example of amplitude error. On the other hand, the 10ns sampling rate of the 32Kb recorder does not suffer from this problem, since there are sufficient data points to define a peak.

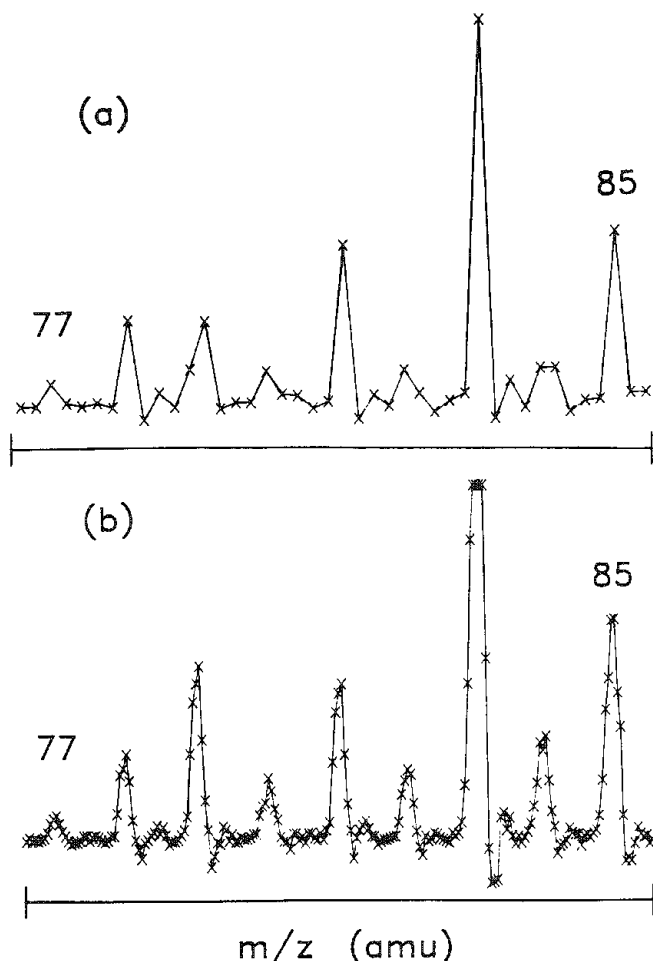


FIG. 3.--Expanded mass spectrum segment:
(a) 50ns sampling rate of 2Kb recorder,
(b) 10ns sampling rate of 32Kb recorder.
(x) are actual data points.

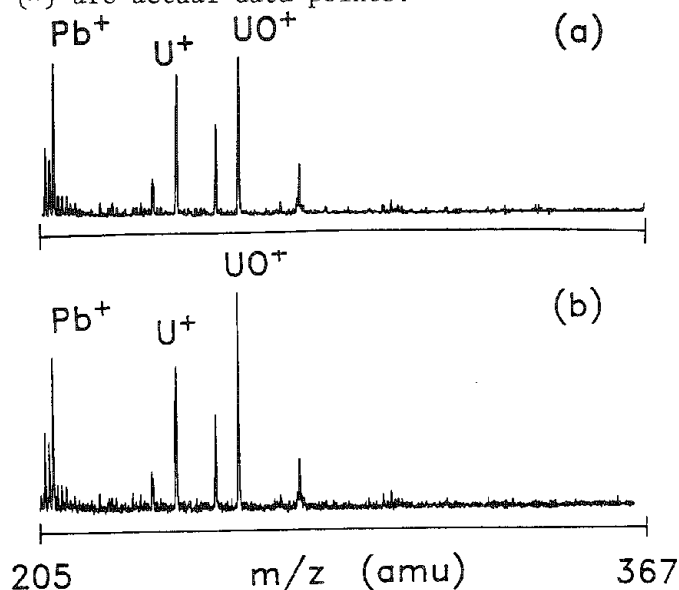


FIG. 4.--The same mass spectrum segment
collected by (a) 2Kb recorder and (b)
32Kb recorder for both devices operating
with 10ns sampling rate.

A further comparison was made between the 2Kb and 32Kb recorders operated at the same gain and same digitization rate of 100 MHz. As above, a LAMMA signal was simultaneously recorded in both digitizers. Under these conditions the 2Kb recorder can only capture a limited portion of the mass spectrum, the onset of which can be controlled by a variable trigger delay. Figure 4 shows a comparison between the two recorders for the high-mass region of the zircon glass film. We have observed that specific peak intensities from the 2Kb unit are lower than corresponding peaks found in the 32Kb spectrum (for example, UO^+ m/z 254 in Fig. 4). It is likely that this apparent biasing is related to the high percentage of missing codes and few available amplitude levels for the 2Kb recorder when the input signal has a high slew rate.

Another observation from Fig. 4 is that the apparent amplitude of baseline noise is larger for the 32Kb recorder, most likely because of its higher frequency bandpass compared with the 2Kb recorder.

Conclusion

Two different transient recorder systems have been compared for use with the Laser Microprobe Mass Analyzer. Although both are capable of providing similar information in a qualitative mode, the larger memory, modular design, and better high-frequency performance of the 32Kb recorder offer substantial advantages for quantitative work. In addition, with the newer recorder no trade off between digitization rate and range of mass spectral coverage need be made.

References

1. Certain commercial equipment, instruments, or materials are identified in this paper. Such identification does not imply recommendation or endorsement by the National Bureau of Standards, nor does it imply that the materials or equipment identified are necessarily the best available for the purpose.
2. D. S. Simons, "Isotopic analysis with the Laser Microprobe Mass Analyzer," *Intern. J. Mass Spectrometry and Ion Processes* 55: 15-30, 1983/1984.
3. *Dynamic Performance Testing of A-to D Converters*, Hewlett-Packard Note 5180A-2.

ISOTOPIC MEASUREMENTS WITH A REFLECTION-GEOMETRY LASER IONIZATION MASS SPECTROMETER (LIMS)

Filippo Radicati di Brozolo and R. W. Odom

This communication presents the results of an evaluation performed in our laboratory of the isotope ratio measuring capabilities of a Laser Ionization Mass Spectrometer (LIMS) (Model LIMA 2A, Cambridge Mass Spectrometry, Ltd., Cambridge, England).¹ The elements investigated in this study include Li, Ti, Mo, and W. The isotope ratios for these four elements were evaluated over a range of laser power densities, and hence ion signal intensities. The results show that the reflection geometry LIMS can provide reproducible isotopic ratio measurements (relative standard deviations on the order of $\pm 10\%$) for these elements, and the errors in accuracy of the measured isotopic ratios range from a few per cent to approximately 50%.

Since isotopic analysis should be entirely free of matrix-related effects, quantitative results should be obtained directly from peak intensities, after correction for obvious instrumental effects.

We have measured the isotopic composition of these four elements because they cover a wide range of atomic weights. The sample materials analyzed included Li_2CO_3 and spodumene ($\text{LiAl}[\text{Si}_2\text{O}_6]$; approximately 3% by weight Li); metallic alloys for Ti and Mo; and pure W metal.

The laser power density was adjusted for each sample so that the intensity of the major isotope signal was $\sim 25\%$ below the saturation level of the detection system. This level corresponds to a peak signal amplitude of approximately 1.4 V. For Li the variability in signal intensity from shot to shot was quite large, as will be discussed later. The ion signal intensities used for the isotope ratio calculations were the integrated peak areas for each isotope.

Table 1 presents the average isotopic composition of each of the elements investigated, along with absolute and relative standard deviations (RSD) of these measurements. The accepted or true isotopic ratios are also listed, along with the fractional deviation of the measured versus the true isotopic value $(I_m - I_t)/I_t$, where I_m and I_t are the measured and true isotopic ratios, respectively. These results are also illustrated in Fig. 1, in which the measured isotopic ratios normalized to true values are plotted for each of the isotopes.

The Li results are tabulated separately for the two samples, spodumene and Li_2CO_3 , since the differences in isotopic composition among natural samples are quite large, and hence there is no preferred "true" isotopic composition. If the true ${}^6\text{Li}/{}^7\text{Li}$ isotopic ratio for spodumene is assumed to be 0.08182 ± 0.00033 ,² then the fractional deviation for this sample is +0.066 (+6.6%). The Li_2CO_3 sample, obtained from D. S. Simons of NBS, is a "working standard" with a true ${}^6\text{Li}/{}^7\text{Li}$ isotopic ratio of 0.0832, and the calculated fractional deviation for our measurements is also 0.066 (6.6%).

The reference isotopic values for the heavier elements are taken from the NBS Tables.

The Li data show a discrimination in favor of the ${}^6\text{Li}$ isotope. This effect can be attributed to the inherent mass-dependent discrimination of the electron multiplier, which exhibits higher detection sensitivity for higher-velocity ions. This electron multiplier mass discrimination for constant energy ions favors the lighter ions by a factor proportional to $(m_1/m_2)^{1/2}$, where m_1 and m_2 are the masses of the heavy and light isotope, respectively. For the case of the Li isotopes, this factor equals 1.08 or an 8% discrimination in favor of detection of ${}^6\text{Li}$, which compares well with the measured discrimination of 6.6%. The RSDs of the Li isotope measurements are 9.1% and 13.4% for Li_2CO_3 and spodumene, respectively.

The Li isotope ratios were also determined as a function of the ${}^7\text{Li}$ ion intensity in order to evaluate the possibility of a nonlinear response of the electron multiplier to various ion signal intensity levels.³ The results of this investigation are illustrated in Fig. 2, which shows the measured Li isotopic ratio versus the ${}^7\text{Li}$ peak area intensity. The data points in the high-intensity region (Category I data) show an essentially constant

Authors Radicati di Brozolo and Odom are at Charles Evans & Associates, San Mateo, CA 94402.

TABLE 1

Major Isotope	n ^a	Isotope Ratios				
		Isotope	Measured	% RSD	True ^b	Error ^c
⁷ Li (Li ₂ CO ₃)	32	6	.0887±.0081	9.1%	.0832	+.066
⁷ Li (spodumene)	14	6	.0872±.0117	13.4%	.0818	+.066
⁴⁸ Ti	29	46	.082 ±.013	15.8%	.1082	-.25
		47	.078 ±.017	21.7%	.1055	-.26
		49	.065 ±.012	18.0%	.0750	-.13
		50	.058 ±.012	21.0%	.0727	-.20
⁹⁸ Mo	15	92	.562 ±.045	8.0%	.6271	-.10
		94	.369 ±.045	12.2%	.3896	-.05
		95	.629 ±.049	7.8%	.6158	+.02
		96	.661 ±.074	11.2%	.6900	-.04
		97	.405 ±.042	10.4%	.400	+.01
		100	.370 ±.032	8.7%	.4033	-.08
¹⁸⁴ W	22	180	.0022±.0014	64.0%	.0041	-.46
		182	.741 ±.060	8.0%	.8587	-.14
		183	.378 ±.039	10.3%	.4661	-.19
		186	.891 ±.060	6.7%	.9347	-.05

^aNumber of measurements.

^bIsotope ratio value accepted in the literature.

^cFractional error in measured isotope ratio; see text.

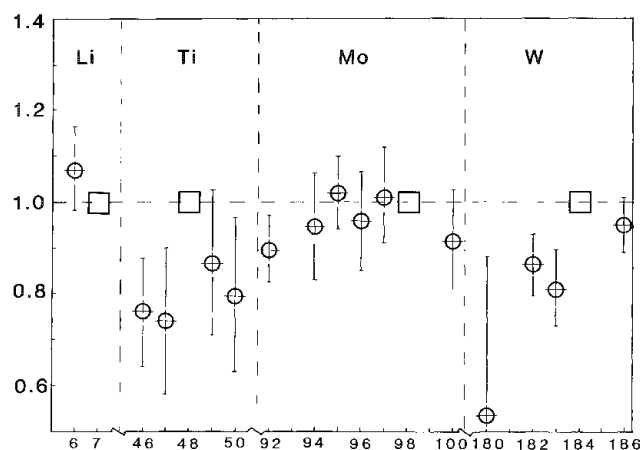


FIG. 1.--Measured isotopic ratios of Li, Ti, Mo, and W., normalized to true isotopic ratios. Without discrimination, all normalized isotopic ratios would fall on reference line.

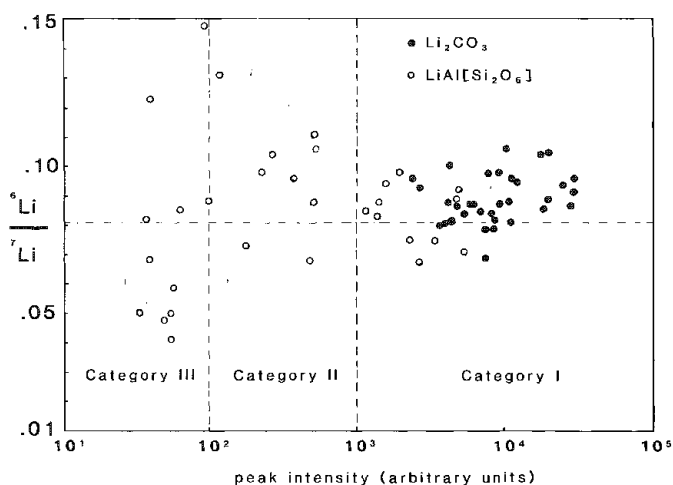


FIG. 2.--Measured ⁶Li/⁷Li as function of ⁷Li signal intensity (arbitrary units); most intense signals correspond to ~7500 ions at the detector (see text). Horizontal dashed line indicates "true" ⁶Li/⁷Li ratio.

$^6\text{Li}/^7\text{Li}$ ratio within our experimental error. Category II data show a larger dispersion, which reflects primarily the poorer counting statistics for these weaker ion signals, but show no systematic difference from the Category I data. Category III data exhibit very large dispersion and data were not included in the computation of results in Table 1. Our data demonstrate that the response of the LIMA 2A electron multiplier is approximately linear with signal intensity, over a range of two orders of magnitude.

The Ti isotopic ratios, normalized to ^{48}Ti , are uniformly low and lie outside the 1 σ error limits except for the $^{49}\text{Ti}/^{48}\text{Ti}$ ratio. This deviation from the true values cannot be attributed to a mass-dependent electron multiplier discrimination. The RSDs for these isotopic measurements range between 16% and 22%. The data show an overrepresentation of ^{48}Ti , which might be explained by an interfering molecular or cluster ion at nominal mass 48. For this sample the most likely interference would be the O_3^+ ion. However, the mass spectra do not show significant O^+ or O_2^+ peaks, and hence the O_3^+ ion intensity is assumed to make a negligible contribution to the mass 48 ion signal.

The Mo isotopic abundances agree with the accepted values except for the $^{92}\text{Mo}/^{98}\text{Mo}$ ratio. As was the case for the Ti isotopes, this deviation cannot be explained by an electron multiplier mass discrimination. The good agreement between measured and accepted values for the other isotopic ratios precludes considering a spectral interference that would overrepresent the ^{98}Mo ion over the ^{92}Mo ion. The RSDs of the Mo isotopic ratios lie between 8% and 12%, which is significantly better than those observed for the Ti measurements. The improved precision must be at least partly due to the fact that Mo isotopic ratios are much closer to unity than the Ti isotopic ratios.

The measured W isotopic ratios are all low relative to the true values, and the only ratio within 1 σ of the true value is the $^{186}\text{W}/^{184}\text{W}$ ratio. The measured $^{180}\text{W}/^{184}\text{W}$ ratio is lower by approximately a factor of two than the accepted value and a detectable ^{180}W peak was observed in only about 50% of the measurements. Excluding the $^{180}\text{W}/^{184}\text{W}$ ratio, the RSDs are between 7% and 10% and are the smallest observed in this work. At least part of this improved precision may be attributed to the fact that the W isotope ratios, with the exception of the $^{180}\text{W}/^{184}\text{W}$ ratio, are close to unity.

Two of the most important factors affecting the precision of the isotopic ratio measurements in these LIMS analysis are the ion counting statistics and dynamic digitization limitations of the transient recorder. The major isotope signals in our experiment were in general of the order of 1.4 V, which corresponds to ~ 7500 ions arriving at the electron multiplier. The Poisson statistical error for this signal is $\sim 1.2\%$. A 0.14V ion signal would have a counting error of $\sim 3.7\%$, and hence the RSD for a 1:10 isotopic ratio--e.g., $^6\text{Li}/^7\text{Li}$ or $^{46}\text{Ti}/^{48}\text{Ti}$ --would be 3.9%. The errors in the precision of all isotope ratios measured in this work are significantly larger than the minimum value obtained from ion counting statistics alone, which indicates that errors of dynamic digitization in the transient recorder are very important. Simons³ has discussed in detail these errors for another apparatus (LAMMA) equipped with a transient recorder similar in many respects to ours (Sony-Tektronix 390 AD), so that his conclusions should be directly applicable to our results.

The Ti and W data suggest a systematic bias in the measurement, which favors the detection of the major isotope. The Li data show a different bias, which favors detection of the lighter isotope, and which can be attributed to the electron multiplier mass discrimination. The Mo data do not show a systematic bias, with the possible exception of the $^{92}\text{Mo}/^{98}\text{Mo}$ ratio. The systematic overrepresentation of the major isotope in our experiment cannot be explained by an electron multiplier nonlinearity. The exact nature of the causes of such a phenomenon is not clear at this time; however, one possible source of error could be in the A/D conversion process in the transient recorder. We are investigating this potential source of error at present.

References

1. C. A. Evans Jr. et al., "Microanalysis of bulk samples by laser-induced ion mass analysis," *Microbeam Analysis--1983*, 101-105.
2. H. J. Svec and A. R. Anderson, "The absolute abundance of the lithium isotopes in natural sources," *Geochim. Cosmochim. Acta* 29: 633-641, 1965.
3. D. S. Simons, "Isotopic analysis with the Laser Microprobe Mass Analyzer," *Int. J. Mass Spectrom. Ion Proc.* 55: 15-30, 1983/1984.

LAMMA/LIMA: A METHOD OF CONTROLLING THE LASER POWER AT THE SPECIMEN FOR MILD FRAGMENTATION OF ORGANIC MOLECULES

F. W. Anderson, Hans Heinen, and J. N. Ramsey

Laser ionization and subsequent mass spectroscopy of the fragments has been successfully used in a transmission mode as the LAMMA 500 for several years.¹ Recently its usefulness was extended to the reflection mode as the LAMMA 1000.² Studies have been aimed at understanding the differences in the fragmentation patterns between laser and electron impact ionization.³

As has been stated earlier,^{4,5} the degree of fragmentation of a molecule controls the amount of useful information leading to molecular identification. As part of a particulate contamination analysis problem, samples of cellulosic material and polypropylene were run on a LAMMA 1000. The spectra are shown in Figs. 1 and 2. The fragmentation has been so severe that it would be very difficult to reconstruct mentally the information into a molecular identity. Precise control and measurement of a very low laser power *applied to the specimen* is essential. Stable operation of the lasers requires a minimum power level. Crossed polarizers were used to reduce and control the power level at the specimen. However, the desired/required power levels were still lower. F. W. Anderson employed the through-focus series concept from his transmission electron microscopy experiments vis-à-vis the LAMMA. Defocusing reduces the energy density of the beam on the sample and allows irradiation of the sample without producing volatilization and ionization. Then, by progressively improving the focus and repeatedly firing the laser, one can go through initial desorption and soft ionization and fragmentation to the point of extreme fragmentation where the spectrum is not recognizable. The laser power is constant and stabilized but the power to the specimen is variable and controlled. Fragmentation recognizable by an experienced organic mass spectroscopist is made possible.^{4,5} Figure 3 shows the through-focus method; the preferred starting point is the lower case, with the beam focused below the surface. If it is focused above, the focal point can provide a hot spot that could further fractionate any vapor.

This technique has been applied to five organics, well characterized by Electron Impact/Mass Spectroscopy (EI/MS):

Figure 4 shows the LAMMA 1000 negative spectrum from benzophenone, an aromatic ketone with a molecular mass of 182. The base peak by LAMMA is 183, probably from protonation by the abstraction of hydrogen from a second molecule of benzophenone. This process could occur because of the high sublimation pressure of benzophenone in the laser beam. Since the reaction would be pressure sensitive, possibly even lower laser power would eliminate the protonation and give the 182 peak. EI/MS also gives the 105 and 77 peaks.

Figure 5 shows the LAMMA 1000 negative spectrum of rhodamine B, an indicator dye. Neither LAMMA nor EI detects the full molecule (478) because HCl is lost, giving a parent peak of 442. As indicated, all EI mass peaks are found in LAMMA along with many extraneous peaks, which might be confusing; however, experienced organic mass spectroscopists can see the pertinent peaks. The skill background required in the early stages of any analytical/characterization technique, especially for organics, is of a high level.

Figure 6 shows the LAMMA 1000 negative spectrum for poly alpha methy styrene, an unzip-pable polymer (that is, it breaks apart sequentially as monomers).

Figure 7 shows the LAMMA 1000 positive spectra of Irganox 1010 (Ciba Geigy®), a high-molecular-weight (1176), multifunctional anti-oxidant and thermal stabilizer. The LAMMA matches the EI spectra well, with the LAMMA giving additional information: the phenyl and benzyl ions suggest an aromatic compound.

Figure 8 shows the LAMMA 1000 negative spectrum of glycerol monostearate, a monoester of glycerine used as an emulsifier and lubricant. As stated, the major EI peaks are also in the LAMMA spectrum. Of particular interest are the strong 358 and 340 peaks by LAMMA, representing a loss of H₂O, typical of the rearrangement loss in alcohol or aldehydes;

Authors Anderson and Ramsey are at IBM Corp., Hopewell Junction, NY 12533; author Heinen is at Leybold Heraeus, Cologne, Federal Republic of Germany. Given as a "late-breaking" paper at the 1984 MAS meeting at Lehigh University, Bethlehem, Pa., in June 1984.

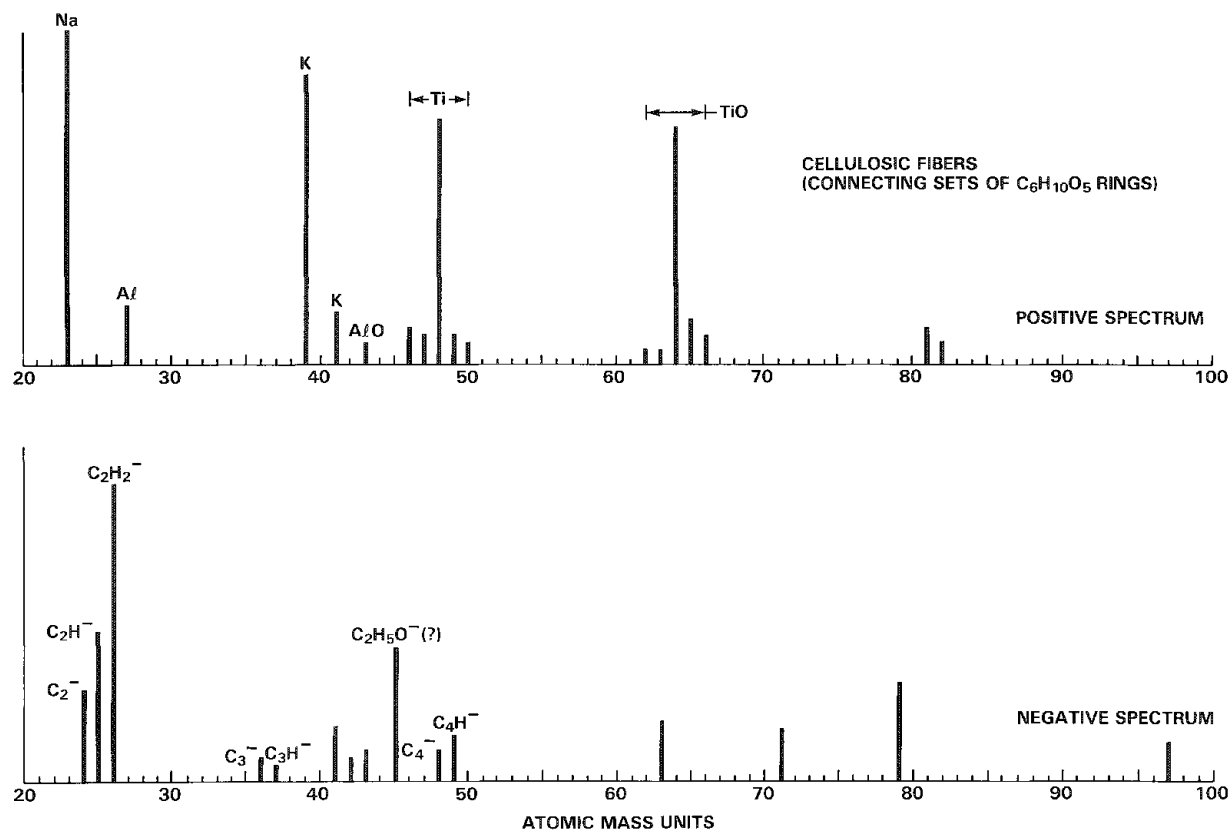


FIG. 1.--Fibrous material.

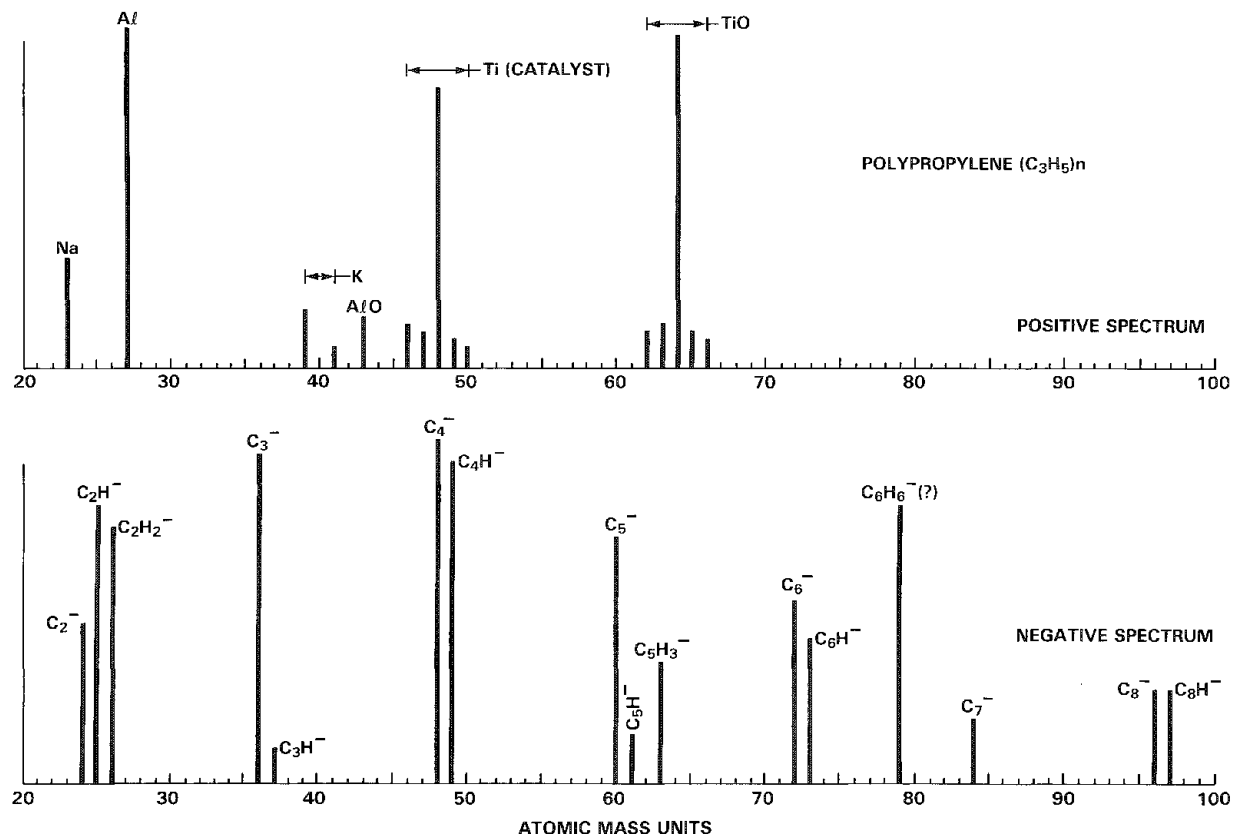


FIG. 2.--Nodules on celulosic fibers.

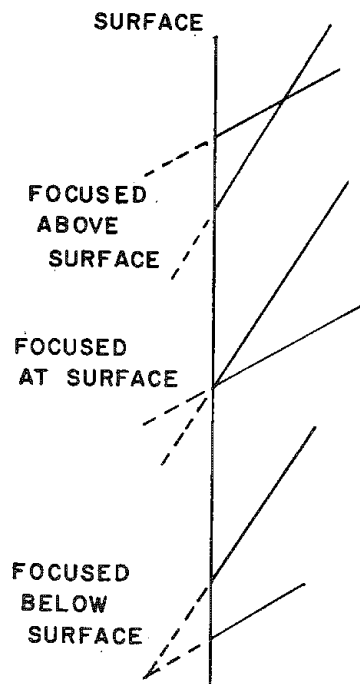


FIG. 3.--'Through-focus' method of reducing laser power density at specimen.

this information is lacking in EI.

These LAMMA successes (defined as recognizable to EI/MS) led the authors to try an unknown; a residue discovered after an etching and cleaning process in device manufacture. Figure 9 showed the material to be nitrobenzene sulfonic acid. (Note the overlap of the two mass range spectra, with 157 on both.)

Figure 10 shows the spectra from 1,4 diphenoxy benzene, a poly phenyl ether, taken recently on the LIMA by the defocused method as outlined above; again, recognizable fragments are produced.⁵ As expected, this result shows that the method is applicable to at least two makes of instrument.

Conclusions

Although it is evident that the spectra of these known organic materials contain recognizable fragments, there are many extraneous peaks beyond EI that add a great deal of uncertainty in the analysis of unknown organic materials. A considerable effort is required to understand this new and different means of ionization in order to sort out factors such as differences in positive and negative spectra, changes in fragmentation path, pressure effects, etc. The technique should be very useful for analysis of organics.

This technique has been applied to five organics, well characterized by Electron Impact/Mass Spectroscopy (EI/MS): benzophenone (Fig. 4), rhodamine B (Fig. 5), poly alpha methyl styrene (Fig. 6), Irganox 1010 (Fig. 7), and glycerol monostearate (Fig. 8).

These LAMMA successes (defined as recognizable to EI/MS) led the authors to try an unknown (Fig. 9); and spectra from 1,4 diphenoxy benzene are shown in Fig. 10.

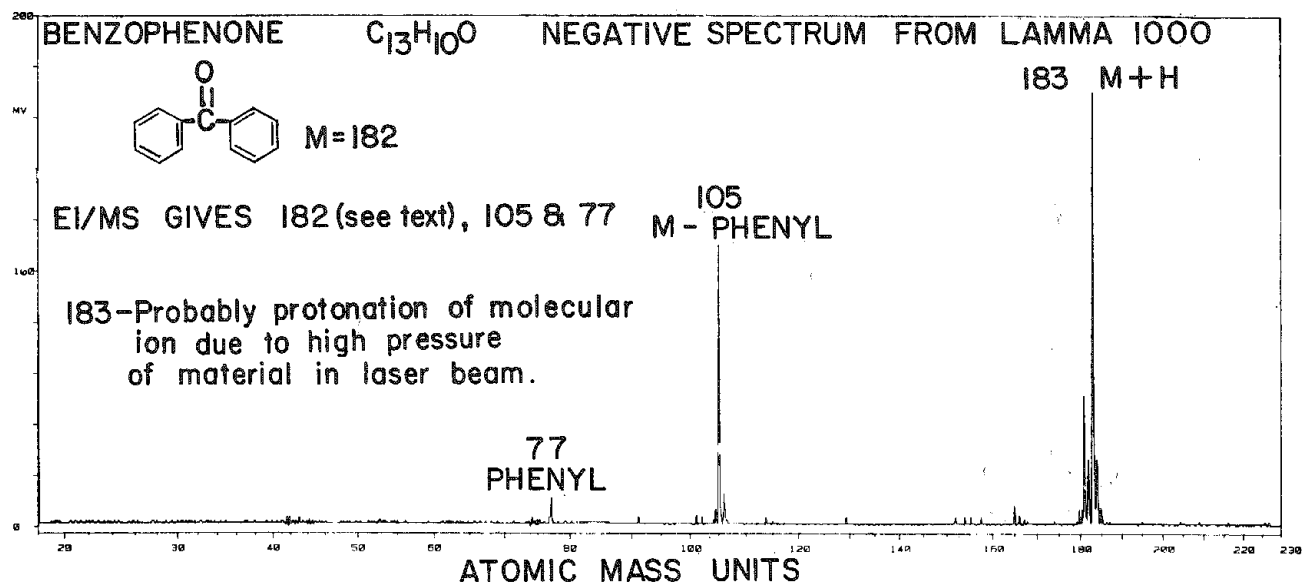


FIG. 4.--LAMMA 1000 negative spectrum from benzophenone, an aromatic ketone with molecular mass of 182. Base peak by LAMMA is 183, probably from protonation by abstraction of hydrogen from second molecule of benzophenone. This process could occur because of high sublimation pressure of benzophenone in laser beam. Since reaction would be pressure sensitive, possibly even lower laser power would eliminate protonation and give 182 peak. EI/MS also gives 105 and 77 peaks.

References

1. R. Kaufman, *Microbeam Analysis--1982*, 341.
2. F. Hillencamp, R. Kaufman, and R. Wechsung, presented at 1983 MAS meeting (unpublished).
3. D. Hercules, *Analy. Chem.* 280, February 1982.
4. J. N. Ramsey, "Small area molecular analysis as applied in the microelectronics industry," *J. de Physique* Supplement C-2: 881, 1984.
5. J. N. Ramsey, "Microelectronics processing problem solving: The synergism of complementary techniques," *Industrial Applications of Surface Analysis*, ACS Symp. Ser. 199 (in press).

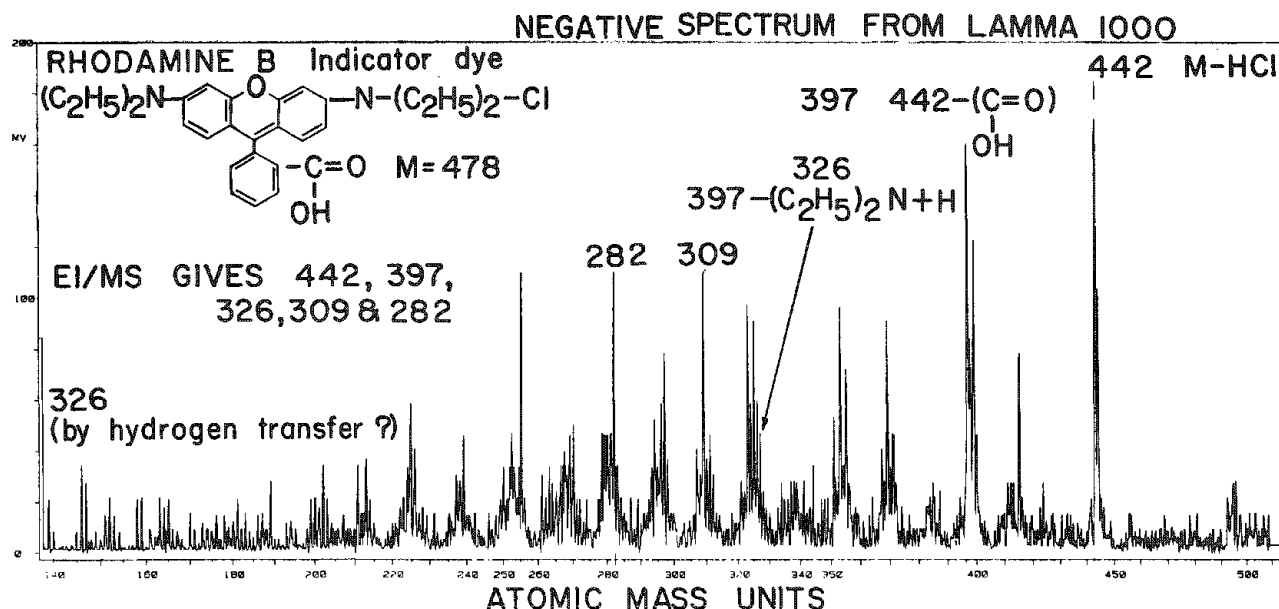


FIG. 5.--LAMMA 1000 negative spectrum of rhodamine B, an indicator dye. Neither LAMMA nor EI detects full molecule (478) because HCl is lost, giving parent peak of 442. As indicated, all EI mass peaks are found in LAMMA along with many extraneous peaks, which might be confusing; however, experienced organic mass spectroscopists can see pertinent peaks. Skill background required in early stages of any analytical/characterization technique, especially for organics, is of high level.

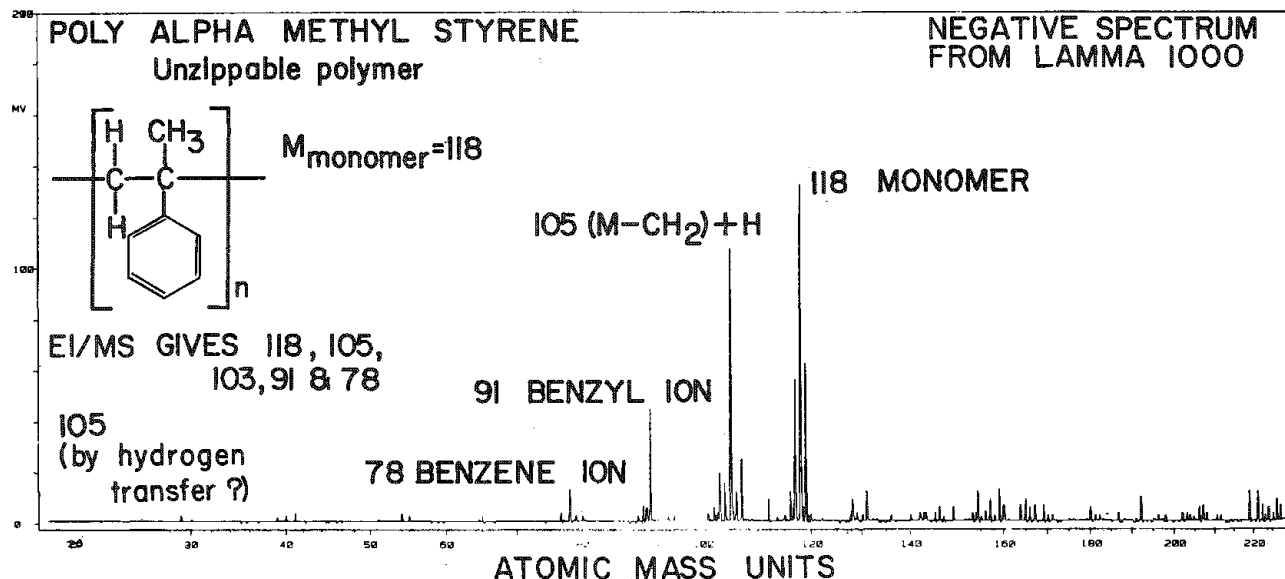


FIG. 6.--LAMMA 1000 negative spectrum for poly alpha methyl styrene, an unzippable polymer (that is, it breaks apart sequentially as monomers).

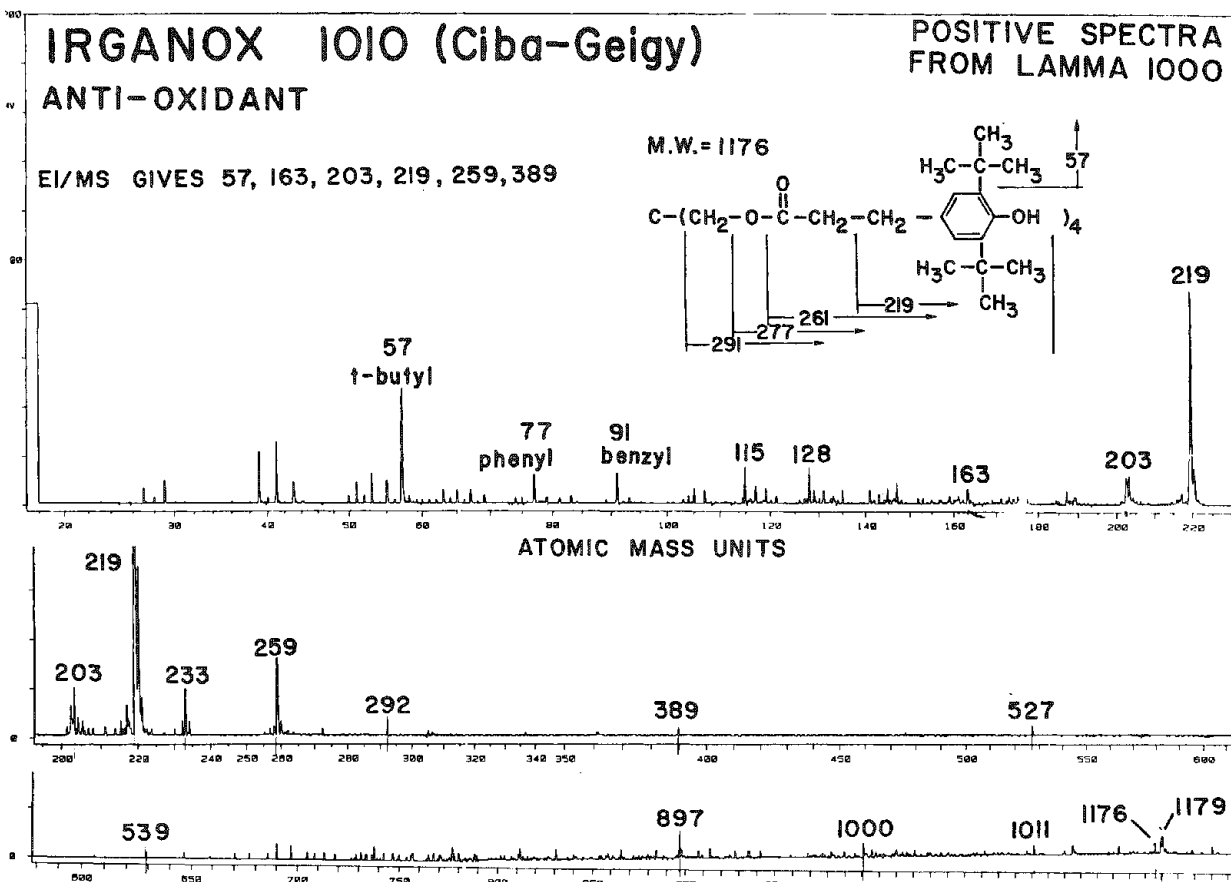


FIG. 7.--LAMMA 1000 positive spectra of Irganox 1010 (Ciba Geigy®), a high-molecular-weight (1176), multifunctional anti-oxidant and thermal stabilizer. LAMMA matches EI spectra well and gives additional information: phenyl and benzyl ions suggest aromatic compound.

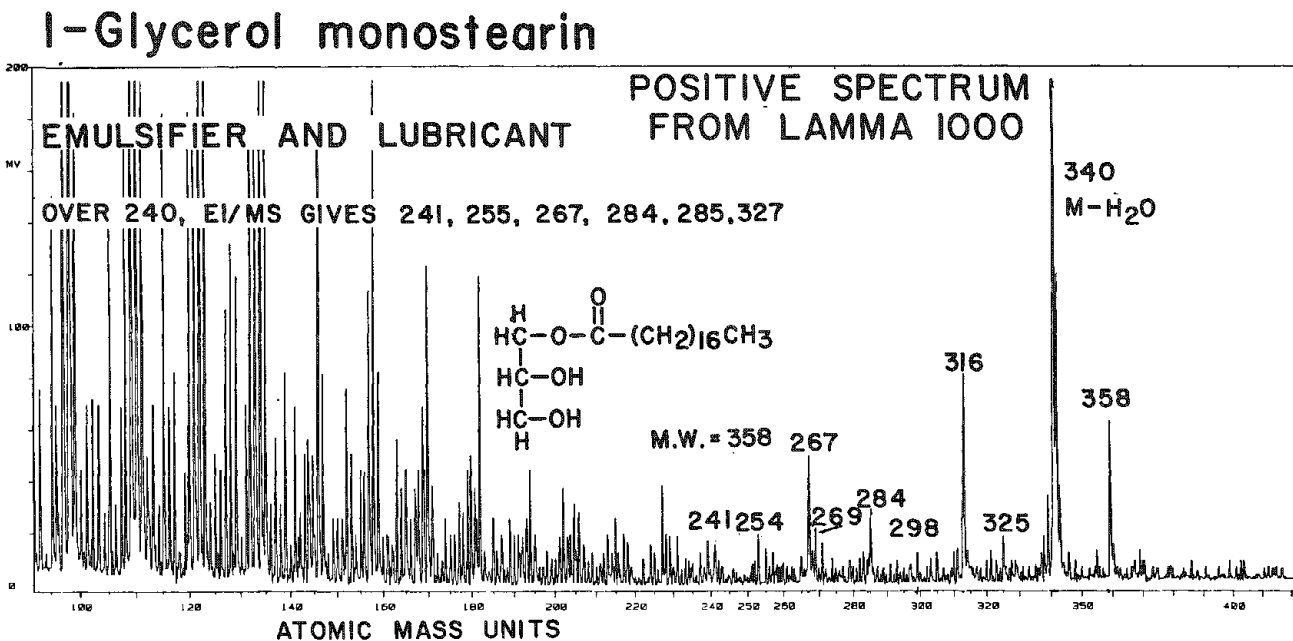


FIG. 8.--LAMMA 1000 negative spectrum of glycerol monostearate, a monoester of glycerine used as emulsifier and lubricant. As stated, major EI peaks are also in LAMMA spectrum. Of particular interest are strong 358 and 340 peaks by LAMMA, representing a loss of H₂O, typical of rearrangement loss in alcohol or aldehydes; this information is lacking in EI.

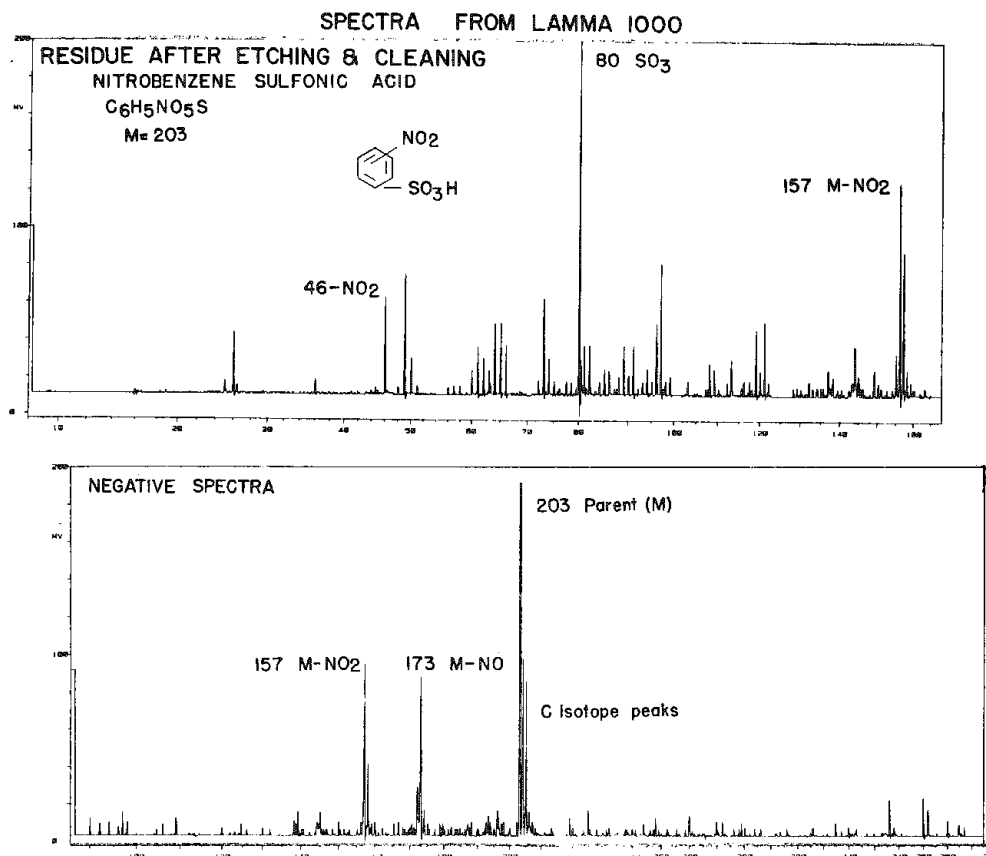


FIG. 9.--LAMMA spectra of unknown, a residue discovered after etching and cleaning process in device manufacture, show it to be nitrobenzene sulfonic acid. (Note overlap of two mass range spectra, with 157 on both.)

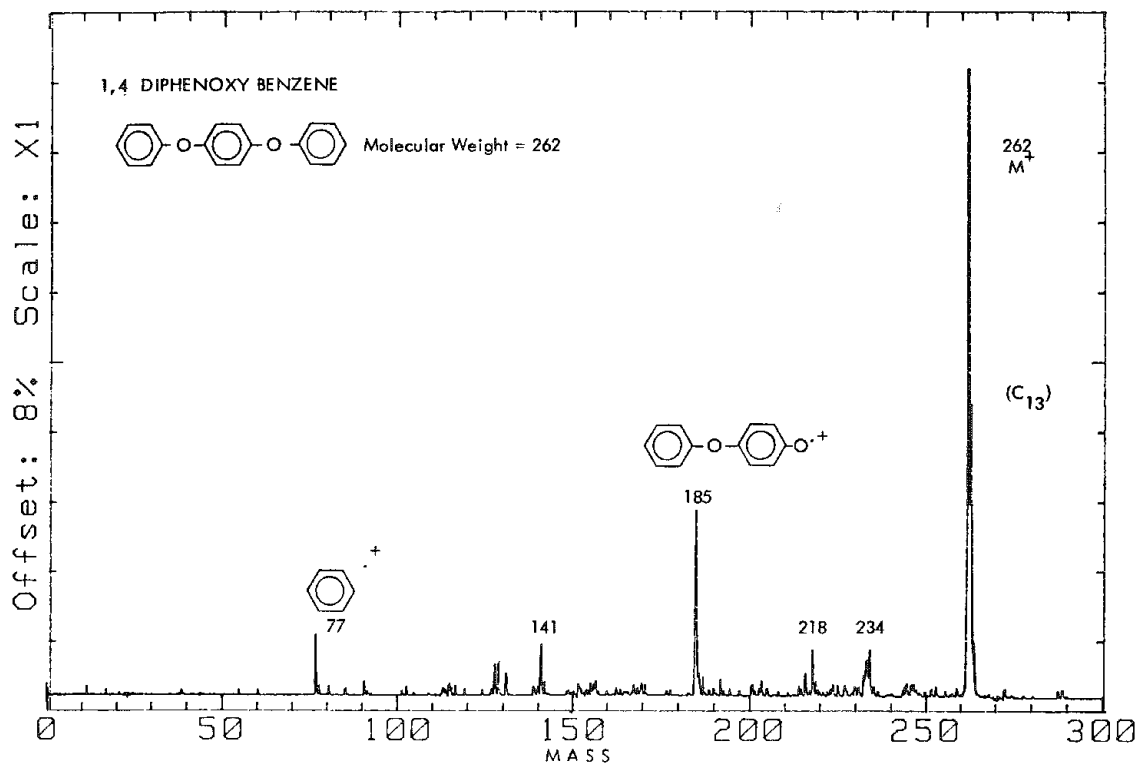


FIG. 10.--Spectra from 1,4 diphenoxy benzene, a poly phenyl ether, taken on LIMA by defocused method. Again recognizable fragments are produced.⁵ Result shows that method is applicable to at least two types of instrument.

LASER MICROPROBE MASS ANALYSIS OF CARBONATE IN APATITE OF BIOLOGICAL CONCRETIONS

P. F. Schmidt, B. Hagen, and D. B. Leusmann

Well-established techniques for the study of biological concretions like urinary calculi are x-ray diffraction and infrared spectroscopy. X-ray diffraction is a useful method in the study of crystalline material and allows a quantitative estimation of the different constituents of stones.^{1,2} An alternative method for stone analysis is infrared spectroscopy. This method demonstrates the major compounds (noncrystalline as well as crystalline) and requires only a small sample.^{3,4} But both methods are less precise in the identification of carbonate in apatite, especially if the carbonate content is low. Moreover, no estimation of an inhomogeneous distribution of carbonate is possible. Therefore, we performed investigations with the laser microprobe mass analyzer (LAMMA).

The aim of these investigations is to demonstrate the ability of laser microprobe mass analysis for the determination of the chemical compounds of human concretions, especially for the detection of carbonate in apatite and for the detection of oxalate. For this purpose, urinary calculi and standards of comparable chemical composition have been analyzed.

Material and Methods

The laser microprobe technique and infrared spectroscopy have been used for the analysis of the standards and the urinary calculi. The laser microprobe mass analyzer (LAMMA 500, Leybold-Heraeus) combines an optical microprobe with a laser source and a time-of-flight mass spectrometer. The light microscope allows observation of the various crystals and focusing of a short and intense pulse of a Nd-YAG-laser onto a selected area to be analyzed. This area is then evaporated and ionized. The ionized part of the evaporated material is analyzed in the time-of-flight mass spectrometer in which ions of different m/e ratios are discriminated according to their different flight time. Each laser shot can yield a complete positive or negative spectrum.⁵ The standards and the stones were powdered and attached to a grid. The bars of the grids were covered with a specific adhesive, so that the small particles of the powder adhere on the grid. The small crystals were analyzed with laser light at grazing incidence on a visible edge. For an analysis LAMMA needs very small amounts of material: 10^{-13} g.

The infrared spectra were registered by means of an infrared spectrophotometer from Beckman, Acculab 10, covering the range of 4000 to 250 cm^{-1} . For this study the potassium bromide pellet technique was used: 250 mg of KBr were thoroughly mixed with 1-2 mg of the sample and pressed to form a pellet.³

Results

Reference Mass Spectra of Standards. To make an exact interpretation of the LAMMA spectra obtained from renal stones possible, analyses of standards were first performed: CaO , Ca(OH)_2 , CaHPO_4 , apatites like $\text{Ca}_{10}(\text{PO}_4)_6 \cdot (\text{OH})_2$ (hydroxyapatite) and $\text{Ca}_{10}(\text{PO}_4)_6 \cdot \text{CO}_3 \cdot (\text{OH})_2$ (carbonate apatite), $\text{MgNH}_4\text{PO}_4 \cdot 6\text{H}_2\text{O}$ (struvite)/ CaCO_3 (carbonate), and $\text{CaC}_2\text{O}_4 \cdot \text{H}_2\text{O}$ (calcium oxalate monohydrate: whewellite), and $\text{CaC}_2\text{O}_4 \cdot 2\text{H}_2\text{O}$ (calcium oxalate dihydrate: weddellite).

The LAMMA mass spectra of these standards were reproducible and were characteristic for the specific chemical compounds. With regard to the problem under discussion, we demonstrate typical mass spectra of calciumoxalate ($\text{CaC}_2\text{O}_4 \cdot \text{H}_2\text{O}$) (Fig. 1) and calcium carbonate (CaCO_3) (Fig. 2). The mass spectra show typical mass lines of the specific chemical compounds. Of great interest is the characteristic mass line at $m/e = 60$, representing CO_3 . By this mass peak the identification of carbonate apatite is possible, which is also demonstrated by the analysis of synthetic carbonate apatite (Fig. 3). This

Author Schmidt is at the Institut für Medizinische Physik and authors Hagen and Leusmann at the Urologische Klinik of the University of Münster in the Federal Republic of Germany. They gratefully acknowledge the technical assistance of Mrs. Schwantge and Mrs. Flammand.

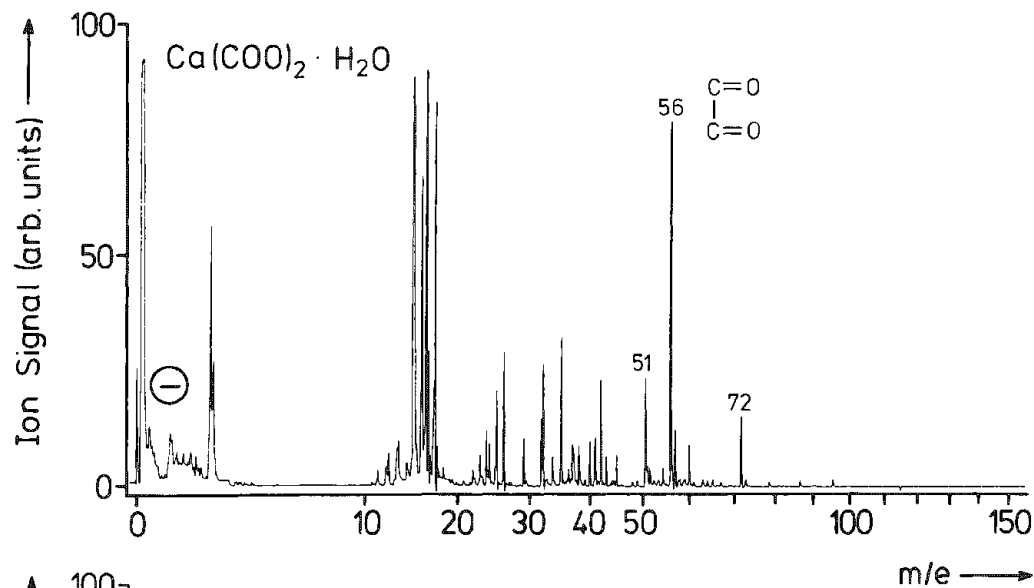


FIG. 1.--LAMMA spectrum of calcium oxalate ($\text{CaC}_2\text{O}_4 \cdot \text{H}_2\text{O}$) with characteristic mass line at $m/e = 56$ (C_2O_2).

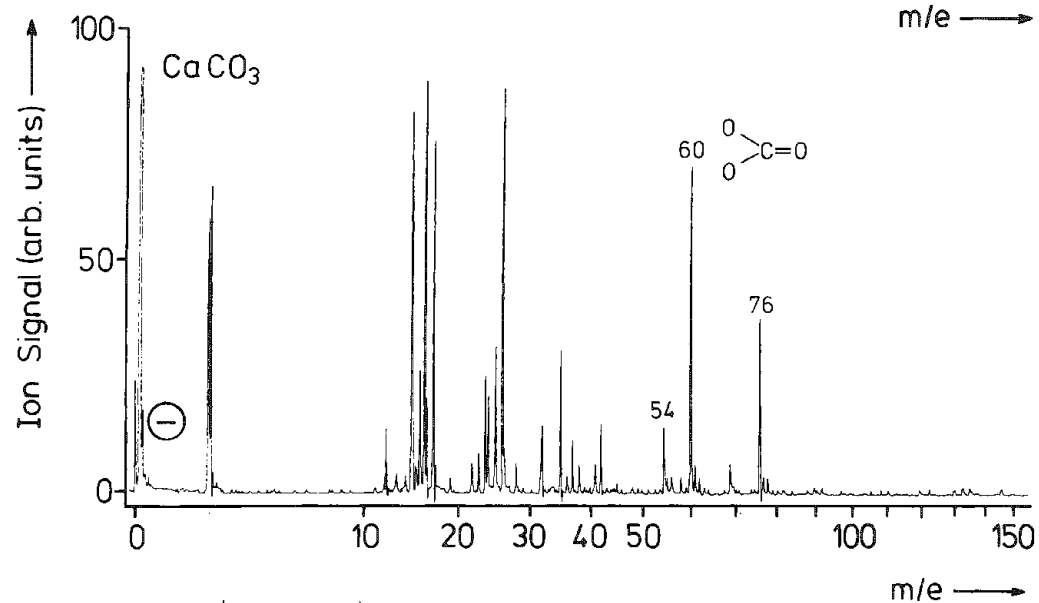


FIG. 2.--LAMMA spectrum of calcium carbonate (CaCO_3) with characteristic mass line at $m/e = 60$ (CO_3).

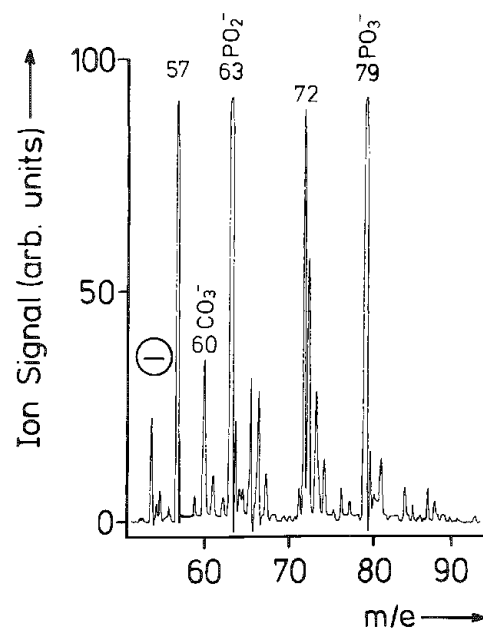


FIG. 3.--Significant region of LAMMA spectrum of synthetic carbonate apatite: $\text{Ca}_{10}(\text{PO}_4 \cdot \text{CO}_3 \cdot \text{OH})_6 \cdot (\text{OH})_2$. Mass line at $m/e = 60$ demonstrates presence of CO_3 .

spectrum shows that besides typical apatite mass lines, the carbonate mass line at $m/e = 60$ are also found.

Stone Analyses. (a) Analyses of urinary calculi show that it is possible to identify various compositions of stones. For example, Fig. 4 shows a mass spectrum of an apatite stone. Besides organic mass lines originating from the organic matrix, mass lines ($m/e = 57, 63, 72, 79$) appear that are typical for phosphate. Figure 5 shows a mass spectrum of a struvite stone ($MgNH_4PO_4 \cdot 6H_2O$). Besides mass lines of phosphate the mass line $m/e = 97$ (NH_4PO_3) indicates struvite. These spectra are comparable with the spectra of the specific reference standards.

(b) The LAMMA analysis of a mixed stone (70% apatite, 20% whewellite: calcium oxalate monohydrate), 10% weddellite (calcium oxalate dihydrate) demonstrates the occurrence of oxalate ($m/e = 51$ and 56) in an apatite (Fig. 6).

(c) Figure 7 shows an infrared spectrum of an apatite stone. The broad absorption maximum at 1420 cm^{-1} and a sharp peak at 875 cm^{-1} indicate the presence of carbonate. The corresponding LAMMA analyses result in an inhomogeneous distribution of carbonate. There are regions within the apatite without carbonate and regions with a high ion signal at $m/e = 60$ (CO_3) (Fig. 8).

(d) One of the advantages of LAMMA is shown by the analysis of a mixed stone: 30% struvite, 30% ammonium hydrogen urate, and 40% apatite, estimated by x-ray diffraction measurements. Figure 9 shows an infrared spectrum of this stone. In this case the identification of carbonate is difficult due to the interference of the CO_3 band at 875 cm^{-1} with bands originated by ammonium hydrogen urate. Since LAMMA permits the light microscopical observation of the specimen, the several constituents of this mixed stone could be separated. Thus it was possible to analyze struvite monocrystals, ammonium acid urate crystals, and apatite spherulites. By this analysis LAMMA was able to demonstrate that only apatite spherulites contain carbonate.

(e) To get more information on the content in apatite we analyzed 7 different hydroxy-apatite stones (noninfection stones) and 7 different struvite stones. The struvite stones were grown in alkaline-infected urine (infection stones). From each sample 100 analyses were performed. Since at present no absolute quantitation is possible we used a relative quantitation⁶ by referring the ion signal of CO_3 ($I_{m/e=60}$) to the ion signal of PO_2 ($I_{m/e=63}$). The results of these evaluations are given in Fig. 10. The carbonate content of infection stones is higher than the carbonate content of noninfection stones.

(f) Analyses of the organic matrix of stones demonstrate no mass peak of carbonate, so that the detected carbonate is incorporated into the apatite.⁷

Conclusions

The detection of carbonate in apatite as well as the mechanisms for incorporation of carbonate into apatite have been the subject of many investigations.⁸ Isolated Ca-carbonate was formerly supposed to be present in urinary calculi. Today, two mechanisms are assumed for incorporation of carbonate ions into apatite: Type A carbonate apatite means the incorporation of carbonate ions into the hydroxyl position;⁹ Type B carbonate apatite, the replacement of phosphate by carbonate ions.¹⁰ With regard to urinary calculi a pH-dependent variable supply of bicarbonate ions (HCO_3^-) is responsible for the incorporation of carbonate in apatite. During an urinary tract infection with urea-splitting bacteria, where CO_2^- and NH_3^- is set free, an alkalic urine is formed by hydrolysis of CO_2^- . Conditioned by the resulting high concentration of HCO_3^- , the apatite formed in such an environment contains a large amount of carbonate (carbonate apatite).

In the mildly acid pH region, nearly no free bicarbonate ions exist. Therefore, apatite crystals grown in urine not infected by urea-splitting bacteria contains only very small amounts of carbonate (hydroxyapatite). For these reasons one can distinguish between hydroxyapatite and carbonate apatite; the latter is regarded as pathognomonic for urine infected by urea-splitting germs.

It is possible to discriminate between hydroxyapatite and carbonate apatite by infrared spectroscopy, which is limited only on its capability for detecting minor components in mixed stones.¹¹

For several years Raman spectroscopy (laser molecular microprobe, MOLE) has been also

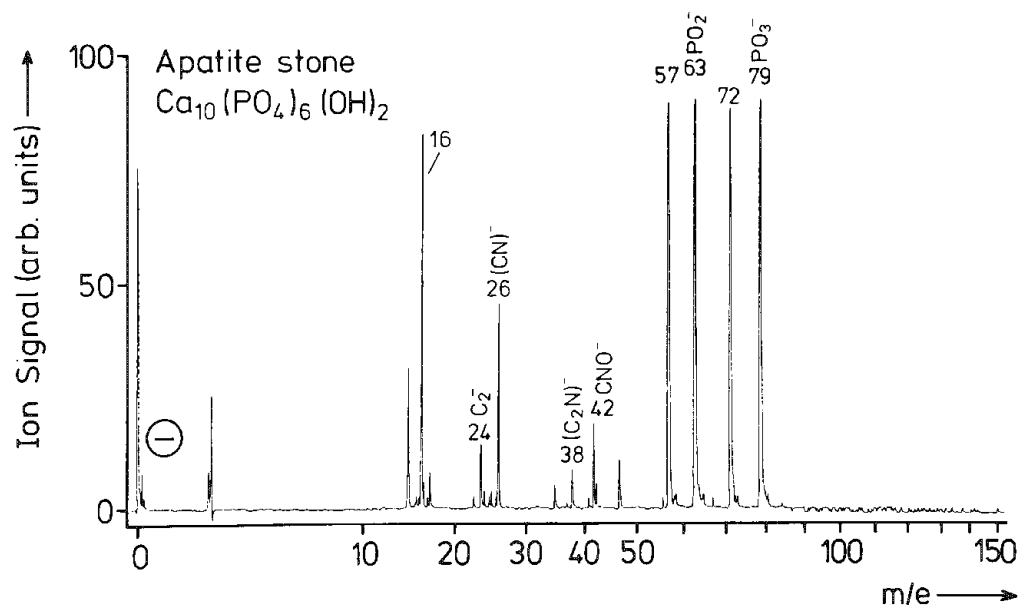


FIG. 4.--LAMMA spectrum of pure apatite stone with typical sequence of mass lines $m/e = 57, 63, 72,$ and 79 (phosphate).

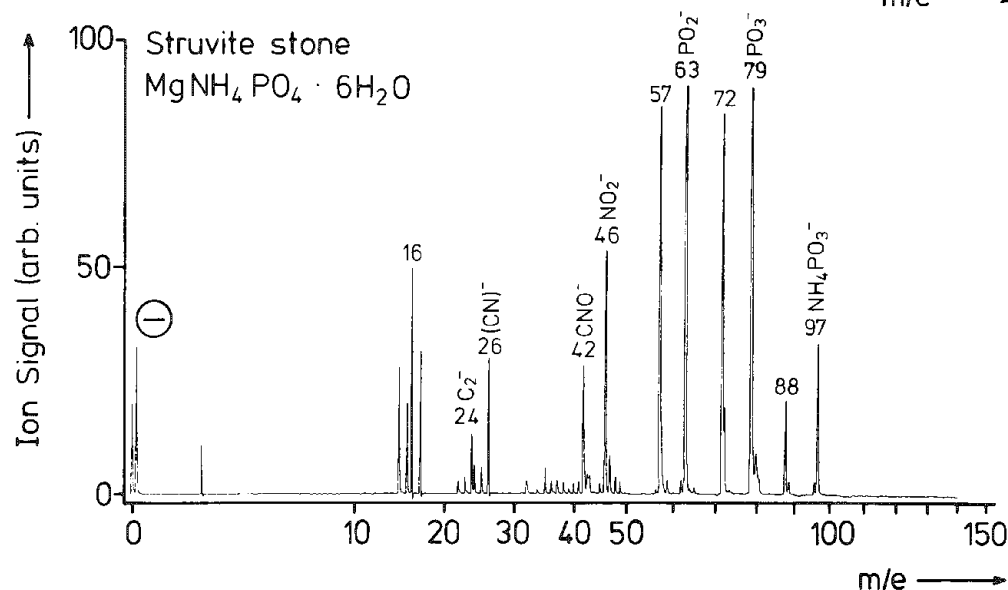


FIG. 5.--Mass spectrum of a struvite stone. A characteristic mass line for struvite is at $m/e = 97$ (NH_4PO_3).

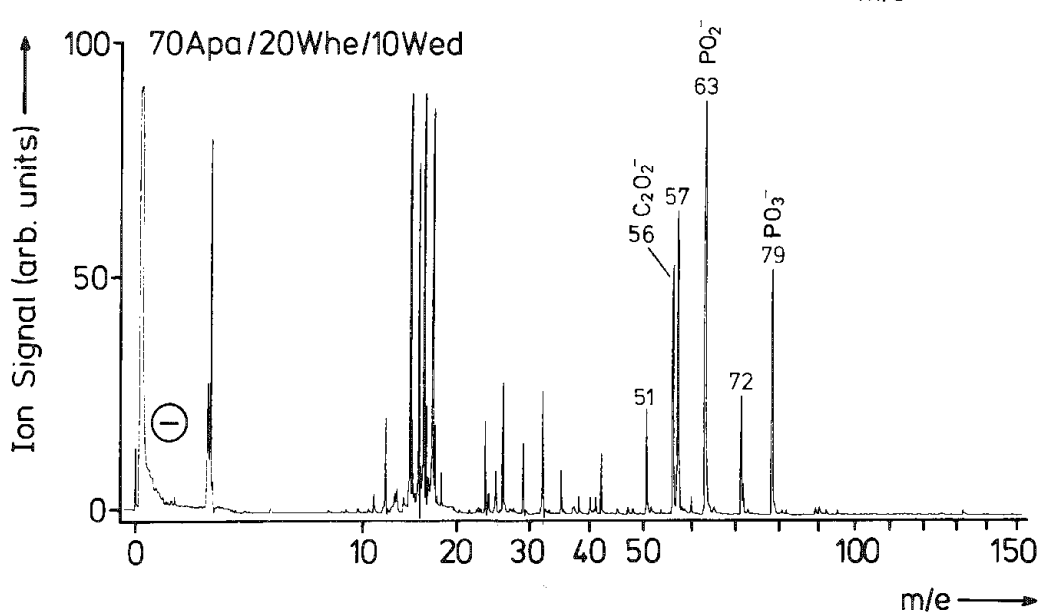


FIG. 6.--LAMMA analysis of mixed stone demonstrating occurrence of oxalate: $m/e = 56$ (C_2O_2).

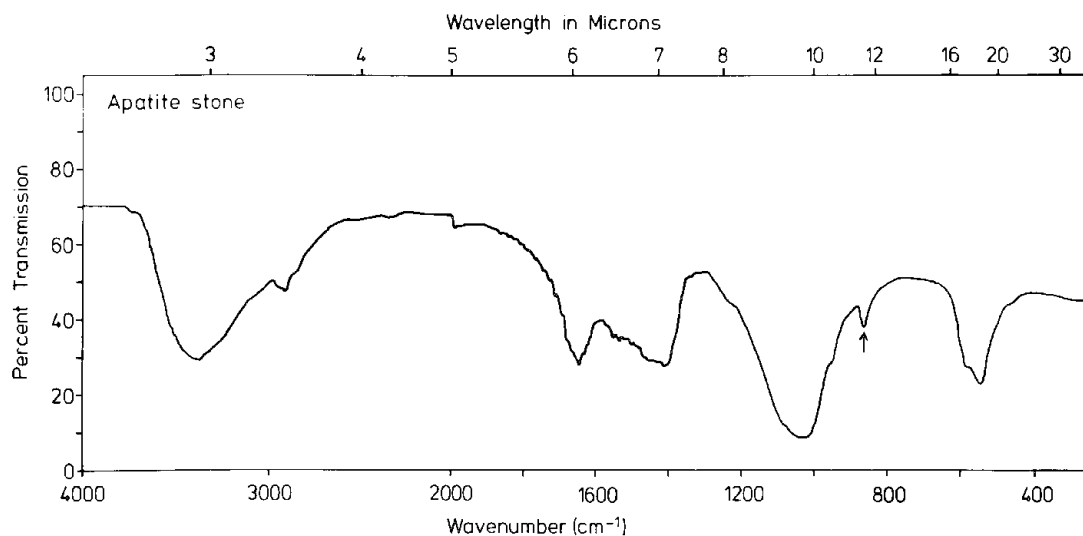


FIG. 7.--Infrared spectrum of apatite stone. Broad absorption band at 1430 cm⁻¹ and sharp peak at 875 cm⁻¹ indicate presence of carbonate.

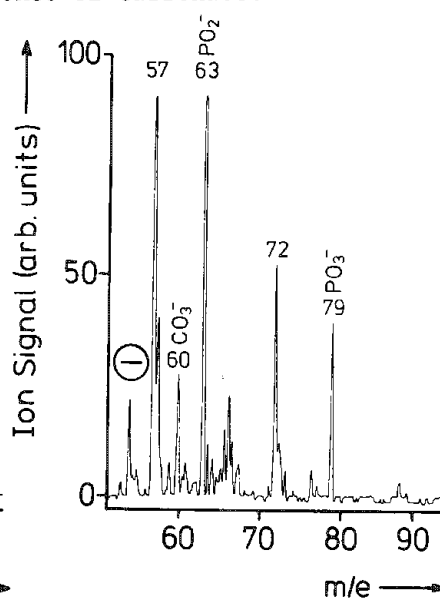
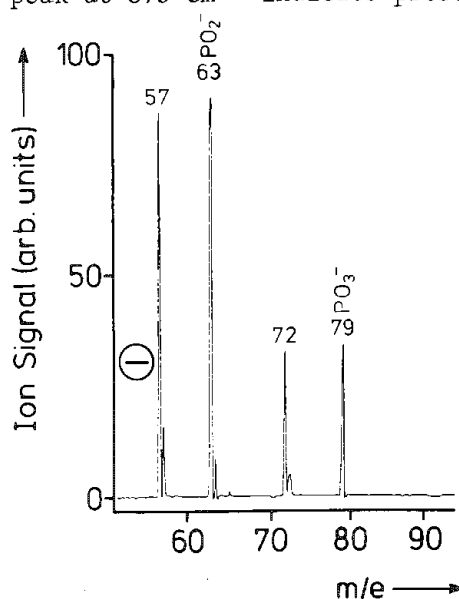


FIG. 8.--LAMMA spectra of apatite showing inhomogeneous distribution of carbonate.

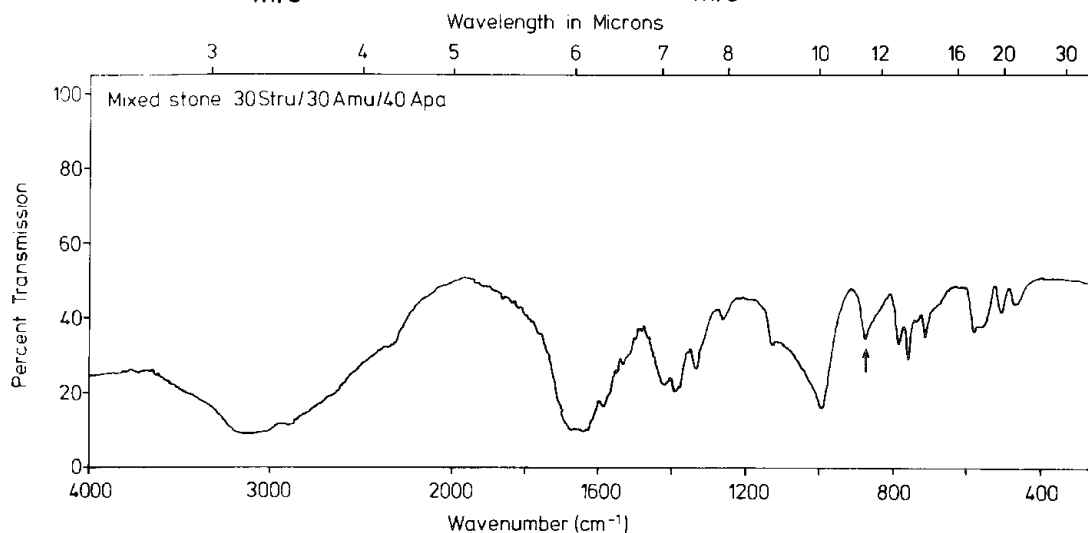


FIG. 9.--Infrared spectrum of mixed stone: 30% struvite, 30% ammonium hydrogen urate, 40% apatite. Due to interference by bands of ammonium hydrogen urate no estimation of carbonate is possible.

applied to the analysis of urinary calculi. MOLE can be used for the analysis of very small samples and for the study of the molecular and crystalline structure of isolated microcrystals of stones.¹²

Our investigations have shown that LAMMA can be used for the study of the molecular structure of urinary calculi. All demonstrated spectra are spectra of negative ions. But LAMMA also makes it feasible to analyze cations, so that it is easy to detect elements of concretions in major as well as in trace concentrations.¹³ This method also allows the distinction between hydroxyapatite and carbonate apatite. One advantage of LAMMA is given by the optical selection of crystals, so that it is possible to analyze small isolated crystals. Thus it could be demonstrated that carbonate is incorporated into apatite spherulites. Furthermore, by relative quantitation it could be shown that the carbonate content in infection stones was increased. Up to now an absolute quantitation has not been accomplished. Investigations of the ability of LAMMA for the study of crystalline structure are in progress.

References

1. S. S. Pollack and G. L. Carlson, "A comparison of x-ray diffraction and infrared techniques for identifying kidney stones," *Am. J. Clin. Path.* 52: 656-660, 1969.
2. D. B. Leusmann, "Routine analysis of urinary calculi by scanning electron microscopy," *SEM/1983*, 387-396.
3. E. Takasaki, "An observation on the analysis of urinary calculi by infrared spectroscopy," *Calc. Tiss. Res.* 7: 232-240, 1971.
4. R. Kisters and B. Terhorst, "Harnsteinanalyse durch Infrarotspektroskopie," *Urologe B-13*: 85-89, 1973.
5. P. F. Schmidt, "Laser microprobe mass analyzer," in P. Echlin, Ed., *Analysis of Organic and Biological Surfaces*, New York: Wiley, 1984, 73-104.
6. P. F. Schmidt and K. Ilseemann, "Quantitation of laser-microprobe-mass-analysis results by the use of organic mass peaks for internal standards," *SEM/1984 I*, 77-85.
7. D. B. Leusmann, B. Hagen, and P. F. Schmidt, "Untersuchungen zum Karbonatgehalt der Harnsteinapatite mit dem Laser-Mikrosonden-Massen-Analysator (LAMMA)," in W. Vahlen-sieck and G. Gasser, Eds., *Pathogenese und Klinik der Harnsteine*, Darmstadt: Steinkopff Verlag, in press.
8. N. S. Chickerur, M. S. Tung, and W. E. Brown, "A mechanism for incorporation of carbonate into apatite," *Calcif. Tissue Int.* 32: 55-62, 1980.
9. P. F. Gonzales-Dias, J. V. Garcia-Ramos, and M. Santos, "Composition of apatites in human urinary calculi," *Calcif. Tissue Int.* 28: 215-225, 1979.
10. W. F. Neumann and B. J. Mulryan, "Synthetic hydrogenapatite crystals: III. The carbonate system," *Calcif. Tiss. Res.* 1: 94-104, 1967.
11. K. Try, "The composition of urinary stones analyzed by infrared spectrophotometry and the precipitation of calcium phosphates from saturated solutions," *Scand. J. Urol. Nephrol.* 15: 263-267, 1981.
12. M. Daudon, M. F. Protat, R. J. Reveillaud, and H. Jaeschke-Boyer, "Infrared spectrometry and Raman microprobe in the analysis of urinary calculi," *Kidney Internat.* 23: 842-850, 1983.
13. P. F. Schmidt, "Localization of trace elements with the Laser Microprobe Mass Analyzer (LAMMA)," *Trace Elements in Medicine* 1: 13-20, 1984.

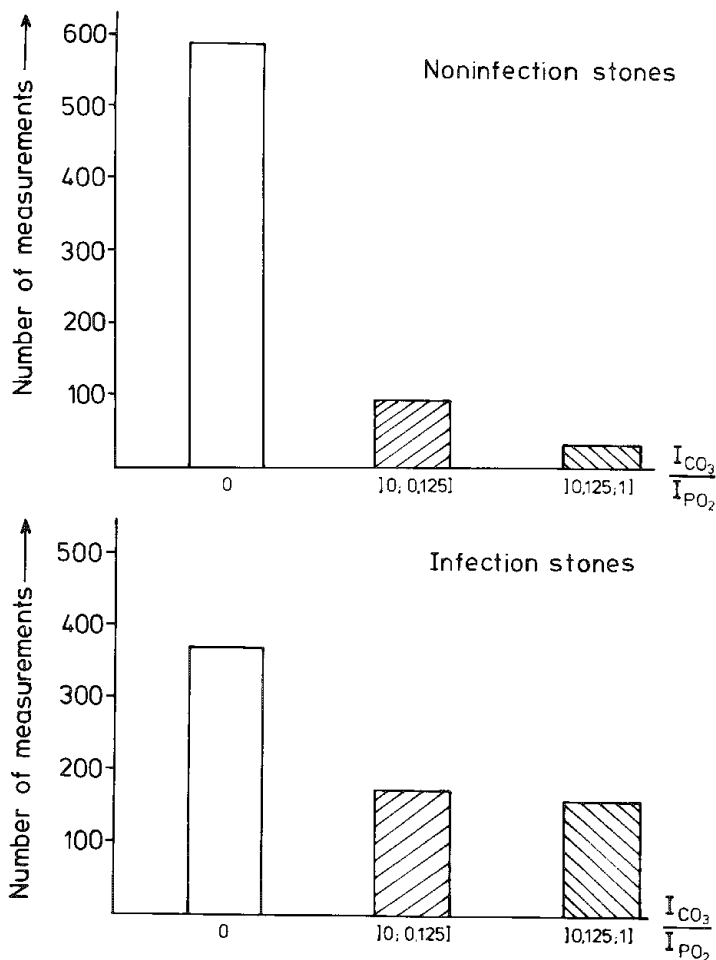


FIG. 10.--Comparison of carbonate content of noninfection stones and infection stones by relative quantitation: I_{CO_3}/I_{PO_2} .

THE USE OF LASER MICROPROBE MASS ANALYSIS FOR NICKEL SPECIATION IN INDIVIDUAL PARTICLES OF MICROMETER SIZE

I. H. Musselman, R. W. Linton, and D. S. Simons

The laser microprobe mass analyzer (LAMMA) is capable of analyzing single inorganic particles of micrometer size. Under favorable conditions, the mass spectra exhibit a high abundance of polyatomic or cluster ions in a unique "fingerprint" pattern that can be used for the identification of compound stoichiometry.¹⁻⁴ In this study, positive and negative ion mass spectra of micrometer-sized particles of five nickel compounds were examined to determine the feasibility of nickel speciation by LAMMA. One species of particular importance in environmental chemistry applications is nickel subsulfide (Ni_3S_2). The subsulfide is a potent animal carcinogen presumed to be a human carcinogen upon inhalation. An ultimate objective is to use LAMMA, in concert with other analytical microprobe and separations techniques, to characterize the various nickel compounds, including the subsulfide, in airborne particles from stationary pollution sources.

Experimental

Micrometer-sized particles of nickel metal (Ni^0) and the Ni-containing compounds nickel oxide (NiO), nickel sulfate heptahydrate ($\text{NiSO}_4 \cdot 7\text{H}_2\text{O}$), nickel sulfide (NiS), and nickel subsulfide (Ni_3S_2) were mounted on Formvar-coated TEM grids and analyzed by use of a Leybold-Heraeus Laser Microprobe Mass Analyzer, LAMMA-500.⁵ A detailed description of the instrument is provided in the literature.⁶⁻⁸ The frequency-quadrupled Q-switched Nd-YAG laser ($\lambda = \text{nm}$, $\tau = 15 \text{ ns}$) was focused onto the sample through a 32 \times optical microscope objective with the aid of a continuous He-Ne laser beam. All spectra were collected and digitized by Biomation model 8100 transient recorders at the 20ns-per-channel time scale. The influences of various instrument operating conditions, such as laser power, were characterized to assess and optimize the possibility of distinguishing the nickel compounds by their characteristic cluster ion "fingerprint" spectra. Positive and negative ion mass spectra of each compound were also obtained and compared.

As a further attempt to distinguish the NiS and Ni_3S_2 compounds, the laser power was increased to maximize fragmentation by use of a Nd-YAG amplifier rod. The S^+/Ni^+ intensity ratios for various nickel isotopes were examined to determine whether they would reliably reflect the inherent stoichiometry difference between NiS and Ni_3S_2 .

Discussion

Positive Ion Mode. Representative positive-ion LAMMA spectra of nickel metal and four nickel compounds are given in Fig. 1. With the exception of NiS versus Ni S , each nickel species produces a unique "fingerprint" spectrum using instrumental conditions to promote the formation and detection of polyatomic or cluster ions. Table 1 summarizes the comparison of the spectra of nickel metal, nickel oxide, nickel sulfate heptahydrate, nickel sulfide, and nickel subsulfide obtained under three conditions. By use of only a few select atomic/cluster ions, one may differentiate four of the five nickel species.

Six positive-ion LAMMA spectra were obtained from nickel metal, nickel oxide, nickel sulfate heptahydrate, nickel sulfide, and nickel subsulfide at low laser power conditions. The spectra are compared in Table 1A. Nickel metal is identified by the presence of Ni^+ and Ni_2^+ without oxygen or sulfur-bearing clusters, whereas nickel oxide has an additional

Author Musselman is doing her thesis research at the National Bureau of Standards while a graduate student at the University of North Carolina. Author Linton is an Associate Professor of Chemistry at the University of North Carolina. Author Simons is a Research Physicist at the National Bureau of Standards, Gaithersburg, MD 20899.

peak for the cluster ion Ni_2O^+ . Nickel sulfate heptahydrate is readily distinguished by the presence of both the Ni_2O^+ and Ni_2S^+ ions. Nickel sulfide and nickel subsulfide are differentiated from nickel metal, nickel oxide, and nickel sulfate by the presence of the NiS_2^+ ion and the absence of the Ni_2O^+ ion.

Six positive-ion LAMMA spectra of nickel metal and the four compounds were also obtained at a higher laser power (Table 1B). As expected, the formation of lower-mass ions was favored at higher laser power, whereas the higher-mass ions were more abundant at lower laser power. The spectra of four of the five nickel species are also unique at this higher laser power. The distinguishing ions for nickel metal, Ni^+ , and nickel oxide, Ni^+ and Ni_2O^+ , are the same as at the lower laser power. The nickel sulfate heptahydrate spectrum

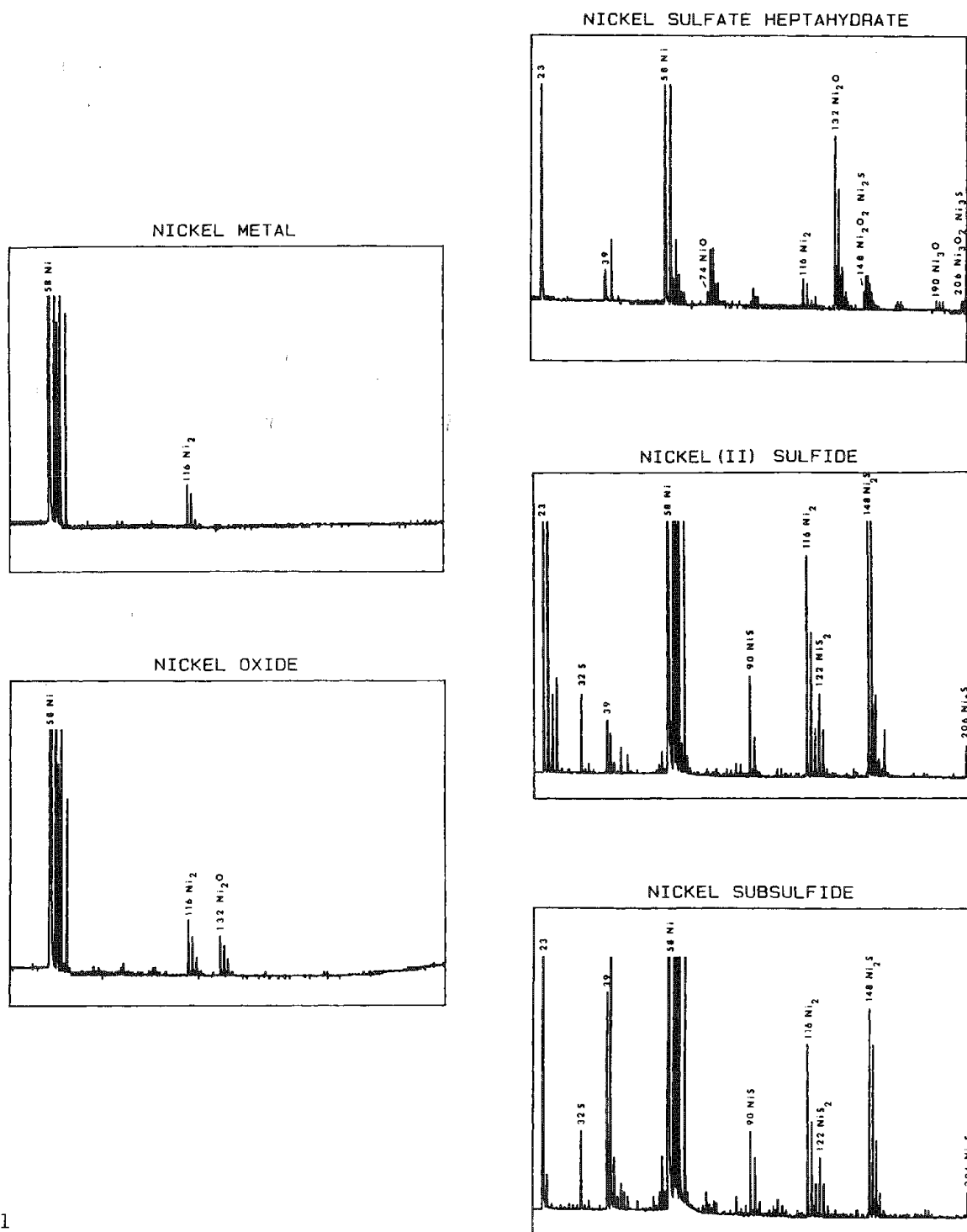


FIG. 1

is unique in the presence of the SO^+ ion. Both the nickel sulfide and nickel subsulfide spectra exhibit sulfur-containing peaks such as S^+ to distinguish them from nickel metal or nickel oxide, and the absence of the SO^+ and NiO^+ ions to differentiate them from nickel sulfate heptahydrate.

As is illustrated by Tables 1A and 1B, the positive-ion spectra of nickel sulfide and nickel subsulfide are qualitatively indistinguishable under both laser power conditions. Indeed, both compounds yield the same atomic/cluster ions including S^+ , Ni^+ , NiS^+ , Ni_2S^+ , Ni_3S^+ , and Ni_3S_2^+ .

TABLE 1

A. Positive Ions Detected at Low Laser Power

Sample	Ni^+	NiS_2^+	Ni_2O^+	Ni_2S^+
Ni^0	X	--	--	--
NiO	X	--	X	--
$\text{NiSO}_4 \cdot 7\text{H}_2\text{O}$	X	--	X	X
NiS	X	X	--	X
Ni_3S_2	X	X	--	X

B. Positive Ions Detected at High Laser Power

Sample	S^+	SO^+	Ni^+	NiO^+	Ni_2O^+
Ni^0	--	--	X	--	--
NiO	--	--	X	1	X
$\text{NiSO}_4 \cdot 7\text{H}_2\text{O}$	X	X	X	X	X
NiS	X	--	X	--	2
Ni_3S_2	X	--	X	--	--

C. Negative Ions Detected at High Laser Power

Sample	Ni^-	$\text{S}_2^-/\text{SO}_2^-$	NiO^-	HSO_4^-	NiS_2^-
Ni^0	X	--	--	--	--
NiO	X	--	X	--	--
$\text{NiSO}_4 \cdot 7\text{H}_2\text{O}$	4	X	4	X	--
NiS	1	X	--	--	X
Ni_3S_2	--	X	--	--	X

X = presence of ion in 6 out of 6 spectra

-- = absence of ion in all spectra

number = number of times ion appeared in 6 spectra

The numbers in Table 1 refer to the number of times the ion appeared in six spectra. The fact that some ion species were only occasionally observed suggests that the magnitude of the ion signal borders on the detection limit of the instrument.

Negative Ion Mode. Six negative-ion LAMMA spectra each of nickel metal, nickel oxide, nickel sulfate, nickel sulfide, and nickel subsulfide were obtained. Four of the five species produce a unique fingerprint LAMMA spectrum, as is illustrated by selected ions in Table 1C. Nickel metal is differentiated from the other compounds in that it shows only a characteristic peak for Ni^- . Nickel oxide is distinguished by the existence of a peak for NiO^- in addition to the Ni^- ion and by the absence of all sulfur-containing peaks. Although the spectrum of nickel sulfate heptahydrate is complex, the formation of the HSO_4^- ion is unique to the compound. Analogous to the positive-ion results, negative-ion spectra of nickel sulfide and nickel subsulfide are qualitatively identical. Both compounds yield peaks for S^- , SO^- , S_2/SO_2^- , NiS^- , NiS_2^- , NiS_3^- , Ni_2S_2^- , Ni_2S_3^- , and Ni_3S_3^- .

Peak Intensity Ratios. In an effort to differentiate the positive-ion spectra of nickel sulfide and nickel subsulfide, a laser amplifier rod was used to increase the maximum laser power by a factor of ten. It was hoped that the use of very high laser power would produce complete fragmentation and create only Ni^+ and S^+ elemental ions. This was generally the case. Positive-ion spectra were obtained from twenty $\sim 1\mu\text{m}$ particles of each compound. Sulfur-to-nickel ratios along with the mean ratio and standard deviation of the mean were calculated for each compound. The results for this data set (Table 2) indicate that the mean of the ion ratio $^{32}\text{S}^+/^{58}\text{Ni}^+$ may be used to distinguish the nickel sulfide and nickel subsulfide compounds at the 95% confidence level when at least twenty particles of each compound are analyzed. The magnitude of the standard deviation of the means for the ion ratios $^{32}\text{S}^+/^{62}\text{Ni}^+$ and $^{32}\text{S}^+/^{60}\text{Ni}^+$ do not permit the distinction. Although one can differentiate multiple sets of the nickel sulfide and nickel subsulfide spectra using the mean of the $^{32}\text{S}^+/^{58}\text{Ni}^+$ ion ratio, the data do not show a sufficient difference to permit a distinction to be made between the two compounds based on the spectrum from a single particle. This is the case even though the two compounds do have a factor of 1.5 difference in the sulfur-to-nickel atom ratios (NiS : 1/1, Ni_3S_2 : 2/3).

In addition, twenty positive-ion spectra were obtained from both the nickel sulfide and nickel subsulfide samples at low laser power to promote the formation of cluster ions. The ratios of various cluster ion peak integrals were plotted versus the integral of a nickel elemental isotope for both compounds. Preliminary results indicate that the slopes of a linear fit to these plots appear to be sufficiently different to serve as an indicator with which to differentiate these two nickel compounds. The difference in the slopes of these plots may reflect a difference in the formation mechanism of the same cluster ions from the two compounds. Additional experiments are being conducted to test this possibility further.

The difficulty in quantitatively distinguishing the spectra of nickel sulfide and nickel subsulfide from various nickel-sulfur intensity ratios has several possible explanations. Variability in energy deposition due to differences in particle size and shape, laser focus, and laser pulse energy result in nonreproducible spectra and are reflected in the standard deviation of the mean.⁶ Michiels and Gijbels observed a similar phenomenon in the analysis of titanium oxides.² They found that compound stoichiometries could be distinguished only when differences between the O/Ti ratios were large, e.g., 2, such as in the compounds TiO_2 and TiO . In this case, the difference in the ion intensity ratios is significant despite the inherent problems with spectral reproducibility. However, when the O/Ti ratio differed by only a factor of 1.5, overlap in the oxide ratios did not allow compound stoichiometry to be distinguished. It is likely that there are also interparticle variations in composition for the individual particles analyzed. The vendor of the nickel subsulfide sample specified that the sample exists as a pure phase as determined by bulk x-ray diffraction measurements. However, background-corrected x-ray intensity ratios of nickel subsulfide particles, from the same sample source as used for the LAMMA measurements, suggests that the nickel subsulfide sample is inhomogeneous on the micro-scale.⁹ Although not critical for distinguishing compounds that produce different cluster ions, the extent of sample microhomogeneity appears to be especially important for differentiating the nickel sulfide and nickel subsulfide compounds which contain the same elemental and cluster ions in their mass spectra. Therefore, it is believed that instrumental effects of the LAMMA as well as variations in particle composition contribute to the standard deviations of the ion intensity ratios (Table 2). The relative contributions of these two

effects will be better assessed after experiments to determine the extent of the micro-homogeneity of both the NiS and Ni_3S_2 samples are completed.

Conclusions

Laser microprobe mass analysis is a useful tool for distinguishing nickel metal, nickel oxide, and nickel sulfate from nickel sulfide and nickel subsulfide. Each of the nickel samples exhibits diagnostic ions in its characteristic positive and negative "fingerprint" spectra. However, the positive and negative ion spectra of nickel sulfide and nickel subsulfide are qualitatively identical. The difficulty in differentiating the nickel sulfide and nickel subsulfide spectra using positive atomic ion intensity ratios as a reflection of compound stoichiometry is related to variations in laser power deposition and possible inhomogeneity in sample composition.

References

1. F. J. Bruynseels and R. E. Van Grieken, "Molecular ion distributions in laser microprobe mass spectrometry of calcium oxide and calcium salts," *Spectrochim. Acta* 38B: 853-858, 1983.
2. E. Michiels and R. Gijbels, "Fingerprint spectra in laser microprobe mass analysis of titanium oxides of different stoichiometry," *Spectrochim. Acta* 38B: 1347-1354, 1983.
3. F. J. Bruynseels and R. E. Van Grieken, "Laser microprobe mass spectrometric identification of sulfur species in single micrometer-size particles," *Anal. Chem.* 56: 871-873, 1984.
4. E. Michiels and R. Gijbels, "Cluster ion distributions and correlation with fragment valence in laser-induced mass spectra of oxides," *Anal. Chem.* 56: 1115-1121, 1984.
5. Certain commercial equipment, instruments, or materials are identified in this paper. Such identification does not imply recommendation or endorsement by the National Bureau of Standards, nor does it imply that the materials or equipment are necessarily the best available for the purpose.
6. H. Vogt et al., "LAMMA 500 principle and technical description of the instrument," *Fresenius Z. Anal. Chem.* 308: 195-200, 1981.
7. E. Denoyer et al., "Laser microprobe mass spectrometry 1: Basic principles and performance characteristics," *Anal. Chem.* 54: 26A-32A, 1982.
8. R. Kaufmann and P. Wieser, "Laser microprobe mass analysis in particle analysis," in John Beddow, Ed., *Particle Characterization in Technology*, Boca Raton, Fla.: CRC Press, Inc., 1984, 21-57.
9. X. B. Cox, J. Rickman, and R. W. Linton, unpublished results, University of North Carolina, Chapel Hill, 1985.

TABLE 2

	$^{32}\text{S}^+ / ^{62}\text{Ni}^+$	$^{32}\text{S}^+ / ^{60}\text{Ni}^+$	$^{32}\text{S}^+ / ^{58}\text{Ni}^+$
Ni_3S_2 Mean	6.94	1.66	0.95
Std. Dev. of Mean	0.31	0.08	0.06
Rel. Std. Dev.	4.5%	4.8%	6.3%
NiS Mean	6.53	1.26	0.60
Std. Dev. of Mean	0.74	0.14	0.06
Rel. Std. Dev.	11%	11%	10%

15

Detectors and Instrumentation Developments

Si(Li) DETECTORS, DEAD LAYERS, AND INCOMPLETE CHARGE

D. C. Joy

Si(Li) x-ray detectors have now been in wide use for nearly two decades but surprisingly little attention has been paid to the way they behave. In general it is assumed that the efficiency of the detector is determined at low energies by the properties of the window in front of the detector, and at high energies by the transmission of photons through the detector. However, careful examination of low-energy x-ray peaks shows significant deviations from the expected Gaussian shape. The low-energy tail on the peak indicates that the detector is not collecting with complete efficiency all the charge produced by the photons. The distortions due to incomplete charge not only cause problems in the determination of peak integrals but also lead to anomalies in the background. This paper examines how this effect can occur, and describes a model to calculate the magnitude of the incomplete charge and its energy distribution across a spectrum.

The Dead Layer

Conventionally the Si(Li) detector is viewed schematically as a p-i-n diode (Fig. 1). The active portion of the diode consists of the p-type front face and the intrinsic region. Because of the high resistivity of the intrinsic material, and the bias applied across the diode, the whole intrinsic region (which may extend for several millimeters) can be space-charge depleted. The p-type region is of much lower resistivity and is therefore only depleted in the immediate vicinity of the junction. The n^+ region insures a fully ohmic back contact. A photon of energy E entering the diode transfers its energy to a photo-electron in a single event. This electron in turn travels through the semiconductor generating electron-hole pairs, the total number n of which for each photon is

$$n = E/e_{eh} \quad (1)$$

where e_{eh} is the energy required to generate one electron hole pair (about 3.6 eV in silicon). These carriers having opposite charge are separated by the bias field and move through the material. The diode behaves as a capacitance C and so the voltage pulse ΔV sensed by the external circuit is

$$\Delta V = (nq)/C \quad (2)$$

where q is the electronic charge. (Note that the use of the intrinsic material also reduces the capacitance and hence maximizes ΔV .) The pulse produced should therefore be linearly proportional to the energy of the photon, provided that all the charge is collected.

The incomplete charge is the result of the presence of a neutral (i.e., not space-charge depleted) region between the surface and the junction, a zone usually referred to as the "dead layer." Conventionally this dead layer is thought of as resulting from the materials processing required to form the diode; the result is a damaged layer several thousand Ångströms deep below the surface. Carriers produced within the intrinsic region are collected with 100% efficiency, but electron-hole pairs generated in the dead layer must diffuse through the dead layer to reach the junction at depth DL . If the minority carrier diffusion length is L then the collection probability for a carrier produced at depth Z is

$$\exp[-(Z - DL)/L] \quad (3)$$

Author Joy is with ATT Bell Laboratories, Murray Hill, NJ 07947.

For all except the trivial limiting case where L is infinite any carriers produced in the dead layer will therefore contribute to the incomplete charge, the magnitude of which will depend on the values of DL and L .

Although it is certain that the fabrication procedure does adversely affect the properties of the detector it was pointed out by Goulding that the experimentally determined values of the dead layer thickness always appeared to be in the range 0.2 to 0.3 μm for detectors operated at liquid-nitrogen temperatures regardless of the details of the processing.¹ More significant, dead-layer thicknesses obtained for the same, or a similar, detector operated at room temperature were typically only a few hundred Angstroms. Goulding explained this paradox by proposing that the dead layer was not the result of processing, but an inherent attribute of the detector. In this model charge carriers may diffuse to the surface of the detector, and be lost, before their drift velocity in the electric field removes them from the vicinity of the surface. If the electron mobility is μ , the diode temperature is T , and k is Boltzman's constant, then the average diffusion distance in time t is

$$(kT\mu t/q)^{1/2} \quad (4)$$

and the drift distance in the electric field is

$$V_s T \quad (5)$$

where V_s is the saturation carrier drift velocity. Assuming that carriers might be lost if the diffusion distance exceeds the drift distance it is reasonable to equate the "dead-layer" thickness DL to these two values

$$DL = V_s t = (kT\mu t/q)^{1/2} \quad (6)$$

Eliminating t then gives

$$DL = (kT\mu/qV_s) \quad (7)$$

Substituting for these variables using standard values for silicon at 77 K ($\mu = 4 \times 10^4 \text{ cm}^2/\text{V}\cdot\text{s}$, $V_s = 10^7 \text{ cm/s}$) gives $DL = 0.28 \mu\text{m}$, which is right in the range of experimentally determined values. Furthermore, since μ varies as about $1/T^{2.2}$, DL at room temperature is predicted to be about 500 Å, again as observed. This analysis is somewhat oversimplified, and also requires the assumption that the depletion layer extends to the front face of the detector, but the result is suggestive and indicates that the detector physics must be considered in any analysis of the dead layer and its effects.

Modeling the Detector

The model used here to compute the effects of the dead layer includes elements from both of the descriptions given above. The depletion field is assumed to begin at the junction positioned at a depth DL from the front surface. The material between the entrance surface and the junction is assumed to be neutral, and to have a minority carrier diffusion length L . The front surface is taken to have a normalized recombination velocity s . Carriers deposited in the depleted region will be collected with 100% efficiency, but carriers deposited at a depth Z such that $0 < Z < DL$ are collected with efficiency

$$\eta = \exp[-(Z - DL)/L_{\text{eff}}] \quad (8)$$

L_{eff} is an effective minority carrier diffusion length, used to take into account the fact that the presence of the surface leads to recombination and hence loss of signal;² L_{eff} is given as

$$L_{\text{eff}} = L\{1 - [s/(s + 1)]\exp(-Z/L)\}^{1/2} \quad (9)$$

The collection efficiency thus depends on the value of s as well as on the diffusion length, and varies continuously with Z rather than falling suddenly to zero as in the Goulding model.

X-ray photons produce photo-electrons in a single scattering event. If the mean free path in SI of a photon of energy E is λ , then the depth distribution $p(Z)$ of the points at which photo-electrons are generated can be simulated in a Monte Carlo model by the function

$$p(Z) = -\lambda \cdot \text{RND}(1) \quad (10)$$

where $\text{RND}(1)$ is an equidistributed random number between 0 and 1. As shown in Fig. 2(a), λ varies from about $0.07 \mu\text{m}$ at carbon $K\alpha$ to $13 \mu\text{m}$ at Si $K\alpha$, falls to about $1.5 \mu\text{m}$ above the Si absorption edge, and then rises again. The photo-electrons produced have kinetic energy E and thus move through the detector, losing energy and creating electron-hole pairs as they travel. This process can be modeled by a second Monte Carlo simulation using a simple multiple scattering approximation.³ The electron range, computed assuming the Bethe stopping power to be valid, is always much smaller than the photon mean free path (Fig. 2b), and consequently errors in its exact value are not likely to be significant. However the motion of the photoelectron is important in determining the form of the incomplete charge distribution and must not be neglected. The range is divided into ten equal steps and the stopping power is used to find the energy at the end of each step. If the energies at the start and finish of the k -th step are E_k and E_{k+1} , respectively, then the number of charge carriers produced on this step is

$$(E_k - E_{k+1})/e_{\text{eh}} \quad (11)$$

If these carriers are produced within the depleted region then all of them are collected; if they are generated outside of the depleted region then Eqs. (8) and (9) are applied. This process is repeated for each of the steps in the trajectory, and the collected charge is summed and stored. A new photon is then put into the system and the procedure is carried out again. If the detector were perfect the summed charge would always be the same value Q

$$Q_E = E/q/e_{\text{eh}} \quad (12)$$

and this value would correspond to the expected energy E in the pulse height analyzer spectrum. When incomplete charge collection occurs the total charge Q collected from a photon is less than Q_E . After simulating a large number of photons a "spectrum" of the distribution $N(Q)$ against Q can be plotted. This can be made to resemble the usual appearance of an x-ray spectrum by convoluting it with a Gaussian function of appropriate width, here chosen as 160 eV. By comparing the total charge collected from M photons with the expected value MQ_E , the incomplete charge fraction can be determined.

Programs to implement these steps were written in BASIC, for an APPLE IIE, and in FORTRAN, for a DEC 11/23. The results shown are typically for 5000 photon events.

Results

The form of the results is best illustrated by taking a particular set of parameters which are typical of those for current detectors, $DL = 0.25 \mu\text{m}$, $L = 0.5 \mu\text{m}$, and $s = 1$. Figure 3(a) shows the computed spectrum for the CA K-line at 3.6 keV. In this case $\lambda = 8 \mu\text{m}$, so that $\lambda \gg DL$. Consequently almost all the charge is deposited into the active area and the result is a good Gaussian peak. However, when displayed on a logarithmic scale the peak is seen to be preceded by a broad plateau of intensity; the computed incomplete charge is 3.9%. The presence of such a tail would probably not be guessed from an electron produced spectrum because of the bremsstrahlung, but it can clearly be seen in x-ray fluoresced spectra.^{1,3} Figure 3(b) shows the equivalent spectrum for sodium for which λ is about $4 \mu\text{m}$. Even on a linear scale the deviation from Gaussian on the low side of the peak is clearly visible, and there is again a step of intensity ahead of the edge, with an intensity equal to about 3% of the maximum peak height. The computed incomplete charge magnitude is 6.9%.

Figure 3(c) shows the computed peak shape for oxygen K at 530 eV. Here λ is about $0.5 \mu\text{m}$, so the mean free path is not much larger than the junction depth. The result of

this is evident in the peak shape. The peak itself is markedly non-Gaussian on the low side, and in addition there is a second "hump" of intensity below the peak due to the significant number of carriers that have had to diffuse through the dead-layer to reach the junction. The presence of this artifact in an experimental spectrum would not only make the determination of the peak integral difficult, but would adversely affect the peak to background ratio for other peaks on the low side of the oxygen. The calculated incomplete charge for oxygen is 38%, indicating the very major corrections that must be applied to raw data when operating in this range.

Finally, Fig. 3(d) shows the carbon K line. The x-ray mean free path for this line is $0.07\text{ }\mu\text{m}$, so that only a small fraction of the photons produces carriers inside the depleted zone. The result is that the majority of the carriers are incompletely collected, and the expected characteristic peak disappears. The peak that is visible is due solely to the incomplete charge tail, which is why it occurs at the wrong energy. Both of these effects, the apparent transition of the lowest energy peak back to a Gaussian form (at least in the comparison with the oxygen line) and an accompanying "nonlinearity" in energy calibration, are observed experimentally, which gives some support to the general assumptions of the model presented here. The form, and hence the apparent position, of the peak depend sensitively on the position of the onset of the depleted region. Changing the applied bias will vary this somewhat and hence seem to alter the calibration. Clearly microanalytical results based on the properties of a peak such as this will require careful attention.

Discussion

The calculations show that incomplete charge is a significant factor for all peaks in the x-ray spectrum with energies below 3 or 4 keV (Fig. 4). It is also seen, however, that the visible evidence may be masked in electron-produced spectra because of the contributions from bremsstrahlung, and consequently its presence is often neglected.

Accurate quantitative microanalysis in the low-energy x-ray range clearly requires a knowledge of the magnitude of the incomplete charge. Experimentally it is difficult to determine because the distortions of the peaks make formulating a measurement method difficult, and because a substantial fraction of the effect may, as mentioned above, be masked in the bremsstrahlung. The best approach would therefore seem to be to calculate the necessary correction. First, the parameters DL, L, and s which describe the detector must be found, most easily by using a program such as that discussed here and empirically finding values which enable experimental spectra, especially spectra produced by x-ray excitation, to be matched.

An approximate value for DL can be obtained by noting the energy at which the calibration appears to deviate from linearity. The mean free path λ corresponding to this (Fig. 2a) is about the junction depth DL. DL can also be deduced from a measurement of the bremsstrahlung jump ratio at the silicon absorption edge; and s and L can also be estimated from the general appearance of an XRF spectrum. Large values of L and small values of s will give peaks with broadening on the low energy side. Small values of L and high values of s lead to the incomplete charge appearing as a rising characteristic in the spectrum as the energy falls.

Conclusions

Several conclusions can be drawn from this preliminary study. First, incomplete charge, particularly in the range below 1 keV, is a major effect requiring significant corrections to data. Second, it is possible that the carbon, and lower energy, peaks visible on some detectors are in reality manifestations of the incomplete charge. As a general rule therefore microanalytical data derived from regions of the spectrum where the calibration is non-linear should be treated with great caution.

Finally, it might be that an analysis of this type could be used to try and improve the design of detectors. Improved materials processing should certainly lead to higher values of L and reduced surface recombination velocities and, in the light of Goulding's analysis, it is possible that the design of materials with deliberately reduced carrier mobility might lead to a reduction in the apparent value of DL. There might also be a case for the design of a dedicated low-energy x-ray detector using a Schottky barrier device. Such diodes exhibit very shallow junctions and even in their unbiased state would have sufficient deple-

tion depth to collect x rays up to 1 keV or so with good efficiency. In this way the low-energy performance could be optimized without the necessity of compromising parameters to achieve acceptable higher energy performance.

References

1. F. S. Goulding, "Some aspects of detectors and electronics for x-ray fluorescence analysis," *Nucl. Instr. and Methods* 142: 213, 1977.
2. L. Jastrzebski et al., "Application of SEM to determination of surface recombination velocity," *Appl. Phys. Lett.* 27: 537, 1975.
3. R. L. Myklebust et al., "NBS Monte Carlo electron trajectory calculation program," in K. F. J. Heinrich, D. E. Newbury, and H. Yakowitz, Eds., *Use of Monte Carlo Calculation*, NBS Special Publication 460, 105, 1976.
4. P. F. J. Statham, "The efficiency of Si(Li) detectors at very low photon energies," in K. F. J. Heinrich, D. E. Newbury, and R. L. Myklebust, Eds., *Energy Dispersive X-ray Spectrometry*, NBS Special Publication 604, 127, 1981.

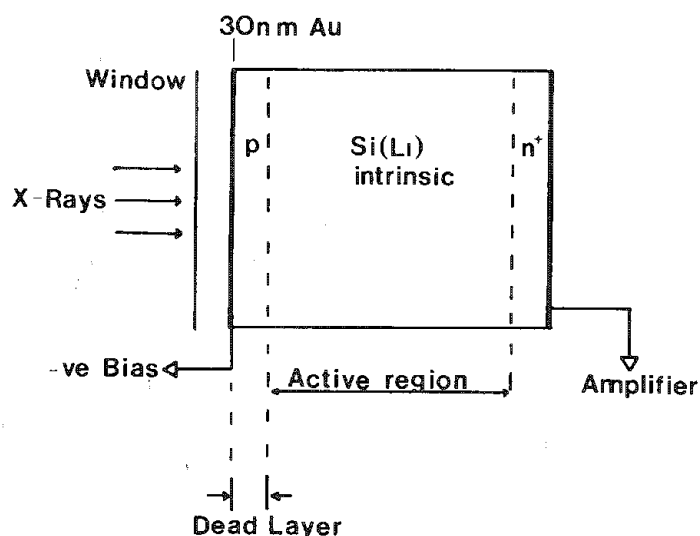


FIG. 1.--Schematic representation of Si(Li) detector.

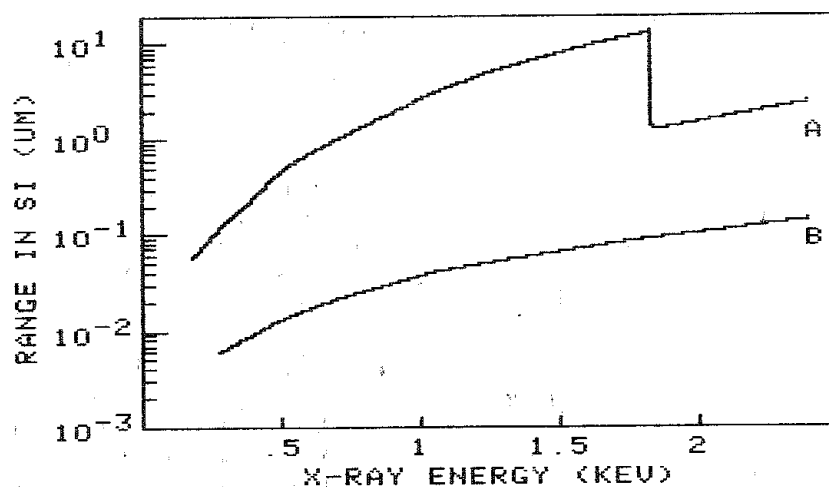


FIG. 2.--Mean free path for x-ray photons in Si (A); photoelectron range in silicon (B).

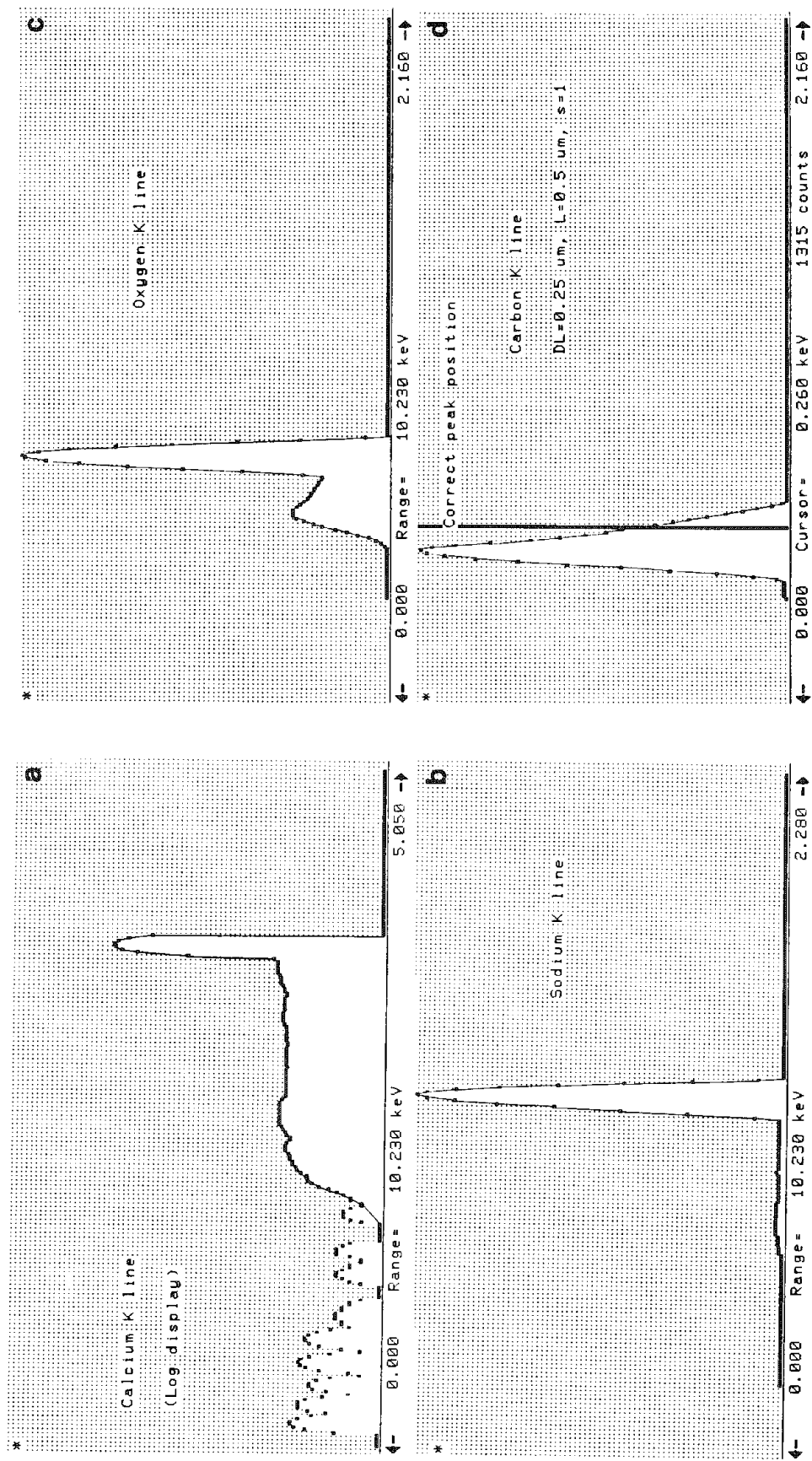
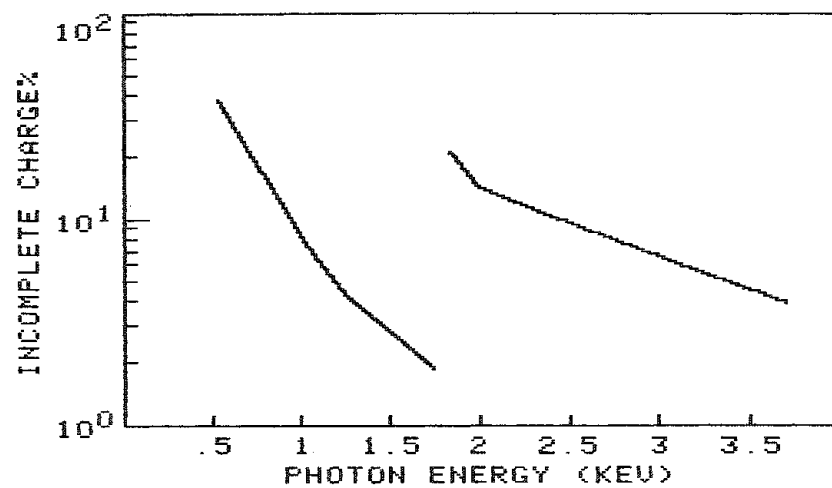


FIG. 3.--Computed spectrum for (a) calcium, (b) sodium, (c) oxygen, and (d) carbon K lines, with DL = 0.25 μm , L = 0.5 μm , s = 1.

FIG. 4.--Computed incomplete charge for detector with parameters of Fig. 3.



16

Analytical Electron Microscopy—EELS

COHERENT BREMSSTRAHLUNG--NEW PEAKS IN EDS: A NEW UNAVOIDABLE ARTIFACT IN THIN-CRYSTAL X-RAY MICROANALYSIS

J. C. H. Spence, J. Titchmarsh, and N. Long

The energy-dispersive x-ray emission spectrum shown in Fig. 1 was obtained with a Philips EM400 transmission electron microscope operating at 100 kV and fitted with an EDAX Energy dispersive spectroscopy (EDS) system from a thin crystal of diamond. The numbered peaks shown are not due to characteristic x-ray emission from impurity atoms in the sample. They result from radiation from the beam electron itself, known as coherent bremsstrahlung,¹ which is due to the juddering motion of the beam electron as it passes down a column of atoms in the crystal. This acceleration of the charged beam electron produces monochromatic, tunable, polarized x-ray emission within the region of the focussed electron probe. It has now been studied in many materials by EDS,² and may have been mistaken for characteristic radiation in earlier microanalytical work.

Simplified Theory of Coherent Bremsstrahlung (CB)

Figure 2 shows the beam electron passing atoms with spacing L in its path as it travels through a thin crystal. The frequency with which it passes these atoms is $\omega_1 = 2\pi v/L$, where v is the electron velocity ($\beta = v/c$). The nonrelativistic energy of the CB emission is then

$$\epsilon_1 = \hbar\omega_1 = 2\pi\hbar v/L \quad (1)$$

This equation also gives the correct relativistic result for a detector take-off angle of $\theta = 90^\circ$. Relativistic effects can be included more generally by replacing L by the relativistically "foreshortened" value L/γ , where $\gamma = (1 - \beta^2)^{-1/2}$; Eq. (1) then gives the emission energy and frequency ω_1 in the frame of the beam electron. To transform to the lab frame we must take account of the relativistic doppler effect, since the beam electron (which is the source of the radiation) is moving. The frequency observed in the laboratory is

$$\omega = \omega_1/\gamma (1 - \beta \cos \theta) \quad (2)$$

Thus the observed CB energy $\epsilon = \hbar\omega$ becomes

$$\epsilon = hc\beta/L (1 - \beta \cos \theta) \quad (3)$$

$$\text{i.e., } \boxed{\epsilon = 12.4\beta/L (1 - \beta \cos \theta)} \quad (4)$$

if the interatomic spacing L is given in Ångströms and ϵ is in keV. The take-off angle θ is measured as in Fig. 2. Thus there is an emission line for every periodic component of the beam electrons' motion, and these components may be associated with the diffraction of the electron.² Quantum mechanically, this radiation which must accompany the acceleration of a charged particle is known as spontaneous emission, and although the simplified classical treatment above cannot be extended to predict the fine structure or intensities of CB lines, Eq. (3) gives the emission energies of CB lines to within an accuracy which is much better than the energy resolution of modern EDS spectrometers. A quantum-mechanical treatment has

Authors Spence and Long are at Arizona State University, Tempe, AZ 85287; author Titchmarsh is at AERE Harwell, Oxon, England. This work was supported by ARO award DAAG29-83-K-0087 and the facilities of the NSF National Center for High Resolution Electron Microscopy at Arizona State University.

been given elsewhere² for the range of energies important in electron microscopy and using the concepts of dynamical electron diffraction.

In the past two related forms of radiation have been distinguished. In the language of electron diffraction, these two forms correspond first to the case where $L = d$ is an interatomic spacing (for coherent bremsstrahlung), and second to the case where $L = \xi_g$ is an extinction distance for dynamical electron diffraction, in which case the radiation is known as channeling radiation (CR). Since $\xi_g \gg d$, CR lines appear in the ultraviolet and soft x-ray region for electron microscopes operating in the 50-400keV range. Before we discuss further the relationship between CR and CB, it is useful to express Eq. (4) in terms of the reciprocal lattice vectors g of the crystal, so that the CB peaks can be indexed crystallographically.

If \hat{n} is a unit vector in the beam direction and we define $\beta = (v/c)\hat{n}$, then the distance L in the beam direction between atoms belonging to the inclined planes g shown in Fig. 2 is $L = (g \cdot \hat{n})^{-1}$. Thus the CB energy becomes

$$\epsilon = hc\beta \cdot g / (1 - \beta \cos \theta) \quad (5)$$

The reciprocal lattice vectors that are important are those which are approximately antiparallel to the beam direction. The energy resolution of EDS is generally not sufficient to resolve lines due to different g vectors in the same reciprocal lattice plane normal to the beam (but not passing through the origin). Hence we find one peak for every plane of reciprocal lattice vectors normal to the beam. The peaks in Fig. 1 are numbered $n = g \cdot H$, where g is any vector in reciprocal lattice plane n and $H = [111]$ (the beam direction). Owing to the symmetry of the diamond lattice, all structure factors for reciprocal lattice vectors on the $n = 2$ and $n = 6$ planes are zero, since here $h + k + l = 2p$ (p odd), and the corresponding CB peaks are absent. Figure 3 shows a relevant section of the reciprocal lattice for diamond.

Whereas CB can be thought of loosely as juddering or dipole radiation with the dipole axis parallel to the beam, CR or "Pendellösung radiation" is more akin to the transverse "wiggler" radiation used in synchrotrons. Thus CB would be most intense at right angles to the beam, were it not for the relativistic searchlight effect, which sweeps the intensity maxima forward to an angle of approximately $\theta \approx 1/\gamma$ (for large γ) as for conventional bremsstrahlung. The connection between CB and CR has been described in detail elsewhere,^{2,3} but a simple picture emerges in the two-beam approximation, since Eq. (5) can be more accurately written as

$$\epsilon = hc\beta S_g / (1 - \beta \cos \theta) \quad (6)$$

where S_g is the excitation error for reciprocal lattice vector g in plane $n \neq 0$. In the two-beam dynamical electron diffraction theory $S_g^{-1} \approx \xi_g$ for large S_g ,⁴ so that CB could be described as "weak-beam" Pendellösung radiation.

The line-shapes of CB peaks differs markedly from those of atomic emission. In addition to the "g vector" broadening there is an additional effect due to CR sidebands,³ and a smaller life-time effect due to either phonon "absorption" or the finite crystal thickness. But the variation of the doppler effect across the detector semiangle is likely to produce the largest line broadening effect; it is

$$\Delta E/E \approx \beta \Delta \theta \quad (7)$$

for a detector at $\theta = 90^\circ$ subtending an angle $\Delta \theta$. The net effect of all these factors has been included in our recent large many-beam calculations.⁵ Generally, at EDS resolution one sees an asymmetrical peak extended toward the low energy side.

Experimental Conditions for the Observation of CB

The most important experimental requirements for the observation of CB is the observation of a "good" transmission electron diffraction pattern, showing strong Bragg disks, weak Kikuchi lines, and little diffuse scattering due to defects. Thus CB cannot be obtained from bulk samples. A particular Bragg condition is not required; however, the detailed in-

tensity distribution of the peaks varies strongly with crystallographic orientation, and this effect, plus the dependence of the emission line energy on accelerating voltage (through β), may be used to distinguish CB from atomic emission. The spectrum in Fig. 1 was acquired over about 10 min with a take-off angle of $\theta = 110^\circ$ and a diamond specimen thickness of about 1000Å. Similar peaks have now been observed in MgO, BN, stainless steel, silicon, and graphite. The zone axis orientation was chosen only for convenience in comparison with calculations, and is not a requirement for the observation of CB. Defects and bending may be expected to broaden CB lines, so that with the decreasing probe sizes of modern TEM instruments and the emphasis on minimum detectable mass, the observation of CB is likely to become more frequent in future.

Significance for Microanalysis

Figure 1 shows that, in crystalline samples, CB makes a large contribution to the background in EDS. Indeed, it has been suggested that there is no other contribution,⁶ since CB is an unavoidable consequence of spontaneous emission coupled with elastic Bragg scattering. It must therefore be considered in detail when estimating the sensitivity of EDS (currently about 0.01 atomic percent in favorable cases). Spontaneous emission is forbidden in vacuum, but made possible for the beam electron in a crystal by "Umklapp" or Bragg diffraction (for CB), and by dynamical dispersion (for CR). *The conventional theory of Bremsstrahlung background⁷ in EDS (derived from that due to Bethe and Heitler) treats the scattering of an energetic electron by a single atom and therefore does not apply to crystals.* For perfect crystals (or small probes illuminating a perfectly crystalline region whose thickness is much less than the mean free path for phonon excitation⁸), the beam electron is strongly Bragg scattered, and so must be modeled by a sum of Bloch waves of appropriate translational symmetry. The experimental evidence for the importance of this Bragg scattering is the transmission electron diffraction pattern. For such a Bloch wave beam electron the momentum conservation law for photon emission becomes

$$\vec{k} = \vec{k}' + \vec{q} + \vec{g} \quad (8)$$

i.e., conservation of "crystal momentum." Here \vec{k} (\vec{k}') is the beam electron wave vector before (after) the spontaneous emission of a photon of wave vector \vec{q} . When combined with the energy conservation law, these equations can predict only the emission of discrete monochromatic photon lines (one for each \vec{g} , together with other CR lines due to dynamical dispersion). Thus, if there were no atomic vibrational motion, this line spectrum would be the only background in EDS due to the sample itself, and these lines would be broadened only by the small lifetime or thickness effect, together with the doppler broadening given in Eq. (7). (The sample thickness broadening is given by Eq. (3), with L now taken as the sample thickness.) In practice, however, even at the absolute zero of temperature an appreciable atomic vibrational amplitude exists,⁸ and the infrequent large-angle inelastic scattering of a beam electron by a phonon limits its contribution to a particular CB peak, and so may contribute to the "continuous" bremsstrahlung background. The other inelastic processes (plasmon excitation and single electron excitation) can be shown to be relatively unimportant. Again, the importance of inelastic phonon scattering can be judged from a glance at the transmitted electron diffraction pattern. The *depletion* of the elastic wavefield by inelastic phonon excitation has been incorporated into CB intensity calculations using a suitable optical potential.^{2,3} In addition there is in practice also an appreciable "systems" contribution to the EDS background (such as copper grid lines) even in instruments with very low "hole counts." In high-voltage microscopes the general bremsstrahlung background from the electron accelerator, and the secondary radiations it generates, is also difficult to eliminate.

In conclusion it is clear that the effect of crystallinity in a sample is to concentrate the otherwise continuous EDS bremsstrahlung background into well-defined peaks. For amorphous materials we anticipate that the shape of the background (leaving aside systems and temperature effects) will also reflect to some extent the degree of atomic ordering in the sample. In the past the theoretical basis for microanalysis has generally commenced with rather simple wave functions for the probe and/or crystal electron, such as plane waves and hydrogenic models. We have now seen three recent examples--Electron Loss Near Edge Structure (ELNES),⁹ Atomic Location by Channeling Enhanced Microanalysis (ALCHEMI),¹⁰ and CB--in

A SHORT STUDY OF k-FACTORS FOR MICROANALYSIS OF THIN FILMS

P. J. Statham and J. E. Wood

Previous studies of k-factors have concentrated mainly on analysis using K lines whereas L and M characteristic lines often have to be used. The commercially available package "RTS2/FLS" used the simple Green and Cosslett log U/U_0 parameterization for ionization cross section (where U is the overvoltage E_0/E_0) as suggested by Goldstein et al.¹ with additional scaling factors of 4 for L lines and 9 for M lines. Recently, Wirmark and Nordén² proposed modifications and we received further suggestions from other investigators that these formulas were inadequate for L and M use. As we also had previous experience of problems with molybdenum specimens (P. Doig, personal communication), a study involving Mo peaks was initiated.

Experimental

Particulate samples of sulfides and oxides of both Mo and Pb were suspended on a Formvar-coated Cu grid, and a self-supporting ion beam thinned disk of pure Mo was prepared. Measurements were made on three different transmission microscopes (not all made by the same manufacturer) in what might be called "routine analysis conditions" as there was not time available to perform exhaustive checks on instrumentation prior to the study. In each installation, a "low background" holder was used and several analyses were carried out at 100, 120, and 200 kV where possible. Data were collected in STEM mode, both from a focused spot and by rastering the beam over an area, and in TEM mode from a focused spot. Areas chosen for analysis were electron transparent although thicker areas were also analyzed to confirm there was no discernible effect from sample self-absorption on the results.

Discussion

Since the Mo L series lines are at energies just above 2 keV and the Mo $K\alpha$ line is at 17.4 keV, the L:K intensity ratio for Mo at a given voltage should be insensitive to differences in EDS detector thickness parameters and should therefore be constant for different microscopes and sample composition provided sample absorption is negligible. However, values quoted in the literature^{2,3} do not agree and even show a different variation with voltage. Our measurements also exhibited a wide range of Mo L/K ratios between instruments and even over points on the same sample, with differences greater than 30%! Furthermore, preliminary results on the MoS_2 specimens showed a fluctuation in Mo L/S K area ratios and corresponding changes in Mo L/K. Careful analysis of the data revealed a number of problems which are summarized below.

Definition of k Factors. It is important to clarify exactly what peaks are used when comparing ratios. In thin film analysis, differential absorption of emission lines within a given series will normally be negligible, so if spectrum processing happens to yield the total area for all lines it is convenient to define k-factors based on total emission from a given atomic shell. This procedure avoids having to estimate a "relative intensity factor" for the major line from a shell although values have been parameterized³ so that comparisons can be made between k-factors defined for total shell, partial shell, or single lines. With Mo $K\alpha$ and $K\beta$ well separated and near the typical upper limit of 20 kV of displayed spectrum, it is easy to ignore Mo $K\beta$ in the interests of simpler spectrum processing, but it must be taken into account in the calculated k factor.

Sample Composition. We observed a small Si peak in a spectrum from MoS_2 that was not apparent in spectra from the Mo film and a small peak in all Mo film spectra close to Ca $K\alpha$ in energy. Although the composition is irrelevant for studies of Mo L/K ratios, we have assumed a composition of MoS_2 and PbS for the sulfides in the calculation of k-factors.

The authors are at Link Systems Ltd., Halifax Road, High Wycombe, Bucks, England HP12 3SE.

Spurious Spectrum Components. Spectra from both oxide and sulfide samples exhibited large Cu peaks of similar size to the Mo L peaks. If the incident beam strikes an electron-transparent sample, it is unlikely that scatter from the sample itself could be responsible for such a large contribution, and we presume it was due to beam tails, electrons scattered from below the specimen, or fluorescence by x rays generated in microscope components. This phenomenon occurred at all three installations and is quite common, perhaps too readily accepted.

The process of modifying an analytical electron microscope to produce clean x-ray spectra has been described in a number of papers⁴ and our experience here only serves to reinforce the notion that this practice is essential if reproducible results are to be obtained. Moreover, the occasional inconsistency in Mo L/K ratios obtained on the same sample suggests that even empirically determined k-factors will not insure accurate results in "unclean" conditions.

In one microscope, a series of spectra were acquired with the beam passing through a hole in the ion-thinned Mo foil specimen. At 200 kV, Mo L/K ratio from the in-hole spectrum was 0.4 whereas the ratios obtained on the specimen were often >2; this result would be expected if there were a source of x radiation (e.g., aperture) within the columns. In this case the relative significance of the hole count would be expected to decrease for thicker areas of a specimen but in one example, an approximate correction for the "hole-count" changed an observed Mo L/K ratio of 1.5 to 2.15.

Spectrum Processing. The overlap between Mo L and S K peaks is severe and slight drift in calibration can produce significant variation in the results of least squares fitting.⁵ By adjusting the effective zero position of the spectrum we observed that a drift of 2 eV could produce a 4% change in Mo L/S K in one sample spectrum. Even with careful calibration, there is statistical uncertainty in the observed ratio which is exacerbated by the severe overlap; thus, the relative error in Mo L/S K ratio was calculated to be around 5% for spectra containing of the order of 200 000 counts.

Results

Table 1 summarizes the average results obtained in this study. Because of the problems described, the values for Mo L/Mo K are probably not of great significance but are quoted for completeness. If we assume that Mo L/S K and Pb M/S K are less sensitive to perturbation because of the proximity of line energies, then these values can suggest suitable values for coefficients to use in cross-section formulas.² Indeed, the Mo L/S K values do at least agree within the calculated statistical error and give an overall average of 0.84; that in turn suggests a factor 3.5 to be used for L lines in a simple log U/U parameterization of cross sections in contrast to the 4.37 proposed by Wirmark and

Table 1.--Experimental ratios from microscopes A, B, and C compared with published data from Wirmark and Nordén² (WN) and parameterizations of Schreiber and Wims³ (SW). Total shell areas have been used and the SW data have been adjusted assuming Mo K α /Mo K TOT = 0.85. Standard deviations are not quoted for the Mo L/Mo K data because of inherent unreliability of these measurements in "unclean" conditions. Compositions of 60% Mo, 40% S, and 87% Pb, 13% S were assumed for the sulfides.

		A	B	C	WN	SW
MoL/MoK	100 kV	1.64	2.79	2.33	2.6	2.31
	120 kV			2.01	2.46	2.12
	200 kV			1.76	2.12	1.73
MoL/SK		0.94	0.77	0.81		0.8
		$\pm .05$	$\pm .07$	$\pm .04$		
PbM/SK		3.62				2.84
		$\pm .1$				

Nordén. The Pb M/S K value suggests a factor of 6.3 for M lines in comparison to 6.6 proposed by Wirmark and Nordén.

Conclusions

Perhaps the most troublesome aspect of this study is that the trivial measurement of Mo L/Mo K ratios gave results with poor reproducibility; published data show further discrepancies, as seen in Table 1. It would be particularly useful for investigators who have already modified and tested their instruments for "cleanliness" of spectra to repeat such measurements and to come to some consensus as to the correct value of Mo L/Mo K at 100 and 200 kV.

Amid controversy concerning the correct form of theoretical formulas for k-factors,⁶ it may seem out of place to discuss "scaling factors" for the simplistic log U/U parameterization. However, until it can be demonstrated in practice that there are indeed sets of k-factors for different voltages that are universally applicable (with corrections for detector efficiency, of course), there seems little justification for more elaborate formulas. If we believe we understand the mechanisms for generation of x rays from a specimen then it is surely preferable to try to match "theoretical" performance by striving for a "clean" column rather than relying on empirical calibration which may provide inadequate compensation for instrumental sources of error.

References

1. J. Goldstein et al., "Quantitative x-ray analysis in the electron microscope," *SEM/77* I, 315.
2. G. Wirmark and H. Nordén, "Experimental determination of x-ray intensity ratios for L, K and M, L lines," *Analytical Electron Microscopy--1984*, 269.
3. P. Schreiber and A. M. Wims, "A quantitative x-ray microanalysis method using K-, L-, and M-lines," *Ultramicroscopy* 6: 323-334, 1981.
4. L. F. Allard and D. F. Blake, "The practice of modifying an analytical electron microscope to produce clean x-ray spectra," *Microbeam Analysis--1982*, 8-20.
5. P. J. Statham, "Pitfalls in linear and non-linear profile fitting procedures for resolving severely-overlapped peaks," *X-Ray Spectrom.* 7: 132, 1978.
6. D. B. Williams et al., "Ionization cross sections in analytical electron microscopy," *J. Microscopy* 136: 209-218, 1984.

COMPARISON OF METHODS FOR QUANTITATIVE THIN-FILM X-RAY MICROANALYSIS FROM STRONGLY OVERLAPPING PEAKS

C. F. Klein, Raghavan Ayer, and D. B. Williams

Quantitative analysis of isolated characteristic peaks in thin film x-ray microanalysis is well established and is an integral part of many of the analyzing systems developed during the past few years.¹ However, there is no equally well-accepted method for quantification in cases where x-ray peaks overlap. In principle, it is possible to calculate the peak intensity of one of the overlapping peaks from a high- or low-energy peak of the same element if present in the spectrum. One can carry out this calculation manually by first carefully establishing the (absorption-corrected) intensity ratio of the two peaks using independent standards of the element, and using this ratio to calculate the intensity of the overlapping peak from the measured intensity of the low- or high-energy peak. Once the individual intensities of the overlapping peaks are determined, they can be converted to absolute elemental concentrations by the standard thin film approach.² However, this manual method suffers from several drawbacks. First, one needs to rely on the presence of a second peak for one of the elements to determine its intensity in the overlapping peak. Second, it is critical to have an accurate knowledge of the specimen thickness since the ratio of the peak intensities is affected by absorption. Finally, the procedure is tedious and time consuming. Therefore, it would be attractive to have a method that overcomes the limitations of the manual procedure and provides reliable quantitative analysis.

Recently, computer software has been introduced in several modern x-ray analyzing systems to deconvolute the overlapping peaks and carry out quantitative analysis.^{3,4} The deconvolution procedure has several advantages over the manual method. First, the method treats only the overlapping peaks whose energies are close and therefore the analysis is virtually independent of the sample thickness. Second, the method is extremely fast and does not require extensive experimental preparation and analysis such as is required for the manual method. Therefore, the current investigation was conducted to compare the quantitative analysis from overlapping x-ray peaks using a manual method and a computer deconvolution procedure available in a modern analyzing system.

Molybdenum sulfide samples were chosen for the present investigation since the S K (2.307 eV) and the Mo L (2.29 eV) peaks overlap and cannot be resolved by EDS analysis. The following four sulfide samples were examined: (1) (natural) molybdenite, MoS₂; (2) synthetic MoS₂; (3) synthetic MoS₃, and (4) synthetic MoCrS₂. The molybdenite was in the form of thin sheets and was used as a standard to determine the k_{MoS} value; the synthetic samples, whose compositions had to be determined, were in the form of powders. In addition, thin samples of pure Mo were also examined. The manual and deconvolution analyses were conducted primarily on an EM 430 electron microscope equipped with an EDAX detector and Tracor Northern 5500 analyzer. For comparison, the molybdenite sample was also analyzed by the manual method in an EM 400-FEG microscope fitted with an EDAX analyzer and EDAX 9100 detector. All the analyses were conducted at an accelerating voltage of 100 kV. With the k_{MoS} value determined from the molybdenite standard, quantitative analysis of the synthetic sulfides was carried out by the manual and the deconvolution methods. Counting time was adjusted to obtain about 100 000 counts in the Mo K α peak.

Manual Method

As mentioned earlier, the first step in the analysis was to determine the k_{MoS} value. This determination was made by a measurement of the intensities in the Mo L and Mo K peaks in the Mo sample and (Mo L + S K) and Mo K peaks in the natural molybdenite samples. Figure 1 shows the shapes of the low- and high-energy peaks of the pure Mo and molybdenite sample, respectively. Peak intensities were measured from windows set to include the entire peak (840 eV for the Mo L and/or S K peaks and 640 eV for the Mo K peak). In each case the thickness of the specimen was determined by convergent-beam electron diffraction.

Authors Klein and Ayer are at Corporate Research Laboratory, Exxon Research and Engineering Co., Route 22 East, Annandale, NJ 08801; author Williams is at the Department of Metallurgy and Materials Engineering, Lehigh University, Bethlehem, PA 18015.

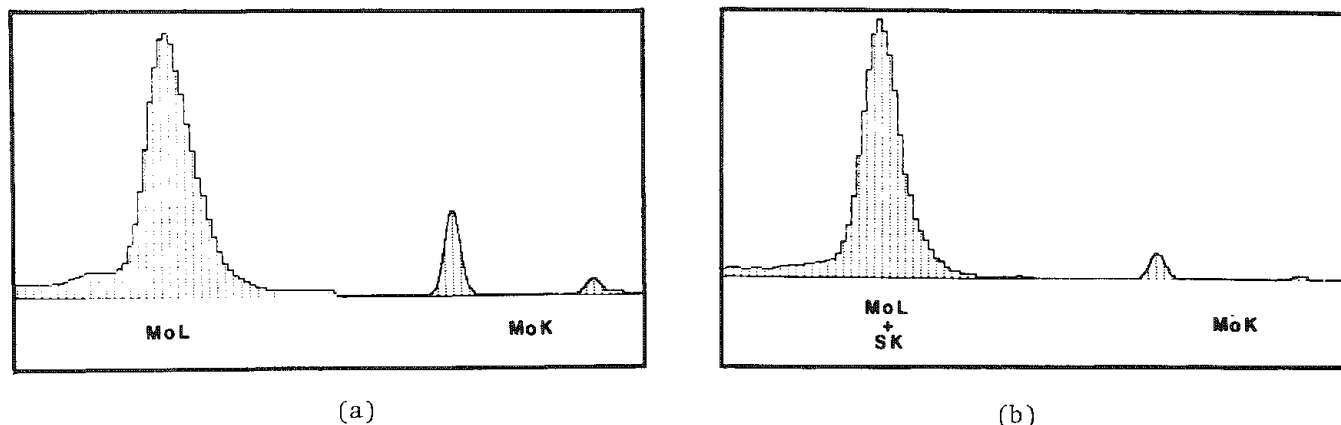


FIG. 1.--(a) Shapes of the Mo L and Mo K peaks in pure Mo sample; (b) shapes of Mo L + S K and Mo K peaks in molybdenite sample.

All the peak intensities were calculated for a fixed 20° take-off angle; the ratios are plotted as a function of thickness in Fig. 2. The plot also shows the ratio of (Mo L + S K)/Mo K for the molybdenite sample. The ratios for both the Mo and molybdenite samples were measured in the EM 400 and EM 430 microscopes and are plotted in Fig. 2. The slopes of the curves were small indicating that absorption is not a severe problem in this system. The curves for the EM 400 and the EM 430 microscopes (both with EDAX detectors) do not superimpose, which means that these ratios must be determined for each microanalytical system.

The k_{MoS} value was calculated by determination of the intensities in the S K and Mo K peaks in the molybdenite sample. The intensity in the S K peak was obtained by calculation of the Mo L peak from the measured Mo K peak and subtraction of the Mo L peak intensity from the overlapping Mo L + S K peaks. From the intensities in the S K and Mo K peaks the k_{MoS} value was found to be 4.43. The results of the quantitative analysis obtained on the synthetic samples by use of the above procedure are listed in Table 1. The results indicate that the mean values of the Mo and S concentrations of the synthetic sulfides determined by the manual method are close to their expected stoichiometries.

Deconvolution Procedure

As mentioned earlier, the deconvolution procedure provides quantitative analysis only by fitting the shape of the overlapping (S K and Mo L) peaks and therefore the intensity in the Mo K peak is not considered. However, library standards of both Mo L and S K peaks are required to carry out the deconvolution. The k_{MoS} value for the Mo L and S K peaks was determined by use of the deconvolution software, which also provides their intensities. The k_{MoS} value for the Mo L and S K peaks based on the molybdenite standard was found to be 1.39. This value was used for the subsequent quantification of the synthetic sulfides. The deconvolution procedure was carried out on the same spectra used for the manual method of the sulfide samples and the results are listed in Table 1. They show that the mean values of the Mo and S concentrations were close to the expected stoichiometries of the sulfides. It was observed that the standard deviation was always slightly higher than that observed in the manual method. To determine the quality of the fitting procedure, both the S K and Mo L peaks were subtracted from the (Mo L + S K) peak of the molybdenite sample and the residual intensity is shown in the bipolar spectrum (Fig. 3). The residual intensity at the peak position shows only minor deviations from the background. The χ^2 value of the fit was 7.4 which indicated that the fitting procedure is acceptable.

Discussion

The results of the present study show that both the manual and the deconvolution methods provide reasonably accurate quantitative analysis of overlapping peaks. For the same spectra, the results of the manual method seem to have a smaller standard deviation compared to the deconvolution method. Since the accuracy of the deconvolution method depends critically on the statistics of the standards and unknown peaks, it should be

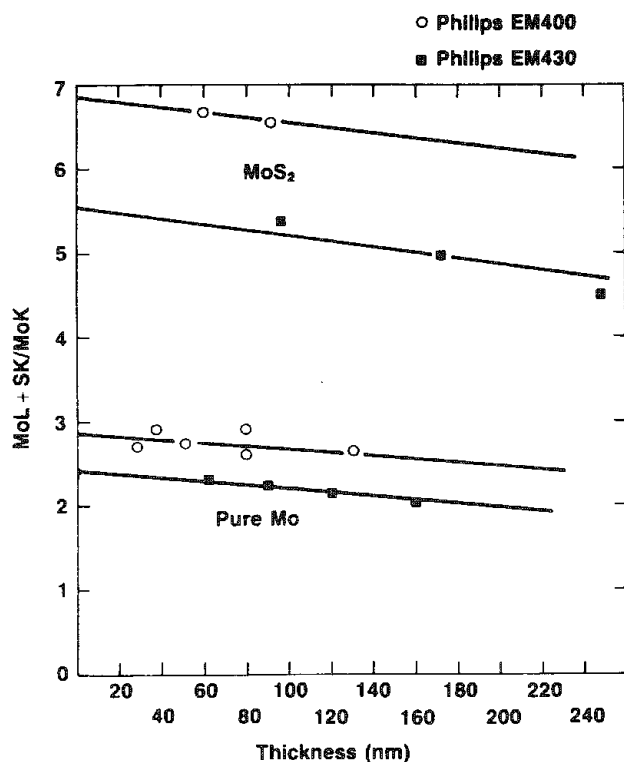


FIG. 2.--Plot of ratios of (Mo L/Mo K) in pure molybdenum sample and (Mo L + S K)/Mo K in molybdenite (MoS) samples as function of specimen thickness in EM 400 and EM 430 electron microscopes. All ratios reported for 20° take-off angle.

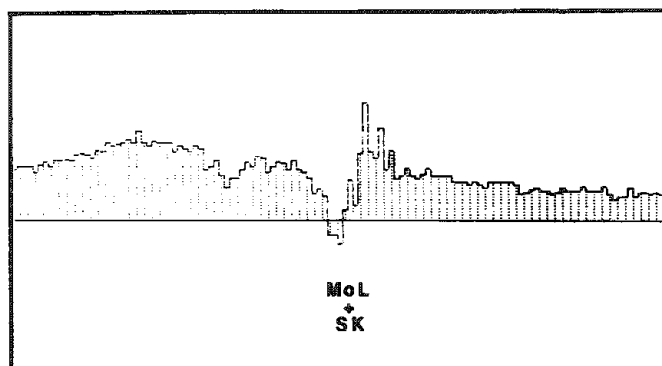


FIG. 3.--Portion of x-ray spectrum showing residual intensity after subtraction of S K and Mo L lines from molybdenite sample.

possible to improve on the scatter in the method by accumulating more counts. Nevertheless, the technique is extremely rapid and does provide reasonably accurate quantification. It has the further advantage that it is less sensitive to specimen thickness and would be ideally suited for amorphous samples where diffraction methods cannot be used for accurate thickness determination. In the present example, the absorption effects were small and the manual method provided satisfactory results. However, in systems where absorption is severe, the manual method may not provide the best results due to additional errors in thickness measurements and subsequent absorption correction.

If an analytical system contains no deconvolution software, the manual method, though tedious, provides a very good alternative. It is apparent from a comparison of the results on the EM 400 and EM 430 systems (Fig. 2) that one must calibrate each system using independent standards and to values reported in the literature only as a first approximation. This requirement should also be extended to the deconvolution method, which requires k_{MoS} values for converting the intensities to absolute concentrations. Once the standards are properly established, both the manual and the deconvolution techniques provide acceptable quantification of overlapping peaks and the choice would depend on the availability of the computer software in the analytical systems.

Conclusions

1. Both the manual method and computer deconvolution procedure of quantitative analysis from overlapping peaks provide comparable results in obtaining concentrations of Mo and S in molybdenum sulfide samples.

2. The accuracy of the techniques depends on establishing acceptable k_{MoS} values from standards and also obtaining good counting statistics.

TABLE 1.--Concentration, at.% ($\pm\sigma$).

Compound	Manual		Computer Deconvolution	
	Mo	S	Mo	S
Molybdenite(MoS_2)	33.3(2.3)	66.7(2.3)	33.65(6.7)	66.35(6.7)
MoS_2	32.0(0.5)	68.0(0.5)	28.9(1.0)	71.1(1.0)
MoS_3	25.9(0.8)	74.1(0.8)	23.8(1.2)	76.2(1.2)
MoCrS_3^*	24.3(1.4)	75.7(1.4)	24.0(2.0)	76.0(2.0)

*Normalized concentrations of Mo and S.

References

1. D. B. Williams, *Practical Analytical Electron Microscopy in Material Science*, Mahwah, N.J.: Philips Electronic Instruments, 1984, 55.
2. G. Cliff and G. W. Lorimer, *J. Microscopy* 103: 203, 1975.
3. F. H. Schamber, *Energy Dispersive X-ray Spectroscopy*, in K. F. J. Heinrich, D. F. Newbury, R. L. Myklebust, and C. E. Fiori, Eds., NBS Special Publication 604, Washington, D.C.: Department of Commerce, 1981, 193.
4. *Ibid.*, p. 233.

Appendix: Solid-state Diffusion as Measured by Microbeam Analytical Techniques A Comprehensive Bibliography

A. D. Romig Jr., D. L. Humphreys, J. I. Goldstein, and M. R. Notis

Over the past two decades microbeam analytical techniques have proven to be powerful tools for the quantitative measurement of composition profiles generated during solid-state diffusion reactions. Unlike earlier analytical techniques, the microbeam methods permit the measurement of concentration profiles at very high spatial resolution, from fractions of a nm to several mm. The techniques included in this bibliography are: (1) Electron Probe Microanalysis, (2) Analytical Electron Microscopy, (3) Auger Electron Spectroscopy and Scanning Auger Microanalysis, (4) Secondary Ion Mass Spectroscopy and Ion Microprobe, (5) Rutherford (and other ion) Backscattering, and (6) Specialized X-ray Techniques including Extended X-ray Absorption Fine Structure and Variable Incidence Angle X-ray Fluorescence. Although the techniques are complementary, few researchers, excluding those intimately involved with diffusion studies, appreciate the way in which these techniques as a group can be used to investigate solid-state diffusion. It is the objective of this bibliography to bring together the literature references which discuss the quantitative analysis of diffusion phenomena as investigated with the group of microbeam techniques. To qualify for inclusion into the bibliography, the paper must address diffusion in a quantitative way, either by dealing with the direct measurement of diffusion coefficients or by the quantitative modeling of solid-state diffusion controlled reactions. Every attempt has been made to make the bibliography as complete as possible through 1984. The bibliography was compiled with a computerized search of the appropriate abstracting services (Metadex, Chemical Abstracts, etc.) and augmented with a manual search through appropriate proceedings and journals. Metals, ceramics, minerals, and semiconductors have been included. Due to the specific nature of this bibliography a new format has been used. The references are divided into categories by technique. Each category has been further subdivided by year and then alphabetically by author. Titles have been included in each citation to help the potential user decide which references may be useful. Since many different materials are included in the references, it is not practical to subdivide or index the bibliography by material. In the small number of cases where more than one technique has been used, the reference appears under all appropriate categories.

Reference

A. D. Romig Jr., D. L. Humphreys, J. I. Goldstein, and M. R. Notis, "Solid state diffusion as measured by microbeam analytical techniques: A comprehensive bibliography," in *Microbeam Analysis--1985*, J. Armstrong, Ed., San Francisco: San Francisco Press, 1985, 361-380.

Authors A. D. Romig Jr. and D. L. Humphreys are with Sandia National Laboratories, Albuquerque, NM 87185, operated for the U.S. Department of Energy under contract number DE-AC04-76DP00789; authors J. I. Goldstein and M. R. Notis are with the Department of Metallurgy and Materials Engineering, Lehigh University, Bethlehem, PA 18015. The authors wish to thank W. Servis, of the Sandia National Laboratory technical library, for performing the computerized literature search.

INDEX

General Reference

J. I. Goldstein, M. R. Notis and A. D. Romig Jr., Atomic transport as measured by electron optical techniques, *Atomic Transport in Concentrated Alloys and Intermetallic Compounds*, G. E. Murch and M. A. Dayananda (Eds.), The Metallurgical Society, AIME, Warrendale, Pa. (1985) in press.

Electron Probe

1960

1. R. F. Mehl and C. F. Lutz, Diffusion in gamma brass, *Trans. TMS-AIME* 221 (1960) 439.
2. N. L. Peterson and R. E. Ogilvie, Diffusion studies in the U-Nb system, *Trans. TMS-AIME* 218 (1960) 439.

1962

1. J. S. Kirkaldy and D. G. Fedak, Nonplanar interfaces in two phase ternary diffusion couples, *Trans. TMS-AIME* 224 (1962) 490.

1963

1. H. A. Froot and L. S. Castleman, Growth kinetics of beta-brass layers in saturated gamma-brass vs alpha-brass diffusion couples, *Trans. TMS-AIME* 227 (1963) 838.
2. N. L. Peterson and R. E. Ogilvie, Diffusion in the U-Nb system. *Trans. TMS-AIME* 227 (1963) 1083.

1964

1. G. W. Powell and J. D. Braun, Diffusion in the Au-In system, *Trans. TMS-AIME* 230 (1964) 694.
2. G. R. Purdy, D. H. Weichert, and J. S. Kirkaldy, The growth of proeutectoid ferrite in ternary Fe-C-Mn austenites, *Trans. TMS-AIME* 230 (1964) 1025.
3. J. A. Wood, The cooling rates and parent planets of several iron meteorites, *Icarus* 3 (1964), 429.

1965

1. J. I. Goldstein, R. E. Hanneman, and R. E. Ogilvie, Diffusion in the Fe-Ni system at 1 atm and 40 kbar pressure, *Trans. TMS-AIME* 233 (1965) 812.
2. J. I. Goldstein and R. E. Ogilvie, The growth of the Widmannstätten pattern in metallic meteorites, *Geochim. Cosmochim. Acta* (1965) 893.
3. R. E. Hanneman, R. E. Ogilvie, and H. C. Gatos, Effect of high pressure on the FeV system: Part II. Chemical interdiffusion, *TMS-AIME* 233 (1965) 691.
4. J. A. Raussel-Colom, T. R. Sweatman, C. B. Wells, and K. Norrish, Artificial weathering of mica, in *Experimental Petrology*, E. G. Hallsworth and D. V. Crawford (Eds.), Butterworth, London (1965) 40.

1966

1. I. B. Borovskiy, I. D. Marchukova, and Y. E. Ugaste, Local x-ray spectral analysis of mutual diffusion in binary systems forming continuous series of solid solutions: Pt. I. The systems Fe-Pd, Co-Pd, Ni-Pd, Cu-Pd, *Phys. Metals Metallogr.* 22 (1966) 43.
2. A. G. Guy and V. Leroy, Diffusion in a ternary substitutional system: Application to the Co-Ni-Cr system, paper from the *Electron Microprobe* (1966) 543.
3. R. F. Hehemann and S. Leber, Chemical diffusion in the Nb-W system, *Trans. TMS-AIME* 236 (1966) 1040.
4. I. D. Marchukova and Y. E. Ugaste, Study of mutual diffusion in binary systems forming a continuous series of solid solutions by local x-ray spectral analysis, *Fiz. Metallov Metalloved.* 22 (1966) 849.
5. D. J. Schmatz, H. A. Domain, and H. I. Aaronson, Diffusion in the disordered Cd-Mg solid solution, *Trans. TMS-AIME* 236 (1966) 543.

1967

1. I. B. Borovsky, I. D. Marchukova, and Y. E. Ugaste, Mutual diffusion in binary systems forming a continuous series of solid solutions as indicated by local spectral analysis 2.-- The systems Fe-Ni, Ni-Co, Ni-Pt, and Co-Pt, *Fiz. Metallov* 24 (1967) 436.
2. J. R. Cahoon and W. V. Youdelis, The diffusion of Cu in Ag-rich/Cu, *Trans. TMS-AIME* 239 (1967) 127.
3. O. Caloni and A. Ferrari, Copper-manganese interdiffusion kinetics studied by x-ray microprobe, *Z. Metallkunde* 58 (1967) 892.

4. J. I. Goldstein and J. M. Short, Cooling rates of 27 iron and stony iron meteorites, *Geochim. Cosmochim. Acta* 31 (1967) 1001.
5. M. M. Janssen and G. D. Rieck, Reaction diffusion and the Kirkendall effect in the Ni-Al system, *Trans. TMS-AIME* 239 (1967) 1372.
6. Y. H. Liu and G. W. Powell, Defect interaction in the diffusion zone of short Au-Ag couples, *Trans. TMS-AIME* 239 (1967) 998.
7. J. A. Wood, Chondrites: Their metallic minerals, thermal histories and parent bodies, *Icarus* 6 (1967) 1.
8. T. O. Ziebold and R. E. Ogilvie, Ternary diffusion in the Cu-Ag-Au system, *Trans. TMS-AIME* 239 (1967) 942.

1968

1. D. Bergner, Measurement of small diffusion coefficients with the microprobe. *Mikrochim. Acta Suppl.* 3 (1968) 19.
2. H. C. Casey Jr. and M. B. Panish, Reproducible diffusion of Zn into GaAs: Application of the ternary phase diagram and the diffusion and solubility analyses, *Trans. TMS-AIME* 242 (1968) 406.
4. M. A. Dayananda, P. F. Kirsch, and R. E. Grace, Ternary diffusion in Cu-Zn-Sn solid solutions, *Trans. TMS-AIME* 242 (1968) 885.
5. J. R. Eifert, D. A. Chatfield, G. W. Powell, and J. W. Spretnak, Interface compositions, motion and lattice transformations in multiphase diffusion couples, *Trans. TMS-AIME* 242 (1968) 66.
6. T. Hehenkamp, Microprobe measurements of material transport in solid metals, *Mikrochim. Acta Suppl.* 3 (1968) 79.
7. S. N. Ruddlesden and A. C. Airey, Some applications of electron-probe microanalyses, *Fourth Symposium on Special Ceramics*, British Ceram. Res. Assoc. (1968) 251.
8. F. A. Veer, B. H. Kolster, and W. G. Burgers, Diffusion in the Cu₃Si phase of the Cu-Si system, *Trans. TMS-AIME* 242 (1968) 669.

1969

1. M. Andreani, P. Azou, and P. Bastien, Chemical diffusion of zinc/nickel intrinsic diffusion coefficients, *Proc. Internat. Congress on X-ray Optics and X-ray Microanalysis*, Springer-Verlag, Berlin (1969) 519.
2. Experimental techniques for the determination of diffusion data, *Diffusion Data* 3 (1969) 241 (no author given).
3. M. G. Hall and C. W. Haworth, Measurement of diffusion fields around precipitate particles by electron-probe microanalysis, *Mechanisms of Phase Transformations in Crystalline Solids*, Institute of Metals, London (1969) 117.
4. J. Kucera and K. Stransky, Indium diffusion in lead single crystals, *Can. Met. Quat.* 8 (1969) 91.
5. S. Steeb and R. Keppeler, Diffusion investigated by microprobe in Mo-Nb, Mo-Al and Nb-Al, *Z. Naturforsch.* 24 (1969) 1601.
6. A. Vignes and J. P. Sabatier, Ternary diffusion in Fe-Co-Ni alloys, *Trans. TMS-AIME* 245 (1969) 1795.

1970

1. I. B. Borovsky, I. D. Marchukova, and Y. E. Ugaste, Local x-ray spectral analysis of mutual diffusion in binary systems forming continuous series of solid solutions: Pt. III: Concentration dependence of the coefficient of mutual diffusion, *Phys. Metals Metallogr.* 29 (1970) 86.
2. I. B. Borovsky, I. D. Marchukova, and Y. E. Ugaste, X-ray microanalysis study of mutual diffusion in binary systems forming a continuous series of solid solutions: Pt. III: Concentration dependence of the mutual diffusion coefficients, *Fiz. Metallov Metallovedenie* 29 (1970) 308.
3. A. W. Bowen and G. M. Leak, Solute diffusion in alpha and gamma iron, *Met. Trans.* 1 (1970) 1695.
4. N. A. Gjostein, Surface, grain boundary and dislocation pipe diffusion, *Physicochemical Measurements in Metals Research Techniques*, Interscience Publishers, New York (1970) 405.
5. S. A. Golovanenko, Electron microprobe investigation of diffusion processes at the layer interface in clad metals, *Protective Coatings on Metals*, Consultants Bureau, New York 2 (1970) 187.
6. A. L. Hurley and M. A. Dayananda, Multiphase diffusion in Ag-Zn alloys, *Met. Trans.* 1 (1970) 139.
7. A. Y. Shinyayev and D. B. Butrymowicz, Interdiffusion in and the phase diagram for V-rich alloys of the V-Al system at pressures 0 to 47 kbar, *Met. Trans.* 1 (1970) 1905.
8. T. S. Lundy, Volume diffusion in solids, *Physicochemical Measurements in Metals Research*, Interscience Publishers, New York (1970) 379.
9. H. Oikawa, T. Obara, and S. Karashima, Interdiffusion coefficients in Cu-rich Al solid solutions, *Met. Trans.* 1 (1970) 2969.

10. C. W. Taylor Jr., M. A. Dayananda, and R. E. Grace, Multiphase diffusion in ternary Cu-Zn-Ni alloys, *Met. Trans.* 1 (1970) 127.
11. G. H. Walker and B. W. Lewis, Cu-Ni diffusion: Electron microprobe study of effects of voids and discontinuities, *Met. Trans.* 1 (1970) 2643.
12. J. D. Whittenberger and M. A. Dayananda, Diffusion studies in Cu-Mn alloys at 850°C, *Met. Trans.* 1 (1970) 2023.
13. J. D. Whittenberger and M. A. Dayananda, Steady-state diffusion in Cu-Zn-Mn alloys, *Met. Trans.* 1 (1970) 3301.

1971

1. A. Brunsch and S. Steeb, Electron microprobe studies of diffusion in the system Nb-Pd, *Z. Metallkunde* 62 (1971) 247.
2. A. Brunsch and S. Steeb, Investigation of diffusion in the Pd-Ta system by electron-probe microanalysis, *Z. Naturforsch.* 26A (1971) 274.
3. A. M. Clark and J. V. P. Long, The anisotropic diffusion of Ni in olivine, in *Thomas Graham Mem. Symp. on Diffusion Processes*, J. N. Sherwood, A. V. Chadwick, W. M. Muir, and F. L. Swinton (Eds.), Gordon and Breach, London (1971) 511.
4. D. E. Coates and J. S. Kirkaldy, Morphological stability of alpha/beta phase interfaces in the Cu-Zn-Ni system at 775°C, *Met. Trans.* 2 (1971) 3467.
5. A. D. Dalvi and D. E. Coates, Concentration profiles in NiO-CoO mixed oxide formed during oxidation, *Oxid. of Metals* 3 (1971) 203.
6. C. E. Shamble and C. J. Rosa, Ti₃Ga and Ti interdiffusion between 660°C and 860°C, *Met. Trans.* 2 (1971) 1925.
7. R. A. Tanzelli and R. W. Heckel, An analysis of interdiffusion in finite-geometry, two-phase diffusion couples in the Ni-W and Ag-Cu systems, *Met. Trans.* 2 (1971) 1779.
8. P. Lamparter, S. Steeb, and A. Gukelberger, Microprobe measurements of diffusion in Pd-V, Pd-Ti and metal-ceramic systems, *High Temp. High Pressures* 3 (1971) 727.
9. G. Vallier, C. Pautet, M. Toitot and P. Bastien, Application of the electron micro-analyzer to the study of diffusion in platings, *Metaux-Corrosion-Ind.* 46 (1971) 272.

1972

1. P. T. Carlson, M. R. Dayananda, and R. E. Grace, Diffusion in ternary Ag-Zn-Cd solid solutions, *Met. Trans.* 3 (1972) 819.
2. J. B. Gilmore, G. R. Purdy and J. S. Kirkaldy, Partition of Mn during the proeutectoid ferrite transformation in steel, *Met. Trans.* (1972) 3213.
3. P. Lamparter, T. Krabichler, and S. Steeb, Microprobe study of diffusion in the Pd-V system, *Z. Naturforsch.* 27A (1972) 960.
4. V. S. Raghunathan, G. P. Tiwari, and B. D. Sharma, Chemical diffusion in the beta phase of the Zr-Ti alloy system, *Met. Trans.* 4 (1972) 783.
5. M. S. Seltzer and B. A. Wilcox, Diffusion of Cr and Al in Ni-20Cr and TDNiCr, *Met. Trans.* 3 (1972) 2357.
6. J. D. Whittenberger, Diffusion in Ni-rich, Ni-Al solid solution at 1260°C, *Met. Trans.* 3 (1972) 2010.
7. W. Zaiss, S. Steeb, and T. Krabichler, Electron-probe microanalysis study of diffusion in the system Mo-Pd, *Z. Metallkunde* 63 (1972) 180.

1973

1. S. Gadea, M. Petrescu, and N. Petrescu, Quantitative evaluation of electron microprobe analysis of diffused metal films, *Coll. Spectros. Internat. Firenze* 2 (1973) 637.
2. B. G. Grinberg, P. P. Pashkov, P. A. Pinchk, Y. V. Knyshev, and L. M. Shtein, X-ray microanalysis of the diffusion layer in a Ti-steel bimetal, *Izvest V.U.Z. Chernaya Met.* 7 (1973) 133.
3. T. R. Heyward and J. I. Goldstein, Ternary diffusion in the alpha and gamma phases of the Fe-Ni-P system, *Met. Trans.* 4 (1973) 2335.
4. J. S. Kirkaldy, P. N. Smith, and R. C. Sharma, Diffusion of Mn in paramagnetic bcc Fe, *Met. Trans.* 4 (1973) 624.
5. J. M. Walsh and M. J. Donachie Jr., On a new intermetallic phase in the Ni-W system, *Met. Trans.* 4 (1973) 2854.

1974

1. A. Brunsch and S. Steeb, Diffusion studies in the system Ti-V by electron probe microanalysis, *High Temp. High Pressure* 6 (1974) 155.
2. H. Engelke and G. Tomandl, Electron microprobe analysis technique to prevent undesirable heating of samples to improve counting statistics and a correction procedure for small diffusion coefficient measurements, *Mikrochim. Acta* 5 (1974) 149.
3. D. J. Misener, Cationic diffusion in olivine to 1400°C and 35 kbar, in *Geochemical Transport and Kinetics*, R. W. Hofmann, B. J. Giletti, H. S. Yoder, and R. A. Yund (Eds.), Carnegie Inst. Washington Publ. 634 (1974) 117.

4. M. Wilhelm, Interdiffusion in the Cu-Ga system, *Z. Naturforsch.* 29a (1974) 733.

1975

1. A. S. Bruk and L. I. Kolesnik, Measurement of short diffusion paths by induced current method with a scanning electron probe, *Ind. Lab.* 41 (1975) 1679.
2. P. T. Carlson, M. A. Dayananda, and R. E. Grace, Atomic mobilities and vacancy wind effects for diffusion in ternary Ag-Zn-Cd solid solutions, *Met. Trans. A* 6A (1975) 1245.
3. G. H. Cheng, M. A. Dayananda, and R. E. Grace, Diffusion studies in Ag-Zn alloys, *Met. Trans. A* 6A (1975) 21.
4. A. A. Korolev and K. P. Smirnova, Applicability of the oblique-section method for studying mutual diffusion in x-ray microanalysis, *Zavod. Lab.* 41 (1975) 1476.
5. R. D. Lanam and R. W. Heckel, Diffusional homogenization behavior in finite Ni-Mo couples, *Met. Trans. A* 6A (1975) 421.
6. N. Matsuno and H. Oikawa, Interdiffusion in Cu-based Cu-Al solid solutions, *Met. Trans. A* 6A (1975) 2191.
7. A. S. Norkiewicz and J. I. Goldstein, Ternary dissolution kinetics in the Fe-Ni-P system, *Met. Trans. A* 6A (1975) 891.
8. E. Randich and J. I. Goldstein, Non-isothermal finite diffusion controlled growth in ternary systems, *Met. Trans. A* 6A (1975) 1553.

1976

1. P. T. Carlson, Interdiffusion and intrinsic diffusion in binary V-Ti solid solutions at 1350°C, *Met. Trans. A* 7A (1976) 199.
2. B. McEnaney and R. D. Mehew, Transport of Cs through a nuclear graphite: Pt. I. Microgravimetric studies and electron probe microanalysis, *J. Nucl. Mater.* 60 (1976) 177.
3. T. D. Moyer and M. A. Dayananda, Diffusion in β_2 Fe-Ni-Al alloys, *Met. Trans. A* 7A (1976) 1035.
4. K. Przybyłowicz and H. Stupnicka, Electron microprobe applied for study of Cu diffusion in Al, *Rudy. Met. Niezależ.* 21 (1976) 293.
5. D. Treheux, D. Marchive, D. Juve-Duc, P. Poyet, and P. Guiraldenq, General Method for determining the coefficients of equivalence in stainless steels (Fe,Cr,Ni) by diffusion couples, *Mem. Sci. Rev. Metall.* 73 (1976) 725.

1977

1. D. Ablitzer and M. Gantois, The measurement of autodiffusion and heterodiffusion coefficients in Nb and Ta by radiotracer and Castaing microprobe techniques, *La Diffusion dans les milieux condensés* 1 (1977) 299.
2. D. Ablitzer, J. P. Haeussler, and A. Vignes, Diffusion anomalies in vanadium: Autodiffusion of vanadium and heterodiffusion of iron in vanadium, *La Diffusion dans les milieux condensés* 1 (1977) 55.
3. I. A. Akimova and R. L. Fogelson, The diffusion of germanium in silver, *Fiz. Strukt. Svoistv. Iverd* 2 (1977) 41.
4. Y. Iijima, K. Hoshino, and K. Hirano, Diffusion of Ti in Cu, *Met. Trans. A* 8A (1977) 997.
5. Y. Iijima, K. Hoshino, and K. Hirano, Interdiffusion in Co-Mn alloys, *Met. Trans. A* 8A (1977) 991.
6. H. Shimizu, M. Ono and K. Nakayama, Microprobe and Auger analysis of heterogeneous oxidation of alloys and determination of grain boundary diffusion constants, *Proc. 3rd Intl. Conf. Solid Surf. Vol. III*, Oesterreichische Studiengesellschaft für Atomenergie GmbH, Vienna (1977) 2359.
7. R. D. Sisson Jr. and M. A. Dayananda, Diffusional and thermodynamic interactions in the Cu-Ni-Zn system at 775°C, *Met. Trans. A* 8A (1977) 1849.
8. L. E. Wirtz and M. A. Dayananda, Diffusion paths and structures in multiphase Cu-Ni-Zn couples at 775°C, *Met. Trans. A* 8A (1977) 567.

1978

1. D. Bergner, Intermetallic diffusion: Microprobe methods for the solution of diffusion problems, *Neue Hütte* 23 (1978) 233.
2. D. Bergner and K. Schwartz, The diffusion of other metals in platinum, *Neue Hütte* 23 (1978) 210.
3. D. B. Butrymowicz and J. R. Manning, Chemical interdiffusion and Kirkendall shifts in Ag-Cd alloys, *Met. Trans. A* 9A (1978) 947.
4. B. Dukiet-Zawadzka, R. Ciach, and W. Wolczynski, Diffusion of zinc during the homogenization of cast aluminum-zinc alloys, *Arch. Hutn.* 23 (1978) 413.
5. E. A. Farah and W. May, Reactions between tungsten carbide-titanium in the region 1000 to 1400°C, *Fifth Interamerican Conf. on Matls. Techn.*, Sao Paulo, Brazil (1978) 513.
6. S. Fujikawa, K. Hirano, and Y. Fukushima, Diffusion of Si in Al, *Met. Trans. A* 9A (1978) 1811.

7. J. I. Goldstein and A. E. Moren, Diffusion modeling of the carburization process, *Met. Trans. A* 9A (1978) 1515.
8. A. Gukelberger and S. Steeb, Diffusion layers within the Zr-Al-O ternary system at temperatures between 1000 and 1300°C: I. The Zr-Zr₂Al₃ system, *Z. Metallkd.* 69 (1978) 255.
9. A. Gukelberger and S. Steeb, Diffusion welding within the Zr-Al-O ternary system at temperatures between 1000 and 1300°C: II. Zr-Al₂O₃ couple, *Z. Metallkd.* 69 (1978) 385.
10. A. Gukelberger and S. Steeb, Diffusion layers within the Zr-Al-O ternary system at temperatures between 1000 and 1300°C: III, *Z. Metallkd.* 69 (1978) 462.
11. V. S. Khlomov, V. N. Pimenov, and K. P. Gurov, The temperature dependence of the coefficients of interdiffusion in the region of the phase transformations in the nickel-vanadium system, *Fiz. Met. Metalloved.* 46 (1978) 199.
12. V. S. Khlomov, V. N. Pimenov, Y. E. Ugaste, and K. P. Gurov, A study of interdiffusion in the Ni-V system, *Fiz. Met. Metalloved.* 46 (1978) 668.
13. V. I. Kostikov and B. A. Dainyak, Kinetics of the process of mutual diffusion in the system W-Zr, *Fiz. Khim. Obrab. Mater.* 6 (1978) 59.
14. B. Million, K. Stransky, and A. Rek, Diffusion of carbon between carbon and austenitic steels in the temperature interval 773-1373 K, *Kovove Mater.* 16 (1978) 279.
15. A. E. Moren and J. I. Goldstein, Cooling rate variations in group IVA iron meteorites, *Earth Planet. Sci. Lett.* 40 (1978) 151.
16. G. Salje and M. Feller-Kniepmeier, The Cu-Fe phase diagram in the temperature range 650-1050°C, *Z. Metallkd.* 69 (1978) 167.
17. W. Schatt, Diffusion study of the Cu-Ti system, *Kristall. Tech.* 13 (1978) 185.
18. S. Shankar and L. L. Seigle, Interdiffusion and intrinsic diffusion in the NiAl phase of the Al-Ni system, *Met. Trans. A* 9A (1978) 1467.
19. R. Sivakumar and L. L. Seigle, Variation of diffusion coefficient with composition in NiAl, *Trans. Indian Inst. Met.* 31 (1978) 336.
20. I. G. Solorzano and F. A. I. Darwish, Formation of an intermetallic compound of the Ti-Al system in the solid state, *Fifth Interamerican Conf. on Matls. Tech.*, Sao Paulo, Brazil, (1978) 171.
21. J. Willis and J. T. Wasson, Cooling rates of group IVR iron meteorites, *Earth Planet. Sci. Lett.* 40 (1978) 151.
22. S. V. Zemskii, G. I. Aleksandrova, D. R. Litvinenko, and V. V. Khangulov, The diffusion saturation of steels with tin, *Zashch. Met.* 14 (1978) 512.

1979

1. G. Bliznakov, Z. Zakhariyev, I. Tzolovski, and S. V. Velichkov, An investigation of the formation of metal-like compounds in the diffusion layer obtained during simultaneous multi-component saturation of Fe with B and Zr, *J. Less Common Metals* 67 (1979) 315.
2. A. V. Byakova, V. F. Loskutov, and G. N. Gordan, The composition of NbC coatings on carbon steel, *Izv. V.U.Z. Chernaya Metall.* 12 (1979) 59.
3. G. H. Cheng and M. A. Dayananda, Multiphase diffusion in the Fe-Ni-Al system at 1000°C: Diffusion structures and diffusion paths, *Met. Trans. A* 10A (1979) 1407.
4. M. A. Dayananda and C. W. Kim, Zero flux planes and flux reversals in Cu-Ni-Zn diffusion couples, *Met. Trans. A* 10A (1979) 1333.
5. R. Freer, An experimental measurement of cation diffusion in almandine garnet, *Nature* 280 (1979) 220.
6. Z. Glowacki and W. Kaluba, Growth kinetics, morphology and formation mechanism of chromium diffusion carbide layers, *Simpozion 1979 Romania* 2 (1979) 24.
7. F. H. Hammad and H. I. Shaaban, Interdiffusion of Zircaloy 4 and Nickel, *J. Nucl. Mater.* 80 (1979) 152.
8. S. N. Kryukov, Y. E. Soklovskaya, Y. A. Soldatov, S. F. Dunayev, and V. I. Gachegov, Investigation of Co diffusion in bimetals, *Vestn. Moskovskogo Univ. (Khim.)*. 20 (1979) 450.
9. V. Leute, H. Bottner, and H. Schmidtke, Chalcogen interdiffusion in the system Pb(S,Se), *Z. Naturforsch.* A34 (1979) 89.
10. A. E. Moren and J. I. Goldstein, Cooling rates of group IVA iron meteorites determined from a ternary Fe-Ni-P model, *Earth Planet. Sci. Lett.* 43 (1979) 182.
11. M. R. Pinnel and J. E. Bennett, On the formation of the ordered phases CuAu and Cu₃Au at a Cu/Au planar interface, *Met. Trans. A* 10A (1979) 741.
12. Y. Sasaki, Y. Iida, and S. Ueda, High temperature phosphidation of Ni-Cr alloys in phosphorous vapor, *J. Electrochem. Soc.* 126 (1979) 1948.
13. K. V. Sathiyaraj, D. Ablitzer, and C. Demangeat, Impurity diffusion and vacancy-impurity binding energy associated with elements of the second transition series in Nb and Mo, *Philos. Mag.* A 40 (1979) 541.
14. F. Storek, B. Kolman, P. Chraska, and J. Dubsky, Measurement of Fe and Ni concentration changes in Au layers: II. X-ray microanalysis method and its comparison with the X-ray diffraction technique, *Prakt. Metalloqr.* 16 (1979) 493.

1. S. J. Budurov, W. S. Boshinov, and P. D. Kovatchev, Interdiffusion in FCC Ni-In alloys, *Kristall. Tech.* 15 (1980) K19.
2. A. V. Byakova, V. F. Loskutov and G. N. Gordan, The composition of chromium carbide coatings on the surface of carbon steels, *Izv. V.U.Z. Chernaya Metall.* 4 (1980) 109.
3. Y. S. Chen and C. J. Rosa, High temperature oxidation of Ti-4.32 wt% Nb alloy, *Oxid. Met.* 14 (1980) 147.
4. T. G. Garbovitsaya and L. N. Paritskaya, The role of impingement in interdiffusion in thin film specimens, *Fiz. Met. Metalloved.* 50 (1980) 623.
5. V. I. Gryzunov, A. S. Sagyndikov, and E. M. Sokolovskaya, Interdiffusion in the Ti-Ni system, *Izv. Akad. Nauk. Kazakh.* 6 (1980) 72.
6. D. E. Holmes and G. S. Kamath, Growth characteristics of liquid phase epitaxy InSb and InGaSb, *J. Electron. Mater.* 9 (1980) 95.
7. Z. Has, P. Kula, and Z. Gawronski, Structure of the sulfonitriding layers on stainless and heat resistant steels, *Arch. Nauki Mater.* 1 (1980) 137.
8. H. Jehn and E. Olzi, Zirconium depletion profiles in a Nb-5at%Zr alloy after high temperature vacuum annealing, *High Temp. High Pressures* 12 (1980) 85.
9. J. D. Katz, H. W. Pickering, and W. R. Bitler, Low-temperature diffusion kinetics in Ni electrodeposits, *Plat. Surf. Finish.* 67 (1980) 55.
10. S. V. Kositsyn, V. S. Litvinov, V. G. Sorokin, and N. A. Gervasev, The effect of Si on diffusion in Ni-Al alloys, *Fiz. Met. Metalloved.* 49 (1980) 1063.
11. M. A. Laheij, F. J. VanLooy, and R. Metselaar, Phase relations in the Fe-Cr-O system at 1200°C investigated by means of a diffusion couple technique, *Oxid. Met.* 14 (1980) 207.
12. M. Morioka, Cation diffusion in olivine: I. Co and Mg, *Geochem. Cosmochim. Acta* 44 (1980) 759.
13. S. D. Mukherjee, C. J. Palmstrom, and J. G. Smith, The thermal stability of thin layer transition and refractory metallizations on GaAs, *J. Vac. Sci. Technol.* 17 (1980) 904.
14. V. I. Neverov and V. N. Pimenov, Phase growth kinetics in the system Fe-Al, *Fiz. Khim. Obrab. Mater.* 5 (1980) 104.
15. K. Okada and K. Nishida, Diffusion of ternary electrodeposited layers of Fe-Ni-Cr and Fe-Cr-Ni, *Jpn. J. Iron and Steel Inst.* 66 (1980) 1343.
16. A. Olsen and F. R. Sale, Growth kinetics, morphologies and structures of vapor deposited nickel silicide layers, *Met. Technol.* 7 (1980) 494.
17. S. K. Pabi, On the dissolution kinetics of Si in an Al-rich matrix, *Mater. Sci. Eng.* 43 (1980) 151.
18. P. Peutner and H. J. Engeu, Electrochemical investigations of the kinetics of formation of the intermetallic phases of the systems Fe-Zn and Fe-Zn-Si, *Arch. Eisenhüttenwes.* 51 (1980) 463.
19. M. R. Pinnel and J. E. Benett, Observations on interdiffusion in planar Cu/Sn-Ni/Au tricouples, *Met. Trans. A* 11A (1980) 587.
20. G. W. Roper and D. P. Whittle, Interdiffusion in ternary Co-Cr-Al alloys, *Met. Sci.* 14 (1980) 21.
21. H. Saito and Y. Ishida, The effect of boundary structure on the diffusion of Sn and Cr along grain boundaries in pure Fe, *J. Jpn. Inst. Met.* 44 (1980) 215.
22. H. Shimizu, N. Koyama, and Y. Ishida, Depletion of Cu from the grain boundary region of Cu-Ni alloys during sputtering at elevated temperatures, *Jpn. J. Appl. Phys.* 19 (1980) L671.
23. P. R. Webber and D. Chadwick, Evaporation limited segregation of Cu-Ni, *Surf. Sci.* 94 (1980) L151.
24. D. J. Young, T. Narita, and W. W. Smeltzer, Diffusional analysis for growth of the monosulfide scale on Co-Fe alloys, *J. Electrochem. Soc.* 127 (1980) 679.

1981

1. D. Ablitzer, J. Haeussler, K. V. Sathiyaraj, and R. Vignes, Diffusion of Fe in V, *Phil. Mag. A* 44 (1981) 589.
2. G. C. Allen and R. K. Wild, Probing the secrets of solid surfaces, *CEGB Res.* 11 (1981) 12.
3. M. Arita, M. Ohyama, K. S. Goto, and M. Someno, Measurements of activity, solubility and diffusivity in alpha and gamma Fe-Sn alloys between 1183 and 1680 K, *Z. Metallkd.* 72 (1981) 244.
4. M. Arita, M. Tanaka, K. S. Goto, and M. Someno, Activity and diffusivity measurements of Cu in gamma and delta Fe by equilibration between solid Fe and liquid Ag, *Met. Trans. A* 12A (1981) 497.
5. G. W. Ashwell and R. Heckingbottom, Interdiffusion of Ti and Au: A comparison of thin films deposited in technical vacuum and ultrahigh vacuum, *J. Electrochem. Soc.* 128 (1981) 649.
6. S. Kanamori, A study on the penetration of Pt in Si in Ti/Pt/Au beam metallization systems, *Thin Solid Films* 75 (1981) 19.
7. Y. P. Khukhryanskii and V. I. Panteleev, Coefficient of mutual diffusion of the

components in solutions of the Al-Ga-As system as a function of temperature, *Izv. Akad. Nauk SSSR Neorg. Mater.* 17 (1981) 204.

8. S. C. Kwon and J. Y. Lee, Interdiffusion in Fe/Fe₂Al₅/Al couples, *Met. Technol.* 8 (1981) 373.

9. V. Leute, H. M. Schmidtke, W. Stratmann, and W. Winking, Interdiffusion in doped and undoped semiconductor alloys Hg_{1-x}Cd_xTe, *Phys. Status Solidi (a)* 67 (1981) 183.

10. P. Lobotka and S. Luby, Influence of the noise driving force on the diffusion of Cu in Al thin films, *Czech. J. Phys.* B31 (1981) 1099.

11. A. D. Romig Jr. and J. I. Goldstein, The diffusivity of Ni in Fe-Ni and Fe-Ni-P martensites, *Met. Trans. A* 12A (1981) 243.

12. A. D. Romig Jr. and J. I. Goldstein, Low temperature phase equilibria in the Fe-Ni and Fe-Ni-P systems: Application the thermal history of metallic phases in meteorites, *Geochim. Cosmochim. Acta* 45 (1981) 1187.

13. Y. Ukyo and K. S. Goto, The interdiffusivity matrix of Fe₂O₃/CaO/SiO₂ melt at 1693 to 1773 K, *Met. Trans. B* 12B (1981) 449.

14. F. J. VanLoo and G. F. Bastin, Phase relations and diffusion paths in the Ti-Ni-Co system at 900°C, *J. Less Common Met.* 81 (1981) 61.

15. F. J. VanLoo, F. M. Smet, G. D. Rieck, and G. Verspui, Phase relations and diffusion paths in the Mo-Si-C systems at 1200°C, *Trends in Refractory Metals, Hard Metals and Special Materials and Their Technology* 2 (1981) 141.

16. D. S. Williams, R. A. Rapp, and J. P. Hirth, Multilayer diffusional growth in Ag-Zn alloys, *Met. Trans. A* 12A (1981) 639.

17. F. J. VanLoo, J. W. Vrolijk, and G. F. Bastin, Phase relations and diffusions paths in the Ti-Ni-Fe system at 900°C, *J. Less Common Met.* 77 (1981) 121.

18. D. S. Williams, R. A. Rapp, and J. P. Hirth, Multilayer diffusional growth in Ag-Zn alloys, *Met. Trans. A* 12A (1981) 639.

19. P. A. Wycliffe, G. R. Purdy, and J. D. Embury, Growth of austenite in the intercritical annealing of Fe-C-Mn dual phase steels, *Can. Metall. Quat.* 20 (1981) 339.

1982

1. N. I. Afanasev and T. F. Elsukova, The role of volume diffusion to discontinuous precipitation, *Fiz. Met. Metalloved.* 53 (1982) 360.

2. V. Amicarelli, G. Boghetich, L. Cento, and G. F. Bocchini, The manganizing process: Comparison between P/M and conventional steels, *Second International Congress on Heat Treatment of Materials* (1982) 147.

3. M. G. Barker and S. A. Frankham, The effects of carbon and nitrogen on the corrosion resistance of type 316 stainless steel to liquid lithium, *J. Nucl. Mater.* 107 (1982) 218.

4. C. Canali, G. Celotti, F. Fantini, and E. Zanon, Interdiffusion and compound formation in the Si/PtSi/(Ti-W)/Al system, *Thin Solid Films* 88 (1982) 9.

5. D. Dayan, U. Atzmony, and M. P. Dariel, Interdiffusion studies of rare earth metals with liquid Ga, *J. Less Common Metals* 87 (1982) 87.

6. Z. Glowacki and W. Kaluba, On some features of chromium carbide diffusion layer formation, *Met. Trans. A* 13A (1982) 753.

7. S. K. Gupta, S. R. Adolph, I. C. Tandon, and L. L. Seigle, Experimental and theoretical concentration profiles at the surface of chromized iron, *Met. Trans. A* 13A (1982) 495.

8. K. Hoshino, Y. Iijima, and K. Hirano, Intrinsic diffusion coefficients and the vacancy flow factor in dilute Cu-Zn alloys, *Met. Trans. A* 13A (1982) 1135.

9. W. Kaluba and A. Wachowiak, On the formation of complex chromium diffusion layers on carbon steel, *Second International Congress on Heat Treatment of Materials* (1982) 411.

10. M. D. Kelly, K. L. Breakall Jr., and D. L. Roesch, Microstructural analysis of Kovar/Mo and Cu-Mo interdiffusion, *Microstructural Science*, vol. 10, Elsevier, New York (1982) 59.

11. A. D. Romig Jr. and R. J. Salzbrenner, Elemental partitioning as a function of heat treatment in an Fe-Si-V-C dual phase steel, *Ser. Metall.* 16 (1982) 33.

12. A. D. Romig Jr. and R. J. Salzbrenner, The kinetics of the ferrite/austenite phase transformation in Fe-Si-V-C alloys: A quantitative analysis of elemental partitioning, *Solid-Solid Phase Transformations*, TMS-AIME (1982) 849.

13. G. Rudolph, Microprobe measurements to determine phase boundaries and diffusion paths in ternary phase diagrams taking a Cu-Ni-Al system as an example, *Progress in Materials Science*, vol. 1, Springer-Verlag, Vienna (1982) 241.

14. A. K. Sarkhel and L. L. Seigle, Interdiffusion coefficients in the Ni₂Al₃ phase of the Ni-Al system, *Met. Trans. A* 13A (1982) 1313.

15. W. Toschkow and T. Tontschew, Morphological features of the diffusion layers from gas and ion nitriding, *Second International Congress on Heat Treatment of Materials* (1982) 363.

16. K. N. Tu, Thermal Stability of Pd₂Si and PdSi in thin film and bulk diffusion couples, *J. Appl. Phys.* 53 (1982) 428.

1983

1. V. Ganesan, V. Seetharaman, and V. S. Raghunathan, Interdiffusion in the type 316 aus-

tenitic stainless steel/iron system, *J. Nucl. Mater.* 118 (1983) 313.

2. O. Kubaschewski, Diffusion, *Atomic Energy Review: Special Issue No. 9. Titanium: Physiochemical Properties of Its Compounds and Alloys*, International Atomic Energy Authority, Vienna (1983) 441.

3. S. Okuda, Z. Okamoto, F. Miyashita, and G. Miyatani, Diffusion heat treatment of Cu-Zn alloys coated with Sn plate, *Jpn. J. Met. Finish Soc.* 34 (1983) 106.

4. A. M. Ovrutskii and I. M. Spiridonova, The kinetics of boride phase formation during electrolytic boriding, *Fiz. Khim. Obrab. Mater.* 3 (1983) 78.

5. A. D. Romig Jr., Interdiffusion in beta phase Cu-Al alloys, *J. Appl. Phys.* 54 (1983) 3172.

6. A. D. Romig Jr. and J. I. Goldstein, Interface equilibrium in alpha/beta phase Cu-Al diffusion couples, *Met. Trans. A* 14A (1983) 1224.

1984

1. J. C. Bierlein, S. W. Gaarenstroom, R. A. Waldo, and A. C. Ottolini, Characterization of multilayer diffusion barriers by electron probe microanalysis and Auger electron spectroscopy, *J. Vac. Sci. Technol. A* 2 (1984) 1102.

2. L. S. Castleman and G. Wo, Ternary diffusion: Solutions with diffusion coefficients linearly dependent on concentrations, *Met. Trans. A* 15A (1984) 1359.

3. C. W. Kim and M. A. Dayananda, Zero-flux planes and flux reversals in the Cu-Ni-Zn system at 775°C, *Met. Trans. A* 15A (1984) 649.

4. S. M. Merchant, M. R. Notis, and J. I. Goldstein, Morphological stability of beta-gamma phase interfaces in Ni-Cr-Al alloys, *Microbeam Analysis--1984*, A. D. Romig Jr. and J. I. Goldstein (Eds), San Francisco Press, San Francisco (1984) 315.

5. A. D. Romig Jr., F. G. Yost, and P. F. Hlava, Intermetallic layer growth in Cu/Sn-In solder joints, *Microbeam Analysis--1984*, A. D. Romig Jr. and J. I. Goldstein (Eds), San Francisco Press, San Francisco (1984) 87.

6. V. D. Rusnyak, S. F. Dunaev, E. M. Slyusarenko, and E. M. Sokolovskaya, Study of the solid phase reaction of Mg with Ni, *Vestn. Mosk. Univ. Khim.* 25 (1984) 264.

7. D. H. StJohn and L. M. Hogan, Solute distribution at the solid/liquid interface during steady state peritectic solidification, *J. Mater. Sci.* 19 (1984) 939.

8. R. Sellamuthu and J. I. Goldstein, Measurement and analysis of distribution coefficients in Fe-Ni alloys containing sulfur and/or phosphorus I: K_{Ni} and K_P , *Met. Trans. A* 15A (1984) 1677.

9. M. A. Shahid, P. J. Topham, B. J. Sealy, and K. E. Puttick, Laser alloyed Sn layers on GaAs, *J. Mater. Sci.* 19 (1984) 2361.

10. U. Siegel and A. Haas, Microanalytical determination of the amount of primary ferrite and distribution coefficients in austenitic Cr-Ni and Cr-Ni-Mo steels, *Neue Hütte* 29 (1984) 211.

11. V. N. Vechkanov, A. N. Khodan, S. M. Chigishev, I. A. Stepanov, and A. A. Gavrish, Volume and grain boundaries mass transport in austenitic steel at high temperature, *International Congress on Metallic Corrosion*, Vol. 3, National Research Council of Canada, Ottawa, Canada (1984) 372.

Analytical Electron Microscopy

1978

1. R. Delhez and E. J. Mittemeyer, Diffraction studies of concentration variations, *Delft Prog. Rept.* 3 (1978) 316.

1979

1. S. A. Al-Salman, G. W. Lorimer, and N. Ridley, Partitioning of silicon during pearlite growth in a eutectoid steel, *Acta Met.* 27 (1979) 1391.

2. R. C. Sharma, G. R. Purdy, and J. S. Kirkaldy, Thermodynamics and Phase equilibria for the Fe-C-Cr system in the vicinity of the eutectoid temperature, *Met. Trans. A* 10A (1979) 1119.

1981

1. J. Chance and N. Ridley, Chromium partitioning during isothermal transformation of a eutectoid steel, *Met. Trans. A* 12A (1981) 1205.

2. I. Ogura, Structures of metals and alloys as examined by means of the ultramicrotomed thin section method, *New Trends of Electron Microscopy in Atomic Resolution Materials Science and Biology*, Science Press, Beijing, China (1981) 94.

3. L. Rivaud, I. D. Ward, A. H. Eltoukhy, and J. E. Greene, Enhanced diffusion and precipitation in Cu-In alloys due to low energy ion bombardment, *Surf. Sci.* 102 (1981) 610.

4. A. D. Romig Jr. and J. I. Goldstein, The diffusivity of Ni in Fe-Ni and Fe-Ni-P martensites, *Met. Trans. A* 12A (1981) 243.

5. P. Wycliffe, G. R. Purdy, and J. D. Embury, Austenite growth in the intercritical annealing of ternary and quaternary dual-phase steels, *Fundamentals of Dual Phase Steels*, TMS-AIME (1981) 59.

1. R. Chopra, M. Ohring, and R. S. Oswald, Low temperature compound formation in Cu/Sn thin film couples, *Thin Solid Films* 94 (1982) 279.
2. P. Doig, D. J. Chastell, and P. E. Flewitt, The stress corrosion susceptibility of a quenched and tempered 12%CrMoV martensitic stainless steel, *Met. Trans. A* 13A (1982) 913.
3. P. Doig and P. E. Flewitt, Segregation of chromium to prior austenite boundaries during quenching of a 2.25%Cr-1%Mo steel, *Acta Met.* 29 (1982) 1831.
4. P. Doig, P. E. Flewitt, B. C. Muddle, H. L. Fraser, and K. Chattopadhyay, Solute redistribution during the formation of α ₁ bainite plates in Cu-Zn and Cu-Au-Zn alloys, *Solid to Solid Phase Transformations*, TMS-AIME (1982) 983.
5. R. Glitz, M. Notis, and J. I. Goldstein, AEM study of early stage growth of Ni₃Al intermediate phase in NiAl-Ni diffusion couples, *Solid to Solid Phase Transformations*, TMS-AIME (1982) 691.
6. J. D. Pan and R. W. Baluffi, Diffusion induced grain boundary migration in Au/Cu and Au/Ag thin films, *Acta Met.* 30 (1982) 861.
7. M. Pohl, H. Oppolzer, and S. Schild, STEM-EDS measurements on grain boundary phenomena of sensitized chrome-nickel steels, *Prog. in Materials Analysis*, vol. 1, Springer-Verlag, Vienna (1982) 281.
8. R. A. Ricks, A microanalytical study of the diffusion fields associated with the growth of NiAl precipitates in an Fe-25%Ni-20%Cr-4%Al alloy, *Solid to Solid Phase Transformations*, TMS-AIME (1982) 751.
9. R. A. Ricks, Study of grain boundary precipitation in Fe-20%Cr-25%Ni-4%Al alloy using STEM/EDS and convergent beam electron diffraction, *Quantitative Microanalysis with High Spatial Resolution*, The Metals Society, London (1982) 217.
10. R. A. Ricks, S. A. Parsons, and P. R. Howell, The application of STEM/X-ray microanalysis to phase transformations in iron-base alloys, *Solid to Solid Phase Transformations*, TMS-AIME (1982) 831.
11. A. D. Romig Jr. and R. J. Salzbrenner, Elemental partitioning as a function of heat treatment in an Fe-Si-V-C dual phase steel, *Scripta Met.* 16 (1982) 33.
12. A. D. Romig Jr. and R. J. Salzbrenner, The kinetics of the ferrite/austenite phase transformation in Fe-Si-V-C alloys: A quantitative analysis of elemental partitioning, *Solid to Solid Phase Transformations*, TMS-AIME (1982) 849.

1983

1. P. Doig and P. E. Flewitt, Intergranular segregation studies in steels using STEM-EDS X-ray microanalysis, *J. Microsc. Spectrosc. Electron.* 8 (1983) 193.
2. E. L. Hall, R. L. Mehan and M. R. Jackson, Phase equilibria and kinetics in the solid state reaction between Si and NiCrAl, *Met. Trans. A* 14A (1983) 1549.
3. H. T. Hentzell, R. D. Thompson and K. N. Tu, Interdiffusion in Cu-Al thin film bilayers: I. Structure and kinetics of sequential compound formation, *J. Appl. Phys.* 54 (1983) 6923.
4. K. Kuroda, P. A. Labun, G. Welsch, and T. E. Mitchell, Oxide-formation characteristics in the early stages of oxidation of Fe and Fe-Cr alloys, *Oxid. Met.* 19 (1983) 117.
5. S. M. Merchant, M. R. Notis, and D. B. Williams, An AEM investigation of the formation of precipitate free zones in an Al-16wt%Ag alloy: Determination of equilibrium and metastable solvus lines, *Met. Trans. A* 14A (1983) 1825.
6. S. Nakahara, J. A. Abys, and S. M. Abys, Room temperature diffusion induced grain boundary migration in the fine grained Pd side of Cu/Pd diffusion couples, *Mater. Lett.* 2 (1983) 155.
7. C. Narayan and J. I. Goldstein, Low-temperature diffusivity measurements in the FeNi system using STEM techniques, *Met. Trans. A* 14A (1983) 2437.
8. A. W. Nicholls and I. P. Jones, Determination of low temperature volume diffusion coefficients in an Al-Zn alloy, *J. Phys. Chem. Solids* 44 (1983) 671.

1984

1. C. Narayan and J. I. Goldstein, Growth of intragranular ferrite in Fe-Ni-P alloys, *Met. Trans. A* 15A (1984) 867.
2. J. R. Michael and D. B. Williams, An analytical electron microscope study of the kinetics of the equilibrium segregation of Bi in Cu, *Met. Trans. A* 15A (1984) 99.
3. N. Pussegoda, W. R. Tyson, P. Wycliffe and G. R. Purdy, Segregation during intercritical annealing of dual phase steels, *Met. Trans. A* 15A (1984) 1499.
4. R. A. Ricks, Cellular precipitation in austenitic stainless steel containing Al and Ti, *Met. Sci.* 18 (1984) 7.
5. N. Ridley and D. Burgess, Partitioning of Co during pearlite growth in a eutectoid steel, *Met. Sci.* 18 (1984) 7.
6. I. G. Solorzano, G. R. Purdy, and G. C. Weatherly, Studies of the initiation, growth and dissolution of the discontinuous precipitation product in Al-Zn alloys, *Acta Met.* 32 (1984) 1709.
7. T. Thorvaldsson and A. Salwen, Measurement of diffusion coefficients for chromium at low temperatures in a type 304 stainless steel, *Scripta Met.* 18 (1984) 739.

Secondary Ion Mass Spectroscopy and Ion Microprobe

1974

1. B. J. Giletti, M. P. Semet, R. B. Kasper, Self-diffusion of potassium in low albite using an ion microprobe, *Geol. Soc. Am. Abstr. Progr.* 6 (1974) 754.

1975

1. H. J. Windhager and G. Borchardt, Tracer diffusion and defects in cobalt orthosilicate, *Ber. Bunsenges. Phys. Chem.* 79 (1975) 1115.

1976

1. B. J. Giletti, M. P. Semet and R. A. Yund, Oxygen self-diffusion measured in silicates using an ion microprobe, *Trans. Am. Geophys. Union* 57 (1976) 350.
2. B. J. Giletti, R. A. Yund and M. P. Semet, Silicon diffusion in quartz, *Geol. Soc. Am. Abstr. Progr.* (1976) 883.

1977

1. H. G. Sockel and D. Hallwig, Determination of small diffusion coefficients in O containing compounds by SIMS, *Mikrochim. Acta Suppl.* 7 (1977) 95.

1978

1. H. E. Beske and H. Holzbrecher, Understanding decomposition products and diffusion with the SIMS, *Mikrochimica Acta* 1 (1978) 201.
2. D. E. Carlson and C. W. Magee, SIMS analysis of D diffusion in hydrogenated amorphous Si, *Appl. Phys. Lett.* 33 (1978) 81.
3. B. J. Giletti, M. P. Semet, and R. A. Yund, Studies in diffusion: III. Oxygen in feldspars: An ion microprobe determination, *Geochim. Cosmochim. Acta* 42 (1978) 45.
4. W. V. McLevige, K. V. Vaidyanathan, B. G. Streetman, J. Comas, and L. Plew, Diffusion studies of Be-implanted GaAs by SIMS and electrical profiling, *Solid State Commun.* 25 (1978) 1003.
5. G. Muller, M. Haubold, R. Schimko, M. Trapp, and G. Schwarz, Investigations on the diffusion of implanted Zn in GaAs by ion microprobe, *Phys. Stat. Solidi* 49 (1978) 279.
6. R. C. Pillier and A. D. Marwick, The radiation induced redistribution of Si in Ni, *J. Nucl. Mater.* 71 (1978) 309.
7. D. L. Smith and V. Y. Pickhardt, Impurity dopant incorporation and diffusion during molecular beam epitaxial growth of IV-VI semiconductors, *J. Electrochem. Soc.* 125 (1978) 2042.
8. P. D. Vyas and B. L. Sharma, Behavior of Au in the vicinity of the Au-Ge/n-GaAs interface during annealing, *Thin Solid Films* 51 (1978) L21.
9. R. A. Yund and T. F. Anderson, The effect of fluid pressure on oxygen isotope exchange between feldspar and water, *Geochim. Cosmochim. Acta* 42 (1978) 235.

1979

1. M. Arita, M. Hosoya, M. Kobayashi, and M. Someno, Depth profile measurement by SIMS for determining the tracer diffusivity of oxygen in rutile, *J. Am. Chem. Soc.* 62 (1979) 443.
2. A. Christou, Interdiffusion in gold/refractory thin film systems studied by a combination of scattering techniques, *Scanning Electron Microscopy/1979/I* (1979) 191.
3. D. Dieumegard and D. Dubreuil, Hydrogenation of amorphous silicon films by plasma treatment, *Intl. Congress on Cathodic Sputtering and Related Applications*, Société Française du Vide, Paris (1979) 189.
4. C. A. Evans Jr., V. R. Deline, T. W. Sigmon, and A. Lidow, Redistribution of chromium during annealing of 80Se-implanted GaAs, *Appl. Phys. Lett.* 35 (1979) 291.
5. B. J. Giletti, J. H. Hickey, and T. E. Tullis, Oxygen diffusion in olivine under hydrous conditions, *Trans. Am. Geophys. Union* 60 (1979) 370.
6. T. Hehenkamp, A. Lodding, H. Odelius, and V. Schlett, Isotope effect in the diffusion of the stable germanium isotopes in copper, *Acta Met.* 27 (1979) 829.
7. M. B. Hintz, *Applicability of SIMS to the Investigation of Foreign Atom Diffusion Demonstrated by the Example of In and Al Volume Diffusion in Ni Single Crystals*, Thesis, Univ. Stuttgart (1979) 128.
8. L. L. Kazmerski, Grain boundary and interdiffusion studies in compound semiconductor thin films and devices utilizing Auger electron spectroscopy and SIMS, *Thin Solid Films* 57 (1979) 99.
9. A. Noya, S. Kuriki, G. Matsumoto, and M. Hirano, A study of gold migration in Au/Yt₂O₃/Yt junctions by SIMS, *Thin Solid Films* 59 (1979) 143.
10. H. Scherrer, G. Pineau and S. Scherrer, Diffusion of ¹¹⁷Sn in tin telluride, *Phys. Lett. A* 75 (1979) 118.

1980

1. S. Abdin, A. Huber, G. Morillot and C. Val, Properties of Ni films prepared by

radiofrequency sputtering and interdiffusion analysis of Ta₂N/Ni films, *Electrocomponent Sci. Technol.* 7 (1980) 159.

2. A. A. Bochvar, Diffusion in tin during the growth of a Nb₃Sn layer, *Metalloved. Term. Obrab. Met.* 12 (1980) 44.

3. R. W. Cahn, J. E. Evetts, J. Patterson, R. E. Somekh, and C. K. Jackson, Direct measurement by SIMS of self diffusion of B in Fe₄₀Ni₄₀B₂₀ glass, *J. Mater. Sci.* 15 (1980) 702.

4. A. B. Campbell III, B. D. Sartwell, and P. B. Needham Jr., Depth profiling in ion implanted alloys, *J. Appl. Phys.* 51 (1980) 283.

5. W. H. Christie and C. W. White, SIMS depth profiling studies: The effect of laser annealing on the distribution of ion implanted B in Si, *Surf. Sci.* 100 (1980) 43.

6. P. Dorner, SIMS investigations on the diffusion of Cu in Ag single crystals, *Acta Met.* 28 (1980) 291.

7. W. K. Hofker and J. Politiek, Ion implantation in semiconductors, *Philips Tech. Rev.* 39 (1980) 1.

8. O. Jaoul, C. Froidevaux, W. B. Durham, and M. Michaud, Oxygen self-diffusion in forsterite: Implications for the high temperature creep mechanism, *Earth Planet. Sci. Lett.* 47 (1980) 391.

9. J. Kasahara and N. Watanabe, Redistribution of Cr in capless annealed GaAs under As pressure, *Jpn. J. Appl. Phys.* 19 (1980) L151.

10. U. Koster and U. Herold, Diffusion in some Fe-Ni-B glasses, *Liquid and Amorphous Metals*, Editions de Physique, Orsay, France (1980) 352.

11. A. Lidow, J. F. Gibbons, V. R. Deline, and C. A. Evans Jr., Ion implanted Se in GaAs, *J. Appl. Phys.* 51 (1980) 4130.

12. S. D. Mukherjee, C. J. Palmstrom, and J. G. Smith, The thermal stability of thin layer transition and refractory metallizations on GaAs, *J. Vac. Sci. Technol.* 17 (1980) 904.

13. Y. I. Nissim, J. F. Gibbons, C. A. Evans Jr., V. R. Deline, and J. C. Norberg, Thermal diffusion of Sn in GaAs from a spin-on SnO₂/SiO₂ source, *Appl. Phys. Lett.* 37 (1980) 89.

14. G. Pineau, H. Scherrer, and S. Scherrer, Heterodiffusion of Sn in n-type PbSe, *Phys. Lett. A* 75 (1980) 234.

15. D. J. Reed and B. J. Wuensch, Ion probe measurements of oxygen self diffusion in single crystal Al₂O₃, *J. Am. Ceram. Soc.* 63 (1980) 88.

16. H. Scherrer, S. Weber, and S. Scherrer, Diffusion of ¹²⁵Te in SnTe, *Phys. Lett. A* 77 (1980) 189.

17. H. G. Sockel, D. Hallwig, and R. Schachtner, Investigations of slow exchange processes at metal and oxide surfaces and interfaces using SIMS, *Mater. Sci. Eng.* 42 (1980) 59.

18. G. J. VanGurp, J. W. Slotboom, F. J. Smolders, W. T. Stacy, and Y. Tamminga, Enhanced diffusion of implanted As and B in Si by low temperature heat treatment, *J. Electrochem. Soc.* 127 (1980) 1813.

19. R. G. Wilson, P. K. Vasudev, D. M. Jamba, C. A. Evans Jr., and V. R. Deline, Chromium concentrations, depth distributions and diffusion coefficients in bulk and epitaxial GaAs in Si, *Appl. Phys. Lett.* 36 (1980) 215.

20. A. K. Zurek and H. L. Marcus, Studies of the deuterium transport mechanism during fatigue of Al alloys, *Hydrogen Effects in Metals*, TMS-AIME (1980) 57.

1981

1. G. C. Allen and R. K. Wild, Probing the secrets of solid surfaces, *CEBG Res.* 11 (1981) 12.

2. D. L. Begley, R. W. Alexander, R. J. Bell and C. A. Goben, Reaction at a Pt/GaAs Interface, *Surf. Sci.* 104 (1981) 341.

3. G. Edelin and C. Tete, Diffusion of phosphorus in amorphous Fe₈₅B₁₅, *Scr. Metall.* 15 (1981) 739.

4. W. Gust, M. B. Hintz, A. Lodding, H. Odelius, and B. Predel, Impurity diffusion of Al in Ni single crystals studied by SIMS, *Phys. Status Solidi (a)* 64 (1981) 187.

5. W. Gust, M. B. Hintz, A. Lodding, and H. Odelius, Measurement of the impurity diffusion of In in Ni single crystals by SIMS, *Phil. Mag. A* 43 (1981) 1205.

6. W. Gust, M. B. Hintz, A. Lodding, H. Odelius, and U. Roll, Application of SIMS for quantitative analysis of grain boundary impurity diffusion, *Mikrochimica Acta*, Suppl. 9 (1981) 307.

7. D. Hallwig, R. Schachtner, and H. G. Sockel, Diffusion of Mg, Si and O in Mg₂SiO₄: Formation of the compound in a solid state, *Proc. 9th Int. Symp. Reactivity of Solids*, K. Dyrek, J. Haber, and J. Nowotny (Eds.) (1981) 166.

8. H. Kotake, Y. Oana, and I. Watanabe, The diffusion barrier effect of a vanadium layer in the formation of nickel silicides, *Thin Solid Films* 75 (1981) 247.

9. A. Lodding, H. Odelius, and U. Sodervall, Applications of SIMS in studies of slow diffusion and isotope diffusion, *Secondary Ion Mass Spectrometry III*, Springer, Berlin (1981) 351.

10. T. J. Magee, C. Leung, H. Kawayoshi, B. K. Furman, and C. A. Evans Jr., Gettering of mobile oxygen and defect stability within back-surface damage regions in silicon, *Appl. Phys. Lett.* 38 (1981) 891.

11. R. Schubert, Secondary ion mass spectrometric analysis of cobalt hardened gold electroplate surfaces, *J. Electrochem. Soc.* 128 (1981) 126.
12. G. J. Scilla and J. J. Wysocki, SIMS study of Al and Cr metallizations on CdSe, *J. Vac. Sci. Technol.* 18 (1981) 37.

1982

1. H. K. Birnbaum, H. Fukushima, and J. Baker, Applications of high resolution SIMS techniques to studies of hydrogen in metals, *Advanced Techniques for Characterizing Hydrogen in Metals*, TMS-AIME (1982) 149.
2. P. Dorner, SIMS investigation of volume diffusion of Al in Ge, *Acta Met.* 30 (1982) 941.
3. P. Dorner, SIMS investigations on the diffusion of In in Ge single crystals, *Z. Metallkd.* 73 (1982) 325.
4. R. C. Frank, J. E. Baker, and C. J. Altstetter, A SIMS study of the diffusion and trapping of deuterium in 302 stainless steel, *Met. Trans. A* 13A (1982) 581.
5. W. Gust, M. B. Hintz, A. Lodding, H. Odelius, and B. Predel, Measurement of the grain boundary diffusion of In in Ni bicrystals by the SIMS technique, *Acta Met.* 30 (1982) 75.
6. Z. A. Iskanderova, L. F. Lifanova, and T. D. Radjabov, Depth distribution of ion implanted Ar in Gd and Sm films, *Vacuum* 32 (1982) 269.
7. M. P. Macht and V. Naundorf, Direct measurement of small diffusion coefficients with SIMS, *J. Appl. Phys.* 53 (1982) 7551.
8. D. P. Valyukhov, M. A. Golubin, D. M. Grebenshchikov, and V. I. Shestopalova, A study of the initial stages of the oxidation of Zr by XPS and SIMS, *Fiz. Tverd. Tela* 24 (1982) 2816.

1983

1. P. Dorner, SIMS analysis of the diffusion of Ge in Si, *DIMETA-82, Diffusion in Metals and Alloys*, Trans. Tech. Publ., Rockport, Mass. (1983) 488.
2. D. M. Gruen, A. R. Krauss, S. Susman, M. Venugopalan, and M. Ron, Gibbsian and radiation induced segregation in Cu-Li and Al-Li alloys, *J. Vac. Sci. Technol. A* 1 (1983) 924.
3. W. Gust, SIMS analysis of the impurity diffusion of In in Cu, *Phil. Mag. A* 47 (1983) 395.
4. W. Gust, A. Lodding, H. Odelius, B. Predel, and U. Roll, Diffusivity of In in Cu along stationary and migrating grain boundaries, *DIMETA-82, Diffusion in Metals and Alloys*, Trans. Tech. Public, Rockport, Mass. (1983) 418.
5. A. F. Henriksen, Y. M. Chiang, W. D. Kingery, and W. T. Petuskey, Enhanced oxygen diffusion at 1400°C in deformed single crystal MgO, *Comm. Am. Ceram. Soc.* 9 (1983) C144.
6. M. Kitajima, M. Fukutomi, and M. Okada, Direct observation of boron diffusion using SIMS for SiC coated molybdenum with a boron underlayer, *Thin Solid Films* 105 (1983) 325.
7. R. Kwor and C. DeAraujo, Multizone modeling of impurity redistribution in ion implanted materials, *J. Electrochem. Soc.* 130 (1983) 1580.
8. A. Lodding and H. Odelius, Applications of SIMS in interdisciplinary materials characterization, *Progress in Materials Analysis*, vol. 1, Springer-Verlag, Vienna, (1983) 21.
9. G. J. Scilla and F. C. Luo, Indium diffusion in cadmium selenide thin-film transistors with indium/gold contacts, *Appl. Phys. Lett.* 42 (1983) 538.
10. U. Sodervall, Isotope effect of Ge diffusion in Si, *DIMETA-82, Diffusion in Metals and Alloys*, Trans. Tech. Publ., Rockport, Mass. (1983) 492.
11. A. S. Wakita, T. W. Sigmon, and J. F. Gibbons, Impurity redistribution studies on laser-formed silicides, *Laser/Solid Interactions and Transient Thermal Processing of Materials*, Elsevier, New York (1983) 721.
12. H. I. Yoo, B. J. Wuensch and W. T. Petuskey, SIMS analysis of oxygen self diffusion in single crystal MgO, *Structure of Property Relationships for MgO and Al₂O₃ Ceramics*, W. D. Kingery (Ed.), Cambridge, Mass. (1983).

1984

1. M. E. Greiner and J. F. Gibbons, Diffusion of silicon in GaAs using rapid thermal processing: Experiment and model, *Appl. Phys. Lett.* 44 (1984) 750.
2. W. T. Petuskey, Diffusion analysis using SIMS, *Nontraditional Methods on Diffusion*, G. E. Murch, H. K. Birnbaum, and J. R. Cost (Eds.), The Metallurgical Society, AIME, Warrendale, Pa. (1984) 179.

Auger Electron Spectroscopy and Scanning Auger Microanalysis

1973

1. M. J. Sparnaay, A. J. VanBommel, and A. VanTooren, Auger electron spectroscopy as a tool for measuring the diffusion of foreign atoms in solids near their surface, *Surf. Sci.* 39 (1973) 251.

1975

1. A. Christou, L. Jarvis, W. H. Weisenberger, and J. K. Hirvonen, Scanning electron

microscopy, Auger spectroscopy and ion backscattering techniques applied to analyses of Au/refractory metallizations, *J. Electron. Mater.* 4 (1975) 329.

1976

1. T. Inoue, S. Horiuchi, H. Iwai, H. Shimizu, and T. Ishida, Microprobe Auger analysis of Si migration in Al metallization for large scale integrated circuits, *Jpn. J. Appl. Phys.* 15 (1976) 63.

1977

1. A. P. Janssen, J. A. Venables, J. C. Hwang, and R. W. Balluffi, Direct observation of grain boundary diffusion by scanning Auger microscopy, *Phil. Mag.* 36 (1977) 1537.

2. H. Shimizu, M. Ono and K. Nakayama, Microprobe Auger analysis of heterogeneous oxidation of alloys and determination of grain boundary diffusion constant, *Third International Conf. on Solid Surfaces*, Vol. 3, Austrian Research Society for Atomic Energy, Vienna (1977) 2359.

1979

1. R. Butz and H. Wagner, Surface diffusion of Pd and Au on W single crystal planes: Spreading behavior of Pd and Au layers, *Surf. Sci.* 87 (1979) 69.

2. M. P. Chearer, C. L. Bauer, and A. G. Jordan, Investigation of interdiffusion in thin film couples of Al and Cu by Auger electron spectroscopy, *Thin Solid Films* 61 (1979) 273.

3. A. Christou, Interdiffusion in Au/refractory thin film systems studied by a combination of scattering techniques, *Scanning Electron Microscopy/1979/I* (1979) 191.

4. L. L. Kazmerski, Grain boundary and interdiffusion studies in compound semiconductor thin films and devices utilizing Auger electron spectroscopy and SIMS, *Thin Solid Films* 57 (1979) 99.

5. J. F. Moulder, D. G. Jean, and W. C. Johnson, Quantitative application of the scanning Auger microprobe to the study of thick film structures, *Thin Solid Films* 64 (1979) 427.

6. J. O. Olowolafe, P. S. Ho, H. J. Hovel, J. E. Lewis, and J. M. Woodall, Contact reactions in Pd/GaAs junctions, *J. Appl. Phys.* 50 (1979) 955.

7. G. J. VanGurp, J. L. Daams, A. VanOostrum, L. J. Augustus, and Y. Tamminga, Aluminum-silicide reactions: I. Diffusion, compound formation and microstructure, *J. Appl. Phys.* 50 (1979) 6915.

1980

1. Y. G. Borodko, The diffusion of aluminum along dislocations in copper, *Fiz. Tverd. Tela* 22 (1980) 3707.

2. R. J. Blattner, An introduction to scanning Auger microscopy and its applications, *Microstructural Science*, vol. 8, Elsevier-North Holland, New York (1980) 63.

3. P. Peutner and H. J. Engau, Electrochemical investigations of the kinetics of formation of the intermetallic phases of the systems FeOZn and Fe-Zn-Si, *Arch. Eisenhüttenwes* 51 (1980) 463.

4. M. R. Pinnel and J. E. Bennett, Observations on interdiffusion in planar Cu/Sn-Ni/Au tricouples, *Met. Trans. A* 11A (1980) 587.

5. H. Saito and Y. Ishida, The effect of boundary structure on the diffusion of Sn and Cr along the grain boundaries of pure Fe, *J. Jpn. Inst. Met.* 44 (1980) 215.

6. H. Shimizu, N. Koyama, and Y. Ishida, Depletion of Cu from the grain boundary region of Cu-Ni alloys during sputtering at elevated temperatures, *Jpn. J. Appl. Phys.* 19 (1980) L671.

1981

1. G. C. Allen and R. K. Wild, Probing the secrets of solid surfaces, *CECB Res.* 11 (1981) 12.

2. T. E. Brady and C. T. Hovland, Scanning Auger microprobe study of Au/Ni/Cu diffusion in thin films, *J. Vac. Sci. Technol.* 18 (1981) 339.

3. G. N. Burland and P. J. Dobson, Pseudomorphic behavior and interdiffusion between palladium films and silver and gold, *Thin Solid Films* 75 (1981) 383.

4. R. Chopra, M. Ohring, and R. S. Oswald, Observations of a marker shift in a Cu/Sn thin film diffusion couple by Auger electron spectroscopy methods, *Thin Solid Films* 86 (1981) 43.

5. K. J. Holub and L. J. Matienzo, Magnesium diffusion in several aluminum alloys, *Appl. Surf. Sci.* 9 (1981) 22.

6. W. Losch and J. Kirschner, Surface segregation kinetics in Cu/Au alloys, *Solid Surfaces*, Société Française du Vide, Paris (1981) 19.

7. G. Luckman, R. A. Didio, and W. R. Graham, Phosphorus interdiffusivity in alpha-binary and alloy systems, *Met. Trans. A* 12A (1981) 253.

8. L. Rivaud, I. D. Ward, A. H. Eltoukhy, and J. E. Greene, Enhanced diffusion and precipitation in Cu/In alloys due to low energy ion bombardment, *Surf. Sci.* 102 (1981) 610.

9. H. Shimizu, N. Koyama, and Y. Ishida, The sputter-induced solute segregation in the surface layer of Cu-Ni alloys during argon ion bombardment at elevated temperatures, *J. Jpn. Inst. Met.* 45 (1981) 768.

10. P. R. Webber, C. E. Rojas, P. J. Dobson, and D. Chadwick, A combined XPS/AES study of Cu segregation to the high and low index surfaces of a Cu/Ni alloy, *Surf. Sci.* 105 (1981) 20.
11. A. K. Zurek and H. L. Marcus, Studies of the deuterium transport mechanism during fatigue of aluminum alloys, *Hydrogen Effects in Metals*, TMS/AIME (1981) 57.

1982

1. C. Canali, G. Celotti, F. Fantini, and E. Zanoni, Interdiffusion and compound formation in the Si/PtSi/(Ti-W)/Al system, *Thin Solid Films* 88 (1982) 9.
2. M. B. Chamberlain, Diffusion of Cu in thin TiN films, *Thin Solid Films* 91 (1982) 155.
3. R. Chopra, M. Ohring, and R. S. Oswald, Low temperature compound formation in Cu/Sn thin film couples, *Thin Solid Films* 94 (1982) 279.
4. M. Eizenberg and R. Brenner, Contact reaction of silicon and thin films of Ir-V alloys, *Thin Solid Films* 89 (1982) 355.
5. J. Massies, P. Delescluse, P. Etienne, and N. T. Linh, The growth of silver on GaAs(001): Epitaxial relationships, modes of growth and interfacial diffusion, *Thin Solid Films* 90 (1982) 113.
6. H. Shimizu, M. Ono, N. Koyama, and Y. Ishida, Sputter enhanced diffusion phenomena in Cu/Ni alloys at elevated temperatures, *J. Appl. Phys.* 53 (1982) 3044.

1983

1. A. Appelbaum, M. Eizenberg, and R. Brenner, Solid state reactions of Ta-W thin films and Si single crystals, *Vacuum* (1983) 227.
2. D. M. Gruen, A. R. Krauss, S. Susman, M. Uenugopalan, and M. Ron, Gibbsian and radiation induced segregation in Cu-Li and Al-Li alloys, *J. Vac. Sci. Technol. A* 1 (1983) 924.
3. S. Nakahara, J. A. Abys and S. M. Abys, Room temperature diffusion induced grain boundary migration in the fine grained palladium side of Cu-Pd diffusion couples, *Mater. Lett.* 2 (1983) 155.
4. R. A. Outlaw and D. T. Peterson, The diffusivity of hydrogen in Nb stabilized stainless steel, *Met. Trans. A* 14A (1983) 1869.

1984

1. O. Aina and K. P. Pande, Schottky contact barrier height modification by ion implantation of Al into GaAs, *J. Appl. Phys.* 56 (1984) 1717.
2. A. Appelbaum and M. Eizenberg, Silicides formation for refractory metal alloys (Ta-V and Ti-V) on silicon, *J. Appl. Phys.* 56 (1984) 2341.
3. J. C. Bierlein, S. W. Gaarenstroom, R. A. Waldo, and A. C. Ottolini, Characterization of multilayer diffusion barriers by electron probe microanalysis and Auger electron spectroscopy, *J. Vac. Sci. Technol. A* 2 (1984) 1102.

Rutherford Backscattering

1959

1. R. F. Sippel, Diffusion measurements in the system Cu-Au by elastic scattering, *Phys. Rev.* 115 (1959) 1441.

1970

1. G. M. Hood, The diffusion of iron in aluminum, *Phil. Mag.* 21 (1970) 305.

1971

1. G. M. Hood and R. J. Schultz, The diffusion of Mn in Al, *Phil. Mag.* 23 (1971) 1479.
2. G. M. Hood and R. J. Schultz, In diffusion in Al, *Phys. Rev. B* 4 (1971) 2339.

1972

1. D. Treheux, D. Marchive, J. Delagrange, and P. Guiraldeng, Determination of the diffusion coefficients for dilute Sn in alpha-Fe, *C. R. Acad. Sci.* 274 (1972) 1260.

1974

1. S. M. Myers, S. T. Picraux, and T. S. Prevender, Study of Cu diffusion in Be using ion backscattering, *Phys. Rev. B* 9 (1974) 3953.

1975

1. A. Christou, L. Jarvis, W. H. Weisenberger, and J. K. Hirvonen, Scanning electron microscopy, Auger spectroscopy and ion backscattering techniques applied to analysis of Au-refractory metallizations, *J. Electron. Mat.* 4 (1975) 329.

1976

1. S. M. Myers, D. E. Amos, and D. K. Brice, Modeling and enhanced diffusion under ion irradiation, *J. Appl. Phys.* 47 (1976) 1812.

1977

1. G. Hettich, H. Mehrer, and K. Maier, Self diffusion in ferromagnetic alpha-iron, *Scripta Met.* 11 (1977) 795.

1978

1. S. U. Campisano, E. Costanzo, F. Scaccianoce, and R. Cristofolini, Growth kinetics of the phase in Al-Cu thin film bilayers, *Thin Solid Films* 52 (1978) 97.
2. W. K. Chu, J. W. Mayer, and M. A. Nicolet, *Backscattering Spectrometry*, Academic Press, New York, (1978).
3. S. M. Myers and H. J. Rack, Ion beam investigation of Sb diffusion and solubility in Fe, *J. Appl. Phys.* 49 (1978) 3246.
4. *Thin Films: Interdiffusion and Reactions*, J. M. Poate, K. N. Tu, and J. W. Mayers (Eds.), John Wiley and Sons, New York (1978) (no author given).

1979

1. A. Christou, Interdiffusion in gold/refractory thin film systems studied by a combination of scattering techniques, *Scanning Electron Microscopy/1979/I* (1979) 191.
2. B. L. Doyle and P. S. Peercy, Technique for profiling II with a 2.5 MeV Van de Graaff accelerator, *Appl. Phys. Lett.* 34 (1979) 811.
3. S. Matteson, J. Roth, and M. R. Nicolet, Ion induced silicide formation in Nb thin films, *Radiat. Eff.* 42 (1979) 217.
4. J. O. Olowolafe, P. S. Ho, H. J. Hovel, J. E. Lewis, and J. M. Woodall, Contact reactions in Pd/GaAs junctions, *J. Appl. Phys.* 50 (1979) 955.
5. G. J. VanGurp, J. L. Daams, A. VanOostrom, L. J. Augustus, and Y. Tamminga, Aluminum silicide reactions: I. Diffusion, compound formation and microstructure, *J. Appl. Phys.* 50 (1979) 6915.

1980

1. S. D. Mukherjee, C. J. Palmstrom, and J. G. Smith, The thermal stability of thin layer transition and refractory metallizations on GaAs, *J. Vac. Sci. Technol.* 17 (1980) 904.
2. Y. I. Nissim, J. F. Gibbons, C. A. Evans Jr., V. R. Deline, and J. C. Norberg, Thermal diffusion of Sn in GaAs from a spin on SnO₂/SiO₂ source, *Appl. Phys. Lett.* 37 (1980) 89.
3. J. M. Vandenberg and E. Kinsbron, Interface reaction of Au films with n-type (GaO)₇(AlO)₃As and GaAs, *Thin Solid Films* 65 (1980) 259.
4. G. J. VanGurp, J. W. Slotboom, F. J. Smolders, W. T. Stacy, and Y. Tamminga, Enhanced diffusion on implanted As and B in Si by low temperature heat treatment, *J. Electrochem. Soc.* 127 (1980) 1813.

1981

1. G. W. Ashwell and R. Heckingbottom, Interdiffusion of Ti and Au: A comparison of thin films deposited in technical vacuum and ultrahigh vacuum, *J. Electrochem. Soc.* 128 (1981) 649.
2. C. Chang, A. Segmuller, L. L. Chang, and L. Esaki, Ge/GaAs superlattices by molecular beam epitaxy, *Appl. Phys. Lett.* 38 (1981) 912.
3. J. M. Mackowski, M. Bendali, P. Normandon, and P. Kumurdjian, Diffusion kinetics in Au/amorphous GeTe₄ thin films, *J. Phys. (Orsay)* 42 (suppl. C4) (1981) 975.
4. I. Suni, M. A. Nicolet, and M. Maenpaa, Interdiffusion of thin bilayers of Cu and Ni, *Thin Solid Films* 79 (1981) 69.

1982

1. M. B. Chamberlain, Diffusion of Cu in thin TiN films, *Thin Solid Films* 91 (1982) 155.
2. B. Ilugsted, L. Buene, T. Finstad, O. Lonsjo, and T. Olsen, Interdiffusion and phase formation in Au/Sn thin film couples with special emphasis on substrate temperature during condensation, *Thin Solid Films* 98 (1982) 81.
3. K. N. Tu and R. D. Thompson, Kinetics of interfacial reaction in bimetallic Cu/Sn thin films, *Acta Metall.* 30 (1982) 947.

1983

1. H. T. Hentzell, R. D. Thompson, and K. N. Tu, Interdiffusion in Cu/Al thin film bilayers: I. Structure and kinetics of sequential compound formation, *J. Appl. Phys.* 54 (1983) 6923.
2. A. S. Wakita, T. W. Sigmon, and J. F. Gibbons, Impurity redistribution studies on laser formed silicides, *Laser/Solid Interactions and Transient Thermal Processing of Materials*, Elsevier, New York (1983) 721.

1984

1. T. Chu, S. U. Campisano, S. Cannavo, and E. Rimini, Phase formation in Au-Al and Cu-Al thin film systems under ion beam bombardment, *J. Appl. Phys.* 55 (1984) 3322.

2. R. A. Hamm and J. M. Vandenberg, A study of the initial growth kinetics of the Cu-Al thin film interface reaction by in situ x-ray diffraction and Rutherford backscattering analysis, *J. Appl. Phys.* 56 (1984) 293.
3. G. Majni, M. Costat, and F. D. Valle, On the growth kinetics and structure of the NiSi compound on Si single crystals, *Nuovo Cimento D* 40 (1984) 27.
4. S. M. Myers, Ion beam analysis and ion implantation in the study of diffusion, *Nontraditional Methods in Diffusion*, G. E. Murch, H. K. Birnbaum, and J. R. Cost (Eds.), The Metallurgical Society, AIME, Warrendale, Pa. (1984) 137.
5. J. Narayan, C. W. White, O. W. Holland, and M. J. Aziz, Phase transformation and impurity redistribution during pulsed laser irradiation of amorphous silicon layers, *J. Appl. Phys.* 56 (1984) 1821.
6. M. A. Shahid, P. J. Topham, B. J. Sealy, and K. E. Putick, Laser alloyed Sn layers on GaAs, *J. Mater. Sci.* 19 (1984) 2361.

Specialized X-ray Diffraction Techniques

1967

1. J. B. Dinklage, X-ray diffraction by multilayered thin film structures and their diffusion, *J. Appl. Phys.* 38 (1967) 3781.
2. H. Herman (Ed), Experimental methods of materials research, vol. 1, *Advances in Materials Research*, Interscience Publishers, John Wiley and Sons, New York (1967).

1968

1. J. Burgeat and D. Taupin, Application of the dynamical theory of x-ray diffraction to the diffusion of B and P in Si single crystals, *Acta Crystallogr.* 23 (1968) 99.
2. R. Fogelson, Method of determining diffusion coefficients by x-ray diffraction, *Fiz. Metall. Metalloved.* 25 (1968) 492.
3. R. Fogelson, Method of determining the diffusion constant from x-ray diffraction analyses, *Phys. Metals. Metallogr.* 25 (1968) 116.

1970

1. C. R. Houska, X-ray diffraction from a binary diffusion zone, *J. Appl. Phys.* 41 (1970) 69.
2. M. M. Naumova and S. V. Semenovskaya, Determination of the activation energy of diffusion by diffuse x-ray scattering, *Fizika Tverdogo Tela* 12 (1970) 3632.
3. M. M. Naumova, S. V. Semenovskaya, and Y. S. Umansky, Investigation of elementary diffusion events by diffuse scattering of x-rays, *Sov. Phys. Solid State* 12 (1970) 764.
4. D. R. Tenney, J. A. Carpenter, and C. R. Houska, X-ray diffraction technique for the investigation of small diffusion zones, *J. Appl. Phys.* 41 (1970) 4485.

1971

1. J. A. Carpenter, D. R. Tenney, and C. R. Houska, Method for determining composition profiles and diffusion generated substructure in small diffusion zones, *J. Appl. Phys.* 42 (1971) 4305.
2. R. L. Fogelson, Y. A. Ugai, A. V. Pokoev, and I. A. Akimova, X-ray diffraction investigation of bulk diffusion in polycrystalline materials, *Sov. Phys. Solid State* 13 (1971) 856.
3. C. A. Mackay, X-ray diffraction determination of the surface concentration of Sn diffused into steel, *J. Appl. Crystallography* 4 (1971) 77.
4. M. M. Naumova and S. V. Semenovskaya, Determination of the activation energy of diffusion by x-ray diffuse scattering, *Sov. Phys. Solid State* 12 (1971) 2954.

1972

1. C. R. Houska, Nondestructive atomic diffusion studies using x-ray diffraction: Experimental considerations, *High Temp. High Pressures* 4 (1972) 417.
2. S. S. Lau and R. C. Sun, Internal stress and interdiffusion of Ti-Pd-Au films studied by X-ray diffraction techniques, *Thin Solid Films* 10 (1972) 273.
3. K. N. Tu and B. S. Berry, X-ray study of interdiffusion in bimetallic Cu-Au film, *J. Appl. Phys.* 43 (1972) 3283.
4. H. Zuchner, X-ray measurements of lattice expansion as a method for determining diffusion coefficients of H in Ta, *Z. Physikal. Chem.* 82 (1972) 240.

1973

1. J. Unnam, J. A. Carpenter and C. R. Houska, X-ray diffraction approach to grain boundary and volume diffusion. *J. Appl. Phys.* 44 (1973) 1957.

1974

1. D. R. Tenney and P. K. Talty, X-ray diffraction investigation of bimetallic diffusion zones in the Cu-Pd systems, *Met. Trans.* 5 (1974) 241.

1975

1. C. R. Houska, X-ray examination of diffused films, *Thin Solid Films* 25 (1975) 451.

1976

1. Y. M. Kulish, D. G. Sherman, and Y. S. Tibabsheva, Determining diffusion coefficients by the x-ray method, *Fiz. Met. Metalloved.* 41 (1976) 1261.
2. Y. M. Kulish, D. G. Sherman, and Y. S. Tibabsheva, Determination of diffusion coefficients by the x-ray method, *Phys. Met. Metallogr.* 41 (1976) 118.
3. M. Murakami and D. deFontaine, X-ray diffraction study of interdiffusion in bimetallic Ag/Cu thin films, *J. Appl. Phys.* 47 (1976) 2857.
4. M. Murakami, D. deFontaine, and J. Fodor, X-ray diffraction study of interdiffusion in bimetallic Au/Pd thin films, *J. Appl. Phys.* 47 (1976) 2850.
5. J. Unnam and C. R. Houska, X-ray study of diffusion in the Cu/Ag system, *J. Appl. Phys.* 47 (1976) 4336.
6. A. Wagendristel, D. Wolf, and H. Bangert, Evaluation of diffusion parameters in thin film diffusion couples by means of Kiessig x-ray interference, *Thin Solid Films* 32 (1976) 307.

1977

1. H. Chen and J. B. Cohen, A comparison of experiment and the theory of continuous ordering, *J. de Physique* 38 (1977) (suppl. C-7) C-7/314.
2. W. M. Paulson and J. E. Hilliard, Interdiffusion in composition modulated Cu-Au thin films, *J. Appl. Phys.* 48 (1977) 2117.

1978

1. R. W. Bicknell, Interpretation of x-ray diffraction data from thin epitaxial Pb-SnTe crystals (Pt 2), *Infrared Phys.* 18 (1978) 133.
2. S. U. Campisano, E. Costanzo, F. Scaccianoce, and R. Cristofolini, Growth kinetics of the Al_2Cu phase in Al-Cu thin film bilayers, *Thin Solid Films* 52 (1978) 97.
3. R. Delhez and E. J. Mittemeijer, On the analysis of x-ray diffraction line profiles from small epitaxial binary diffusion couples: Determination of concentration profile and influence of thermal diffuse scattering, *J. Appl. Phys.* 49 (1978) 4770.
4. R. Delhez and E. J. Mittemeijer, The determination by x-ray diffraction of the concentration profile in a thin epitaxial binary diffusion couple, *Acta Crystallogr. A* 34 (1978) 5376.
5. R. Delhez, E. J. Mittemeijer, and E. A. vandenBergen, X-ray diffraction line profile analysis of diffusional homogenization in powder blends, *J. Mater. Sci.* 13 (1978) 1671.
6. C. R. Houska, Broadening of x-ray diffraction lines from small subgrains containing gradients of spacing, *J. Appl. Phys.* 49 (1978) 2991.
7. K. N. Tu and J. W. Mayer, Silicide formation, in *Thin Films--Interdiffusion and Reactions*, J. M. Poate, K. N. Tu and J. W. Mayer (Eds.), John Wiley, New York (1978) 359.

1979

1. L. G. Chow, S. K. Decker, D. J. Pocker, G. C. Pendley, and J. Papadopoulos, Interdiffusion in titanium permalloy thin films, *IEEE Trans. Magn.* 15 (1979) 1833.
2. A. H. Eltoukhy and J. E. Greene, Compositionally modulated sputtered InSb/GaSb superlattices: Crystal growth and interlayer diffusion, *J. Appl. Phys.* 50 (1979) 505.
3. V. Holy and J. Kubena, X-ray rocking curves on inhomogeneous surface layers on silicon single crystals: I. Diffusion layers, *Czech. J. Phys.* B29 (1979) 1161.
4. G. P. Martynova, G. A. Obukhova, and A. V. Pokoev, An x-ray study of diffusion in single crystals, *Fiz. Strukt. Svoistv. Tverd.* 3 (1979) 29.
5. M. Murakami and K. N. Tu, Diffusion in thin metal films studied by x-ray diffraction techniques, *Bull. Jpn. Inst. Met.* 18 (1979) 262.
6. J. O. Olowolafe, P. S. Ho, H. J. Hovel, J. E. Lewis, and J. M. Woodall, Contact reactions in Pd/GaAs junctions, *J. Appl. Phys.* 50 (1979) 955.
7. A. E. Pontau and D. Lazarus, Diffusion of Ti and Nb in BCC Ti-Nb alloys, *Phys. Rev. B. Cond. Matter.* 19 (1979) 4027.
8. A. Wagendristel, H. Bangert, and W. Tonser, Diffusional alloying in polycrystalline Ag-Al thin film couples studied by means of Kiessig x-ray interference, *Surf. Sci.* 86 (1979) 68.

1980

1. R. I. Barabash, X-ray scattering by polycrystals with multiphase diffusion layers, *Dop. Akad. Nauk Ukr. RSR CAJ* 7 (1980) 84.
2. R. M. Fleming, D. B. McWhan, A. C. Gossard, W. Wiegmann, and R. A. Logan, X-ray diffraction study of interdiffusion and growth in $(\text{GaAs})_n(\text{AlAs})_m$ multilayers, *J. Appl. Phys.* 51 (1980) 357.
3. C. Gloede, H. Muller, N. Kaiser, and M. Trapp, Influence of $\text{Bi}_{1-x}\text{Sb}_x$ and Sb overlayers on the annealing behavior of Ag films, *Kristall. Tech.* 15 (1980) 965.
4. C. R. Houska, The investigation of composition variations by diffraction, *Treatise on*

Materials Science, H. Herman (Ed), vol. 19, Pt. A, Academic Press, New York (1980) 63.

5. A. Olsen and F. R. Sale, Growth kinetics, morphologies and structures of vapor deposited nickel silicide layers, *Met. Technol.* 7 (1980) 494.

6. M. P. Rosenblum, F. Spaepen and D. Turnbull, Diffusion and structural relaxation in compositionally modulated amorphous metal films, *Appl. Phys. Lett.* 37 (1980) 184.

7. A. Wagendristel, H. Schurz, E. Ehrmann-Falkenau, and H. Bangert, An x-ray optical study of layered phase growth in Au/Al thin film couples, *J. Appl. Phys.* 51 (1980) 4808.

1981

1. C. Chang, A. Segmuller, L. L. Chang, and L. Esaki, Ge-GaAs superlattices by molecular beam epitaxy, *Appl. Phys. Lett.* 38 (1981) 912.

2. W. H. Gries and F. T. Wybenga, Determination of the centroid depths of shallow impurity profiles by x-ray fluorescence spectrometry, *Surf. Interface Anal.* 3 (1981) 251.

3. S. Kanamori, A study on the penetration of platinum into silicon in Ti/Pt/Au beam lead metallization systems, *Thin Solid Films* 75 (1981) 19.

4. H. Kotake, Y. Oana, and I. Watanabe, The diffusion barrier effect of a vanadium layer in the formation of nickel silicides, *Thin Solid Films* 75 (1981) 247.

5. M. Marcus, Siting and dynamics of Cu impurity in Ti lattice, *Solid State Commun.* 38 (1981) 251.

6. M. Murakami, Interdiffusion in bilayered Pb/In thin films studied by x-ray diffraction, *Trans. Jpan Inst. Met.* 22 (1981) 567.

7. I. Suni, M. A. Nicolet, and M. Maenpaa, Interdiffusion of thin bilayers of Cu and Ni, *Thin Solid Films* 79 (1981) 69.

8. T. Tsakalakos, Composition modulated films: New materials for studying stability and critical phenomena in solid solutions, *Thin Solid Films* 86 (1981) 79.

9. J. Unnam, D. R. Tenney, and C. R. Houska, An x-ray study of diffusion in the Cu-Au system, *Met. Trans. A* 12A (1981) 1147.

10. M. I. Zakharova and A. A. Aminov, Structural transformations during the decomposition of the beta solid solution in alloys of Zr with Mo, Al, Nb, V and Ta, *Fiz. Met. Metalloved.* 51 (1981) 333.

1982

1. C. Canali, G. Celotti, F. Fantini, and E. Zanoni, Interdiffusion and compound formation in the Si/PtSi/(Ti-W)/Al system, *Thin Solid Films* 88 (1982) 9.

2. M. Cramak, Determination of the phase composition and the thickness of thin layers by x-ray quantitative phase analysis, *Kovove Mater.* 20 (1982) 111.

3. M. Eizenberg and B. Brener, Contact reaction of Si and thin films of Ir-V alloys, *Thin Solid Films* 89 (1982) 355.

4. R. L. Fogelson, An x-ray study of the concentration dependence of the diffusion coefficient, *Fiz. Met. Metalloved.* 53 (1982) 796.

5. K. N. Tu, Single intermetallic compound formation in Pd-Pb and Pd-Sn thin film couples studied by x-ray diffraction, *Mater. Lett.* 1 (1982) 6.

6. K. N. Tu, Thermal stability of Pd₂Si and PdSi in thin film and bulk diffusion couples, *J. Appl. Phys.* 53 (1982) 428.

7. K. N. Tu and R. D. Thompson, Kinetics of interfacial reaction in bimetallic Cu-Sn thin films, *Acta Met.* 30 (1982) 947.

8. J. M. Vandenberg, F. J. den Broeder, and R. A. Hamm, Formation of intermetallics and grain boundary diffusion in Cu-Al and Au-Al thin film couples, *Thin Solid Films* 93 (1982) 277.

1983

1. I. A. Akimova, V. M. Mironov, and A. V. Pokoev, The diffusion of Al in Fe, *Fiz. Met. Metalloved.* 56 (1983) 1225.

2. A. Appelbaum, M. Eizenberg, and R. Brener, Solid state reactions of Ta-W thin films and Si single crystals, *Vacuum* 33 (1983) 227.

3. H. T. Hentzell, R. D. Thompson and K. N. Tu, Interdiffusion in Cu-Al thin film bilayers: I. Structure and kinetics of sequential compound formation, *J. Appl. Phys.* 54 (1983) 6923.

4. V. B. Rao and C. R. Houska, Reactions and diffusion between an Al film and a Ti substrate, *Met. Trans. A* 14A (1983) 61.

1984

1. A. Appelbaum and M. Eizenberg, Silicides formation for refractory metal alloys (Ta-V and Ti-V) on silicon, *J. Appl. Phys.* 56 (1984) 2341.

2. T. Chu, S. U. Campisano, S. Cannavo, and E. Rimini, Phase formation in Au-Al and Cu-Al thin films under ion beam bombardment, *J. Appl. Phys.* 55 (1984) 3322.

3. T. Claeson, J. B. Boyce, W. P. Lowe, and T. H. Geballe, NbZr multilayers: II. Extended x-ray absorption fine structure study, *Phys. Rev. B Condens. Matter.* 29 (1984) 4969.

4. R. A. Hamm and J. M. Vandenberg, A study of the initial growth kinetics of the Cu-Al

thin film interface reaction by in situ x-ray diffraction and Rutherford backscattering analysis, *J. Appl. Phys.* 56 (1984) 293.

5. G. E. Henein and J. E. Hilliard, Interdiffusivities in Ag-Pd compositionally modulated foils, *J. Appl. Phys.* 55 (1984) 2895.

6. S. Mantovani, F. Nava, C. Nobili, G. Queirolo, and G. Celotti, Pt/Ni bilayers on n-type silicon: Metallurgical and electrical behavior, *J. Appl. Phys.* 55 (1984) 899.

7. Y. Oya, S. Ochiai, T. Shinoda, and T. Suzuki, Continuous solid solution in the pseudo quaternary Ni/AlNi₃/GaNi₃/GeNi₃/Si system, *Z. Metallkd.* 75 (1984) 53.

8. T. Tsakalakos and J. E. Hilliard, Effect of long-range interaction on diffusion in Cu-Ni compositionally modulated alloys, *J. Appl. Phys.* 55 (1984) 2885.

9. V. V. Vasekin, V. I. Gryzunov, M. V. Raevskaya, N. N. Golikova, and E. M. Sokolovskaya, Mutual diffusion in the Pt-Ru-Rh system, *Vestn. Mosk. Univ. Khim.* 25 (1984) 272.

Author Index

- Abe, 85
 Adar, 19,41,53
 Albee, 255
 Alvarez, 65,71
 Andersen, M. E., 33,75
 Anderson, F. W., 325
 Armstrong, 273
 Ayer, 357

 Barbillat, 15
 Barbour, 68
 Bastin, 1
 Baughman, 137
 Bell, 151
 Benjamin, 235,285
 Bernius, 123
 Bohning, 197
 Brenna, 123
 Bright, 101,155,159,163
 Brown, 97
 Brownlee, 269
 Bruja, 119
 Butler, 49

 Calvo, 199
 Campbell, 53
 Carr, 189
 Chandra, 125
 Chiovetti, 125
 Church, 253
 Cieslak, 179
 Clark, 287
 Conner, 235,285
 Crow, 209
 Cvikevich, 85

 Da Silva, 15
 Davis, 193
 Deason, 65
 Delhaye, 15
 Delly, 33
 Dennemont, 305
 DeNoyer, 7
 Dhamelin-court, 15
 Diem, 19
 Dingle, 315
 Dodd, 7
 Doyle, 68,71
 Duffy, 235,285
 Dunn, 60

 Etz, 60
 Fauchet, 53
 Fine, 241
 Fiori, 219
 Fisanick, 29
 Fletcher, 319
 Follstaedt, 173
 Friel, 167

 Goldstein, 259,361
 Gómez de Salazar, 199
 Gordon, 227
 Gorlen, 219
 Grasseli, 68
 Grayzel, 19
 Grice, 60
 Griffiths, 315
 Grossman, 266
 Guilemany, 199

 Hagen, 331
 Hagler, 119
 Hanson, 227
 Hare, 133
 Harris, 310
 Harvey, 49
 Hazle, 68
 Headley, 79,189
 Heidersbach, 57
 Heijligers, 2
 Heinen, 325
 Heinrich, 79
 Hellman, 189
 Helmold, 107
 Heyman, 122
 Hollander, 285
 Humphreys, 367
 Hutcheon, 273
 Hutt, 19

 Ingram, F. D., 109
 Ingram, M. J., 109

 Jones, J. H., 285
 Jones, K. W., 227
 Joy, 342

 Klein, 357
 Kohler, 310
 Kuptsis, 85

 Landry, 305
 Laskowski, 193
 Le Clercq, 19
 Leapman, 219
 Lee, 153
 Leusmann, 331
 Levi-Setti, 209
 Lewis, 287
 Linton, 337
 Livi, 241
 Long, 349
 Love, 82,93

 McCarthy, 153
 McGuire, 253
 McKay, 291
 Mackinnon, 291
 McMillan, 137
 Maggiore, 235,285

 Marinenko, 101,159
 Mauney, 299
 Mehicic, 68
 Mendenhall, 241
 Moore, 287
 Morrison, 125,123
 Mugli, 75
 Mullock, 310
 Murata, 85
 Musselman, 337
 Myers, 129
 Myklebust, 101,151,159

 Nagahara, 282
 Newbury, 60,101,159,204
 Nielsen, 145
 Noether, 41
 Notis, 170,361

 Odom, 322
 Ono, 145

 Packwood, 97
 Pasteris, 25
 Pichoir, 104
 Pounds, 227
 Pouchou, 104
 Purcell, 57

 Radicatti di Brozolo, 322
 Raghavan Ayer, 357
 Ramsey, 325
 Reitmeijer, 291
 Reuter, 259
 Rivers, 227
 Roeder, 170
 Rogers, 235,285
 Romig, 173,179,361
 Roussel, 15
 Russ, J. C., 133,141
 Russ, J. Ch., 141

 Sastri, 97
 Sauberman, 122
 Schamber, 137
 Schidlovsky, 227
 Schmidt, 331
 Scott, 82,93
 Seitz, 25
 Seo, 145
 Sewell, 82
 Short, 107
 Simons, 319,337
 Sorsenson, 189
 Southon, 310
 Spence, 349
 Statham, 230,354
 Steel, 151,155,163
 Stewart, 141
 Stolper, 241

Tagata, 145
Tesmer, 235
Titchmarsh, 349
Tombrello, 241
Tormey, 113,116

Vale, 148
Vander Wood, 75

Wallach, 310
Walker, 153
Walsh, 113
Wang, 209
Warner, 129
Was, 246
Wheeler-Clark, 116
Williams, 259,357
Wood, 354
Wopenka, 25
Zolensky, 291

NOTES

NOTES